AN INVESTIGATION OF ONGOING DISPLACEMENTS OF ACTIVE FAULTS IN THE GOBI DESERT USING PERSISTENT SCATTERER INTERFEROMETRIC SYNTHETIC APERTURE RADAR TECHNIQUE TO SUPPORT THE PERMANENT DISPOSAL OF HIGH-LEVEL WASTE IN BEISHAN, CHINA

A thesis submitted to Imperial College London in partial fulfillment of the requirements for the degree of Doctor of Philosophy

Zixiao Wang (CID: 00811233)

February 2023

Department of Civil and Environmental Engineering

Imperial College London

South Kensington Campus, London SW7 2AZ, UK

Abstract

This research demonstrated the application of PSInSAR method in identifying and characterising the micro-displacements along active faults in Beishan to support the selection of GDF host rock. This research first distinguishes and separates the tectonic induced and non-tectonic induced deformation within three study areas at Suanjingzi, Jiujing and Xinchang. Through the application of coherence change detection, it found the granite outcrop areas characterised by high coherence provide more robust results of tectonic activity. The Quaternary sediments covered areas which are characterised by low coherence usually show higher deformation rates due to the impacts of erosion and deposition. The tectonic induced displacements generally range from -0.4 to 0.4 mma^{-1} and are dominated by fault bound tectonic movements.

As a part of wrench faut zone, Beishan is impacted by a NE-SW trended maximum in situ compressive stress field (σ1). To correlate the visible valleys, gullies, or cracks in Google Earth imagery with the SAR image deformation discontinuities, this study mapped and characterised more than 40 active faults in the three study areas, these include (1) the NE-SW trended sinistral strike-slip faults triggered by extension and (2) the NW-SE/W-E trended reverse faults triggered by maximum compression. The fault activity is characterised by subtle (minor) displacement rate value difference between the two sides of the fault plane.

This research successfully improved the understanding of local structural geology and provided moderate guidance for the selection of HLW disposal sites in China. It was indicated that Xinchang has the highest tectonic stability, and this is then followed by Jiujing and Suanjingzi. This kind of displacement rate difference is possible due to the angle difference towards the Sanweishan Fault Zone. To trace and characterise the undiscovered active fault planes, the PSInSAR approach also benefits the prediction of earthquake by improving the positioning of the potential epicentres.

Key words

Interferometric Synthetic Aperture Radar (InSAR), Persistent Scatterer (PS), micro-displacement, active fault, strike-slip, deformation, Line of Sight (LoS) distance, time series analysis, granite outcrop, maximum compression, extension, Gobi Desert, precipitation, Beishan, Quaternary Sediments, erosion, deposition, geomorphological processes, coherence, Geological Disposal Facility (GDF), High-level waste (HLW), China, SARScape

Declaration of Originality

This is to certify that the content of this thesis is my own work except where work by others has been properly referenced.

Zixiao Wang

30/Jan/2023

Copyright Declaration

The copyright of this thesis rests with the author. Unless otherwise indicated, its contents are licensed under a Creative Commons Attribution-Non-Commercial 4.0 International Licence (CC BY-NC). Under this licence, you may copy and redistribute the material in any medium or format. You may also create and distribute modified versions of the work. This is on the condition that: you credit the author and do not use it, or any derivative works, for a commercial purpose. When reusing or sharing this work, ensure you make the licence terms clear to others by naming the licence and linking to the licence text. Where a work has been adapted, you should indicate that the work has been changed and describe those changes. Please seek permission from the copyright holder for uses of this work that are not included in this licence or permitted under UK Copyright Law.'

Acknowledgement

Completing a PhD has never been an easy job. First, I want to take this opportunity to thank my parents. It is under their financial sponsor I have the chance to finish 8 years' study in London both in undergraduate and PhD levels. I hope they keep healthy and happy.

This PhD project is completed under the inspirational supervision of Dr. James Lawrence, Prof. Richard Ghail and Dr. Philippa Mason. Dr. James Lawrence led the supervision and provided precious guidance on research project design and progression. Prof Richard Ghail and Dr. Philippa Mason provided very professional guidance on InSAR technique and Sentinel-1 data analysis. Obviously, this project could not have been completed without their support. I would also like to thank my colleagues Anthony Carpenter and Stewart Agar. The guidance they provided on satellite data reprocessing using SARScape and ICSAR software significantly improved the efficiency of data analysis.

The submission of this thesis marks the end of my eight years' student life at Imperial College. I believe this period will become one of the most memorable and fulfilling times in my life. My achievements have been far more than academic. I appreciate the support from my peers especially when elected to be the President of Graduate Students' Union in 2020. This provided me opportunity to represent the Postgraduate community. I am proud of my campaign to pursue a better student experience for all at Imperial and to minimize the impact of COVID and lockdown which affected all researchers.

List of Figures

Figure 1.1 Location of Beishan area in Gansu Province, northwest China……15
Figure 1.2 The monthly rainfall in Beishan from September 2017 to April 2020. 16
Figure 1.3 The location of the Beishan Region (A, B, and C)..... 17
Figure 1.4 The seismic distribution around Beishan (A, B, and C) 17
Figure 2.1 The illustration of Beishan area and the regional structure geology. 25
Figure 2.2 The geological map of Jiujing study area 32
Figure 2.3 The geological map of Xinchang study area 37
Figure 2.4 The geological map of Suanjingzi study area 41
Figure 3.1 The map of descending LoS deformation rates in Morelia between 2003 and 2010 from Cigna (2012) [97])..... 66
Figure 3.2 An illustrative example shows the correlation between variations in groundwater level and time-series analyses in Nevada..... 67
Figure 4.1 The schematic figure illustrates how phase difference is observed by comparing two SAR images to infer line of sight (LoS) distance changes in angular unit..... 76
Figure 4. 2 The geometry of InSAR system 77
Figure 4.3 The satellite SAR imaging geometry along the ascending and descending orbits..... 81
Figure 4. 4 The estimation of northingand horizontal displacement rates 83
Figure 4. 5 The schematic illustrations of (A) normal fault and (B) reverse fault..... 85
Figure 4. 6 The schematic figure illustrates the combination of SAR images to form interferograms through Coherence Change Detection (CCD) method..... 88
Figure 4.7 Time-Baseline Plot (A) and Time-Position Plot (B) obtained from descending Sentinel-1 dataset from 11/March/2017 to 31/January/2020. 89
Figure 4.8 Time-Baseline Plot (A) and Time-Position Plot (B) obtained from ascending Sentinel-1 dataset from 08/October/2017 to 07/February/2020. 90
Figure 4. 9 The flowchart of Sentinel-1 data reprocessing through PSInSAR method from software ENVI SARScape..... 92
Figure 5.1 Patterns of displacement rate in LoS-ascending (A), LoS-descending (B), vertical (C) and horizontal (D) direction across the Suanjingzi study area 100
Figure 5.2 Patterns of displacement rate in LoS-ascending (A), LoS-descending (B), vertical (C) and horizontal (D) direction across the Jiujing study area..... 104
Figure 5.3 Patterns of LoS displacement rate in LoS-ascending (A), LoS-descending (B), vertical (C) and horizontal (D) directions across the Xinchang study area 108
Figure 5.4 The relationship between ascending and descending displacement geometries..... 112
Figure 5.5 (A) to (H). The spatial variations of Sentinel-1 (ascending) coherence at 8 time-periods in Suanjingzi study area 118
Figure 5.6 (A) to (I). Frequency distribution curves for coherence at selected blocks in the Suanjingzi study area between 08/10/2017 and 26/01/2020. 128
Figure 5.7 The average time-series analysis at Block SJZ0 in ascending and descending scenes..... 131
Figure 5.8 (A) to (F). The temporal variation of coherence in relation to precipitation between 08/10/2017 to 26/01/2020 in Suanjingzi region. 133
Figure 5.9 (A) to (H). The spatial variations of Sentinel-1 (ascending) coherence at 8 time-periods in Jiujing study area 135
Figure 5.10 (A) to (E). Frequency distribution curves for coherence at selected blocks in Jiujing study area between 08/10/2017 and 26/01/2020..... 146
Figure 5.11 (A) to (E). The temporal variation of coherence in relation to precipitation between 08/10/2017 to 26/01/2020 in Jiujing region..... 147

Figure 5.12 (A) to (F). Frequency distribution curves for coherence at selected blocks in Xinchang study area between 08/10/2017 to 26/01/20220 150
Figure 5.13 (A) to (H). The spatial variations of Sentinel-1 (ascending) coherence at 8 time-periods in Xinchang study area 151
Figure 5.14 (A) to (G). The temporal variation of coherence in relation to precipitation between 08/10/2017 to 26/01/2020 in Xinchang region 160
Figure 5.15 The schematic figure illustrates the generation of interferograms and the calculation of threshold coherence within PSInSAR. 161
Figure 6.1 The schematic diagram illustrates the sinistral shearing of the Jiujing granite region due to NE compression 166
Figure 6.2 Schematic figures (A, B, C, D, E, and F) illustrates the correlation between maximum compression (σ1) and the vertical shearing properties along fault. 167
Figure 6.3 Schematic illustration of the shearing properties of high angle faults (antithetic strike-slip faults) and low angle faults (synthetic strike-slip faults) under NE compression. 169
Figure 6.4 (A to E) Schematic illustration of the correlation between fault striking angle, maximum compression direction and horizontal shearing properties. 170
Figure 6.5 The |θ-α| related dip-slip and strike-slip shearing properties along fault plane. 172
Figure 6.6 The patterns of displacement in LoS-ascending (A), LoS-descending (B), easting (C), and vertical (D) directions illustrate the correlation between surface deformations and active faults over the Suanjingzi study area 174
Figure 6.7 The aerial frequency distribution of vertical displacement rates at Block SJZ1 and SJZ2 (A), Block SJZ6b and SJZ11 (C), and the easting displacement rates at Block SJZ1 and SJZ2 (B), Block SJZ6b and SJZ11 (D) 180
Figure 6.8 The average time series displacements of Block SJZ1 (A), SJZ2 (B), SJZ6b (C), SJZ11 (D) and SJZ14 (E) in ascending (01/10/2017 to 07/02/2020) and descending (11/03/2017 to 31/01/2020) scene. 183
Figure 6.9 (A) and (B). The distribution of vertical displacement and horizontal displacement rates along cross-section AA' in Figure 6.6 184
Figure 6.10 (A) and (B). The distribution of vertical displacement and horizontal displacement rates along cross-section BB' in Figure 6.6 184
Figure 6.11 (A to C) illustrates three possible horizontal shearing conditions along F_1 depends on the direction of maximum horizontal compression 186
Figure 6.12 The schematic figure illustrates the formation of sinistral shearing along F_b 188
Figure 6.13 The schematic sketch explains the existence of divergence at Block SJZ6b, SJZ7a, SJZ8 and SJZ7b along F_h and F_e through a perspective of geomechanics 189
Figure 6.14 The schematic sketch illustrates a positive flower relationship between F_5 and F_6 in Suanjingzi. 192
Figure 6.15 The patterns of displacement rate in LoS-ascending (A), LoS-descending (B), easting (C) and vertical (D) directions illustrtate the correlation between surface deformations and active faults over Jiujing study area 195
Figure 6.16 The aerial frequency distribution of vertical displacement rates at Block JJ6 and JJ8 (A), Block JJ4 and JJ5 (B), Block JJ3 and JJ12 (D), Block JJ19, JJ20 and JJ21 (F), and the easting displacement rates at Block JJ4 and JJ5 (C), Block JJ3 and JJ12 (E), Block JJ19, JJ20 and JJ21 (G) 202
Figure 6.17 The average time-series displacemnt of Blocks JJ6 (A), JJ7 (B), JJ3 (C), JJ12 (D), and JJ19 (E) in the ascending (01/10/2017 to 07/02/2020) and descending (11/03/2017 to 31/01/2020) scene.. 206
Figure 6.18 (A) and (B). The distributions of vertical and horizontal displacement rates along cross-section AA' in Figure 6.15 207

Figure 6.19 (A) and (B). The distributions of vertical and horizontal displacement rates along cross-section BB' in Figure 6.15 208
Figure 6.20 (A) and (B). The distributions of vertical and horizontal displacement rates along cross-section CC' in Figure 6.15. 209
Figure 6.21 The schematic figure illustrates the spatial correlation between F_d and the maximum horizontal compression 212
Figure 6.22 The schematic figure illustrating the direction of σ_1 and D_H in Step 1 and 2 due to direction change and the two horizontal deformation components (D_E and D_N) along F_{I-1} 215
Figure 6.23 The patterns of displacement rate in LoS-ascending (A), LoS-descending (B), vertical (C) and easting (D) directions illustrtate the correlation between surface deformations and active faults over Xinchang study area 217
Figure 6.24 The aerial frequency distribution of vertical displacement rates at Block XC6 and XC8 (A), Block XC9 and XC10 (B), and the easting displacement rates at Block XC9 and XC10 (C) 223
Figure 6.25 The average time-series displacement of Blocks XC6 (A), XC7 (B), XC8 (C), XC9(D), and XC10 (E) in the ascending (01/10/2017 to 07/02/2020) and descending (11/03/2017 to 31/01/2020) scene. 225
Figure 6.26 (A) and (B). The distributions of vertical displacement and horizontal displacement rates along cross-section AA' in Figure 6.23. 226
Figure 6.27 (A) and (B). The distributions of vertical displacement and horizontal displacement rates along cross-section BB' in Figure 6.23 227
Figure 6.28 (A) and (B). The distributions of vertical displacement and horizontal displacement rates along cross-section CC'C'' in Figure 6.23. 228
Figure 6.29 (A to D) The schematic graphs illustrate the spatial correlation between maximum horizontal compression (σ1) and fault strike angle along Fault F_{31}, ,,F_{29}, F_h, and F_{22-4} 230
Figure 6.30 The schematic graph illustrates the spatial correlation between maximum horizontal compression and fault strike angle along Fault F_b 231
Figure 7.1 Patterns of LoS displacement rate in descending direction across the Jiujing study area over period 11/03/2017 reprocessed by ICSAR 243

List of Tables

Table 1. 1 The volume of Chinese radioactive waste.....13
Table 2.1 The characteristics of faults in Beishan area.....26
Table 2.2 The measurements of compression in Beishan 29
Table 2.3 The description of major Jiujing granite units.....32
Table 2.4 The description of major exposed stratigraphy in Jiujing 33
Table 2.5 The characteristics of major fault structures in Jiujing study area 34
Table 2.6 The description of major granite units in Xinchang study area 38
Table 2.7 The description of major exposed stratigraphy in Xinchang study area.....38
Table 2.8 The characteristics of major fault structures in Xinchang study area.....39
Table 2.9 The description of major granite units in Suanjingzi study area.....41
Table 2.10 The description of major exposed stratigraphy in Suanjingzi study area 42
Table 2.11 The characteristics of major fault structures in Suanjingzi study area 42
Table 2.12 The geochemical properties of groundwater in Beishan.....45
Table 2.13 A summary of granite and fracture zones permeability in Beishan.....46
Table 3.1 The application of the InSAR time-series analysis on erosion susceptible surface (rural areas) 53
Table 3.2 The application of InSAR time-series analysis in rural-urban continuum area.....57
Table 3. 3 The application of InSAR time-series analysis in robust surface (urban and rocky outcrop) 59
Table 4.1 The parameter value setting in Sentinel-1 data reprocessing.....93
Table 4.2 The processing stages, script name and script purposes of ICSAR 87
Table 5.1 The displacement rates of selected blocks in Suanjingzi 97
Table 5.2 The displacement rates of selected blocks in Jiujing 98
Table 5.3 The displacement rates of selected blocks in Xinchang.....99
Table 5.4 The cumulative percentage of coherence at Blocks SJZ0, SJZ1, SJZ2, SJZ6b, SJZ11, SJZ12, SJZ14, SJZ15 and Fluvial Channel 2 in Suanjingzi study area between 08/10/2017 to 26/01/2020. 117
Table 5.5 The erosional rates of granite and granodiorite in various environment.....129
Table 5. 6 The cumulative percentage of coherence at Block BB1, BB2, JB1, JJ5, and JJ12 in Jiujing study area between 08/10/2017 to 26/01/2020. 146
Table 5.7 The cumulative percentage of coherence at Block XC4, XC5, XC6, XC9, XC10 and Qh1 in Xinchang study area between 08/10/2017 to 26/01/2020. 148
Table 6.1 The characteristics of active faults in Suanjingzi.....173
Table 6.2 The characteristics of newly identified active faults in Jiujing.....202
Table 6.3 The characteristics of active faults in Xinchang 223
Table 7.1 The vertical offset rates and long-term elevation difference along major active faults in Suanjingzi, Jiujing and Xinchang..... **Error! Bookmark not defined.**
Table 8.1 A summary of the active fault identified in Suanjingzi, Jiujing, and Xinchang.....248

Publication

Wang, Z., Lawrence, J., Ghail, R., Mason, P., Carpenter, A., Agar, S. and Morgan, T., 2022. Characterizing Micro-Displacements on Active Faults in the Gobi Desert with Time-Series InSAR. Applied Sciences, 12(9), p.4222. Available at: https://www.mdpi.com/2076-3417/12/9/4222

Contents

Contents 9

1.Introduction 11

1.1 Contribution to knowledge 11

1.2 Research background 11

1.3 The required geological conditions for a Geological Disposal Facility (GDF) 12

1.4 Radioactive waste inventory and disposal policy in China 13

1.5 Progression of GDF host rock selection in China 14

1.6 Beishan, China: the region of interest 15

1.7 InSAR ground monitoring 20

1.8 Research aims and objectives 21

1.9 An overview of the thesis 22

2. Literature Review: The geology in Beishan 24

2.1 Introduction 24

2.2 A review of the overall tectonic background around Beishan 24

2.3 The history of magmatic activities and exposed stratigraphy in Beishan 30

2.4 A review of the geology in Jiujing study area 31

2.5 A review of the geology in Xinchang study area 36

2.6 A review of the geology in Suanjingzi study area 40

2.7 The origin and evolution of groundwater 43

2.8 Other hydrogeology related studies 44

2.9 Summary 46

3. The applications of the InSAR technique in engineering geology 48

3.1 InSAR detection of surface displacement 48

3.2 InSAR algorithms for time series analysis model 49

3.3 The application of various InSAR time series analysis methods in engineering geology 52

3.4 Coherence for surface change detection 70

3.5 Summary 73

4. Methodology 75

4.1 InSAR technique 75

4.2 The application of PSI for displacement rate measurements in Beishan 78

4.3 PSInSAR method 79

4.4 The estimation of vertical and horizontal displacement rates 81

4.5 Alternative method for estimating northward displacement rates 83

4.6 Method to determine active faults 84

4.7 Method to characterise active fault 85
4.8 The application of Coherence Change Detection (CCD) to identify surface alteration 85
4.9 Sentinel-1 data and data reprocessing software 88
4.10 Method to validate PSInSAR results using ICSAR 94
5. The preliminary interpretation of surface deformation and the role of geomorphological processes 96
5.1 Ground displacement maps 96
5.2 Factors contributing to surface deformation 112
5.3 Surface deformation at Suanjingzi and its geomorphological effects 116
5.4 Surface deformation in Jiujing and its geomorphological effects 133
5.5 Surface deformation in Xinchang and its geomorphological effects 147
5.6 The feasibility of geomorphological rates measurements using PSI method 160
5.7 Discussion 161
5.8 Conclusion 162
6. Mapping and characterizing micro-displacements on active faults in granite outcrops areas under the context of geomechanics 164
6.1 Introduction 164
6.2 The theory of kinematics 165
6.3 Characterizing active faulting at Suanjingzi granodiorite outcrop 172
6.4 Characterizing active faulting at Jiujing granite outcrop 194
6.5 Characterizing the active faults at Xinchang granite outcrop 216
6.6 Summary 234
7. Discussion 236
7.1 Regional tectonic 236
7.2 The potential contributing sources of the data standard deviations 238
7.3 The result validation 239
7.4 The validation of fault micro-displacements using ICSAR 242
7.5 Limitations and suggested future works 244
8. Conclusion 246
8.1 Introduction and research background 246
8.2 Research achievements 246
8.3 The significance of this research 248
9. Reference 250
10. Supplementary materials 266

1.Introduction

1.1 Contribution to knowledge

This work contributes to overall knowledge from several novel perspectives. Firstly, by identifying, mapping and characterizing the active faults, this research improves the understanding of the stress regime and the structural geology in Beishan, Northwestern China, which would ultimately benefit the permanent disposal of high-level wastes in this area.

Second, the results explain the correlation between the maximum compression direction and the strike- and dip-slipped characteristics of active faults. This supports the existing relevant studies [32, 33, 34, 235, 36, 37, 38] regarding the tectonic activities around Arjen Fault Zone, Shulehe Fault Zone and Sanweishan Fault zone in the northern boundary of Qinghai-Tibetan Plateau.

Thirdly, this research successfully demonstrates a new approach to map and characterize the active faults using the InSAR technique. The approach demonstrates observable micro movements which trace the InSAR deformation pattern discontinuities improving the accuracy in positioning the fault plane and make the fault mapping in rural areas with harsh environment (such as Gobi Desert) more feasible.

Lastly, this research demonstrates the feasibility of using PSInSAR method in measuring slow erosional and depositional rates. If the geomorphological processes continuously but slightly change the surface, it is possible to generate an interferogram with coherence at the chosen threshold value (0.65 to 0.75), this allows for the monitoring of slow geomorphological processes using PSI, such as the development in incised ephemeral channels.

As a result of this research one paper had been accepted and published by Applied Science journal:

Wang, Z., *Lawrence, J., Ghail, R., Mason, P., Carpenter, A., Agar, S., & Morgan, T. (2022). Characterizing Micro-Displacements on Active Faults in the Gobi Desert with Time-Series InSAR. Applied Sciences, 12(9), 4222. Available at: https://www.mdpi.com/2076-3417/12/9/4222*

Two further papers are in preparation:

Wang, Z., Lawrence, J., Ghail, R., and Mason, P., 2023. The kinematical interpretation of active faults across the granite outcrop area in Xinchang, Beishan (China) through the application of Persistent Scatterer InSAR method (in preparation).

Wang, Z., Lawrence, J., Ghail, R., and Mason, P., 2023. An investigation of the geomorphological processes over Suanjingzi granite outcrop in Beishan, Northwestern China through the application of Coherence Change Detection (CCD) and Persistent Scatterer InSAR methods (in preparation).

1.2 Research background

Nuclear energy releases very little amount of carbon dioxide into the atmosphere compared with other energy sources, hence the nuclear energy source is a clean alternative to fossil fuels which importantly does not contribution to climate change. It is generated through the processes of fission, decay, and even fusion of radioactive elements such as uranium and plutonium.

However, nuclear fuels produce a radioactive waste. Usually, 1 GW nuclear power station can produce 4 m^3 of high-level wastes, 20 m^3 of intermediate level wastes, and 140 m^3 of low level wastes every year [1], if this waste left untreated then it could pose regional environmental problems & serious health threats for living organism due to radiation. Therefore, the safe handling and disposal of these kinds of radioactive waste affects the sustainable functioning of nuclear power plants.

Based on their radioactivity and half-life the International Atomic Energy Agency (IAEA) has classified these radioactive wastes into six types, which are high level wastes (HLWs), intermediate level wastes (ILWs), low level waste (LLWs), very short-lived wastes (VSLWs), very low-level wastes (VLLWs) & exempt waste (EWs) [2,3]. HLWs contain the highest concentration of both short- and long-lived radionuclides and these wastes need safe isolation and management for 10s of thousands of years.

Internationally, the discussion of HLW disposal has been ongoing since the 1950s. The initial disposal ideas include using radioactive wastes as weapon material, space disposal, and ice-sheet disposal. Deep well injection had been used until the 1980s at Oak Ridge National Laboratory in Tennessee in the USA, and this method was also adopted by the Soviet Union after the disastrous HLW explosion at Kyshtym near the Ural Mountains. However, the uncertainties in the underground sites and the high operational costs for borehole drilling have been obvious disadvantages for this method. Another historical disposal method has been ocean dumping and burying HLW below the abyssal clay, however, this may generate significant pollution into the oceanic environment, and has been criticised by international communities [4]. Therefore, from the 1980s onwards permanent geological disposal of higher-level radioactive waste (such as High-Level Waste and Intermediate Level Waste) in a purpose built, engineered Geological Disposal Facility (GDF) has become the internationally accepted platform to deal with HLWs.

1.3 The required geological conditions for a Geological Disposal Facility (GDF)

The GDF is designed to isolate the radioactive wastes permanently in an engineered permanent storage facility, which aims to stop the radionuclides from entering the biological and hydrological cycles. Ideally, the radionuclides are expected to be kept under the subsurface for longer than ten

times their half-lives that is more than 100,000 years, so that their radioactivity and toxicity will be effectively eliminated [5].

The permanent disposal of the HLW under the subsurface requires a long-term stable geo-environment site. This long-term stability is challenged by two factors. First due to tectonic instability and secondly due to groundwater flow. Therefore, the factors such as topography, tectonics and seismicity, subsurface conditions, geological structures, physical & chemical properties of rocks, hydrology & hydrogeology, future nature events, and even the general geological and engineering conditions combined with social considerations must be taken into consideration for the GDF site selection [6,7,8,9]. The disposal site is expected to have low population density with good transportation conditions and with minimal economic activities. Each country is responsible for its own radioactive waste. Four broad generic lithological rock types are considered as adequate for HLW disposal site, which are mudstone, salt rock, crystalline (igneous) rock, & tuff.

1.4 Radioactive waste inventory and disposal policy in China

It was estimated China has around 10,000 m^3 of radioactive waste (which includes High Level Waste (HLW), Intermediate Level Waste (ILW), and Low-Level Waste (LLW)) coming from the application of nuclear technology (nuclear power plants), 5000 m^3 from scientific research work, and in the order of 10,000 m^3 from military production [1]. As High-Level Waste (HLW) only occupy around 3% of the total volume of radioactive waste [3], it is estimated that China currently has 450 m^3 of spent fuel reprocessing wastes (including 300 m^3 from nuclear power plants and 150 m^3 from research work (institutional wastes)) dominantly composed of plutonium and americium, and >300 m^3 of military wastes composed of strontium and caesium. So, in total more than 750 m^3 HLW wastes are waiting for safe disposal.

Table 1.1 The volume of Chinese radioactive waste

	Radioactive Waste Volume (m^3)	High-Level Waste Volume(m^3)	Elemental Composition
Nuclear Power Plant (NPP)	10,000	300	U, Pu and Am
Research Work	5,000	150	
Military	n×10,000 (n>1)	n×300 (n>1)	Sr and Cs

The HLW geological disposal program conducted in China is based on the option of a GDF at depths of between 500 and 1000 m, and this program consists of three steps (add the year) [10]:

Step 1: Laboratory studies and site selection for HLW repository (2006-2020).

Step 2: Underground in-Situ test (2021-2040).

Step 3: Repository construction (2041-2050).

Currently China is nearing the end of Step 1 and at early stages of Step 2.

1.5 Progression of GDF host rock selection in China

China has granite mainly distributed in the Eastern offshore area and Qinghai-Tibetan plateau in West part, which occupies around 9% of its continental area [11]. China also has thick mudstone layers distributed in Qaidam Basin, Tarim Basin, Zhungeer Basin, Ordos Basin, Erlian Basin, Bayingebi Basin, etc. [11, 12]. The wide distribution of the potential hosting rocks provides huge opportunities and options for GDF site selection in China.

Igneous rocks have received the most attention during the process of GDF site selection in China. In general, the the Xinchang region in Beishan region in Gansu province was widely considered as the most suitable igneous GDF site in China [6, 13], although, no final decision has been made yet. Currently in the end of Step 1 (site selection for HLW repository), the published literature suggests the screening of igneous rocks at a regional level and detailed site investigations works are being conducted at the Beishan region with a focus on several key granite masses in Xinchang, Jiujing and Suanjingzi which are the focus of this thesis. Some historical studies dating back to 2000 have also been conducted on the granite masses Shazaoyuan and Yemaquan [14].

Site selection work has been conducted in other major nuclear countries such as United States, France, Belgium, Switzerland, Germany, Sweden and Finland. France, Switzerland, and Belgium are all focusing on Lower strength sedimentary rocks (LSSR) Led by the Department of Energy (DOE), salt was recommended as the suitable hosting rock for GDF in 1957 in the US Waste Isolation Pilot Plant (WIPP), waste emplacement started in 1999 [8]. Meanwhile, potential tuff rock at Yucca Mountain in Nevada were investigated along with several other sites as the disposal site for spent fuel and other high-level wastes. The Yucca Mountain site was approved to be qualified for a GDF in 2002. Unfortunately, due to political interference this process was ended [8]. Germany also investigated a salt site at Gorleben, but the process halted in 2000 [15]. Similar to China, Sweden and Finland chose crystalline rock as their GDF host rock for spent fuel and high-level wastes [16]. Started in 1983, the crystalline rock on Olkiluoto Island was finally chosen as the GDF host rock in Finland by Teollisuuden Voima Oyj (TVO) and Posiva by 2012. The excavation work of the Finnish GDF ONKALO is being conducted at Olkiluoto, and the wastes are expected to be put in place in the 2020s. In comparison, the site selection and GDF construction in Sweden is slightly slower. Enacted by the Swedish Nuclear Fuel and Waste Management Company (SKB), the site selection work in Sweden started in 1992, after the processes of site investigation, Östhammar was finally chosen as the GDF site in 2009.

France currently has the most advanced GDF site selection programme in mudstone. There is no final decision to be made about the HLW disposal site in Belgium and Switzerland. Meanwhile, Finland and

Sweden provide reference for the crystalline site selection and GDF construction in Beishan, China, and the US experience in Yucca Mountain and the Waste Isolation Pilot Plant (WIPP) are important for the future tuff and salt site selection in China depends on governmental policy.

1.6 Beishan, China: the region of interest

1.6.1 location, population, and economy



Figure 1.1 Location of Beishan area in Gansu Province, northwest China (highlighted by red box)

Beishan is considered as the most promising HLW disposal site in China and has received most research attention at this stage of the process and that is the reason it forms the focus of this research. Beishan is located in the northwest region of Gansu province in China (Figure 1.1) with geographical coordinates from 40°00'-42°00'N to 96°40'-98°40'E and a total area more than 12,000 km^2. It is jointly administrated by the Subei County and Yumen City (county-level division) in Jiuquan, Gansu Province, and the Ejin Banner (county-level division) in Alexa, Inner Mongolia Autonomous Region (Province-level division). The south part of preselection area is topographically flat and crossed by Lanxin Railway and No. 312 National Highway, this obviously provides convenience for the transportation of radioactive wastes from the nuclear power stations, which are mostly suited in east coastal areas [17].

This area is characterised by low population density, low economic level and poor development prospect. The surface area is largely covered by the Gobi Desert and therefore unpopulated, where the average population density is less than 1 km^{-2}. The economies in Subei and Ejin are dominated by animal husbandry with annual GDP only 1.94 and 0.4 billion RMB respectively. Most population and economic production are concentrated in Yumen City, the largest urban community in this region due

to the petroleum and mining industries. Yumen is around 40km away from the potential GDF host rocks sites such as Xinchang and Jiujing [18, 19, 20]. In this way, the disposal of HLW in Beishan granites has very limited social, economic and even ecological impacts on local communities, indicating Beishan region from a socio-economic perspective is an ideal site for GDF.

1.6.2 Climate (precipitation and temperature)

The Beishan Region is a semi-arid climate with very low annual precipitation (78.9 mm a^{-1}). However, the annual evaporation is 3130.9mm. This indicates a poor atmospheric groundwater recharge in general. The temporal distribution of the precipitation is uneven, where most precipitation is concentrated in summer months (June, July and August) in terms of short intense rainfall, this in turn leads to the formation of torrential flood and debris flow. Meanwhile, the monthly precipitation in autumn and winter months are very low [17]. This is illustrated in Figure 1.2, which presented the monthly precipitation in Jiuquan from September 2017 to April 2020.

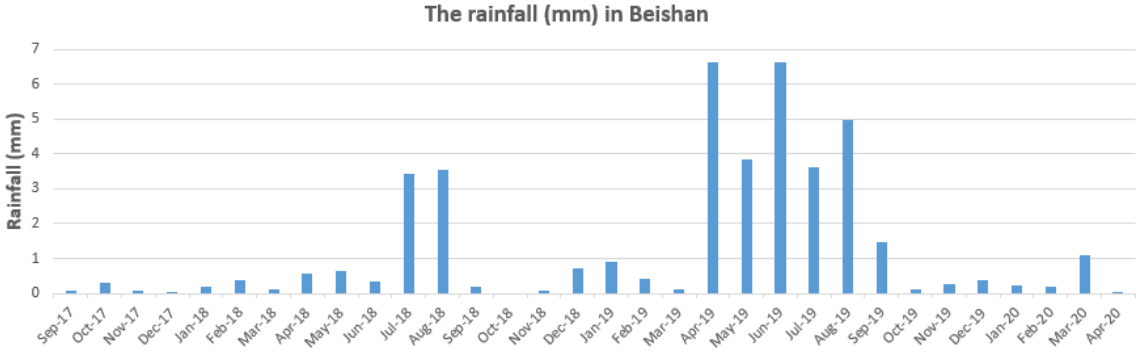


Figure 1.2 The monthly rainfall in Beishan from September 2017 to April 2020, where most precipitation was concentrated in summer months [21].

The average wind speed in Beishan is about 3.7 ms^{-1} and the average temperature is about 4-6°C. However, the temperature difference over the year is highly variable, which can reach up to 37°C in summer months and fall to -28°C in winter months. Therefore, from November to March in the following year, the soil in the area is frozen, and the depth of permafrost could be around 30 to 244 mm. The soil becomes unfrozen in April [17].

1.6.3 Geo-environments in Beishan

Tectonically, Beishan is a part of Tarim Basin in the northeast end of the Aerjin Fault system, and it has an annual uplift rate of 0.6–0.8 mm a^{-1} [13]. The Aerjin Fault system has been an active strike-slip fault zone since the Cenzoic era, however, due to the buffer impact of the Qilian Mountains which absorbs most of the energy generated by the fault zone, Beishan has historically been considered tectonically stable. Therefore, Beishan has been described as “the most stable region within the active zone” [22]. This is the reason why Beishan had been chosen as a potential HLW disposal site in national and regional level selection.

The ground surface in Beishan is characterised by typical Gobi landscape, limited vegetation, flat plains and small hills with elevations between 1400 m and 2000 m [10, 23]. The overall regional terrain shows a north-south trending "V" shape valley. Therefore, the drainage pattern of water converges to the lowland in middle and then flows eastwards [24]. Due to the dry climate, there are no perennial rivers on the surface, but when daily precipitation is high (5 mm) in summer months it causes seasonal floodwater in surface gullies. This occurs several times per year (5-6 times in wet years and at least once in dry years). Most floodwater infiltrates downwards and recharges the groundwater, the rest flows to the lowland area and forms surface water which then rapidly evaporates [25]. Based on the regional aquifer the shallow groundwater can be classified into three types, based on the underlying rocks: (1) pore-fissure water in loosening rocks, (2) pore-fracture water in clastic rocks and (3) bedrock fracture water [26].

The surface processes in Beishan region have led to the upland areas being composed of granite masses whilst Quaternary wind-blown sediments line the valleys. These granite masses predominantly strike E-W. The spatial distribution of Xinchang, Jiujing, Jijicao, Yemaquan, Suanjingzi and Shazaoyuan granite masses are shown in Figure 1.3 and have been recognised as potential GDF host rocks. This is the focus of Chapter 2.

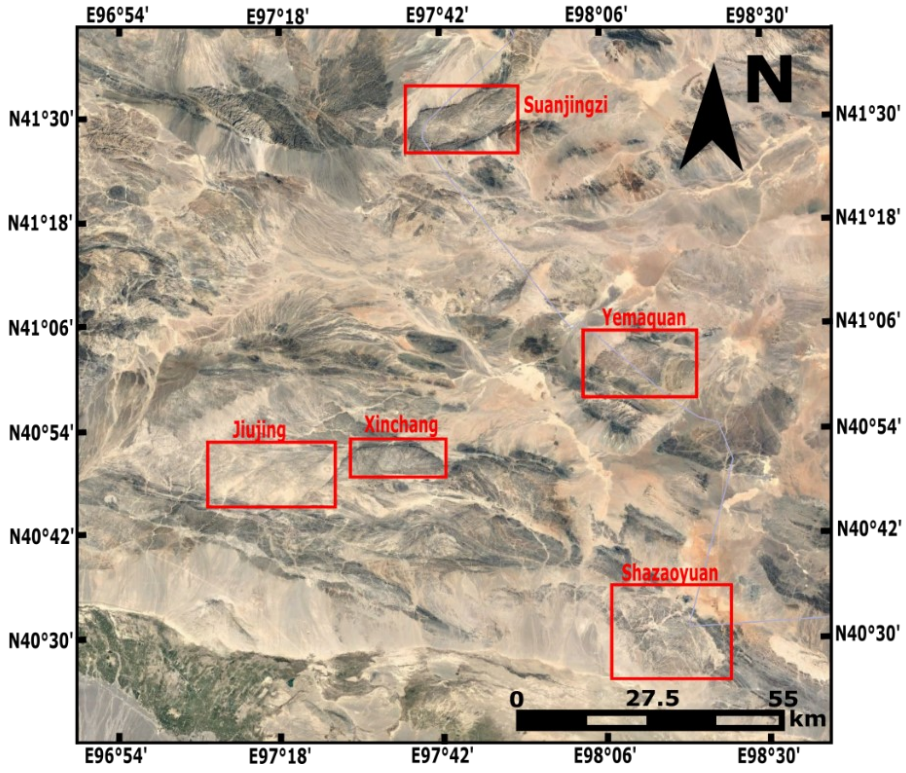


Figure 1.*3 (A)* The Google Earth image of the Beishan Region, showing the spatial distribution of potential GDF host rocks at Xinchang, Jiujing, Yemaquan, Shazaoyuan and Suanjingzi.

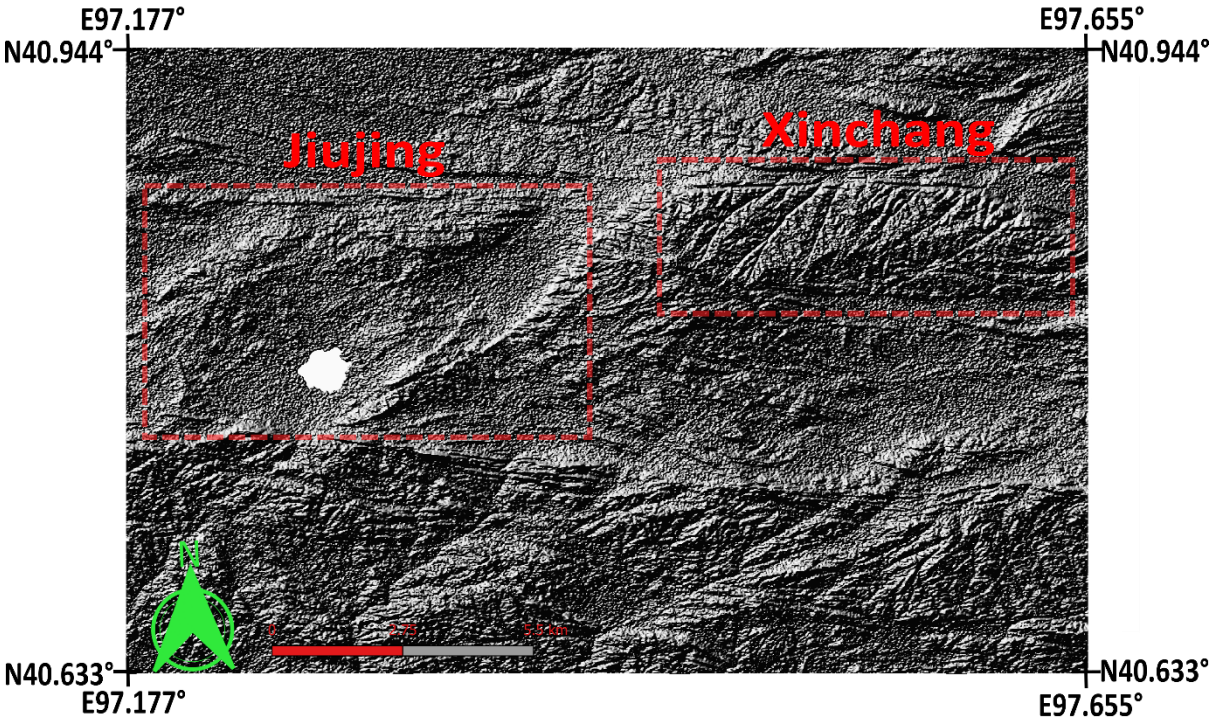


Figure 1.3 (B) The hill-shaded topographic map shows the detail locations of Jiujing and Xinchang study areas in Figure 1.3 (A).

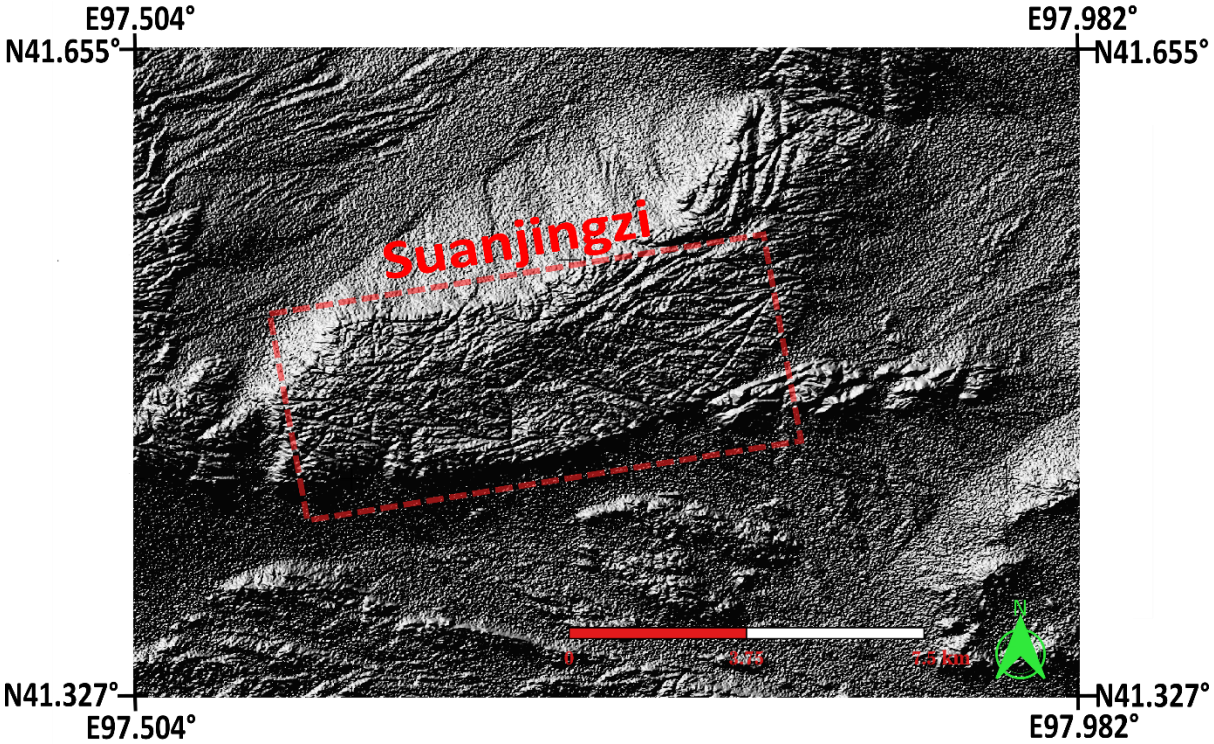


Figure 1.3 (C) The hill-shaded topographic map shows the detail locations of Suanjingzi study area in Figure 1.3 (A).

1.6.4 The seismic distribution around study area

The Qilian Mountains absorb most of the energy generated by Arjen fault zone, therefore, Beishan has been described as the most stable region within the active zone. The term “stability” is relative and characterised by a seismic distribution with a low density and low magnitude. Figure 1.4a shows the number and magnitudes of earthquakes in relation to the Beishan region [233]. Although figure 1.4a shows no evidence of earthquake epicentres, as shown in Figure 1.4b and 1.4c some seismically controlled faulting and ground motion may be expected.

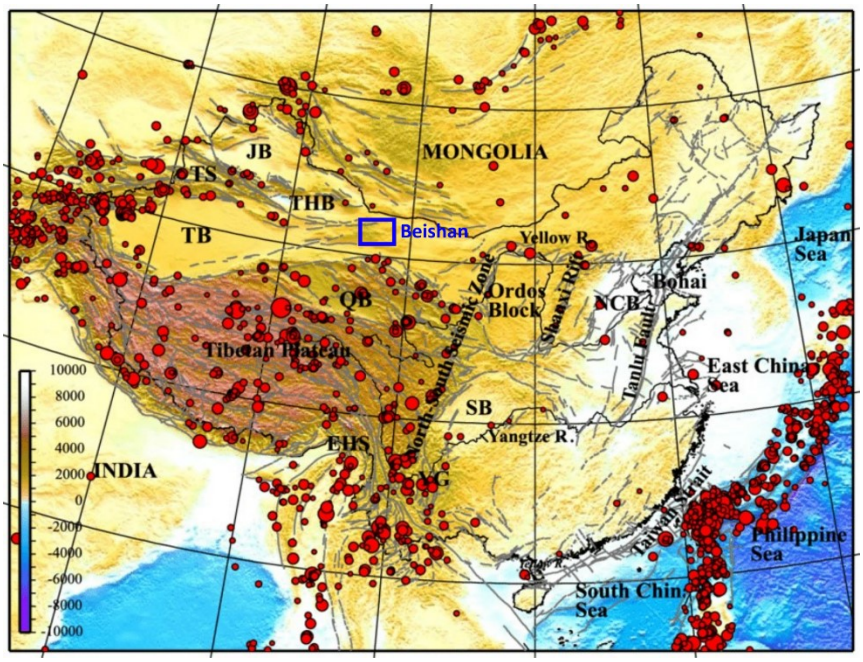


Figure 1.4 (A) The topographic map illustrates the correlation between elevation and seismic distribution in China. The Beishan study area has been highlighted by the blue box. Red circles indicate earthquakes of magnitude >5.0 recorded between 1978 and 2004; circle size is proportional to magnitude [233].

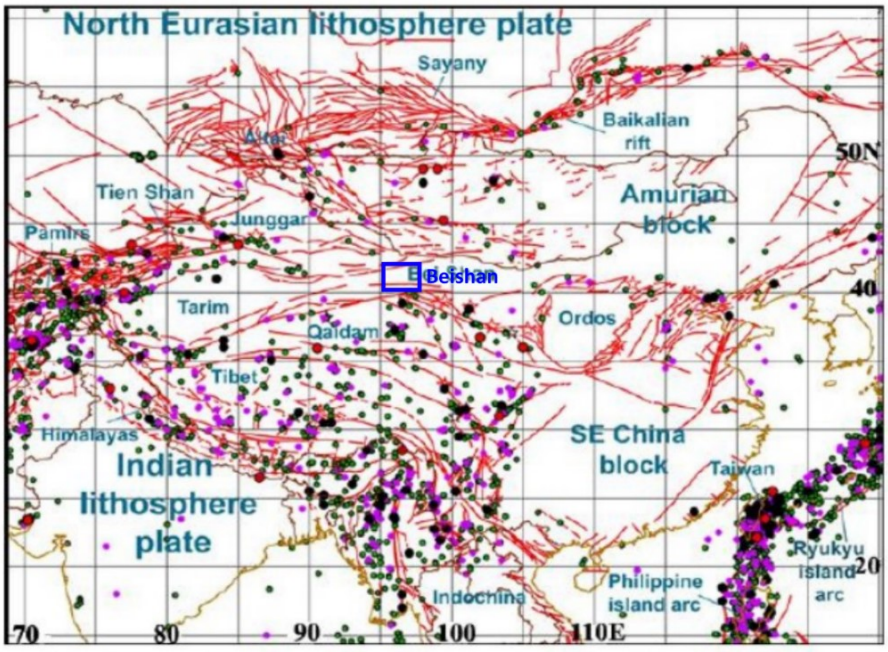


Figure 1.4 (B) The national map shows the correlation between active faults (red lines) and seismic distribution in China. The Beishan study area has been highlighted by the blue box. Small circles

show epicentres of earthquakes after NEIC Catalog with magnitudes: red–7.9 - 8.9, black–6.9 - 7.9, violet–5.9-6.9, and green–4.9 - 5.9 [234].

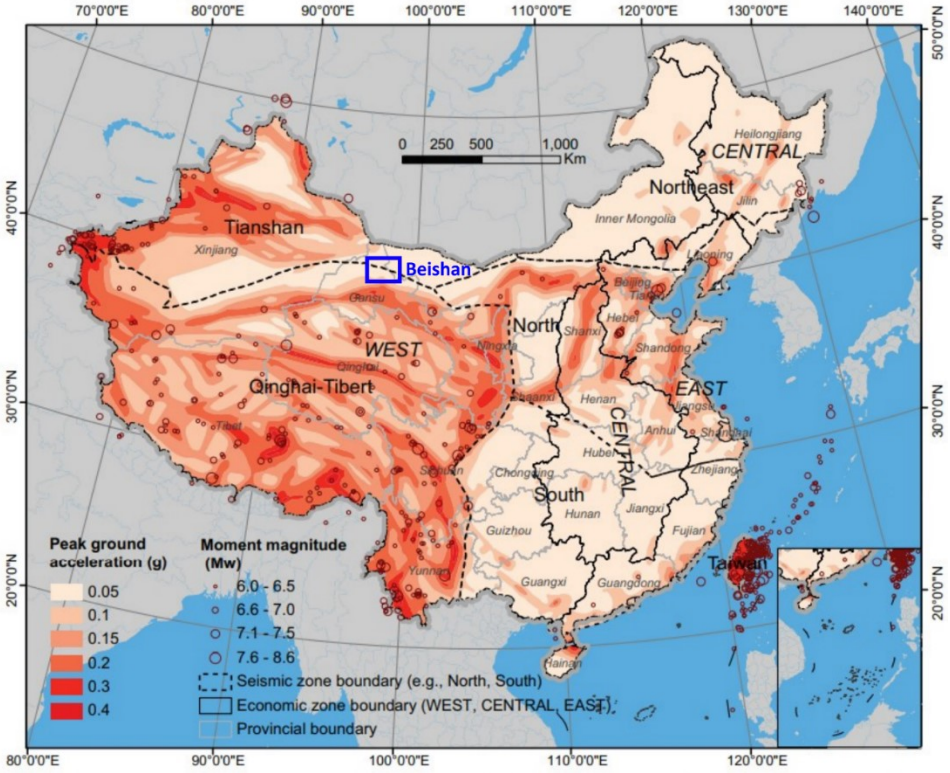


Figure 1.4 (C) The seismic ground motion parameter zonation map (the peak ground acceleration with a 10% probability of exceedance in 50 years) and major earthquakes (with magnitudes greater than 6) from 1950 to 2015 in China (data source: China Earthquake Administration). The Beishan study area has been highlighted by the blue box [235].

1.7 InSAR ground monitoring

The GDF host rock is expected to have long term geological stability, therefore, quantifying the tectonic activity is a key process for in establishing a safety case for the safe disposal of radioactive waste. This research has used the Earth Observation technique Interferometric Synthetic Aperture Radar (InSAR) to interpret the earth surface processes and structural geology. InSAR is a remote sensing method to measure the surface deformation at the millimetre scale. It is an active system whereby Satellites emit electromagnetic (EM) waves and collect the returned energy from target points, so that the phase difference can be monitored to define the satellite-surface distance change between two image acquistration time [27, 28]. This kind of surface deformation rate is estimated using Persistent Scatterer Interferometry (PSI) method. Ground movement can be caused by a range of processes from tectonic activity to factors such as erosion and deposition of materials. In this way, another ambition of this research is to identify the impact of geomorphological processes and define the tectonically induced deformation through the application of InSAR coherence.

1.8 Research aims and objectives

The granite masses of Beishan Region are the focus of the Chinese sting process for radioactive waste in a GDF. To improve the understanding of local tectonic stability and support the GDF site selection process a new approach to discover unknown active faults through remote sensing has been established, this research has chosen Xinchang, Jiujing and Suanjingzi regions in Beishan as case studies to demonstrate how PSInSAR technique can be applied to investigate earth surface process. This includes two aims and eight objectives:

Aim 1: To develop a new approach to identify, map, and characterise the micro-displacements along active faults in the studies area through the combination of vertical (D_U) and horizontal (D_E) deformation through the application of the PSInSAR technique. This includes 4 objectives:

Objective 1.1: to understand the structural, petrological, hydrogeological, sedimentary and geomechanical environments in Beishan through literature review. This is achieved in first literature review chapter (Chapter 2).

Objective 1.2: to process the Sentinel-1 data in both ascending and descending orbits to quantify the vertical and easting deformation rates within study area through the application of Persistent Scatterer InSAR (PSI) method. This is introduced in methodology chapter.

Objective 1.3: to distinguish the spatial distribution of tectonically induced deformation (triggered by active faults) and geomorphologically induced deformation (surface erosion and deposition triggered by fluvial processes) through the application of Coherence Change Detection Method (CCD). This is discussed in Chapter 5.

Objective 1.4: to identify, trace, map and characterise the active faults within study areas based on vertical and easting deformation rates. This is discussed in Chapter 6.

Aim 2: to assess and conceptualise the structural regime in the Jiujing, Suanjingzi and Xinchang regions from the perspective of tectonic activity and future structure evolution considered within the context of a GDF.

1.9 An overview of the thesis

This research investigates the geology of Beishan through the application of InSAR to better understand the tectonic and geomorphological processes in the area. This thesis includes 8 chapters, the introduction, geology and InSAR related literatures, the methodology, the geomorphological and tectonic influence and impact on the region, followed by a discussion and conclusion. The thesis structure is outlined below:

Chapter 1 is the introduction providing the research context and the aims and objectives. It briefly introduces the study area (Beishan) from the perspectives of social economic, climate and geo-environments perspectives. The chapter addresses why permanent geological disposal of HLW is important in China and how the results in this project can contribute the ongoing GDF site selection work.

Chapter 2 is the first literature chapter which focuses on providing an understanding of the geological background in Beishan. The review centres on 4 elements of geology which are tectonic and structural history, granite petrology, stratigraphy and hydrogeology. The geological understanding developed in this chapter is vital to in assisting with the interpretation of InSAR deformation patterns (Chapter 6).

Chapter 3 is the second literature review chapter which aims to better understand the theoretical techniques underpinning InSAR and the basis for their applications in geological and civil engineering. The review in this chapter includes the theories of Persistent Scatterer (PS) and Distributed Scatterer (DS) related InSAR time series analysis algorithms, their applications in measuring active faults and geomorphological processes, and the application of coherence change detection (CCD) in quantifying surface alterations.

Chapter 4 is the methodology chapter which introduces the working theories of the InSAR techniques in details in relation to this project, which include the InSAR geometry, Interferogram composition, PSInSAR, the decomposition of Line of Sight (LoS) deformations and the working theories of CCD. It also provides an alternative method for estimating northwards displacement rates and the methods to determine active faults based on the knowledge developed in Chapter 3.

Chapter 5 interprets the PSInSAR deformation patterns in Suanjingzi, Jiujing, and Xinchang by distinguishing the impacts of geomorphological processes from tectonic activity through the application of the Coherence Change Detection (CCD) method over thee 3 study regions. It also generates maps to show the spatial variation of coherence and time series analysis curves to illustrate

the temporal correlation between decoherence and precipitation. This facilitates and supports the result interpretation in Chapter 6.

Based on the conclusion in Chapter 5, Chapter 6 maps and characterizes the identifies, characterizes and quantifies active faults in granite outcrops at Suanjingzi, Jiujing, and Xinchang. It first introduces the kinematic correlation among the fault shearing properties, the fault strike direction and the maximum compression direction. Then the active faults throughout the granite outcrop areas in three study areas are identified based on the interpretation of InSAR deformation patterns.

Chapter 7 is the discussion chapter which aims to explain and validate the results in Chapter 6. It first explains the results from the perspective of regional tectonics, then explains the potential contributing sources and validates the results using literature data and ICSAR software. Finally, Chapter 7 discusses the suitability of Beishan granite as GDF host rock from the perspectives of groundwater flow and tectonic activity.

Chapter 8 is conclusion chapter which summarizes the thesis, highlighting the key outcomes, then it discusses the significance of this research and identifies next steps for future works.

2. Literature Review: The geology in Beishan

2.1 Introduction

Beishan has been considered as the most promising area for HLW disposal in China. This is mainly due to its stable tectonics and depleted groundwater. To assess the suitability of permanent HLW disposal, the granite outcrops in Suanjingzi, Jiujing, and Xinchang (location shown in Figure 1.1 and 2.1) have been chosen as study areas.

To improve the knowledge of study areas in Jiujing, Xinchang and Suanjingzi, the review in this chapter focuses on the perspectives of tectonic structures, granite petrology and stratigraphy. This section started by taking a regional overview of the tectonic stability in Beishan by introducing several key structural features (faults) and reviewed the local tectonic regimes by summarising the characteristics of some major pre-mapped faults (Section 2.2). The review in this section improves the knowledge of fault activation in threes study areas through a perspective of geomechanics and dramatically facilitates the interpretation of InSAR deformation pattern in Chapter 6. Then Section 2.3 reviewed and summarised the history of magmatic activities and exposed stratigraphy in Beishan. This assists the observation of geomorphological impacts on surface change using coherence phase difference in Chapter 5. After that, Section 2.4, 2.5 and 2.6 reviewed the stratigraphy, granite lithology and structural geology at Jiujing, Xinchang, and Suanjingzi in details. Finally, Section 2.8 and 2.9 reviewed the hydrogeology related studies in Beishan, this includes the groundwater origin, groundwater geochemistry, and granite rock and fracture zone permeability. The review in this section not only assist the interpretation of InSAR deformation pattern in Chapter 6 but also supports the discussion of the GDF suitability assessment.

2.2 A review of the overall tectonic background around Beishan

As a part of the Tarim Basin, Beishan is located between the Central Asian Orogenic Belt and the Qilianshan Orogenic Belt (location shown in Figure 1.3 and 2.1). The northern and southern boundaries of Tarim Basin are delineated by the Hongliuhe strike-slip fault zone and the Arjen strike-slip fault zone respectively. Tectonically, the area around Beishan can be divided into four parts: the weak uplift area around Beishan (I), the differential sedimental areas in Anxi (II) and the Hexi Corridor (III), and the strong uplift area in Qilianshan (IV) [32], these are shown in Figure 2.1.

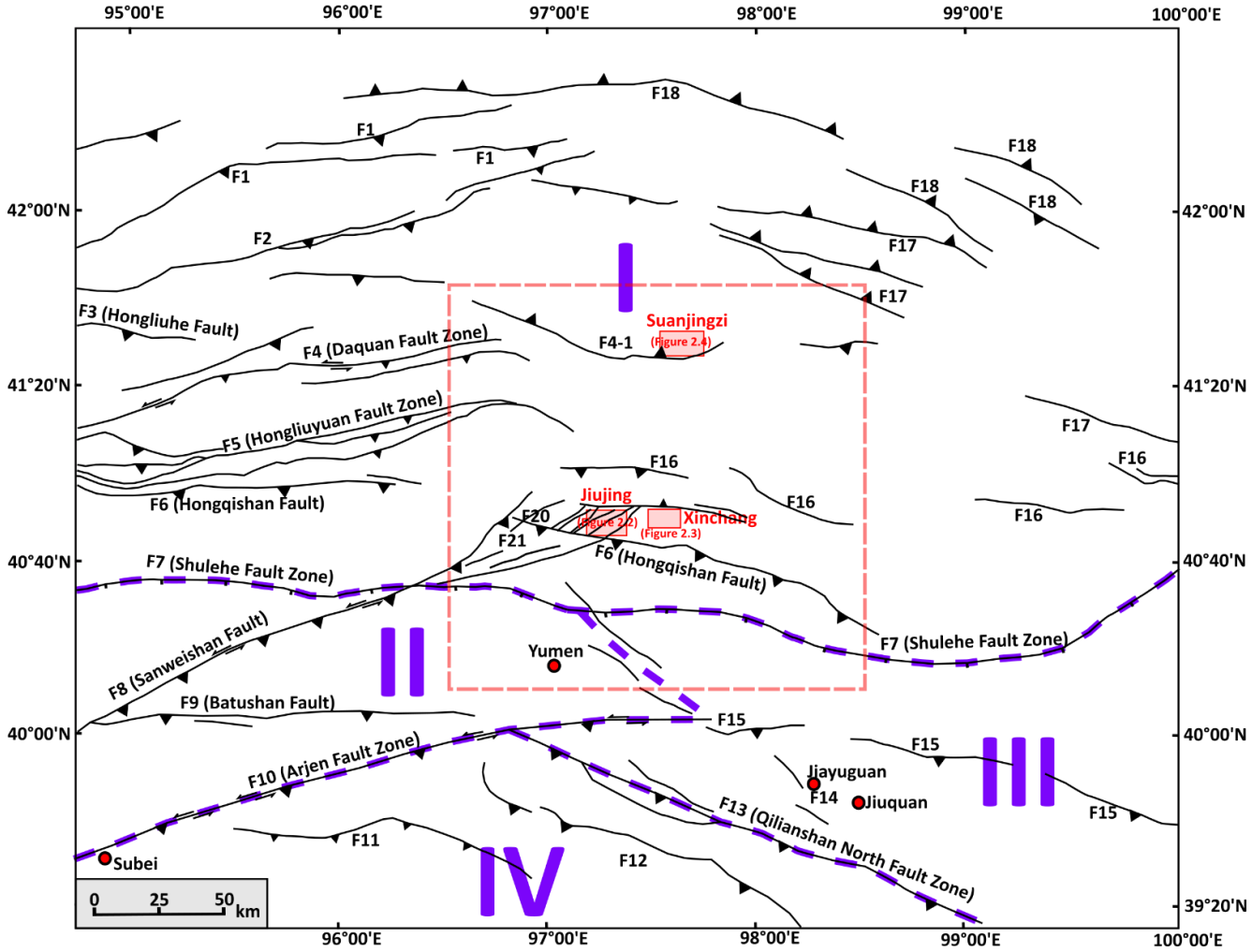


Figure 2.1 The illustration of Beishan area (highlighted by dashed red box and the location labelled in Figure 1.3) and the regional structure geology. This figure was adapted from Yun [32] and Niu [33]. The granite outcrops at Suanjingzi, Jiujing and Xinchang are highlighted by solid red rectangles. The solid black lines represent the major faults, and their characteristics are summarised in Table 2.1. The area can be divided into four parts: the weak uplift area around Beishan (I), the differential sedimental areas in Anxi (II) and the Hexi Corridor (III), and the strong uplift area in Qilianshan (IV).

Table 2.1 The characteristics of faults in Beishan area (location shown in Figure 2.1). Reference: Yun [32]

Fault No.	Fault name	Dipping direction	Shearing Properties	Dip angle	Activation period
F_1	Aqikuduke Fault Zone	SE	Reverse	50°-80°	Early& Mid Pleistocene
F_2	Shaquanzi-Niya Fault Zone	SE	Reverse	50°-80°	Early& Mid Pleistocene
F_3	Hongliuhe Fault Zone	S	Reverse	60°-70°	Early& Mid Pleistocene
F_4	Daquan Fault Zone	SE	Reverse	33°-70°	Early& Mid Pleistocene
F_5	Hongliuyuan Fault Zone	S	Reverse	60°-80°	Pre-Quaternary
F_6	Hongqishan Fault Zone	S	Reverse	60°	Pre-Quaternary
F_7	Shulehe Fault Zone	S	Normal	50°-80°	Early& Mid Pleistocene
F_8	Sanweishan Fault Zone	SE	Reverse (sinistral)	50°-70°	Holocene
F_9	Batushan Fault	S	Reverse (sinistral)	50°-80°	Late Pleistocene
F_{10}	Arjen Fault Zone	SE	Reverse (sinistral)	50°-80°	Holocene
F_{11}	Daxueshan Fault Zone	SW	Reverse (sinistral)	50°-70°	Holocene
F_{12}	Changma-Ebo Fault Zone	SW	Reverse (sinistral)	60°-80°	Holocene
F_{13}	Qilianshan-North Fault Zone	SW	Reverse (sinistral)	40°-80°	Holocene
F_{14}	Jiayuguan-Wenshushan Fault	SW	Reverse (dextral)	73°-85°	Holocene
F_{15}	Jintananshan Fault Zone	SW	Reverse	60°-80°	Holocene
F_{16}	Baiyunshan Fault Zone	S	Reverse	50°-70°	Pre-Quaternary
F_{17}	Shibanjing Fault Zone	S	Reverse	60°-70°	Pre-Quaternary
F_{18}	Liutuofeng Fault Zone	S	Reverse	50°-70°	Pre-Quaternary
F_{19}	Jiujing Faults	NW	Normal	50°-80°	Pleistocene
F_{20}	Qiaowan Faults	NW	Normal	49°-80°	Early& Mid Pleistocene

As indicated by Yun [32], GPS data suggests the collision between the Indian Plate and Eurasian Plate led to a ground rotation around Beishan towards the east since Cenzoic period. This generated the NE-SW trending horizontal compression and finally led to the formation of left-strike slip (sinistral) thrust faults trending in the NW and NWW directions. As indicated by Wang [34], these NW or NWW trending reverse faults are generally older and more deformed than normal NE trended faults within Beishan.

Yun [32] also suggested most faults around Beishan are distributed along the edge of mountains, such as the Yingjushan Fault, Yemashan Fault, Tulaishan Fault, Daxueshan Fault, Qilianshan Fault, Sanweishan Fault and Batushan Fault. These faults were formed in the early Cenzoic era during the uplift of the Qinghai-Tibet Plateau and remain active today. The deformations along these faults are thrust-dominated during Paleogene to early Pleistocene and then converted to strong sinistral strike slip in middle Pleistocene.

Within the faults presented in Figure 2.1 and Table 2.1, it is important to note the overall tectonic activities in Beishan are controlled by Arjen Fault Zone and Sanweishan Fault Zone. Arjen Fault Zone

controls the northern boundary of Qinghai-Tibetan Plateau, which activates the Sanweishan Fault Zone and in turn trigger the displacements in Suanjingzi, Jiujing and Xinchang. The detail description about Arjen Fault Zone and Sanweishan Fault Zone are presented as follows, these assists the interpretation of local tectonic structures.

2.2.1 Arjen Fault Zone (F_{10} in Figure 2.1)

As indicated by Guo [35], the Arjen Fault Zone is a NE trending left-strike-slip (sinistral) reverse fault dipping towards the southeast, which controls the northern boundary of the Qinghai-Tibetan Plateau. The movement of Indian subcontinent towards the north-east since Cenozoic led to the uplift of Qinghai-Tibetan Plateau, which then led to the activation of the Arjen Fault zone. According to Guo [36], Ritts [37], Matte [38] and Meng [44], the distance of the displacement ranges from 320 km to 600 km. In general, according to Guo [35], the horizontal displacement decreases towards the east, where the strike-slip rate is 20-30 mma^{-1} at the west end of the fault, 17.5±2 mma^{-1} in the middle and 11±3.5 mma^{-1} in the east between Subei and Shibaocheng.

The Arjen Fault Zone played a dominant role in the formation of Cenzoic structures and tectonic activity in Beishan. As suggest by Guo [35], the effects of sinistral strike-slip and the folding of Qilianshan Mountain largely absorbed the activation energy triggered by the movement of the Qinghai-Tibetan Plateau within the north side of the fault zone. According to Molnar [45], this absorption rate is around 10% to 25%. Therefore, as indicated by Guo [22] and [35], the tectonic activity is weak at the north-east end of Arjen Fault. As the Qilianshan Mountain and the foreland thrust impeded further deformations of the Arjen Fault, the strike-slip component of the Arjen fault in turn led to the formation of the Sanweishan-Shuangta Fault (F_8), Aqike-Daquan Fault (F_4) and Hongliuhe Fault (F_3) in Figure 2.1. The striking directions of above faults are all parallel with the Arjen Fault having sinistral shearing properties.

Wang [34] suggested the compressive stress which transmitted from the Arjen Fault zone (F_{10} in Figure 2.1) towards the north is characterised by the effects of hysteresis and attenuation, where the Cenzoic tectonic structures in Beishan are both weaker and younger than those in the Qinghai-Tibetan Plateau (the strong uplift area (IV) shown in Figure 2.1). Guo [35] suggested the Sanweishan-Shuangta Fault Zone, Daquan Fault Zone and their associated EW trending branch faults were activated in the Pliocene, 1.5-1.2 Ma and after 400 ka, which indicates these faults are more recent towards the further north-west and suggested the Arjen fault zone is currently expanding in this direction. It is predicted that these reverse faults will become increasingly deformed during the uplift of Qinghai-Tibetan Plateau. Since Sanweishan-Shuangta and Daquan Fault Zones are derivative faults of Arjen

Fault Zone and the activation energy driven by the movement of Qinghai-Tibetan Plateau are attenuating northwardly, this explains why the deformation rates along these two faults are way lower than that along the Arjen Fault. The reviews about the Sanweishan Fault Zone are as follows.

2.2.2 Sanweishan Fault Zone (F_8 in Figure 2.1)

The Sanweishan Fault zone (F_8) is widely believed to be a NE50-70^o trending sinistral strike-slip fault dipping towards the south-east with a reverse component [32, 35, 46]. There is debate concerning this activity between Guo [35] and Yun [32]. Guo [35] first suggested F_8 was active in the early Cenozoic before finally becoming locked in the late Pleistocene. This led to a 100-500m sinistral displacement along the fault plane. Then, Yun [32] suggested since the late Pleistocene the Sanweishan Fault, Jiujing Fault and Bantan Fault have been active, most recently 7.4-2.4 k years ago for the Sanweishan Fault and 22 k years ago for the Jiujing Fault. According to Yang [46], since the late Pleistocene, the sinistral shearing rate and vertical displacement rate have been estimated to be 0.06-1.25 mma^{-1} and 0.05-0.08 mm a^{-1} along F_8. The Sanweishan Fault Zone is still in active.

2.2.3 In-situ measurements of tectonic stress

The movement and collision of tectonic plates controls tectonic forces, which therefore creates the regional stress field [47]. As indicated by Zhao [48], the in-situ stress in the rock mass at depth is influenced by gravity, Earth's tectonic plate movement, underground water pressure, and heat. Where the gravity of overlaying rock mass governs the magnitude of vertical stress, and the tectonic movements govern the horizontal stress orientation. In this way, the maximum horizontal compression (S_H) reflects the direction of tectonic movement.

In the case of Beishan, as indicated by Ma [49], the general direction of maximum horizontal stress (S_H) is NNE-NEE, for which the detailed measurements from Niu [33] and Ma [49] based on Boreholes BS01, BS05, BS06, BS15, BS16, BS17, BS18, and BS19 in Jiujing (borehole location shown in Figure 2.2), Xinchang and Jijicao regions are presented in Table 2.2. In general, as described by Ma [49] and Zhao [48], the magnitude of compressive stress gradually increases with depth and 81% of S_H values are larger than S_V values, suggesting the in-situ stress field in Beishan is controlled by tectonic processes.

Table 2.2 The measurements of maximum horizontal compression (σ_1), minimum horizontal compression (σ_3), and vertical compression (σ_v) in Beishan. Data sources: Niu [33] and Ma [49].

Location	Borehole	Depth (m)	σ_1 (MPa)	σ_3 (MPa)	σ_v (MPa)	σ_1 Direction
Jiujing	BS01	166.5	7.11	4.12	4.49	N25°E
		252.4	7.71	4.71	6.81	N30°E
		339	6.51	4.72	9.15	N38°E
		413.3	12.56	8.37	11.15	N45°E
Jijicao	BS05	114	11.62	6.47	2.96	N2°E
		198.5	9.86	6.26	5.16	N13°W
		305	12.41	8.08	7.94	N22°W
Xinchang	BS06	113.5	7.93	4.97	2.95	N53°E
		341.5	11.2	7.96	8.88	N67°E
		502.5	13.89	9.93	13.07	N52°E
Jijicao	BS015	65.97	6.77	3.78	1.75	N60°E
		81	5.11	3.65	2.15	N25°E
		107.05	5.22	3.67	2.84	N48°E
		146.6	5.55	4.13	3.88	N79°E
		318.77	7.28	5.18	8.45	N74°E
		426.13	8.41	7.16	11.29	N10°E
Jijicao	BS016	118	6.6	4.36	3.13	N73°E
		150.19	7.74	4.9	3.98	N47°E
		206.5	8.64	5.4	5.47	N18°E
		248.5	6.62	4.87	6.59	N5°E
		287.5	12.29	7.85	7.62	N17°E
		471.5	14.64	9.82	12.49	N7°E
		570.5	17.7	11.79	15.12	N10°E
Xinchang	BS017	158.2	6.76	4.86	4.19	N67°E
		254	10.59	6.91	6.73	N56°E
		314.6	7.07	5.56	8.33	N60°E
		446.5	19	12.72	11.83	N53°E
		482	23.76	14.99	12.77	N60°E
Xinchang	BS018	223	12.14	7.82	5.91	N45°E
		406	11.58	8.35	10.76	N50°E
		431	11.76	8.6	11.42	N45°E
		493	18.82	12.28	13.06	N73°E
		512	16.78	11.19	13.57	N56°E
Xinchang	BS019	167	7.27	5.38	4.43	N62°E
		180	9.73	6.48	4.77	N54°E
		263	9.8	6.34	6.97	N59°E
		441	16.08	11.04	11.69	N60°E
		484	13.41	10.33	12.83	N63°E
		508.6	19.67	12.8	13.48	N77°E

2.3 The history of magmatic activities and exposed stratigraphy in Beishan

The stratigraphy in Beishan was formed in 6 eras, chronologically, these include Early Proterozoic to Archaean, Middle and late Proterozoic, Early Paleozoic, Late Paleozoic, Mesozoic, and Cenozoic [50].

According to Tian [50], the oldest stratigraphy found in study area can be traced to the Archaean-Early Proterozoic era. It is a set of formation composed by terrestrial clastic, carbonate, and volcanic rocks that were deposited in neritic facies. These formed the Dunhuang Rock Group (include the Huayaoshan, Yujishan, Dakouzi, and Laojunmiao Formations, described in Table 2.4). The earliest massive intrusion started in Middle Proterozoic era (1229 to 1589Ma), this led to the formation of Jiujing Tonalite Unit ($Pt_2^2J\delta o\beta$, distribution shown in Figure 2.2). A strong shear stress field was formed due to the intrusion of Tonalite magma, this led to the formation of gneissic schistosity and EW trended ductile shear zone.

The Porphyritic monzogranite in Bantan Unit ($Pt_2^3B\eta\Upsilon$, distribution shown in Figure 2.2) was intruded in middle and late Proterozoic era (609 ~ 619Ma) along with the formation of some tensile fractures filled by amphibolite dikes. In late Proterozoic, the Xianshuijing Group (Chxs, distribution shown in Figure 2.2) formed in Mid-Proterozoic is metamorphized by low temperature dynamic processes. No evidence of depositional activities was found in middle and late Proterozoic and Early Paleozoic eras, but the Quartz diorite in Jiazijing Unit ($S_3J\delta o$, distribution shown in Figure 2.2) was intruded in end Silurian. This period is accompanied by weak deforming activities symbolised by the formation of the EW trended folding in the stratigraphy of Dunhuang Rock Group [50].

The weathering denudation continued in late Paleozoic. The collision induced orogenesis led to the activation of ductile shear zone. This period is characterised by intense tectonic deformation and magmatic intrusive activities triggered by Hercynian movement. The Suanjingzi granodiorite was formed in early carboniferous, the diagenetic age is around 350 to 359 Ma. Due to the impact of Piedmont faults which trend NE and NW, the Suanjingzi granodiorite is distributed NE-SW. This is in alignment with the direction of main structure line [51]. The Suanjingzi granodiorite can be divided into three units, which are Sandaomingshui North Unit ($CS^1\Upsilon\delta$), Sandaomingshui Unit ($CS^2\Upsilon\delta$), and Sandaomingshui East Unit ($CS^2\Upsilon\delta$) (distribution shown in Figure 2.4). These three units interlocked spatially and originated in same felsic magma but crystallised in different stage. They intruded into the Silurian Gongpoquan Group (S_2gp) and lower Carboniferous Baishan Formation (C_1b), then get covered by upper cretaceous Chijinbao Formation (K_1c) in an unconformity [51, 52].

During Permian, the Xinchang granite, which includes Hongliujing-Nanshan unit (Pt^2_2H), Xinchang unit (O_1X), Jijinggou unit (O_1J) and Yuanyanggou unit (Pt^2_2Y) (distribution shown in Figure 2.3), were first

intruded [65]. Then at the end of Permian, the muscovite monzogranite in Jiujing Shimenkan Unit ($P_2S\eta\Upsilon$, distribution shown in Figure 2.2) was intruded. After that, the tectonic stabilised and no deposition was found until Mesozoic [50].

Cenozoic is characterised by a slow ground uplift. The weathering and erosional processes formed the planation surface and led to the exposure of the intruded granite plutons in Xinchang, Jiujing and Suanjingzi. Meanwhile, the diluvium and alluvium sediments were accumulated in Quaternary sedimentary basins. These form the geomorphology observed in modern time [50].

2.4 A review of the geology in Jiujing study area

2.4.1 The lithology of the Jiujing granite outcrop and the exposed stratigraphy

The granite outcrop in Jiujing can be divided into four units, the Jiujing (middle-Proterozoic), Bantan (middle-Proterozoic), Jiazijing (Silurian) and Shimenkan (Permian) [53]. The Jiujing unit is composed of tonalite with an area of 220 km^2 and the Bantan unit is composed of porphyritic-monzonitic granite with an area of 53 km^2 [54]. Their distribution and full descriptions are presented in Figure 2.2 and Table 2.3.

Most of the exposed stratigraphy in Jiujing were formed in the Early Proterozoic to Archaean periods. Their lithologies are summarised in Table 2.4. Overlying the granite, there are Quaternary sediments such as Alluvial and Diluvium distributed on the surface of granite rocks in the Bantan Basin, Ba'antan Basin and Jiujing (Shiyuejing) Basin (shown in Figure 2.2), which are mainly composed of loose sandy gravel, coarse sand, and clay [55]. Due to the subsidence caused by faulting (F_{16}, F_{18} and F_{20}), the Bantan Basin, Ba'antan Basin and Jiujing Basin have lower elevations compared to surrounding blocks, which results in the discharge of shallow groundwater, surface water and floodwater towards the centre of the basins [34, 55, 56], leading to the sediments being eroded and deposited during the wet season.

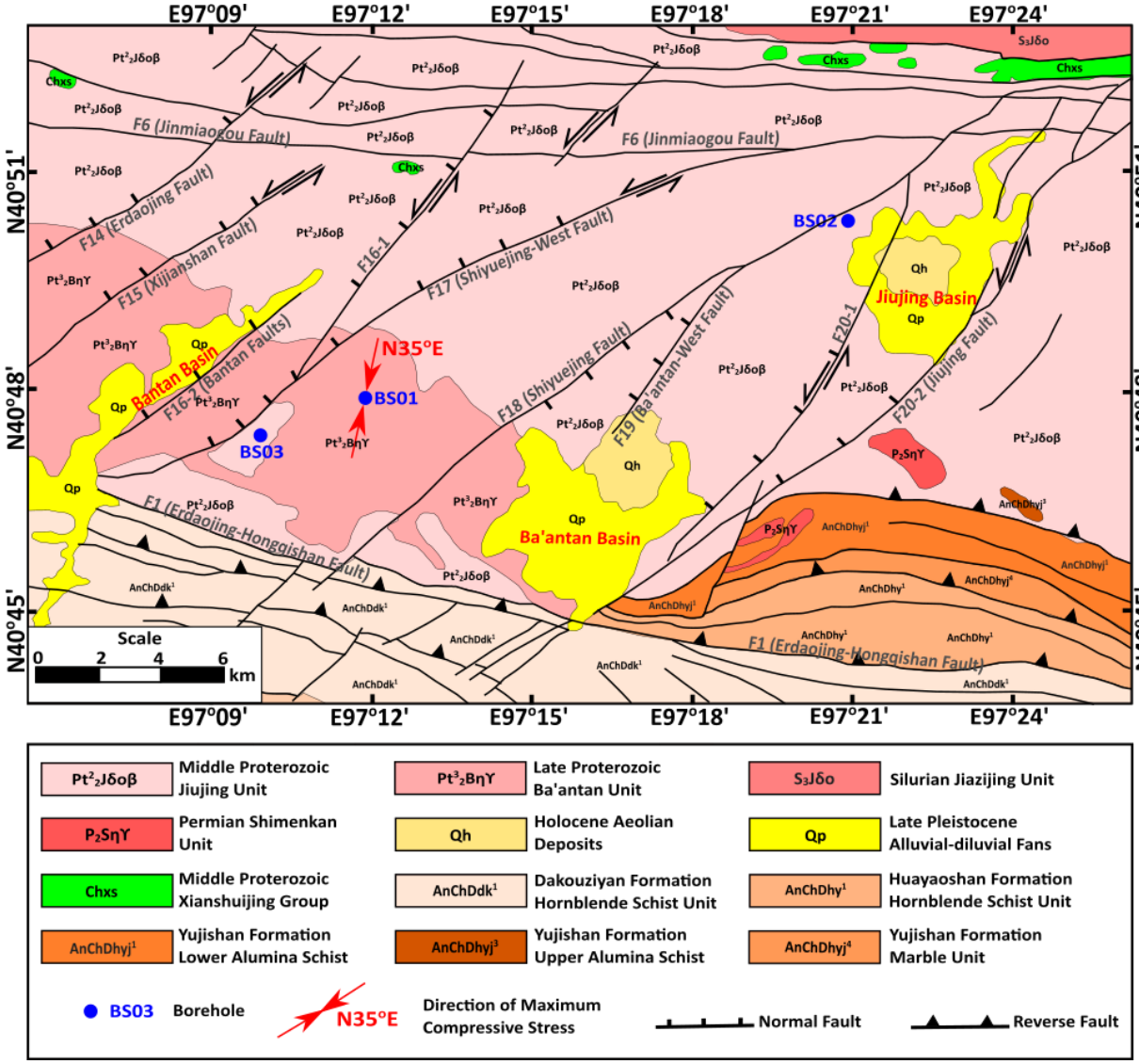


Figure 2.2 The geological map of Jiujing study area shows the distribution of major faults (characteristics summarised in Table 2.5), granite units (lithology summarised in Table 2.3) exposed stratigraphy (lithology summarised in Table 2.4), Quaternary sediments at Jiujing, Bantan, and Ba'antan Basins, and the locations of boreholes BS01, 02, and 03. (Figure adapted from Wang [53] Guo [57], and Yun [58])

Table 2.3 The description of major Jiujing granite units. Distribution shown in Figure 2.2. Reference: [53]

Unit	Jiujing Unit	Bantan Unit	Jiazijing Unit	Shimenkan Unit
Code Number	$Pt_2^2J\delta o\beta$	$Pt_2^3B\eta\Upsilon$	$S_3J\delta o$	$P_2S\eta\Upsilon$
Geological Period	Mid Proterozoic	Late Proterozoic	Silurian	Permian
Lithology	Tonalite	Porphyritic monzogranite	Quartz diorite	Muscovite monzogranite
Area	220km^2	53km^2	4.3km^2	2.5km^2
Depth	13-20km	6.5-13km	--	--
Age	1589.13Ma	609.62Ma	--	244Ma

Table 2.4 The description of major exposed stratigraphy in Jiujing. Distribution shown in Figure 2.2. Reference: [53]

Geological Period	Formation/Group	Unit	Code	Lithology
Holocene	--	--	Qh	clay and loam
Late Pleistocene	--	--	Qp	loose sand and gravel
Mid-Proterozoic	Xianshuijing	--	Chxs	Basalt, andesite, tuff
Early Proterozoic to Archaean	Huayaoshan	Hornblende Schist	$AnChDhy^{1}$	Hornblende schist, chlorite schist, dolomite schist, biotite quartzite, biotite calcite schist
	Yujishan	Marble	$AnChDhyj^{4}$	Marble, quartz marble, biotite quartz schist, biotite plagioclase granulite
		Upper Alumina Schist	$AnChDhyj^{3}$	Biotite schist, mica schist, dolomite schist
		Lower Alumina Schist	$AnChDhyj^{1}$	Biotite schist, mica schist, chlorite schist
	Dakouziyan	Hornblende Schist	$AnChDdk^{1}$	Hornblende schist

2.4.2 The structural geology in Jiujing outcrop

Tectonically, Jiujing is at the north-east end of the Sanweishan fault zone, which controls the crustal stability in this region. As indicated by Yun [32], the strong left-strike-slip (sinistral shearing) of the Sanweishan Fault led to an extensional environment at the north-east end, which in turn formed the extensional sinistral branch faults F_{14}, F_{15}, $F_{16\text{-}2}$, F_{17}, F_{18}, F_{19}, F_{20} and $F_{20\text{-}1}$ in Jiujing. Altogether with the main fault (Sanweishan Fault, F_8 in Figure 2.1), these faults have a flower-shaped distribution. According to Guo [35], these branch faults in Jiujing generally form in a 30^{o} to 50^{o} eastwards inclination compared with the main fault. These faults are rotating in a clockwise direction and showing a domino structure. According to Yun [32], the branch faults with the lowest angle to the main fault (Sanweishan Fault Zone) usually have the highest tectonic activity. This can therefore explain why the Jiujing Fault (F_{20}) has a higher deformation than the Bantan Fault (F_{16}).

Overall, according to Guo [35], the small branch faults at the north-east end of the Sanweishan Fault Zone act to disperse the energy they transmitted, which further weakens any potential for activation and significantly reduces the deformation along each fault plane. This is also the reason why Beishan, especially Jiujing and Xinchang, have been described as the most stable region within in active zone. Therefore, the selection of these areas to host a GDF would support a more robust safety case.

Table 2.5 The characteristics of major fault structures in Jiujing study area. Distribution shown in Figure 2.2.

Fault No.	Fault name	Dipping direction	Shearing Properties	Dip angle	Reference
F_1	Erdaojing-Hongqishan Fault	S or N	Reverse (Dextral or sinistral)	--	[34, 59]
F_6	Jinmiaogou Fault	S or N	Normal (sinistral)	60^o-75^o	[60, 61]
F_{14}	Erdaojing Fault	NW	Normal (sinistral)	63^o	[59]
F_{15}	Xijianshan Fault	NW or SE	Normal (sinistral)	$\approx 90^o$	[59]
$F_{16\text{-}1}$	Bantan Faults	NW	Normal	--	[59]
$F_{16\text{-}2}$	Bantan Faults	NW	Normal (sinistral)	75^o	[59]
F_{17}	Shiyuejing-West Fault	NW	Normal (sinistral)	80^o	[59]
F_{18}	Shiyuejing Fault	NW or SE	Normal	70^o-80^o	[34, 59]
F_{19}	Ba'antan-West Fault	NW	Normal	$\approx 90^o$	[59]
$F_{20\text{-}1}$	Jiujing Faults	NW	Normal (sinistral)	--	[34, 59]
$F_{20\text{-}2}$	Jiujing Faults	NW	Normal (sinistral)	--	[34, 59]
$F_{20\text{-}3}$	Jiujing Faults	NW	Normal (sinistral)	--	[34, 59]
$F_{20\text{-}4}$	Jiujing Faults	NW	Normal (sinistral)	--	[34, 59]

As shown in Figure 2.2, there are two main sets of faults that divide the Jiujing region into rhombus-shaped blocks. The published literature on the characteristics of the above faults is summarised in Table 2.5.

The first set of faults are northeast-trending (around 50°N) strike-slip faults with clear sinistral shearing properties, this is mainly due to the maximum horizontal compressive stress in the direction of NE-SW. These include the Erdaojing Fault (F_{14}), Xijianshan Fault (F_{15}), Bantan Faults ($F_{16\text{-}1}$, $F_{16\text{-}2}$), Shiyuejing-West Fault (F_{17}), Shiyuejing Fault (F_{18}), Ba'antan-West Fault (F_{19}) and Jiujing Faults ($F_{20\text{-}1}$, $F_{20\text{-}2}$, $F_{20\text{-}3}$, and $F_{20\text{-}4}$), which were most active in the late Pleistocene era (126,000–12,000 years ago) [62]. These faults cut the Jiujing granite outcrops into several parallelograms.

The F_{20} fault cluster control the east boundary of the Jiujing Basin and Bantan Basin. Guo [35] suggested the fault started to be active approximately 350 ka BP, and the last activity was in the late Pleistocene to Holocene [46, 58, 59]. Wang [34] suggested the last tectonic activity along F_{20} is around 17.56±1.49ka to 8.55±1.49ka. This time was estimated through the measurements of fault wedge age using thermoluminescence dating techniques. The vertical and horizontal displacement rates along fault plane are estimated as 0.03±0.01 mma^{-1} and 0.18 mma^{-1} respectively. These rates were calculated based on the extents of vertical and horizontal offsets. Yun [59] then suggested the timing of the movement started around 22ka (estimated through thermoluminescence dating) with horizontal displacement extent around 1.3 to 3.5m (estimated through the offsets of the stratigraphy). Yun [58] confirmed the Jiujing faults had been reactivated in the last 20ka (late period of the Late Pleistocene) due to the northward's movements of the Qinghai-Tibetan Plateau. The three authors

have slightly different views about the fault's last activity time. This might be due to two reasons. First, the activities vary along the fault plane and the observation points chosen by each study are different. Second, the sediment samples which selected for thermoluminescence dating might be different, this further influence the results. However, the above literatures remain arguable regarding the activities along F_{20} in recent time, this will be discussed in Section 6.4.

Yun [59] suggested $F_{16\text{-}2}$ controls the east boundary of the Bantan Basin, with an elevation difference of around 20 m between the east and west sides of the fault, where $F_{16\text{-}1}$ and $F_{16\text{-}2}$ were weakly activated since the late Pleistocene, hinting that $F_{16\text{-}1}$ and $F_{16\text{-}2}$ may still be active today. Based on these comments $F_{16\text{-}1}$ (Section 6.4.1) and $F_{16\text{-}2}$ have been investigated and the results can be found in section 6.4. It was this ongoing uncertainty regarding the tectonic activity in the region which in part lead to this investigation.

Yun [59] also indicated the Holocene sediments covering the F_{17} and F_{18} show no evidence of displacement along fault planes concluding no activities has been found since the Holocene and suggested F_{17} and F_{18} were locked in the early to middle Pleistocene. However, Wang [34] suggests the last activity event along F_{18} was around 46.30±3.94ka (Late Pleistocene), this indicated F_{18} was in fact active since the late Pleistocene, and it slipped towards the dipping direction (southeast). The investigation of the recent tectonic activity along F_{17} and F_{18} can be found in Section 6.4.1.

The second set of faults include the Erdaojing-Hongqishan Fault (F_1) and Jinmiaogou Fault (F_6). They are formed much earlier than the above NE trended sinistral normal faults. These two east-west trending fault zones control the south and north boundaries of the Jiujing region respectively. Wang [34] indicated the last activity of the Jinmiaogou Fault (F_6) and Erdaojing-Hongqishan Fault (F_1) was about 500ka (Middle Pleistocene) and 111.98±9.52ka (late Pleistocene) respectively through the estimation of fault wedge age using thermoluminescence dating techniques. Several studies considered them as south dipping reverse faults with sinistral shearing components, but as presented in Table 2.5, their dipping directions, and shearing properties are still in arguable. That is because the above studies interpreted the fault characteristics based on field observations. F_1 and F_6 are fault zones with widths more than 1km [59] and are characterised by multiperiodic activities in the Middle Pleistocene [62]. These lead to complex structures within fault zones and make it is difficult to interpretate the fault characteristics solely based on field observations. Through the application of InSAR displacement pattern along fault plane, this research attempted to understand their characteristics in Section 6.4.

2.5 A review of the geology in Xinchang study area

2.5.1 The lithology of the Xinchang granite outcrop and the exposed stratigraphy

The total exposure area of Xinchang granite pluton is around 100km^2, which can be divided into four units based on lithology, including Hongliujing-Nanshan unit (Pt^2_2H), Xinchang unit (O_1X), Jijinggou unit (O_1J) and Yuanyanggou unit (Pt^2_2Y). Their characteristics are summarised in Table 2.6.

The exposed stratigraphy around Xinchang includes the Early Proterozoic to Archaean Yujishan Formation (AnChDyj), Mid-Proterozoic Xianshuijing Formation (Chxs), Jurassic Jijigou Formation (J_1j), Jinmiaogou Formation (J_2jm) and Shazaohe Formation (J_3S), Cretaceous Hongliujing-Gedajing Formation (K_1xn^1) and Holocene sediments (Qh). Their lithological characteristics are described in Table 2.7 and distributions are shown in Figure 2.3

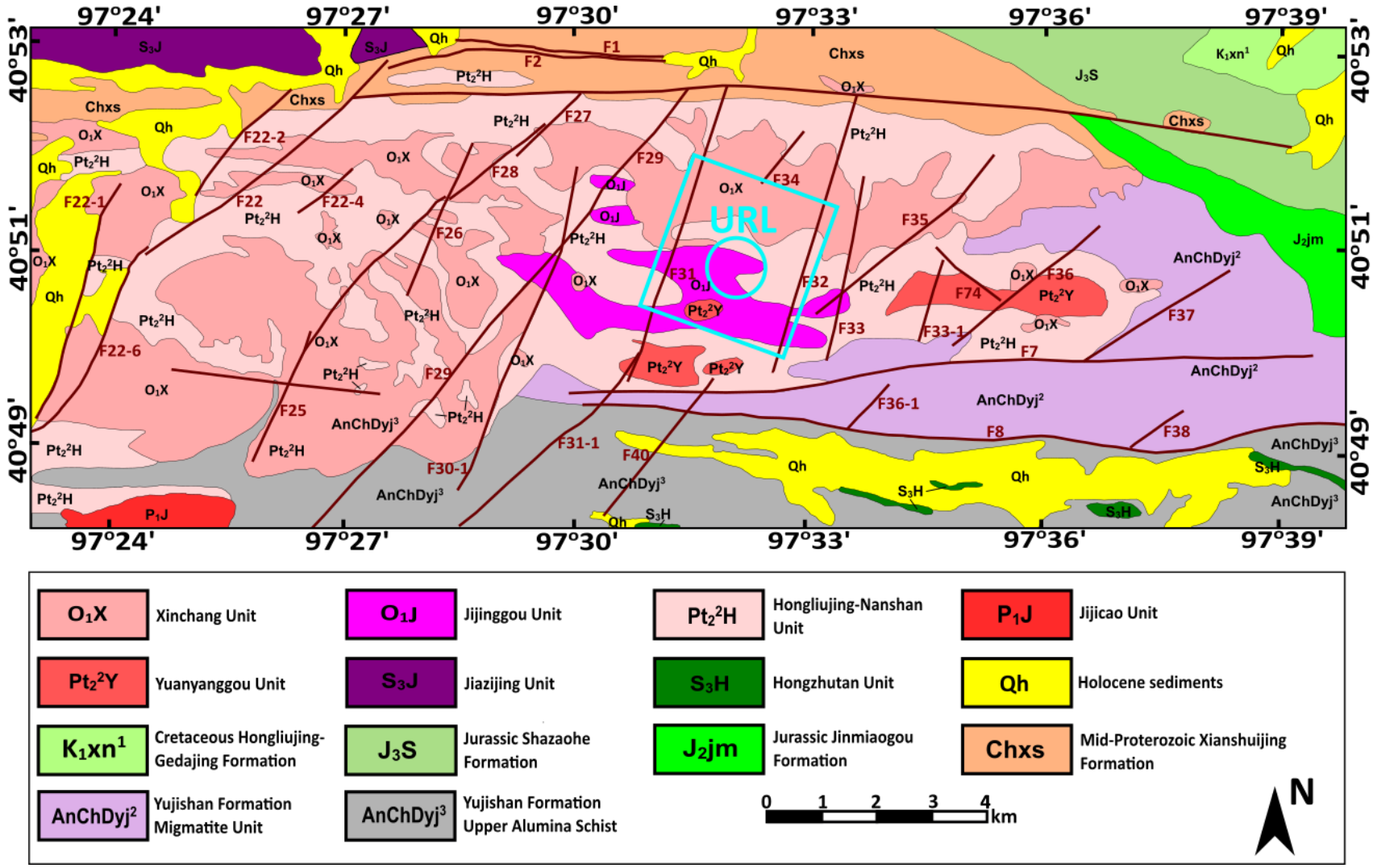


Figure 2.3 The geological map of Xinchang study area shows the distribution of major faults (characteristics summarised in Table 2.8), granite units (lithology summarised in Table 2.6) exposed stratigraphy (lithology summarised in Table 2.7), Quaternary (Holocene) sediments, and the location of the Underground research laboratory (URL). (Figure adapted from Luo [60] and Wang [63])

Table 2.6 The description of major granite units in Xinchang study area. Distribution shown in Figure 2.3. Reference: [60, 63, 64]

Unit	Hongliujing-Nanshan Unit	Xinchang Unit	Jijinggou Unit	Yuanyanggou Unit
Code	Pt^2_2H	O_1X	O_1J	Pt^2_2Y
Age	235-296 Ma	235-296 Ma	235-296 Ma	235-296 Ma
Lithology	Gneissic biotite granodiorite	Biotite monzogranite	Fine sized granodiorite	Gneissic monzogranite
Mineral composition	Quartz:25%, Plagioclase:40-45%, Alkali feldspar:15%	Quartz:20%-25%, Plagioclase:35-40%, Microcline:30-35%, Biotite:5%	Quartz:15-20%, Plagioclase:70%, Alkali feldspar:5-10%, Hornblende:5-7%, Biotite:7-8%	Quartz:25%, Alkali feldspar:32%, Plagioclase:36%, Others:6%
Area	--	42 km^2	--	--

Table 2.7 The description of major exposed stratigraphy in Xinchang study area. Distribution shown in Figure 2.3. Reference: [60]

Geological Period	Formation/Group	Code	Lithology
Holocene	--	Qh	Composed by diluvial and alluvial sandy gravel, sand, and loam deposits. The thickness is around 5-10m.
Cretaceous	Hongliujing-Gedajing	K_1xn^1	Composed by grey-brown coloured boulder conglomerate. The lithologies of conglomerate are granite, schist, gneiss, and quartzite.
Jurassic	Shazaohe	J_3S	The Shazaohe Formation can be divided into two units: Upper unit (J_3S^1): composed by grey coloured conglomerate, sandstone, and argillaceous siltstone. Lower unit (J_3S^2): composed by red brown coloured conglomerate, silty mudstone, and mudstone.
	Jinmiaogou	J_2jm	The Jinmiaogou Formation can be divided into two units: Upper unit (J_2jm^2): grey-green coloured fine and coarse sandstone and brown coloured conglomerate sandstone, fine sandstone, sandy mudstone, and mudstone. Lower unit (J_2jm^1): light grey coloured sandy mudstone, mudstone, siltstone, and fine sandstone.
	Jijigou	J_1j	The Jijigou Formation can be divided into two lithological units: Conglomerate unit (J_1j^1): purple coloured conglomerate. Sandstone unit (J_1j^2): yellow brown coloured siltstone, medium and fine sized sandstone, sandy mudstone, and coarse sandstone.
Mid-Proterozoic	Xianshuijing	Chxs	Composed by metamorphized basalt, andesite, sandstone and phyllite, tuff and slate.
Early Proterozoic to Archaean	Yujishan	AnChDyj	Migmatite unit ($AnChDhyj^2$): stripped, striation and augen shaped migmatite. Upper Alumina Schist ($AnChDhyj^3$): Biotite schist, mica schist, dolomite schist.

2.5.2 The structural geology in Xinchang outcrop

Luo [60] suggested the faults in the Xinchang region can be divided into three groups based on the trending directions NE, NW, and EW. Most EW trended faults are reverse or compressive strike-slip faults characterised by multiperiodic activity, this includes F_6, F_7 and F_8 (Figure 2.3 and Table 2.8).

These EW trended reverse faults led to the formation of NE trended extensional left-strike slipping faults with lengths of around 2-5 km. Typical examples include F_{28}, F_{29}, F_{30}, F_{31}, F_{32}, F_{33}, F_{34}, F_{35} and F_{36}. This is mainly due to the shear stress inserted by a maximum compressive stress in NE-SW direction. The detailed explanation in a perspective of geomechanics can be found in Section 6.2 and the distribution and characterisations of these faults in Xinchang outcrop are presented and summarised in Figure 2.3 and Table 2.8.

Table 2.8 The characteristics of major fault structures in Xinchang study area. Distribution shown in Figure 2.3

Fault No.	Fault name	Dipping direction	Shearing properties	Dip angle	Reference
F_6	Jijing-Jinmiaogou-Hongliuquan Fault	S or N	Early period: reverse Late period: normal (sinistral)	60°-75°	[34, 59, 61, 60,65]
F_7	Yuanyanggou Fault	S	Reverse (dextral)	50°-70°	[59, 60, 61, 65]
F_8		S	Normal or reverse	75°	[59, 61, 65]
F_{28}	Xinchang Fault	SE	--	80°	[59]
F_{29}		NW	Normal (sinistral)	54°-70°	[59, 60]
F_{29-1}		S	Normal	85°	[60]
F_{30}		NW	Normal	80°	[60]
F_{31}	Jijing Fault	NW	Normal (sinistral)	62°-86°	[59, 60, 61]
F_{32}	Jijing East Fault	NW	Normal or reverse (sinistral)	60°-80°	[59, 60, 61]
F_{32-1}		SE	Reverse	70°-79°	[60]
F_{33}		NW	Normal (sinistral)	60°-75°	[60, 61]
F_{34}		NW or SE	Normal	72°-87°	[59, 60]
F_{35}		NW	Normal (sinistral or dextral)	66°-70°	[59, 60]
F_{36}		NW or SE	--	60°-88°	[59, 61, 65]

In general, F_7 and F_6 control the south and north boundaries of the Xinchang, and the faults have a depth of around 2-3km [60]. As described by Yun [59], the Jinmiaogou Fault Zone (F_6) is a 1-3km width mylonite shearing zone, which was initially considered to be compressive in and then inverted into a sinistral normal fault. That might be due to the change of maximum compressive stress direction. The potential Underground Research Laboratory (URL), which may evolve into a GDF, is around the junctions of NE trended F_{31}, F_{32}, F_{33}, F_{34} and NW trended F_{32-1} (shown in Figure 2.3) and has been described as a "tectonic safe island" due to the inactivation of above fault in Quaternary period [60]. These fault planes have widths between 0.80 and 3.56m, where F_{32} and F_{33} extend to depths of more than 700m whilst the other faults have depths less than 300m estimated through the inversion of magnetic waves [60]. In Section 6.5 these "inactive" faults are investigated, understanding the potential for faults movement when developing any nuclear facility in essential to the development of the safety case.

Yun [59] suggested that F_7, F_8, F_{28}, F_{29}, F_{30}, F_{31}, F_{32}, F_{33}, F_{34} and F_{35} were formed more than 200 million years ago. Luo [60] indicated they were most active in the pre-Quaternary period, and then became less active in the early and middle Pleistocene and (most of them) finally became inactive in the late Pleistocene. This is approximately the same period as some Jiujing faults such as F_{20} (Section 2.1.2). As the Holocene talus and other sediments covered the fault region including the fault planes they were rarely disturbed by the fault-induced displacements, these faults can indeed be confirmed to be inactive during the Holocene [59]. However, the SAR detection in this research suggests that F_{29}, and F_{31} are in fact active or partially active, albeit the displacement rates are slight. This will be discussed in Section 6.5.

2.6 A review of the geology in Suanjingzi study area

2.6.1 The lithology of the Suanjingzi granite outcrop and the exposed stratigraphy

Suanjingzi is in the north part of Beishan study area around 200km from Yumen City (locations shown in Figure 2.1). The Suanjingzi granite is EW trending with a total outcrop area of around 200 km^2 (25km×8km) (Figure 2.4) [66]. Within the study area, the main exposed stratigraphy includes the Lower Cretaceous Chijinbao Formation (K_1c), Neoproterozoic Qingbaikou Series Dahuoluoshan Formation (Qbd), Lower Carboniferous Baishan Formation (C_1b), Middle Silurian Gongpoquan Group (S_2gp) and Holocene Sediments (Qh). Descriptions of these are presented below.

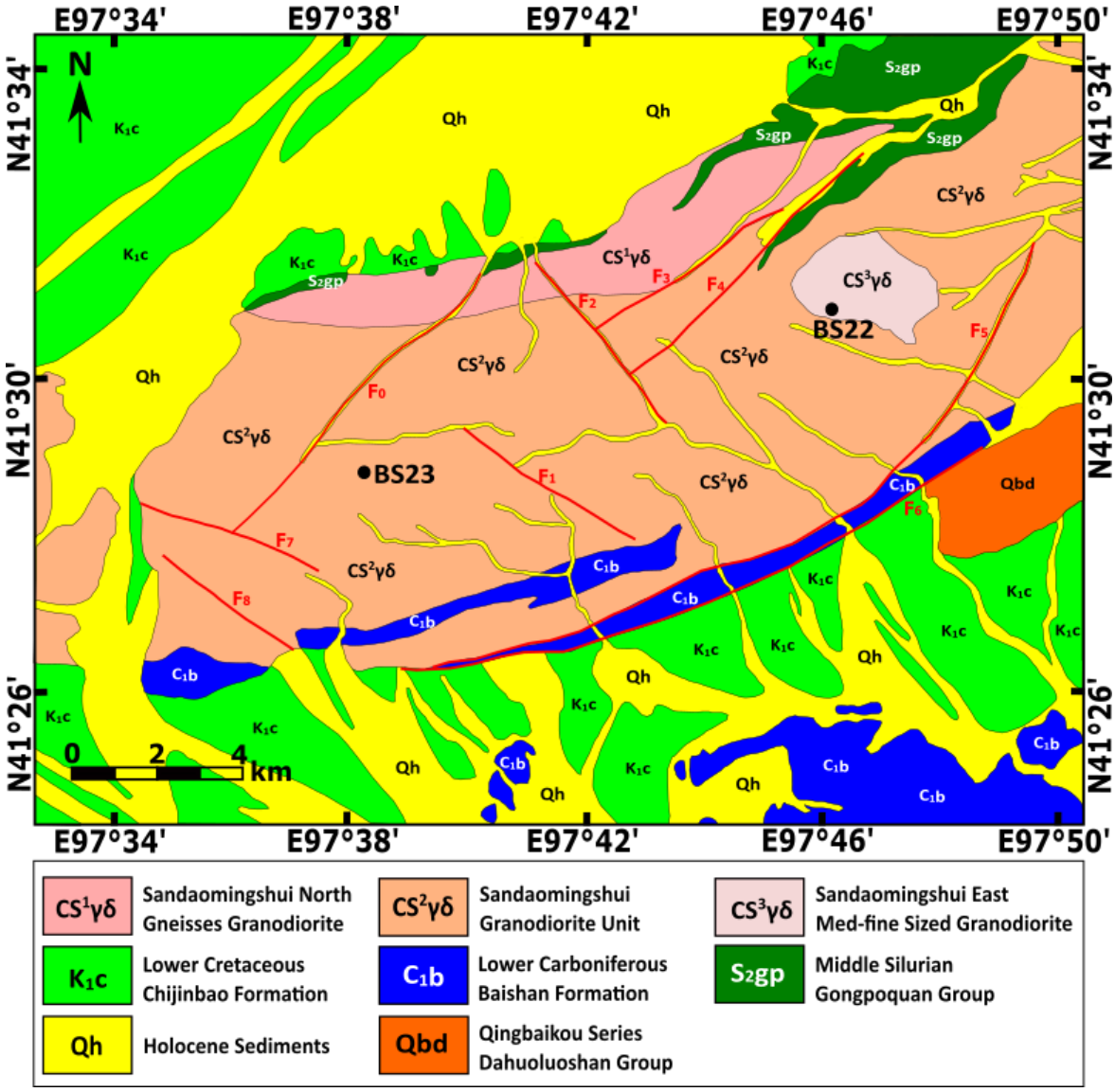


Figure 2.4 The geological map of Suanjingzi study area shows the distribution of major faults (characteristics summarised in Table 2.12), granite units (lithology summarised in Table 2.9) exposed stratigraphy (lithology summarised in Table 2.10), Quaternary (Holocene) sediments, and the location of the borehole BS22 and 23. (Figure adapted from Jiang [51])

Table 2.9 The description of major granite units in Suanjingzi study area. Distribution shown in Figure 2.4. Reference: [51]

Unit	Sandaomingshui North Unit	Sandaomingshui Unit	Sandaomingshui East Unit
Code Number	$CS^1\gamma\delta$	$CS^2\gamma\delta$	$CS^3\gamma\delta$
Geological Period	Early Carboniferous	Early Carboniferous	Early Carboniferous
Lithology	Gneisses granodiorite	Granodiorite	Medium and fine sized Granodiorite
Area	18.88km^2	150.71km^2	5.89km^2
Age	350-359Ma	350-359Ma	346-355Ma

Table 2.10 The description of major exposed stratigraphy in Suanjingzi study area. Distribution shown in Figure 2.4. Reference: [67, 69, 70, 71].

Geological Period	Formation/Group	Code	Lithology
Holocene	--	Qh	composed of loose, dry, and yellowish coarse sand (composed of quartz and feldspar), conglomerate and sandy gravel (composed of quartz schist, gneiss, and granite).
Lower Cretaceous	Chijinbao	**K_1c**	upper part: composed of grey-purple coloured fine conglomerate and pebbled coarse sandstone, which reflects an oxidised alluvial depositional environment. middle part: composed of greyish-green siltstone and claystone with little silty dolomite inside, which reflects a transition from oxidised alluvial to sub-lacustrine depositional environment. lower part: composed of grey-green coloured sandstone, siltstone, and mudstone, which reflects a shallow sub-lacustrine depositional environment.
Lower Carboniferous	Baishan Formation	**C_1b**	a set of neritic facies with deposited volcanic rock and sedimentary clastic rock. The main lithology includes andesite, rhyolite, rhyolitic tuff lava, basalt and metamorphized sandstone and siltstone.
Neoproterozoic	Qingbaikou Dahuoluoshan Formation	**Qbd**	composed of grey coloured siliceous calcium dolomite and striped dolomite.
Middle Silurian	Gongpoquan Group	**S_2gp**	composed of a set of tuffaceous quartz sandstone, feldspar quartz sandstone, siliceous slate, andesitic basalt, spilite, tuff and siliceous dolomite.

2.6.2 The structural geology in Suanjingzi outcrop

The tectonic environment around the Suanjingzi region has been outlined by Jiang [51] and Yun [68]. Jiang [51] outlined 9 faults within the Suanjingzi granite outcrop, labelled as F_0 to F_8 in Figure 2.4 and summarised in Table 2.11. They split these faults into three groups based on trending directions: NE trended F_0, F_3 and F_4, NW trended F_1, F_2, F_7 and F_8 and EW trended F_5 and F_6.

Table 2.11 The characteristics of major fault structures in Suanjingzi study area. Distribution shown in Figure 2.4. Reference: Jiang [51].

Fault No.	Dipping direction	Shearing properties	Dip angle	Length	Activation period
F_0	Northwest	Reverse strike-slip	68°-86°	8.5km	Pre-Quaternary
F_1	Northeast	Reverse strike-slip	75°-85°	5.0km	Pre-Quaternary
F_2	Southwest	Reverse strike-slip	57°-72°	5.5km	Pre-Quaternary
F_3	Southeast	Reverse strike-slip	65°	5.3km	Pre-Quaternary
F_4	Northwest	Reverse strike-slip	67°-72°	7.0km	Pre-Quaternary
F_5	Northwest	Reverse strike-slip	53°	19.0km	Pre-Quaternary
F_6	Northwest	Reverse strike-slip	83°	20.0km	Pre-Quaternary
F_7	Southwest	Reverse strike-slip	55°-65°	4.5km	Pre-Quaternary
F_8	Northeast	Reverse strike-slip	58°-82°	3.8km	Pre-Quaternary

The faulting structures in Suanjingzi study area were controlled by Mazongshan Fault system, which is labelled as F_6 in Figure 2.4. It was formed during the period between Sinian and Caledonian [51, 68]. F_5 is believed to form in Carboniferous, which controls the south boundary of the Suanjingzi

granodiorite. The rest faults in Table 2.11 were formed during the period between Late Paleozoic (Variscan) and Jurassic, and the spatial relationships deduced that NE trended F_0, F_3 and F_4 were formed later than NW trended F_1, F_2, F_7 and F_8 [51].

Both Yun [68] and Jiang [51] recognised the activation period of above faults were in the pre-Quaternary. This is mainly because Quaternary sediments such as piedmont diluvial fans which covers on the top of the fracture lines, were not clearly disturbed, or offset by fault activities. This led them to conclude the faults have been inactive throughout the Quaternary Period. This conclusion will be challenged and discussed in Section 6.3.

2.7 The origin and evolution of groundwater

There are two main types of groundwater in Beishan: deep water and shallow water reservoirs. The shallow groundwater can be further classified based on the types of water bearing aquifer. These include (1) pore-fissure water in loose rocks, (2) pore-fracture water in clastic rocks and (3) fracture water in bedrock.

Liu [26] described the existence of the three types of shallow groundwater in Beishan, which suggests that: (1) the fissure water is mainly found among the loose rocks in gullies and ravines, and is mainly recharged by the lateral inflows of bedrock fracture groundwater and the infiltration of flood water; (2) the fracture water in clastic rocks is mainly distributed in the Cretaceous and Tertiary sand and gravel and is recharged by surface flood water and the lateral inflow of bedrock fracture groundwater; and (3) the bedrock fracture groundwater which is mainly distributed in the fractures of metamorphic, magmatic, clastic and carbonate rocks (bedrocks) and is recharged by the infiltration of rainfall and flood water Li [55] and Guo [23].

Li [55] and Guo [23] determined the most widely distributed shallow groundwater type in Beishan is bedrock fracture water in the joints and fractures. However, Li [55] suggested the interconnectivity and the permeability of the bedrock fracture aquifers are poor, therefore, the bedrock fracture water is weakly developed with a very low circulation rate. According to the groundwater table variations observed by Guo [72] in Jiujing and Yemaquan, it is suggested that the dynamic mechanism of bedrock fracture water is infiltration-runoff, and for pore-fissure water is infiltration-evaporation-runoff. This shows that the shallow groundwater originated from modern atmospheric precipitation.

The overall recharge rate of shallow groundwater in Beishan was estimated by Li [24] and Zhou [25]. Li [24] first suggested the regional shallow recharging rate is 0.25 mm a^{-1} on average, which is less than 0.5% of annual precipitation. However, within permeable gullies, the vertical recharging rate can be

range from 0.07 to 2.03 mm a^{-1} (1.0 mm a^{-1}). Zhou [25] and Li [55] also estimated the average recharge rate of 0.28 mma^{-1} which is less than 1% of total atmospheric precipitation. In general, these estimations all indicate the overall atmospheric precipitation to groundwater is poor, which might be due to the high levels of evaporation in local area.

The chemical difference and vertical interaction between shallow groundwater and deep groundwater had also been investigated. Based on the hydrogen-oxygen isotopic ratios and CFC data from Guo [23], Xiao [73]and the chemical ion component data from Zhou [25] which measured the shallow groundwater as Na-Cl-SO_4 and Na-Ca-Cl-SO_4 type and deep groundwater as Na-Cl-SO_4 type, it can be interpreted that deep water is older than shallower water and had a longer water-rock interaction and lower circulation rate. It is outlined by Guo [23] and Zhou [25] that the Beishan groundwater originated from the infiltration of local precipitation, where shallow groundwater is mainly recharged by modern and local precipitation, and deep groundwater originated from ancient precipitation.

Finally, Zhou [25] estimated the deep groundwater residence time to be 3.8 ka to 5.0 ka with flow velocity ranges of 9.8×10^{-4} m a^{-1} to 9.5×10^{-4} m a^{-1} and renewal rates of about 0.006% to 0.012%. It is suggested there are two main sources of deep groundwater, where the majority of the deep groundwater was laterally recharged by the adjacent ancient groundwater, the rest was recharged by the shallow groundwater originating in modern precipitation (young water).

It is important to note, the recharging of the groundwater in aquifer can cause seasonal ground uplifts. This may impact the SAR deformation observed in this study. Further, the released radionuclides which dissolved into the groundwater might be transported into biosphere through the migration of the groundwater. Therefore, to facilitate the selection of GDF host rock, the impacts of groundwater will be discussed in Chapter 6 through the curves of time-series displacements.

2.8 Other hydrogeology related studies

The geochemical properties of the groundwater not only control the corrosive and adsorption behaviours of the groundwater, but also reflect the circulation rate and flow velocity in reservoir. This facilitates the selection of GDF host rock.

There are series studies investigating the geochemical properties of groundwater in Beishan. Overall, the regional groundwater is dominated by Na^+, Cl^-, SO_4^{2-} ions with a high degree of mineralization and slight alkaline due to the process of strong evaporation [55, 74, 75]. The detailed groundwater geochemical data in three study areas (Xinchang, Jiujing and Suanjingzi) are presented in Table 2.12.

Table 2.12 The geochemical properties of groundwater in Beishan

Region	Borehole	TDS (mg/L)	pH	Type	Water depth	Reference
Xinchang	BS06, 15	1111.5-3750.9	7.4-9.6	Cl-SO_4-Na	near-surface	[75, 76]
Xinchang	BS06, 15	1317.6-2731	7.4-8.0	Na-Cl-SO_4/Na-Ca-Cl-SO_4	shallow	[55, 25, 76]
Xinchang	BS06, 15	1750.1-4140	7.5-8.5	Na-Cl-SO_4	deep	[25, 76]
Xinchang	rainwater	33.4-53.5	6.86-7.13	Ca-HCO_3	Surface	[25]
Xinchang	snow	125.9	7.57	Ca-Na-HCO_3	Surface	[25]
Jiujing	BS01, 02, 03	--	7.45-7.48	Cl-SO_4-Na/SO_4-Cl-Na	deep	[17]
Suanjingzi	BS23	690.7-3315.9	7.8	Cl-SO_4-Na-Ca	near-surface	[76]

Further to groundwater geochemical properties, the permeability (hydraulic conductivity) at major granite masses and fracture zones have also been reviewed. These have been presented in Table 2.13. The fracture zones which have higher permeability than granite are the most important areas for shallow groundwater recharging in Beishan [55] and the released radionuclides are expected to be transported through the pathways of groundwater flow. In this way, the fracture zones also played an important role in navigating radionuclides to surface ecosystem.

Table 2.13 A summary of granite and fracture zones permeability in Beishan

Study Area	Geological units	Borehole	Permeability	Reference
Xinchang	Granite	BS05, BS06	10^{-13} to 10^{-7} m a^{-1}	Xiao [56]
Xinchang	Granite	BS17, BS18, BS19	Less than 10^{-8} ms^{-1}	Zhang [77]
Xinchang	Granite		10^{-12} to 10^{-10} ms^{-1}	Wang [63]
Xinchang	Fracture zone		1.28×10^{-13} to 3.22×10^{-6} ms^{-1}	Wang [63]
Suanjingzi	Granite	BS23	3.96×10^{-9} ms^{-1}	Ling [66]
Suanjingzi	Fracture zone	BS23	7.71×10^{-7} ms^{-1}	Ling [66]
Xinchang	Fracture zone		2.75×10^{-4} ms^{-1}	Li [55]
Jijicao	Fracture zone		9.37×10^{-5} ms^{-1}	Li [55]
Jiujing	Fracture zone (Shiyuejing Fault)		4.02×10^{-6} to 7.48×10^{-5} ms^{-1}	Guo [78]
Jiujing	Fracture zone (Shiyuejing Fault)		fault gouge: $10^{-9}ms^{-1}$ breccia: 10^{-5} to 10^{-7} ms^{-1} cataclasite: 10^{-4} to $10^{-7}ms^{-1}$	Zhang [79]

2.9 Summary

In conclusion, this chapter review the structural geology, granite petrology and stratigraphy and hydrogeology in Beishan to improve the understanding of local geology.

The collision between the Indian Plate and Eurasian Plate activated the Arjen Fault zone and further led to the activation of Sanweishan Fault zone. This triggers the fault movements in Jiujing and Xinchang granite outcrop. Suanjingzi might be activated in a similar way, however, the tectonic relations between Mazongshan Fault (F_6 in Figure 2.4) and Arjen Fault Zone are still unknown. The review in this section summarised the major faults in Jiujing, Xinchang and Suanjingzi study areas. These faults can be divided into two types, which includes the NE-SW trended sinistral normal faults and the E-W trended reverse faults. Most of them are believed as in active since Quaternary or with very low displacement rates (less than 0.5 mma^{-1}). In this way, Beishan has been widely believed as the most stable region within in active zone. To robustly supports the selection of GDF host rock in this area, these results will be reassessed in Chapter 6 through the application of InSAR deformation.

Finally, this chapter reviewed the hydrogeology related studies in Beishan such as groundwater origin, groundwater geochemistry, and granite rock and fracture zone permeability. The recharging of the groundwater leads to the seasonal uplifts of the ground surface. Therefore, understanding the

condition of subsurface groundwater movement supports the interpretation of InSAR deformation pattern. Meanwhile, the measurements of rock permeability facilitate the estimation of radionuclides migration time. Altogether with the review in structural geology, these all support the assessment of long-term HLW disposal.

3. The applications of the InSAR technique in engineering geology

The aims and objectives listed at Section 1.8 in Chapter 1 require the precise measurements of surface displacements over time. This could be achieved through the application of InSAR technology. InSAR technology has been widely applied in detecting and measuring surface deformations. This is achieved through the measurements of the phase difference by comparing two SAR images to infer the changes in Line of Sight (LoS) distance in the angular unit (degree or radians) and the extraction of coherence phase difference.

This literature review aims to improve the understanding of InSAR technology by focusing on InSAR applications in resolving real geological engineering problems. The emphasis of the review in this Chapter is on the application of different InSAR methods and the theoretical aspects of InSAR and data reprocessing will be incorporated into the Methodology Chapter (Section 4.1, 4.2, and 4.3).

Several different InSAR algorithms have been developed to measure the surface deformation rates through Time Series Analysis. This research first reviews these algorithms and then summarizes the most-frequently used in Section 3.2. These include Persistent Scatterer (PS) (Section 3.2.1), Distributed Scatterer (DS) (sub-Section 3.2.2) and combined PS-DS (Section 3.2.3). A review of their application in measuring active faults (Section 3.3.1) and geomorphological processes (Section 3.3.2) follows in section 3.3, providing guidance and underpinning the data interpretations in Chapters 5 and 6. The literature review is grouped according to surface susceptibility in both natural and urban environments in three summary tables 3.1, 3.2, and 3.3, based on erosional susceptible surface (rural areas, Table 3.1), robust surface (urban and rocky outcrop areas Table 3.2), and soft-robust combined surface (rural-urban continuum area, Table 3.3). The purpose of doing this is to assist with the selection of suitable InSAR algorithms for this research.

Finally, this research reviews the application of the coherence phase difference (Coherence Change Detection, CCD) method in identifying and quantifying the surface change at the micro-scale (Section 3.4). The literature review in this Section improves the understanding of geomorphological impacts in Chapter 5 and validates the InSAR deformation data in Chapter 6.

3.1 InSAR detection of surface displacement

This research argues the surface deformations are usually caused by two factors: ground movements and surface changes. Ground movement refers to the temporal and spatial variations of surface displacements caused by uplifting, subsiding and horizontal movements. In the published literature,

the most common factors causing ground movements are fault activity, landslides, subsurface projects (mining and tunnelling), surface building loading, and subsurface fluid (groundwater, oil, and gas) extraction and recharging. Surface changes are usually caused by geomorphological processes such as erosion and deposition. These alter the surface topography (on micro and macro scales) through down-wearing and accumulation of deposits over time and, collectively, they lead to a change in LoS distance.

The Differential Interferometric SAR (DInSAR) technique relies on the processing of two SAR images covering the same area of the earth's surface [80]. It is a conceptual method of extraction of the phase difference measured over a set time period, within which a movement event has occurred. The DInSAR measurements are suitable for displacements caused by discrete events such as earthquakes and landslides, which trigger movements that cause distinct deformation.

However, the limitations of DInSAR are significant: there is no atmospheric error removal, very low coherence threshold (approximately 0.3), it suffers from baseline-dependent DEM accuracy and DInSAR involves low interferograms stacking number (only 2). This all means DInSAR has low monitoring precision, equivalent only to the centimetre scale [81] and thus it can provide neither accurate deformation rates nor constraint on the temporal character of deformation.

3.2 InSAR algorithms for time series analysis model

3.2.1 PSI methods

IPTA, PSInSAR and DePSI have been developed from the theory of PS Interferometry and are collectively referred to as PSI. They comprise stack-processing methods that use multiple SAR images, acquired at regular intervals, to achieve millimetre-scale measurement precision [81, 82]. These time-series analysis models are built based on PS which have lower spatial dimension than the SAR resolution cell [27, 82]. According to the amplitude dispersion method, scatters which have been selected as PS usually have standard deviation-mean ratios of less than 0.25 [82], and they represent coherent targets showing high phase stability over the observation period [83]. Compared to DS methods, PS methods are unaffected by baseline decorrelation, which indicates that all the acquired SAR scenes can be used to form interferograms [27, 84]. In general, PS are more abundant in hard and stable surfaces such as buildings, man-made surfaces, and rocky outcrops. PSI methods are therefore suitable for making deformation measurements in urban areas and hard rocky outcrops [27, 83, 85, 86].

Ferretti [81], described the processes of phase unwrapping and space-time estimation, and then In 2001, Ferretti [82] presented a complete procedure for interferometric estimation of Digital Elevation Models (DEMs), PS identification and selection, Atmospheric Phase Screen (APS) and ensemble coherence estimation. These ground-breaking works collectively form the basic theory of the PSInSAR method.

IPTA and DePSI can be treated as optimized versions of PSI. IPTA is developed from Werner [87] (2003) and aims to achieve a more complete use of the available data, through exploiting point targets and, importantly, interferometric pairs with long baselines can be used. This improves the observation numbers which, in turn, reduces the atmospheric errors and leads to better temporal coverage. This leads to an overall improvement in height accuracy, linear deformation rate, atmospheric phase estimation, information quality, refined baselines, and non-linear deformation histories.

Kampes [88] revisited the PSI technology in 2005 and 2006 to improve the quality of estimated displacement parameters by introducing the STUN (Spatio-Temporal Unwrapping Network) algorithm, which led to the development of DePSI. The first step of DePSI is to establish a reference network of coherent points selected by amplitude stability through the time-series, which is expected to be indicative of low phase dispersion. A variance component model is developed to define the dispersion of double differenced phase observation. The estimations are performed between nearby points with distances of less than 2 km to limit the atmospheric signal. This guarantees the precision and accuracy of the results. To prevent the use of wrapped phase data, the unwrapped phase is obtained through the selection of reliable points and the utilisation of minimal cost flow sparse grid phase unwrapping within DePSI. A hypothesis is carried out to identify incorrectly estimated parameters and incoherent points and the displacement model is used to estimate non-linear displacement through wrapped data. Once the parameters at these points are computed, further points are selected and estimated with respect to the reference network.

3.2.2 Distributed Scatterers (DS) based method (SBAS)

SBAS differs from PSI in that it generates the time-series analysis model solely from DS, not PS. The reference and secondary pairs for interferograms are selected from average baseline parameters, and only the shortest baselines are selected, regardless of the spatial separation of the acquisition position [27]. Lanari [89] introduced the basic methods involved in SBAS, these include the selection of coherent pixels, the estimation and filtering out of topographic artifacts and atmospheric phase signals, the two stepped phase unwrapping, and the selection and expression of a generic (reference) SAR interferogram. Berardino [90] first explained the rationale of the SBAS technique as linking the

interferograms computed from separate data subsets, then described the overall data processing procedure, which includes the unwrapping of DInSAR interferograms, low-pass (LP) temporal deformation, residual topography estimations and removal, unwrapping of the residual phase component and the deformation estimate via the singular value decomposition (SVD) approach. In general, DS are contiguous point clusters with a lower individual amplitude and coherence than PS. The measured output from SBAS is characterized by higher spatial resolution than PS in rural areas (semi-arid with short vegetation, or arid deserts), and they are, therefore, more applicable for the deformation measurements in such regions [83].

3.2.3 PS-DS combined method

a. StaMPS method

StaMPS differs from PSI in its method of PS selection. Both methods use amplitude dispersion for initial candidate PS selection but the threshold value for StaMPS is higher (0.4) than that used in PSI. PSIs methods tend to characterize scatterers on the basis of phase stability in space and time, regardless of amplitude and they select Persistent Scatterer Candidates (PSCs) with stable temporal behaviours only. However, StaMPS calculates the PSC coherence using other neighbouring PSCs [27]. Hooper [90] suggests StaMPS identifies the PS pixels primarily from phase characteristics and that it can find low-amplitude pixels with phase stability that are not identified by existing amplitude-based algorithms. Meanwhile, StaMPS can observe temporally variable processes by using spatial phase correlation rather than a well-defined phase history. This therefore allows StaMPS to be used for measuring deformation in non-urban areas. Hooper [91] indicates StaMPS is a new method that combines PSI and Small Baseline Subset (SBAS). The Slowly-Decorrelating Filtered Phase (SDFP) and PS form two distinct but overlapping sets of pixels which are selected using both PSI and SBAS methods. This improves the spatial sampling by increasing the number of scatterers with lower coherence in rural areas.

b. SqueeSAR method

SqueeSAR is regarded as a 'second generation' PSI method, and it is developed through the combination of Point and Distributed Persistent Scatters (PPS and DS) and aims to improve the resolution of deformation measurements in non-urban areas which are difficult to obtain via PSI [27, 92]. Ferretti [93] described how a reliable estimation of the coherence matrix can be carried out using DS. It expands the amplitude stability index concept and shows how local amplitude statistics can be adopted to find DS rather than individual pixels containing point scatterers. Ferretti [85] presents the DespecKS algorithm for the identification of statistically homogeneous pixels (SHP) families, then introduces the Point Target Analysis (PTA) algorithm to provide a bridge that could jointly reprocess the DS and PPS through N phase values. After that, it described the details of the SqueeSAR algorithm,

which includes (1) application of the DespecKS algorithm to identify the family of SHP; (2) defining DS; (3) estimating the sample coherence matrix; (4) applying the PTA algorithm to the coherence matrix associated with each DS; (5) selecting DS with PTA value coherence higher than a threshold level and (6) estimating the displacement time series via the selected DS and PPS.

3.3 The application of various InSAR time series analysis methods in engineering geology

This section reviews the application of above-mentioned time-series InSAR methods that are used to help solve real-world problems in engineering geology. The strength of the ground surface in the monitoring area influences the density and quality of the selected scatterers. This will further influence the monitoring resolution and efficiency of the adopted time-series analysis model. To explore the correlation between surface strength and the application of proper time-series analysis models, more than 60 pieces of research have been reviewed. The research is roughly grouped into three according to the type of environment in each study area: (1) rural areas (soft surface), (2) urban and rocky surface areas (hard surface), and (3) rural-urban continuum areas (soft and hard surface). These groups are summarised in Table 3.1, 3.2 and 3.3 respectively.

Table 3.1 The application of the InSAR time-series analysis on erosion susceptible surface (rural areas)

Reference	Method	Software	Study area	Satellite data information	Causes of deformation	Description
Rosi (2018) [94]	PSI		Tuscany	ERS1–2 (1992 to 2000), ENVISAT (2002 to 2010)	unstable slopes	Identified 672 active landslides, analysed landslide distribution and geomorphological features, and generated a landslide density map
Bozzano (2017) [95]	PSI, QPSI		Dendalo stream basin	ERS and Envisat (1992 to 2010)	unstable slopes	Investigated 27 landslides and indicated the basin is characterised by more than 90 slope deformation with detected velocity of up to 20 mm a^{-1}. Concluded PSI is effective for mapping and analysing landslide deformation patterns.
Oommen (2018) [96]	PSInSAR	ENVI SARscape	Palos Verdes Peninsula	34 ENVISAT 40 COSMO-SkyMed	unstable slopes	Mapped 263 landslides across the peninsula, including 67 previously undiscovered.
Deffontaines (2018) [97]	PSInSAR		Hengchun Fault	PALSAR ALOS (2007 to 2011).	fault activity	It confirmed the Hengchun Fault as an active left lateral transpressive fault.
Declercq (2017) [98]	PSInSAR		Merchtem, Belgium.	67 descending ERS (Apr 1991 to Jan 2001), 73 descending Envisat (Mar 2003 to Oct 2010), 50 descending TerraSAR-X (Oct 2011 to Apr 2014)	groundwater recharging	Some previously subsiding zones in Aalst had recently been uplifted by 3 mm a^{-1} due to groundwater level increase.
Grzovic (2015) [99]	SBAS and PSInSAR	ENVI SARscape	Springfield, Illinois, USA	39 ascending ERS-1/2 (Jun 1992 to Aug 2000), 14 ascending PALSAR (Jun 2007 to Feb 2011)	subsurface projects	The maximum subsidence rates increased from 4.1 mm a^{-1} during 1992-2000 to 35.9 mm a^{-1}during 2007-2011. The scatterers density at PSI is coarser than that at SBAS because of the vegetation and SBAS and PSI results are consistent.
Zhao (2018) [100]	SBAS and IPTA		Jinsha River valley	20 ascending ALOS/PALSAR (Jan 2007 to Mar 2011)	unstable slopes	Identified and mapped 22 suspected landslides on two sides of Jinsha River valley using IPTA (threshold coherence 0.65).

						Measured Jinpingzi landslide has maximum deformation rate 390 mm a^{-1} using SBAS and indicated deformation was sensitive to heavy precipitation with about 1 to 2 months' time lag.
Jia (2019) [101]	ADS-InSAR		Shuibuya Town in Enshi, China	18 Sentinel-1A (Mar 2016 to Apr 2017)	unstable slopes	Estimated a regional deformation rate varying from -38.7 mm a^{-1} to 46.3 mm a^{-1} and detected 7 suspected landslide areas
Liu (2010) [102]	StaMPS	ROI_PAC, DORIS, StaMPS	L'Aquila, Central Italy	59 ENVISAT ASAR (2003 to 2009)	fault activity	
Motagh (2017) [103]	StaMPS	DORIS, GAMMA	Rafsanjani Plain, South-eastern Iran	16 descending Envisat (Apr 2003 to May 2008), 23 ascending Envisat (Jun 2004 to Aug 2007), 10 ascending ALOS PALSAR (Sept 2007 to Nov 2010), 32 Sentinel-1 (May 2015 to May 2016)	groundwater extraction	Study area subsided over 50 mm a^{-1} and locally exceeding 300 mm a^{-1} during 2007-2017 due to the overexploitation of groundwater.
Champenois (2012) [104]	StaMPS		Longitudinal Valley Fault (LVF), Taiwan	10 L-band ALOS (2007 to 2010)	fault activity	Indicated there was a clear velocity discontinuity along LVF with 30 mm a^{-1} velocity offset due to shallow interseismic creep.
Yazici (2020) [105]	StaMPS		Havuzlu, Artvin City, Turkey	25 Sentinel-1	unstable slopes	1608 Persistent scatterers were generated and measured a total displacement rate between -25 mm a^{-1} to 28 mm a^{-1}
Cetin (2014) [106]	StaMPS		Ismetpas, Turkey	Descending Envisat ASAR (2003 to 2010)	fault activity	Measured a maximum creep rate of around 20 mm a^{-1} along North Anatolian Fault (NAF).
Siles (2015) [107]	SBAS		north of the Valley of Mexico	51 ENVISAT (Nov 2002 to Jun 2010)	building loading	Showed subsidence had a linear behaviour and found the areas with maximum subsidence rates up to 285 mm a^{-1} were mainly covered by thick clay deposits with dense populations.
Fatholahi (2020) [108]	SBAS		Marun area, Southwest Iran	18 ENVISAT ASAR (2003 to 2010)	hydrocarbon extraction, fault activity	Revealed a maximum subsidence of around 17.3 mm a^{-1} due to combined effects of tectonic activities and oil extraction in Zagros fold-thrust belt.

Tong and Schmidt (2016) [109]	SBAS		Red Bluff landslide, Columbia River Gorge	ALOS-1 (2007-2011)	unstable slopes	Measured a 25cm LOS displacement over a 4-year period (2007-2011)
Lauknes (2010) [110]	SBAS and StaMPS		Troms County, Norway	18 ERS-1/2 (1992 to 1999)	unstable slopes	
Yang (2014) [111]	SBAS		Datong Basin, China	40 Envisat ASAR	fault activity	Ascertained a 6 mm a^{-1} subsidence difference between the two sides of F8, and suggested ground subsidence was controlled by Kou-Quan and Datong-Yanggao faults and surrounding fissures
Yang (2016) [112]	StaMPS		Taiyuan Basin, China	ALOS PALSAR (2007 to 2011)	fault activity	Suggested the subsidence is controlled and bounded by faults, and the distribution of faults controls ground subsidence occurrence trends.
Funning (2007) [113]	PSInSAR		Rodgers Creek Fault, San Francisco Bay	30 descending Sentinel-1 (1992–2001)	fault activity	Observed a significant LoS velocity discontinuity around 10 mm a^{-1} and measured a shallow creep rate up to 6 mm a^{-1} in the immediate north of Santa Rosa ascribed to local transtension.
Parcharidis (2009) [114]	IPTA		Rio-Antirio strait in western Greece	42 ERS-1 and 2	fault activity	Measured the linear subsidence rates between -1.8 to -6.2 mm a^{-1} in Rio and the subsidence rates less than -2 mm a^{-1} in Antirio. Indicated Rio and Antirio are hanging wall and footwall respectively.
Liu (2010) [102]	StaMPS	ROI_PAC, DORIS and StaMPS	L'Aquila, Central Italy	59 ENVISAT ASAR (2003 to 2009)	fault activity	Found a distinct uplift area in the northwest of study region with velocity 4.6 mm a^{-1} and two subsidence areas in the south and northeast part of the city. These are associated to the NW-SE strike fault in study region.
Champenois (2012) [104]	StaMPS		Longitudinal Valley Fault (LVF), Taiwan	10 L-band ALOS (Jan 2007 to Feb 2010)	fault activity	Revealed a LoS velocity offset around 30 mm a^{-1} attributed to the creep of LVF and improved fault tracing by identifying and characterising new structures at the southern end of the valley.
Cetin (2014) [106]	PSI	StaMPS	North Anatolian Fault (NAF), Ismetpas	2 descending Envisat ASAR (2003 to 2010)	fault activity	Found a maximum creep rate of around 20 mm a^{-1}.
Deffontaines (2018) [97]	PSInSAR	StaMPS	Hengchun Fault	13 ascending PALSAR ALOS (Jan 2007 to 28 Jan 2011).	fault activity	Revealed a clear continuous difference in LoS velocities across Fault: western Hengchun Peninsula was uplifting by 10 mma^{-1} and eastern

						part was subsiding by 0 to -2.5 mm a^{-1}. confirmed the Hengchun Fault as an active left lateral transpressive fault.
Jin (2017) [115]	StaMPS		northernmost Rodgers Creek Fault, Californian	33 descending Envisat ASAR (Mar 2003 to May 2010) 39 ascending Envisat ASAR (Aug 2003 to Apr 2010)	fault activity	Identified seven locations with creep rates in the range 1.9–6.7 mm a^{-1}, confirmed the northernmost segment of the Rodgers Creek fault is creeping. Indicated the fault remained inactive in the immediate southeast of Santa Rosa.
Hallden (2017) [116]	PSInSAR and SBAS	ENVI SARScape	Ystad, Sweden	32 ENVISAT (Nov 2002 to Aug 2005); 24 ERS-2 (Mar 1996 to Aug 2002)		Indicated that both PSInSAR and SBAS methods are unsuited for deformation measurements in Ystad due to vegetation induced low coherence. But shown that SBAS is more promising than PSInSAR in measuring the coastal erosion.
Jiang (2019) [117]	PSInSAR and SBAS	ArcGIS and ENVI	Dongzhiyuan Plateau, China	21 ALOS PALSAR (2007 to 2011)	Erosion	Detected an average subsidence rate of around 6.3 mm a^{-1} due to the impacts of erosion.
Mider (2020) [118]	PSInSAR	ENVI SARScape	Chalk littoral zone between Brighton and Eastbourne, South England	184 Sentinel-1 (3.5 years)	Erosion	Demonstrated the overall down wearing rate is 0.33 mm a^{-1}: the protected sections of coast are down wearing at an average rate of -0.33 mm a^{-1} and the unprotected sections are down-wearing more rapidly at -1.10 mm a^{-1} with a threshold coherence 0.65.
Jiang (2021) [119]	SBAS		Dongzhiyuan Plateau, China	22 descending ALOS PALSAR (Jan 2007 to Feb 2011)	Erosion	An average surface subsidence rate of around -13.5 mm a^{-1} with a variance of 11.0 mm a^{-1} was estimated, which is equivalent to an average gully head erosional rate around 7.5 $m^3 m^{-2} a^{-1}$.
Sajinkumar (2021) [120]	PSInSAR	ENVI SARscape	Thaickal and Munambam in western India	22 Sentinel-1 (Mar 2016 to Jun 2017)	Erosion and deposition	The highest subsidence (-24.9 mm) at Thaickal and the highest uplifting (7.6 mm) at Chellanam showed the co-existing milieus of erosion and deposition.
Aswathi 2022 [121]	PSInSAR	SARproz	Muvattupuzha River Basin (MRB), southwestern India	30 Sentinel-1 (Feb 2015 to Dec 2019)	Erosion and deposition	PSI values ranged from 18.46 to −13.89 mm a^{-1}, showed a mean rate of net soil loss of 6.8 $ton^{-1} ha^{-1} a^{-1}$, and nearly 8% of the area experiences deposition.

Mason (2022) [122]	SqueeSAR		Volcán de Colima, Mexico	147 ascending and descending Sentinel-1 (May 2017 to Feb 2019)	Volcanic activity	Observed a pattern of lava subsidence less than 150 mm over 2 years' period and indicated an apparent westward lateral movement.

Table 3.2 The application of InSAR time-series analysis in rural-urban continuum area

Reference	Method	Software	Studying area	Satellite data information	Causes of deformation	Deformation description
Dehghani (2013) [123]	StaMPS		Southwestern Tehran Basin, Iran	22 descending ENVISAT ASAR (2003 to 2008) 19 ascending ENVISAT ASAR (2004 to 2009)	groundwater extraction	Measured a subsidence rate around 2.5mm a^{-1}
Jin (2017) [115]	StaMPS		Rodgers Creek fault, northern California.	33 descending Envisat ASAR (Mar 2003 to May 2010) 39 ascending Envisat ASAR (Aug 2003 to Apr 2010)	fault activity	identified seven locations with creep rates 1.9 to 6.7 mm a^{-1} and confirming the northernmost segment of the Rodgers Creek fault is active. Analysed the patterns of velocities and indicated the fault remained inactive in the immediate southeast of Santa Rosa.
Dang (2021) [124]	StaMPS		Ha Long and Cam Pha, Vietnam	5 ALOS- PALSAR (2007 to 2009)	subsurface projects	Indicated a maximum subsidence rate of 14.5 mm a^{-1} as a result of underground coal mining exploitation in Hon Gai Formation
Qu (2015) [125]	StaMPS		Houston–Galveston (HG) region, Texas	29 descending ERS-1/2 21 descending Envisat 12 ascending ALOS PALSAR	groundwater extraction, hydrocarbon extraction	Indicated the subsidence rates in the NW region reduced from 53 mm a^{-1} (1990s) to less than 30 mm a^{-1} (2004–2011) and the uplift remains at 20 mm a^{-1} in the SE region.
Chen 2012 [126]	IPTA	DORIS	Greater Pearl River Delta (GPRD), China	61 ascending Envisat ASAR	subsurface projects, building loading	Measured the deformation rates range from −15 to 15 mm a^{-1}.
Zeng (2014) [127]	PSInSAR		Lanzhou, China	40 ENVISAT ASAR (2003 to 2010)	unstable slopes	Measured a ground subsidence rate up to 10 mma^{-1} due to previously unknown unstable slopes

Yang (2018) [128]	StaMPS	SARPROZ	Eastern Beijing	39 Envisat (2003 to 2010) 55 TerraSAR-X (2010 to 2016)	groundwater extraction, building loading, fault activity	Measured the surface displacement rate in the Beijing urban area ranged from -109 to 13 mma^{-1} (2003–2010) and -151 to 19 mm a^{-1} (2010–2016). Identified two most significant subsidence areas in eastern Chaoyang District caused by groundwater extraction, compressible layer, and geological faults. Indicated the newly constructed blocks had higher spatial deformation than old ones.
Hu (2019) [129]	SBAS	GAMMA	Eastern Beijing	22 Sentinel-1A (Jul 2015 to Apr 2017)	fault activity, groundwater extraction	Suggested east Beijing is subsiding with maximum by 140 mm a^{-1} mainly due to groundwater over-extraction. This subsidence is also spatially controlled by geological faults (Nankou-Sunhe fault and Shunyi-Liangxiang fault), showing a correlation with fault distribution.
Haghighi (2019) [130]	SBAS		Tehran Plain, Iran	Envisat (2003 to 2010) ALOS (2003 to 2010) Sentinel-1 (2015 to 2017)	groundwater extraction, fault activity	Identified 3 distinct subsidence bowls in western Tehran Plain, International Airport, and Varamin Plain with subsidence rates 250 mm a^{1}, 50 mm a^{-1} and 220 mm a^{-1} respectively. Suggested the subsidence in Varamin is controlled by Pishva Fault, and the subsidence in the western Tehran Plain and international airport are controlled by permanent aquifer compaction triggered by excessive groundwater extraction.
Zhang (2015) [131]	DS-PS combined		Huainan City, Anhui, China	20 ascending Radarsat-2 (Sept 2012 to May 2014)	subsurface projects	Indicated the coal-mining areas has subsidence rate greater than 107 mm a^{-1} and confirmed underground mining is the primary cause of land subsidence.
Yang (2014) [111]	SBAS		Datong Basin, China	40 Envisat ASAR	groundwater extraction, fault activity	ascertained a 6 mm a^{-1} subsidence difference between the two sides of F8 ground fissure. the velocity patterns indicate the ground subsidence was controlled by Kou-Quan and Datong-Yanggao faults and surrounding fissures
Yang (2016) [112]	StaMPS		Taiyuan Basin, China	ALOS PALSAR (January 2007 to March 2011)	fault activity	Identified more than 30 active faults in NNE, NEE, and NNW study areas with maximum displacement range -75 to 15 mm a^{-1}.

Table 3.3 The application of InSAR time-series analysis in robust surface (urban and rocky outcrop)

Reference	Method	Software	Studying area	Satellite data information	Causes of deformation	Deformation description
Osmanoğlu (2011) [132]	DePSI	DORIS	Mexico City	23 Envisat (Jan 2004 to Jul 2006)	groundwater extraction	Indicated a maximum subsidence rate of 300 mm a^{-1} and suggested PSI measurements are more accurate than GPS method.
Cigna (2012) [133]	DePSI	GAMMA/DORIS	Morelia, Mexico	23 ENVISAT (2003 to 2010)	groundwater extraction	Measured a 10 mm a^{-1} velocity difference between the hanging wall and footwall sides of the Central Camionera fault and a maximum land subsidence of 70 to 80 mm a^{-1} in Morelia, Mexico.
van der Horst (2018) [134]	DePSI		Yangon, Myanmar	33 ascending Sentinel-1 (Dec 2014 to Apr 2017)	groundwater extraction, building loading	Revealed the average subsidence rate is over 10 mm a^{-1} due to the groundwater extraction and identified 4 distinct zones with severe subsidence of over 20 mm a^{-1} located in young alluvium deposits.
Parcharidis (2009) [114]	IPTA		Rio-Antirio, West Greece	42 ERS-1/2	fault activity	Measured the subsidence rates at Rio (-1.8 to -6.2 mm a^{-1}) were much higher than that at Antirio (-2.0 mm a^{-1} or less) due to the presence of active faults. Rio is part of the hanging wall in fault zone.
Bonì (2016) [135]	IPTA		London Basin, United Kingdom	27 ascending ERS-1/2 (Jun 1992 to Jul 2000) 45 descending ENVISAT (Dec 2002 to Sept 2010)	groundwater extraction	
Temporim (2017) [136]	IPTA	Gamma	Carajás Mineral Province, Brazil (hard surface)	33 TerraSAR-X (Mar 2012 to Apr 2013)	subsurface projects, groundwater recharging	Demonstrated the highest subsidence displacements in the north of the pit (mapped as landfill) with subsidence extent 94.92mm in dry seasons and 118.76 mm in rainy seasons.
El Kamali (2021) [137]	P-PSI	DORIS/StaMPS	Remah, United Arab Emirates (hard surface)	53 ERS1/2 (1992–2000) 23 ENVISAT (2003–2010)	groundwater extraction	Detected an extensive subsidence bowl with maximum subsidence 40 mm a^{-1} due to a 12m groundwater level decline.
Jiang (2016) [138]	PSI	DORIS	Shanghai Pudong	15 TerraSAR-X (Sept 2011 to Oct 2012)	building loading	Measured the subsidence rate of the three runways are less than 15 mm a^{-1}, higher than 25 mm a^{-1} and higher than 20 mm a^{-1}.

			International Airport			
Catalao (2020) [139]	PSI		Singapore	49 descending TerraSAR-X (2011 to 2016)	building loading	Measured the areas of Kallang geological formation and reclaimed land with sea level below 5m is subsiding by more than 2 mm a^{-1}.
Ng (2012) [140]	PSI	GEOS-PSI	Jakarta	17 ascending ALOS (Jan 2007 to Sept 2010)	groundwater extraction	Identified two distinct subsidence bowls with maximum subsidence rates of 260 mm a^{-1} in northern Jakarta due to groundwater extraction.
Mason (2015) [141]	PSInSAR		London		fault activity groundwater extraction	revealed there were systematic patterns of both vertical and horizontal ground displacement across London, demonstrated the effectiveness of bidirectional PSI in discriminating low rates of horizontal and vertical ground movements through InSAR geometry.
Bell (2008) [142]	PSInSAR		Las Vegas Valley, Nevada	50 descending ERS (Apr 1992 to Aug 2000) 19 descending ENVISAT (Oct 2002 to May 2005)	fault activity, groundwater recharging	Measured the seasonal amplitude at the east and west sides of the Valley View Fault are 2-3 mm and 1-2 mm respectively during 1995 to 1998 due to the seasonal recharging of groundwater.
Kim (2010) [143]	PSInSAR		Mokpo City, Korea	23 JERS-1 SAR (Sept 1992 to Oct 1998)	building loading	Measured a maximum subsidence rate over 60 mm a^{-1} with an acceleration about −0.3 to −4 mm a^{-2}.
Heleno (2011) [144]	PSInSAR		Lisbon Metropolitan Area		groundwater extraction	Revealed two subsiding areas in Laranjeiras and Vialonga with subsidence rates 11-12 mm a^{-1} and 14-15 mm a^{-1} respectively.
Smolianinova (2020) [145]	PSInSAR	ENVI SARscape	Olympic Park, Sochi, Russia	18 ALOS-1 (2007–2010), 13 Envisat (2011–2012), 300 Sentinel-1 (2015–2019)	building loading	Six subsidence areas were identified with maximum subsidence 150mm over past 2 years.
Khan (2014) [146]	PSInSAR	ENVI SARScape	greater Houston area	8 ERS-1 and 17 ERS-2 (1992 to 2002)	groundwater extraction, hydrocarbon extraction	A strong correlation between groundwater level decline (4 m a^{-1}) and hydrocarbon withdrawal (70 million $m^3 a^{-1}$) and land subsidence were found in north-west Harris County.

Ge (2021) [147]	PSInSAR	GAMMA	Baotou City, Inner Mongolia, China	43 ALOS PALSAR (Dec 2006 to Jan 2011)	groundwater extraction, building loading	estimated an overall slow subsidence (0-10 mma^{-1}) and identified 4 high subsidence areas (10 mm a^{-1}) due to soft soil consolidation and compaction under the action of gravity stress and the excessive exploitation of confined groundwater.
Agarwal (2020) [148]	PSInSAR	ENVI SARScape	central London	47 descending ENVISAT (Dec 2002 to Dec 2010)	groundwater extraction, groundwater recharging	Measured the surface displacement rate varied from −6 to 6 mm a^{-1}
Funning (2007) [113]	PSInSAR		Northern San Francisco Bay	30 Sentinel-1 (1992 to 2001)	fault activity	Measured a shallow creep rate up to 6 mm a^{-1} and indicated the lowered normal stresses may play a role in the distribution of creep
Razi (2018) [149]	PSInSAR		Kelok Sembilan bridge, Sumatra, (hard surface)	13 ascending ALOS PALSAR (Jul 2007 to Nov 2010)	unstable slopes	Measured a land movement rates more than 100 mma^{-1} with erroneousness less than 0.3%.
Beladam (2019) [150]	PSInSAR		Constantine city, Algeria	72 descending SAR images (Aug 2015 to Dec 2017), 80 ascending SAR images (Feb 2015 to Jul 2017)	unstable slopes	Identified several potentially dangerous slides and suggested the landslides in Constantine move constantly with annual average velocity around a few centimetres.
Pratesi (2016) [151]	PSInSAR		Florence, central Italy	79 descending ERS-1/2 (1992–2000), 70 ENVISAT ASAR (2003–2010), 101 RADARSAT-1 (2003–2007)	groundwater extraction, unstable slopes	Measured the NW and SW quarters subsidised up to 30-40 mm a^{-1} due to groundwater exploitation and the southern and NE quarters deformed by ±1.5 mm a^{-1} (maximum subsidence less than -3.5 mm a^{-1}) due to natural slope instability.
Gao (2016) [152]	SBAS	StaMPS, MTI	Capital International Airport, Beijing	47 descending ASAR (Jun 2003 to Aug 2010) 18 TerraSAR (Apr 2010 to Dec 2011), 15 TerraSAR (Jan 2012 to Nov 2013)	groundwater extraction, fault activity, building loading	Measured the deformation rate ranging from −66.2 mm a^{-1} (sinking) to 8.2 mm a^{-1} (uplift) due to intense groundwater extraction (main reason), active faults, quaternary sediments compression and urbanisation.

Cigna (2014) [153]	StaMPS		Rome, Italy	32 COSMO-SkyMed (Mar 2011 and Jun 2013)	building loading	Found a subsidence rate around 7 mm a^{-1} in recently urbanised areas such as Marconi and the valleys of Caffarella and Grotta Perfetta.
Declercq (2017) [154]	StaMPS	ROI_PAC, DORIS, StaMPS, SARPROZ	Brussels region of Belgium	78 descending ERS1/1 (1992 to 2006), 73 descending Envisat (2003 to 2010), 74 descending TerraSAR-X (2011 to 2014), 64 Sentinel-1 (2014 to 2017)	groundwater recharging	Highlighted an uplift area in city centre: the uplift rate decreased from 2-4 mm a^{-1} (1992–2006) to 0.5–1 mm a^{-1} (2014–2017) attributed to the reduction of deep groundwater extraction due to the deindustrialization
Cigna (2012) [155]	DePSI	GAMMA, DORIS	Morelia, Mexico	23 ENVISAT (2003–2010)	groundwater extraction, fault activity	Measured a 10 mma^{-1} average velocity difference between the hanging wall and footwall side of the Central Camionera fault and a maximum land subsidence around 7-8 mma^{-1}.
Hu (2019) [129]	SBAS	GAMMA	Beijing	22 Sentinel-1A (July 2015 to April 2017)	groundwater extraction, fault activity	reported that east Beijing is subsiding with a maximum rate of 140 mm a^{-1} mainly due to the over-extraction of groundwater. Indicated the subsidence is spatially controlled by geological faults due to the correlation between uneven subsidence and fault distribution.

Tables 3.1, 3.2 and 3.3 categorise the application of InSAR time-series analysis methods based on the surface characteristics of the study areas. These include 'soft' surfaces (rural areas), robust surface (rural and rocky outcrop areas) and semi-rural (semi-urban) areas. These show that most time-series displacement rates are estimated using less than 40 SAR scenes, and that the general time span ranges from 1 to 10 years.

PSInSAR, StaMPS and SBAS are three most widely adopted InSAR time-series methods for estimating displacement rates. It is important to note, SqueeSAR is proprietary to TRE Altamira, this limits its use frequency. PSI (PSInSAR, IPTA, and DePSI) are more commonly applied in urban related studies. Around 80% of urban--related studies reviewed in this research adopted PSI methods for displacement estimation (Table 3.3). This value was only 25% in rural-related studies (Table 3.1). That is because the PSI selects the scatterers based on their stability in term of coherence. PS with high stability are more abundant in hard and stable surfaces. Their densities are low in rural areas due to the impacts of geomorphological processes (erosion and deposition) and the presence of vegetation (meaning unstable scatterers). This reduces the monitoring resolution.

The lack of PS in rural areas is compensated by DS. The DS related methods (SBAS and StaMPS) form the interferogram pairs based on the averaging of the baseline parameters. Then the DS are chosen as contiguous scatterers clusters which have lower individual amplitude and coherence than PS. This improves the density of the scatterers selected in soft and unstable surfaces and in turn improves the quality of monitoring. This can therefore explain why DS related methods are more commonly applied in rural and semi-rural areas (Table 3.1 and 3.2).

However, it is important to note, that satellite monitored deformation may also be caused by erosion and/or deposition. These processes change the LoS distance through eroding down and depositing up. According to Jiang (2019) [117], Mider (2020) [118], Jiang (2021) [119], Sajinkumar (2021) [120], and Aswathi 2022 [121], these processes are measurable via InSAR time-series analysis methods (Section 3.3.2). In this way, the contribution of geomorphological processes should be considered when DS methods are applied to measure the ground movements in rural areas.

3.3.1 The measurements of micro-displacements caused by active faults

InSAR time-series analysis models have been widely applied to measure and investigate tectonically induced displacements and, usually, those caused by known (pre-mapped) active faults. The most straightforward way to identify the fault plane is to trace discontinuities revealed in patterns of LoS displacement rates (velocities) in profiles (cross-sections) and maps. Typical case studies which used

this method include Deffontaines (2018) [97], Champenois (2012) [104], Funning (2007) [113], and Jin (2017) [115]. With the support of published geological maps, precisely identifying the fault valley locations and defining the sides of footwalls and hanging walls can be achieved.

To characterise the strike slipe (creep) properties of the fault, it requires the estimation of horizontal deformation rates. The combination of ascending and descending LoS displacement rates has been demonstrated as an effective way to estimate the horizontal displacement rates. An unpublished work by Mason (2015) [141] (unpublished) revealed the vertical and horizontal ground displacement across London using the PSInSAR method. It demonstrated the effectiveness of bidirectional PSI in discriminating low rates of horizontal and vertical ground movements through InSAR geometry. Values that are positive in the left-looking (ascending) data and negative in the right-looking (descending) data indicate eastward ground motion, and those which are negative in left-looking (ascending) and positive in right-looking (descending) data indicate westward motion. If the two values are negative in both the ascending and descending observations, the net movement in vertical direction can be derived as downward (this is published in Mason (2022) [122, 141]). Jin (2017) [115] revisited the Rodgers Creek fault introduced by Funning [113] and demonstrated the measurements of horizontal deformation by decomposing the LoS velocities in ascending and descending orbits. This was achieved in four steps:

Step 1: they expressed the ascending and descending LoS deformation (ṙ) as the scalar product of the three-component vector of the ground deformation (v) and the unit pointing vector from the satellite to the ground target ($\hat{\mathrm{p}}$).

Step 2: they decomposed the ground deformation velocity (v) into a vertical component (v_z) and a horizontal component (v_h) in a selected direction defined by a 2D unit vector $\hat{\mathrm{v}}_{\mathrm{h}} = [\sin\sin\gamma \ \cdot \cos\gamma]$, where γ represents the unit vector in the average fault strike direction. These were expressed as:

$$\dot{\mathrm{r}}_{\mathrm{a}} = \mathrm{v}_{\mathrm{h}}(\hat{\mathrm{p}}'_{\mathrm{a}} \cdot \hat{\mathrm{v}}_{\mathrm{h}}) + \mathrm{v}_{\mathrm{z}}\hat{\mathrm{p}}_{\mathrm{za}}$$

$$\dot{\mathrm{r}}_{\mathrm{d}} = \mathrm{v}_{\mathrm{h}}(\hat{\mathrm{p}}'_{\mathrm{d}} \cdot \hat{\mathrm{v}}_{\mathrm{h}}) + \mathrm{v}_{\mathrm{z}}\hat{\mathrm{p}}_{\mathrm{zd}}$$

Where $\hat{\mathrm{p}}'_{\mathrm{a}}$ and $\hat{\mathrm{p}}'_{\mathrm{d}}$ are 2D vectors containing the horizontal components of the ascending and descending unit pointing vectors and $\hat{\mathrm{p}}_{\mathrm{za}}$ and $\hat{\mathrm{p}}_{\mathrm{zd}}$ are corresponding vertical components of the unit pointing vectors.

Step 3: they recast the above equations as normal equations in matrix form: $Am = \dot{r}_a + e$, where:

$$\mathrm{A} = (\hat{\mathrm{p}}'_{\mathrm{a}} \cdot \hat{\mathrm{v}}_{\mathrm{h}} \ \hat{\mathrm{p}}_{\mathrm{za}} \ \hat{\mathrm{p}}'_{\mathrm{d}} \cdot \hat{\mathrm{v}}_{\mathrm{h}} \ \hat{\mathrm{p}}_{\mathrm{zd}})$$

$$\mathrm{m} = [\mathrm{v}_{\mathrm{h}} \cdot \mathrm{v}_{\mathrm{z}}]^{\mathrm{T}}$$

$$\dot{\mathrm{r}} = [\dot{\mathrm{r}}_{\mathrm{a}}, \dot{\mathrm{r}}_{\mathrm{d}}]^{\mathrm{T}}$$

Step 4: the equation system was inverted using standard least squares methods, weighting by the inverse of the variance of the range change rates to obtain best fitting estimates of m. They constructed a variance-covariance matrix *E* as:

$$E = \begin{pmatrix} e_a^2 & 0 \\ 0 & e_d^2 \end{pmatrix}$$

The best fitting model velocities was expressed as:

$$m = (A^T E^{-1} A)^{-1} A^T E^{-1}$$

With corresponding model velocity covariance given by:

$$C = (A^T E^{-1} A)^{-1}$$

These allowed the estimation of horizontal and deformation rates. However, since the satellites are moving in a north-south direction, only the displacement rates in east-west directions are estimable.

Through the projection of LoS velocities into ground surface, the displacement rates in vertical direction can also be estimated. This is demonstrated by Cigna (2012) [133]. Cigna (2012) [133] estimate land subsidence in Morelia, Mexico using the DePSI. They converted the LoS displacements (d_{LOS}) to vertical displacements (d_V) through the equation $d_V = d_{LOS}/\cos\theta$ and corresponded to an increase of LoS displacements by 7%. The research finally measured a 10 mm a^{-1} average vertical velocity difference between the hanging wall and footwall side of the Central Camionera fault and a maximum land subsidence around 7-8 mma^{-1} in Morelia, Mexico.

However, tectonic induced ground displacements are usually closely correlated with groundwater movements, often caused by extraction (or less commonly by recharge). This phenomenon is especially distinct in densely populated urban areas (Yang (2014) [111], Funning (2007) [113], Hu (2019) [129], Cigna (2012) [133], Bischoff (2019) [156], and Bell (2008) [142]). In general, there are three methods to distinguish tectonic-induced and groundwater-induced subsidence. First, this is achieved through the spatial comparison between deformation patterns and fault distribution. The active faults usually define the geometry of the deformation pattern and lead to elongated patterns of subsidence or uplift oriented parallel to the striking direction of active faults (Figure 3.1) (Cigna (2012) [133]). Second, the groundwater extraction induced subsidence are usually in a purely vertical direction, which means the deviation between ascending and descending LoS velocities is insignificant. Hence the estimated horizontal velocities (in E-W direction) are low (Mason (2015) [122]). Third, the ground movements impacted by groundwater are expected to swell seasonally with the atmospheric precipitation. This leads to the formation of sinuous displacement variation trends and is visible from

the time-series analysis curve (Figure 3.2) (Bell (2008) [142]). These facilitate the identification of groundwater impacts on SAR deformation in this research.

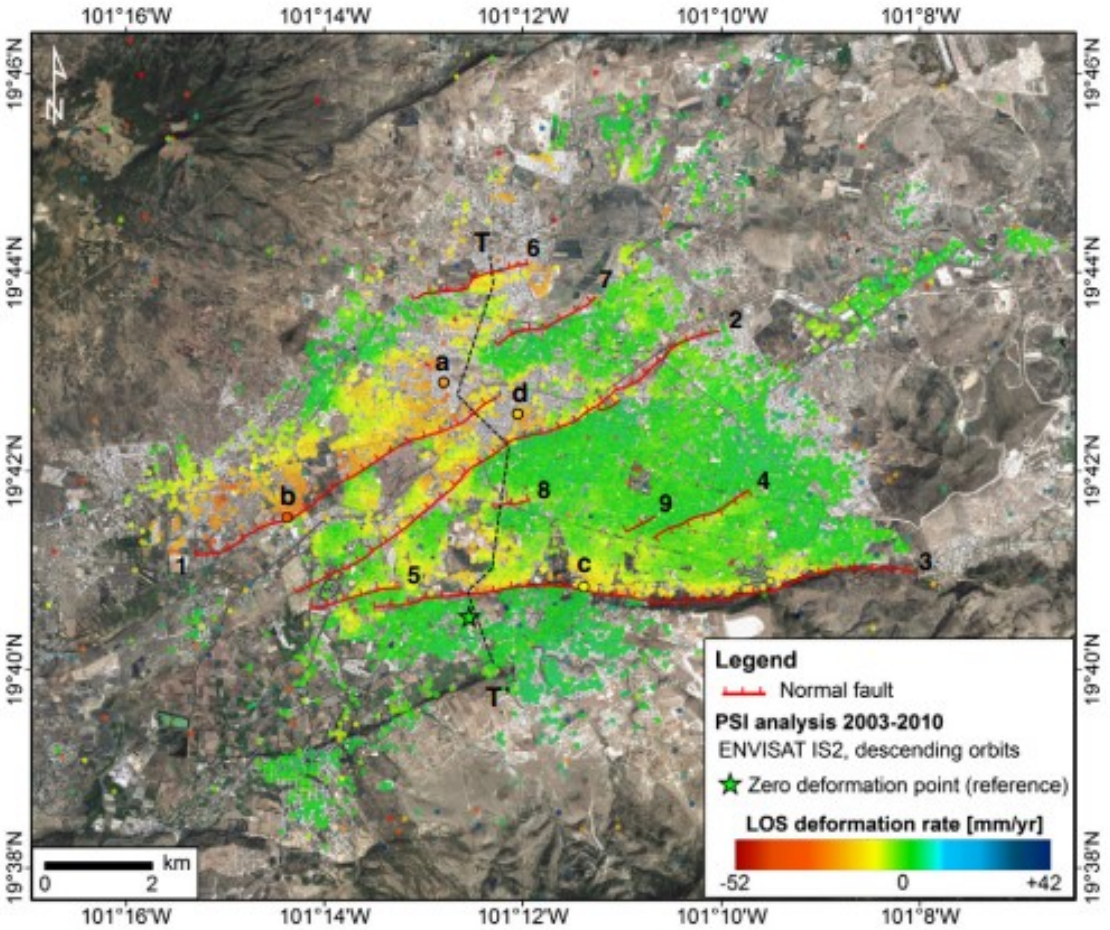


Figure 3.1 The map of descending LoS deformation rates in Morelia between 2003 and 2010, obtained through the PSI analysis of 23 ENVISAT images with normal faults La Colina (1), Central Camionera (2), La Paloma (3), Chapultepec (4), Torremolinos (5), El Realito (6), La Soledad (7), Cuautla (8) and Ventura Puente (9). The map is a typical example which illustrates how active faults define the geometry of the deformation pattern and shows an elongated patterns of subsidence or uplift oriented parallel to the striking direction of faults Cigna (2012) [133]).

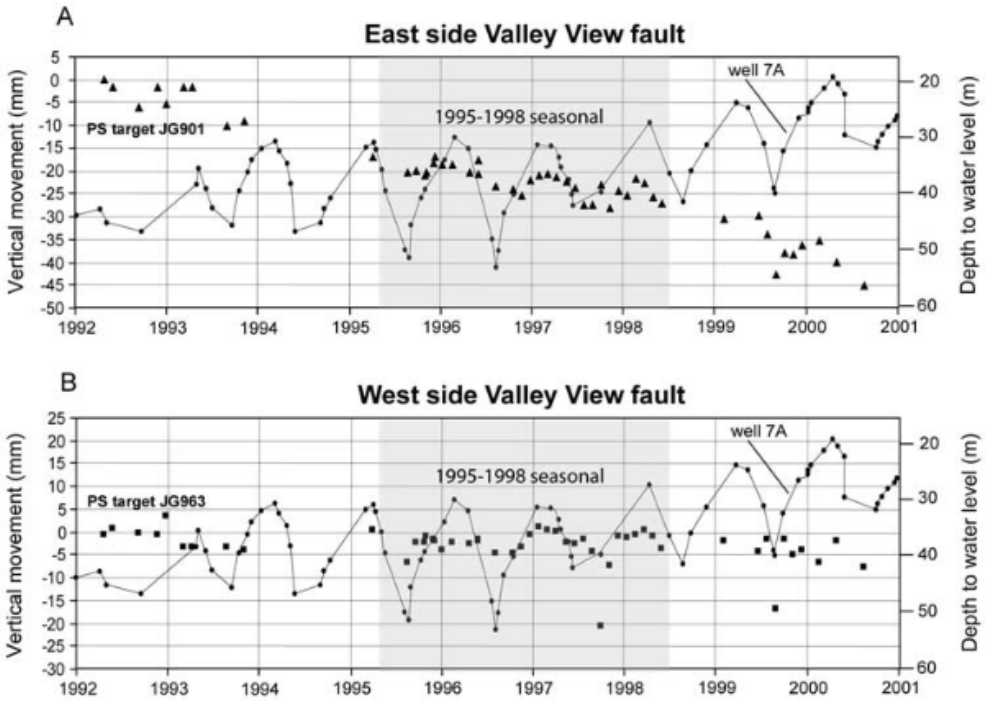


Figure 3.2 This is an illustrative example showing the correlation between variations in groundwater level (solid line) and time-series analyses (black triangles (A) and squares (B)) for Persistent Scatter targets from Bell (2008) [142]. The study area is at the east (A) and west (B) side of Valley View Fault in Nevada. The seasonal sinusoidal model indicates the ground impacted by groundwater swells seasonally with the atmospheric precipitation over 1992 to 2000, which is visible from the time-series analysis curve with 2-3 mm amplitudes in A, and 1-2 mm in B. The sinusoidal curves and the seasonal amplitudes facilitate the identification of groundwater impacts on SAR deformation.

3.3.2 Quantifying geomorphological processes

Geomorphological processes cause topographic changes which, in turn, influence the measured LoS distance. The studies below reviewed the efficiency of DS (Jiang 2021 [119]) and PS (Mider (2020) [118], Sajinkumar (2021) [120], Aswathi 2022 [121]) methods in measuring the erosional and depositional rates.

Hallden (2017) [116] first applied the PSInSAR and SBAS methods to measure the coastal erosion rates along the coast of Ystad municipality in Sweden. Their study area consisted of soft sand landscapes characterised by sand dunes, where erosion is mainly driven by storms and wave action. The results indicated both PSInSAR and SBAS methods are unsuited for use in Ystad because of low surface coherence caused by dense vegetation cover, but also suggested that SBAS is more promising than PSInSAR in measuring the coastal erosion.

Jiang (2019) [117] analysed time-series deformation of the Dongzhiyuan Plateau, as caused by erosion, through a combination of SBAS and PSInSAR methods. They detected an average subsidence rate of around 6.3 mm a^{-1} caused by process of head-cut (major impact), water and gravity erosion. They revisited the Dongzhiyuan Plateau study area in 2021 [119] and measured the gully head erosional rates using the SBAS method. The threshold coherence for unwrapping was set as 0.35. An average surface subsidence rate of around -13.5 mm a^{-1} with a variance of 11.0 mm a^{-1} was estimated, which is equivalent to an average gully head erosional rate of *ca* 7.5 m a^{-1}. It is indicated the results are reasonable consistency and reflected SBAS is a reliable method for measuring erosion rates.

Mider (2020) [118] used the PSInSAR method in measuring the erosional down-wearing rate of the chalk littoral zone platform between Brighton and Eastbourne in southern England. A total of 184 Sentinel-1 SAR scenes, collected over a 3.5-year period, were processed using ENVI SARScape software using a threshold coherence of 0.65. The results demonstrated the overall down wearing rate is 0.33 mm a^{-1}; the protected sections of coast are down-wearing at an average rate of -0.33 mm a^{-1} and the unprotected sections more rapidly at -1.10 mm a^{-1}. A 4 mm overall ground displacement over 3.5-years period indicates the result is well above the uncertainty level of the data.

Sajinkumar (2021) [120] monitored the morpho-dynamics (erosion and deposition) along the coastline between Thaickal and Munambam in western India. A total of 22 Sentinel-1A SAR scenes, acquired between 4 March 2016 and 3 June 2017 were processed using the PSInSAR method in ENVI SARscape. Erosion and deposition are correlated with the onset and offset of the monsoon wave. The highest subsidence (-24.9 mm) at Thaickal and the highest uplift (7.6 mm) at Chellanam showed the co-existing

milieus of erosion and deposition. The PSInSAR results concurred with corresponding Google Earth images and were further corroborated by the sediment texture in the beach segment. All indicating that PSInSAR is a capable and reliable tool for monitoring erosional and depositional processes. However, the threshold coherence value set was not mentioned in this study, which therefore makes it difficult to determine the correlation between threshold coherence and the feasibility of PSInSAR in measuring geomorphological rates.

Aswathi 2022 [121] measured the soil erosion in the Muvattupuzha River Basin (MRB), southwestern India through the PSInSAR method. Some 30 Sentinel-1A SAR scenes (Feb 2015 to Dec 2019) were processed by SARproz and a threshold coherence less than 0.75 was selected. The measured displacement velocities ranged from 18.46 to −13.89 mm a^{-1}, where the upward ground movements (positive) imply uplift or deposition and the downward ground movements (negative) which refer to subsidence or erosion.

The literature review in this section demonstrates the feasibility of SBAS and PSI in measuring depositional and erosional rates. Overall, it appears that SBAS is more efficient and reliable than PSI in measuring geomorphological processes in rural and semi-rural areas. That is because geomorphological processes lead to low scatterer stability and the threshold coherence is a trade-off between scatterers' density and stability. A lower coherence threshold leads to higher scatter density but lower stability and enables more effective geomorphological processes monitoring. This explains why Hallden (2017) [116] and Aswathi (2022) [121] attempted to apply some low threshold coherence in PSInSAR to improve the resolution in measuring the rates of erosion and deposition.

The main aim of this research is to measure the surface deformation rates induced by tectonic activity. To guarantee the measured results reflect actual ground movements, an effective removal of the geomorphologically induced deformations is required. The conventional method is to set a high threshold coherence to filter out the scatterers impacted by erosional and depositional processes in rural areas. However, Mider (2020) [118] and Aswathi 2022 [121] demonstrated geomorphological processes are in fact measurable by PSI with high threshold coherence (0.65 to 0.75). The correlation between threshold coherence and measurement of geomorphological processes remains unknown. It remains debatable how far a high threshold coherence can effectively remove the geomorphological impacts and remove all unstable scatterers. This could be answered through the application of coherence phase difference. The relevant studies are reviewed in Section 3.4.

3.4 Coherence for surface change detection

The phase coherence of two SLC SAR images is a measure of the local correlation of the radar reflection characteristics of the surface target between the two observations. It can be estimated by ensemble averaging of *N* neighbouring pixels of complex SAR data, it is usually used to describe how a system can preserve the phase of the received signal. The coherence value ranges from 0 (no coherence) to 1 (total coherence), and the two waves are coherent when they are in phase [157, 158]. The coherence quantifies the changes between SAR images at different acquisitions over the observation time, where the coherence loss is cumulative in time. Hence, the coherence loss can be spatial and/or temporal. Coherence Change Detection (CCD) is a remote sensing method used to identify the alteration of a surface over the observation time through coherence phase difference. It is important to note that there are many factors that lead to surface change and coherence loss, including geomorphological processes (aeolian [159, 160, 161] and deposition [162, 163, 164, 165, 166, 167, 168, 169, 170, 171, 172, 173, 174] of surface materials) which lead to movements of surface sand, winnowing and etc., human activities such as vehicle movements [175, 176], construction works [177, 178, 179], mining activities [180] and the spatial and temporal variation of vegetation (growth and movement) [181, 182, and 183]. Meanwhile, CCD has also been used to assess the impacts of geohazards such as volcanic eruptions [155, 184], earthquakes [185] and landslides [186, 187, 188]. These all indicate coherence phase difference is a mature remote sensing method in detecting surface changes.

Geomorphological processes alter the ground surface and lead to decoherence through temporal decorrelation caused by erosion and/or deposition, changing the phase of the returning radar signal and therefore leading to a phase difference and ultimately a decrease in coherence. This phenomenon is more common in rural areas where aeolian and fluvial processes cause rapid changes and so loss of coherence. In general, there are two opinions regarding the geomorphologically induced decoherence. Ullmann [189] indicated the prime factor affecting decorrelation is the change in the topography induced by particle migrations, while Lee [190] suggested this is controlled by the slope effect except the cases of slope effect caused by small temporal/spatial baseline observations [160].

This is improved through the development of the time-series coherence method. The new method involves choosing the first SAR image (the one with earliest time) as the reference, then co-registers it with all secondary SAR images, separately, to form a series of interferograms with the same beginning time but different end times in the same area. This method was not only adopted by Havivi (2018) [159] and Cabré (2020) [169] to investigate the temporal variation of surface processes, but also applied by Brisco (2017) [182] to detect the temporal variation of vegetation.

3.4.1 Aeolian processes

There are many studies which demonstrate the application of CCD in detecting aeolian processes. Havivi (2018) [159] exploited the geomorphic stability of Ashdod-Nizzanim coastal dunes using 14 TerraSAR-X images from February 2012 to July 2012. They first co-registered all SAR images relative to the reference image acquired on 9 February 2012. Then they created a series of coherence maps, where each represented the magnitude of the correlation of the complex information from two interferometric SAR images of the same area taken at different times. Finally, the spatial and temporal variation of the coherence was mapped. Havivi (2018) [159] demonstrated the CCD method was able to distinguish between active and inactive dune surfaces, where dune crests are characterised by higher coherence values (0.4-0.45) and windward slopes are characterised by lower values (0.33-0.34). This was mainly due to aeolian induced particle movement (saltation and creep). The higher rainfall events in winter led to high coherence values due to the high soil moisture preventing particle transport. During the period between winter and spring, the wind became stronger, moisture content decreased, and transport was therefore enabled.

Kim (2020) [160] reconstructed the aeolian surface erosion of Southern Mongolia through inter-comparisons of phase coherence signals. They revealed the geological structures in southern Mongolia as sediment transportation pathways which significantly contributed to dust (clay, silt and sand particles) generation in the Gobi Desert over southern Mongolia. Then Kim 2021 [161] investigated the Kubuqi Desert in Inner Mongolia using the same method and successfully monitored the surface changes that occurred before and after the activities to combat desertification.

3.4.2 Fluvial processes

CCD has been widely applied across drainage basins to map the extents of inundation by flooding rivers. This is because the fluvial induced erosion and deposition, which alter the arrangement of ground surface scatterers, may cause significant decoherence. In a chronological order, Geudtner (1996) [170] first mapped the 1993/94 flood event in the river Rhine, Germany using InSAR coherence, then Giordano (2005) [174] detected the damage caused by the Yangtze River flooding in the summer of 1998 through a multitemporal coherence map. After that, Selmi (2014) [165] extracted the surface flooding zone around the Mellegue river in northwest Tunisia in 2005 and enhanced the detection of flooded areas.

Further to the river flood inundation in drainage basin, CCD has also been applied to investigate the rain-induced flooding in desert regions. Liu (2004) [191] demonstrated the effectiveness of multi-temporal coherence imagery in detecting rapid erosion triggered by rainfall events in Southeast Spain.

Schepanski (2012) [166] detected the coherence loss in north-western Sahara, to identify flash floods through coherence ratios using SAR pairs of differing temporal separation to derive coherence maps for each time period. This identified a unique decorrelation related to rainfall events. The research indicated a high coherence during dry periods and significant decoherence during wet seasons.

Gaber (2018) [163] investigated fluvial and aeolian morpho-dynamics and mapped surface change along two paleochannels in the Egyptian Sahara through coherence change detection (CCD). This showed the eroded bedrock and the rounded sand grains deposited in downstream depressions have very low coherence, being close to 0 (high change). Meanwhile, the deposits in ephemeral river channels had low to moderate coherence, ranging from 0.2 to 0.4 (high to moderate change), and the country rocks have high coherence close to 1.

Cabré (2018) [168] evaluated the erosion of the southern Atacama Desert in response to a heavy rain event of March 2015 by constructing time-series of InSAR coherence images. They first split the decoherence triggered by surface erosion or sediment transport from soil moisture variation by examining the temporal evolution of the coherence, then revealed a positive correlation between erosion, precipitation amount and lithology. Finally, the areas with anthropic influence were subjected to continuous decoherence and the caldera and hydrothermal alteration zones were found to be intensively influenced by the event.

Jordan (2020) [162] investigated the impacts of soil types on the temporal and spatial variation of soil moisture in the Atacama Desert, Chile through the observation of coherence change. They demonstrated that calcium sulfate rich soil has longer decoherence response than silicate mineral-based soil due to its high rainwater retaining ability. Meanwhile, decoherence usually occurs in areas such as river channels, steep slopes, playas, and sites of anthropogenic activity (roads, mines, or telescope construction).

Cabré (2020) [169] further investigated and mapped the erosive impact of the March 2015 storm in the Atacama Desert using coherence change detection (CCD) analysis. They indicated that temporal decoherences were the result of soil moisture variation and permanent decoherence is related to soil texture modification caused by erosion and sedimentation. Cabré (2020) [91] demonstrated the temporal variation of InSAR coherence and explored their correlation with major rainfall events. They indicated permanent decoherence is more apparent on gentle slopes, which contradicts the previous claim that steeper hillslopes are more prone to erosion.

CCD has also been adopted to detect the flooding in urban areas characterised by robust surface. This is achieved through the temporal decoherence caused by the absorption of radio wave by surface water. That is because the wet soil contributes less backscattered signal from the scatterers, this leads to low coherence. Li (2019) [164] investigated the roles of SAR intensity and interferometric coherence in urban flooding in Houston, Texas in August 2017. They indicated adding multi-temporal coherence to multi-temporal intensity could make flooded and unflooded areas more distinctive and therefore considerably increase the accuracy and reliability of the inundation map. Chini (2019) [172] also observed the 2017 floods in Houston using InSAR coherence. the obtained floodwater maps agreed with the visual analysis of VHR optical images acquired shortly after the hurricane's passage and showed consistency with most affected buildings. This confirmed the reliability of this approach in mapping flooded urban areas. Chini (2019) [173] presented probabilistic flood maps using the intensity data and InSAR coherence features based on the 2017 flood event case study in Houston (Texas), which improved the information content of a binary SAR-based floodwater map which does not give any indication on the uncertainty in the pixel state.

3.5 Summary

This chapter reviewed the application of InSAR technology in resolving real geological engineering problems. The literature review in this chapter can be divided into two parts: the measurements of surface displacement rates and the quantification of geomorphological processes (erosion and deposition) on the ground surface. Reviewing these processes provides the background required to support and guide the data interpretation in later chapters.

Section 3.2 and 3.3 highlighted that PS related methods (PSI) are more commonly applied in urban related studies or areas with very limited vegetation and that are characterized by a stable surface, the DS related methods are more widely applied in rural studies, and the PS and DS combined methods (StaMPS and SqueeSAR) are more suitable for rural-urban continuum areas. The aim in this research is to measure the surface displacement rates across the granite outcrops at Suanjingzi, Jiujing and Xinchang in Beishan which is a rural environment. Therefore, the review in Section 3.2 and 3.3 would imply that the PSI method is the most appropriate for approach to data processing for this research project.

Section 3.3 reviewed the application of InSAR in fault detection and associated deformation patterns. This was followed by a review of the application of InSAR technology in measuring the rates of erosion

and deposition in relation to geomorphological processes. Understanding these approaches provides guidance for interpreting the deformation pattern observed and discussed in Chapter 5 and 6.

Lastly, the application of coherence changes detection method in quantifying aeolian and fluvial processes has been reviewed in Section 3.4. The review in this section demonstrated how the temporal and spatial variations of the ground surface can be detected in relation to major rainfall events. This supports the coherence data interpretation in Chapter 5.

4. Methodology

The investigation of GDF host rock requires the understanding of local geological stability. To map, interpret and characterise the active fault and predict the future structural geology evolution, it requires the precise measurements of surface displacement rates. This could be achieved through the application of Interferometric Synthetic Aperture Radar (InSAR) technique. This chapter aims to introduce the theories and the methods for displacement rates measurements and geomorphology identification.

This chapter first introduced the basic theory related to InSAR, which include InSAR geometry, Interferogram component, the current algorithms for Time Series Analysis model estimation, the working processes of PSInSAR method, and the 3D decomposition of LoS displacements. As the accurate measurement of northing displacement rate (D_N) is technically unachievable, this chapter also introduced an alternative method for D_N estimation using maximum compression direction in Section 4.5. After that, the methods to interpret measured displacement data are introduced in Section 4.6 and 4.7. The geomorphological processes such as erosion may trigger surface deformation. To identify the geomorphologically impacted areas, Section 4.8 introduced the theory of coherence change detection method. Finally, the data reprocessing flowcharts by ENVI SARScape software were introduced.

4.1 InSAR technique

InSAR is a remote sensing technique to observe the surface deformation in millimetres scales through the comparison of two radar images from Reference (initial) acquisition and Secondary (second) acquisition satellites. It emits the radar (microwave) waves and collects the returned energy from target points, so that the phase difference can be monitored to define the satellite-surface distance change between two image acquistration time [27, 28]. This is illustrated in Figure 4.1. Phase represents the fractional part of a whole wave cycle received by the sensor, which can be measured in angular unit such as degree or radians [192]. The radar wave has a sinusoidal radiation pattern with each wavelength equivalent to 2π radians. The wavelength defines the unit distance for SAR phase measurements [27]. The wave phase varies between -π to π and the change in relative position of the sensor and target is obtained from the difference in cycle position (phase) between observations.

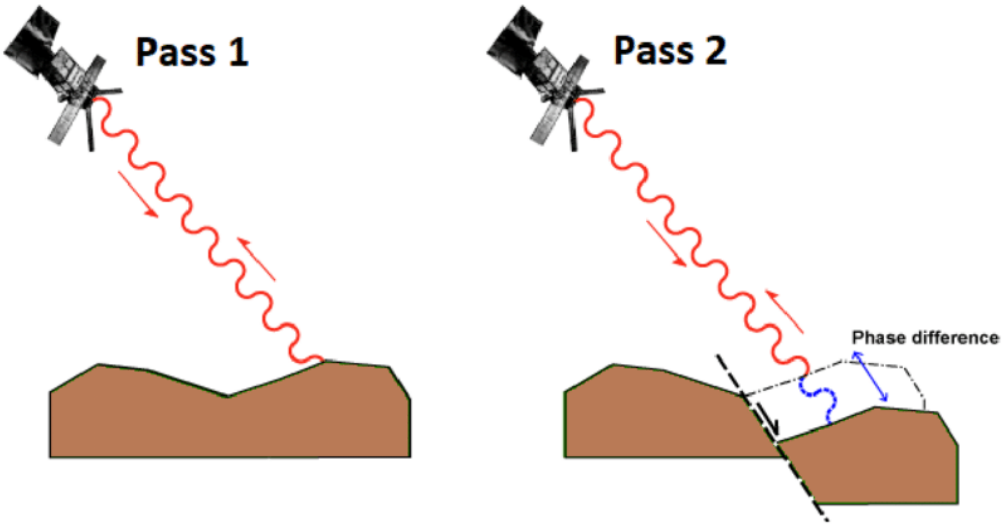


Figure 4.1 The schematic figure illustrates how phase difference is observed by comparing two SAR images to infer line of sight (LoS) distance changes in angular unit (degree or radians) [193].

4.1.1 InSAR geometry

Figure 4.2 illustrates the geometry of InSAR system, where θ is incident angle, β is tilt angle, H is the height of the sensor, ΔR is the relative scattered displacement in line of sight (LoS) direction and h(x) is elevation relative to Earth ellipsoid. The Sentinel-1 satellite observes the same area at different times from slightly different look angles. Usually, the interval of repeat acquisitions is 12 days. When the ground targets slightly change their relative positions during the time interval between two observations, the interferometric phase can be detected [194]. However, the position between the satellite acquisitions does not coincide with each other at the time of imaging. This leads to the spatial separation between Reference acquisition satellite and Secondary acquisition satellites. This kind of spatial difference is defined as the SAR interferometric baseline, which is a spatial vector consisting of the satellite platform orbital positions [195].

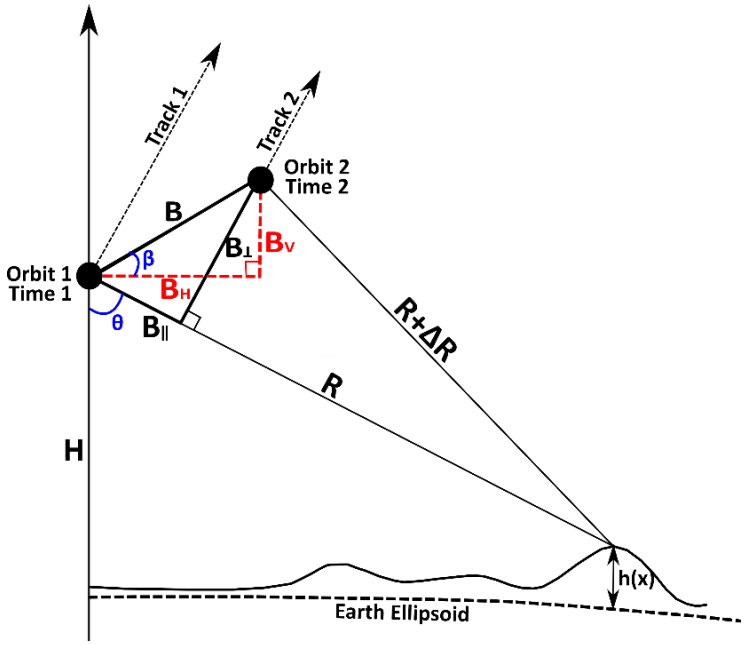


Figure 4.2 The geometry of InSAR system. Figure edited from [194, 195, 196, 197].

The baseline represents the spatial separation between satellites. As illustrated in Figure 4.2, there are two ways to decompose baseline (B), which are (1) horizontal baseline (B_H) and vertical baseline (B_V) and (2) perpendicular baseline ($B_\perp$) and parallel baseline ($B_\parallel$) [196]. The parallel baseline ($B_\parallel$) refer to the baseline component along the LoS and the perpendicular baseline ($B_\perp$) refers to the component that is perpendicular to LoS. These two can be expressed as [195]:

$$\mathbf{B}_{\parallel} \approx \left|\vec{\mathbf{B}}\right| \cdot \mathbf{sin}(\boldsymbol{\theta} - \boldsymbol{\beta}) \quad \textbf{Eq. 4.1}$$

$$\mathbf{B}_{\perp} \approx \left|\vec{\mathbf{B}}\right| \cdot \mathbf{cos}(\boldsymbol{\theta} - \boldsymbol{\beta}) \quad \textbf{Eq.4.2}$$

The flat Earth phase and topography phase are close related to $B_\parallel$ and $B_\perp$, this will be described in following section.

4.1.2 Interferogram composition

Further to the spatial separation between satellites, several factors can contribute to the phase difference between Reference and Secondary acquisition, these include the shape of the Earth, elevation, surface deformation, atmosphere, and the target's electrical properties [27]. The typical model for these phase terms is expressed in Equation 4.3 [27, 81, 82]:

$$\boldsymbol{\Phi} = \boldsymbol{\Phi}\,\mathbf{flat} + \boldsymbol{\Phi}\,\mathbf{dem} + \boldsymbol{\Phi}\,\mathbf{orb} + \boldsymbol{\Phi}\,\mathbf{def} + \boldsymbol{\Phi}\,\mathbf{atm} + \boldsymbol{\Phi}\,\mathbf{scat} + \boldsymbol{\Phi}\,\mathbf{noise} \quad \textbf{Eq. 4. 3}$$

Where Φ is a measured total phase change between Reference acquisition and Secondary acquisition, $\Phi\,\mathrm{flat}$ is the flat Earth phase due to the phase difference between flat Earth surface and actual Earth surface (curved), which is related to parallel baseline ($B_\parallel$) and can be expressed as:

$$\boldsymbol{\Phi}\,\mathbf{flat} = \frac{4\pi}{\lambda}\,\mathbf{B}_{\parallel} \quad \textbf{Eq. 4. 4}$$

Where λ is the wavelength. The term $\Phi\,\mathrm{dem}$ is a topographic phase contribution refers to the topography above the reference ellipsoid. It is controlled by the perpendicular baseline ($B_\perp$), which can be expressed as:

$$\boldsymbol{\Phi\ \mathrm{dem} = \frac{4\pi}{\lambda R} B_\perp(\underline{x}) \frac{h(x)}{\sin\theta}} \quad \textbf{Eq.4.5}$$

Where R is the master sensor-target distance, θ is the local incidence angle with respect to reference ellipsoid, and h is elevation. $\Phi\ \mathrm{def}$ is the surface deformation which is a function of radar wavelength (λ) and the monitored deformation induced radar displacement (ΔR_{def}) in line-of-sight (LoS) direction, this is expressed as Equation 4.6:

$$\boldsymbol{\Phi\ \mathrm{def} = \frac{4\pi}{\lambda} \Delta R_{def}} \quad \textbf{Eq. 4. 6}$$

$\Phi\ \mathrm{atm}$ is an atmospheric phase delay, according to Osmanoğlu [27], $\Phi\ \mathrm{atm}$ can be further divided into tropospheric phase contribution ($\Phi\ \mathrm{tropo}$) and ionospheric phase contribution ($\Phi\ \mathrm{iono}$), which can be expressed as:

$$\boldsymbol{\Phi\ atm = \Phi\ tropo + \Phi\ iono} \quad \textbf{Eq. 4. 7}$$

The tropospheric phase contribution ($\Phi\ \mathrm{tropo}$) is generally referred as the atmospheric phase screen (APS), which can be expressed as:

$$\boldsymbol{\Phi\ tropo = \frac{4\pi}{\lambda} \Delta R_{tropo}} \quad \textbf{Eq. 4. 8}$$

Where ΔR_{tropo} indicates the range change due to atmospheric delay. APS is the mean value of atmospheric components; it can be calculated by averaging the atmospheric phase contribution relative to the master image. This will be described in later section. Ionospheric phase contribution ($\Phi\ \mathrm{iono}$) refers to the interferometric phase change due to the changes in ionospheric conditions, which affects L-band and lower frequency radars more significantly. This is expressed as:

$$\boldsymbol{\Phi\ iono = 1.69 \times 10^{-6}\, N\, \lambda} \quad \textbf{Eq. 4. 9}$$

Where N refer to the number of electrons per unit area. $\Phi\ \mathrm{orb}$ is a satellite orbital errors generated by inaccurate orbit determination, $\Phi\ \mathrm{scat}$ is phase contribution related to scatterers' electronical properties, which are very slight and therefore assume negligible for topography and deformation observations. $\Phi\ \mathrm{noise}$ is the combined noise term linked to coherence and can be divided into four decorrelation terms, these include: spatial baseline decorrelation, temporal decorrelation, Doppler centroid decorrelation and thermal decorrelation.

4.2 The application of PSI for displacement rate measurements in Beishan

The Time Series Analysis of InSAR data reflects the temporal variation of deformation ($\Phi\ \mathrm{def}$) at targeted scatterers during the data acquisition period. This is achieved through the removal of satellite orbital errors ($\Phi\ \mathrm{orb}$), topography ($\Phi\ \mathrm{dem}$), atmospheric phase delay ($\Phi\ \mathrm{atm}$) and temporal and geometrical decorrelation noise ($\Phi\ \mathrm{noise}$) [81, 82].

To estimate the temporal variation of deformation (Φ def), several Time Series Analysis algorithms have been developed to produce continuous records of displacements, these includes IPTA, PSInSAR, DePSI, SBAS, SqueeSAR™, and StaMPS. These methods can be grouped into three, which are persistent scatterers (PS) based (PSI: IPTA, PSInSAR™, and DePSI), distributed scatterers (DS) based (SBAS) and PS-DS combined (StaMPS and SqueeSAR™). These have been described in Section 3.2.

The three study areas (Suanjingzi, Jiujing and Xinchang) in Beishan are mainly exposed by hard granite outcrops with some soft Quaternary sediments covering around. In this research, the main aim is to measure the tectonically induced displacement rates on these outcrops to provide guidance for long term HLW isolation. However, the observed surface deformation, especially the Quaternary covering areas, might be severely impacted by geomorphological processes. In general, DS are contiguous point clusters with a lower individual amplitude and coherence than PS, which are more suitable for the deformation measurements in rural areas with unstable surfaces. To guarantee the measured surface deformation reflecting the real tectonic activities rather than depositional accumulation and erosional wearing down, this requires the selection of stable (persistent) scatterers. In this way, PSI is chosen to filter out the impacts of geomorphological noise in a maximum attempt.

Further, PS can also be geolocated more accurately and achieve a DEM with sub-meter precision [27, 84]. Compared to DS methods, PSI is not affected by baseline decorrelation. This indicates all acquired satellite data can be used to form interferograms. Meanwhile, the hard granite outcrops lead to high PS density. This guarantees the number of available interferograms and scatterer abundance and hence the accuracy of time series analysis on granite outcrops.

Among PSI, the PSInSAR algorithm introduced by Ferretti [81] and [82] is the most widely used method of time-series analysis, adopted in hundreds of peer reviewed papers, and received highest citations [27]. This indicates the reliability of PSInSAR methods, which have been widely verified and accepted by academics. In this way, PSInSAR has therefore been chosen for this research to estimate the surface displacement rates.

4.3 PSInSAR method

Developed by Ferretti [81, 82], the time series analysis model at PSInSAR can be summarised as four steps:

(1) Interferogram formation, where K interferograms are formed from K+1 SAR images.

(2) DEM and differential interferograms formation with orbital error removal.

(3) preliminary estimation of the LoS motion, elevation error, and atmospheric contribution, where only scatterers with high coherence are considered.

(4) Refinement of step (3) by removing the atmospheric phase screen (APS) through phase residuals spatial smoothing, which allows extra scatterers to be identified. The mean value of atmospheric components (APS) is calculated by averaging the atmospheric phase contribution relative to the master image (expressed in Eq. 4.10). This is impacted by the number of interferograms, the density of PS and the reliability of zero baseline steered interferometric phases ($\Delta\Phi$) [82].

$$\boldsymbol{APS_{master}^{T} = \frac{1}{K}\left\{\mathbf{1}^{T} \cdot \widehat{E'_{atmo}} + (\hat{a}\mathbf{1}^{T} + \widehat{p_{\xi}}\boldsymbol{\xi}^{T} + \widehat{p_{\eta}}\boldsymbol{\eta}^{T})\right\}} \quad \textbf{Eq. 4. 10}$$

Where K is the number of available interferograms, E'_{atmo} is atmospheric phase residue, $\hat{a}$, $\widehat{p_{\xi}}$, and $\widehat{p_{\eta}}$ are three linear components of the APS, and ξ and η are azimuth and slant (LoS) range coordinates respectively.

The contribution of $\Phi\,\mathrm{dem}$ can be reduced through the application of DEM regression to find the relationship of the phase and slight variations in the satellite's position, indicative of DEM error; $\Phi\,\mathrm{orb}$ and $\Phi\,\mathrm{atm}$ can be reduced through spatio-temporal filtering [198]. During these steps, the target site with strong stable signals and subsequently low $\Phi\,\mathrm{noise}$ are selected.

The selected scatterers are expected to be only slightly affected by geometrical and temporal decorrelation and exhibit a very stable sequence of amplitude values despite the high temporal and geometrical baseline dispersion. These scatterers are usually characterized by low phase residue with high ensemble coherence greater than a threshold value calculated by means of a time series analysis of the phase values. This can be expressed in Eq. 4.11 [82]:

$$|\Upsilon| = \left|\frac{1}{K}\sum_{k=1}^{K} e^{j\varphi_k} \cdot e^{-j\left(C_q B_{\perp} \cdot \Delta q + C_v T_k \cdot v\right)}\right| \quad \textbf{Eq. 4. 11}$$

Where K is the number of available interferograms, φ_k is the phase value of kth differential interferogram relative to the generic image pixel after APS removal, $B_{\perp}$ is perpendicular baseline and T_k is time interval. C_q and C_v can be further determined in Eq. 4.12 and 4.13 as:

$$\boldsymbol{C_q = \frac{4\pi}{\lambda R} sin\,\alpha} \quad \textbf{Eq. 4. 12}$$

$$\boldsymbol{C_v = \frac{4\pi}{\lambda}} \quad \textbf{Eq. 4. 13}$$

In this research, this threshold coherence value has been set as 0.75, this is also a most widely accepted threshold coherence by other PSI-related studies such as Jiang [199] Hu [200], and Farova [201]. Finally, the Φ def can be estimated by minimising the additional phase change contributors on a PS-by PS basis [81].

4.4 The estimation of vertical and horizontal displacement rates

The vertical, eastward, and northward displacements (D_U, D_E, D_N) are three components that can be estimated from the measured LoS surface displacement (ΔR) illustrated in Figure 4.2. These displacements are derived from the decomposition of LoS displacements in both ascending and descending directions (Figure 4.3).

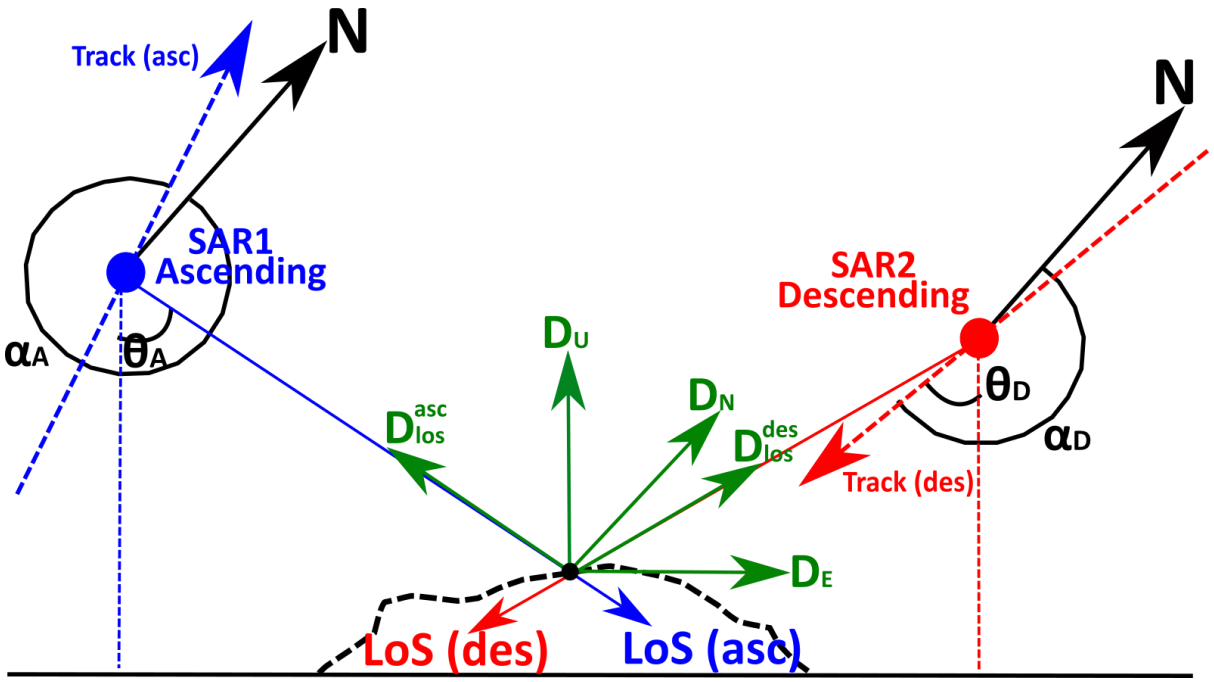


Figure 4.3 The satellite SAR imaging geometry along the ascending and descending orbits illustrates the projection relation between the LoS displacements (D_{los}^{des} and D_{los}^{asc}) and 3D motion components (D_U, D_E, and D_N). θ is incidence angle and α is the azimuth angle measured clockwise from the north. Figure edited from Dai [202].

In theory, the 3D displacement can be expressed in Eq. 4.14 [203, 204, 205]:

$$\mathbf{U} \cdot \begin{bmatrix} \mathbf{D_U} \\ \mathbf{D_E} \\ \mathbf{D_N} \end{bmatrix} = \mathbf{\Delta R} \quad \mathbf{Eq.4.14}$$

Where ΔR is monitored radar LoS displacement (ΔR) that can be expressed as:

$$\mathbf{\Delta R} = \begin{bmatrix} \mathbf{R^A_{los}} \\ \mathbf{R^D_{los}} \\ \mathbf{R^A_{azo}} \\ \mathbf{R^D_{azo}} \end{bmatrix} \textbf{ Eq. 4.15}$$

Where R^A_{los}, R^D_{los}, R^A_{azo}, and R^D_{azo} are four independent displacement vectors for LoS displacement from ascending orbit, LoS displacement from descending orbit, azimuth displacement from ascending orbit, and azimuth displacement from descending orbit respectively.

U is the projection matrix, which can be expressed as [205]:

$$\mathbf{U} = \begin{bmatrix} \mathbf{cos\theta_A} & \mathbf{-cos(\alpha_A - 1.5\pi)\,sin\,\theta_A} & \mathbf{-sin(\alpha_A - 1.5\pi)\,sin\,\theta_A} \\ \mathbf{cos\theta_D} & \mathbf{-cos(\alpha_D - 1.5\pi)\,sin\,\theta_D} & \mathbf{-sin(\alpha_D - 1.5\pi)\,sin\,\theta_D} \\ \mathbf{0} & \mathbf{sin(\alpha_A - 1.5\pi)} & \mathbf{-cos(\alpha_A - 1.5\pi)} \\ \mathbf{0} & \mathbf{sin(\alpha_D - 1.5\pi)} & \mathbf{-cos(\alpha_D - 1.5\pi)} \end{bmatrix} \textbf{Eq. 4.16}$$

Where α_A and α_D are azimuth angles of the satellite heading vector for ascending and descending orbits and θ_A and θ_D are pixel-based radar incidence angles at the reflection points from ascending and descending orbits.

The observations can be further divided into U_{los} and U_{azo}, which can be expressed in Eq. 4.17 and 4.18 respectively [205]:

$$\mathbf{U_{los}} = \begin{bmatrix} \boldsymbol{cos\theta_A} & \mathbf{-cos(\alpha_A - 1.5\pi)\,sin\,\theta_A} & \mathbf{-sin(\alpha_A - 1.5\pi)\,sin\,\theta_A} \\ \mathbf{cos\theta_D} & \mathbf{-cos(\alpha_D - 1.5\pi)\,sin\,\theta_D} & \mathbf{-sin(\alpha_D - 1.5\pi)\,sin\,\theta_D} \end{bmatrix} \textbf{Eq.4.17}$$

$$\mathbf{U_{azo}} = \begin{bmatrix} \mathbf{0} & \mathbf{sin(\alpha_A - 1.5\pi)} & \mathbf{-cos(\alpha_A - 1.5\pi)} \\ \mathbf{0} & \mathbf{sin(\alpha_D - 1.5\pi)} & \mathbf{-cos(\alpha_D - 1.5\pi)} \end{bmatrix} \textbf{Eq.4.18}$$

the consistent geometry in current Sentinel-1 SAR satellite images makes it difficult to measure D_N accurately, because the azimuthal offsets are typically much less precise than the LoS displacements [204]. This is because the satellite flies in a north-south orbit, which makes interferometry insensitive to the surface displacements in that direction [205]. Therefore, the contribution of D_N to the total LoS displacement (ΔR) is insignificant and negligible.

The large errors introduced by atmospheric noise and orbit error residual may further reduce the accuracy of the D_N estimation [203]. Altogether with the imprecise azimuthal offset measurements, the LoS displacements are strongly sensitive to D_U, modestly sensitive to D_E, and least sensitive to D_N [204], so that accurate estimation of the D_N rate from the LoS displacements is not possible.

To neglect northward displacement (D_N), Eq. 4.14 can be simplified to Eq. 4.19 to estimate the vertical displacement (D_U) and eastward displacement (D_E). This can be expressed as [203, 204]:

$$\mathbf{U_{los}}\begin{bmatrix}\mathbf{D_U}\\ \mathbf{D_E}\end{bmatrix} = \begin{bmatrix}\mathbf{R^A_{los}}\\ \mathbf{R^D_{los}}\end{bmatrix} = \mathbf{\Delta R} \quad \mathbf{Eq.\,4.19}$$

4.5 Alternative method for estimating northward displacement rates

D_N and D_E are two components of horizontal movements (D_H), where the orientation of horizontal stress is governed by the tectonic movements [145]. The direction of tectonic movements is dominated by maximum horizontal stress (σ1), in this way, D_H should be in line with σ1. In this way, based on the measurement of maximum horizontal stress, the direction of D_H can be estimated from the E-W component and the knowledge of the stress orientation. This is illustrated in Figure 4.4.

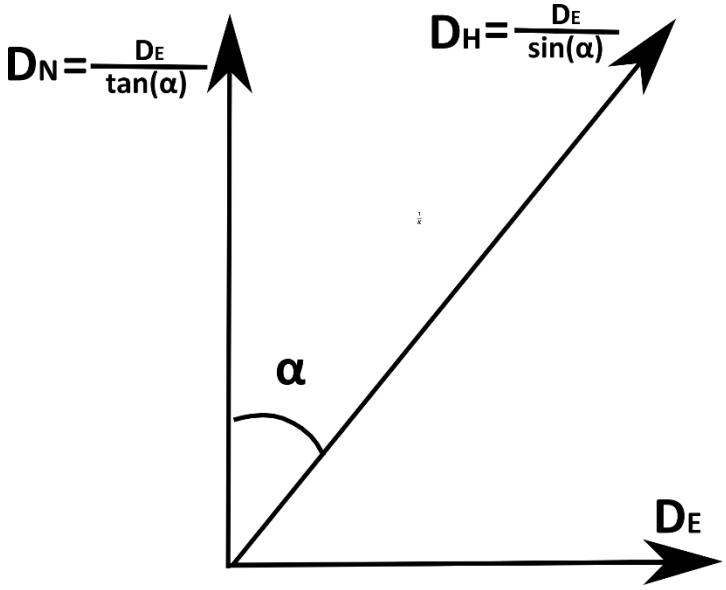


Figure 4. 4 The estimation of northing (D_N) and horizontal displacement (D_H) rates along maximum horizontal compression direction (α) based on the measured easting displacement rate (D_E).

The in-situ stress measurements suggest the Beishan area is in a compressive stress field with maximum horizontal stress generally in the direction of northeast-southwest. The measurements have been conducted at Boreholes BS01, BS05, BS06, BS15, BS16, BS17, BS18, and BS19 in Jiujing, Jijicao and Xinchang regions. This indicates the general direction of horizontal movements (D_H) should be along the maximum horizontal compression direction (α). As D_N and D_E are two components of D_H and D_E can be estimated, based on this value, the estimation of D_N and D_H, which is towards the maximum horizontal compression direction (α) can be achieved using trigonometric method. This has been schematically illustrated in Figure 4.4 and expressed is in Eq. 4.20 and 4.21 respectively.

$$\mathbf{D_N} = \frac{\mathbf{D_E}}{\mathbf{\tan(\alpha)}} \qquad \mathbf{Eq.\,4.20}$$

$$\mathbf{D_H = \frac{D_E}{\sin(\alpha)}} \qquad \mathbf{Eq.\,4.\,21}$$

This estimation is based on two assumptions, where the direction of horizontal deformation is in line with the stress field and the maximum horizontal displacement is almost homogeneous across the whole granite section.

4.6 Method to determine active faults

The active faults should first be supported by discontinuities (which might be valleys, gullies, or cracks) on the surface of the granite that are visible in Google Earth satellite imagery. Then, the observed discontinuities are correlated with the SAR image deformation rate patterns. To have confidence in the data, blocks with displacement rate differences along a fault plane should have an overall coherence greater than 0.7 over 2-3 years' observing period, to remove the impacts of geomorphologically induced surface deformation (see Section 4.7). The observed (Google Earth) discontinuities are correlated with the PSI data deformation rate patterns. By coupling optical imagery (Google Earth) with the SAR images, fault movements are observed in the SAR images with distinct displacement rate discontinuities between the two sides of the fault plane. In addition, using Google Earth satellite imagery also helped to differentiate potentially active faults from geomorphological features and atmospheric effects (APS).

It should be noted that the faults marked in this research are the most conspicuous features and it is likely that there are other, smaller faults within these blocks that may also be active but could not be quantified using this technique. To clearly express the deformation discontinuities along the two sides of fault valley, in addition to deformation pattern figures, there are three ways to reflect this kind of displacement rate difference, which are through time series analysis curves, frequency distribution curve and cross sections.

The time-series analyses conducted across several major blocks present the temporal variation and deviation of vertical displacement in ascending and descending views. This is achieved through the averaging of the displacement values of thousands of PSs within each block. They are conducted using the ENVI Region of Interest (ROI) Tool. The frequency distribution curves demonstrate the occurrence frequency of the displacement rate as a variable, which provides a more comparable way to reflect the displacement rates difference among blocks. They are also conducted through the ENVI ROI Tool.

Cross-sections are generated to show the spatial variation of displacement rates. It is conducted using the ENVI Arbitrary Profile Tool.

4.7 Method to characterise active fault

The significant velocity pattern contrasts or discontinuities between the two sides of the fault plane reflect the activation of the observed fault and in addition the fault properties can be characterised by the combination of vertical (D_U) and horizontal (D_E and D_N) deformations along the fault plane.

The normal faults triggered by extension show crustal extension and a divergent horizontal displacement pattern, where the hanging wall is expected to move downward relative to the footwall as shown in Figure 4.5(A). The reverse faults triggered by compression are showing crustal shortening, the horizontal deformation is expected to show a convergence pattern, in which the hanging wall moves upwards relative to the footwall side, as shown in Figure 4.5(B). Based on the horizontal and vertical displacement comparison along the two sides of the fault plane, the fault type and dipping direction can be postulated.

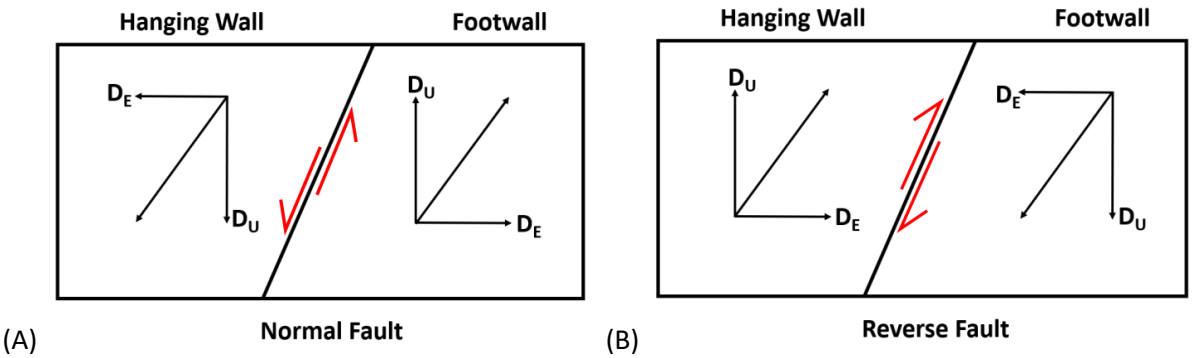


Figure 4. 5 The schematic illustrations of (A) normal fault and (B) reverse fault

4.8 The application of Coherence Change Detection (CCD) to identify surface alteration

The surface deformation in study areas might be triggered by tectonic activities and geomorphological processes. Both PS and DS methods introduced in Section 4.3 can remove the effects of geomorphology in urban areas or rocky outcrops due to their high strength. However, the displacement rate measurements in Quaternary sediments covering rocky outcrops show the effects of erosion. This is mainly due to Quaternary sediments' low strength and susceptibility to erosion. However, the geomorphological processes would always lead to surface alteration and in turn decrease the coherence. In this way, the application of coherence allows the identification of

geomorphologically impacted areas and assess the confidence of PSI results in reflecting tectonic deformation.

Coherence (ϒ) is a measure of the correlation between repeated of radar observations, which is usually used to describe how well the phase of the received signal is preserved. Coherence ranges from 0 (no correlation) to 1 (perfect correlation), and the two waves are coherent when both are in phase [157, 158]. The coherence quantifies the changes between SAR images at different acquisitions, which therefore allows us to identify the alteration of a surface over time. Geomorphological processes that lead to surface alteration, such as erosion or deposition, therefore cause lower coherence.

The coherence can be expressed in Eq. 4.22 [158]:

$$\Upsilon = \frac{\left|\sum_{i=1}^{L}\ \sum_{j=1}^{M}\ \mathbf{Im_1}(x_i, z_j)\ \mathbf{Im_2}(x_i, z_j)\right|}{\sqrt{\sum_{i=1}^{L}\ \sum_{j=1}^{M}\ \left|\mathbf{Im_1}(x_i, z_j)\right|^2\ \sum_{i=1}^{L}\ \sum_{j=1}^{M}\ \left|\mathbf{Im_2}(x_i, z_j)\right|^2}} \quad \textbf{Eq. 4.22}$$

Where Im_1 and Im_2 refer to the complex signals of master image and slave image due to the coherence of a pixel, which is estimated by the means of kernels with L × M pixels.

The coherence can be affected by many factors, including local slope, surface properties, time span between passes, baseline, poor coregistration and poor sampling [158]. These factors can be generalised as follows in Eq. 4.23 [180, 206]:

$$\mathbf{\Upsilon = \Upsilon_{thermal}\ \Upsilon_{doppler}\ \Upsilon_{processing}\ \Upsilon_{temporal}\ \Upsilon_{geom}\ \Upsilon_{vol}} \quad \textbf{Eq. 4.23}$$

$\Upsilon_{thermal}$ is thermal noise decorrelation, which can be expressed in Eq. 4.24 [207], where $SNR_{1\&2}$ refers to signal to noise ratios:

$$\mathbf{\Upsilon_{thermal} = \frac{1}{\sqrt{1+SNR_1{}^{-1}}\sqrt{1+SNR_2{}^{-1}}}} \quad \textbf{Eq. 4.24}$$

$\Upsilon_{doppler}$ is doppler centroid decorrelation.

$\Upsilon_{processing}$ is data processing decorrelation.

$\Upsilon_{temporal}$ is temporal decorrelation caused by surface changes between SAR acquisitions.

Υ_{geom} is geometric (baseline) decorrelation, caused by change in the looking angle of the sensor, which can be expressed as [207]:

$$\mathbf{\Upsilon_{geom} = 1 - \frac{2B_L r_y cos\theta}{\lambda R}} \quad \textbf{Eq. 4.25}$$

Within Eq. 4.25, $B_\perp$ is perpendicular baseline, θ is the projecting angle, r_y is the range resolution of the radar, λ is the wavelength, and R is the range to the target point.

Υ_{vol} is volumetric scattering decorrelation, which can be determined by [207]:

$$\Upsilon_{vol} = \frac{2sin(\kappa_z h_v/2)}{\kappa_z h_v} \quad \textbf{Eq. 4.26}$$

$$\kappa_z = \frac{4\pi B_\perp}{\lambda R sin\theta} \quad \textbf{Eq. 4.27}$$

Where h_v is scattering height and κ_z is vertical wavenumber. In general, Υ_{vol} can be impacted by the vegetation coverage and the steep slopes oriented towards the satellite LoS, which usually leads to the low coherence [158].

Coherent Change Detection (CCD) refers to the process of gathering two time-separated high-resolution satellite radar images of one geographic area on the surface for coherence comparison in order to detect and measure the surface changes [208]. In this research, 69 ascending Sentinel-1 observations spanning from 08/10/2017 to 07/02/2020 have been chosen for coherence estimation.

The Sentinel-1 data on acquistration date 08/10/2017 was chosen as Reference image and the other 68 images, with acquistration dates from 01/11/2017 to 07/02/2020, were used as Secondary images. The reference SAR image is expected to form interferograms with the Secondary images one after another, so that 68 interferograms with time periods 08/10/2017-01/11/2017 to 08/10/2017-07/02/2020 were generated. Collectively, these 68 interferograms demonstrate the temporal variation of coherence in respect to Reference image over the study areas. The working idea of CCD in this research is illustrated in Figure 4.6.

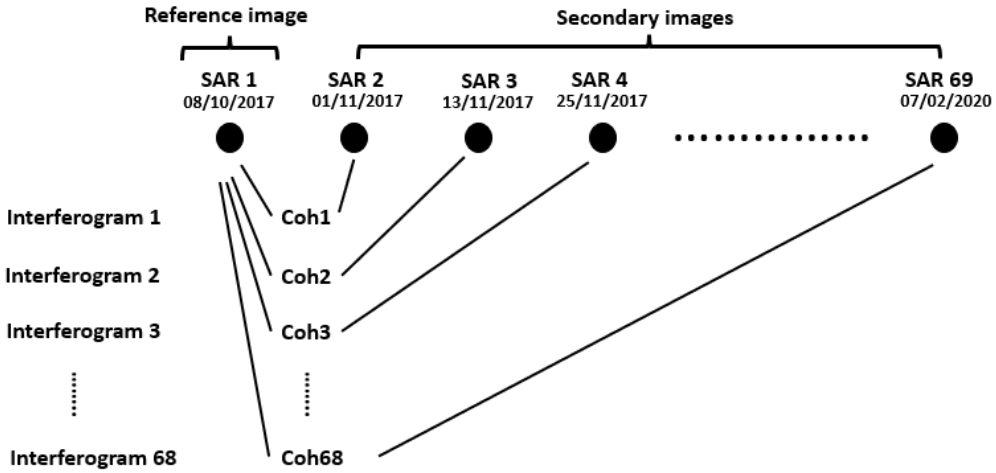
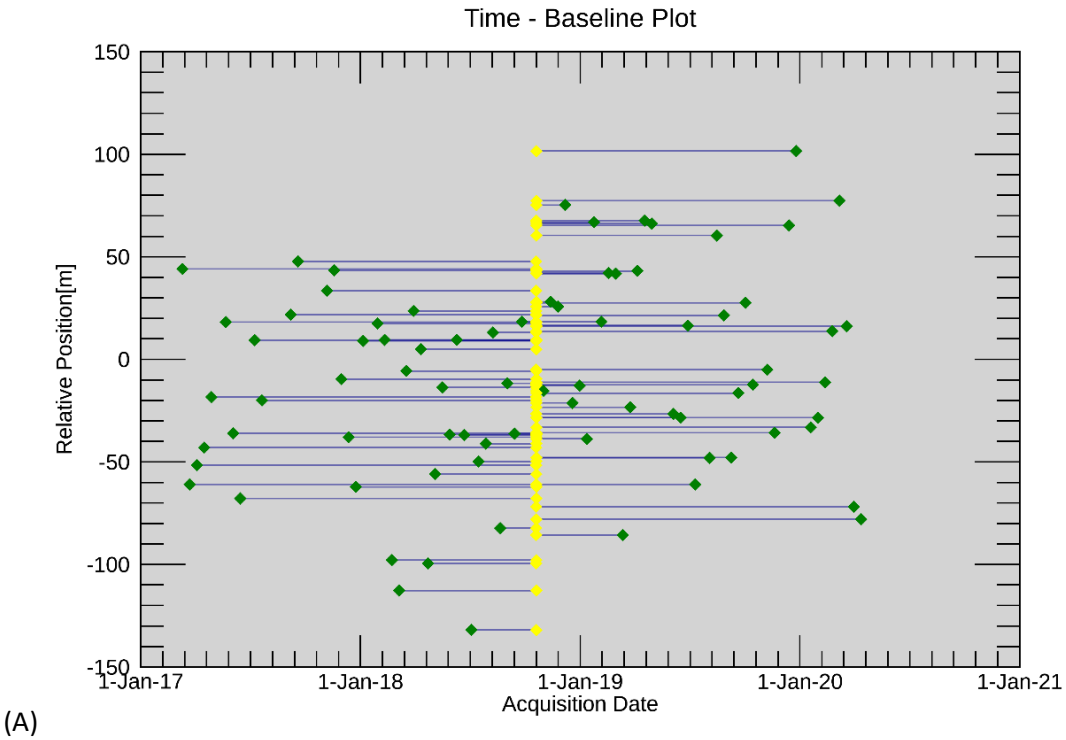


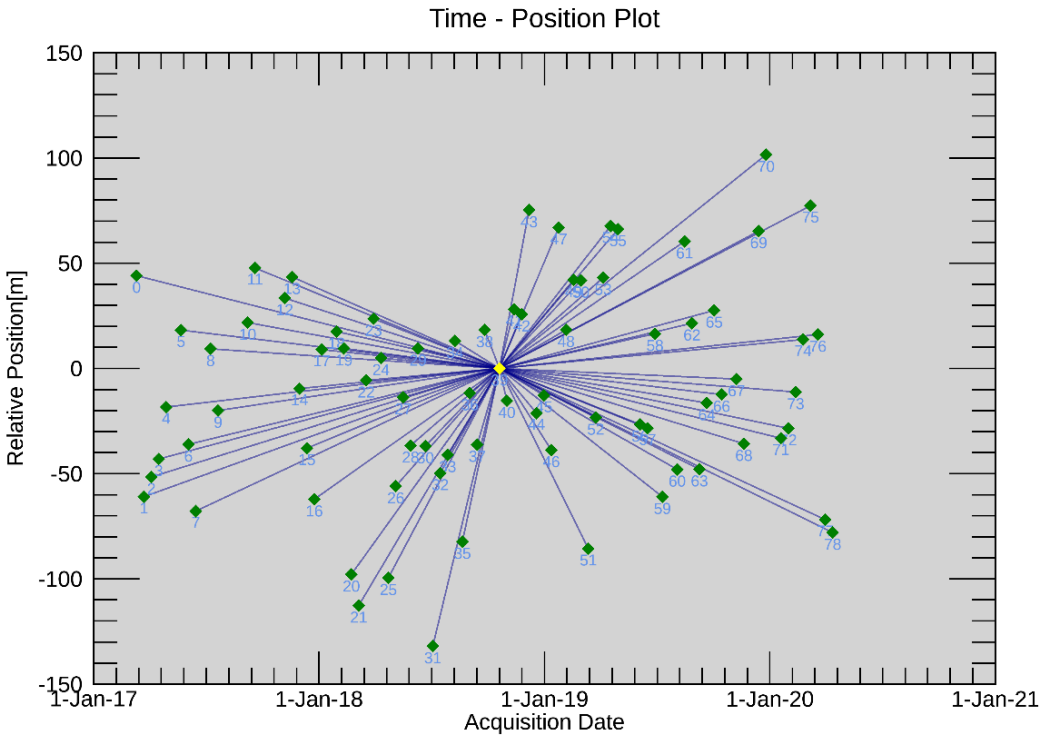
Figure 4. 6 The schematic figure illustrates the combination of SAR images to form interferograms through Coherence Change Detection (CCD) method in this study.

4.9 Sentinel-1 data and data reprocessing software

The SAR images were obtained by the Sentinel-1 satellite from the European Space Agency (ESA) over Beishan area. These images were downloaded from Alaska Satellite Facility's website (https://search.asf.alaska.edu/). For this research project, 72 descending images from 11/March/2017 to 31/January/2020 and 69 ascending images from 08/October/2017 to 07/February/2020 were downloaded. The complete information about these data points is presented in Appendix at Table S1 and S2. The descending data on 02/09/2018 and the ascending data on 12/02/2019 have been chosen as Master images respectively. This is illustrated in Figure 4.7 and 4.8.

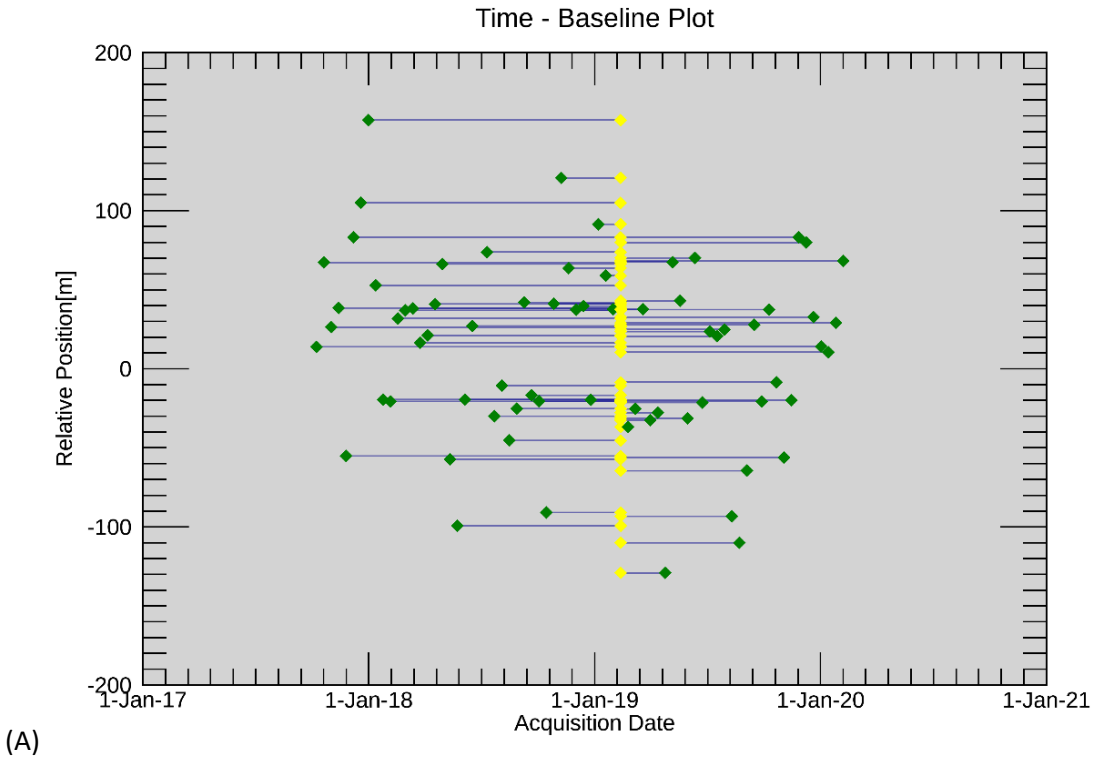


(A)

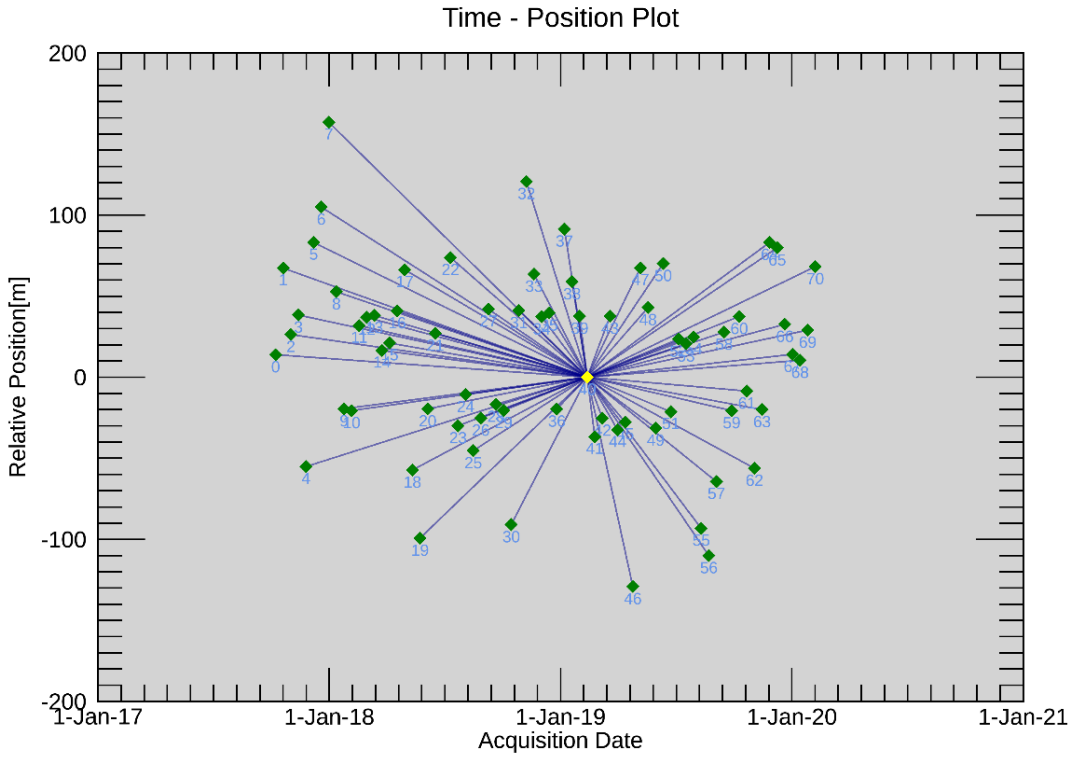


(B)

Figure 4.7 (A) and (B). The connection graphs between the Reference (yellow dot) and Secondary (green dots) images which present the Time-Baseline Plot (A) and Time-Position Plot (B) obtained from descending Sentinel-12 dataset from 11/March/2017 to 31/January/2020. The blue line between yellow and green dots represents an interferogram. The graphs are generated using the PSInSAR method through ENVI SARScape.



(A)



(B)

Figure 4.8 (A) and (B). The connection graphs between the Reference (yellow dot) and Secondary (green dots) images which present the Time-Baseline Plot (A) and Time-Position Plot (B) obtained from ascending Sentinel-12 dataset from 08/October/2017 to 07/February/2020. The blue line between yellow and green dots represents an interferogram. The graphs are generated using the PSInSAR method through ENVI SARScape.

These Sentinel-1 data were reprocessed in ENVI SARScape software (version 5.5.2.1) from Harris Geospatial Solutions (https://www.l3harrisgeospatial.com/Software-Technology/ENVI-SARscape), which is well-reputed for PSI processing of Sentinel-1 data (e.g., Agarwal [148], Trevoho [209], Smolianinova [145] and Khan [146]). Within this software, the PSI technique was developed using the algorithm introduced by Ferretti [81] and [82], and includes five processing steps [210], illustrated in Figure 4.9.

(1) **Connection graph:** this is used to connect all images to create connection network and define the SAR pair combination (Reference and Secondary), which can be used to generate the multiple differential interferograms. The Time-Position plot shows the normal distance from the Master (y axis) and the input acquisition dates (x axis) and Time-Baseline plot which shows the normal baseline (y axis), and the input acquisition dates (x axis). The connected graphs of the datasets in this research have been presented in Figure 4.7 and 4.8.

(2) **Interferometric workflow:** is used to generate the flattened interferograms and intensity images, which can be further divided into two processes: 'Correlated registration' and 'Interferogram generation and flattening'.

2.1 Correlated registration: It is the process of superimposing of multiple images with same acquisition geometry. This includes the spatial registration & resampling to correct the relative transitional shift, rotational, and scale differences.

2.2 Interferogram generation and flattening: The purpose of this process is to generate a flattened interferogram with constant phase since the acquisition geometry and topographic phase being removed. This can be achieved through the measurement of phase difference between two complex co-registered SAR images by multiplying one image with the other's complex conjugate, so that an interferogram is formed in each period.

(3) PS first inversion: This generates the first displacement, velocity and height related results without atmospheric phase removal. This approach is based on the identification of the persistent scatterers introduced in Section 4.2.

(4) PS Second inversion: This inversion includes the estimation and removal of the atmospheric phase components related to the spatial and temporal variations and to generate the final displacements. A linear model is applied to estimate height and displacement velocity, which can be produced by:

$$\mathbf{Disp} = \mathbf{K} + \mathbf{V}(\mathbf{t} - \mathbf{t_0}) \quad \textbf{Eq. 4.28}$$

Where Disp is the displacement at time t, K is the constant used for final fitting process, and V is the displacement velocity. The previously estimated linear model is subtracted date-by-date to estimate the atmospheric effects, and the atmospheric correction i.e., performed by two procedures:

a. Atmosphere Low Pass: To account for the spatial distribution of the atmospheric variations through square window.

b. Atmosphere High Pass: To account for the temporal distribution of the atmospheric variations through temporal window.

(5) Geocoding: To project all PS related products (displacement velocities, residual heights, displacement time series, kml, and shape files, etc.) onto the cartographic system in formats of raster and/or shape.

The key parameter values were set during the Sentinel-1 data reprocessing (ascending and descending) and are summarised in Table 4.1.

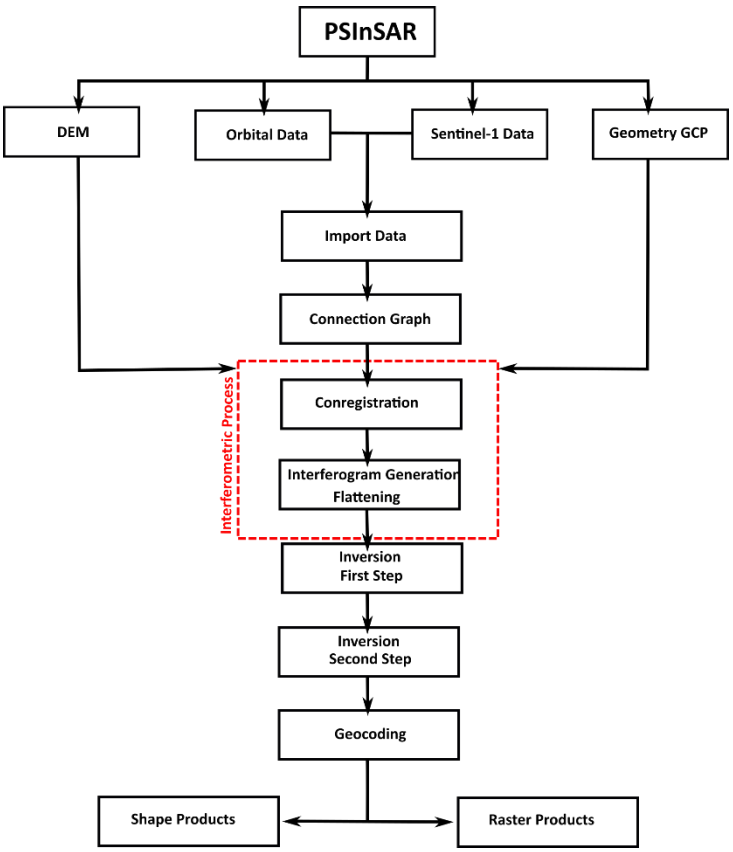


Figure 4.9 The flowchart of Sentinel-1 data reprocessing through PSInSAR method from software ENVI SARScape. Figure edited from reference [211].

Table 4.1 The parameter value setting in Sentinel-1 data reprocessing

Processing Step	Parameter	Setting
Coregistration	Initialization From Orbit	TRUE
	Orbit Accuracy	TRUE
	Estimate From Amplitude	TRUE
	Estimate From Coherence	TRUE
	Range/Azimuth Dependency	3/3
	Range/Azimuth Window Number	10/15
	Range Window Size	256
	Azimuth Window Size	512
	Cross Correlation Threshold	0.25
	Fine Range Window Number	40
	Fine Azimuth Window Number	60
	Fine Range/ Azimuth Window Size	32/32
	SNR Threshold	3.2
Interferometry	Range Looks	-4
	Azimuth Looks	1
	pectral Shift Filter	FALSE
	Doppler Filter	FALSE
Displacements First Inversion	Sub-Area size(km^2)	25
	Overlap (%)	30
	Coherence used for Merging all Sub-Areas	0.66
	Minimum velocity[mm/year]	-25
	Maximum velocity[mm/year]	25
	Sampling rate velocity[mm/year]	1
	Minimum height[m]	-70
	Maximum height[m]	70
	Sampling rate height[m]	2
Displacements Second Inversion	Low Pass Filter Size[m]	1200
	High Pass Filter Size[days]	365
	Minimum velocity[mm/year]	-25
	Maximum velocity[mm/year]	25
	Sampling rate velocity[mm/year]	1
	Minimum height[m]	-70
	Maximum height[m]	70
	Sampling rate height[m]	2
Threshold and Geocoding	Coherence Threshold	0.75
	Geocode using Mu/Sigma Threshold	FALSE
	Mu/Sigma Threshold	0
	Water Body Mask	0
	Refinement GCP File	Not OK
	Geocoded Shape Products	TRUE
	Geocoded Raster Products	TRUE
	X Dimension	25
	Y Dimension	25

4.10 Method to validate PSInSAR results using ICSAR

Chapter 3 reviews a series of peer reviewed studies [145, 146, 148, and 209] to demonstrate the reliability and accuracy of the SARScape results when monitoring ground movements, the algorithm of SARScape is proprietary and a commercial product. Therefore, the end users cannot fully understand the software's working mechanisms from a technical perspective, an element of "black-box". In this way, the reliability of the results could potentially be questioned.

To validate the SARScape results, it requires an alternative way to re-estimate the surface displacement rates over same study area. The Imperial College SAR (ICSAR) was chosen in this research. ICSAR is a new satellite data reprocessing algorithm developed by Stewart Agar at the Department of Civil and Environmental Engineering in Imperial College London, which intends to provide a reference PSI implementation with practically feasible computational requirements for testing and developing data processing approaches in rural areas. It has been developed as an expansible, easy-to-use and easily reproducible system for processing Sentinel 1 data into MTI result sets, since the open-source software allows for easier review, collaboration and the wider adoption and utilisation by the research community. Therefore, it has also been called as OpenInSAR [231]. This project was seen as an opportunity to test ICSAR against SARScape and as a chance to validate the regional results.

ICSAR is a collection of MATLAB scripts designed to implement InSAR data processing through PSI with a similar approach with PSInSAR, IPTA, and DePSI. But the code algorithm is open-source and can be freely downloaded at: https://github.com/insar-uk/OpenInSAR [231]. The satellite data are stored and reprocessed via the Imperial College Research Data Store (RDS). This includes 16 stages with 20 scripts [232]. The details are presented in Table 4.2.

Table 4.2 The processing stages, script name and script purposes of ICSAR [232]

Stage	Script Name	Script Purpose
Stage 0	ICS_0_Initialise	Convert user inputs and other variables into the 'Settings' structure.
	ICS_U_WriteReload	Create script for reloading investigation data.
Stage 1	ICS_1_CheckCatalogue	Find Sentinel-1 data in the given image folder.
Stage 2	ICS_2_ImportAnnotations	Load annotations from the files in the Settings variable.
Stage 3	ICS_3_ImportOrbits	Imports orbital file for each image we have annotations for.
Stage 4	ICS_4_PreProcessing	Get information about each individual burst. Choose which burst covers the AOI. Choose a master image.

Stage 5	ICS_5_Burst stitching	Crop and join all bursts into a continuous image of the AOI.
Stage 6	ICS_6_SubRegions	Divide the image into smaller sections for processing.
	ICS_U_CheckDataConsistency	Check all the files are valid (no download errors or deletions).
Stage 7	ICS_7_GeocodeMaster	Geocode master image to flat Earth.
Stage 8	ICS_8_DemImport	Import digital elevation model.
Stage 9	ICS_9_GeocodeMasterWithDEM	Geocode master image with a DEM.
Stage 10	ICS_10_Coregister	Co-register slave images onto the master's latitude-longitude grid.
Stage 11	ICS_11_Resample	Resample all images onto a common grid.
Stage 12	ICS_12_Interferograms	Create interferograms from all regions.
	ICS_Flattening	Interferogram flattening.
Stage 13	ICS_13_PSCs	Identify persistent scatterer candidates based on amplitude stability (mean and variance).
Stage 14	ICS_14_FirstInversion	PSI inversion.
Stage 15	ICS_15_AtmosphericCorrection	Load residuals from previous step. Filter in space and time to estimate atmospheric contribution. Remove this from the raw interferometric data.
	ICS_16_SecondInversionSingle	Second inversion and writing shapefiles.

To validate the SARScape results, the descending Sentinel-1 data set (Table S2) which were previously reprocessed by SARScape over Jiujing study area were re-analysed using the ICSAR algorithm. The typical deformation patterns of SARScape can be validated through the comparison with ICSAR results.

5. The preliminary interpretation of surface deformation and the role of geomorphological processes

To support the long-term disposal of HLW, the aim of this study is to quantify the tectonic activities within Beishan. However, the literature review in Chapter 3 suggested there are many factors that may change the Line of Sight (LoS) distance and therefore cause the surface deformation. These include groundwater variation, landslides, geomorphological processes (erosion and deposition), volcanic activities and tectonic (fault) activities. Further, the atmospheric residue during the data reprocessing may also impact the monitored deformation.

The objective of this chapter is to preliminarily interpret the SAR deformation data by identifying the impacts of these factors on monitored InSAR deformation patterns. The emphasis in on discovering the influence of geomorphological processes. This objective is achieved through the application of Coherence Change Detection (CCD) method over three study areas (Suanjingzi, Jiujing and Xinchang). The explanation are as follows.

5.1 Ground displacement maps

To discover the surface deformation, a total of 72 images from the descending orbital node of Sentinel-1 (acquired between 11/03/2017 and 31/01/2020) and 69 from the ascending node (acquired between 01/10/2017 and 07/02/2020) have been processed using PSInSAR method within SARScape over three study regions.

As introduced in Methodology Chapter (Chapter 4), the combination of descending and ascending LoS deformation data sets allow us to compute the deformation rates in vertical (perpendicular to ground) horizontal (east-west) directions. This would ultimately benefit the characterization of active faults. The patterns of deformation rates in LoS ascending direction (D_{los}^{asc}), LoS descending direction (D_{los}^{des}), vertical direction (combined ascending-descending) (D_U) and easting direction (D_E) at three study regions (Suanjingzi, Jiujing and Xinchang) are presented in Figures 5.1 (A, B, C, D), 5.2 (A, B, C, D) and 5.3 (A, B, C, D) respectively. These figures illustrate the patterns of deformation, the areas covered by Quaternary sediments (include Holocene sediments) have been circled by black dash lines.

Within each study region at Figures 5.1 to 5.3 (A, B, C, D), the locations of ROIs (Regions of Interest) are highlighted by red dashed boxes. The ROIs are selected based on the distribution of deformation patterns. These represent and reflect the overall deformation trends within each Block. The mean deformation rates with standard deviations of pixels at each ROIs were calculated through the ENVI

Region of Interest (ROI) Tool. These data have been summarized in Tables 5.1, 5.2 and 5.3 respectively. It is important to note the standard deviations presented are measurements of uncertainty or relative accuracy of measured displacements. The standard deviation is a widely adopted measure of the error on PSI measurements, and the mean value and standard deviation are calculated from the spatial average of persistent scatterer points within each block area. There are various reasons contribute the standard deviations. These will be discussed in Chapter 7.

Table 5.1 The displacement rates of selected blocks in Suanjingzi

Sub-area	Number of pixels	D_{los}^{des} (mma^{-1})	D_{los}^{asc} (mma^{-1})	D_U (mm a^{-1})	D_E (mm a^{-1})
SJZ0	14463	-0.12±1.01	-0.94±1.37	-0.68±1.14	0.65±1.26
SJZ1	8125	-0.02±0.56	-0.47±0.76	-0.32±0.61	0.36±0.72
SJZ2	11622	-0.01±0.63	0.28±0.87	0.17±0.70	-0.23±0.83
SJZ3	4116	-0.11±0.67	-0.30±0.94	-0.27±0.73	0.16±0.90
SJZ4	2795	-0.04±0.57	0.16±0.75	-0.08±0.60	-0.15±0.72
SJZ5	5476	-0.35±0.62	-0.13±0.85	-0.32±0.68	-0.16±0.81
SJZ6a	9381	0.16±0.57	0.23±0.79	0.24±0.63	-0.12±0.74
SJZ6b	9710	0.05±0.63	0.21±0.87	0.17±0.68	-0.13±0.83
SJZ7a	12818	0.22±0.63	-0.10±0.89	0.09±0.70	0.25±0.83
SJZ7b	12683	0.17±0.63	-0.21±0.82	-0.01±0.67	0.29±0.79
SJZ8	4457	-0.87±0.66	0.11±0.97	-0.53±0.75	-0.73±0.91
SJZ9	6531	-0.14±0.56	-0.37±0.75	-0.33±0.60	0.19±0.72
SJZ10	11004	-0.58±0.69	-0.30±0.94	-0.59±0.75	-0.20±0.90
SJZ11	6272	-0.18±0.62	-0.22±0.83	-0.26±0.66	0.04±0.79
SJZ12	6782	0.10±0.50	0.23±0.56	0.21±0.49	-0.12±0.57
SJZ13	6848	0.40±0.83	-0.58±1.08	-0.10±0.90	0.75±1.02
SJZ14	3219	0.27±0.69	0.25±0.79	0.35±0.69	0.00±0.79
SJZ15	2569	0.23±00.71	-0.36±0.81	-0.07±0.69	0.46±0.84

Table 5.2 The displacement rates of selected blocks in Jiujing

Block	Number of pixels	D_{los}^{asc} (mma^{-1})	D_{los}^{des} (mma^{-1})	D_E (mma^{-1})	D_U (mma^{-1})
JJ1	16350	0.66±0.71	-0.05±0.52	-0.46±0.81	0.33±0.64
JJ2	20420	none	none	none	0.60±0.57
JJ2-1	8099	0.61±0.68	0.25±0.46	-0.38±0.63	0.65±0.53
JJ2-2	12321	0.17±0.69	0.38±0.46	-0.10±0.63	0.59±0.54
JJ3	9177	0.49±0.67	0.10±0.47	-0.26±0.66	0.42±0.53
JJ4	5600	-0.07±0.68	0.16±0.46	0.18±0.63	0.06±0.53
JJ5	6205	-0.22±0.62	-0.21±0.44	0.02±0.59	-0.26±0.51
JJ6	4919	-0.04±0.69	-0.30±0.50	-0.20±0.66	-0.20±0.70
JJ7	7253	0.06±0.61	-0.12±0.46	-0.15±0.62	-0.04±0.49
JJ8	4719	0.30±0.54	-0.26±0.39	-0.43±0.51	0.02±0.43
JJ9	21904	0.42±0.66	-0.14±0.46	-0.33±0.70	0.17±0.54
JJ10	16514	0.42±0.75	-0.07±0.53	-0.38±0.74	0.26±0.59
JJ11	33052	-0.21±0.75	-0.13±0.60	0.27±0.90	-0.18±0.71
JJ12	40877	-0.25±0.67	0.19±0.46	0.22±0.64	-0.05±0.53
JJ13	10104	-0.14±0.62	0.18±0.43	0.22±0.56	0.04±0.45
JJ14	3316	-0.54±0.77	0.06±0.50	0.29±0.63	-0.32±0.60
JJ15	8204	-0.14±0.67	0.02±0.44	0.12±0.68	0.01±0.58
JJ16	10274	0.24±0.75	0.01±0.50	-0.10±0.67	0.16±0.60
JJ17	4556	0.26±0.62	0.00±0.46	-0.29±0.70	0.16±0.51
JJ19	31958	0.76±0.73	-0.08±0.54	-0.54±0.69	0.35±0.60
JJ20	9683	0.28±0.71	-0.02±0.51	-0.20±0.69	0.16±0.59
JJ21	15449	-0.04±0.70	0.06±0.48	0.05±0.64	-0.03±0.58
JJ22	9472	-0.28±0.83	-0.20±0.58	0.06±0.79	-0.41±0.74
JJ23	25539	0.00±0.60	-0.39±0.41	-0.28±0.65	-0.32±0.58
JJ24	11776	-0.08±0.60	-0.41±0.40	-0.30±0.56	-0.28±0.56
JJ25	6855	-0.38±0.72	-0.32±0.47	0.03±0.66	-0.39±0.56
JJ26	50474	-0.10±0.71	-0.15±0.54	-0.04±0.75	-0.19±0.64
JJ27	9895	0.74±0.71	-0.02±0.55	-0.51±0.85	0.47±0.58
JJ28	5759	0.05±0.68	0.09±0.47	0.09±0.65	0.14±0.54
JJ29	7139	-0.19±0.70	-0.23±0.49	-0.03±0.66	-0.28±0.56
JJ30	5286	-0.26±0.66	-0.24±0.42	0.01±0.61	-0.33±0.51

Table 5.3 The displacement rates of selected blocks in Xinchang

Block	Number of pixels	D_{los}^{des} (mma^{-1})	D_{los}^{asc}(mma^{-1})	D_U (mma^{-1})	D_E (mma^{-1})
XC1	2351	-0.44±0.63	-0.09±0.70	-0.35±0.58	-0.27±0.71
XC2	3838	-0.26±0.51	0.40±0.60	0.09±0.49	-0.51±0.60
XC3	4515	-0.04±0.45	0.09±0.53	0.03±0.44	-0.10±0.52
XC4	2303	-0.31±0.51	0.06±0.61	-0.17±0.48	-0.28±0.61
XC5	4199	-0.36±0.47	-0.12±0.55	-0.32±0.45	-0.18±0.55
XC6	3790	-0.13±0.51	-0.21±0.59	-0.22±0.48	0.06±0.59
XC7	6257	0.11±0.41	-0.18±0.50	-0.04±0.40	0.22±0.49
XC8	2116	0.14±0.56	0.15±0.55	0.19±0.49	-0.01±0.58
XC9	11083	0.06±0.53	0.08±0.53	0.09±0.47	-0.02±0.57
XC10	7211	0.05±0.50	-0.29±0.59	-0.15±0.48	0.27±0.58
XC11	4416	0.06±0.59	-0.51±0.66	-0.29±0.55	0.45±0.67
XC12	10961	0.09±0.60	-0.63±0.58	-0.34±0.52	0.56±0.63
XC13	6500	0.15±0.56	-0.02±0.55	0.09±0.49	0.13±0.59

As presented in Figures 5.1 to 5.3 and Tables 5.1 to 5.3, most observed displacements in the study areas lie in the range between -1 to 1 mma^{-1}, this reflects a very low surface displacement overall. There are some deviations between the ascending (D_{los}^{asc}) and descending (D_{los}^{des}) LoS displacements. This is especially distinct at Blocks SJZ0, SJZ8, SJZ13 in Suanjingzi, Blocks JJ1, JJ8, JJ14, JJ19, JJ27 in Jiujing and XC2 and XC12 at Xinchang, where the difference between D_{los}^{asc} and D_{los}^{des} is more than 0.5mma^{-1}. This indicates horizontal displacement in the east-west direction. This concept is schematically illustrated in Figure 5.4.

In general, the displacements measurements from ascending and descending orbits are expected to be equal if the displacement is purely vertical. However, the east-west oriented horizontal displacements lead to asymmetric variations of LoS distance, where a high horizontally displacement rate usually leads to a large difference between D_{los}^{asc} and D_{los}^{des}. The westward displacement of a scattering point would decrease the line of sight (LoS) distance between scatterer and ascending node satellite position, which make the ascending views appears to have subsidized less (or uplifted more). On the descending node, the westwards displacement will increase the LoS distance, making it appears to have subsidized more (or uplifted less). Conversely, eastward displacement increases the ascending LoS distance and reduces the descending LoS distance, which therefore makes the descending patterns appear more uplifted (less subsided) and ascending patterns appear less uplifted (more subsided).

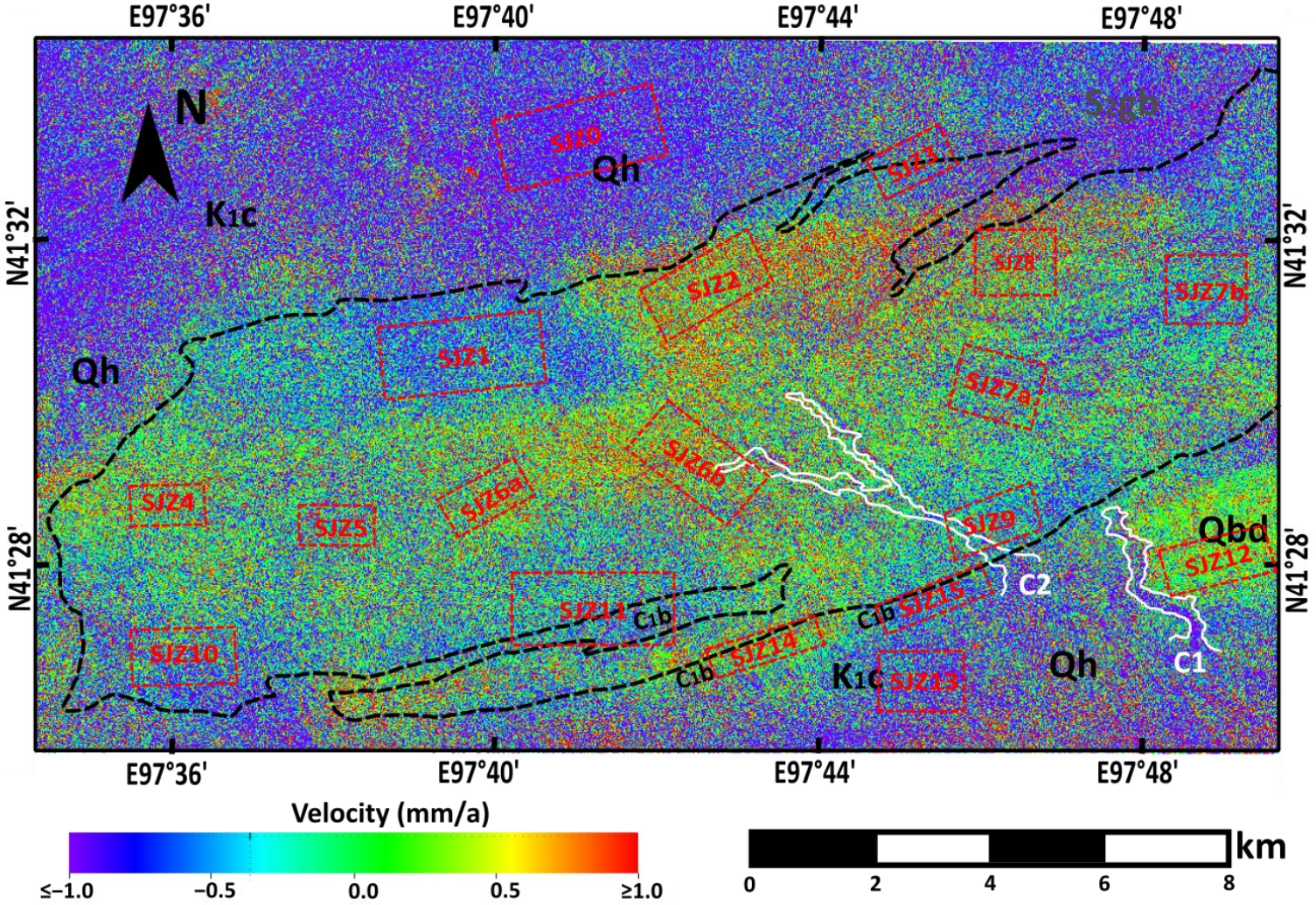


Figure 5.1 (A) Patterns of LoS displacement rate in ascending (D_{los}^{asc}) direction across the Suanjingzi study area. In Figure 5.1 (A), the positive values (green-to-red colours) indicate uplift, and the negative values (blue-to-green colours) indicate to subsidence. The black dash outline shows the extent of the Suanjingzi granodiorite pluton. The black labels indicate: Holocene sediments (Qh), lower Cretaceous Chijinbao Formation (K1c), lower Carboniferous Baishan Formation (C1b), Qingbaikou Series Dahuoluoshan Group (Qbd) and Middle Silurian Gongpoquan Group (S2gb). The white dash lines indicate the major fluvial channels.

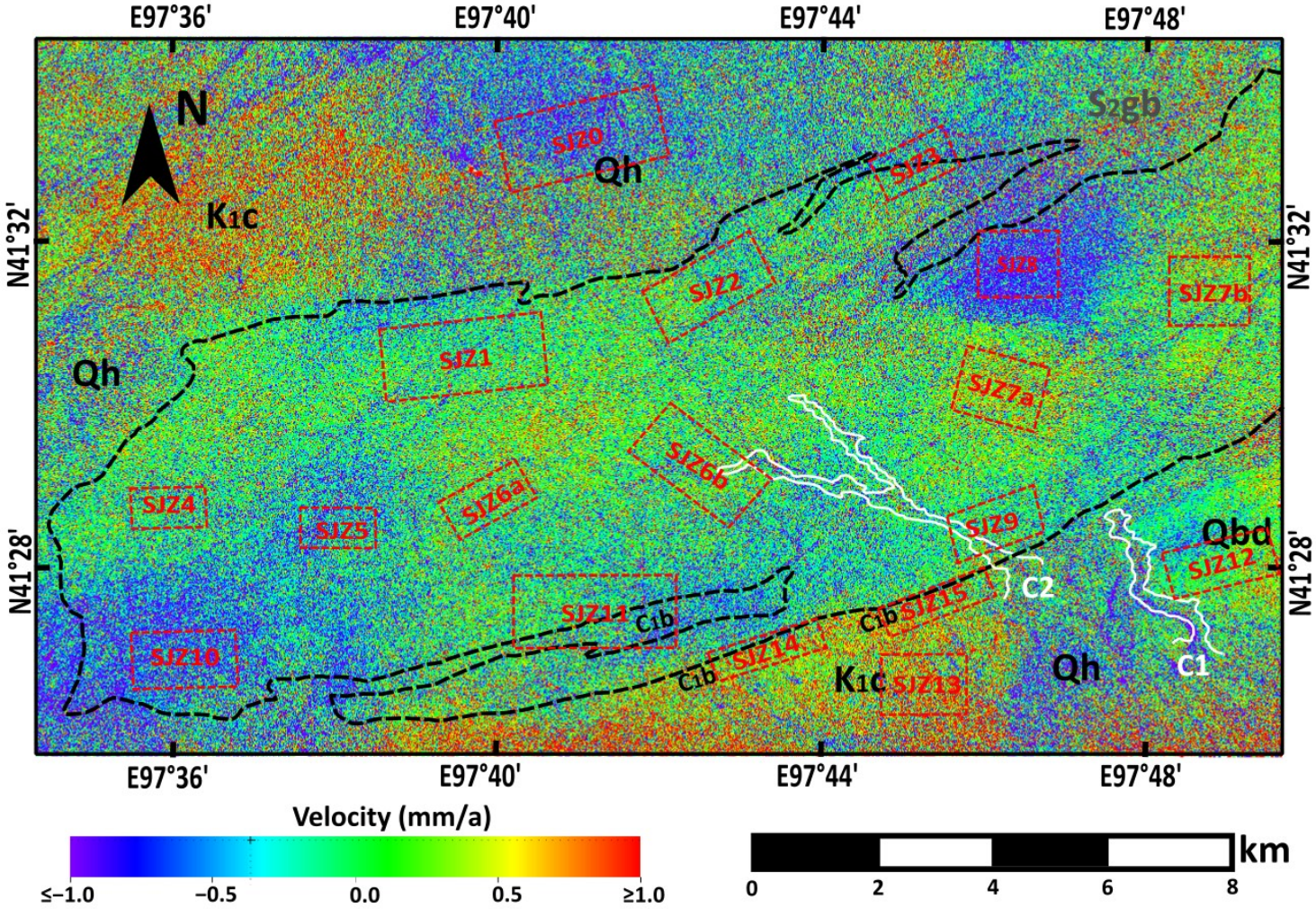


Figure 5.1 (B) Patterns of LoS displacement rate in descending (D_{los}^{des}) direction across the Suanjingzi study area. In Figure 5.1 (B), the positive values (green-to-red colors) indicate uplift, and the negative values (blue-to-green colours) indicate to subsidence. The black dash outline shows the extent of the Suanjingzi granodiorite pluton. The black labels indicate: Holocene sediments (Qh), lower Cretaceous Chijinbao Formation (K1c), lower Carboniferous Baishan Formation (C1b), Qingbaikou Series Dahuoluoshan Group (Qbd) and Middle Silurian Gongpoquan Group (S2gb). The white dash lines indicate the major fluvial channels.

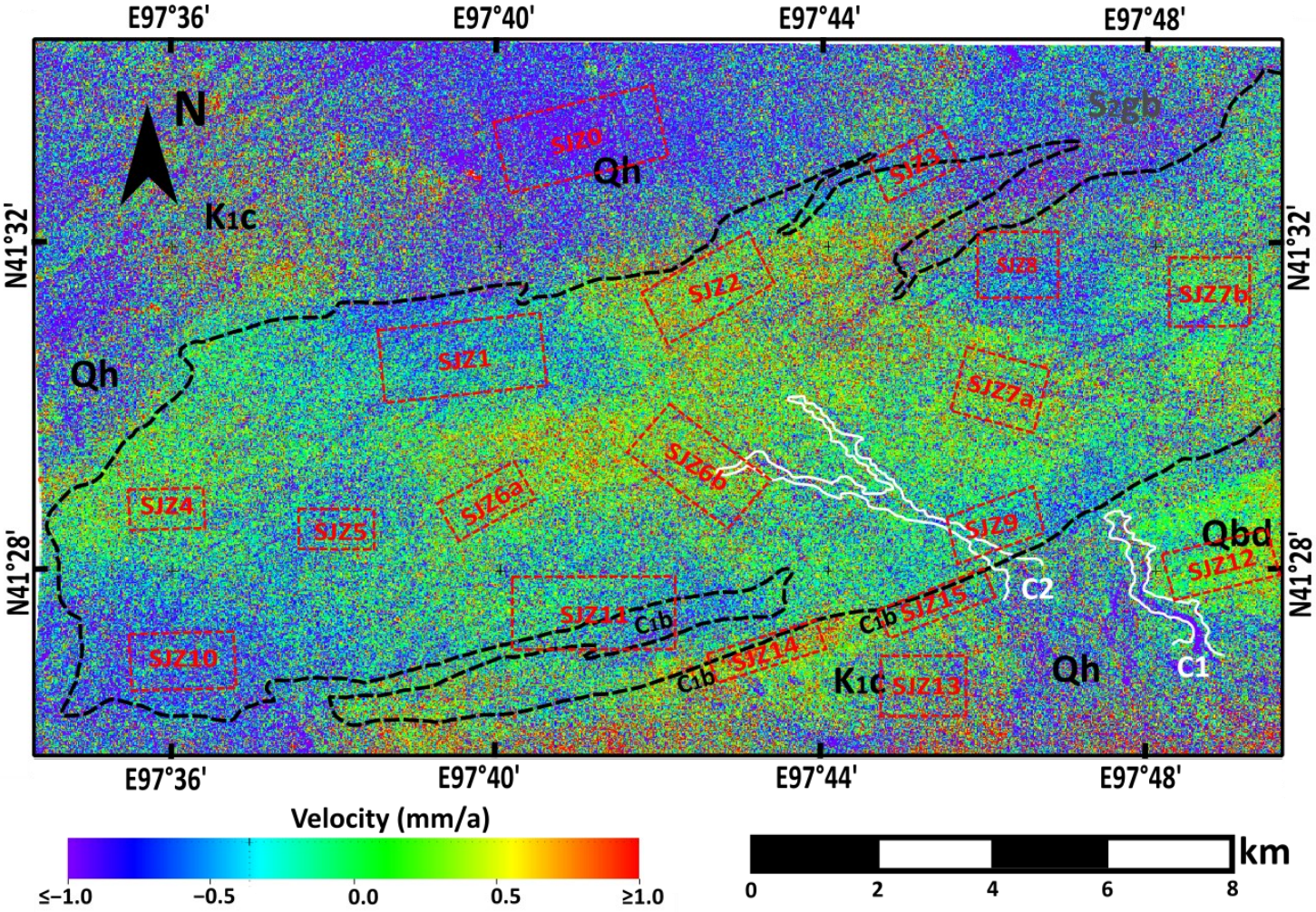


Figure 5.1 (C) Patterns of displacement rate in vertical direction (D_U) computed through the combination of ascending and descending LoS value across the Suanjingzi study area. In Figure 5.1 (C), the positive values (green-to-red colours) indicate uplift, and the negative values (blue-to-green colours) indicate to subsidence. The black dash outline shows the extent of the Suanjingzi granodiorite pluton. The black labels indicate: Holocene sediments (Qh), lower Cretaceous Chijinbao Formation (K1c), lower Carboniferous Baishan Formation (C1b), Qingbaikou Series Dahuoluoshan Group (Qbd) and Middle Silurian Gongpoquan Group (S2gb). The white dash lines indicate the major fluvial channels.

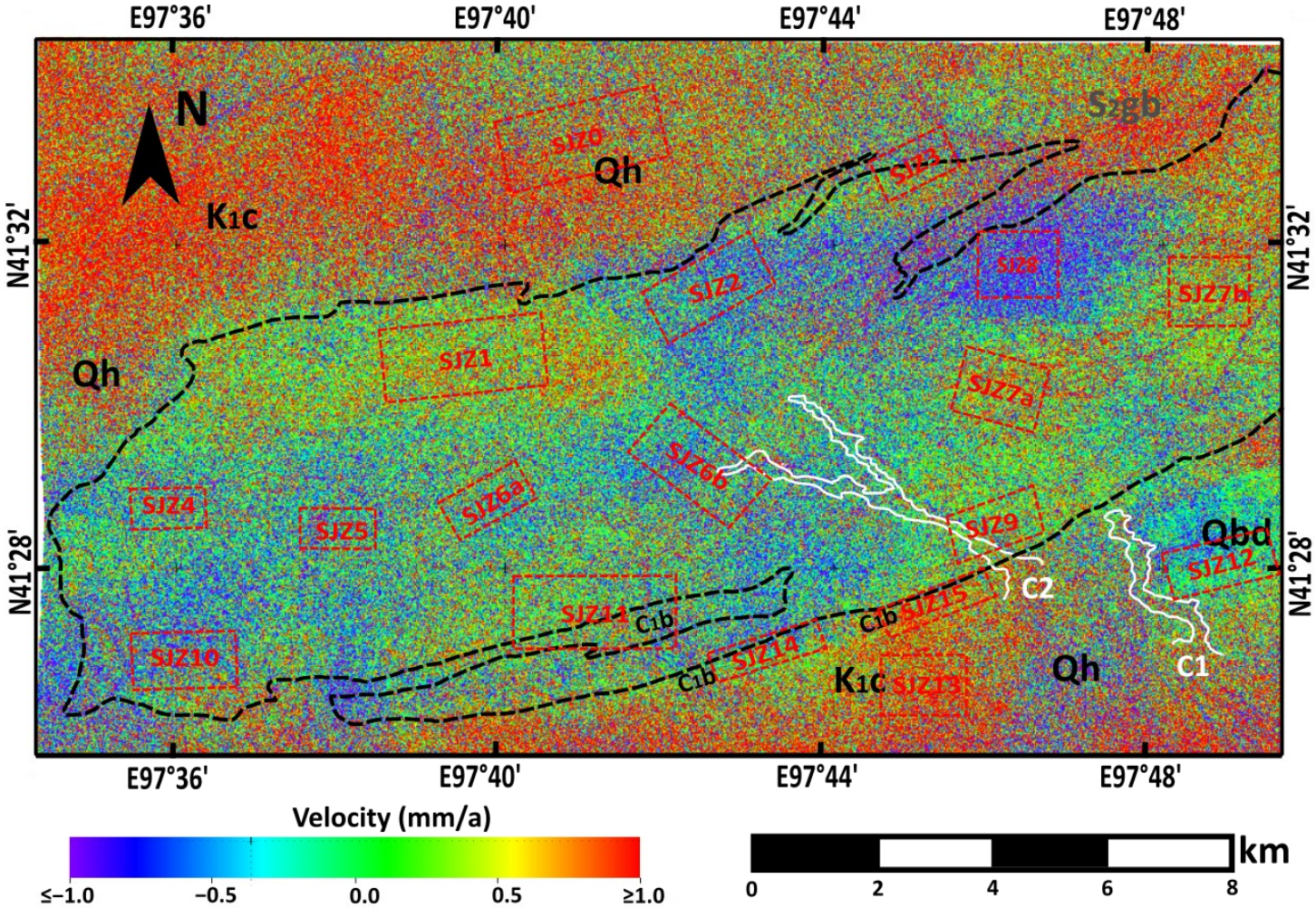


Figure 5.1 (D) Patterns of horizontal displacement rate in east-west direction (D_E) computed through the combination of ascending and descending LoS value across the Suanjingzi study area. In Figure 5.1 (D), the positive values indicate eastward motions and negative values indicate westward motions. The black dash outline shows the extent of the Suanjingzi granodiorite pluton. The black labels indicate: Holocene sediments (Qh), lower Cretaceous Chijinbao Formation (K1c), lower Carboniferous Baishan Formation (C1b), Qingbaikou Series Dahuoluoshan Group (Qbd) and Middle Silurian Gongpoquan Group (S2gb). The white dash lines indicate the major fluvial channels.

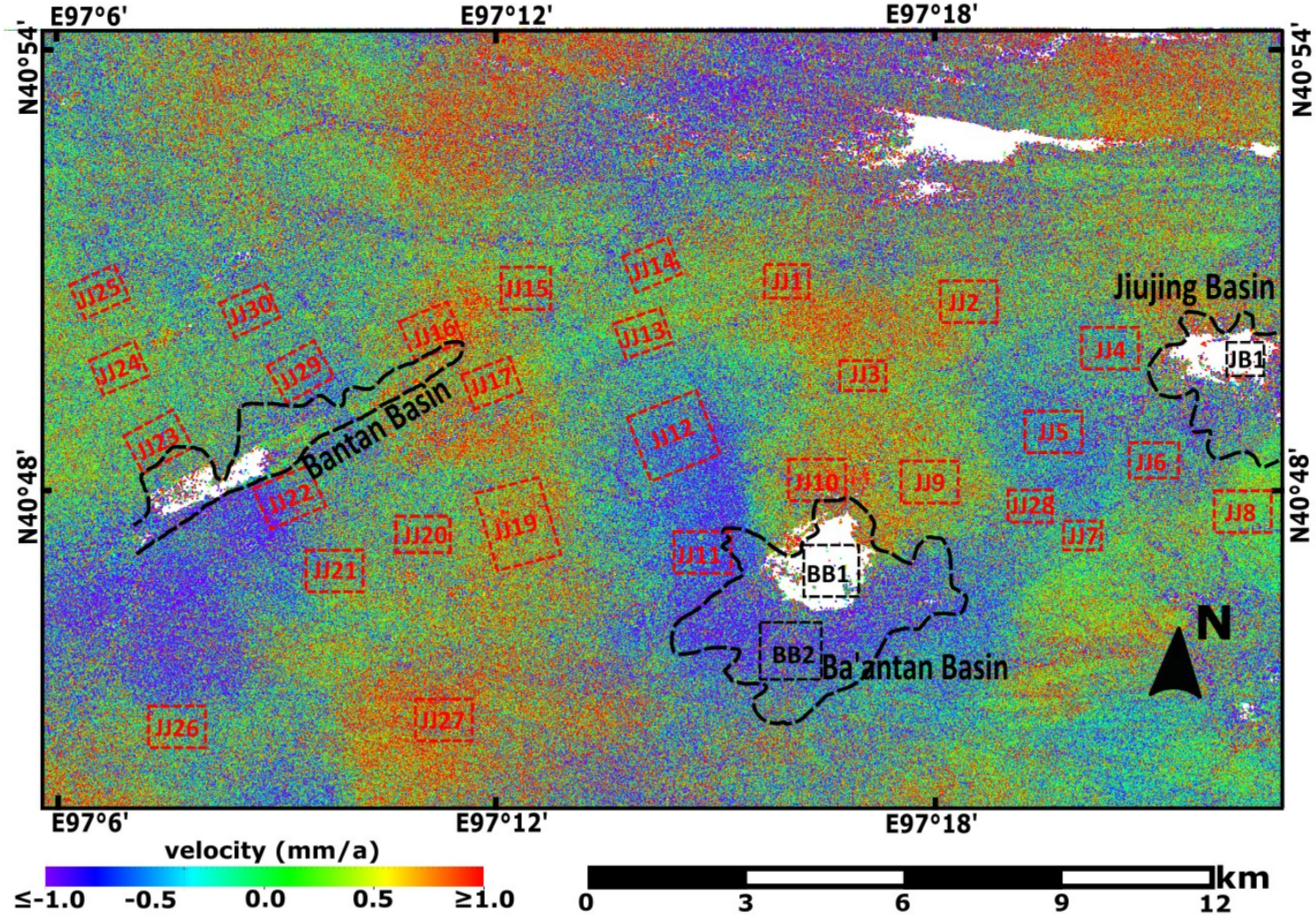


Figure 5.2 (A) Patterns of LoS displacement rate in ascending (D_{los}^{asc}) direction across the Jiujing study area. In Figure 5.2 (A), the positive values (green-to-red colours) indicate uplift, and the negative values (blue-to-green colours) indicate to subsidence. The black dash lines outline the locations of Jiujing Basin, Ba'antan Basin and Bantan Basin which are covered by Quaternary Sediments.

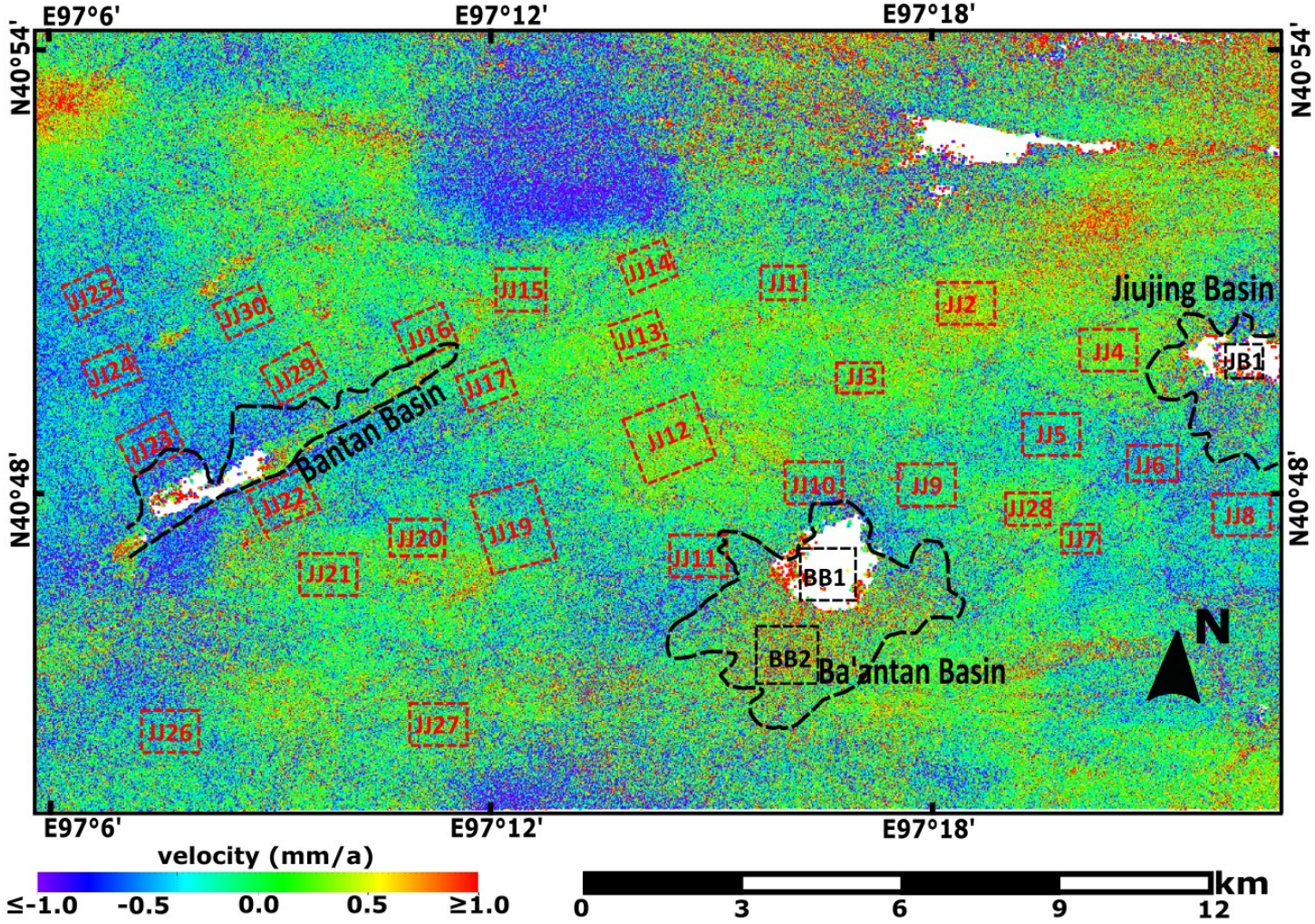


Figure 5.2 (B) Patterns of LoS displacement rate in descending (D_{los}^{des}) direction across the Jiujing study area. In Figure 5.2 (B), the positive values (green-to-red colours) indicate uplift, and the negative values (blue-to-green colours) indicate to subsidence. The black dash lines outline the locations of Jiujing Basin, Ba'antan Basin and Bantan Basin which are covered by Quaternary Sediments.

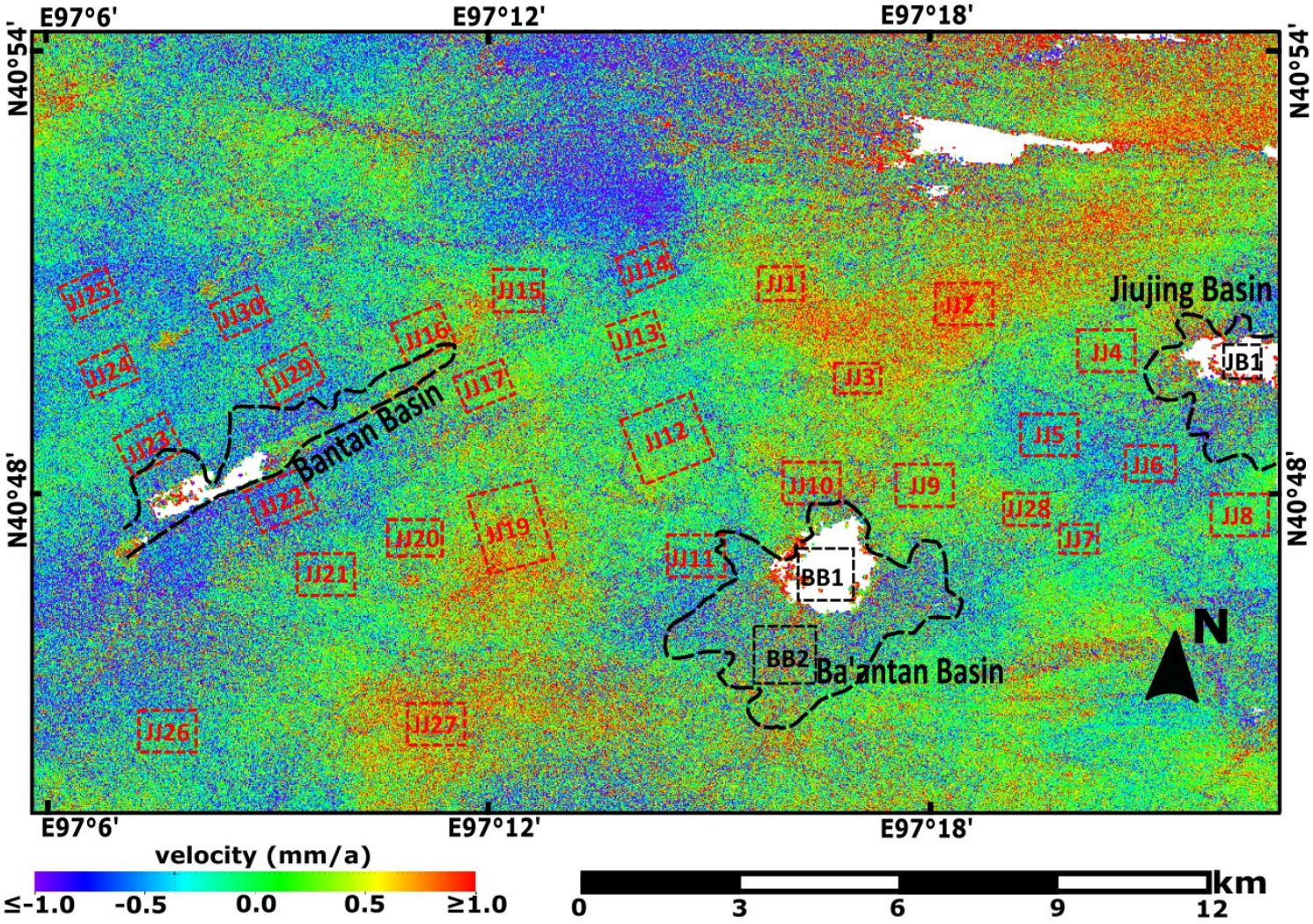


Figure 5.2 (C) Patterns of displacement rate in vertical direction (D_U) computed through the combination of ascending and descending LoS value across the Jiujing study area. In Figure 5.2 (C), the positive values (green-to-red colours) indicate uplift, and the negative values (blue-to-green colours) indicate to subsidence. The black dash lines outline the locations of Jiujing Basin, Ba'antan Basin and Bantan Basin which are covered by Quaternary Sediments.

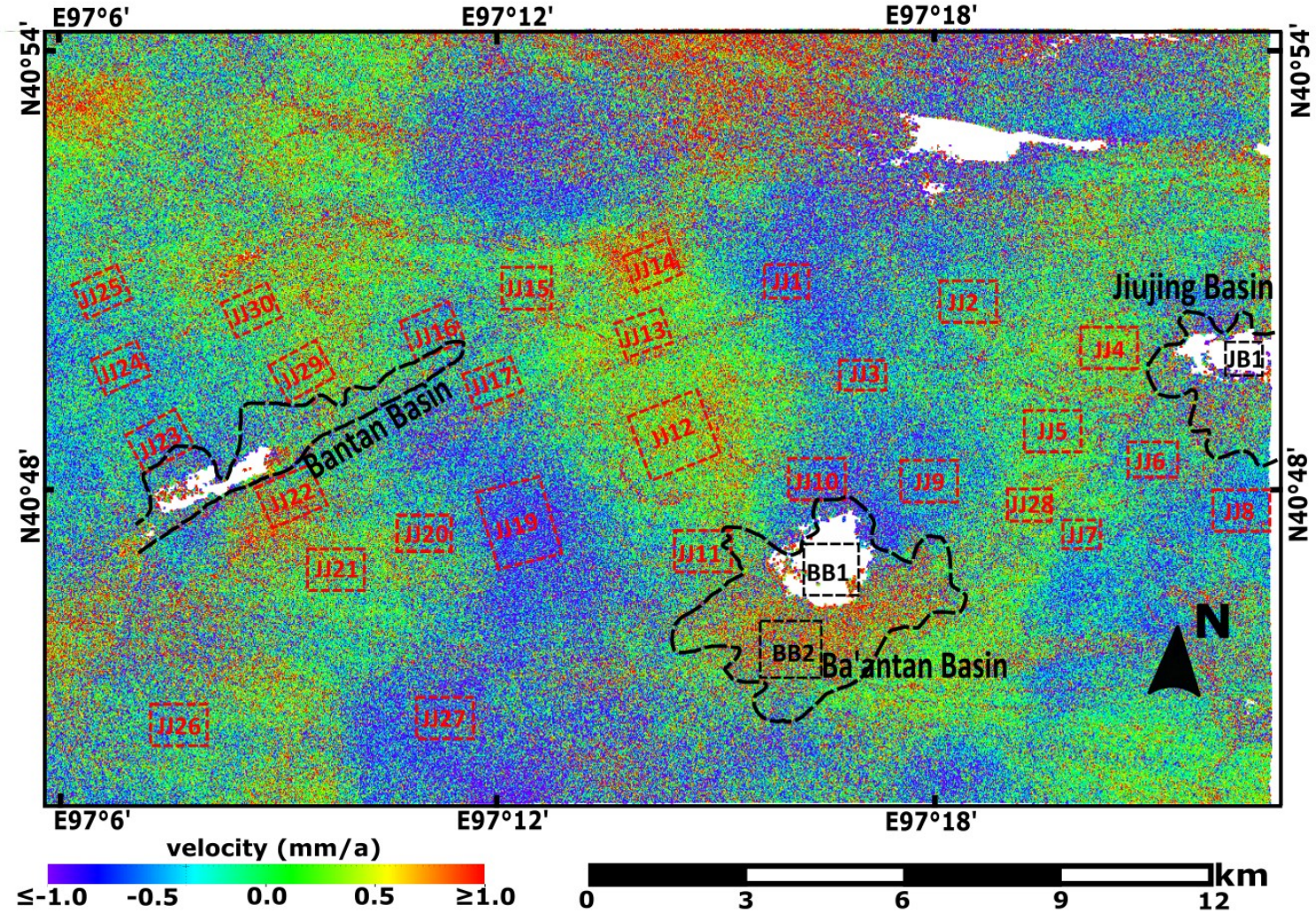


Figure 5.2 (D) Patterns of horizontal displacement rate in east-west direction (D_E) computed through the combination of ascending and descending LoS value across the Jiujing study area. in Figure 5.2 (D), the positive values indicate eastward motions and negative values indicate westward motions. The black dash lines outline the locations of Jiujing Basin, Ba'antan Basin and Bantan Basin which are covered by Quaternary Sediments.

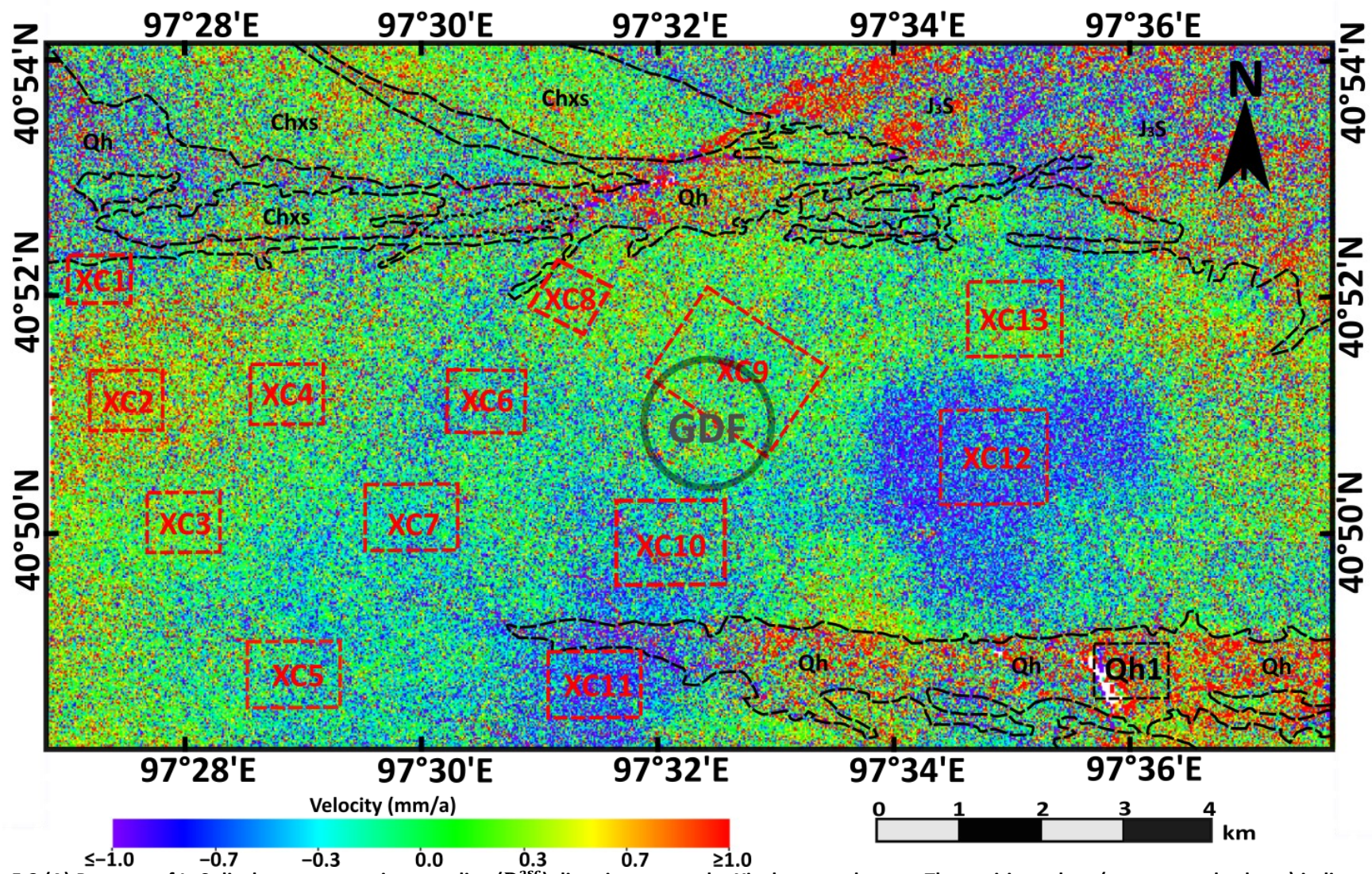


Figure 5.3 (A) Patterns of LoS displacement rate in ascending (D_{los}^{asc}) direction across the Xinchang study area. The positive values (green-to-red colours) indicate uplift, and the negative values (blue-to-green colors) indicate to subsidence. The black circle highlights the rough position of purposed GDF, and the black dash lines highlight the distribution of Qh (Holocene Sediments), Chxs (Mid-Proterozoic Xianshuijing Formation), and J_3S (Jurassic Shazaohe Formation) around the Xinchang granite.

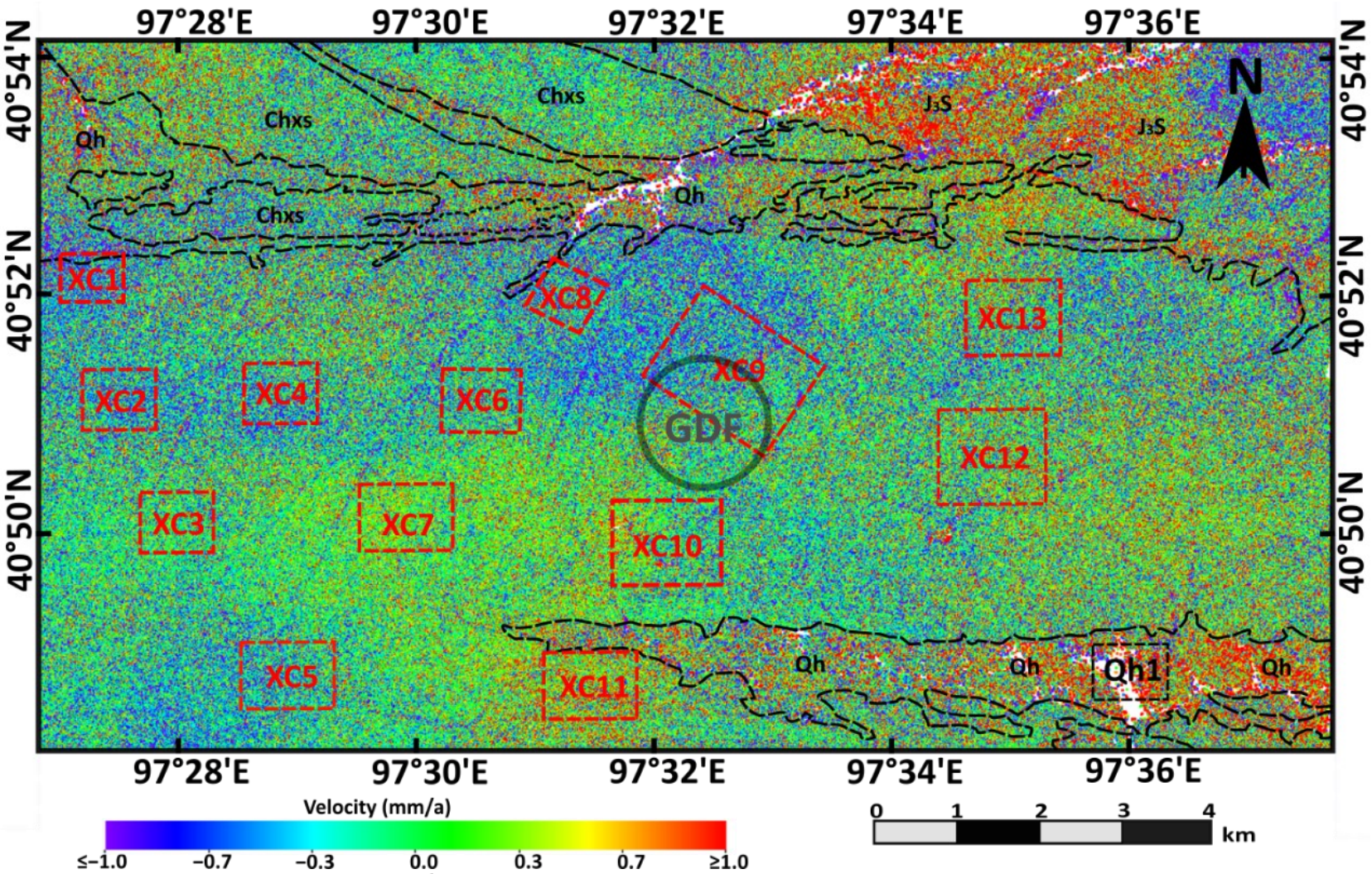


Figure 5.3 (B) shows the pattern of the descending viewed (D_{los}^{des}) deformation rates at Xinchang study area. The positive values (red and yellow coloured) refer to uplift and the negative values (blue, lower side of colour axis) refer to subsidence. The black circle highlights the rough position of purposed GDF, and the black dash lines highlight the distribution of Qh (Holocene Sediments), Chxs (Mid-Proterozoic Xianshuijing Formation), and J_3S (Jurassic Shazaohe Formation) around the Xinchang granite.

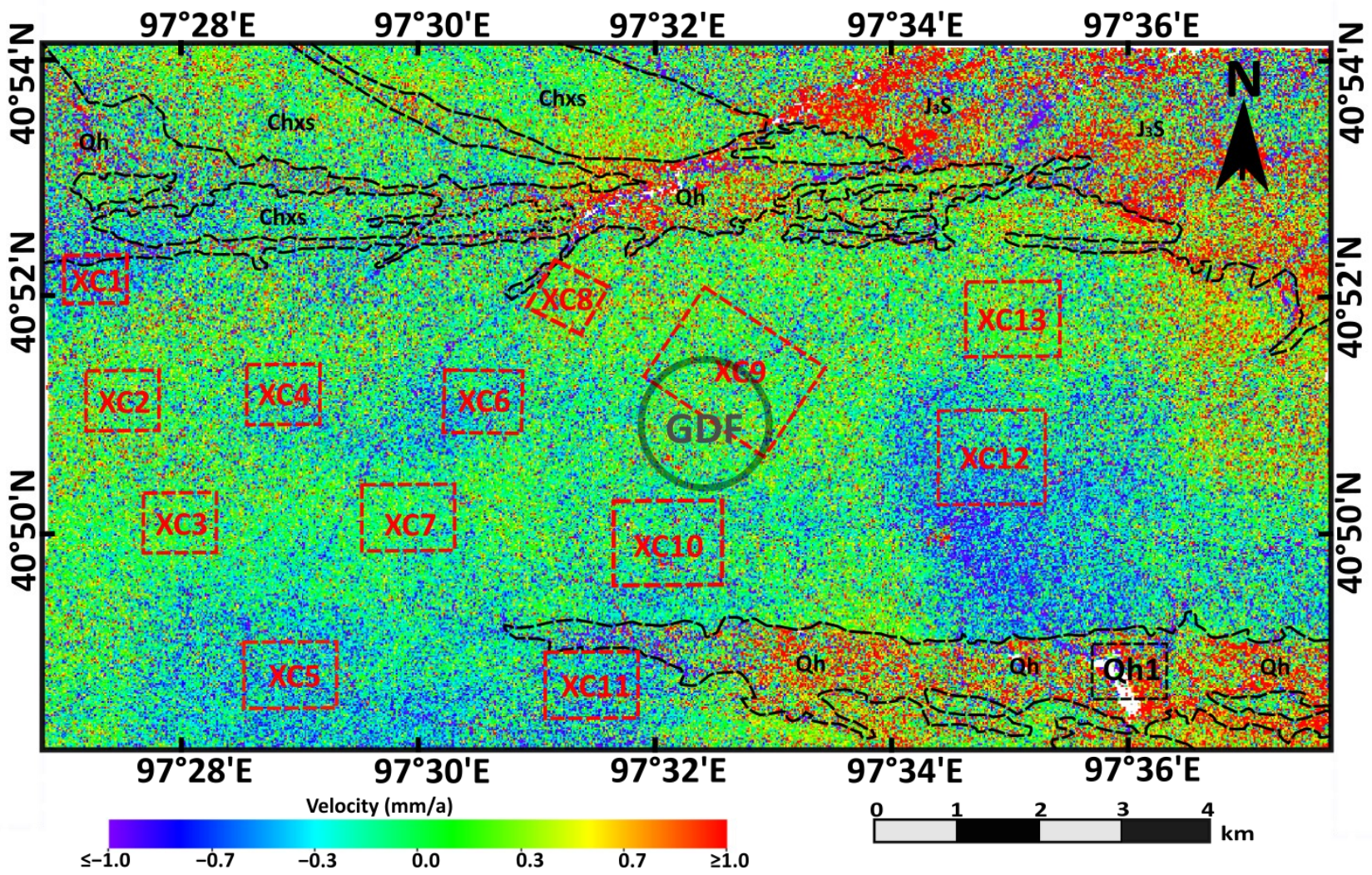


Figure 5.3 (C) shows the pattern of the vertical deformation rates (D_U) at Xinchang study area. The positive values (red and yellow coloured) refer to uplift and the negative values (blue, lower side of colour axis) refer to subsidence. The black circle highlights the rough position of purposed GDF, and the black dash lines highlight the distribution of Qh (Holocene Sediments), Chxs (Mid-Proterozoic Xianshuijing Formation), and J_3S (Jurassic Shazaohe Formation) around the Xinchang granite.

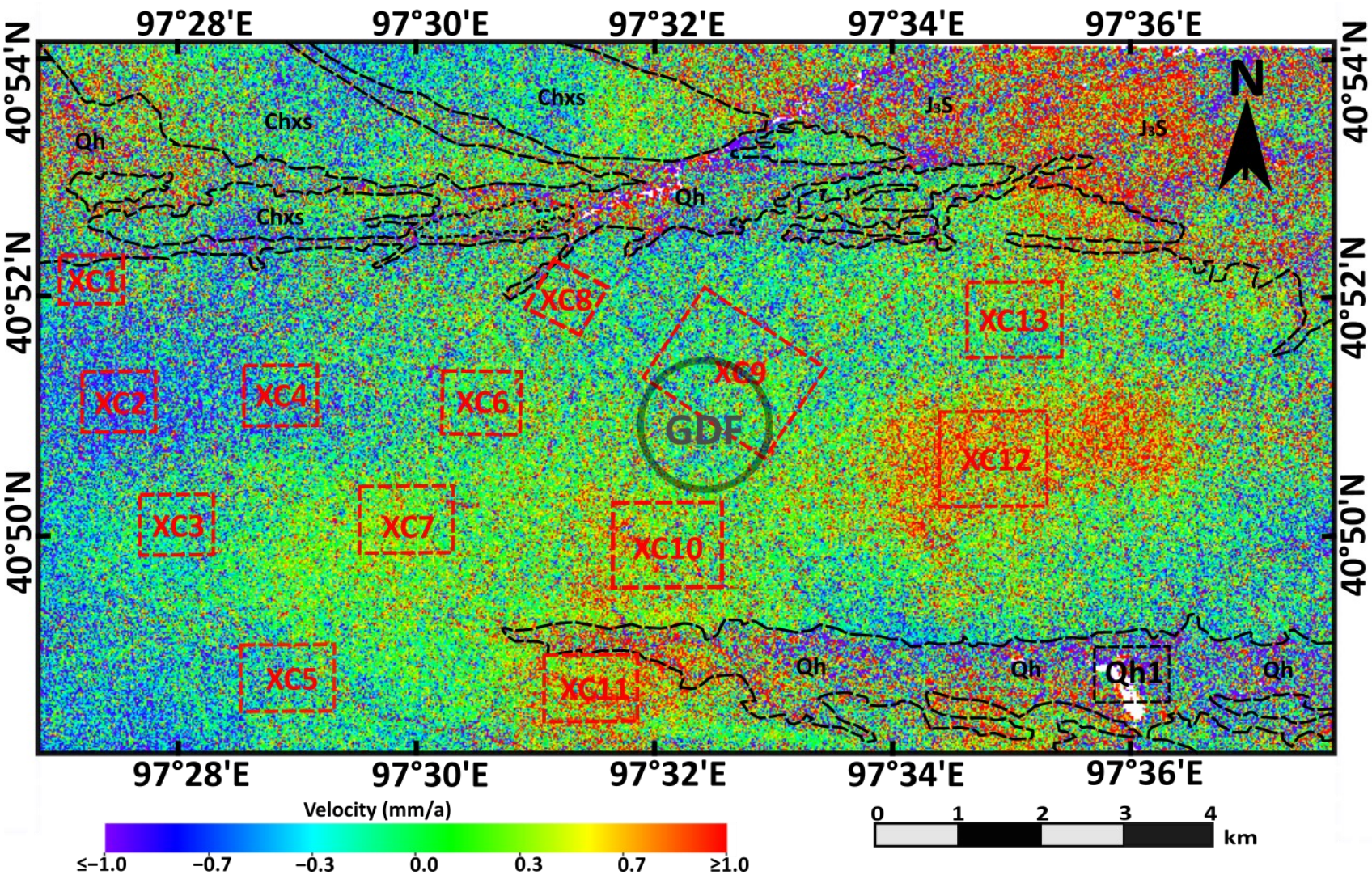


Figure 5.3 (D) shows the pattern of the horizontal deformation rates (D_E) in east-west direction at Xinchang study area. The positive values refer to eastward horizontal displacements and the negative values refers to westward displacements. The black circle highlights the rough position of purposed GDF, and the black dash lines highlight the distribution of Qh (Holocene Sediments), Chxs (Mid-Proterozoic Xianshuijing Formation), and J_3S (Jurassic Shazaohe Formation) around the Xinchang granite.

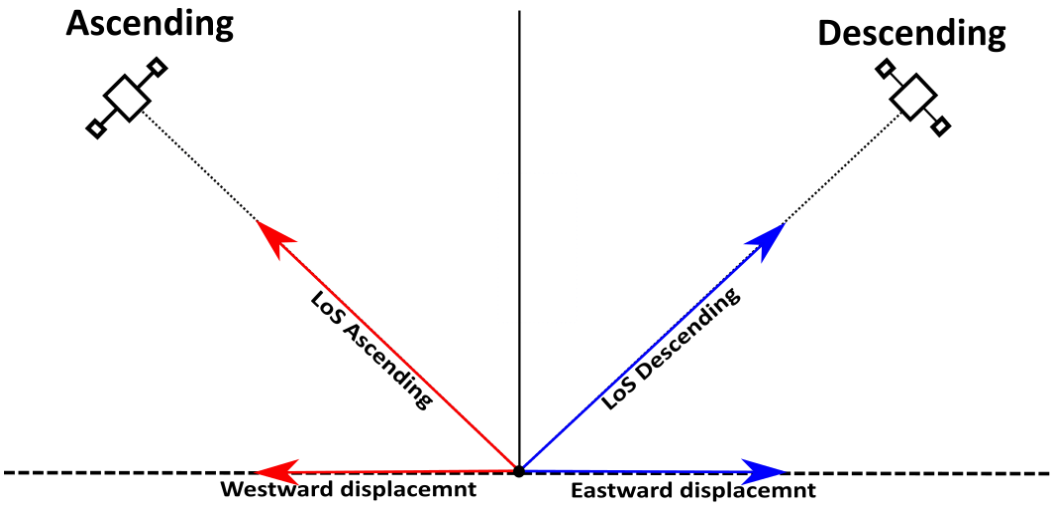


Figure 5.4 The schematic graph shows the relationship between ascending and descending displacement geometries

5.2 Factors contributing to surface deformation

The study area has been considered as a potential long-term HLW wastes disposal site, so understanding the tectonic stability, identifying the active faults and predicting the future tectonic evolution are key processes for the selection of GDF host rock, where the active faults can be identified based on the discontinuities of surface deformation patterns at Figures 5.1, 5.2 and 5.3. There are many factors that may impact the deformation data observed from Sentinel-1 satellite both in ascending and descending orbits. Understanding the influence of these factors is important when predicting the future evolution of local tectonic structures and assessing the long-term performance of the GDF. Identifying and quantifying these factors supports the understanding of tectonically impact on surface deformation. This section aims to discuss those potential factors that may influence the monitored displacement rates.

Along with tectonic activity (discussed in Chapter 6), groundwater variation, geomorphological processes (erosion and deposition) and vegetation can make significant contributing to the measured surface displacements. These processes may also impact on the GDF safety case so are important to consider. Meanwhile, the residual of atmospheric effects (APS) during the Sentinel-1 data reprocessing may also impact the final deformation pattern. These will be discussed as follows.

5.2.1 Vegetation

As Beishan lies within the semi-arid environment of Gobi Desert, the ground is largely bare and thus the impact of vegetation can be excluded. This is observable through the Google Earth image.

5.2.2 Volcanic activity

The raising of magma in subsurface leads to the movement of ground surface, this therefore varies the surface displacement rates. However, the volcanic activity in Beishan have been extinct for tens of thousands of years, and hence it can also be assumed to have negligible effect.

5.2.3 Atmospheric effects (APS)

The atmospheric effects (APS) may impact the measured displacement rates. But as it was described in Methodology Chapter, these errors can be properly corrected during the PSI processing. Need to be noted, there might be a few circumstances when displacement rates are impacted by APS residual during the data processing, but this could be easily identified due to kinematical incompatibility with surrounding deformation pattern and its spatial decorrelation with surface discontinuities. Details will be discussed in Chapter 6 and 7.

The APS is usually considered to be random in variance and distribution both spatially and temporally. At troposphere, it is mainly impacted by the thickness and coverage of clouds in the sky. In general, the displacement rates being significantly impacted by APS would show high variance and randomness with low linear properties in temporal. However, the time-series analysis, which are presented in chapter 6, show consistent trends of uplift or subsidence. This further demonstrates the atmospheric effects have very limited impacts on our results. In addition to the proper atmospheric error correction by SARScape software, another reason might be the dry and hot climate in Gobi Desert leads to low cloudy coverage on sky, this contributes relatively low APS effects at Beishan than humid areas.

5.2.4 Groundwater and precipitation

In general, anthropogenic groundwater extraction and meteoric recharge are two processes that lead to variations in groundwater level. Variations in groundwater level alters the hydraulic pressure in an aquifer, which in turn leads to a vertical effect on the ground surface above.

The literature review in Chapter 3 indicated the over-extraction of groundwater can lead to the consolidation of the rocks in groundwater aquifers, this in turn can lead to the subsidence of ground surface. Through the application of InSAR, this correlation has been well investigated by Motagh [103], Qu [125], Yang [128], Bonì [135], El Kamali [137], Ge [147], Pratesi [151], and Declercq [154]. This phenomenon usually happens in populated areas such as Florence in central Italy [151] and the London Basin [135] which have huge water demand and can lead to an annual subsidence rate around 5mm. However, it should be recognized Beishan is a largely rural area in the centre of Gobi Desert with average population density less than 1 person per km^2 (Chapter 1, Section 1.6.1), this means the

exploitation of groundwater is very rare. Therefore, human activity has been assumed to have no impact on surface deformation.

Naturally, the groundwater in Beishan is recharged by atmospheric precipitation. As highlighted in Chapter 1 Section 1.6.2, annual precipitation is only between 60 mm and 120 mm, however, the annual evaporation is 3200 mm [55]. This therefore indicated the groundwater in Beishan is overall depleted. Figure 1.2 presents the monthly rainfall data in Jiuquan (a city in Beishan) from September 2017 to April 2020 (in line with the acquistration period of Sentinel-1 data), which indicates most of the annual precipitation was concentrated in summer months, especially the July and August in 2018 and the April, May, June, July and August in 2019. However, the high temperature in summer months lead to high evaporation, where the seasonal floodwater in surface gullies and lowland areas produced by intense rainfall are usually quickly removed by evaporation before fully infiltrates downwards to recharge the groundwater [25]. In this way, the groundwater recharging in summer months is low, and the peak groundwater recharging at Beishan is in April [137, 212].

The groundwater recharge by precipitation is expected to increase seasonally in relation to the temporal variations of local precipitation and evaporation. In the case of Beishan, this should occur shortly after the month of April.

The case study from Bell [142] focused on the Valley View Fault in Nevada, which has as similar dry climate to Beishan, and presents a typical example to illustrate how seasonal groundwater recharging could influence the time-series displacements of the ground surface observed by SAR images. As illustrated in Figure 3.2, the surface generates a maximum of 3 mm's seasonal amplitude in the case of Valley View Fault due to the hydraulic pressure induced by groundwater recharging. In the case of Beishan (Jiujing, Xinchang, and Suanjingzi), this kind of seasonal amplitude on the time series analysis figures was not significant around April month, which means the temporal variations of surface deformation cannot be correlated with the precipitation. This therefore indicates the groundwater changes in Beishan do not generate significant hydraulic pressure to uplift the ground.

Further, as previously introduced in InSAR literature chapter, the groundwater induced movements are usually characterized by pure vertical displacement with low ascending and descending LoS velocity difference [122]. However, the horizontal displacements measured in this research is significant relative to vertical displacements. This confirms that groundwater has very little impact on surface deformation and is not observed in the InSAR results.

In general, this research believes that the impacts of groundwater on surface deformation in Beishan might be very slight so that can be ignored. In this way, tectonic activity, causing very small movements on active faults, and geomorphological processes (erosion and deposition) might be the main contributors to the patterns of surface displacement in the study area, where the geomorphology induced deformation can be distinguished from tectonic activities induced through correlation with coherence patterns; as discussed later in Sections 5.4, 5.5 and 5.6.

5.2.5 Conclusion

The above discussion excluded the impacts of vegetation, volcanic activities, groundwater change and atmospheric effects on monitored surface deformation pattern. In this way, this leaves geomorphological processes (erosion and deposition) and fault activity as the only two factors that may cause the deformation. Therefore, the objective of Section 5.3, 5.4 and 5.5 is to distinguish the impacts of geomorphological processes and fault activities over Suanjingzi, Jiujing and Xinchang regions respectively. This could be achieved through the application of coherence

5.3 Surface deformation at Suanjingzi and its geomorphological effects

The vertical (D_U) and horizontal (D_E) deformation patterns at Suanjingzi are presented in Figure 5.1. Having excluded the impacts of groundwater, vegetation, APS and volcanic activity, the factors which may trigger the InSAR deformation in Suanjingzi (similarly, in Jiujing and Xinchang) are fault activities and geomorphological processes. This section aims to integrate the deformation, geological and coherence maps to distinguish the impact of geomorphological processes and tectonic activity related to surface deformation at Suanjingzi.

Figure 2.4 illustrates the spatial distribution of Holocene sediment and Suanjingzi granodiorite. The Holocene sediments are mainly composed of loose, dry and yellowish diluvial and alluvial sandy gravel, sand and loam deposits. To integrate Figure 2.4 with Figure 5.1 and Table 5.1, Block SJZ0 (D_U= -0.68 mm a^{-1}, D_E=0.65 mm a^{-1}) has high deformation rates and are covered with surficial Holocene deposits (Figure 2.4). In comparison, the deformation rates at where granite is exposed at surface such as at Blocks SJZ1 to SJZ11, SJZ14 and SJZ15, are much lower, and generally ranging between -0.3 mm a^{-1} to 0.3 mm a^{-1} in both vertical and horizontal directions.

The high deformation rates related to the Holocene sediment covered areas are mainly distribute surrounds the lower deformed Suanjingzi granodiorite (Figure 2.4). These low deformation rates appear to be related to the blocks where the granodiorite is exposed at surface (Figure 5.1). The displacement rates difference between Holocene sediments and granodiorite looks both kinematically and mechanically incompatible. As it was introduced in sub-Section 3.3.1 in Chapter 3, the deformation patterns which are impacted by active faults are expected to have elongated geometry parallel to the striking direction of active faults. In this way, it is believed such deformation pattern distribution might be influenced by surface sedimentary strata rather than tectonic activity. Therefore, this cannot be merely explained in the tectonic perspective. The geomorphological processes could potentially account for the large ground deformation in this region. The explanations are as follows.

5.3.1 The spatial variation of coherence

It is easy to assume that this is dominantly due to the impacts of fluvial and aeolian induced erosions. The evidence comes from the coherence map. Geomorphological processes such as erosion and deposition can alter the arrangement of random surface scatterers and will lead to decoherence. The spatial variations of coherence in Figure 5.5 indicate that areas covered by Holocene sediments labelled by SJZ0, and Fluvial Channels 1 and 2 (C1 and C2) have significantly lower coherence than areas of granite exposed area (SJZ1, SJZ2, SJZ6b and SJZ11) and the Dahuoluoshan Group formation

area (SJZ12) over the eight time periods (08/10/2017 to 13/11/2017, 08/10/2017 to 13/03/2018, 08/10/2017 to 11/07/2018, 08/10/2017 to 27/10/2018, 08/10/2017 to 24/02/2019, 08/10/2017 to 12/06/2019, 08/10/2017 to 28/09/2019 and 08/10/2017 to 26/01/2020).

As presented in Table 5.4, and Figure 5.6, over a 2.5-year period (08/10/2017 to 26/01/2020), more than 70 % of pixels across granodiorite exposed blocks (SJZ1, SJZ2, SJZ6b and SJZ11) have coherence greater than 0.7; whilst in the areas covered by the Holocene sediment (Block SJZ0 and C1&2), only 0.50% and 12.73% pixels respectively have coherence of greater than 0.7. The temporal variation of coherence in Figure 5.8 indicates Block SJZ0 and C1&2 show permanent decoherence around 0.4, whilst the permanent decoherence of the granodiorite exposed blocks was only around 0.2 over the 2.5-year period. This reflects Holocene sediment covered areas have a more significant surface change than the areas where the granodiorite exposed area.

Table 5.4 The cumulative percentage of coherence at Blocks SJZ0, SJZ1, SJZ2, SJZ6b, SJZ11, SJZ12, SJZ14, SJZ15 and Fluvial Channel 2 in Suanjingzi study area between 08/10/2017 to 26/01/2020.

Percentage	Block SJZ0	Block SJZ1	Block SJZ2	Block SJZ6b	Block SJZ11	Block SJZ12	Block SJZ14	Block SJZ15	Fluvial Channel 2
$P_{(coh>0.3)}$	96.037%	100%	100%	99.832%	100%	100%	100%	99.979%	100%
$P_{(coh>0.4)}$	81.235%	99.944%	100%	99.523%	99.977%	100%	100%	99.707%	98.735%
$P_{(coh>0.5)}$	42.855%	99.675%	99.906%	98.821%	99.492%	100%	100%	98.555%	88.659%
$P_{(coh>0.6)}$	10.489%	98.079%	97.691%	95.507%	95.873%	99.923%	99.500%	94.075%	57.125%
$P_{(coh>0.7)}$	0.501%	85.555%	74.833%	72.789%	74.885%	98.737%	91.549%	70.603%	12.732%
$P_{(coh>0.8)}$	0.012%	33.932%	18.69%	17.313%	21.531%	81.155%	40.073%	20.184%	1.054%
$P_{(coh>0.9)}$	0	0.651%	0.031%	0.014%	0.346%	8.643%	0.500%	0.858%	0

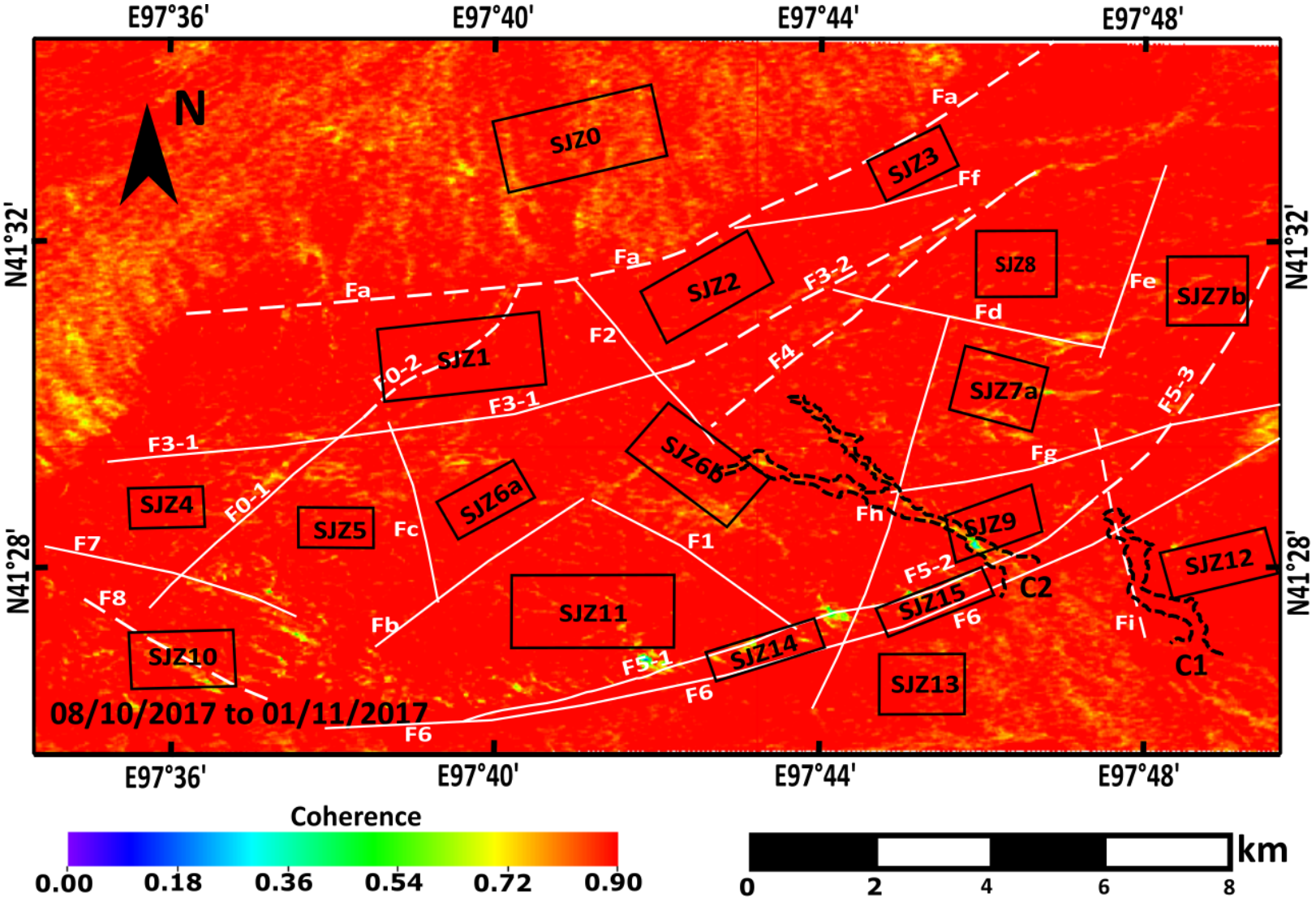


Figure 5.5 (A). The spatial variations of Sentinel-1 (ascending) coherence at time-periods in Suanjingzi study area between 08/10/2017 to 13/11/2017

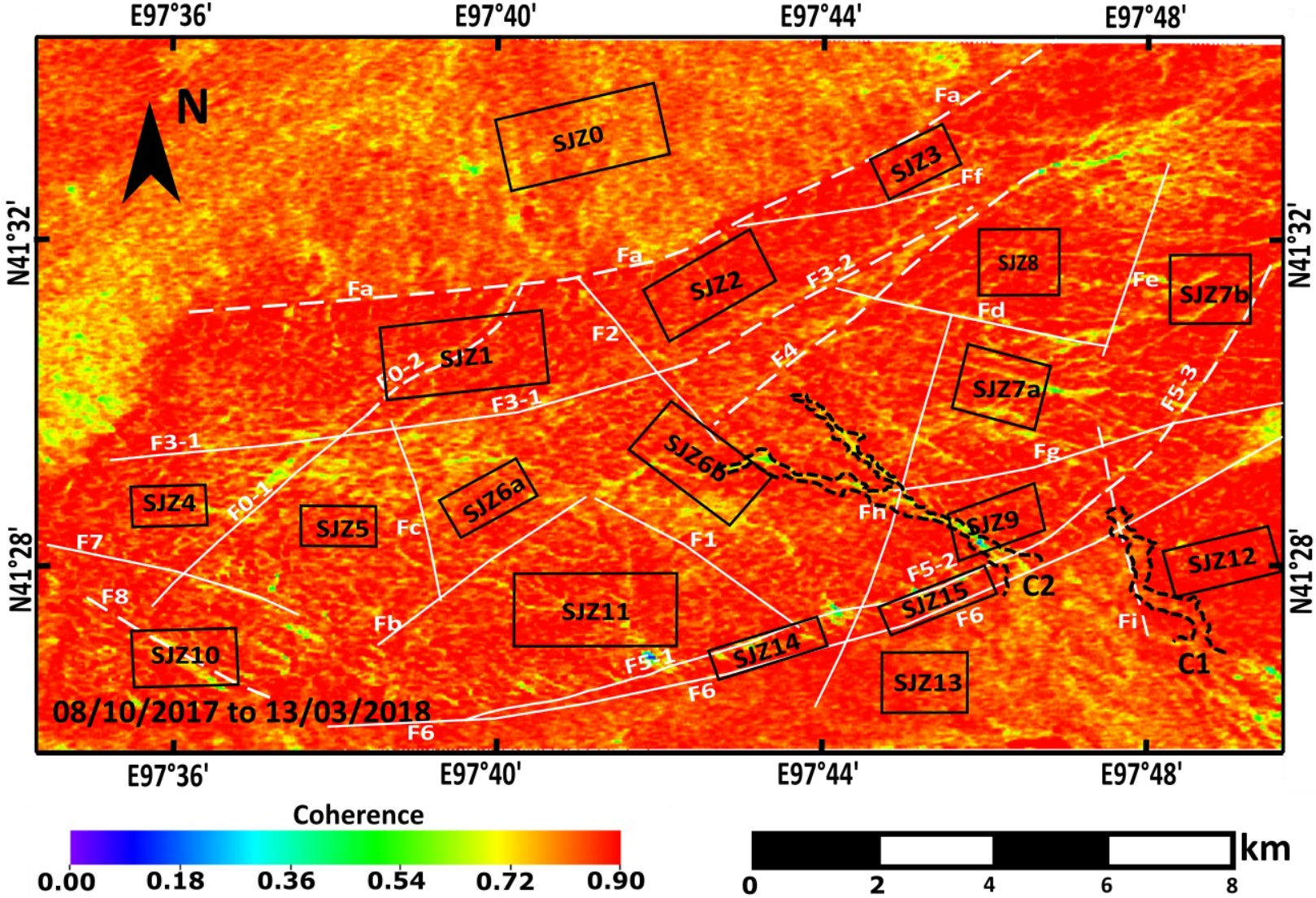


Figure 5.5 (B). The spatial variations of Sentinel-1 (ascending) coherence at time-periods in Suanjingzi study area between 08/10/2017 to 13/03/2018

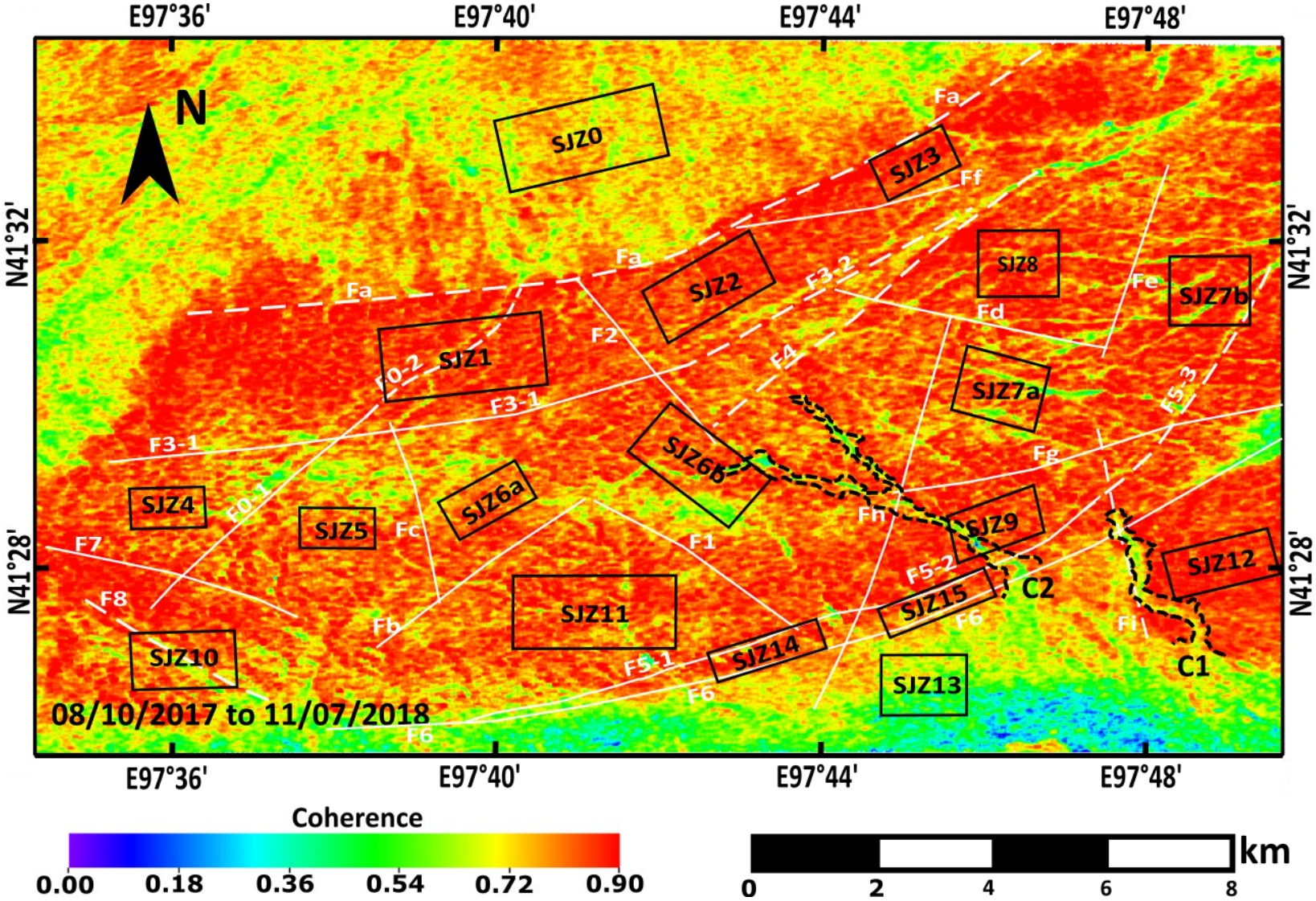


Figure 5.5 (C). The spatial variations of Sentinel-1 (ascending) coherence at time-periods in Suanjingzi study area between 08/10/2017 to 11/07/2018

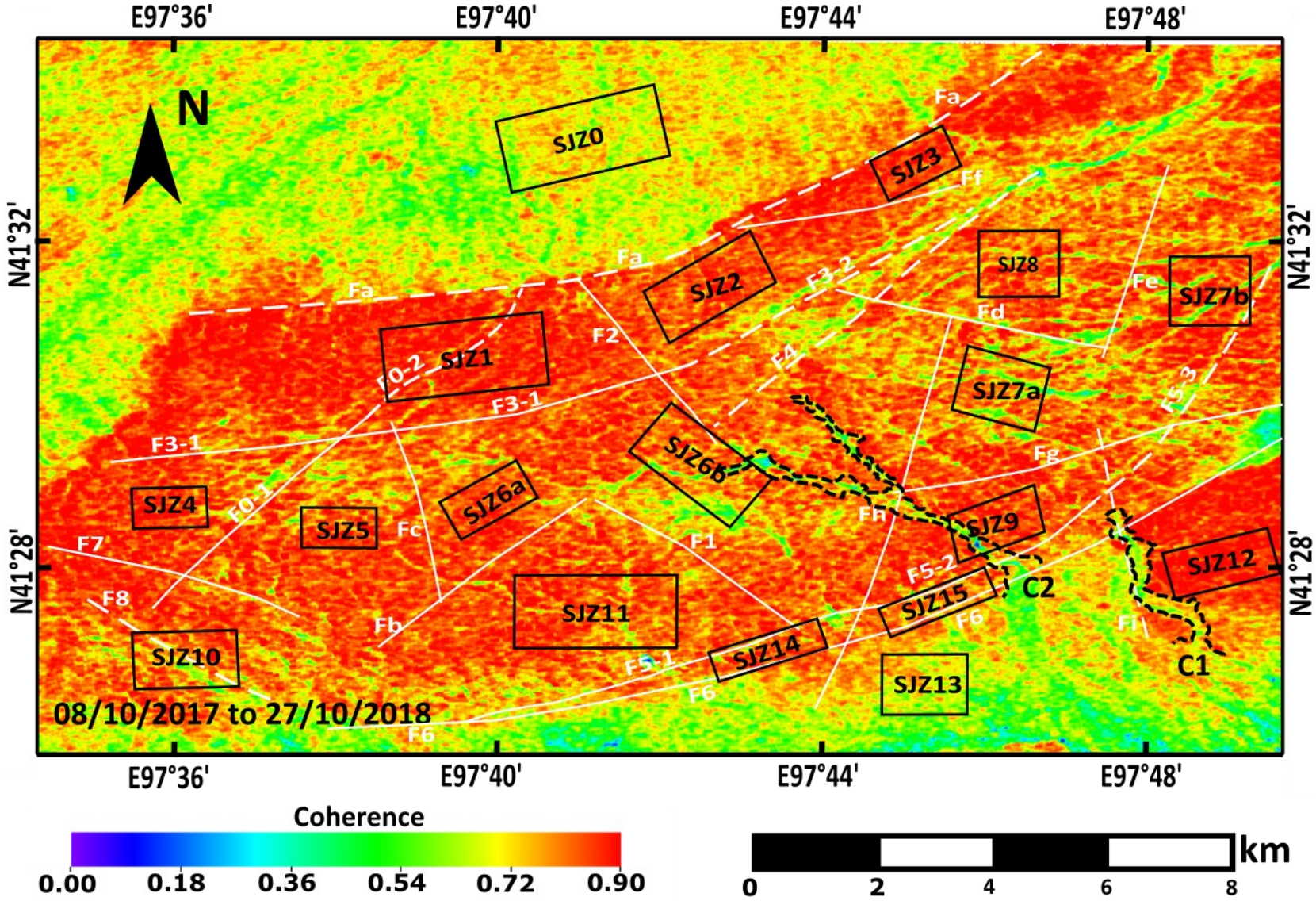


Figure 5.5 (D). The spatial variations of Sentinel-1 (ascending) coherence at time-periods in Suanjingzi study area between 08/10/2017 to 27/10/2018

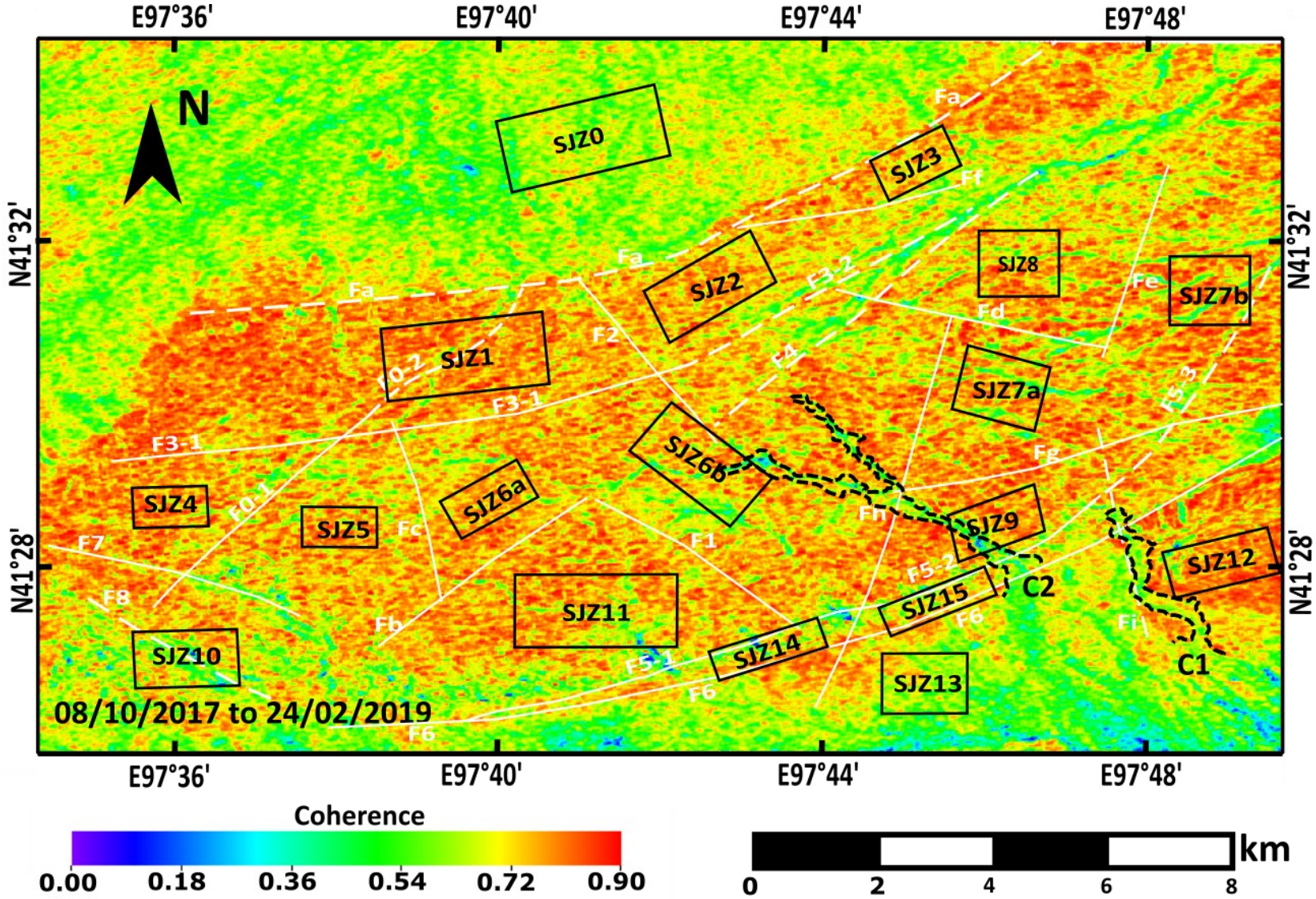


Figure 5.5 (E). The spatial variations of Sentinel-1 (ascending) coherence at time-periods in Suanjingzi study area between 08/10/2017 to 24/02/2019

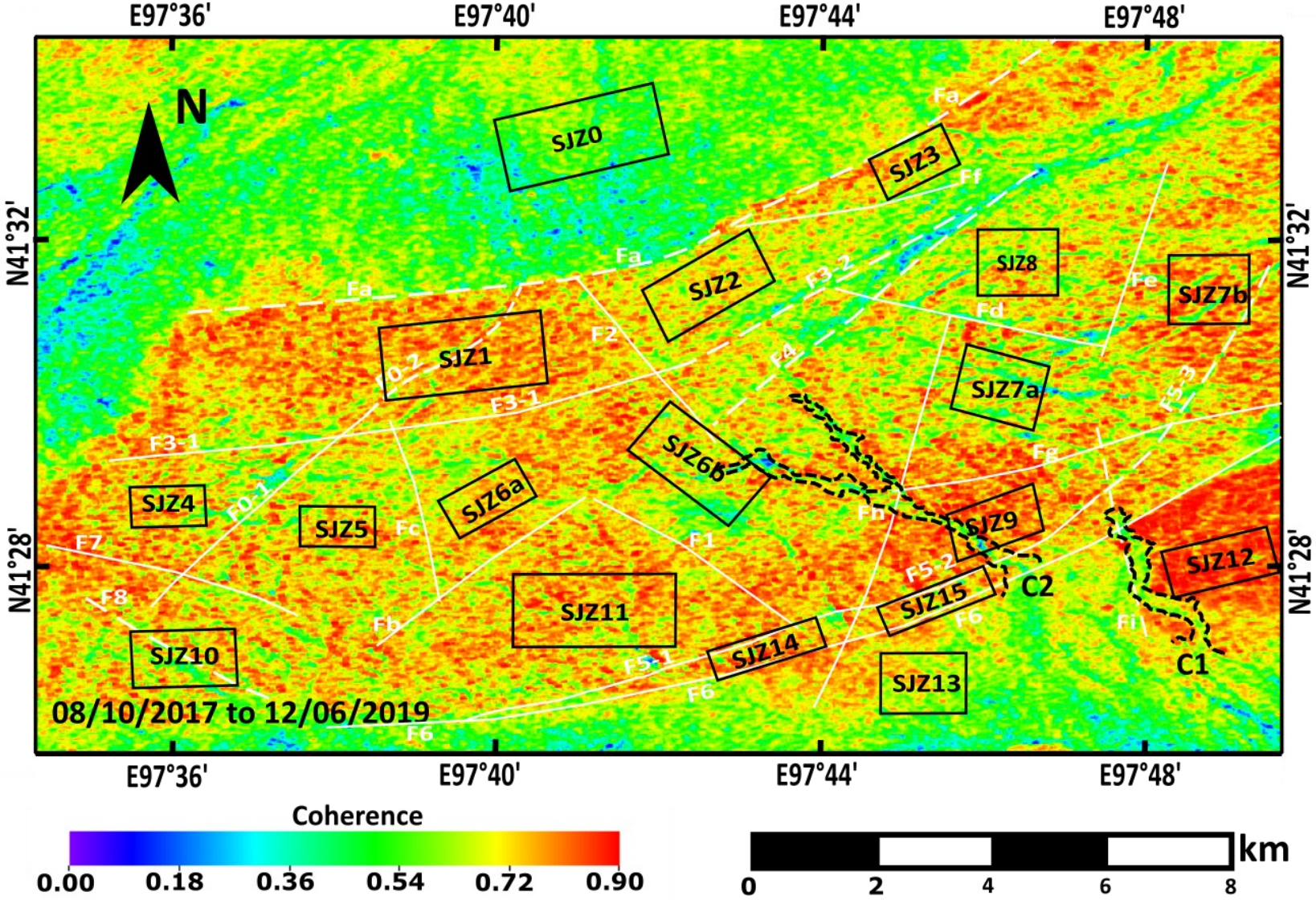


Figure 5.5 (F). The spatial variations of Sentinel-1 (ascending) coherence at time-periods in Suanjingzi study area between: 08/10/2017 to 12/06/2019

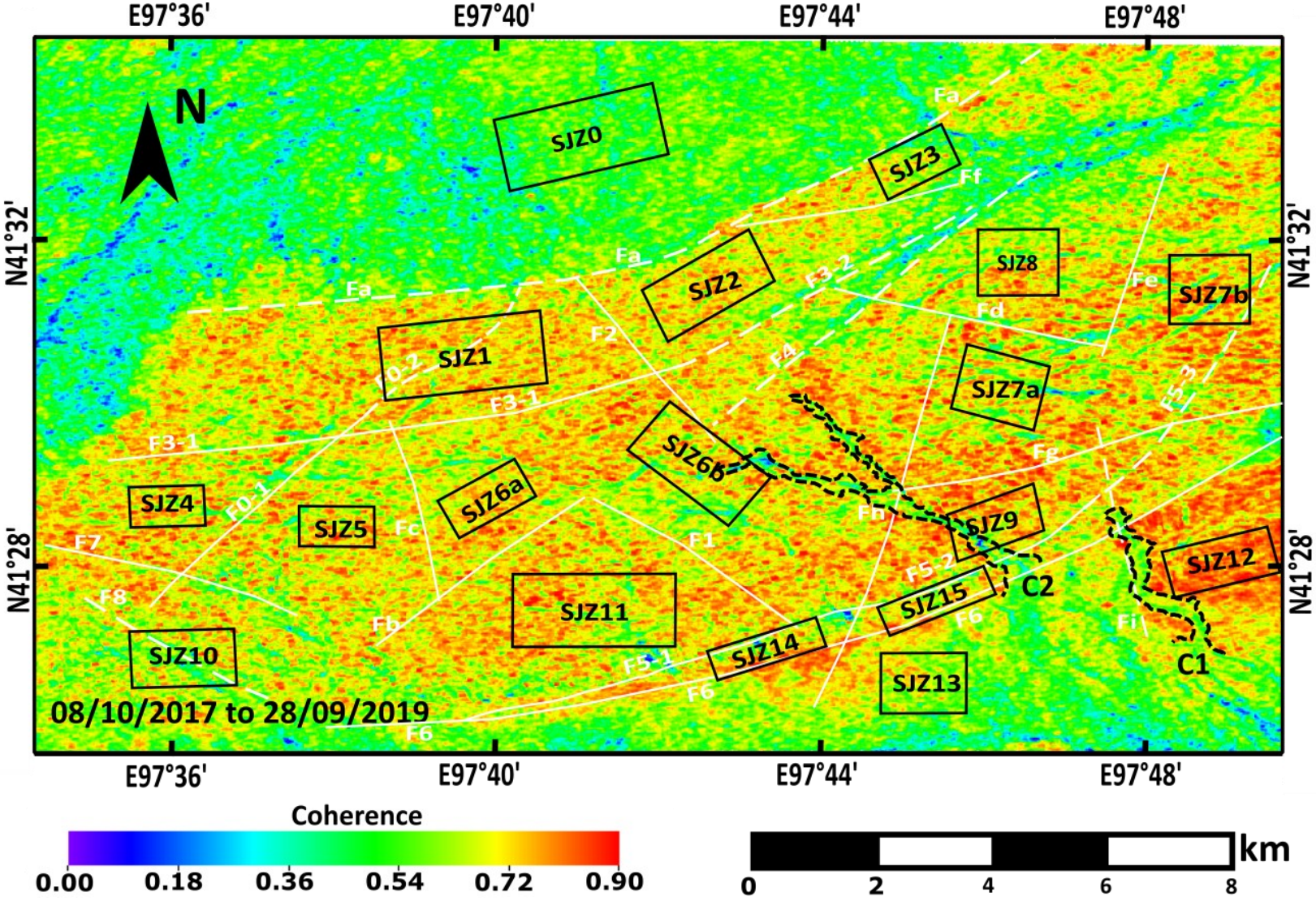


Figure 5.5 (G). The spatial variations of Sentinel-1 (ascending) coherence at time-periods in Suanjingzi study area between 08/10/2017 to 28/09/2019

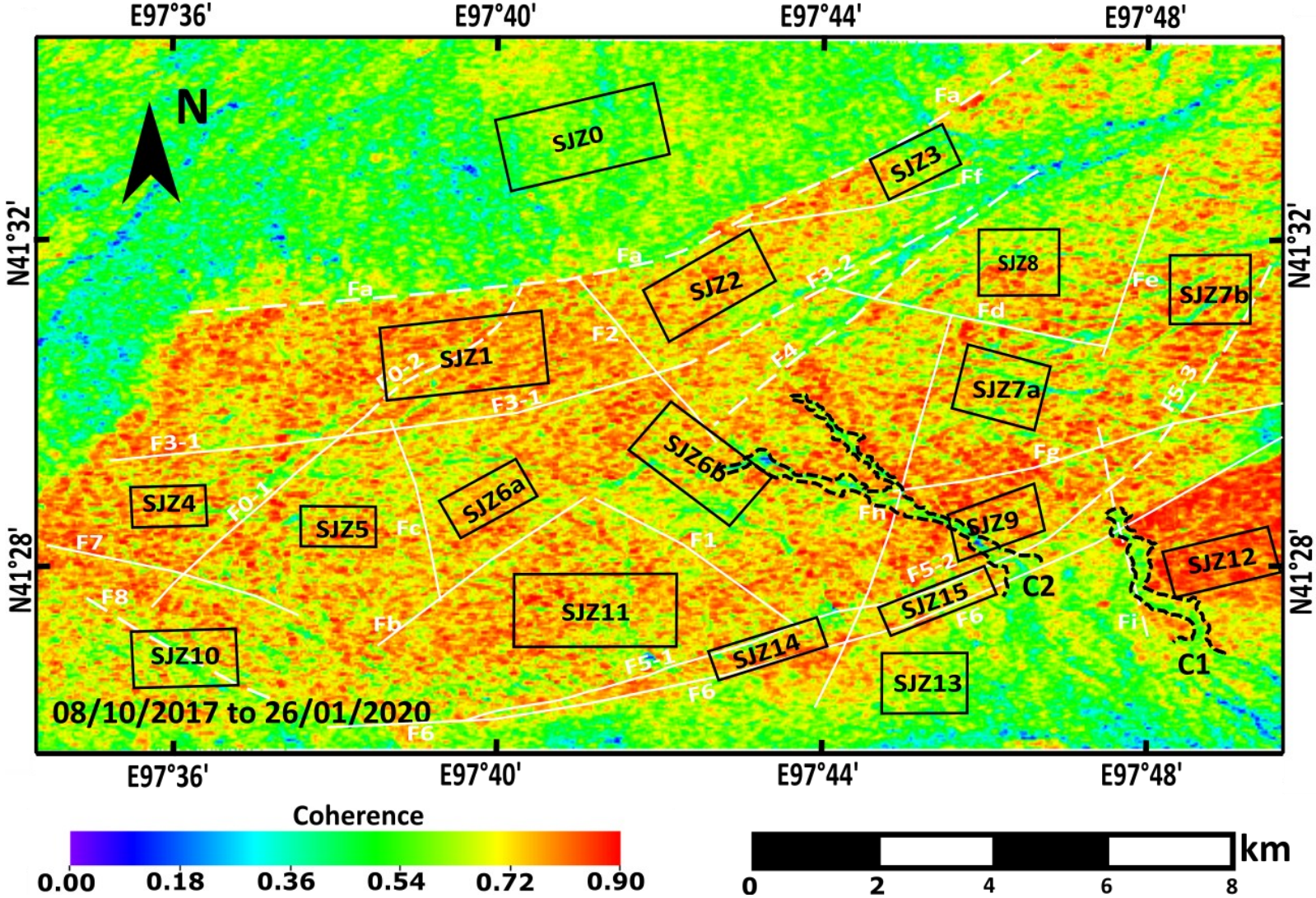
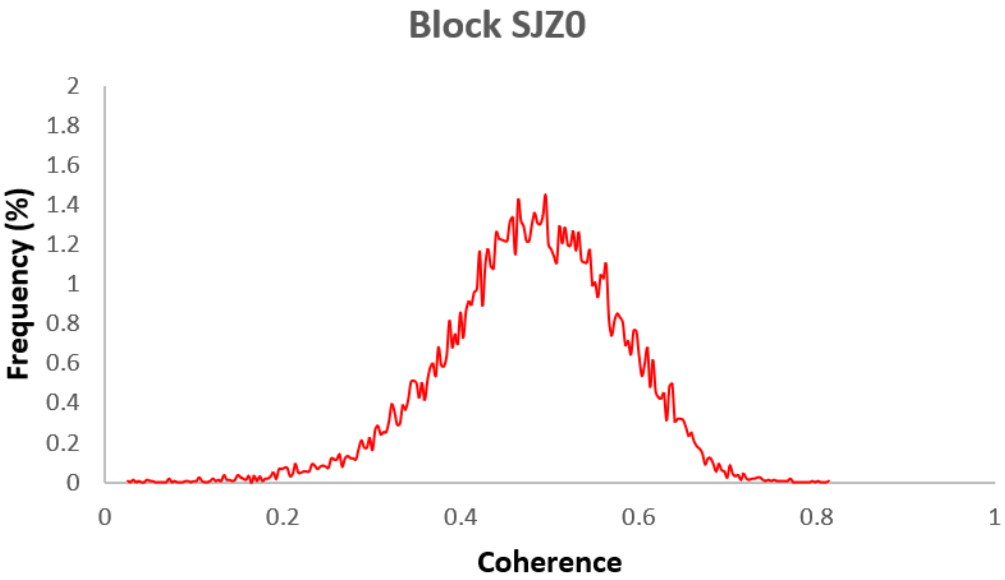
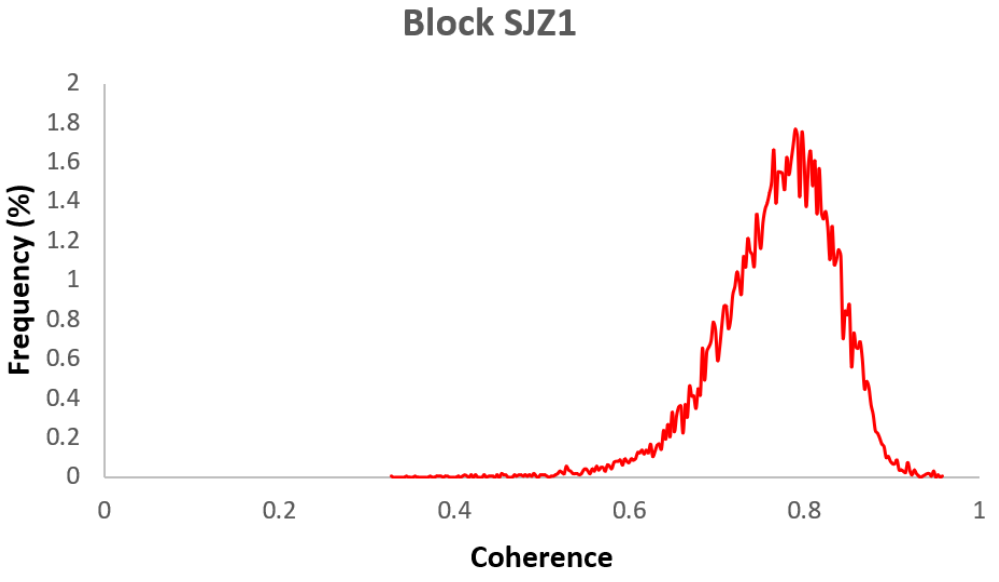


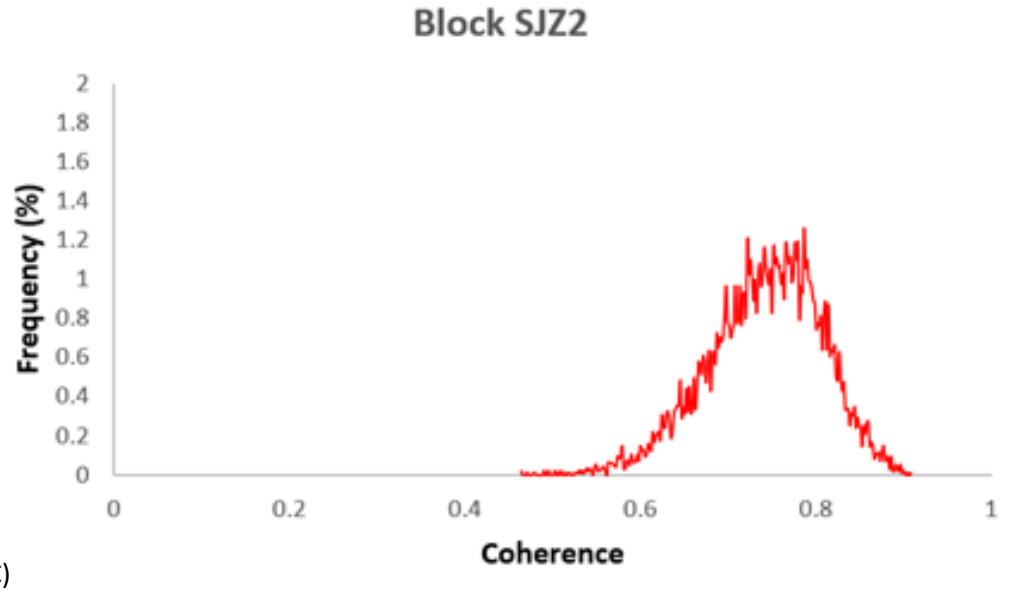
Figure 5.5 (H). The spatial variations of Sentinel-1 (ascending) coherence at time-periods in Suanjingzi study area between 08/10/2017 to 26/01/2020.


Block SJZ0
Frequency (%)
2
1.8
1.6
1.4
1.2
1
0.8
0.6
0.4
0.2
0
0
0.2
0.4
0.6
0.8
1
Coherence

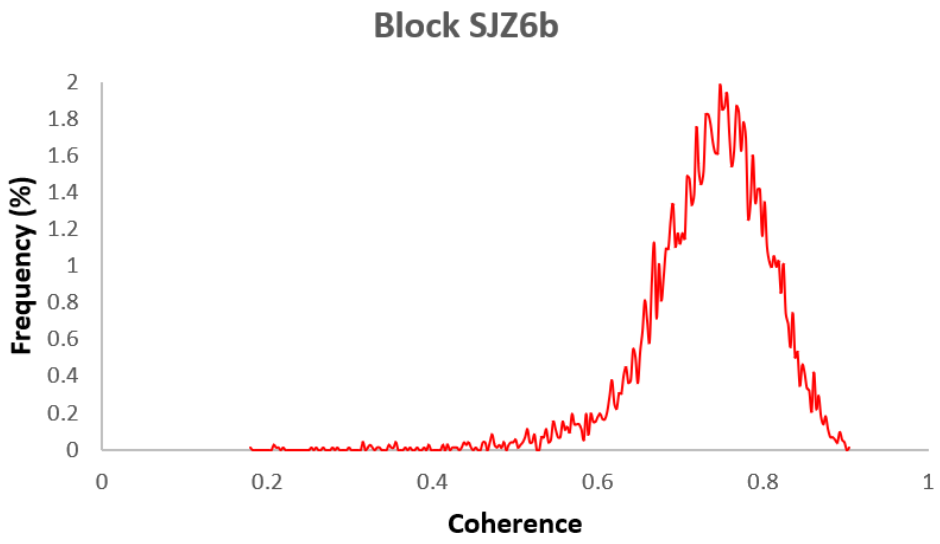
(A)


Block SJZ1
Frequency (%)
2
1.8
1.6
1.4
1.2
1
0.8
0.6
0.4
0.2
0
0
0.2
0.4
0.6
0.8
1
Coherence

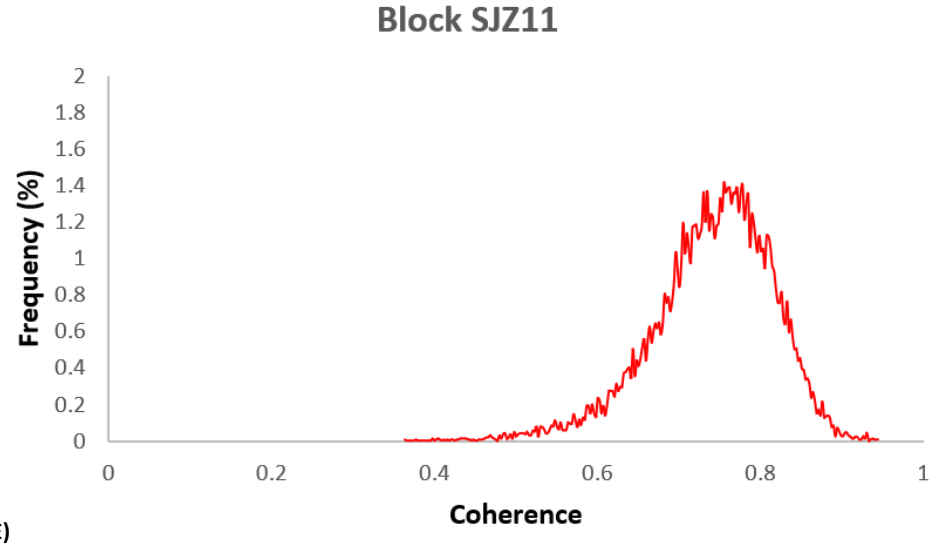
(B)


Block SJZ2
Frequency (%)
2
1.8
1.6
1.4
1.2
1
0.8
0.6
0.4
0.2
0
0
0.2
0.4
0.6
0.8
1
Coherence

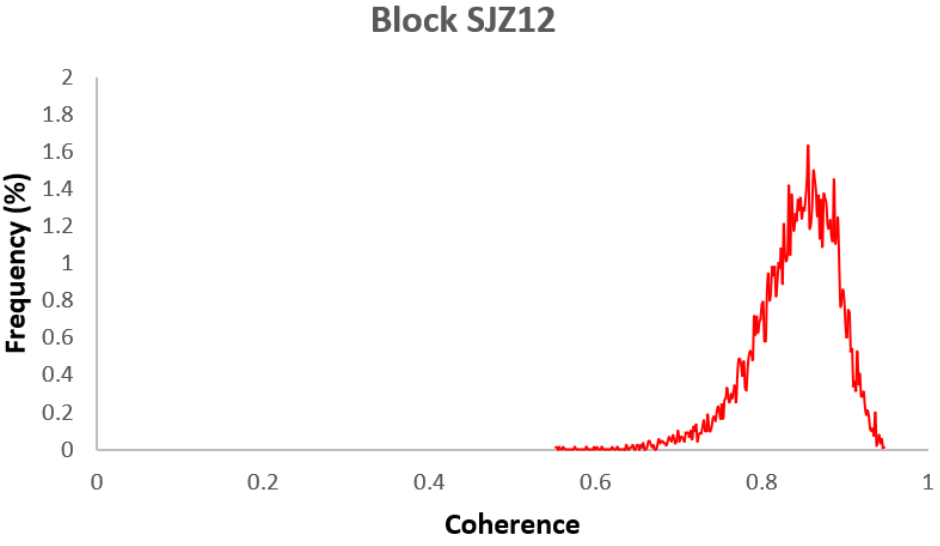
(C)


Block SJZ6b
Frequency (%)
2
1.8
1.6
1.4
1.2
1
0.8
0.6
0.4
0.2
0
0
0.2
0.4
0.6
0.8
1
Coherence

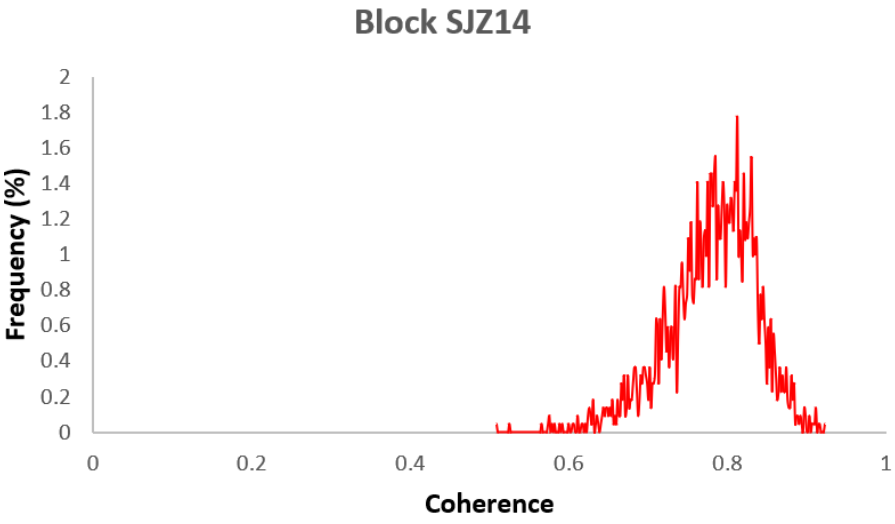
(D)


Block SJZ11
Frequency (%)
2
1.8
1.6
1.4
1.2
1
0.8
0.6
0.4
0.2
0
0
0.2
0.4
0.6
0.8
1
Coherence

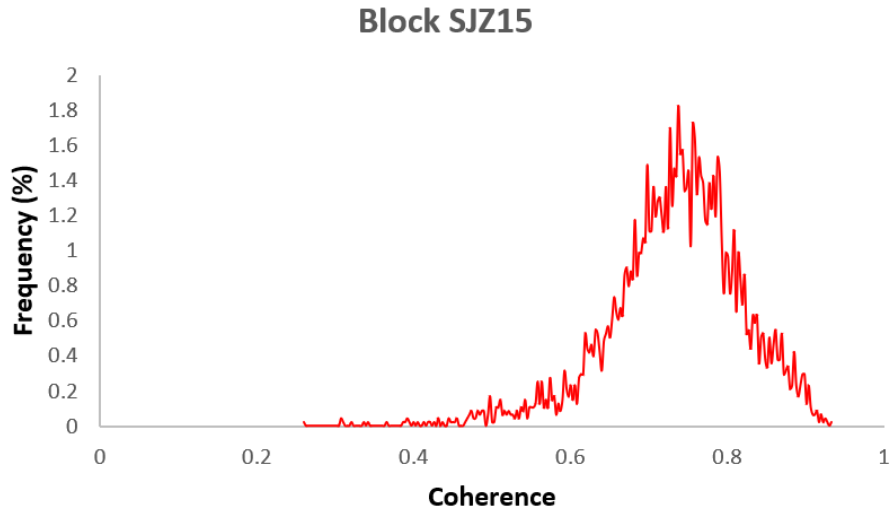
(E)


Block SJZ12
Frequency (%)
2
1.8
1.6
1.4
1.2
1
0.8
0.6
0.4
0.2
0
0
0.2
0.4
0.6
0.8
1
Coherence

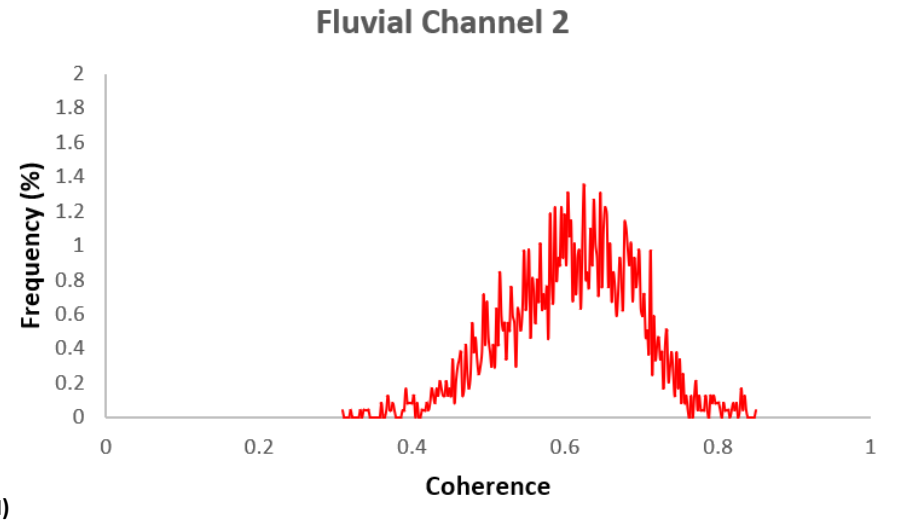
(F)



(G)



(H)



(I)

Figure 5.6 (A) to (I). Frequency distribution curves for coherence at Block SJZ0 (Figure 5.6A), SJZ1 (Figure 5.6B), SJZ2 (Figure 5.6C), SJZ6b (Figure 5.6D), SJZ11 (Figure 5.6E), SJZ12 (Figure 5.6F), SJZ14 (Figure 5.6G), SJZ15 (Figure 5.6H), and Fluvial Channel 2 (Figure 5.6I) in the Suanjingzi study area between 08/10/2017 and 26/01/2020.

The geomorphological processes (erosion and deposition) change the LoS distance, this further impacts the monitored deformation. The erosional processes (either fluvial or aeolian) remove the upper part of the objects will therefore have surface get lowered. This will therefore increase the LoS distance and make the InSAR imageries appear more subsidized. In opposite, the deposition which decrease the LoS will make the InSAR imageries appear more uplifted.

The erosional rates between the granodiorite and the surrounding unconsolidated sediments are different. This is controlled by the strength the of the rock. The Holocene covering area suffers more erosional impacts than the granodiorite covering area. That is because the Holocene sediments are composed of loose sand and loam deposits which are weaker so are more susceptible to erosion than the hard granodiorite. Due to the impacts of high erosional rates, the Holocene covering area has much higher SAR deformation rates than the granodiorite exposing area in Figure 5.1.

This speculation is further supported by the published erosion rates for various exposed felsic plutonic rocks (see Table 5.5). In general, the measured annual erosional rates of granite and granodiorite rock in arid, semi-arid, alpine, and temperate climates are usually in the region of 10^{-3} mm a^{-1} (data summarized in Table 5.5). Beishan in the Gobi Desert is in a similar climate, therefore, the natural erosional rates of the Suanjingzi granodiorite, and even the Jiujing and Xinchang granite, may have similar erosional rates to those highlighted in Table 5.5. However, the vertical and horizontal deformation rates (D_U and D_E) at Suanjingzi granodiorite blocks, as measured in this work, are in the region of 0.1 to 1 mm a^{-1}, mostly in the range between 0.1 to 0.5 mm a^{-1}. These are much higher than the granodiorite surface deformation rates in Table 5.5. This indicates the erosional process only slightly impact the surface displacement at Suanjingzi granodiorite. This granite erosional rate is very low compared to the monitored displacement rates, which is assumed to be negligible. Having excluded the impacts of geomorphology, it can be speculated that the displacements at granite exposed area are highly likely due to the impacts of tectonic activity. This will be discussed in Chapter 6.

Table 5.5 The erosional rates of granite and granodiorite in various environment.

Location	Rock Type	Erosion rate (mma^{-1})	Climate	Reference
Gross Spitzkoppe, Namib	Granite	0.001 to 0.005	Arid	Matmon [214]
Western Mountain Ranges, USA	Granite	0.0076±0.0039	Alpine	Small et al [215]
Mount. Evans, Colorado, USA	Granite	0.008	Alpine	Nishiizumi [216]
Grand Tetons, Wyoming, USA	Granodiorite	0.048	Alpine	Nishiizumi [216]
Himalayas	Granodiorite	0.014 and 0.056	Alpine	Nishiizumi [216]
Georgia Piedmont, Georgia, USA	Granite	0.008	Temperate	Bierman [217]
Llano Uplift, Texas, USA	Granite	0.012	Semi-arid	Bierman [217]
Alabama Hills, California, USA	Granite	0.007	Semi-arid	Bierman [217]
Eyre Peninsula, Australia	Granite	0.0005 to 0.001	Semi-arid	Bierman [218]
Fort Sage Mountains, California, USA	Granodiorite	0.05	Semi-arid	Granger [219]

5.3.2 The impacts of aeolian process

Erosional processes are interpreted as impacting the areas covered by Holocene sediments significantly (SJZ0, C1 and C2), this involves contributions of both aeolian and fluvial processes. The progressive decoherence (Figures 5.8A and 5.8F) and subsidence (Figure 5.7) at Holocene sediments covered SJZ0 might be caused by aeolian processes. Beishan lies in the centre of Gobi Desert in northwest China, an area widely accepted as a potential source for dust storms [220, 221]. The late Pleistocene and Holocene sediments are composed of clay, silt, sand, and/or gravels covering the surface of study area [222], generating dust through the processes of aeolian collision, abrasion and corrosion, which ultimately lead to the formation of dust storms in this dry area [221].

A combination of field investigations, wind tunnel experiments, and wind field analyses suggest that the modern erosion rates at Gobi Desert vary between 0.41 to 0.89 mm a^{-1}[222]. This range is in general agreement with our measured subsidence rate at Block SJZ0 (D_U = -0.68 mm a^{-1}). Since the persistent decoherence level of around 0.4 (Figure 5.8) represents significant surface change, it can be speculated that the 0.68 mm annual subsidence at SJZ0 which is very high for the region is highly possible due to the removal of topmost sedimentary grains by aeolian erosion and winnowing. The granodiorite exposing blocks suggest that most tectonic induced movements at Suanjingzi are only in the range between -0.3 to 0.3 mm a^{-1}. This is much lower than the aeolian induced erosional rates (0.41 to 0.89 mma^{-1}) and InSAR measured deformation rates (-0.68 mm a^{-1}). In this way, it can be speculated that the aeolian erosion has contributed most deformation rates at the surface of Holocene covering area (such as SJZ0). As the tectonic movements have been obscured by geomorphological processes, the exact individual contribution of the geomorphology and tectonics at SJ20 in Figure 5.1 cannot be accurately estimated.

At Block SJZ0, there is a significant deviation between the ascending (D_{los}^{asc} = -0.94 mma^{-1}) and descending (D_{los}^{des}=-0.12 mma^{-1}) LoS displacement rates (Figure 5.7). This deviation reflects a significant shift towards the side of the descending path, which is equivalent to an eastwards deformation rate (D_E) around 0.65 mma^{-1}. This is interpreted as being driven by the aeolian wind, as the general wind direction around Beishan is blowing from west/northwest to east/southeast [222, 223], this may lead to the eastwards creeping and saltation of sand grains in Holocene sediments covering area.

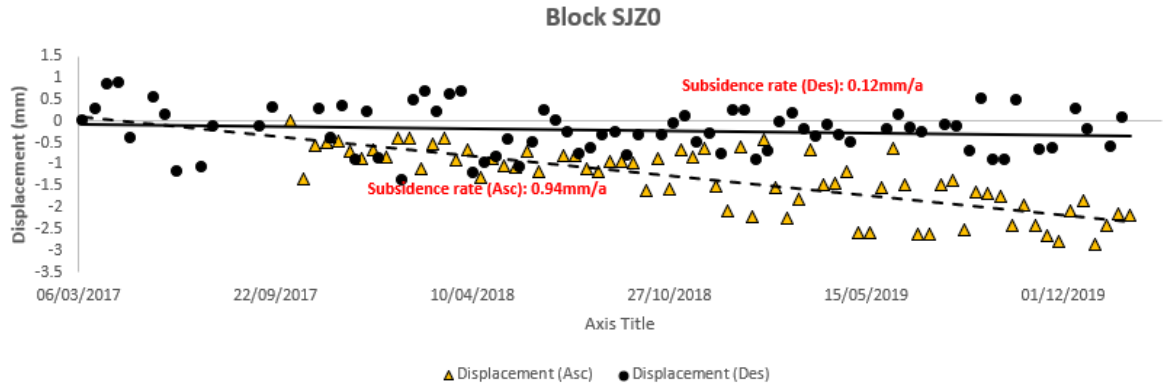


Figure 5.7 The average time-series analysis at Block SJZ0 in ascending (01/10/2017 to 07/02/2020) and descending (11/03/2017 to 31/01/2020) scene. Dashed lines represent the trends of ascending orbit displacements, and solid lines represent the descending orbit displacements. The gradients of the linear trendlines show that rates of subsidence are 0.12 mma^{-1} and 0.94 mma^{-1} from descending and ascending orbits respectively.

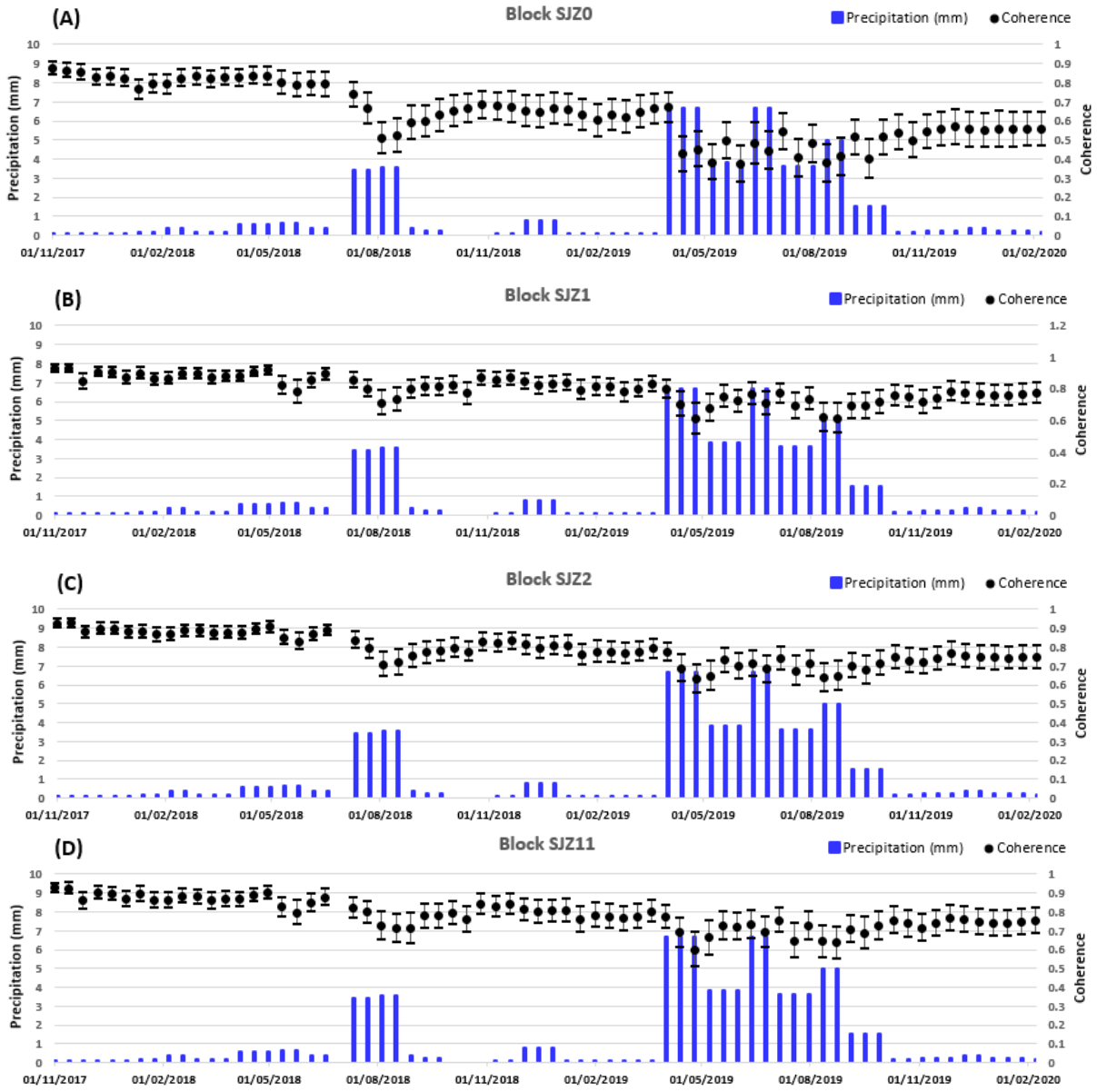
5.3.3 The impacts of fluvial process

The variation in coherence shown in Figure 5.8 demonstrates that two significant periods of decoherence occurred during July-August 2018 and April-May 2019 (highlighted by blue box) during the acquisition period, which showed a clear three stepped (zigzag shaped) reduction. For example, in the Holocene sediment covered areas SJZ0, C1, and C2 the initial coherence has remains at around 0.85 - 0.9 from November 2017, until July 2018 when it decreased to around 0.65 and then decreased to 0.55 in April 2019 (Figure 5.8(A) and 5.8(F)). As illustrated in Figure 5.8 (A) to (F), the timing of these two periods of decoherence are generally associated with the intense summer rainfall (Figure 1.2), where a high precipitation rate (in the summer months) corresponds to an apparent coherence reduction.

There is no direct evidence, either from the experimental results or fieldtrip observations to prove there is a direct causation relation between fluvial processes and decoherence. However, in sub-section 3.4.2, which focuses on a series published studies [165, 166, 167, 168, and 169] it is demonstrated that the major rainfall events can lead to decoherence. Especially in Cabre [169], the same method (CCD) was applied to investigate the impacts of intense rainfall in Atacama Desert (where the climate is comparable to that in Gobi Desert). It indicates that the permanent loss of coherence is related to modification of soil texture by erosion and sedimentation.

In Beishan area, the climate records [17, 21] indicate the temporal distribution of the precipitation is uneven, where most precipitation is concentrated in summer months (June, July and August) in terms of short intense rainfall, this in turn leads to the formation of torrential floods and debris flows. Meanwhile, the monthly precipitation in the autumn and winter months is very low. These of

torrential floods and debris flows occur five to six times in wet years and at least once in dry years [17]. Based on the experience from Atacama Desert study [169], it is possible that the permanent decoherence which temporally coincidence with intense rainfall is due to the soil texture modification by floodwater, and the floodwater rapidly eroding the surface sediments and in turn leading to the significant decoherence observed in Figure 5.8. In comparison, the extent of coherence reduction in the Holocene sediment covered areas (SJZ0, C1, Figure 5.8 A and F) is much higher than that on the granodiorite exposed areas (SJZ1, 2, 11, and 12, in Figure 8 (B, C, D and E)). That might because the Holocene sediments are softer and weaker than the granodiorite, therefore, more susceptible to erosion.



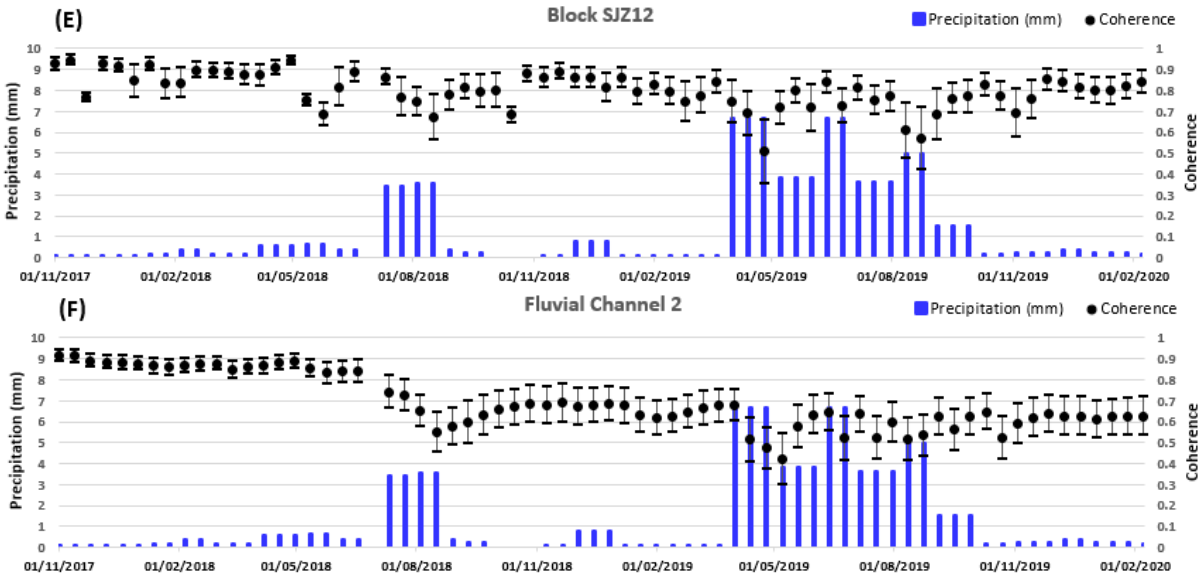


Figure 5.8 (A) to (F). The temporal variation of coherence in relation to precipitation at Block SJZ0, SJZ1, SJZ2, SJZ11, SJZ12 and Fluvial Channel 2 (location shown in Figure 5.1 and Figure 5.5) between 08/10/2017 to 26/01/2020 in Suanjingzi region.

A bounce can be observed (Figure 5.8(A) and 5.8(F)) following the end of the wet period, these two temporal periods of decoherence happened in August 2018 and May 2019. Cabre suggested this temporal loss of coherence is related to variations in soil moisture [169]. The surface rainwater absorbs the Sentinel-1 microwave radiation to decrease the backscattered signal, which in turn causes further decoherence. This can lead to very low coherence of around 0.4. However, when the rainwater evaporated due to the high temperature, the coherence partially but not completely bounces back.

5.3.4 The volumetric scattering decorrelation

Further to the impact of aeolian and fluvial erosion, the low coherence at C1 and C3 may also be due to the impacts of volumetric scattering decorrelation (Υ_{vol}). The volumetric scattering decorrelation is a component of coherence (Chapter 4), which can be affected by the slope angle variation towards the direction of satellite LoS [31]. The steep channel at C1 and C2 may increase the local volumetric scattering decorrelation significantly, making them appeared low coherence in SAR images.

5.4 Surface deformation in Jiujing and its geomorphological effects

5.4.1 Quaternary sediments covered area (low coherence)

Based on the information extracted from Figure 2.2, Block BB1 and JB1 represent the area covered by the Holocene aeolian deposits in Ba'antan Basin and Jiujing Basin respectively, which are characterized by very low coherence (less than 0.3, shown in Figure 5.11A and 5.11C). There may be for two reasons. First, the sediments at Block BB1 and JB1 may be saturated throughout the year. This is because the subsidence triggered by normal faults F_{16}, F_{18} and F_{20} lowered the topographic height of Bantan,

Ba'antan and Jiujing Basins. Such lowering would cause the discharging of shallow groundwater, surface water and flood water towards the basin centres [55, 56]. This increases the saturation of the sediments. As water absorbs the Sentinel-1 microwave radiation [**224**] and wet soil contributes less backscattered signal from the scatterers, leading to the low coherence. Or second, the continuous deposition of aeolian sediments in the Bantan, Ba'antan and Jiujing Basins alters the ground surface may lead to a further loss of local coherence. It has been estimated that the Holocene sediments are still accumulating with an average rate about 0.1 to 0.4 mma^{-1} in Ba'antan and Jiujing Basins [34], this might contribute to uplift within Ba'antan and Jiujing Basin areas observed in Figure 5.2, but further investigations are needed. As the threshold coherence was set at 0.75 during the processing for this research and more than 95% of pixels at Block JB1 and BB1 are below 0.3 during the period 08/10/2017 to 26/01/2020 (Table 5.6). This therefore made it difficult to identify stable scatterers around Block BB1 and JB1, which further leads to deformation data loss around Ba'antan, Bantan and Jiujing Basin areas in Figure 5.2.

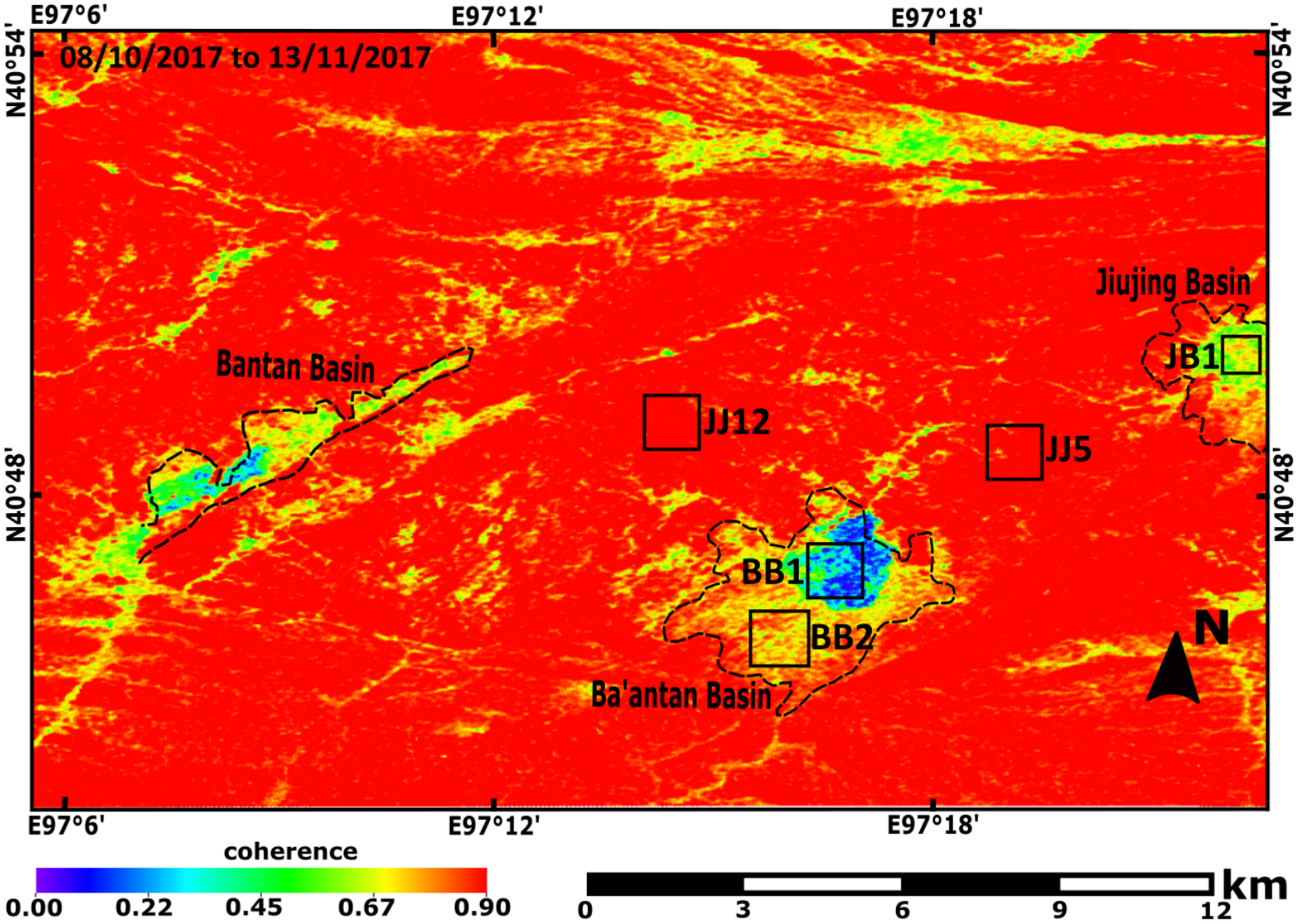


Figure 5.9 (A). The spatial variations of Sentinel-1 (ascending) coherence at time periods in Jiujing study area between 08/10/2017 to 13/11/2017.

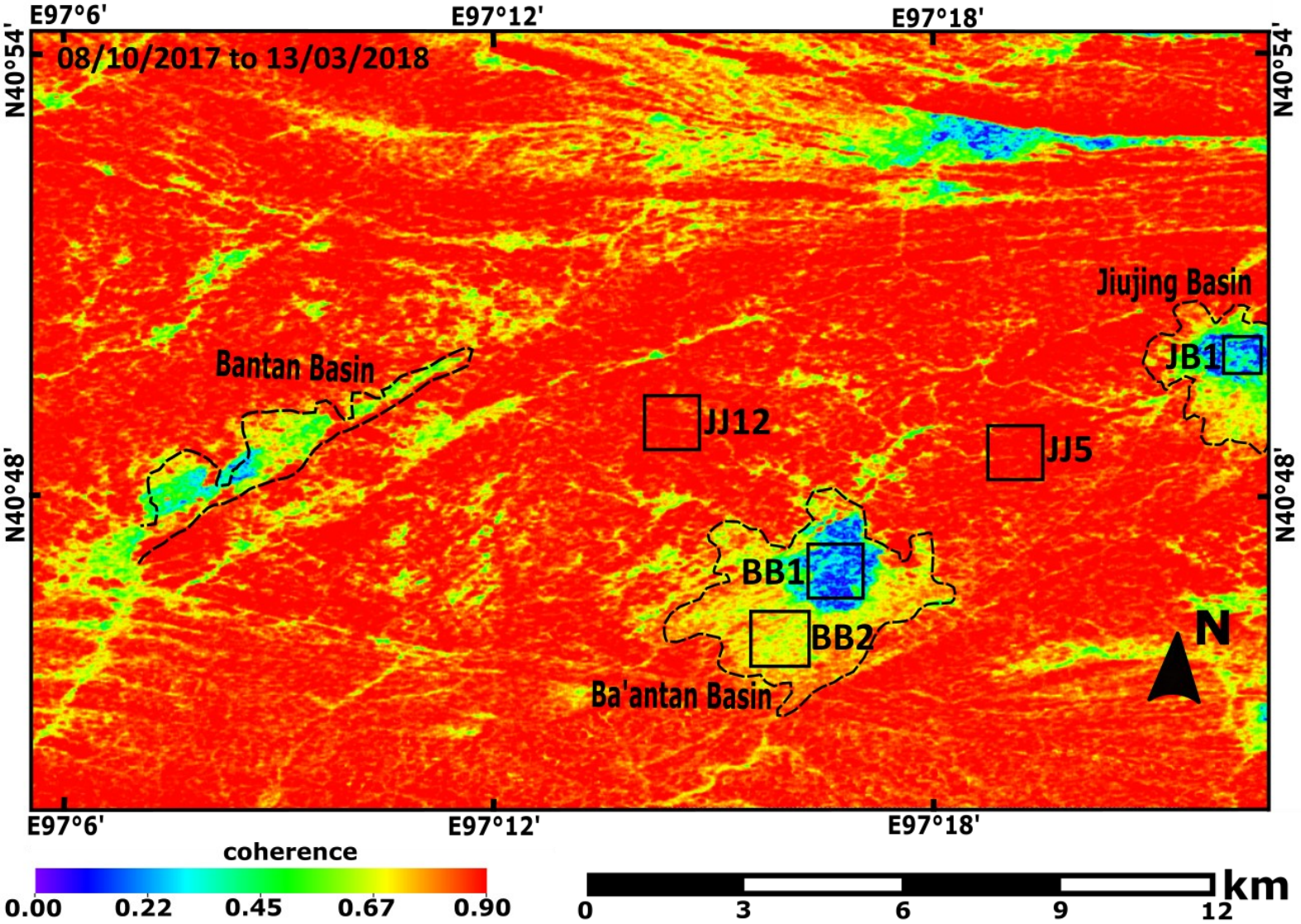


Figure 5.9 (B). The spatial variations of Sentinel-1 (ascending) coherence at time periods in Jiujing study area between 08/10/2017 to 13/03/2018.

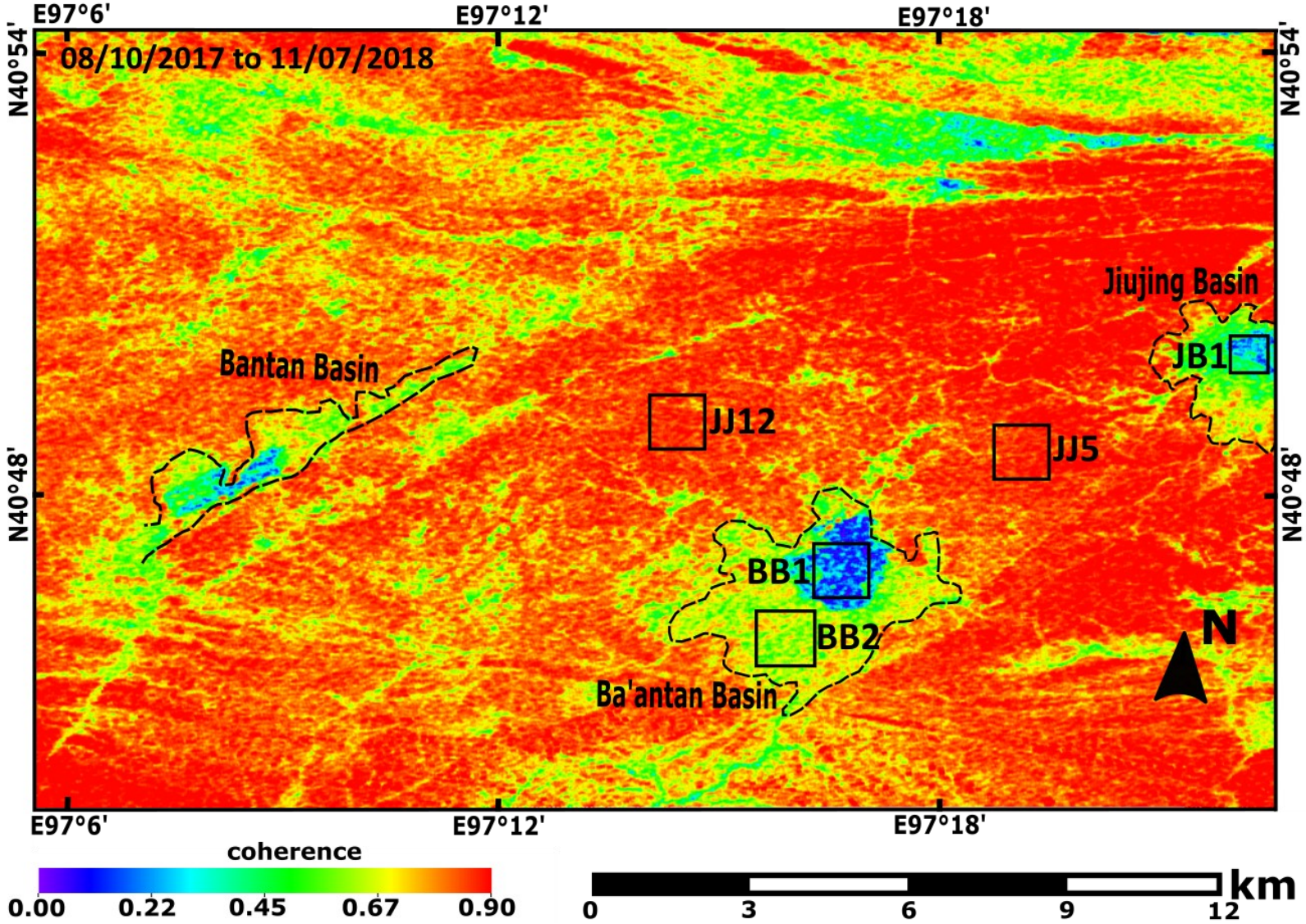


Figure 5.9 (C). The spatial variations of Sentinel-1 (ascending) coherence at time periods in Jiujing study area between 08/10/2017 to 11/07/2018.

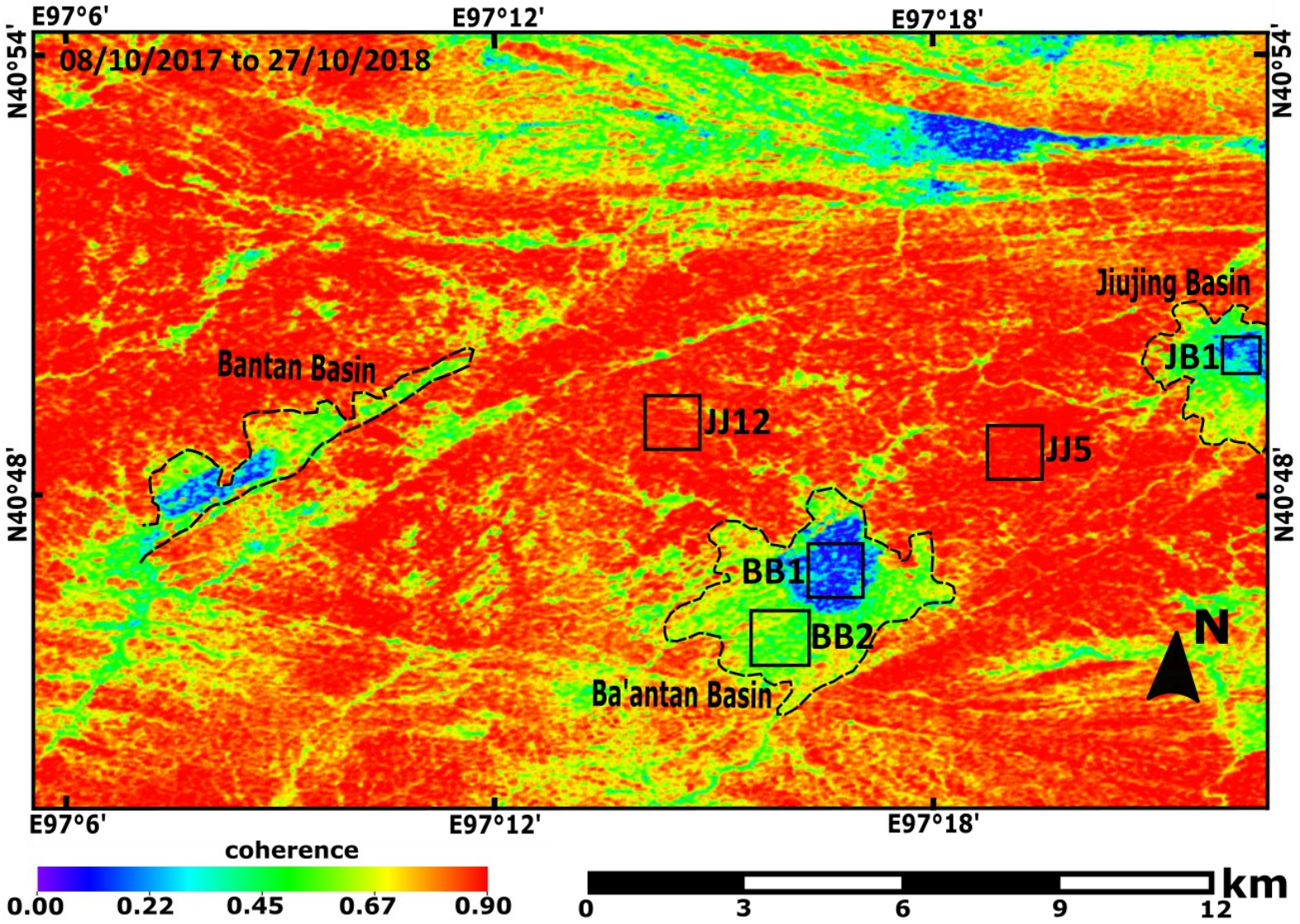


Figure 5.9 (D). The spatial variations of Sentinel-1 (ascending) coherence at time periods in Jiujing study area between 08/10/2017 to 27/10/2018.

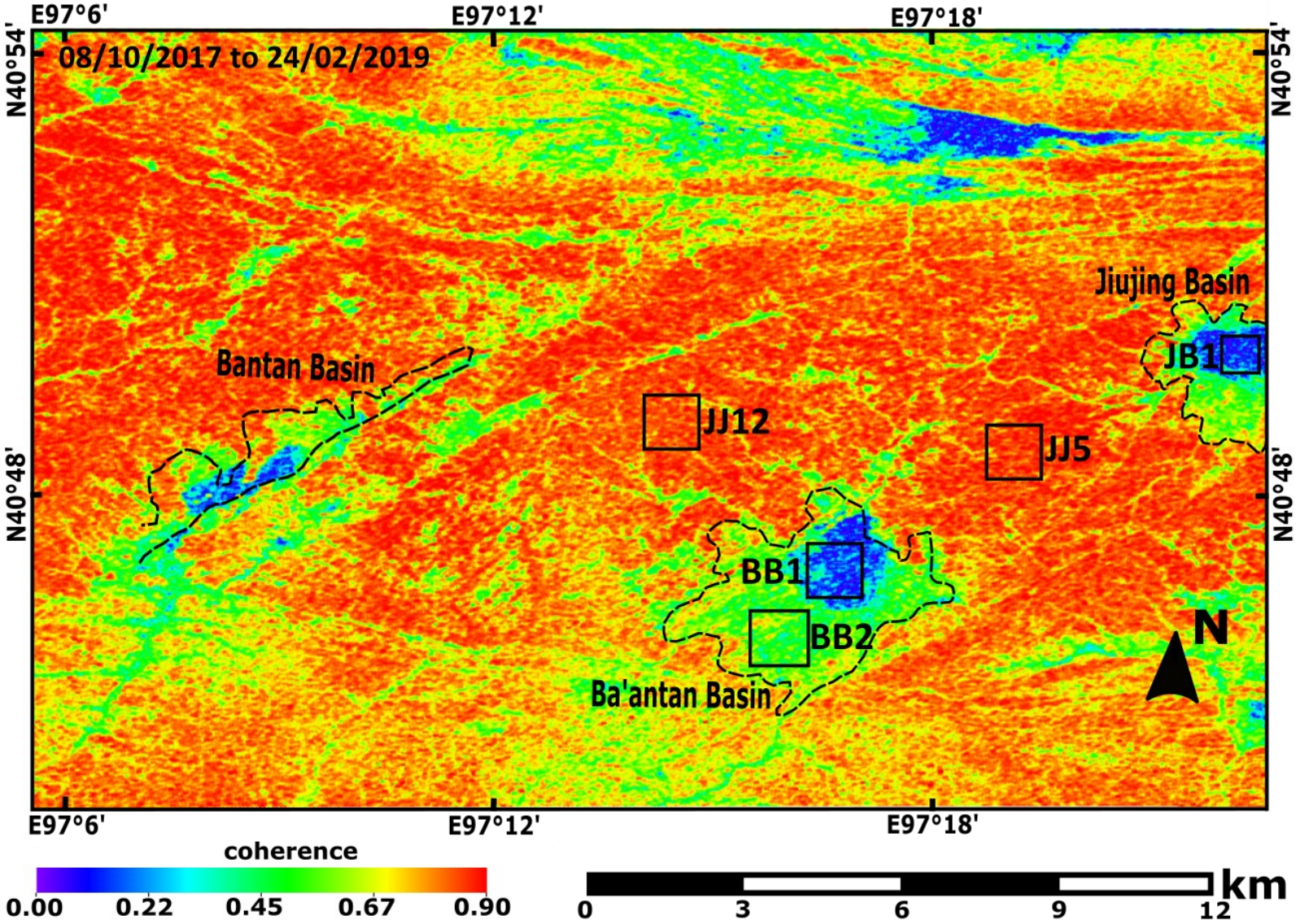


Figure 5.9 (E). The spatial variations of Sentinel-1 (ascending) coherence at time periods in Jiujing study area between 08/10/2017 to 24/02/2019.

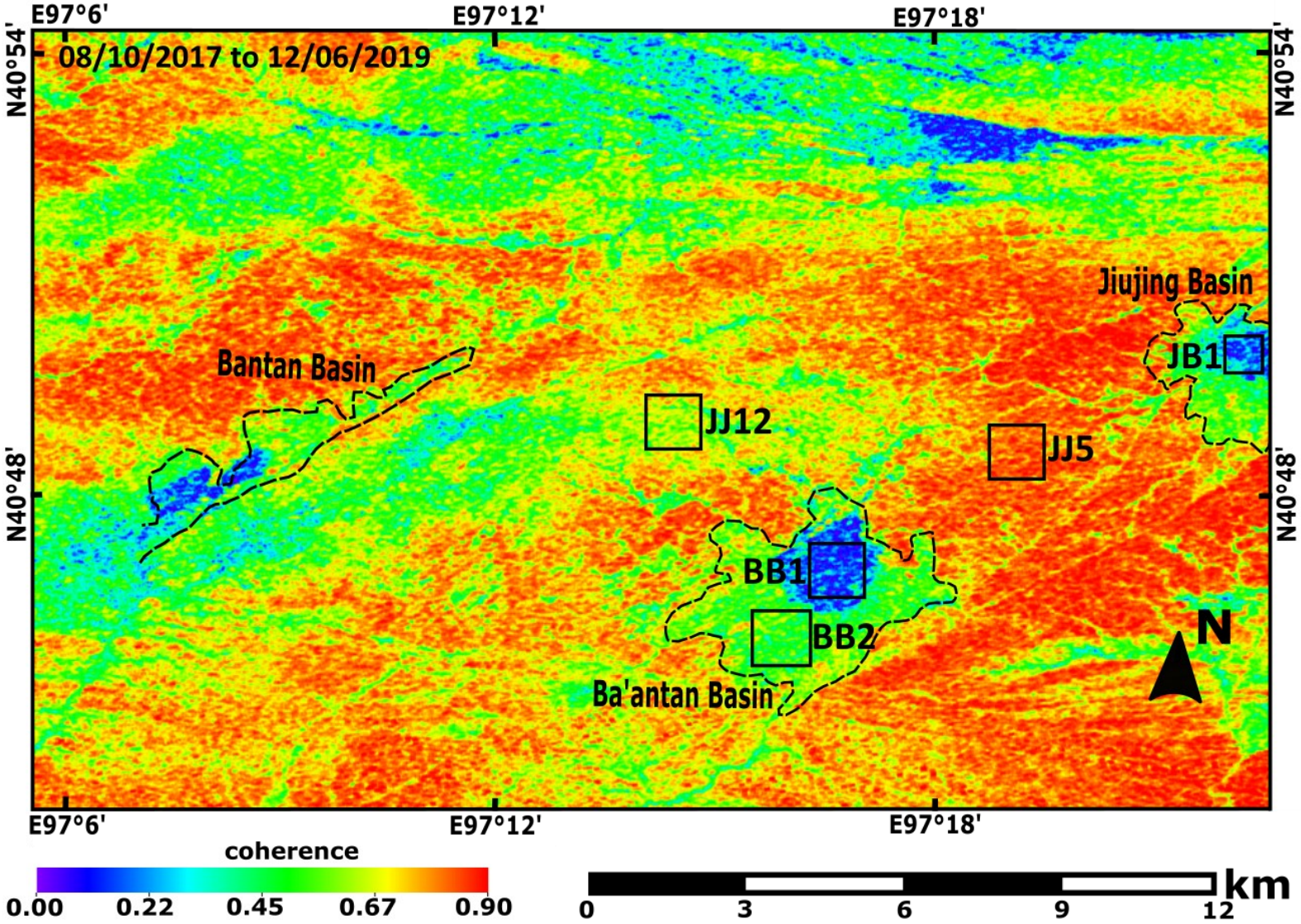


Figure 5.9 (F). The spatial variations of Sentinel-1 (ascending) coherence at time periods in Jiujing study area between 08/10/2017 to 12/06/2019.

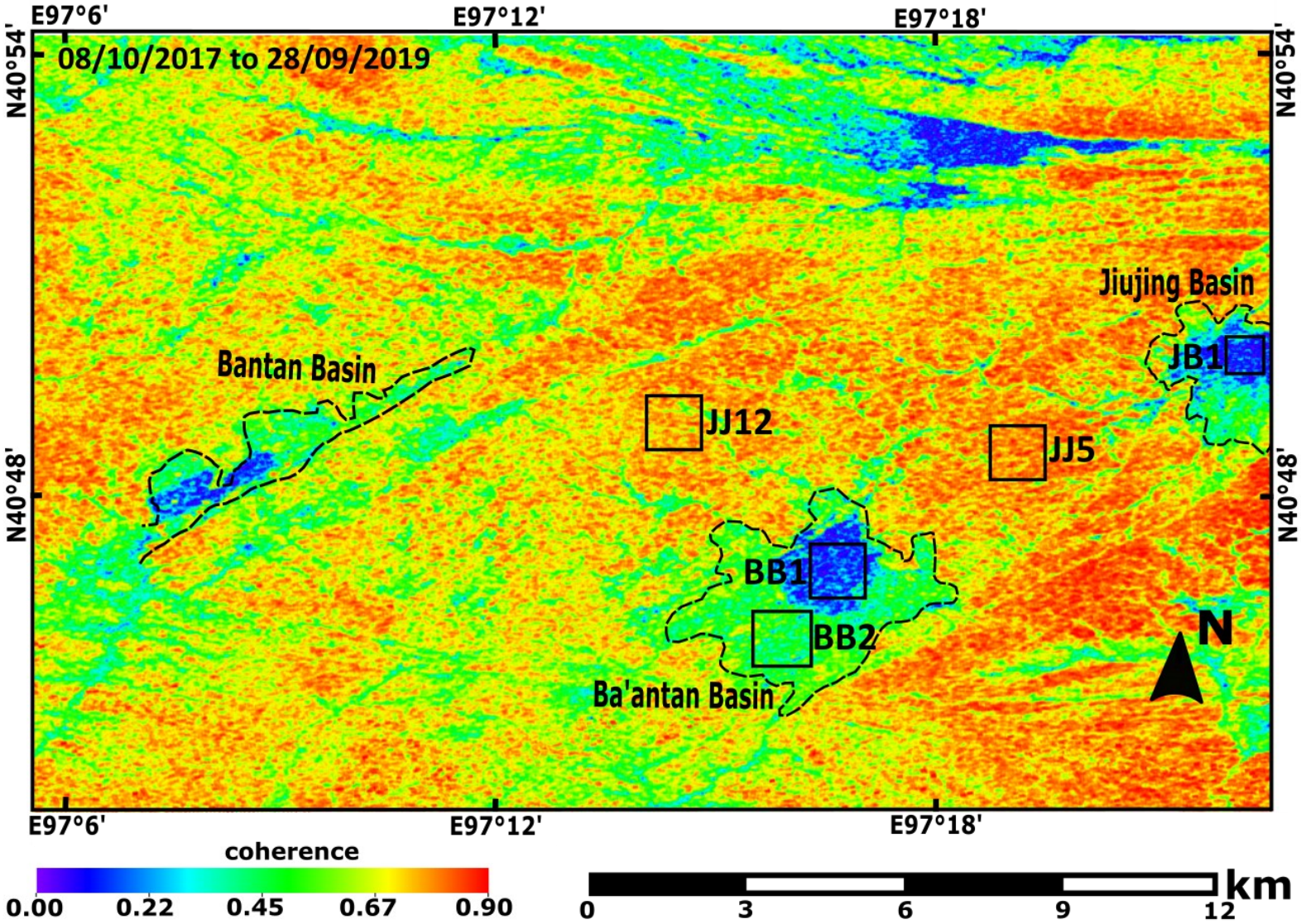


Figure 5.9 (G). The spatial variations of Sentinel-1 (ascending) coherence at time periods in Jiujing study area between 08/10/2017 to 28/09/2019

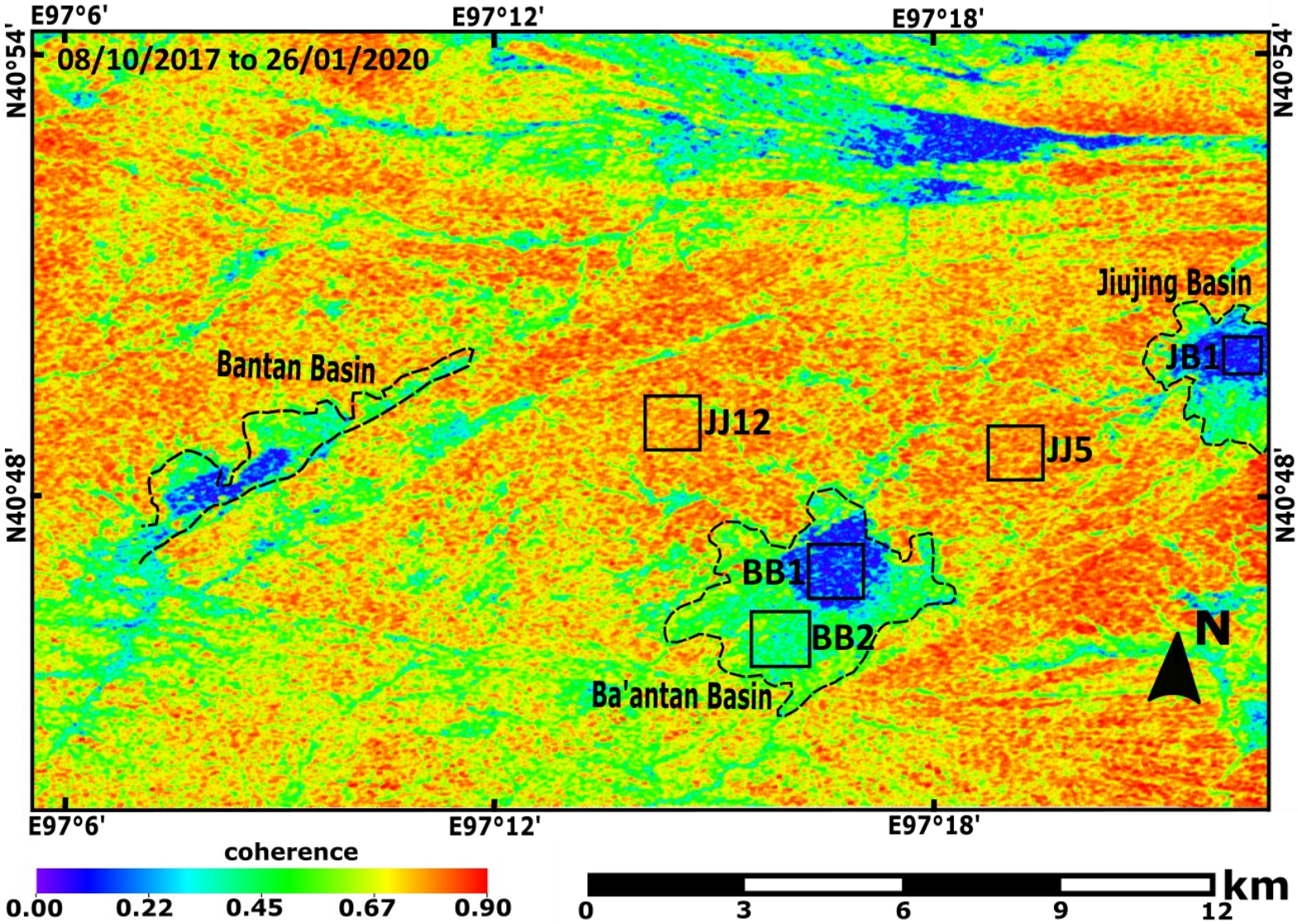
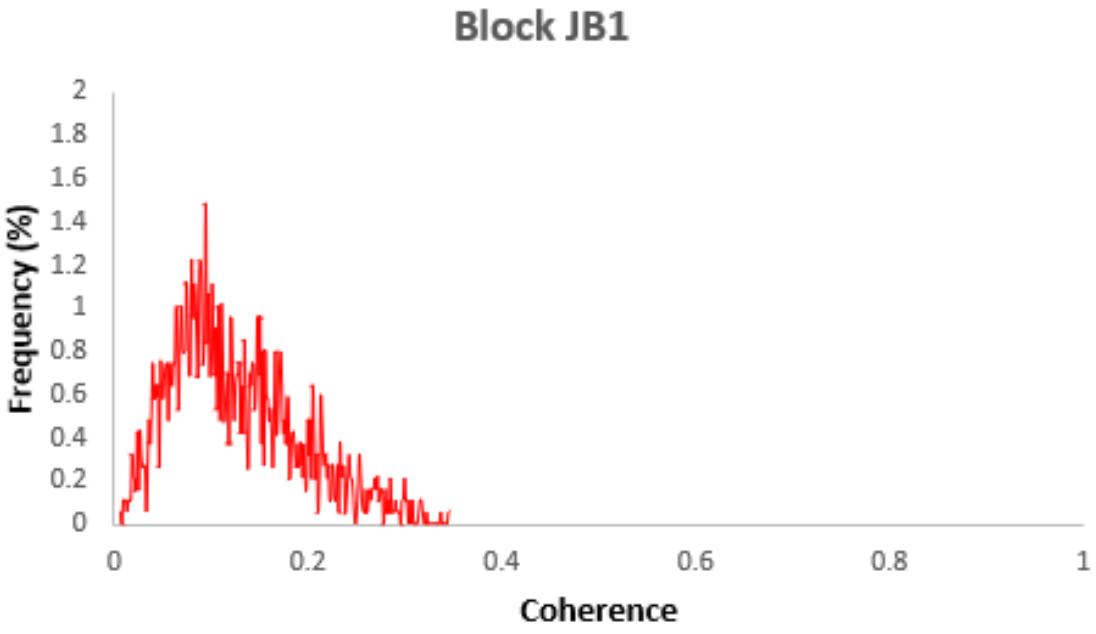


Figure 5.9 (H). The spatial variations of Sentinel-1 (ascending) coherence at time periods in Jiujing study area between 08/10/2017 to 26/01/202

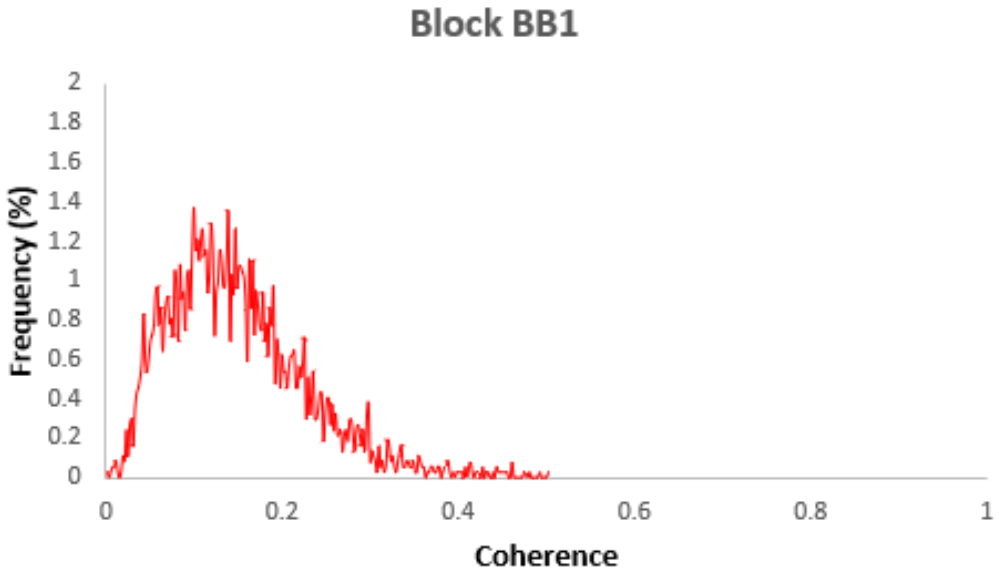
Block BB2 represents the late Pleistocene alluvial sediments covering areas in Ba'antan Basin (Figure 5.11(B)). Similar to Block SJZ0 at Suanjingzi study area (Section 5.4), Block BB2 also shows a two staged decoherence trends reducing from 0.8 to 0.5 due to the heavy summer rainfall in July-August 2018 and April-May 2019 respectively over 2.5 years' period. This has been highlighted in Figure 5.11(B). As in Block SJZ0 this has been interpreted as rainwater can reduce the coherence by direct erosional impact between rain drops and sediment particles and by sediment deposition transported by floodwater. Overall, only about 2.4 % of pixels have coherence values above 0.7 over 08/10/2017 to 26/01/2020.

5.4.2 Granite exposed area (high coherence)

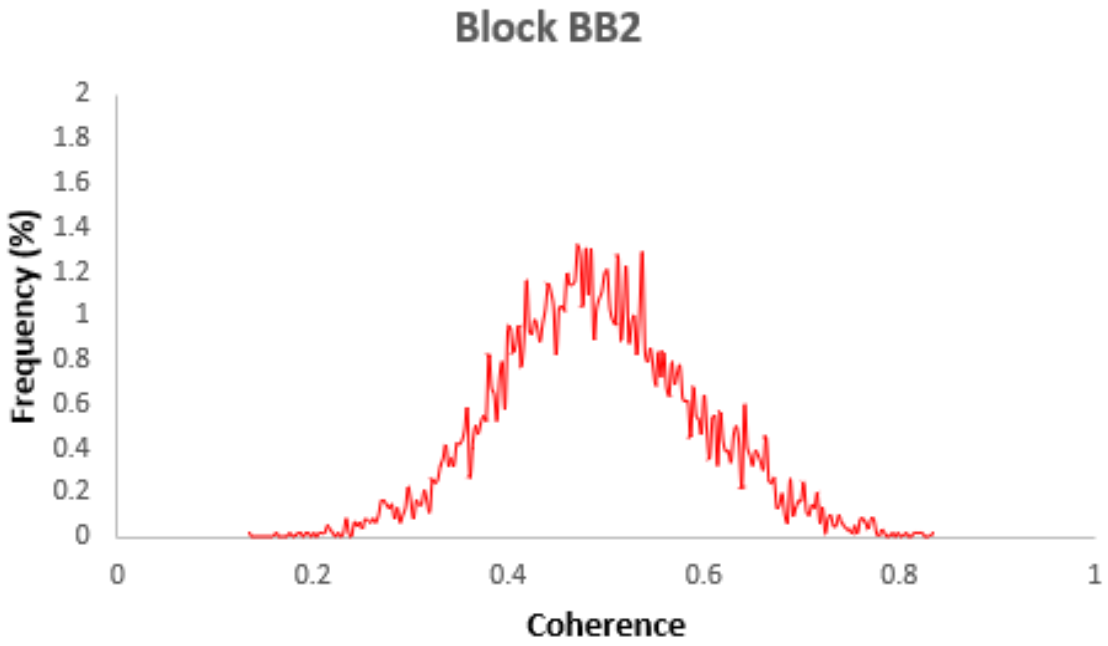
Blocks JJ12 and JJ5 were selected to represent the area exposed by Middle Proterozoic granite. As presented in Figures 5.11 (D) and 5.11 (E), the overall coherence loss is about 0.15 over the time scale 08/10/2017 to 26/01/2020 with 95% and 98% pixels having a coherence above 0.7 respectively. This indicates geomorphological processes have very limited effect on surfaces composed of granite bedrock due to its high resistance, which therefore suggests that tectonic activity might be the main cause of the surface movement.



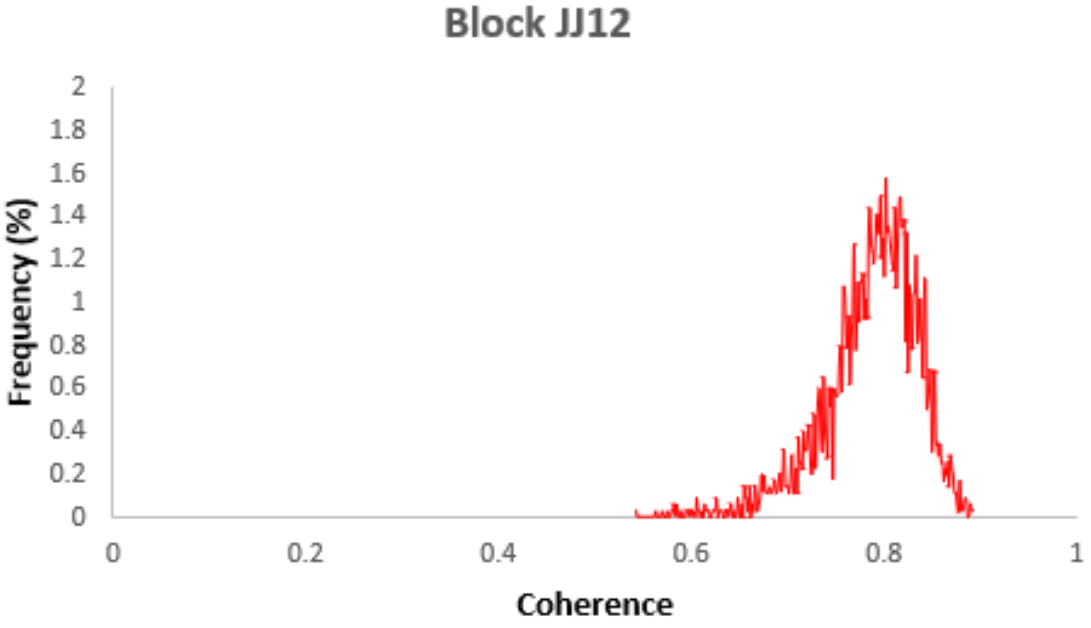
(A)



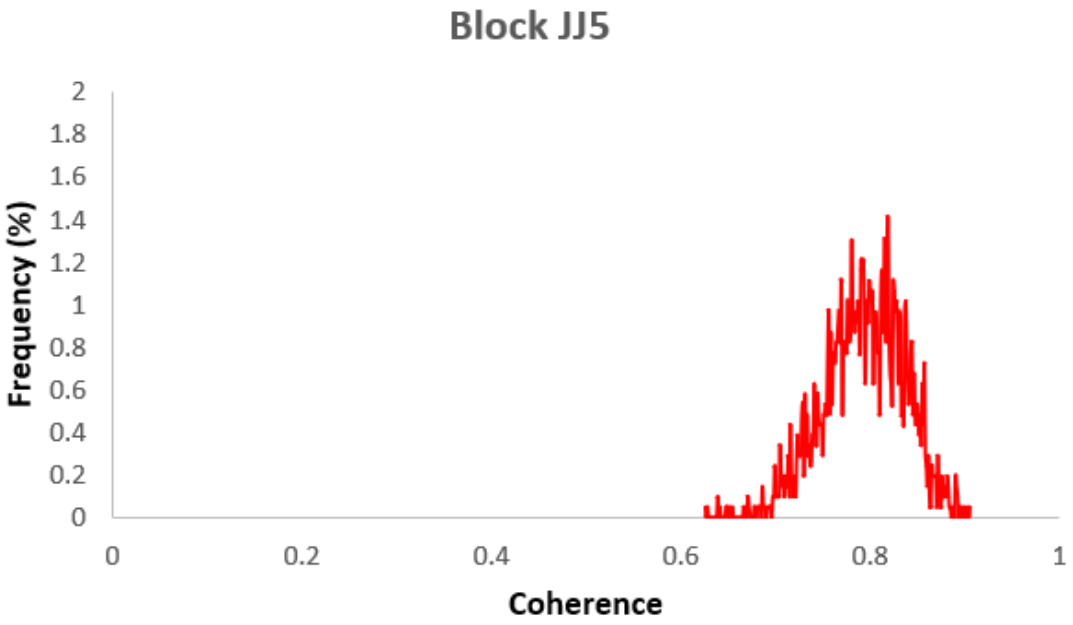
(B)


Block BB2
Frequency (%)
2
1.8
1.6
1.4
1.2
1
0.8
0.6
0.4
0.2
0
0
0.2
0.4
0.6
0.8
1
Coherence

(C)


Block JJ12
Frequency (%)
2
1.8
1.6
1.4
1.2
1
0.8
0.6
0.4
0.2
0
0
0.2
0.4
0.6
0.8
1
Coherence

(D)

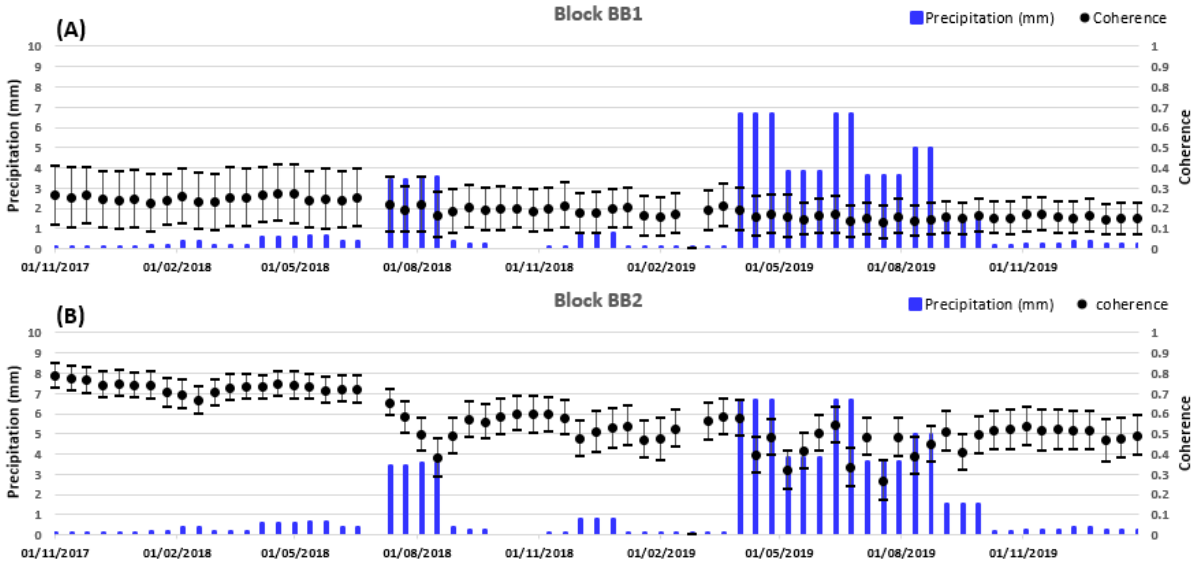


(E)

Figure 5.10 (A) to (E). The frequency distribution of coherence at Block JB1 (Figure 5.10A), BB1 (Figure 5.10B), BB2 (Figure 5.10C), JJ12 (Figure 5.10D) and JJ5 (Figure 5.10E) in Jiujing study area between 08/10/2017 to 26/01/2020, where Block JJ5 and JJ12 represent the granite exposing area and Block BB1, BB2, and JB1 represent the Quaternary sediments covering area.

Table 5.6 The cumulative percentage of coherence at Block BB1, BB2, JB1, JJ5, and JJ12 in Jiujing study area between 08/10/2017 to 26/01/2020.

Percentage	Block JB1	Block BB1	Block BB2	Block JJ5	Block JJ12
$P_{(coh>0.3)}$	0.848356%	4.084923%	97.46978%	100%	100%
$P_{(coh>0.4)}$	0	0.913733%	82.14343%	100%	100%
$P_{(coh>0.5)}$	0	0.026875%	44.49637%	100	100%
$P_{(coh>0.6)}$	0	0	14.71394%	100%	99.57603%
$P_{(coh>0.7)}$	0	0	2.369057%	98.16159%	94.62973%
$P_{(coh>0.8)}$	0	0	0.096696%	46.10547%	44.43188%
$P_{(coh>0.9)}$	0	0	0	0.145138%	0



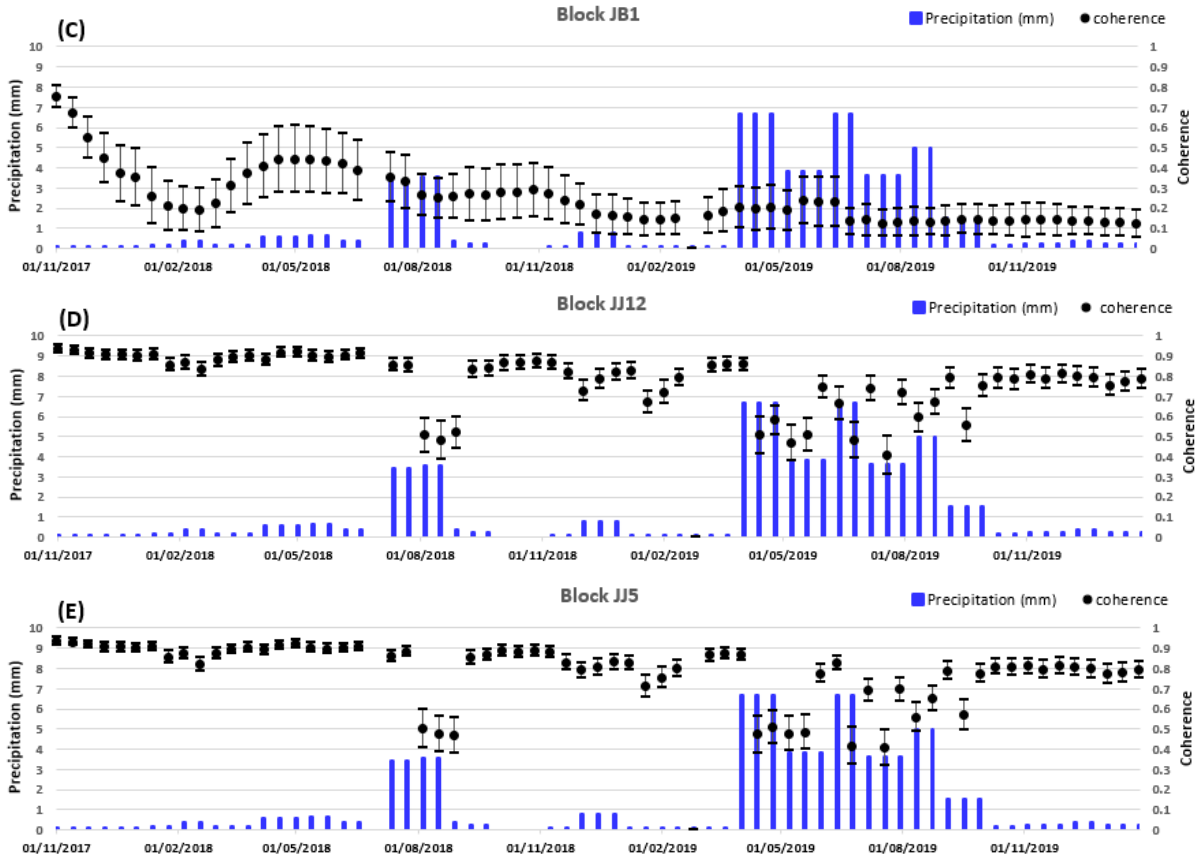


Figure 5.11 (A) to (E). The temporal variation of coherence in relation precipitation to precipitation at Block BB1, BB2, JB1, JJ5, and JJ12 (location shown in Figure 5.2 and Figure 5.9) between 08/10/2017 to 26/01/2020 in Jiujing region, where Blocks JJ5 and JJ12 represent the granite exposed area and Blocks BB1, BB2, and JB1 represent the Quaternary sediments covered area.

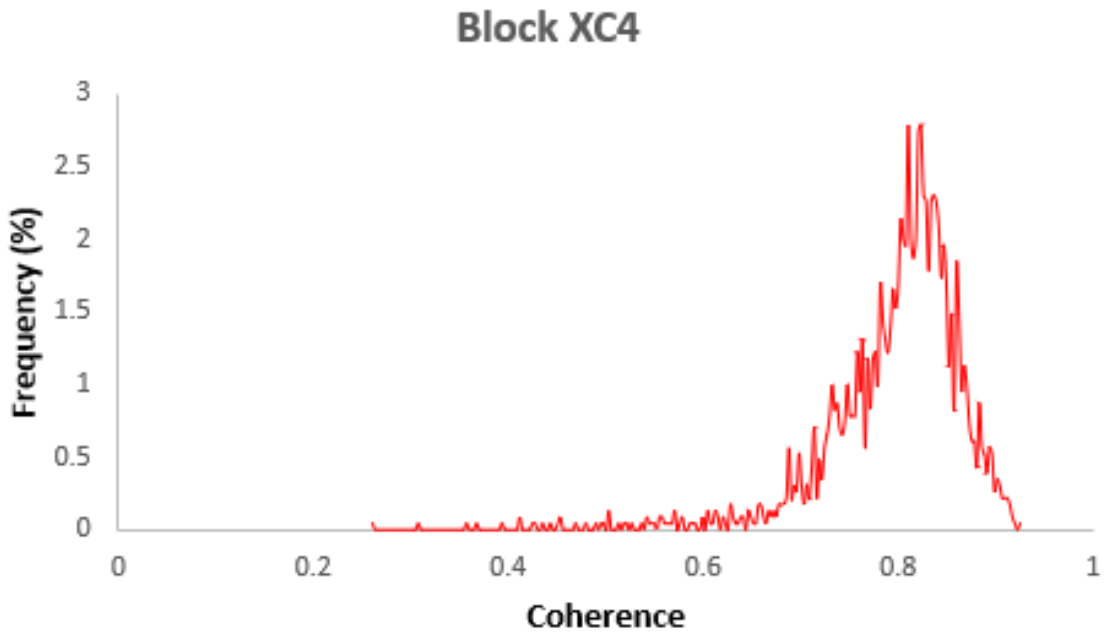
5.5 Surface deformation in Xinchang and its geomorphological effects

Overall, more than 95% pixels at Blocks XC5, XC6, XC9 and XC10 and 90% pixels at Blocks XC4 have coherence higher than 0.7 (Table 5.7, Figure 5.12) with low temporal coherence variation (Figure 5.14) over the period of 08/10/2017 to 26/01/2020, which suggests that the granite exposed area in Xinchang is barely impacted by geomorphology. As it has been discussed previously in Section 5.3 and 5.4, the surface displacements in this area are likely due to the impact of tectonic activity. This will be discussed in Chapter 6.

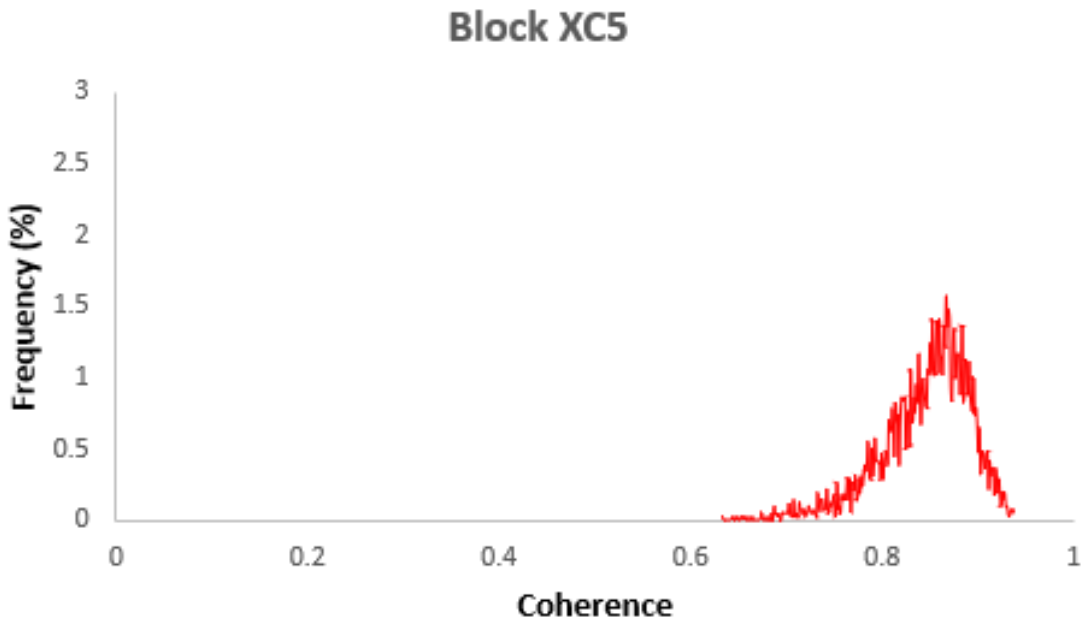
The significant low coherence mainly coincides with the Holocene sediments covering area (Figure 5.13 (A) to (H)). At Block Qh1, only 2.28% pixels have coherence more than 0.7 and the coherence decrease continuously from 0.75 to 0.45 during 08/10/2017 to 26/01/2020. Figure 5.3 (A - C) indicates that the Holocene sediments covering area around Block Qh1 are generally in uplifting, this might be caused by modern sediment deposition and/or the presence of soil moisture and was previously discussed in Section 5.4 and 5.5.

Table 5.7 The cumulative percentage of coherence at Block XC4, XC5, XC6, XC9, XC10 and Qh1 in Xinchang study area between 08/10/2017 to 26/01/2020.

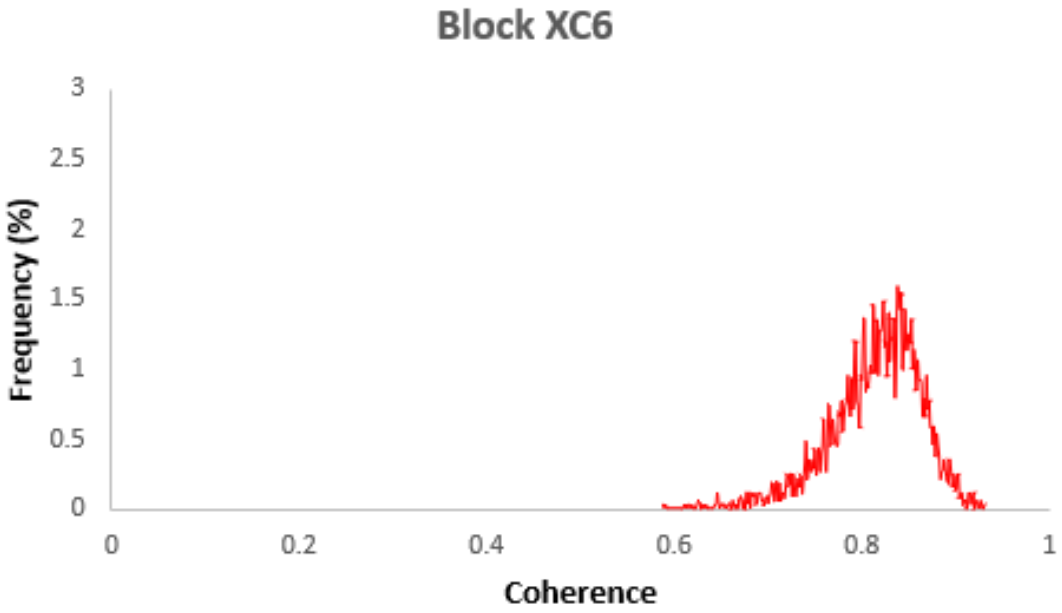
Percentage	Block XC4	Block XC5	Block XC6	Block XC9	Block XC10	Block Qh1
$P_{(coh>0.3)}$	99.95662%	100%	100%	99.90976%	100%	56.80807%
$P_{(coh>0.4)}$	99.78308%	100%	100%	99.72027%	100%	35.44942%
$P_{(coh>0.5)}$	99.1757%	100%	100%	99.28713%	99.93082%	17.11658%
$P_{(coh>0.6)}$	97.87419%	100%	99.9472%	98.79083%	99.15606%	7.445862%
$P_{(coh>0.7)}$	92.88503%	99.19067%	97.67687%	95.41599%	95.19923%	2.284189%
$P_{(coh>0.8)}$	58.35141%	85.14639%	67.37064	62.84967%	66.43608%	0
$P_{(coh>0.9)}$	1.64859%	8.33135%	1.451954	2.905613%	1.521859%	0



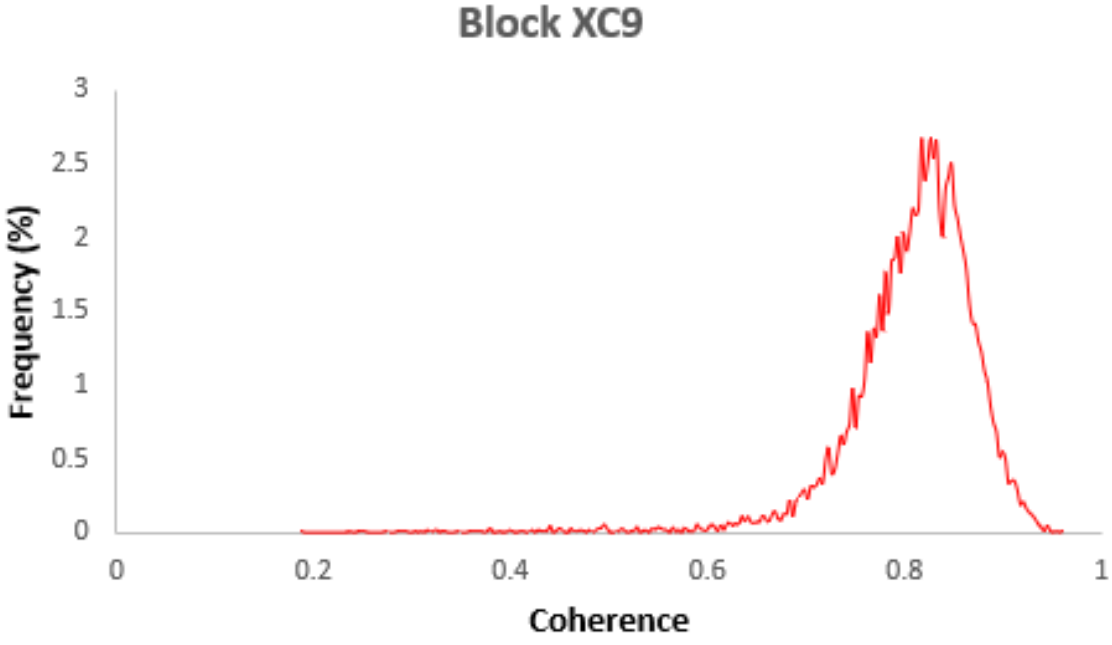
(A)



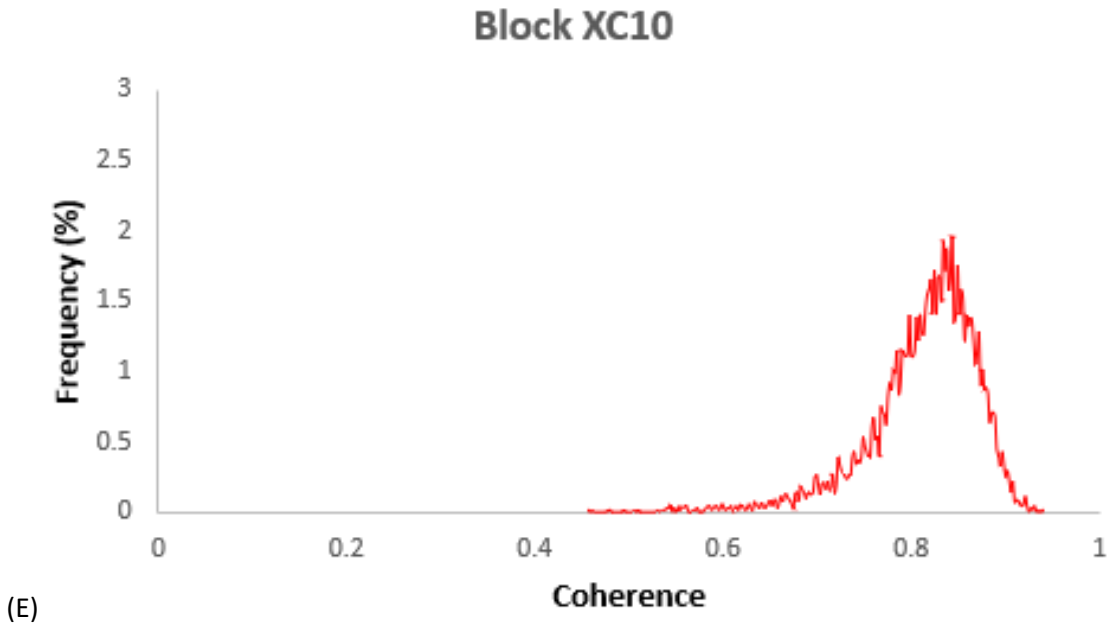
(B)


Block XC6
Frequency (%)
3
2.5
2
1.5
1
0.5
0
0
0.2
0.4
0.6
0.8
1
Coherence

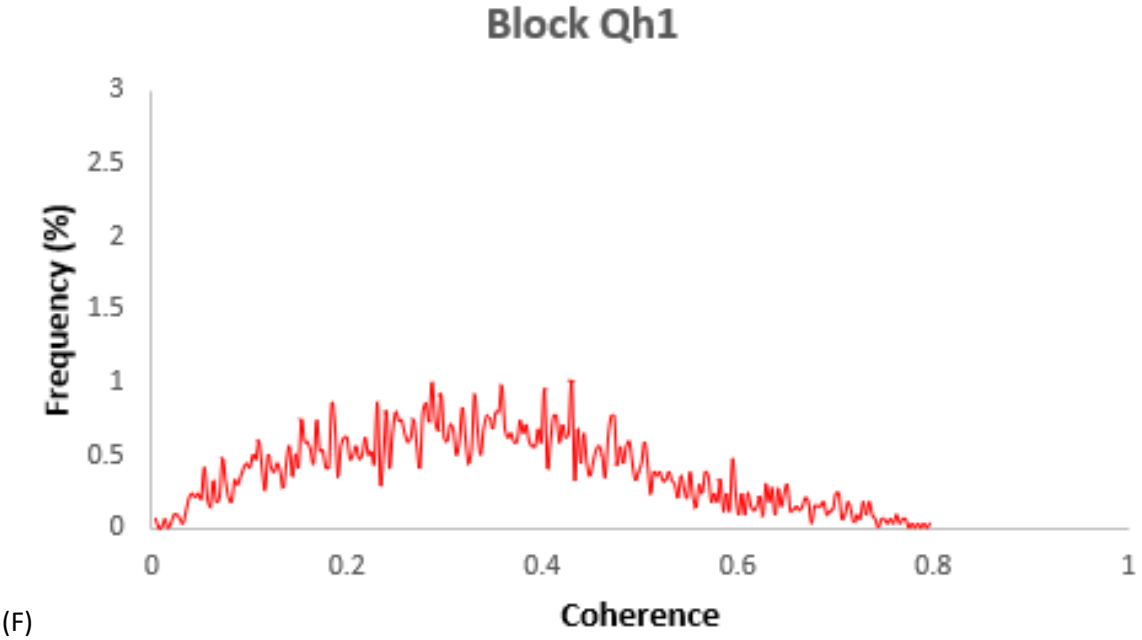
(C)


Block XC9
Frequency (%)
3
2.5
2
1.5
1
0.5
0
0
0.2
0.4
0.6
0.8
1
Coherence

(D)



(E)



(F)

Figure 5.12 (A) to (F) The frequency distribution of coherence at Block XC4 (Figure 5.12A), XC5 (Figure 5.12B), XC6 (Figure 5.12C), XC9 (Figure 5.12D), XC10 (Figure 5.12E) and Qh1 (Figure 5.12F) in Xinchang study area between 08/10/2017 to 26/01/2020, where Block XC4, XC5, XC6, XC9, and XC10 represent the granite exposing area and Block Qh1 represents the Quaternary sediments covering area.

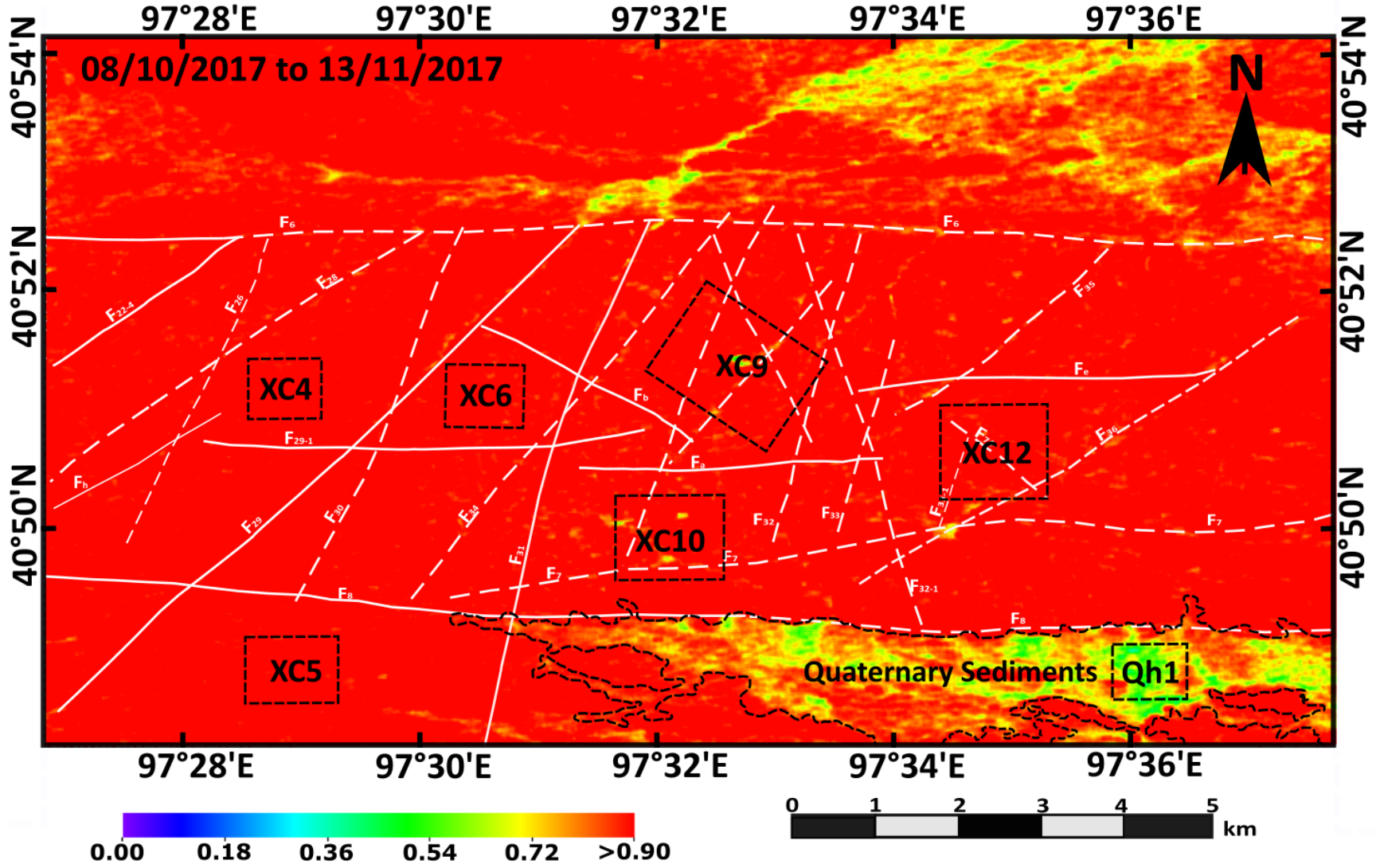


Figure 5.13 (A). The spatial variations of Sentinel-1 (ascending) coherence at time periods in Xinchang study area between 08/10/2017 to 13/11/2017 。

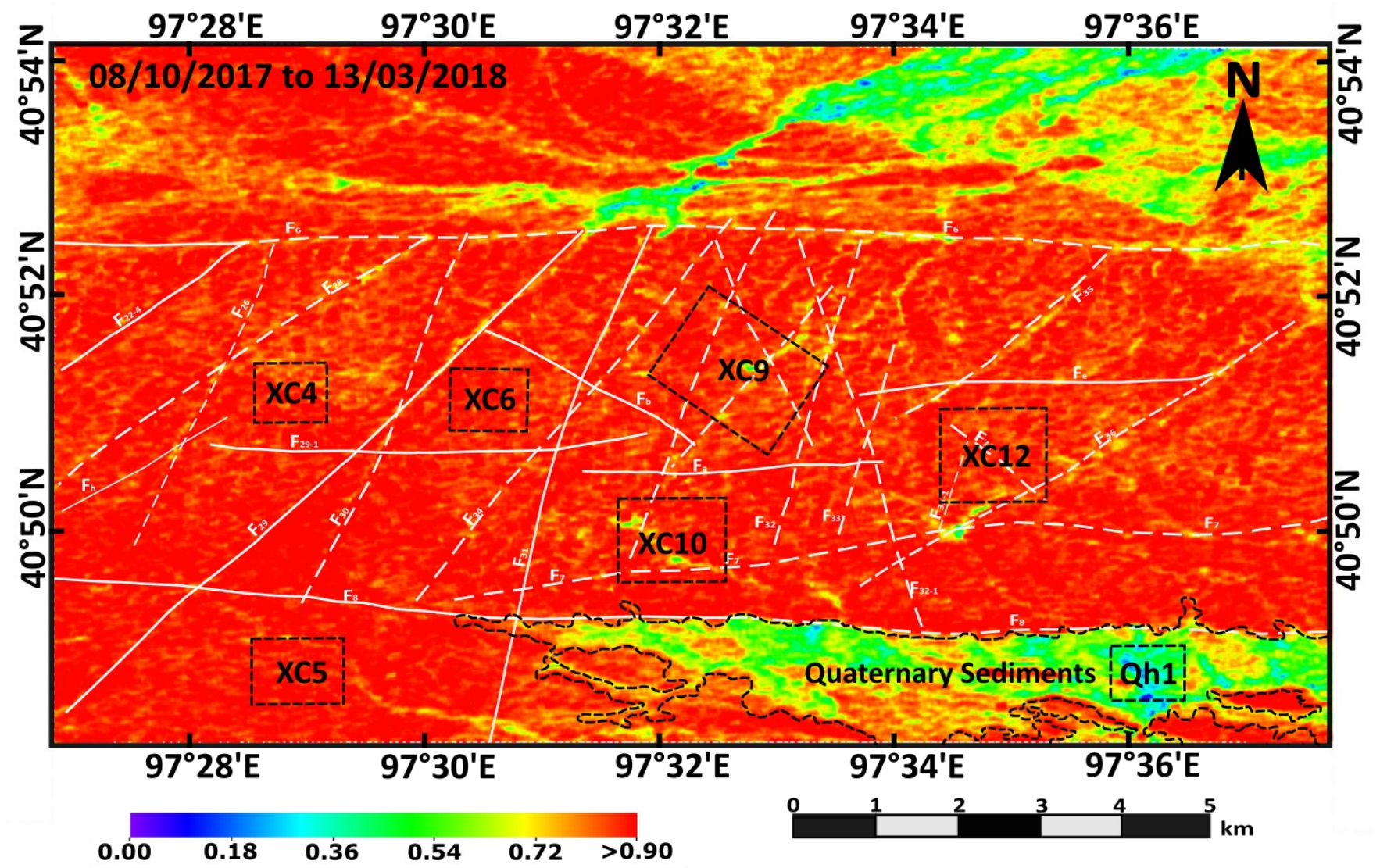


Figure 5.13 (B). The spatial variations of Sentinel-1 (ascending) coherence at time periods in Xinchang study area between 08/10/2017 to 13/03/2018

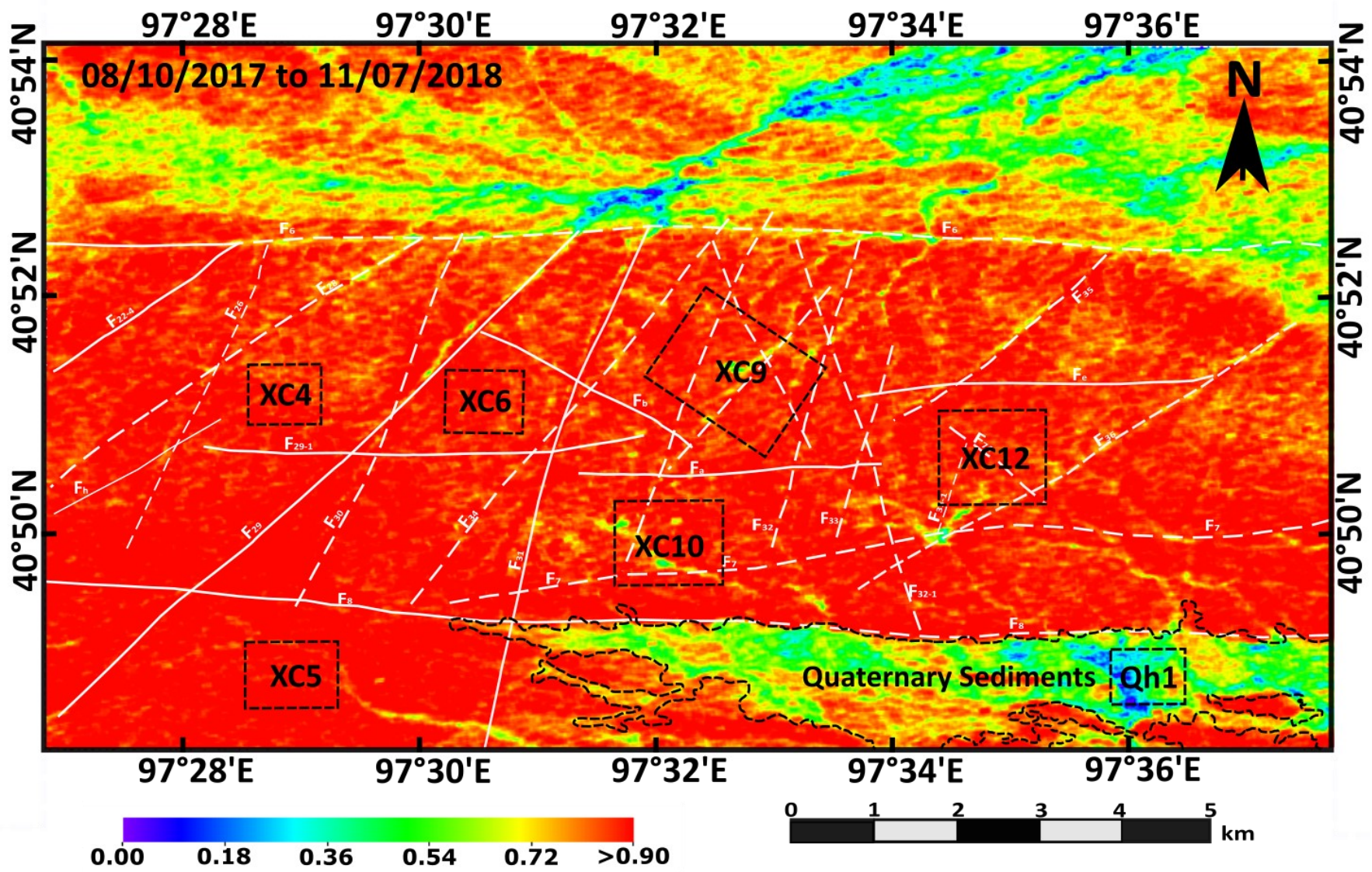


Figure 5.13 (C). The spatial variations of Sentinel-1 (ascending) coherence at time periods in Xinchang study area between 08/10/2017 to 11/07/2018

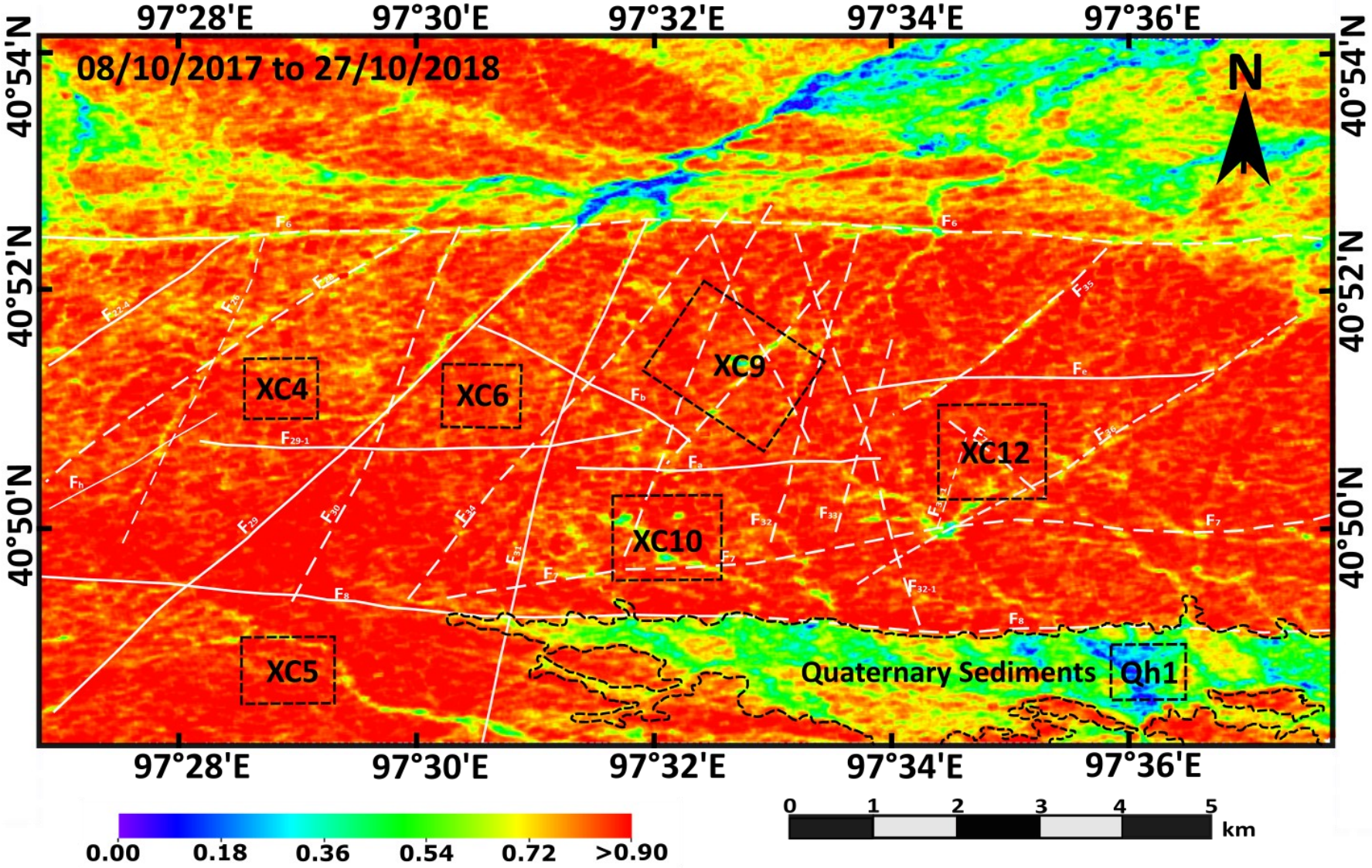


Figure 5.13 (D). The spatial variations of Sentinel-1 (ascending) coherence at time periods in Xinchang study area between 08/10/2017 to 27/10/2018

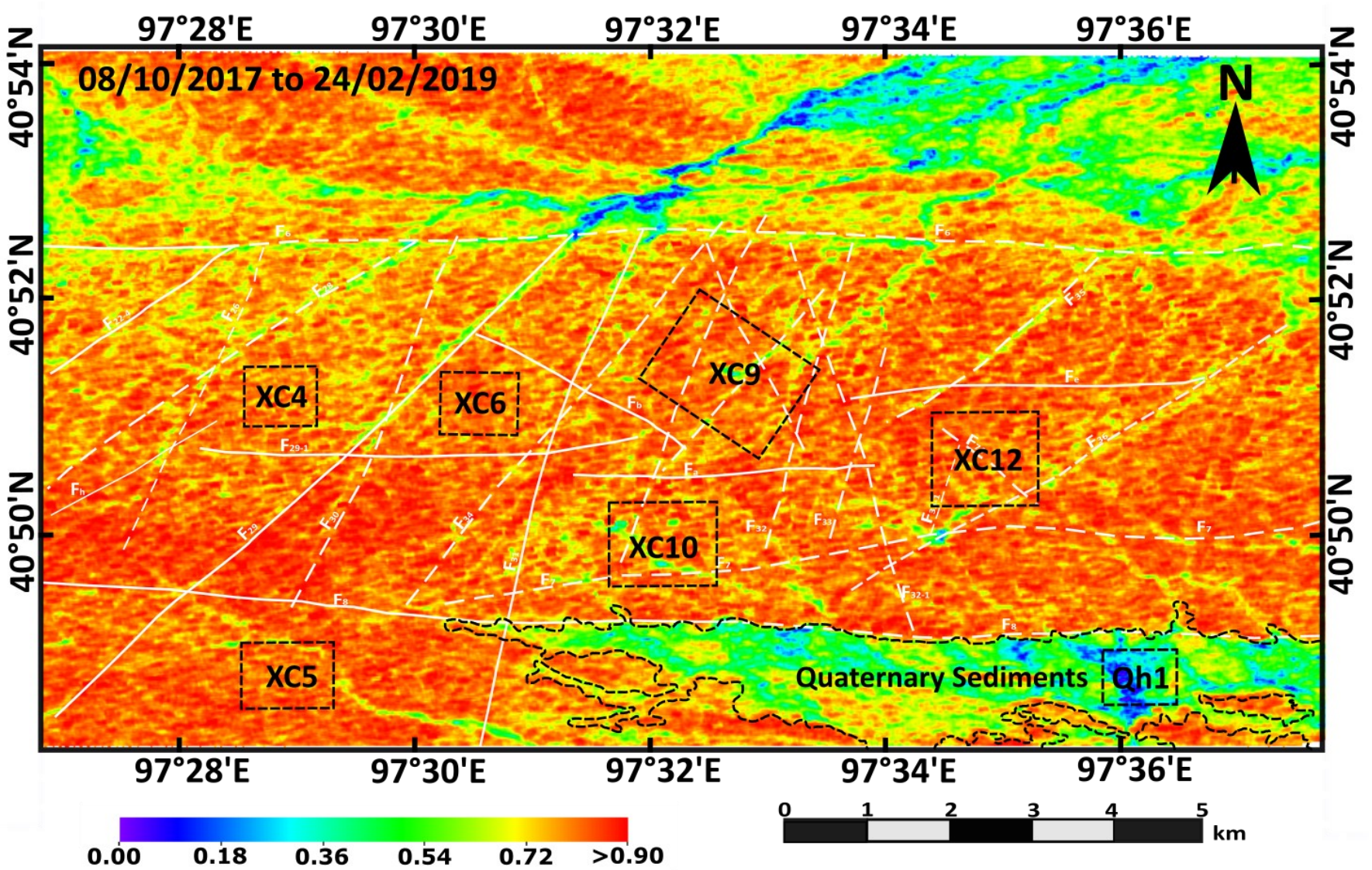


Figure 5.13 (E). The spatial variations of Sentinel-1 (ascending) coherence at time periods in Xinchang study area between 08/10/2017 to 24/02/2019

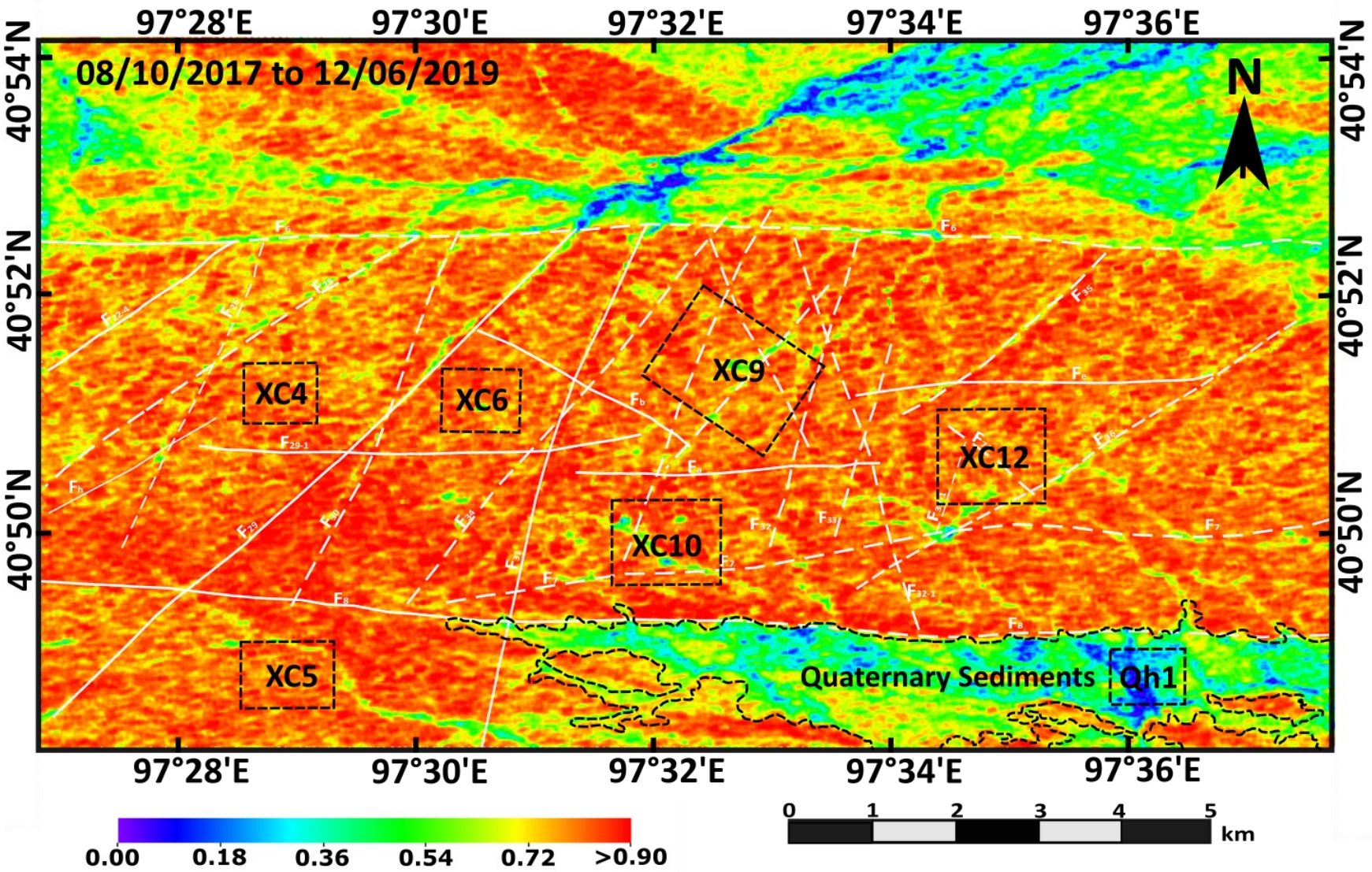


Figure 5.13 (F). The spatial variations of Sentinel-1 (ascending) coherence at time periods in Xinchang study area between 08/10/2017 to 12/06/2019.

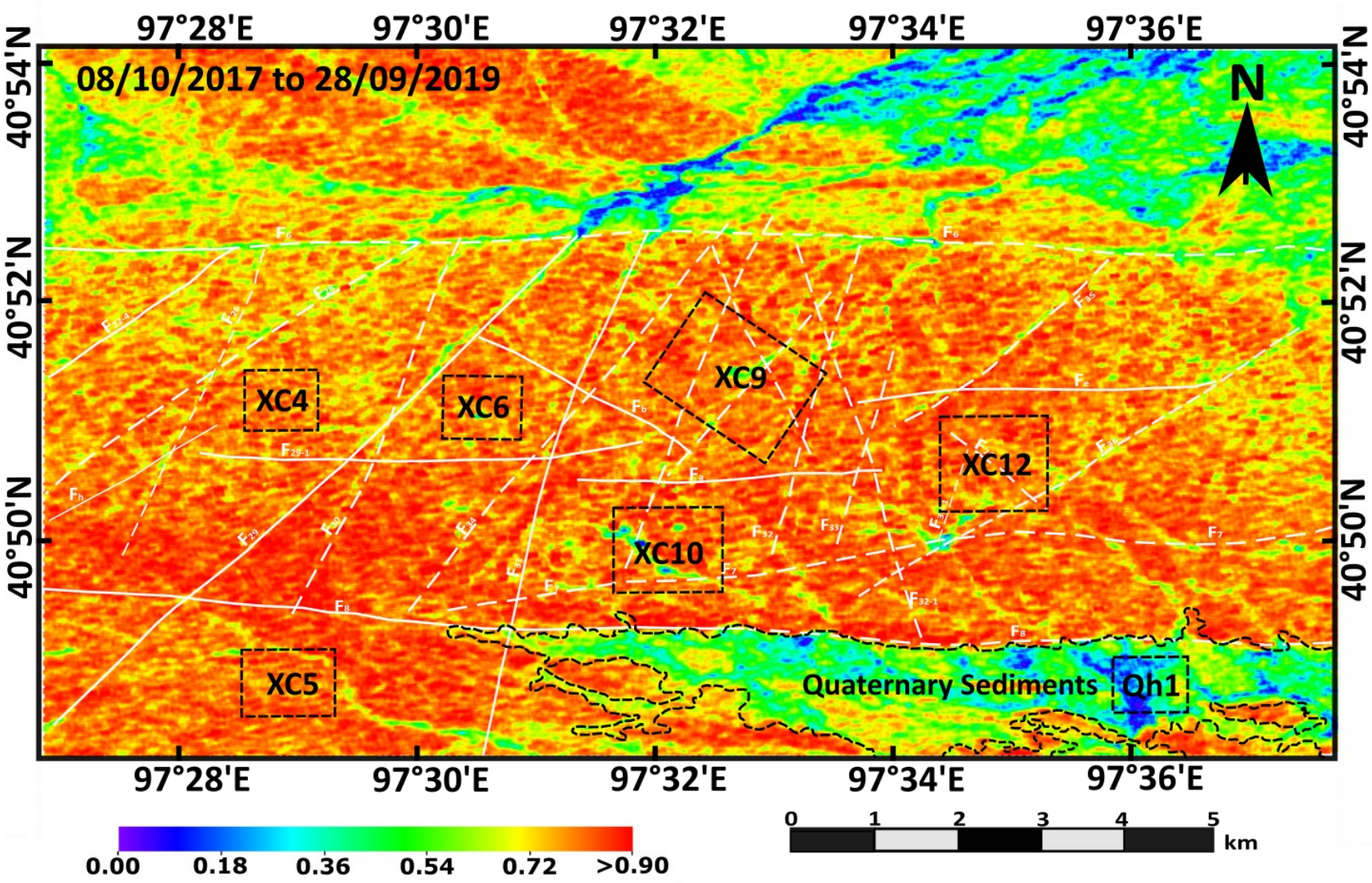


Figure 5.13 (G). The spatial variations of Sentinel-1 (ascending) coherence at time periods in Xinchang study area between (G) 08/10/2017 to 28/09/2019

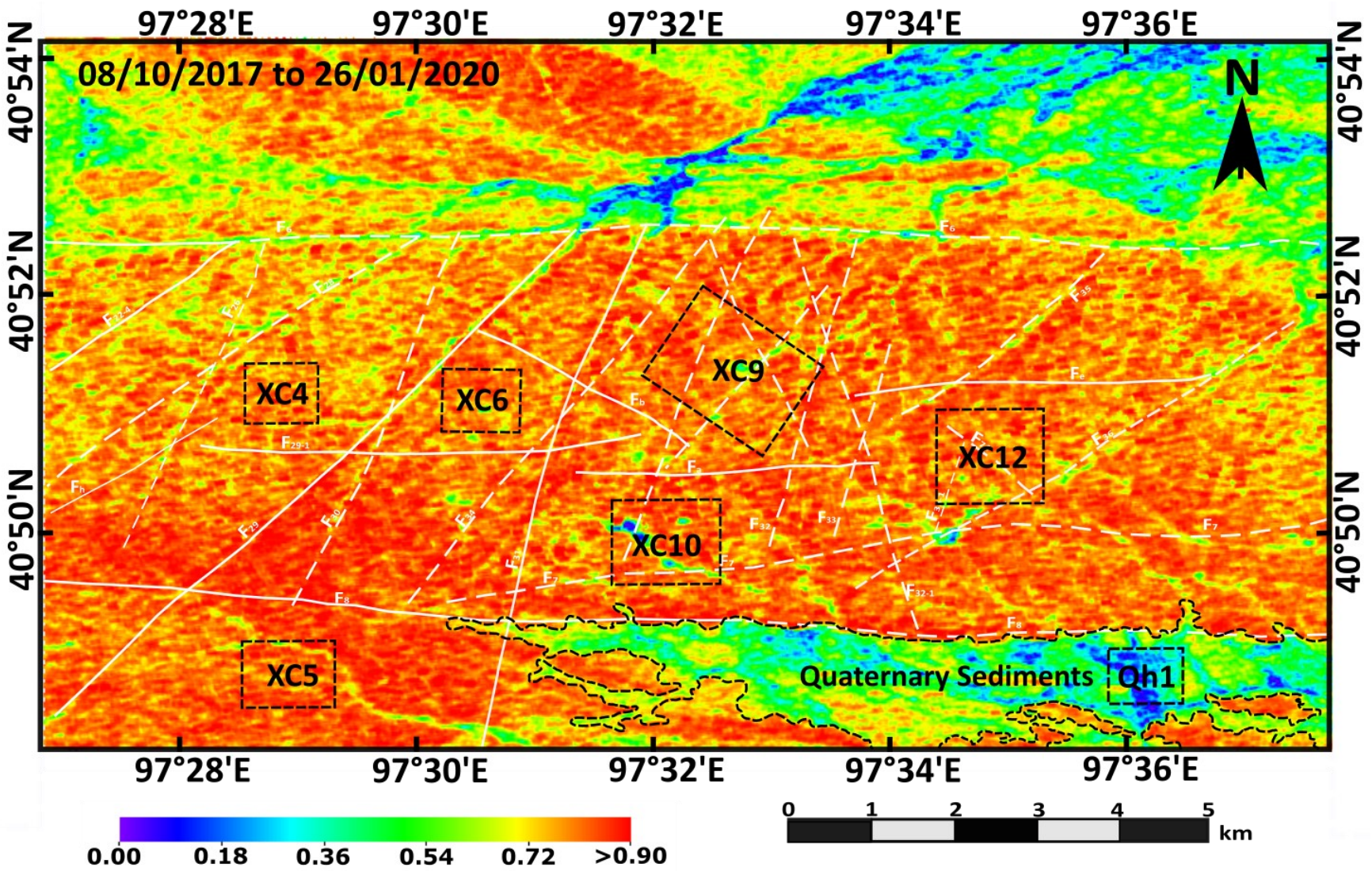
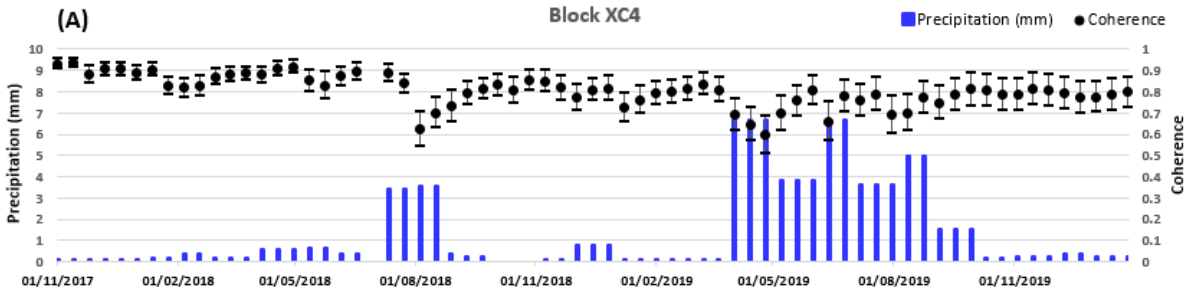
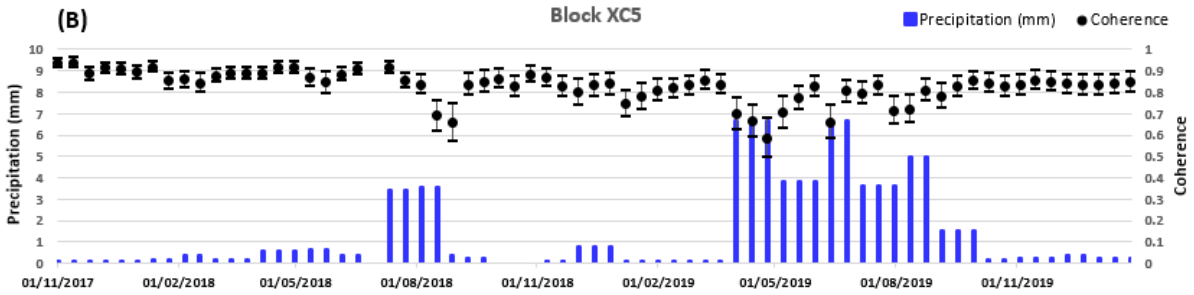
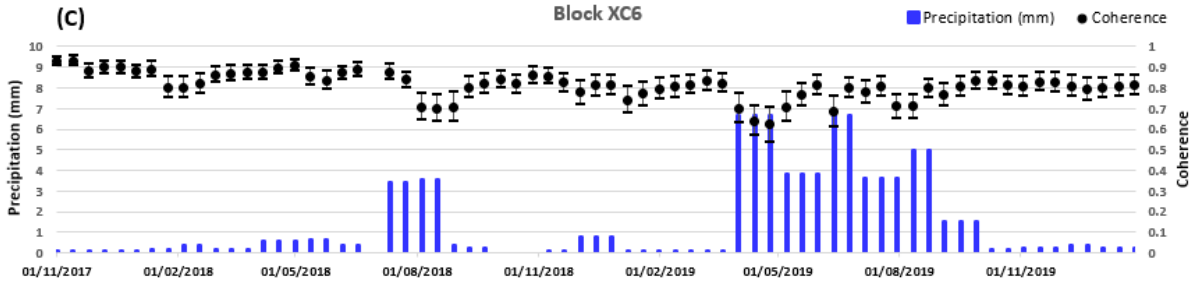
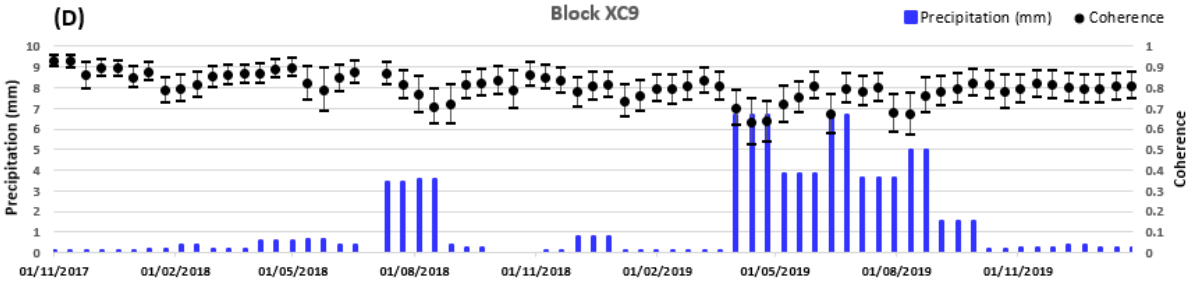


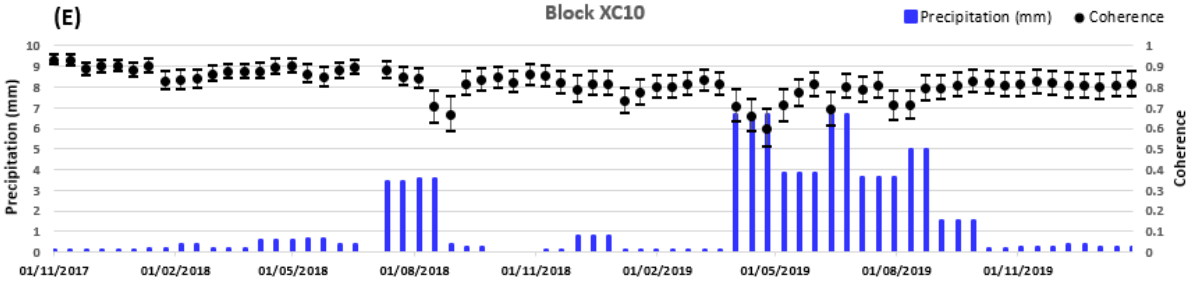
Figure 5.13 (H). The spatial variations of Sentinel-1 (ascending) coherence at time periods in Xinchang study area between 08/10/2017 to 26/01/2020.


(A)
Block XC4
Precipitation (mm)
Coherence
Precipitation (mm)
Coherence
01/11/2017
01/02/2018
01/05/2018
01/08/2018
01/11/2018
01/02/2019
01/05/2019
01/08/2019
01/11/2019


(B)
Block XC5
Precipitation (mm)
Coherence
Precipitation (mm)
Coherence
01/11/2017
01/02/2018
01/05/2018
01/08/2018
01/11/2018
01/02/2019
01/05/2019
01/08/2019
01/11/2019


(C)
Block XC6
Precipitation (mm)
Coherence
Precipitation (mm)
Coherence
01/11/2017
01/02/2018
01/05/2018
01/08/2018
01/11/2018
01/02/2019
01/05/2019
01/08/2019
01/11/2019


(D)
Block XC9
Precipitation (mm)
Coherence
Precipitation (mm)
Coherence
01/11/2017
01/02/2018
01/05/2018
01/08/2018
01/11/2018
01/02/2019
01/05/2019
01/08/2019
01/11/2019


(E)
Block XC10
Precipitation (mm)
Coherence
Precipitation (mm)
Coherence
01/11/2017
01/02/2018
01/05/2018
01/08/2018
01/11/2018
01/02/2019
01/05/2019
01/08/2019
01/11/2019

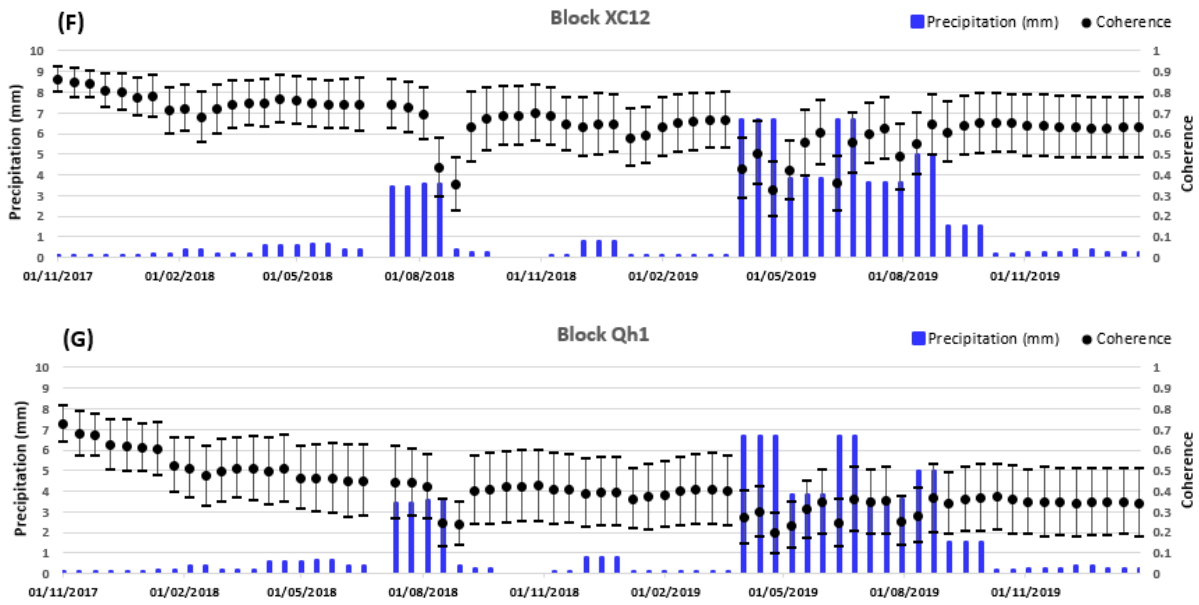


Figure 5.5 (A) to (G). The temporal variation of coherence in relation to precipitation at Block XC4, XC5, XC6, XC9, XC10, XC12 and Qh1 (location shown in Figure 5.3 and Figure 5.13) between 08/10/2017 to 26/01/2020 in Xinchang region, where Block XC4, XC5, XC6, XC9, XC10, XC12 represent the granite exposing area and Block Qh1 represents the Holocene sediments covering area.

5.6 The feasibility of geomorphological rates measurements using PSI method

Traditionally, the impact of geomorphological processes such as erosion and deposition are regarded as data noise in PSI method and are assumed to be removed automatically by default during the processes of PS candidate selection. That is because the PSI selects scatterers based on their stability. The scatterers impacted by geomorphological processes are likely to be destabilized and therefore should be excluded from the process of PS candidate selection due to their low coherence and high dispersion.

The threshold coherence is a trade-off between detection probability (scatterer density) and data noise [82], where a low noise rate correlates to low scatter density. To balance these two and guarantee a low data noise and a proper PS density, the most accepted threshold coherence from previous studies is usually 0.65 to 0.75 (with 0.75 used in this study). However, it is not clear that even this high threshold coherence can remove all geomorphologically-induced displacements by deselecting all geomorphological impacted scatterers. This research shows that the measurement of erosional rate using PSI is feasible even with a threshold coherence of 0.75, as explained below.

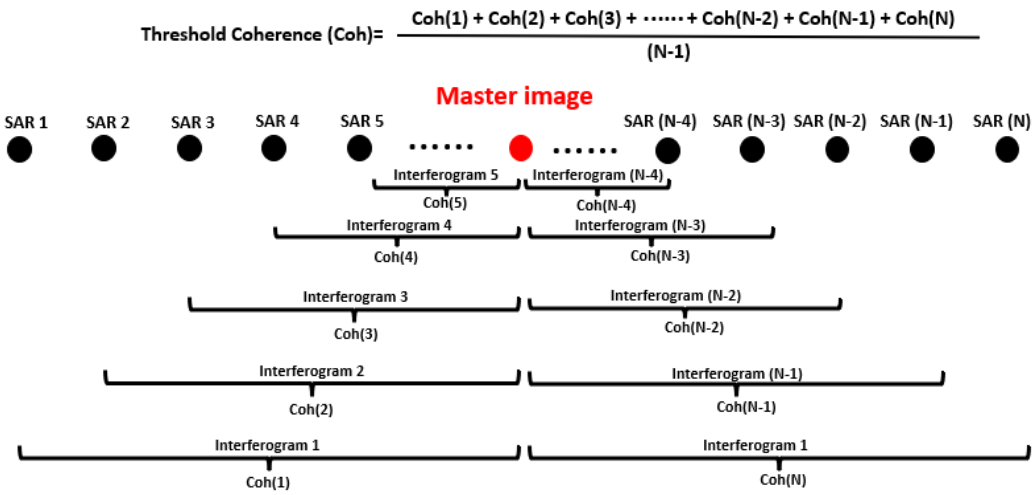


Figure 5.15 The schematic figure illustrates the generation of interferograms and the calculation of threshold coherence within PSInSAR.

Chapter 4 (Methodology) shows that the threshold coherence is an ensemble phase coherence calculated by averaging the coherence of each individual interferogram. The interferogram is formed through the comparison of two radar images, the Master (Reference) acquisition and the Slave (Secondary) acquisition (Figure 5.15). The coherence of each interferogram is controlled by the time interval between the Master and Slave SAR images. Usually, a longer time interval leads to a lower coherence due to more significant geomorphological surface change. The time interval for this study is 2 to 3 years, with 72 descending SAR images from 11 March 2017 to 31 January 2020 and 69 ascending SAR images from 08 October 2017 to 07 February 2020. The minimum time interval between two SAR acquisitions is 12 days, and the longest is up to 3 years, depending on the choice of Master image. In this research, the Master images on 02/09/2018 from descending view and 12/02/2019 from ascending view are chosen.

In the circumstance that geomorphological processes such as aeolian erosion are continuously but only slightly changing the surface, it is possible to generate an interferogram with coherence above the chosen threshold value (0.65 to 0.75), especially so for shorter time interval observations. Figure 5.17 shows that the threshold coherence is calculated by means of a series of individual (short time interval) interferogram coherence estimates, leading to a high coherence. Collectively, these then allow for the monitoring of slow geomorphological processes using PSI.

5.7 Discussion

To compare the coherence at Suanjingzi, Jiujing and Xinchang where the granite is exposed (Tables 5.4, 5.6 and 5.7) during the monitoring period of 08/10/2017 to 26/01/2020, it was found the Xinchang granite has the highest coherence, followed by Jiujing granite and lastly Suanjingzi granodiorite. In

general, more than 95% pixels at Jiujing and Xinchang granite blocks have coherence above 0.7, while this percent at Suanjingzi was only around 70% to 85%. 58% to 85% of pixels at Xinchang granite blocks have a coherence above 0.8, and this percentage at Jiujing granite blocks is around 45% and below 35% at Suanjingzi granite. This research believes this might be due to Suanjingzi granodiorite is more fractured than granites at Jiujing and Xinchang. The fractures could accumulate the sediments, which becomes saturated and susceptible to erosion. This further decreases the coherence. However, this requires further investigations to confirm.

5.8 Conclusion

This Chapter has successfully identified the geomorphologically induced deformation within three study areas (Suanjingzi, Jiujing and Xinchang) are mainly distributed over the Quaternary sediments covering areas through the application of coherence. The displacements are generally in the range of -0.4 to 0.4 mma^{-1} among three study areas. The impacts of groundwater on surface displacements in Beishan are too slight to be ignored. These results hint the InSAR deformation over granite outcrop areas might be dominantly driven by the tectonic movements. This hypothesis can be confirmed in next chapter (Chapter 6) by finding the geometrical correlation between fault planes and InSAR deformation pattern based on the methods introduced in Chapter 3.

The geomorphological processes are interpreted as impacting the Quaternary sediments covering area significantly. These led to high deformation rates over these areas and involved contributions of both aeolian processes and fluvial processes. In general:

(1) The granite/granodiorite areas are characterized by high coherence of greater than 0.7 and retain 70% to 95% pixels over the monitoring period 08/10/2017 to 26/01/2020. This reflects the very limited change to surface scatterers and suggests the observed InSAR deformations are reliable to reflect the real surface LoS distance change and they are likely related to tectonic activity (which will be confirmed in Chapter 6).

(2) The Quaternary sediments areas are characterized by low coherence, less than 20% of pixels have coherence greater than 0.70. This reflects significant geomorphological processes both aeolian and fluvial and corresponds to deformation that may be erosional or depositional. Another maybe some ongoing tectonic activity. However, it was unable to separate the processes.

(3) The granodiorite at Suanjingzi had a lower overall coherence than Jiujing and Xinchang. This might because Suanjingzi granite is more fractured than Jiujing and Xinchang granite. The features are accumulated by sediments and therefore more susceptible to erosion.

In addition to the above conclusion, this chapter also demonstrates the feasibility of PSInSAR method in measuring slow erosional and depositional rates. The geomorphological impacts have traditionally considered as noise in PSInSAR measurements. Through careful analysis of the data, this research believes they can in fact be identified by forming interferograms with short time span. It is accepted that this is at the limits of the current Sentinel 1A and 1B technology, however new improved InSAR satellites currently in development should make this type of geomorphological regional micro scale analysis more feasible and common place.

This chapter determined the possible impacts of geomorphological processes on InSAR deformations. Based on this chapter's results, Chapter 6 will investigate the possible impacts of active faults on granite exposed areas in three study areas. This is achieved through mapping and characterizing the active faults based on the patterns and discontinuities in tectonically induced displacements. This will provide moderate guidance for the selection of HLW disposal sites.

6. Mapping and characterizing micro-displacements on active faults in granite outcrops areas under the context of geomechanics

6.1 Introduction

In Chapter 5 it was demonstrated that the geomorphologically induced deformations are largely distributed over the Quaternary sediments covering areas and could be identified in InSAR results using coherence, however this did not account for large scale regional ground deformation over granite outcrop areas due to the high coherence. In this way, it was concluded that the tectonic movements are very likely responsible for these ground movements in granite outcrop areas within Suanjingzi, Jiujing and Xinchang. This chapter will confirm this hypothesis by finding the spatial correlation between InSAR deformation discontinuities and fault planes.

Having established that the geomorphological processes can be identified in the PSI results but do not account for all the displacements observed, the PSI results in the chapter are compared to the underlying geology. This has been done to determine whether on-going micro-displacement ground movements observed in the PSI can be applied to any geological features such as faults.

This is an area of focus for a GDF in China and as shown in chapter 2 the structural geology of the region is considered to be relatively stable, but as the PSI results could not be explained by the geomorphology the next step was to critically challenge the view of a tectonically stable region and investigate any potential fault movements in the region. To investigate faulting using PSI this chapter will first introduce the theory of fault kinematics offering a wrench fault zone concept for Beishan in Section 6.2. This section aims to explain the possible shearing properties (in both dip-slipped and strike slipped directions) that fault is expected to behave in relation to its striking direction and established NE-SW oriented regional compression as discussed in Chapter 2. This supports the interpretation of SAR displacement rate patterns (D_U and D_E) and improves the understanding of the formation of recent structural features in study areas. Based on the theory introduced in Section 6.2, the Section 6.3, 6.4 and 6.5 investigate whether, mapped faults can be characterized and whether the faults are still active in the Suanjingzi, Jiujing and Xinchang study areas. In addition, this chapter will investigate where any previously unknown structures can be recognized and quantified. This will be achieved from InSAR deformation patterns using the methods introduced in Chapter 4, Section 4.5, 4.6, and 4.7. This chapter aims to enhances the understanding of regional tectonic regimes and the stress mechanisms behind them. As the InSAR displacements rates over Quaternary sediments covering areas are significantly impacted by the geomorphological processes (concluded in Chapter 5), the

active faults mapping and characterizing in this research will avoid these low coherence areas and focus on the granite outcrop areas which are characterized by high coherence.

6.2 The theory of kinematics

In the Beishan Region the current literature has identified a number of faults along with current stress fields, however no regional conceptual model has been produced to explain the faulting observed within the context of the regional tectonic regime. This section explores the possible fault shearing behaviour under the current compressional tectonic environment in Beishan because if the potential fault movements are understood this could potentially support interpretation of the InSAR results (Section 6.3, 6.4, and 6.5). The literature review in Chapter 2 indicates Beishan lies in a convergent wrench zone [13, 49], which is a term referring to a high angle strike-slip fault of great linear extent, formed in response to horizontal pure shear [29]. Such faults often occur in regional-scale basement rocks and are characterized by attributes such as evidence of lateral-slip movement, steep fault planes, and complex deformation zones of subsidiary faults. The collision between the Eurasian and Indian Plates along the Himalayan Mountain belt has resulted in prominent compressional wrench faulting in NW China, and thus in the Beishan area [225].

The literature review in Chapter 2 suggested the in-situ stress measurements implied that the orientation of the average maximum compressive stress (σ1) is NE-SW and a minimum horizontal compressive stress (or extension) (σ3) in NW-SE in Beishan, but is understood to vary with depth [34, 226]. According to Wilcox [29], this leads to a maximum compression in NE-SW and an extension in NW-SE.

The horizontal stress orientation is governed by the tectonic movements [48], with trends of maximum horizontal compression reflected in the displacement direction of the shifting granite regions. As introduced in Chapter 4, this allows a rough estimate of the northing displacement rates (D_N) based on available easting displacement rates (D_E). The combination of horizontal (D_N, D_E) and vertical (D_U) reflects the vertical (extension or compression) and horizontal (sinistral or dextral) shearing properties of the fault. This can arguably be controlled by the relative trending directions of fault planes and maximum horizontal compression (σ1). Further details will be discussed in Sections 6.2.1 and 6.2.2.

6.2.1 Dip-slip shearing

As illustrated in Figure 6.1 (A), the maximum horizontal compression (σ1) which triggers the crustal shortening (BB' in Figure 6.1 (A)) and leads to reverse faulting (mainly trending NW-SE and/or E-W).

Meanwhile, the extension or minimum horizontal compression (σ3) in the NW-SE direction, which is perpendicular to σ1, leads to elongation in the NW-SE direction (AA' in Figure 6.1 (A)). This can lead to the formation of NE-SW (and/or E-W) trending normal faults. In general, these explain the coexistence and superposition of compressional and extensional structures within study areas.

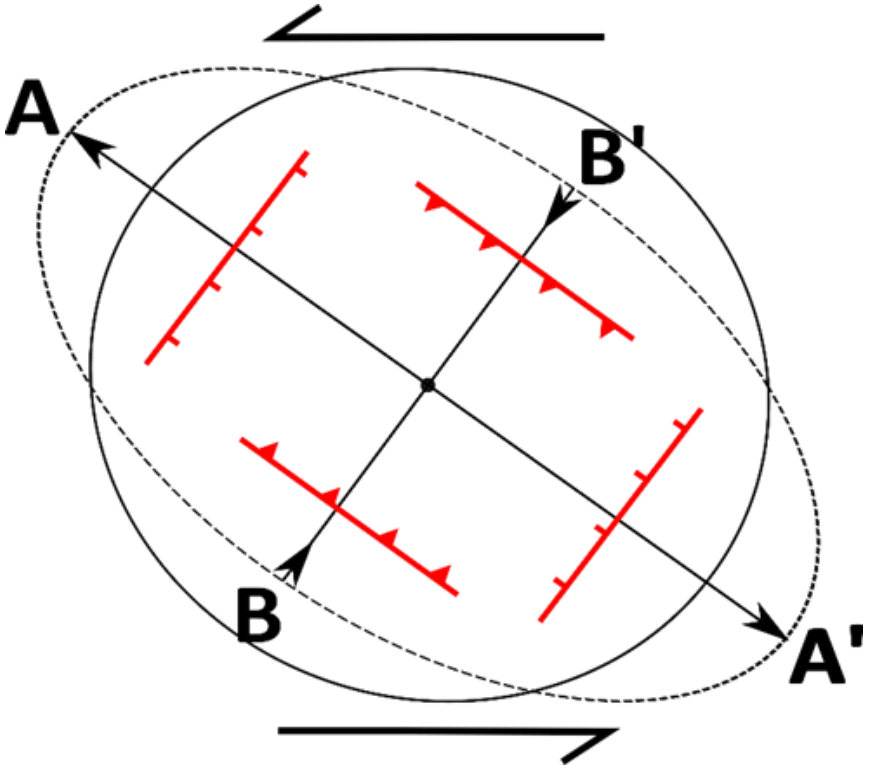


Figure 6.1 The schematic diagram illustrates the sinistral shearing of the Jiujing granite region due to the impacts of NE compression, where the long ellipse axis (AA') marks the direction of elongation and the short axis (BB') marks the direction of shortening. Adapted from Wilcox [29].

When the fault strike (θ) and the magnitude of maximum horizontal compression (σ1) remain constant, the fault vertical shearing property is believed to be controlled by the direction of σ1 (α). This has been illustrated in Figure 6.2, where Figure 6.2 (A, B and C) describes the situation when the fault is NW-SE trending, while Figure 6.2 (D, E and F) describes the situation when the fault is NE-SW trending.

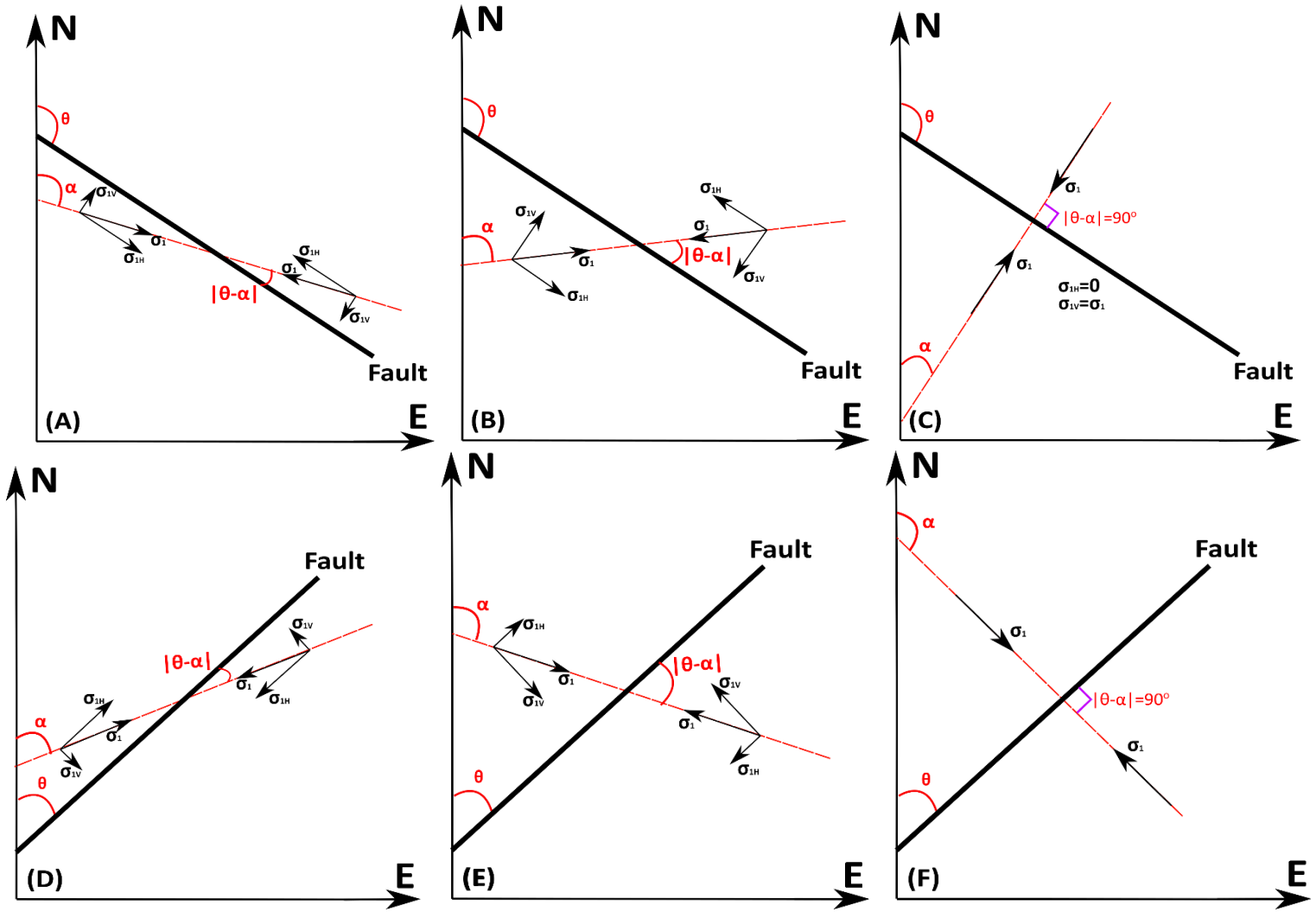


Figure 6.2 Schematic figures (A, B, C, D, E, and F) illustrating the correlation between maximum compression (σ1) and the vertical shearing properties along fault, where σ1 refers to the maximum horizontal compression, σ_{1H} and σ_{1V} refers to the two components of σ1 that are parallel and perpendicular to the fault plane respectively. D_H refers to the displacement in horizontal direction that is parallel to ground surface and D_E and D_N are two components of D_H in the east and north directions respectively.

In general, the maximum horizontal compression σ1 can be decomposed orthogonally as σ_{1H} and σ_{1V}, which refers to the pressure components that are parallel and perpendicular to the fault plane (Figure 6.2). This can be expressed as:

$$\boldsymbol{\sigma_{1H} = \cos(|\theta - \alpha|)\sigma_1} \quad \textbf{Eq. 6.1}$$

$$\boldsymbol{\sigma_{1V} = \sin(|\theta - \alpha|)\sigma_1} \quad \textbf{Eq. 6.2}$$

In this way, as shown in Figure 6.2 (A - C) and Figure 6.2 (D - F), the rotation of the σ1 axis along the fault plane increases the value of |θ-α|, leading to an increase in σ_{1V} and decrease in σ_{1H}. When |θ-α|tends to be 90°, σ_{1V} is maximized ($\sigma_1=\sigma_{1V}$), and the compressional effect towards the fault is maximized. This leads to crustal shortening and the formation of reverse faults. Conversely, when |θ-α| tends to be 0° or 180°, σ1 tends to be parallel with the fault plane ($\sigma_{1V}=0$ and $\sigma_1=\sigma_{1H}$), minimizing the compressive effects along the fault plane. This leads to the formation of a strike-slip fault and may generate some crustal elongation in the wrench fault zone.

6.2.2 Strike-slip shearing

The strike-slip shearing property of a fault is regulated by the relative trending directions of the maximum compression and fault. Based on Wilcox's theory [29] illustrated in Figure 6.3, the faults with a high angle to wrench strike (XX' in Figure 6.3) are classified as high angle faults or antithetic strike-slip faults (DD' in Figure 6.3), which are expected to shear dextrally due to NE compression. Meanwhile, the low angle faults (synthetic strike-slip faults, CC' in Figure 6.3) which are sub-parallel to wrench strikes and directly impacted by the sinistral straining tend to rotate anticlockwise, leading to prominent sinistral shearing properties.

The classification of high angle faults (antithetic strike-slip faults) and low angle faults (synthetic strike-slip faults) in Figure 6.3 is determined by the angle between fault and maximum stress direction. This is further illustrated in Figure 6.4 (A - E).

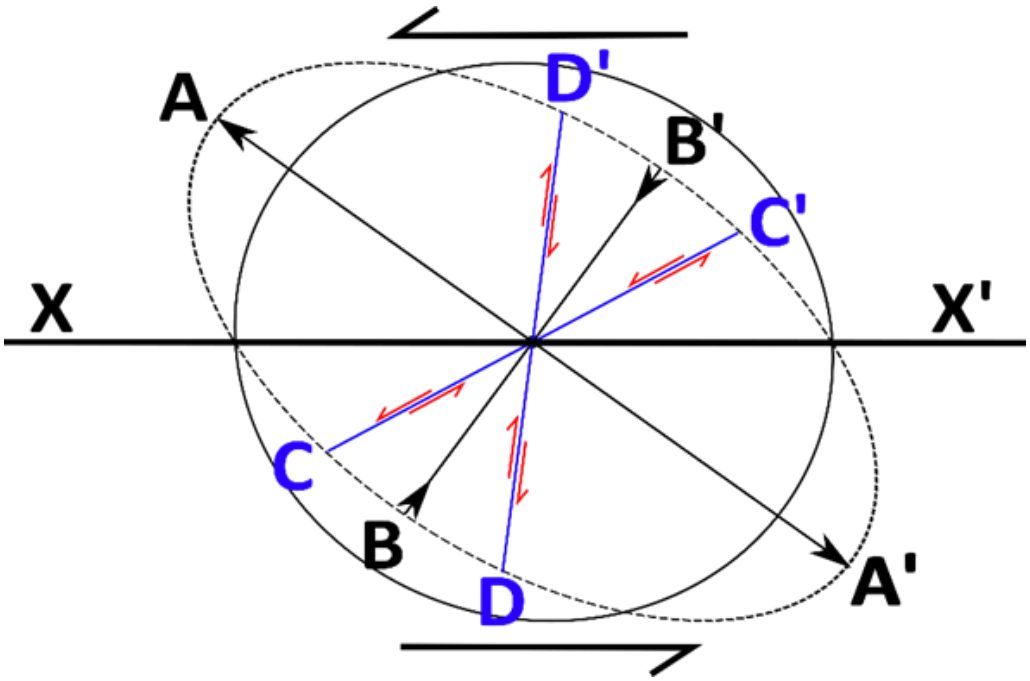


Figure 6.3 Schematic illustration of the shearing properties of high angle faults (antithetic strike-slip faults, marked by axis DD') and low angle faults (synthetic strike-slip faults, marked by axis CC') under the NE compression. Axis XX' refers to wrench strike. Adapted from Wilcox [29].

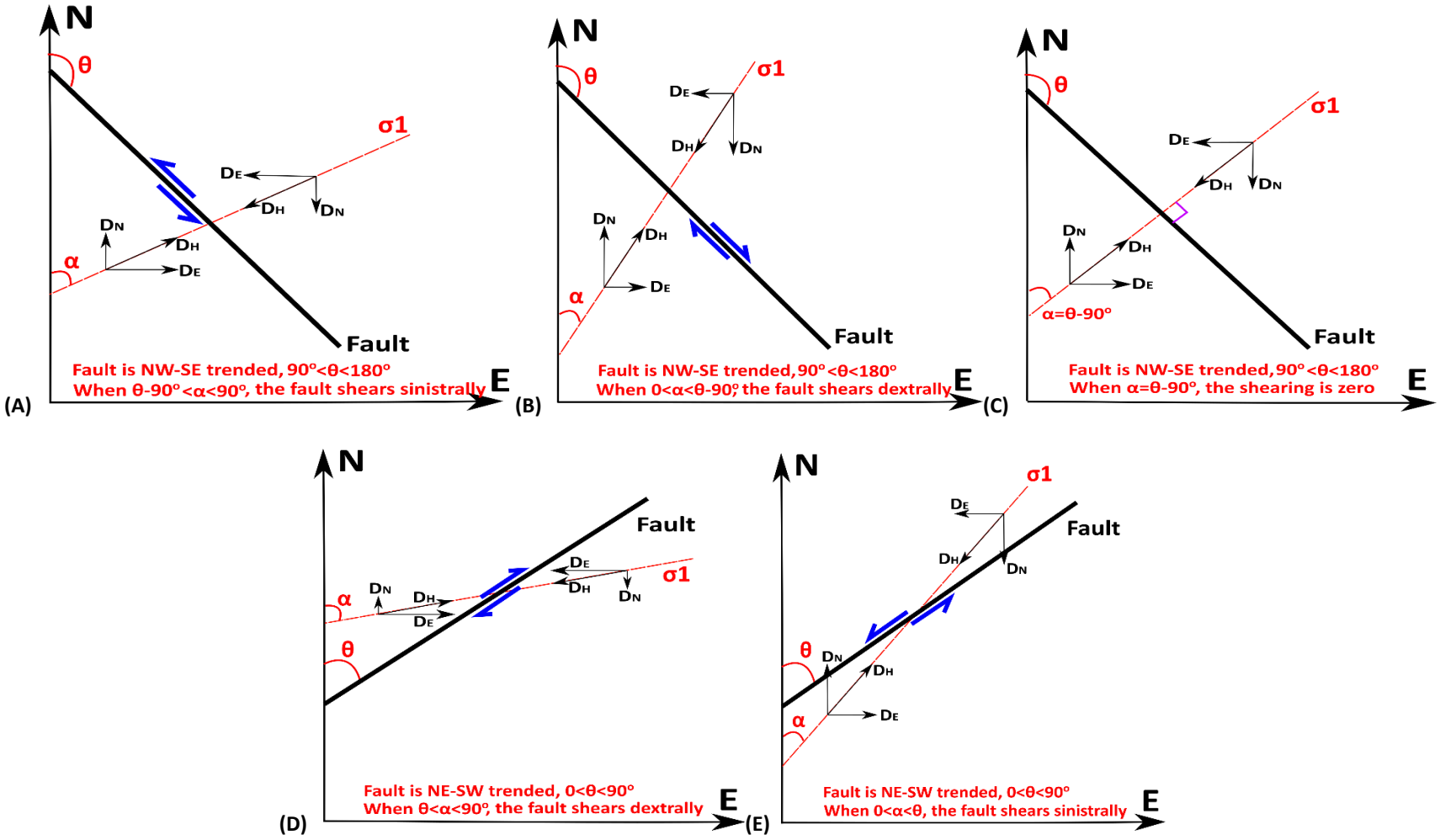


Figure 6.4 (A, B, C, D and E) Schematic illustration of the correlation between fault striking angle (θ), maximum compression direction (α) and horizontal shearing properties. D_H refers to the displacement in horizontal direction that is parallel to ground surface and D_E and D_N are two components of D_H in the east and north directions respectively.

The strike-slip shearing properties along a fault plane are arguably determined by the fault striking angle (θ) and maximum compression direction (α). Beishan is impacted by a NE-SW trended maximum compression, indicating that α is in the range between 0° to N90°E. Depending on the strike direction of the fault plane, as seen in Figure 6.4 (A to E), five situations need to be theoretically considered, it is assumed that the fault strike (θ) remains constant.

From Figure 6.4 it can be seen that there are three situations when the fault trends NW-SE ($90^o<\theta<180^o$):
(1) When σ1 is at a low angle ($\theta-90^o<\alpha<90^o$, as in Figure 6.4 (A)), D_H tends to push the two blocks sliding in an anti-clockwise direction along the fault plane, leading to the formation of sinistral shearing (Figure 6.4(A)).
(2) Conversely, when α is at a high angle ($0<\alpha<\theta-90^o$, as in Figure 6.4 (B)), the horizontal deformation (D_H) is dominated by D_N and tends to push the blocks sliding in a clockwise direction, leading to the formation of dextral shearing (Figure 6.4 (B)).
(3) When $\alpha=\theta-90^o$, σ1 tends to be perpendicular to the fault (Figure 6.4 (C)), the block will have relatively low horizontal deformation (D_H, D_N, and D_E) due to being impeded by the opposite block. This forms a reverse dip slip fault where the blocks have mostly shifted vertically (Figure 6.4 (C)).

There are two other conditions identified in Fig 6.4 when the fault trend is NE-SW ($0<\theta<90^o$):
(1) When σ1 is at a low angle ($\theta<\alpha<90^o$, as in Figure 6.4 (D)), D_H tends to push blocks sliding in a clockwise direction, which leads to the formation of dextral shearing (Figure 6.4 (D)).
(2) Conversely, when σ1 is at a high angle ($0<\alpha<\theta$), D_H tends to push blocks to rotate in an anticlockwise direction along the fault plan (Figure 6.4 (E)), which leads to the formation of sinistral shearing (Figure 6.4(E)).

In general, if σ1 remains constant, the strike-slip shearing rate is controlled by the relative direction of σ1 and fault (hence controlled by θ and α). When $|\theta-\alpha|$ tends to be 0 or 180°, σ1 tends to be parallel to the fault plane. This would generate the highest σ1H (the component of σ1 that is parallel to the fault plane) value, and subsequently lead to the highest horizontal shearing along the fault plane, and the fault would be strike-slip. This may lead to significant horizontal InSAR deformation discontinuities along the fault plane. When angle $|\theta-\alpha|$ equals to 90°, σ1 tends to be perpendicular to the fault plane and so the horizontal shearing rates would be minimized. The fault will be a pure reverse fault dominated by vertical deformation. This may lead to reverse dip slip fault with indistinct horizontal deformation discontinuities due to the low horizontal displacement offsets along the fault plane.

6.2.3 Summary of Kinematic Theory

In summary, the dip-slip and strike-slip shearing properties of the fault plane are controlled by the correlation between fault strike (θ) and σ1 direction (α). This is tenable under the assumption that the magnitude of σ1 remains constant. A decrease in |θ-α| would lead to a reduction in fault compression and an increase in fault horizontal shearing rates. This would cause the fault motion to be purely strike-slip when |θ-α|tends to be zero. In contrast, an increase in |θ-α|would lead to an increased compression and a decrease in fault horizontal shearing rates. This, in turn, would generate a purely reverse fault with no horizontal shearing when |θ-α|is 90°, as summarize in Figure 6.5. Adopting this kinematic theory is pertinent to support the characterization of fault active in the following Sections 6.3, 6.4 and 6.5.

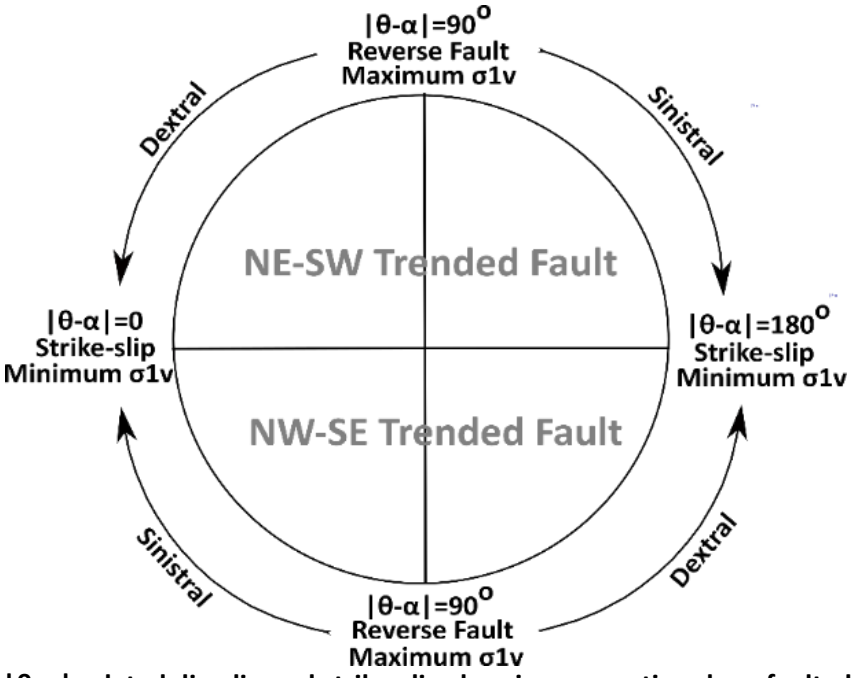


Figure 6.5 The |θ-α| related dip-slip and strike-slip shearing properties along fault plane.

6.3 Characterizing active faulting at Suanjingzi granodiorite outcrop

Based on the kinematic theories introduced in Section 6.2, this section aims to characterize the pattern of displacements in the Suanjingzi granite outcrop. Figure 6.6 (A), (B), (C), and (D) show the patterns of PSI displacement rates in LoS-ascending (D_{los}^{asc}), LoS descending (D_{los}^{des}), easting (D_E), and vertical (D_U) directions. The literature review in Section 2.6 presented the structural geology map in Suanjingzi (Figure 2.4) published by Jiang [51], which mapped 9 major faults on the Suanjingzi granodiorite outcrop and were marked as F_0 to F_8. Jiang [51] indicated these faults have remained inactive since early Quaternary because the Quaternary sediments which cover on the top of the fracture lines were not disturbed by fault activity. The locations of these faults are shown in Figure 6.6 (A) to (D), and their interpreted characteristics are presented in Table 6.1.

Table 6.1 The characteristics of active faults in Suanjingzi region

Fault No.	Activity	Dipping direction	Vertical shearing properties	Horizontal shearing properties
F_{0-1}	Active	Northwest	Reverse	--
F_{0-2}	Inactive	--	--	--
F_1	Active	Northeast	Reverse	Sinistral
F_2	Active	Northeast	Reverse	--
F_{3-1}	Active	North or south	Normal or reverse	Dextral
F_{3-2}	Inactive	--	--	--
F_4	Inactive	--	--	--
F_{5-1}	Active	Southeast	Reverse	Sinistral
F_{5-2}	Active	Southeast	Reverse	Sinistral
F_{5-3}	Inactive	--	--	--
F_6	Active	North	Reverse	--
F_7	Active	South	Normal	Dextral
F_8	Inactive	--	--	--
F_b	Active	Southeast	Normal	Sinistral
F_c	Active	Northeast	Reverse	--
F_d	Active	Southwest	Reverse	Sinistral
F_e	Active	Northwest	Normal	--
F_f	Active	North	Normal	Dextral
F_g	Active	South	Normal	--
F_h	Active	Southeast	Normal	Sinistral
F_i	Active	East	Reverse	--

Statistically, the displacement rate/frequency distribution curves are used to present the displacement rate difference between each block. These are presented in Figure 6.7 (A) to (D). The following sections will investigate the displacement around some of the faults and their adjacent blocks, describing their characteristics and evidence of ground movements, which provides evidence that faults that have previously been described as inactive are actually still active.

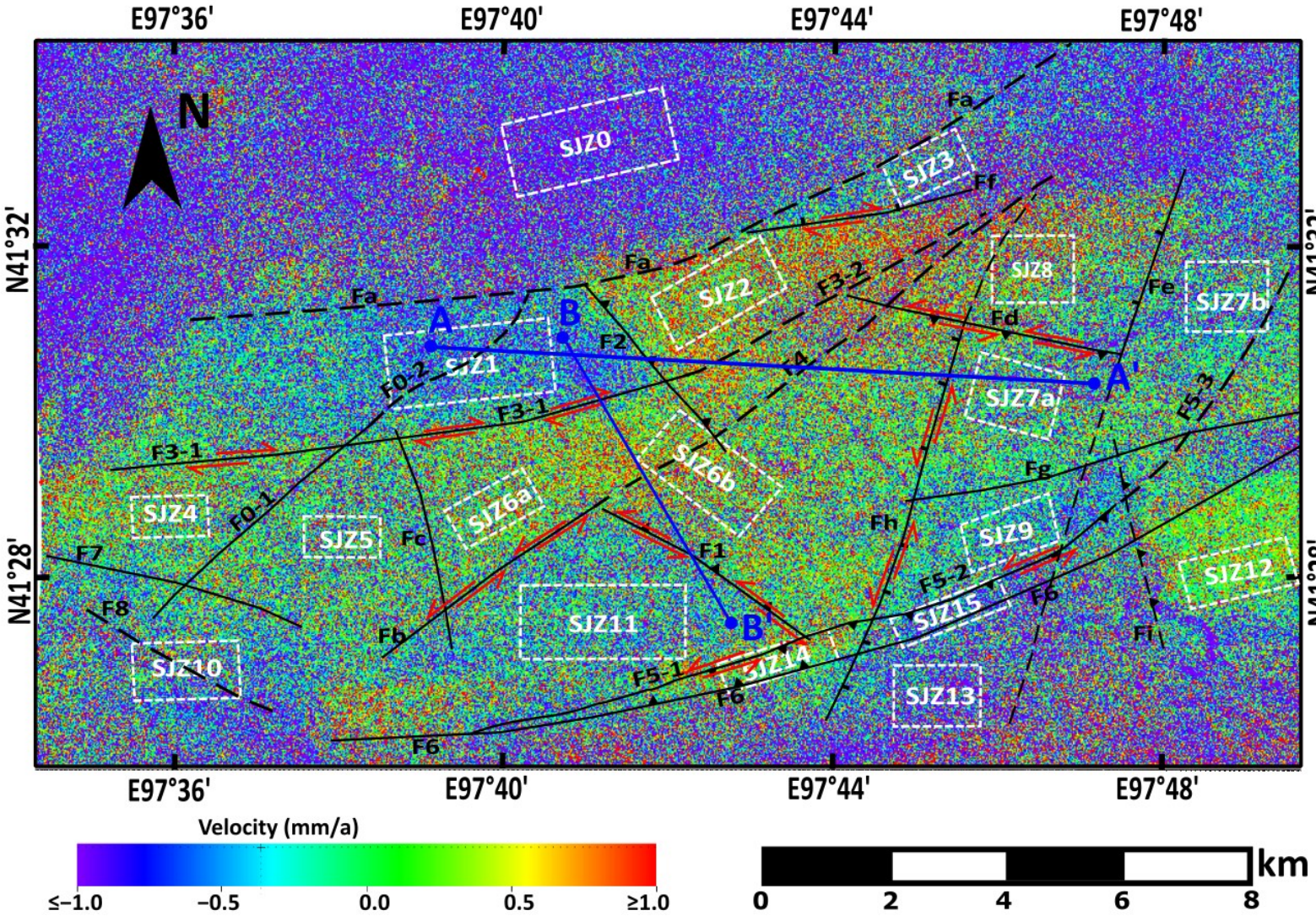


Figure 6.6 (A) The LoS displacement (D_{los}^{asc}) pattern of Suanjingzi region reprocessed from ascending Sentinel-1 data, where the positive values (upper, red side of colour axis) refer to the uplift and negative values (blue, lower side of colour axis) refers to subsidence. It illustrates the correlations between active faults and deformation patterns.

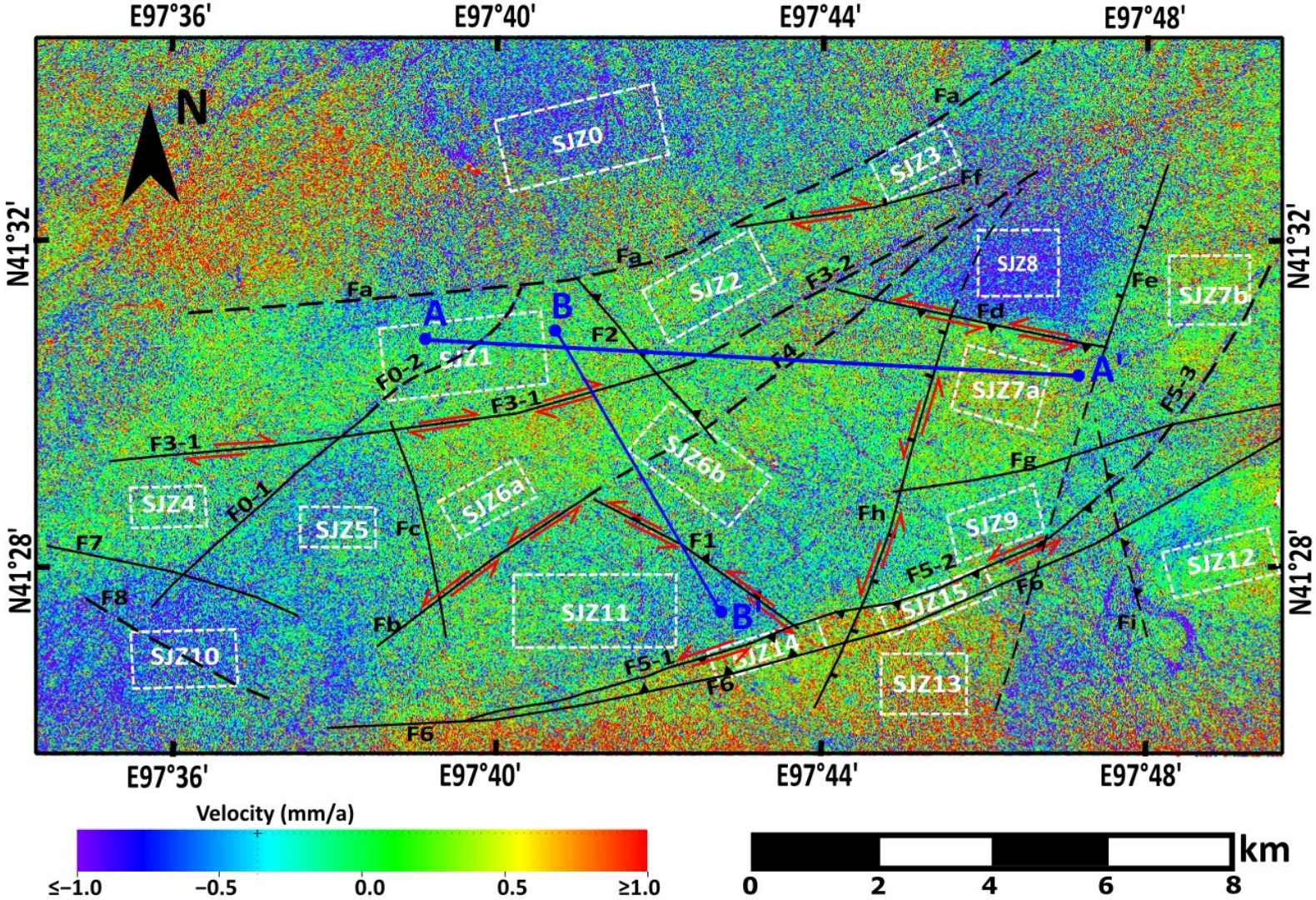


Figure 6.6(B) The LoS displacement (D_{los}^{des}) pattern of Suanjingzi region reprocessed from descending Sentinel-1 data, where the positive values (upper, red side of colour axis) refer to the uplift and negative values (blue, lower side of colour axis) refers to subsidence. It illustrates the correlations between active faults and deformation patterns.

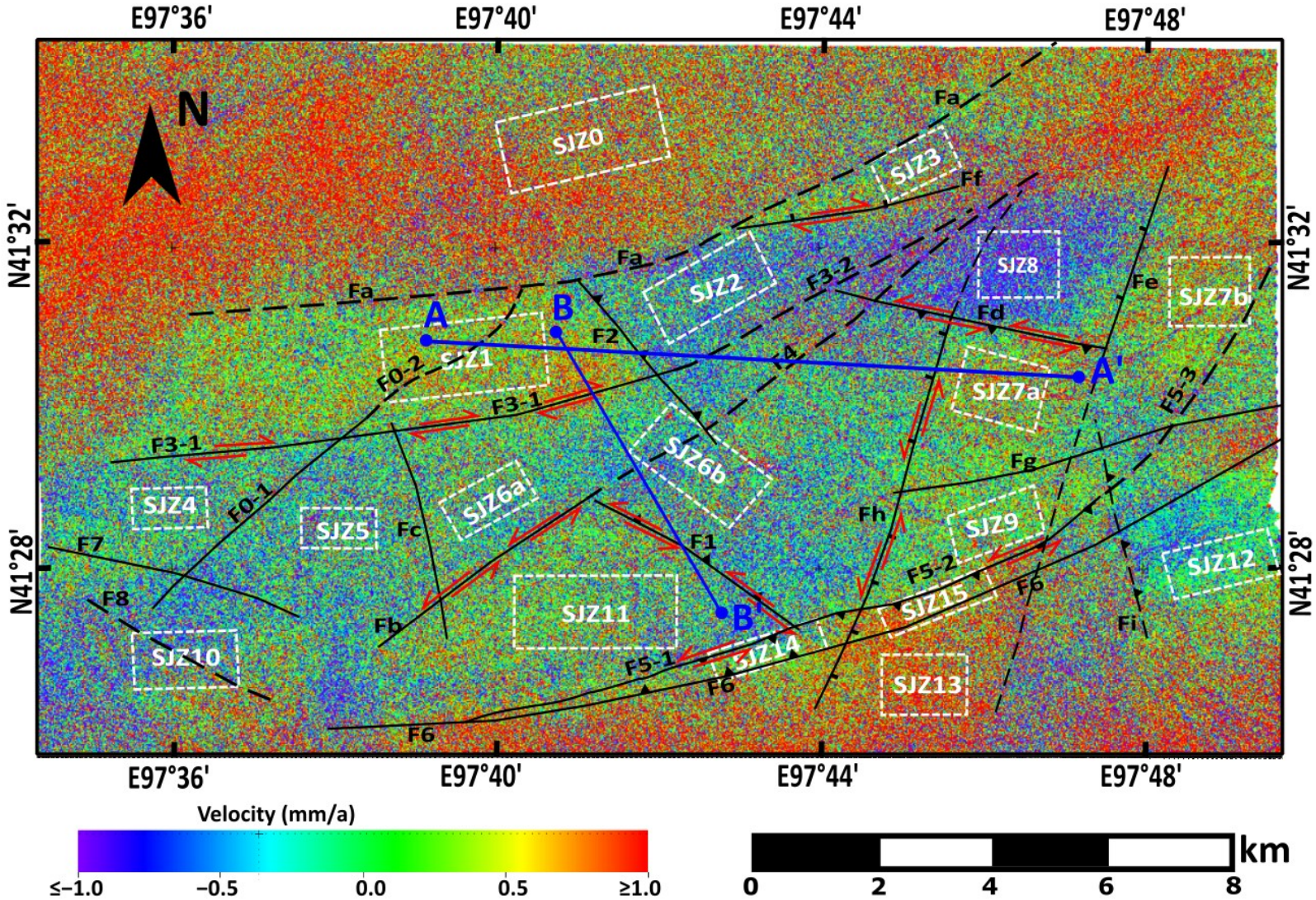


Figure 6.6(C) The pattern of horizontal displacement (D_E) in the Suanjingzi region computed through the combination of descending and ascending Sentinel-1 data based on the theory introduced in Section 4.3, where the positive values (red and yellow coloured) refer to eastward horizontal displacements and the negative values (blue coloured) refers to westward displacements. It illustrates the correlations between active faults and deformation patterns.

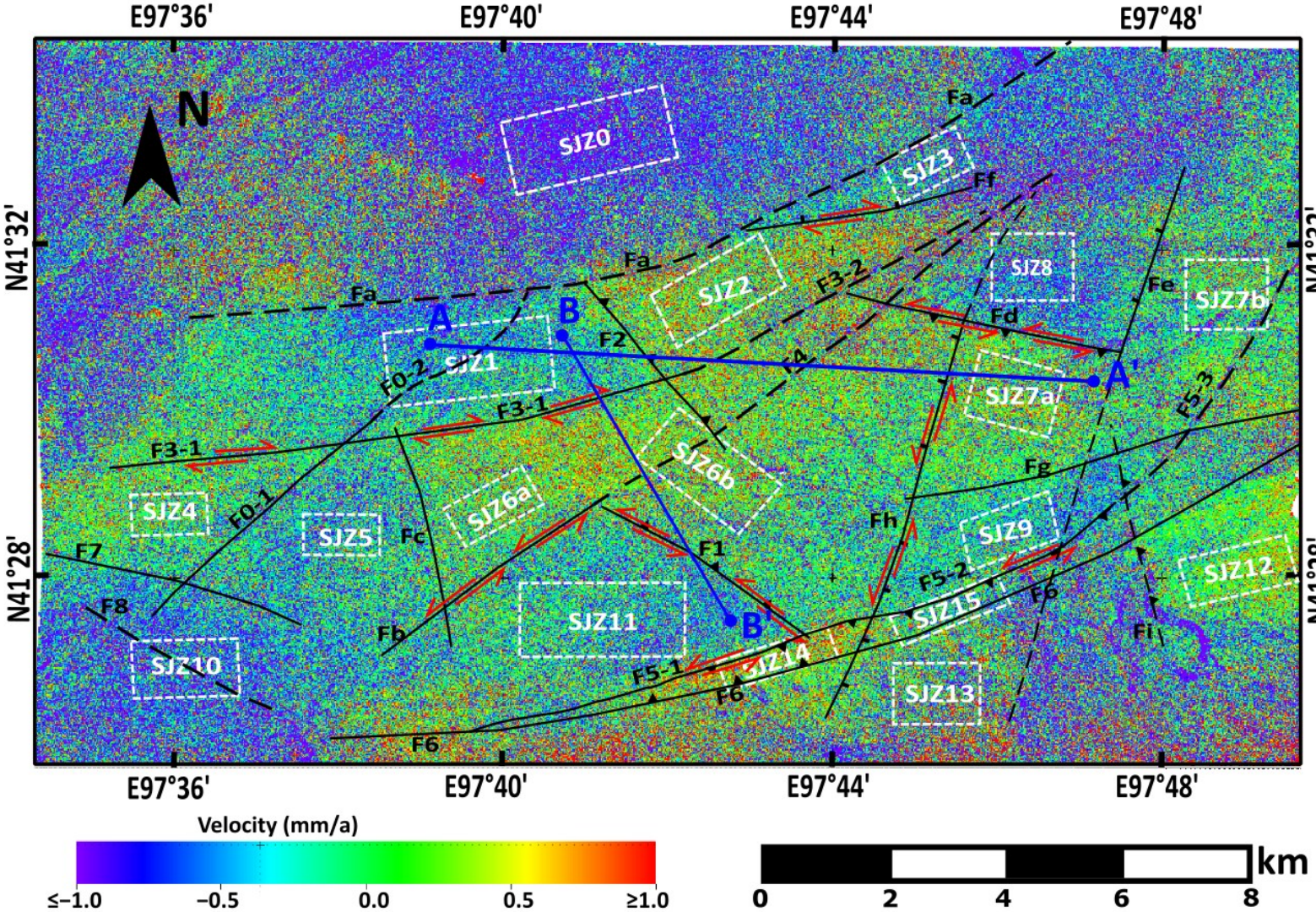


Figure 6.6(D) The pattern of vertical displacement (D_U) in the Suanjingzi region computed through the combination of descending and ascending Sentinel-1 data based on the theory introduced in Section 4.3, where the positive values (upper, red side of colour axis) refer to the uplift and negative values (blue, lower side of colour axis) refers to subsidence. It illustrates the correlations between active faults and deformation patterns.

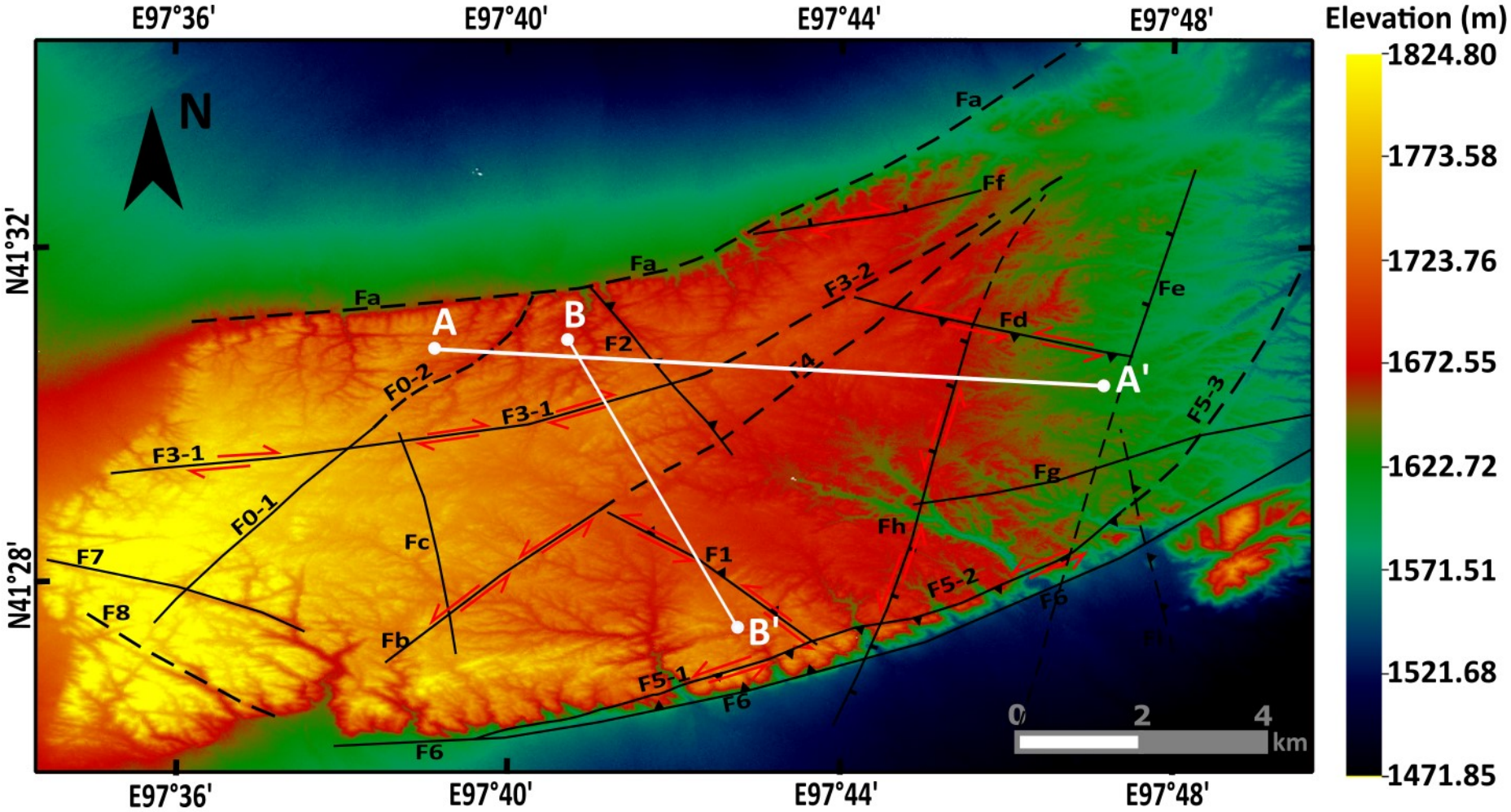


Figure 6.6 (E). The digital elevation model (DEM) across the Suanjingzi study area illustrates the spatial correlation between faults and the topography. The DEM is a third-party product provided by the NASA Shuttle Radar Topography Mission (SRTM). This provides a topographic representation of the earth surface. The solid line represents the on-going active faults and the dash line represent the recent inactive faults (or those whose activity cannot be sorely interpreted based on D_E and D_U deformation).

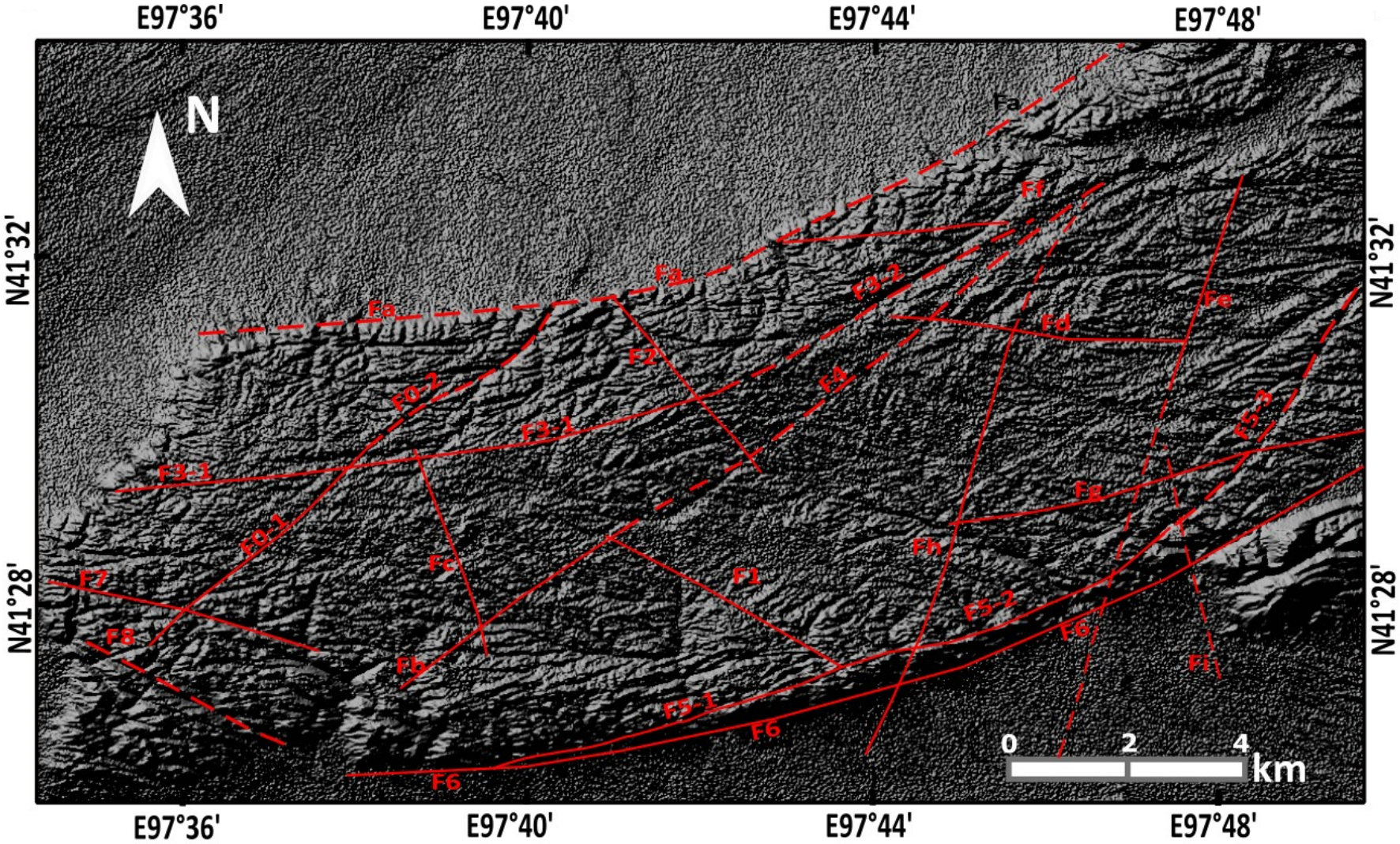


Figure 6.6 (F). The hill-shaded Digital Elevation Model map which overlays the location of active (solid lines) and inactive (dash lines) faults across the Suanjingzi study area. The figure is produced through the processing of DEM data in Figure 6.6 (E) using the QGIS Hillshade analysing tool.

Figure 6.6 (A) to (D) illustrate the correlations between fault traces and the PSI deformation patterns (D_{los}^{asc}, D_{los}^{des}, D_U, and D_E). These results demonstrate that the majority of faults are active (Table 6.1), not inactive as previous suggested by Jiang [51]. To better describe the deformation patterns, the Suanjingzi region has been divided into 18 blocks, labelled from SJZ0 to SJZ15 (Figure 6.6). The deformation rates had been presented at Table 5.1 in Chapter 5.

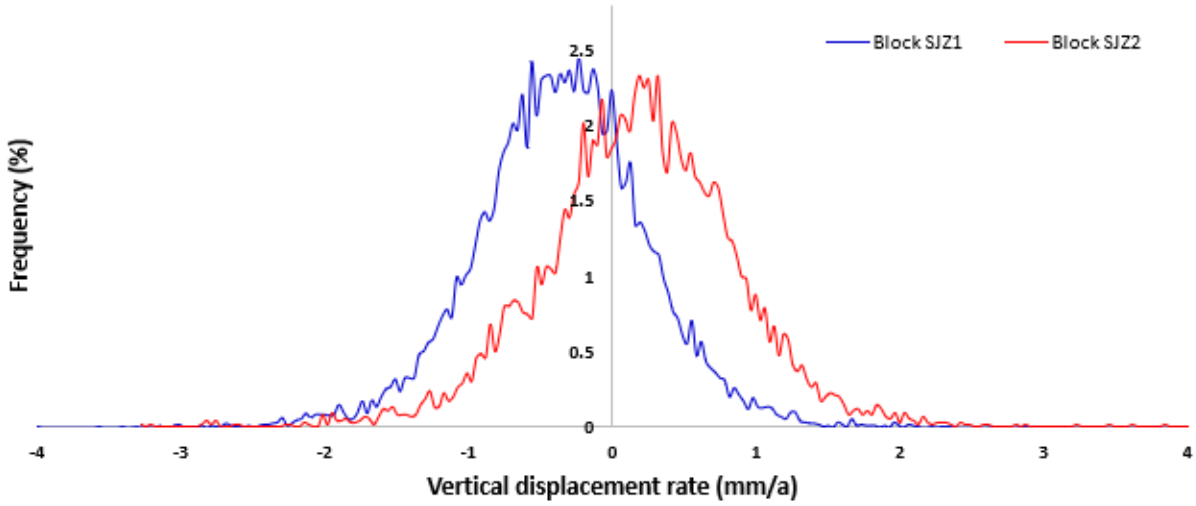


Figure 6.7 (A) illustrates the aerial frequency distribution of vertical displacement rates (D_U) at Block SJZ1 and SJZ2. Statistically, around 73.1% scatterers at SJZ1 are displacing downward and 67.2% at SJZ2 are displacing upward. The means and standard deviations at SJZ1 and SJZ2 are -0.32±0.61 mm $a^{-1}$and 0.17±0.70 mma^{-1} respectively.

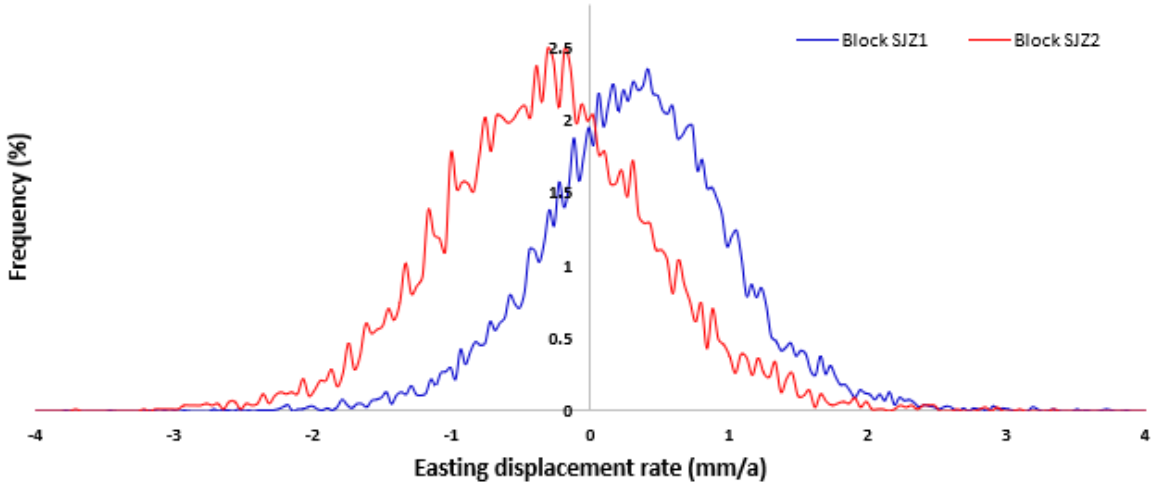


Figure 6.7 (B) illustrates the aerial frequency distribution of easting displacement rates (D_E) at Block SJZ1 and SJZ2. Statistically, around 70.7% scatterers at SJZ1 are displacing eastwards and 65.7% at SJZ2 are displacing westwards. The means and standard deviations at SJZ1 and SJZ2 are 0.36±0.72 mm a^{-1} and -0.23±0.83 mma^{-1} respectively.

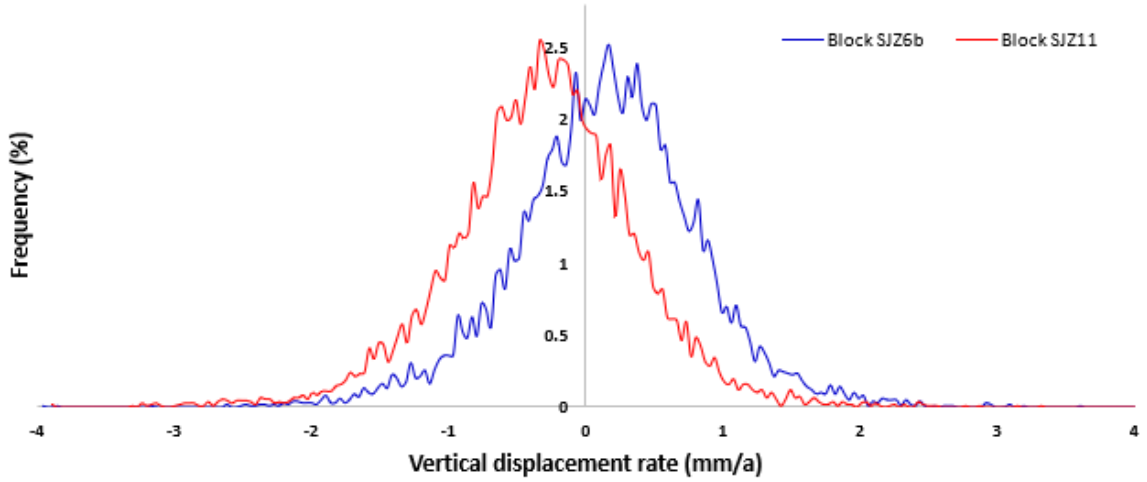


Figure 6.7 (C) illustrates the aerial frequency distribution of vertical displacement rates (D_U) at Block SJZ6b and SJZ11. Statistically, around 50.9% scatterers at SJZ6b are displacing upwards and 63.9% at SJZ11 are displacing downwards. The means and standard deviations at SJZ6b and SJZ11 are 0.17±0.68 mma^{-1} and -0.26±0.66 mma^{-1} respectively.

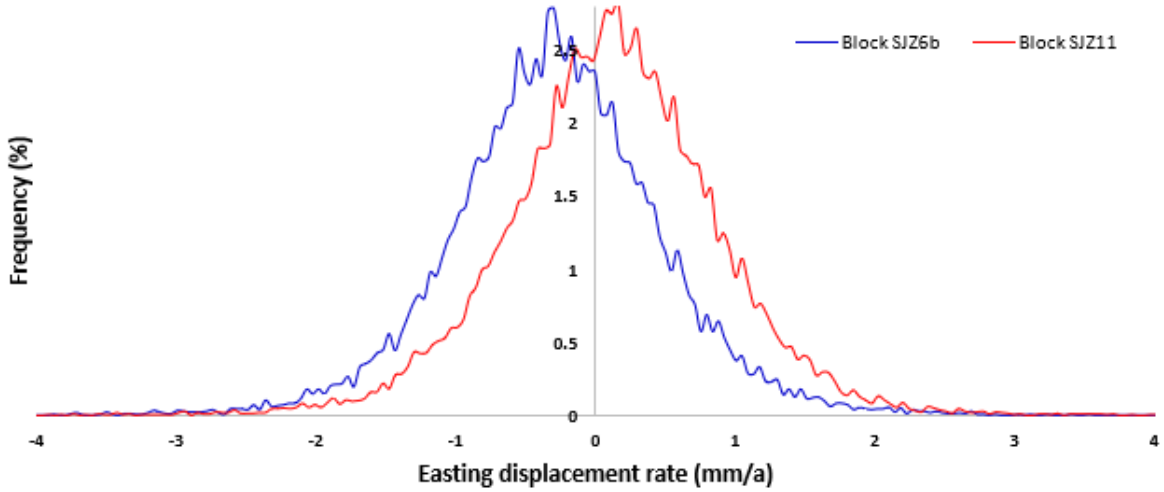
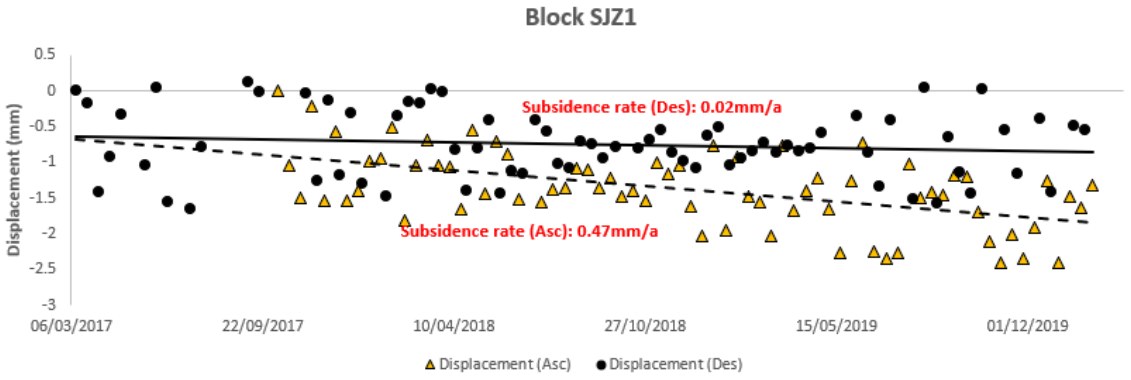
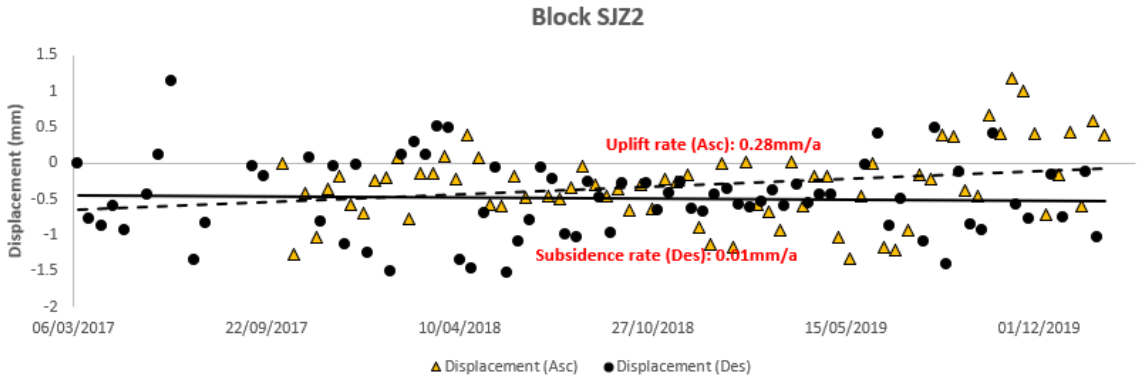


Figure 6.7 (D) illustrates the aerial frequency distribution of easting displacement rates (D_E) at Block SJZ6b and SJZ11. Statistically, around 63.1% scatterers at SJZ6b are displacing westwards and 57.1% at SJZ11 are displacing eastwards. The means and standard deviations at SJZ6b and SJZ11 are -0.13±0.83 mma^{-1} and 0.04±0.79 mma^{-1} respectively.

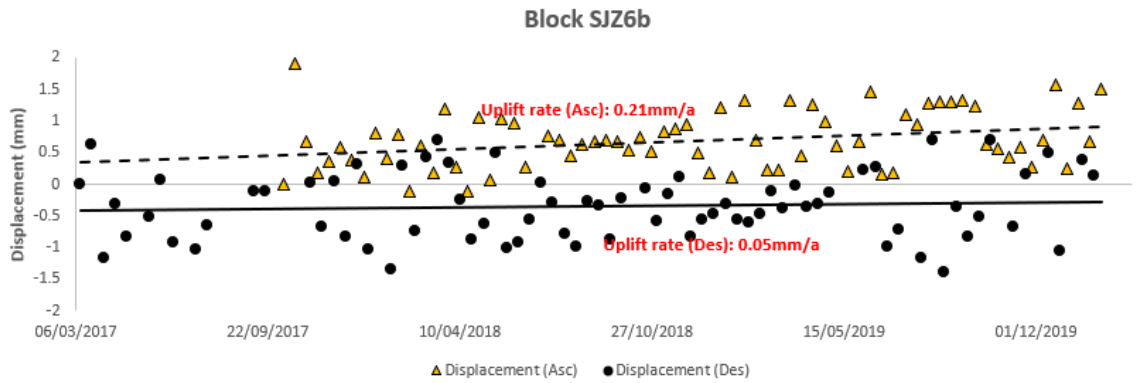
The time-series analyses conducted across several major blocks (Block SJZ1, SJZ2, SJZ6b, SJZ11, and SJZ14) presents the temporal variation and deviation of vertical displacement in ascending and descending views. These are presented in Figures 6.8 (A) to (E), and the original data are presented in Supplementary Materials (Table S3 and S4). This has been achieved through the averaging of the displacement values of thousands of PS points within each block (number presented at Table 5.1 in Chapter 5), where only the scatterers with a coherence greater than 0.7 over the observation period 8/10/2017 to 26/01/2020 were selected.


Block SJZ1
Displacement (mm)
0.5
0
-0.5
-1
-1.5
-2
-2.5
-3
Subsidence rate (Des): 0.02mm/a
Subsidence rate (Asc): 0.47mm/a
06/03/2017
22/09/2017
10/04/2018
27/10/2018
15/05/2019
01/12/2019
Displacement (Asc)
Displacement (Des)

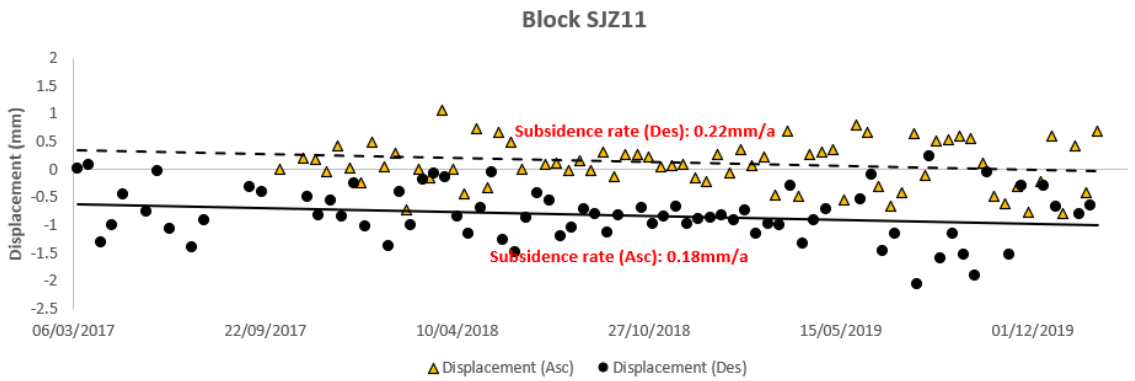
(A)


Block SJZ2
Displacement (mm)
1.5
1
0.5
0
-0.5
-1
-1.5
-2
Uplift rate (Asc): 0.28mm/a
Subsidence rate (Des): 0.01mm/a
06/03/2017
22/09/2017
10/04/2018
27/10/2018
15/05/2019
01/12/2019
Displacement (Asc)
Displacement (Des)

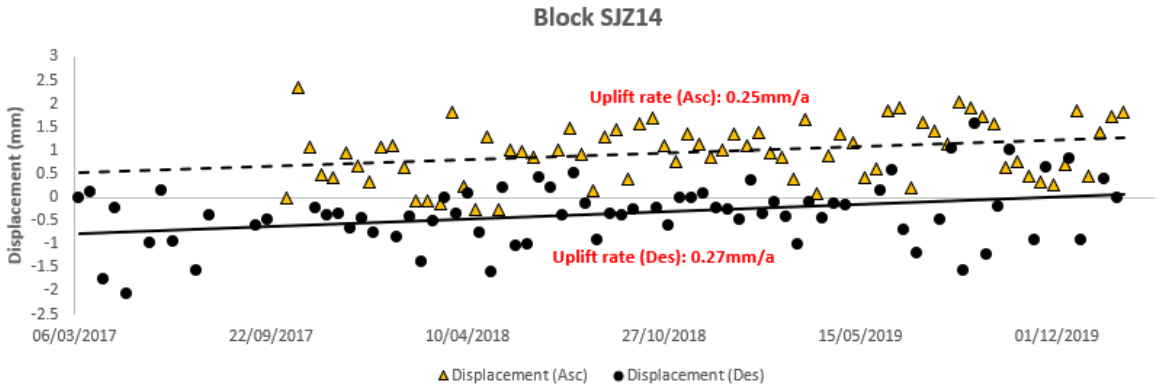
(B)


Block SJZ6b
Displacement (mm)
2
1.5
1
0.5
0
-0.5
-1
-1.5
-2
Uplift rate (Asc): 0.21mm/a
Uplift rate (Des): 0.05mm/a
06/03/2017
22/09/2017
10/04/2018
27/10/2018
15/05/2019
01/12/2019
Displacement (Asc)
Displacement (Des)

(C)


Block SJZ11
Displacement (mm)
2
1.5
1
0.5
0
-0.5
-1
-1.5
-2
-2.5
Subsidence rate (Des): 0.22mm/a
Subsidence rate (Asc): 0.18mm/a
06/03/2017
22/09/2017
10/04/2018
27/10/2018
15/05/2019
01/12/2019
Displacement (Asc)
Displacement (Des)

(D)



(E)

Figure 6.8 (A) to (E). The average time series displacements of Block SJZ1 (A), SJZ2 (B), SJZ6b (C), SJZ11 (D) and SJZ14 (E) in ascending (01/10/2017 to 07/02/2020) and descending (11/03/2017 to 31/01/2020) scene. The dash lines represent the trends of ascending viewed displacements, and the solid lines represent the descending viewed displacements. The gradients of the linear trend lines show the rates of subsidence or uplift. A positive gradient refers to an upward displacement and a negative gradient refers to a downward displacement. The uplift or subsidence rates are highlighted by the text in red on the figures.

Meanwhile, two cross-sections, AA' and BB' highlighted in blue in Figure 6.6, were generated to show the spatial distribution of displacement in vertical and horizontal directions. These are presented in Figures 6.9 (A, B) and 6.10 (A, B) and show the average annual displacement. It should be recognized that these results are estimated from a ~2.5-year time-series of SAR data acquisitions, and they represent continuous ground movement with consistent downward or upward trends over that time. Thus, they are sufficiently accurate to reflect the temporal surface movement. The Sentinel-1 data were analysed in terms of potential structural phenomena and the measured displacements were interpreted and compared against independent priori data sources. As discussed in Chapter 5 potential explanations for apparent movements in InSAR data were analysed for the area as-a-whole, but the only feasible explanation when all else was considered is that a number of the faults are active (Figure 6.9 and 6.10).

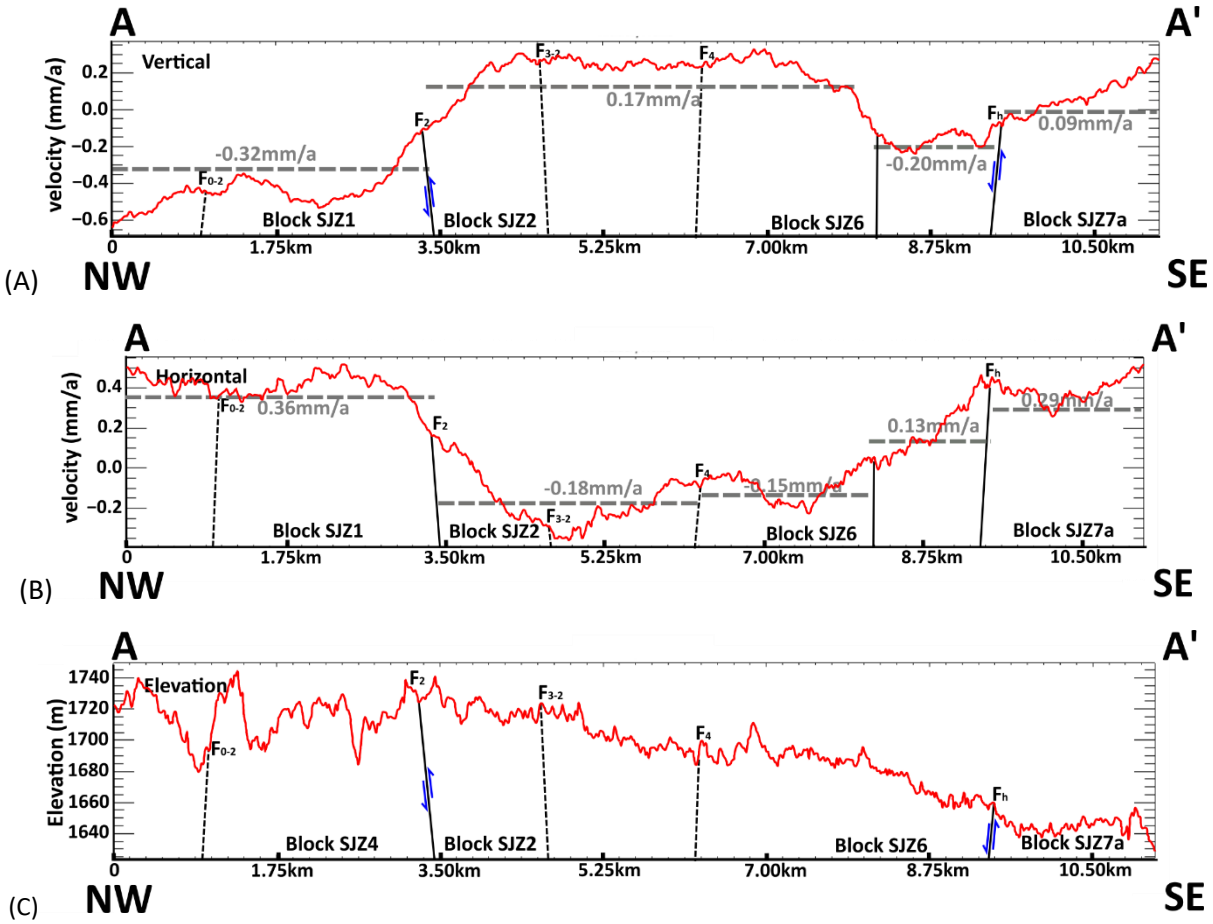
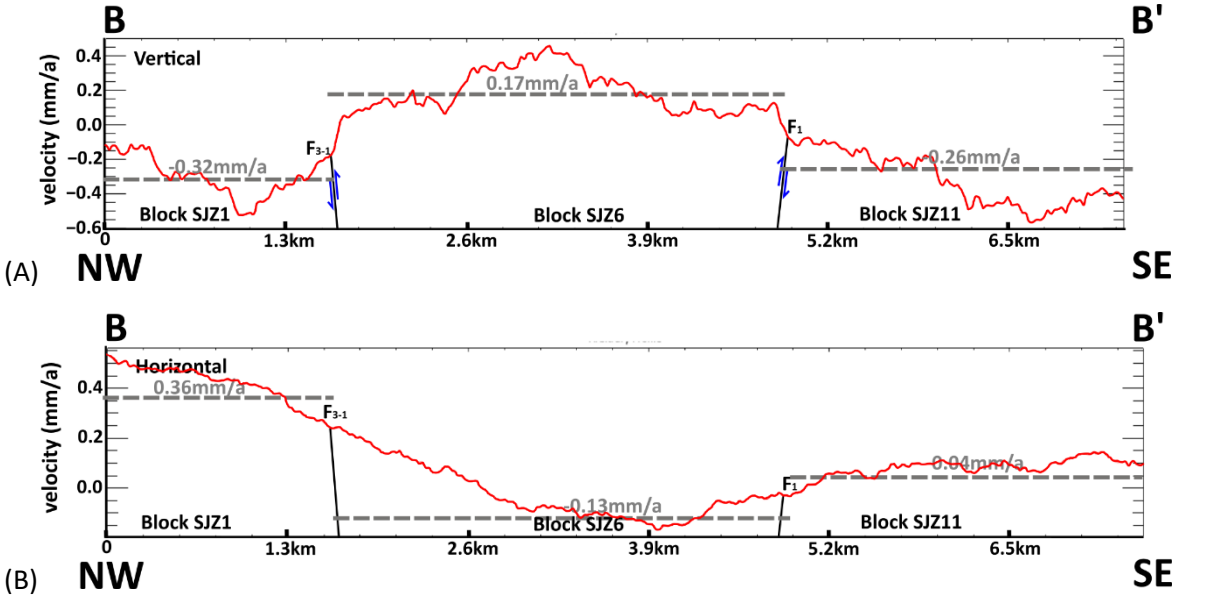


Figure 6.9 (A), (B) and (C). The distribution of vertical displacement (D_U), horizontal displacement (D_E), and elevation along cross-section AA' in Figures 6.6. The cross-section is formed from Persistent Scatterer (PS) values sampled along the cross-section line and shows the annual relative movements within each fault block (Block SJZ4, SJZ2, SJZ6, and SJZ7a). The solid marked faults (F_2 and F_h) are tectonically active, and the dash marked are believed as inactive (F_{0-2}, F_{3-2}, and F_4). These faults are illustrative, showing the sense of fault movement and general direction of faults. They are either interpreted from the PS or extracted from published literature. The horizontal gray dash lines highlighted the average displacement rates along the cross section over each block.



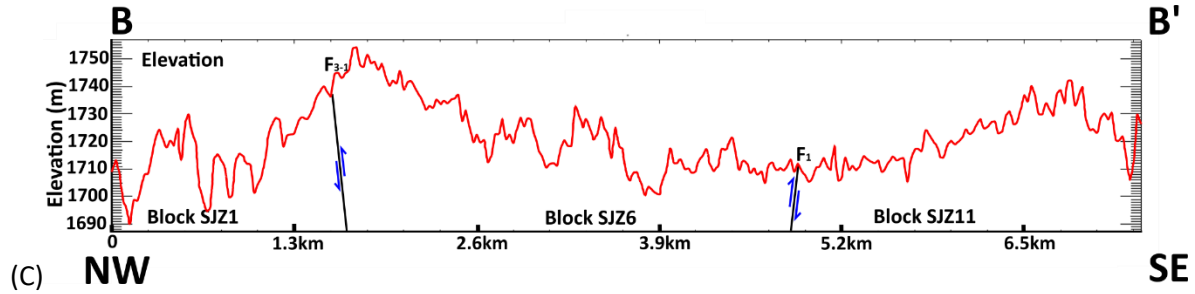


Figure 6.10 (A), (B) and (C). The distribution of vertical displacement (D_U), horizontal displacement (D_E), and elevation along cross-section BB' in Figures 6.6. The cross-section is formed from Persistent Scatterer (PS) values sampled along the cross-section line and shows the annual relative movements within each fault block (Block SJZ1, SJZ6, and SJZ11). The solid marked faults (F_{3-1} and F_1) are tectonically active. These faults are illustrative, showing the sense of fault movement and general direction of faults. They are either interpreted from the PS or extracted from published literature. The horizontal gray dash lines highlighted the average displacement rates along the cross section over each block.

6.3.1 F_2 Northeast dipping reverse fault

The average vertical (D_U) velocity discontinuities between Block SJZ1 (-0.32 mm a^{-1}) and SJZ2 (0.17 mm a^{-1}), suggest that F_2 is vertically active (Figure 6.6D). This discontinuity is presented in Figure 6.9. Statistically, as presented in Figure 6.7 (A), 73.1% of scatterers at SJZ1 are displaced downward, and 67.2% at SJZ2 are displaced upward. The velocity difference between the two sides along the fault plane indicates F_2 is vertically displacing. In general, the ascending scene demonstrates a more distinct velocity discontinuity (-0.47 mma^{-1} VS 0.28 mma^{-1}) than the descending scene (-0.02 mma^{-1} VS -0.01 mma^{-1}), which is clearly illustrated in the PS maps in Figure 6.6 (A, B), in the time-series displacements in Figure 6.8 (A, B) and the velocity cross sections in Figure 6.9 (A, B). The deviation between the ascending and descending viewed velocities is mainly due to the horizontal displacement between blocks SJZ1 and SJZ2. Through the combination of descending and ascending vertical deformation, block SJZ1 is estimated to be displacing eastwards by 0.36 mm a^{-1}, while block SJZ2 is displacing westwards by 0.23 mm a^{-1} (Figure 6.7B). The eastwards displacement of block SJZ1 reduces the descending LoS distance, which therefore makes it appears more uplifted. Meanwhile, the westwards displacements of block SJZ2 decreases the descending LoS distance and makes it appear more subsidized. This explains the slightly difference between the LoS ascending and descending data sets in Figure 6.6. It provides more certainty that there are velocity discontinuities between blocks SJZ1 and SJZ2.

This horizontal displacement pattern (D_E) indicates crustal shorting along F_2, demonstrating that it is a reverse fault, in agreement with the description in Jiang [51]. The relative uplift of SJZ2 compared to

SJZ1 indicate that SJZ1 and SJZ2 are the footwall and hanging wall of the reserve fault respectively, suggesting F_2 is dipping towards the northeast.

6.3.2 Compressive dip-slipped F_1 and sinistral strike-slipped F_b

The previous sections have shown that Fault No. 1 and 2 (F_1 and F_2) are still tectonically active. The direct evidence came from the displacement rate difference between blocks SJZ11 and SJZ6b along the fault. Vertically, SJZ11 is subsiding by 0.26 mma^{-1} and SJZ6b is uplifting by 0.17 mma^{-1}. This is clearly illustrated in Figures 6.6 (D), Figure 6.7 (C), and Figure 6.10 (C).

Horizontally, SJZ11 is displacing eastwards by 0.04 mma^{-1} and SJZ6b is displacing westwards by 0.13 mma^{-1}. This is demonstrated by the difference between descending and ascending LoS deformation rates. The time-series displacement for block SJZ11 presented in Figure 6.7(D), shows the ascending view (-0.22 mma^{-1}) is subsiding slightly more than the descending view (-0.18 mma^{-1}), suggesting that the block is slowly moving away from the ascending satellite (therefore towards east). The time-series displacement for block SJZ6b presented in Figure 6.8(C), shows the ascending view (0.21 mma^{-1}) is uplifting more than the descending view (0.05 mma^{-1}), indicating SJZ6b is moving towards an ascending satellite at a higher speed (therefore towards the west). This can be interpreted as crustal shorting along F_1 due to compression, hence F_1 is believed to be a reverse fault. Finally, the upwards movement of SJZ6b relative to SJZ11 indicates that F_1 is dipping towards the northeast, where SJZ11 and SJZ6b are the footwall and hanging wall respectively. This agrees with the findings of Jiang [51].

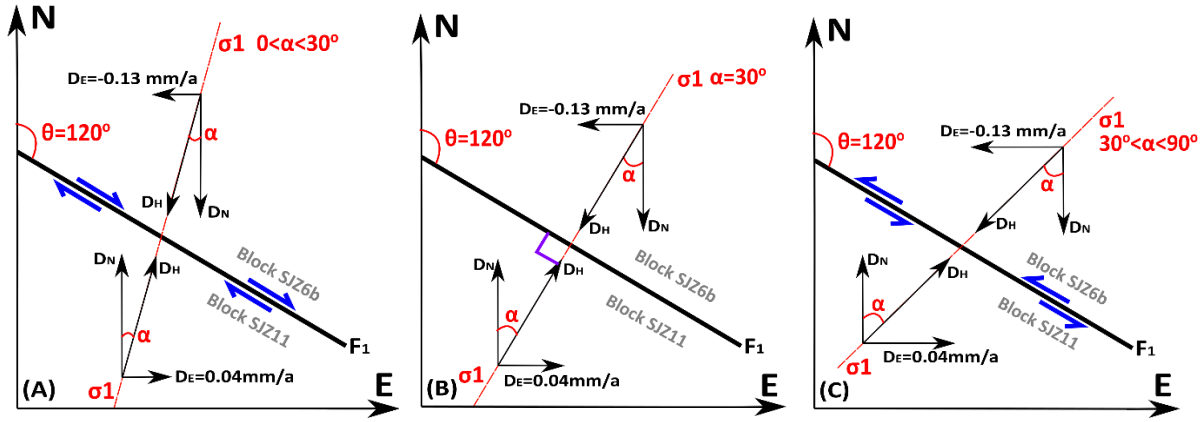


Figure 6.11 (A to C) illustrates three possible horizontal shearing conditions (dextral, pure reverse and sinistral) along F_1 depends on the direction of maximum horizontal compression (α). The striking angle of F_1 (θ) is around 120°.

There is no direct in-situ measurement regarding σ1 direction (α) in Suanjingzi and F_1 is trending NW-SE, therefore it is hard to interpret the horizontal shearing properties of F_1 directly from Figure 6.6C. The entire Beishan region is in a NE-SW compressive field, and the orientation of horizontal stress is

governed by the tectonic movements [48]. In this way, it can be speculated that σ1 and D_H are trending NE-SW and α is generally in the range between N0°E to N90°E.

The horizontal shearing property along F_1 depends on the direction of maximum horizontal stress (α). As illustrated in Figure 6.11, blocks SJZ11 and SJZ6b on the two sides of F_1 are sliding in the opposite direction, measured at D_E are 0.04 mma^{-1} and -0.13 mma^{-1} respectively. A low maximum horizontal compression angle ($0<\alpha<30^o$) which has deformation dominated by northing displacements (D_N) should lead to dextral shearing (Figure 6.11A). Meanwhile, a high maximum horizontal compression angle ($30^o<\alpha<90^o$) with relatively low D_N should lead to sinistral shearing (Figure 6.11C). Finally, when $\alpha=30^o$, σ1 would be perpendicular to F_1 (Figure 6.11B). F_1 would therefore behave in pure reverse (dip-slip fault) and no strike-slip would exist along the fault plane.

The vertical and horizontal displacement rates difference between SJZ6a and SJZ11 indicates that F_b is another active fault in Suanjingzi. In general, SJZ6a is uplifting (D_U = 0.24 mma^{-1}) relative to SJZ11, which also is displacing westward by 0.12 mma^{-1} (Figure 6.6C and D). This form of horizontal displacement is reflected by a difference in descending and ascending vertical deformation, where the descending view is uplifting at a slower rate (0.16 mma^{-1}) than the ascending view (0.23 mma^{-1}). This can be interpreted as a slow movement towards the ascending satellite (i.e., west).

F_b is trending NE-SW, and its striking angle (θ) is around 55°. The south side SJZ11 is displacing eastwards slightly by 0.04 mma^{-1} and the north side SJZ6a is displacing westwards by 0.12 mma^{-1}. Considering the tectonic background that the Suanjingzi region and even the entire Beishan area are under the impact of NE-SW maximum compression, it can be speculated that SJZ11 and SJZ6a are displacing northeast and southwest respectively. In this manner, the D_E deformation patterns demonstrate a sinistral shearing along F_b.

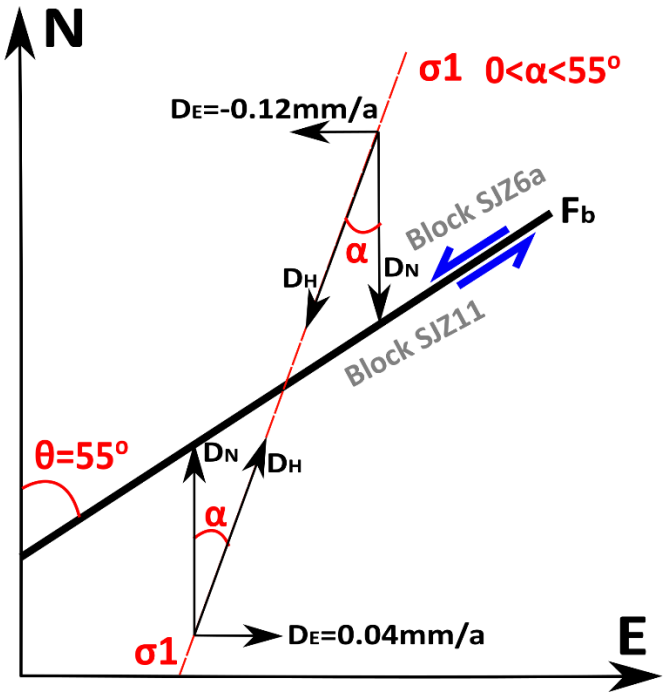


Figure 6.12 illustrates the formation of sinistral shearing along F_b, where the fault strike angle (θ) is around 55° and the direction of maximum horizontal compression (α) ranges from 0 to N55°E.

Based on the arguments in Section 6.2.2, a sinistral shearing refers to a positive ϒ value (θ>α). The fault striking angle (θ) is around 55°. This indicates that α<55°. Meanwhile, the study area is in a NE-SW compressive field. Therefore, α should also be higher than 0. In this way, the maximum compression direction (α) at Suanjingzi is estimated to be within the range of 0<α<55°. It is hard to estimate the vertical shearing properties of F_b directly from Figure 6.6 (C and D) through the patterns of D_U and D_E. Depending on the exact value of α along the fault, F_b can be extensional or compressive. However, compared to NW-SE trended faults such as F_1 and F_2, F_b is arguably less compressive, and might be more dominated by strike slip.

6.3.3 Thrust with sinistral strike-slip, F_d

F_d is another previously unmapped active fault, which is believed to be a sinistral reverse fault. Along F_d, block SJZ8 is subsiding by 0.53 mma^{-1}, whilst adjacent block SJZ7a is uplifting by 0.09mma^{-1}. This kind of vertical discontinuity first indicates that F_d is vertically active. However, within SJZ8, there is a very significant LoS displacement rates difference between the descending (D_{los}^{des}= -0.87 mma^{-1}) and ascending (D_{los}^{asc}= 0.11 mma^{-1}) views, this reflects a strong displacement toward the side of ascending satellite (west), which can be interpreted as a westwards displacement rate (D_U) estimated at 0.73 mma^{-1}. As SJZ7a is displacing towards the east by 0.25 mma^{-1}, the trending angle of F_d is around N100°E, and the whole granodiorite outcrop is influenced by a NE-SW maximum compression. This indicates there is sinistral shearing along F_d, (Figure 6.13).

In general, the orientation of horizontal stress is governed by tectonic movements [48]. There is no in-situ borehole stress measurement at Suanjingzi but various studies [33, 48, 49] have suggested the whole Beishan area is in a compressive stress field with maximum horizontal stress generally in the direction of the Northeast. This, therefore, indicates the real horizontal displacement in Suanjingzi blocks generally aligns with the NE-SW trend. In this way, it can be speculated that SJZ8 is displacing towards the southwest and SJZ7a is displacing towards the Northeast (as illustrated in Figure 6.13). Therefore, F_d is believed to be a south dipping oblique fault that is thrusting towards the NE with clear dip-slipped and strike-slipped displacements, where SJZ7a and SJZ8 are the hanging wall and foot wall of the reverse fault respectively.

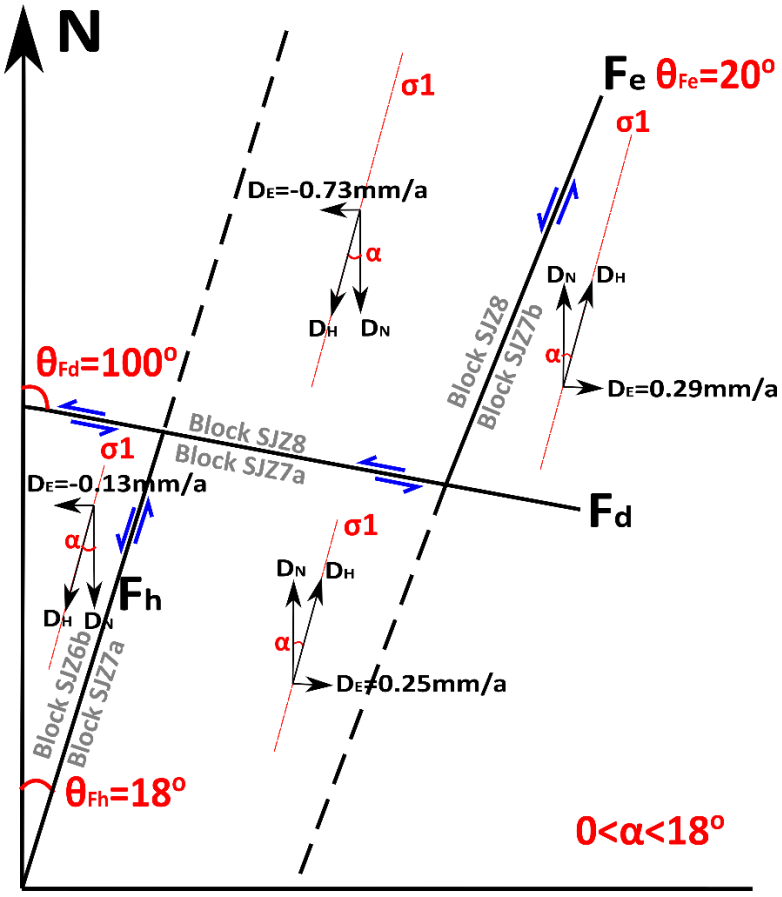


Figure 6.13 The schematic sketch explains the existence of divergence at Block SJZ6b, SJZ7a, SJZ8 and SJZ7b along F_h and F_e in Figure 6.5 (C) through a perspective of geomechanics, where σ1 refers to maximum horizontal compression, α refers to direction of σ1, and θ refers to the striking angle of faults. The dash fault lines are inferred and refer to the linear extension of F_h and F_e which were interpreted as inactive based on the deformation patterns of D_E and D_U in Figure 6.6 (C) and (D).

6.3.4 Sinistral strike-slip faults, F_h and F_e

This research identifies F_h and F_e as previously unmapped faults. They have similar strike angles of N18°E and N20°E respectively. They are interpreted to be sinistral strike slip faults and most likely in extension (very weak compression compared to NW-SE trended faults). there is no significant vertical

(D_U) displacement contrast between the two sides of F_h in ascending view. However, in the descending scene on the east side of F_h, there is vertical displacement of Block SJZ7a (D_U = 0.22 mma^{-1}) suggesting uplift as opposed to the ascending scene which suggests a small amount of subsidence (D_U= -0.10 mma^{-1}) (Figures 6.9D and 6.5). A similar contrast occurs in SJZ9, where the descending LoS displacement (D_{los}^{des}= -0.14 mma^{-1}) is uplifting more than ascending LoS displacement (D_{los}^{asc}= -0.37 mma^{-1}). This slight contract can be explained by horizontal movements, if both SJZ7a and SJZ9 are displacing towards the direction of descending satellite, which has eastward displacement rates of 0.25 mma^{-1} and 0.19 mma^{-1} respectively. Meanwhile, the west side (block SJZ6b) is displacing westwards by 0.13mma^{-1}. This indicates that F_e is vertically and horizontally active. Similarly, the vertical and horizontal deformation at SJZ8 and SJZ7b indicates that F_e is another active fault which demonstrates similar characterization with F_h. A potential explanation for the deformation patterns observed in the InSAR results along F_h and F_e is presented in Figure 6.13.

Figure 6.13 illustrates the horizontal shearing properties along F_h, F_e and F_d when correlated with a possible maximum compression direction (α) and surface deformation in Figures 6.6 C and D. The striking angles (θ) of F_h and F_e are approximately 18° to 20°. According to the theories that were presented in Figure 6.4 and 6.5, if α<θ, F_h and F_e behave sinistrally, this can explain the divergent patterns at Block SJZ6b and SJZ7a along F_h and SJZ8 and at SJZ7b along F_e which was observed in Figure 6.6 (C). Otherwise, if α>θ, F_h and F_e behave dextrally, D_E in Figure 6.6 would present convergent patterns which do not match the SAR data. In this way, the direction of σ1 should fall within the range of 0 to N18°E.

The displacements along F_h, and F_e are strike-slip dominated. It is hard to confirm the vertical shearing properties along them due to the lack of in-situ stress measurements and northing displacement (D_N). However, according to the theory introduced in Section 6.2.1, the low angle difference between α and θ indicates they are more likely to be extensional, at least, much less compressive than F_d. It is important to note, the active faults F_h and F_e are expected to extend beyond F_d as illustrated by inferred dash fault lines in Figure 6.13 and theoretically should be characterised by strike-slip. However, this displacement cannot be observed in Figure 6.6 and is inferred to make the model more kinematically feasible. This may be because this strike-slip shearing is north-south trending and the limitations of the recent InSAR satellite technology mean the northing displacement (D_N) cannot be accurately estimated. Therefore, this strike-slip fault displacement along the inferred dash line illustrated fault planes is hard to observe sorely based on D_E and D_U.

6.3.5 Major thrusts, F_5 and F_6

F_5 controls the south boundary of the Suanjingzi pluton. According to Jiang [51], it is a south-dipping reverse fault. This means SJZ11 and SJZ9 are footwall blocks on the north side, and SJZ14 and SJZ15 on the south side are hanging wall blocks. As presented in Table 5.1, SJZ14 is uplifting by 0.35 mma^{-1} and SJZ11 is subsiding by 0.26 mma^{-1}, which is demonstrated by a significant vertical velocity difference across the fault. Block SJZ14 shows uplift displacement rate values (0.27mma^{-1} and 0.25 mma^{-1}, time series displacements presented in Figure 6.8E) it both the ascending and descending, indicating that the deformation might be vertically dominated.

As a result of block SJZ14 being on the southern edge of the Suanjingzi pluton, which is characterized by a steep slope, it is possible some of the observed movement may be the result of an elevation error. However, the impact of surface alteration due to geomorphological processes can be excluded. As measured in Chapter 5, Section 5.3 (in Table 5.4), around 91.5% of pixels at SJZ14 have a coherence greater than 0.7 from 08/10/2017 to 26/01/2020, which indicates very limited geomorphological impacts during the acquisition period. Although the deformations at SJZ14 could be partly the result of the slope elevation the clear fault relationship to SJZ15 are due to the impact of tectonics, therefore the evidence suggests F_5 and F_6 might be active.

SJZ9 and SJZ15 show similar vertical velocity displacement, where SJZ15 is subsiding at 0.07 mma^{-1} but SJZ9 is subsiding more rapidly at 0.33 mma^{-1}. Both SJZ15 and SJZ9 are displacing eastwards (Figure 6.6 C), which may mainly be due to the activities of F_h that leads to a displacement rate difference between the two sides of the fault plane. SJZ15 (0.46 mma^{-1}) has a higher eastward displacement rate than SJZ9 (0.19 mma^{-1}), which indicates sinistral shearing properties along $F_{5\text{-}2}$. Furthermore, as the orientation of horizontal stress is governed by the tectonic movements, SJZ15 is, therefore, displacing towards the northeast at a higher rate than SJZ9. This, in turn, indicates a crustal shorting along $F_{5\text{-}2}$, indicating $F_{5\text{-}2}$ is compressive. There is no clear velocity discontinuity along $F_{5\text{-}3}$, therefore, $F_{5\text{-}3}$ is considered tectonically inactive. Overall, the Sentinel-1 data confirm the literature description of F_5 as an inactive, south-dipping reverse fault.

F_6 is another reverse fault controlling the southern boundary of Suanjingzi forming a conjugate set with F_5, which is dipping towards the north [51]. The hanging wall side (Block SJZ14, 0.35 mma^{-1}) shows a significant uplift rate compared to the footwall side (Block SJZ13, -0.10 mma^{-1}). The horizontal deformation pattern in Figure 6.6 (C) also indicates a sinistral shearing property along F_6, where block SJZ15 (hanging wall side in the north) and block SJZ13 (footwall side in the south) have eastward displacement rates of 0.46 mma^{-1} and 0.75 mma^{-1} respectively. Considering the description in the

literature by Jiang [51] of F_6 as a northward dipped reverse fault, this explains the formation of uplifting deformation patterns observed in the InSAR data at SJZ14 and SJZ15 along the F_6 fault plane in Figure 6.6 (D). In a further step, it is also reasonable to speculate that F_6 forms a sinistral positive (reverse) flower structure with F_5 in the subsurface due to the impact of NE-SW compression, which is illustrated in Figure 6.14.

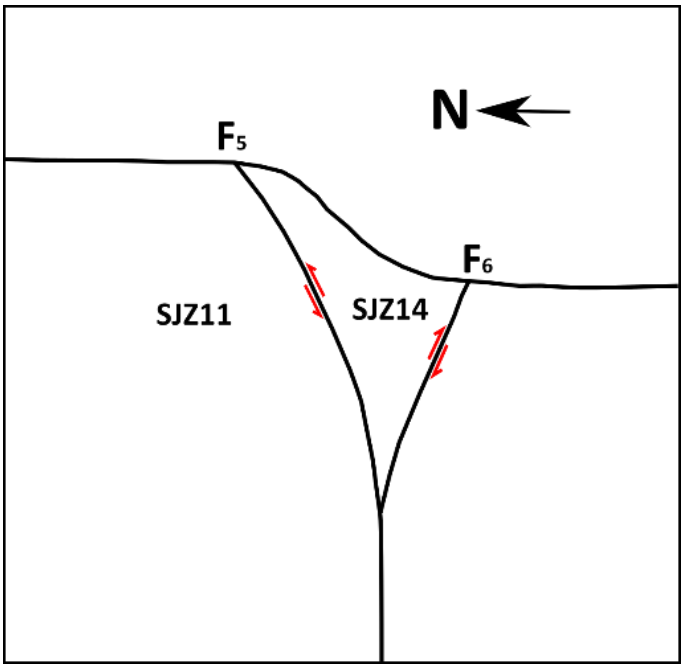


Figure 6.14 The schematic sketch illustrates a positive flower relationship between F_5 and F_6 in Suanjingzi. This indicates Block SJZ14 is a part of F_5 and F_6 hanging wall and explains the uplifting from a tectonic perspective.

The tectonic cause of ground movements observed in the InSAR along F_6 are still questionable. This is due to Block SJZ13 being composed of lower Cretaceous, Chijinbao Formation (Section 5.4). As presented in Figure 5.7 (H). Whilst block SJZ13 has a good coherence at around 0.7 over a timescale from 08/10/2017 to 26/01/2020, this value is lower than the granite exposed blocks exposed although much higher than the Holocene sediment covered blocks (SJZ0). This indicates the geomorphology may partially impact the deformation at Block SJZ13 and require further investigation to finally conclude the activity along F_6.

6.3.6 Fault of indeterminate type, F_a

There is significant deformation discontinuity along F_a as presented in Figure 6.6, both vertically and horizontally. High coherence on the southern side (Blocks SJZ1 and SJZ2) reinforces the interpretation that the results are tectonic in origin. However, the northern side (SJZ0) is characterized by very low coherence. As summarized in Table 5.4 in Section 5.4, only 0.5% of pixels in Block SJZ0 have a

coherence higher than 0.7 over the timescale from 08/10/2017 to 26/01/2020. This indicates the deformation at SJZ0 is severely impacted by geomorphological processes, which obscures the tectonic activities. In this way, it is hard to characterize the activity of F_a based on current data.

6.3.7 Faults of indeterminate type, $F_{0\text{-}1}$, F_c, and F_7,

There are distinct vertical deformation discontinuities along $F_{0\text{-}1}$, F_c and F_7, (Figure 6.6 D), however, the easting deformation (D_E) discontinuities along these faults are unclear (Figure 6.6 C). This vertical deformation indicates these faults are active, but the lack of any horizontal movement component might be due to two reasons: (1) the σ1 is almost perpendicular with the fault, where the faults are purely reverse with little horizontal shearing; and/or (2) there is significant north-south displacement (D_N) at SJZ4, SJZ5 and SJZ6a, which can't be observed by the Sentinel satellite because D_N is unmeasurable based on the combination of ascending and descending polar orbit data.

Since F_0 is dipping towards the northwest [51], the uplift of SJZ4 relative to SJZ5 suggests $F_{0\text{-}1}$ is likely compressive, where SJZ4 and SJZ5 are the hanging wall and footwall respectively. F_c is NW-SE trending, which indicates F_c is likely to be impacted by σ1 trending NE-SW. In this way, F_c is a reverse fault, which is more likely to dip towards the east/northeast. F_7 is dipping towards the southwest, with the subsidence of block SJZ10 against the uplift of block SJZ4 indicating F_7 is a normal fault, where block SJZ10 and block SJZ4 are the hanging wall and footwall respectively.

6.3.8 Identifying inactive faults

$F_{0\text{-}2}$, $F_{3\text{-}2}$, F_4, $F_{5\text{-}3}$ and F_8 have no impacts on surface deformation. This is because there are no clear deformation pattern discontinuities along these fault planes. This has been clearly presented in Figures 6.5 A to D and the cross sections AA' and BB' in Figures 6.9 and 6.10. In this way, $F_{0\text{-}2}$, $F_{3\text{-}2}$, F_4, $F_{5\text{-}3}$ and F_8 are believed to be tectonically inactive.

6.3.9 Summary

Through a comparison with the structure geology map published by Jiang [51], Section 6.3 has successfully identified 15 active faults in the Suanjingzi granodiorite area. It confirmed that F_1, F_2, F_6 and F_7 remain tectonically active and F_0, F_3 and F_5 are partially active. It also traced 8 previously unmapped faults, labelled as F_b, F_c, F_d, F_e, F_f, F_g, F_h, and F_i shown in Figure 6.6.

There are no borehole in-situ stress measurements in the Suanjingzi granodiorite region, however, by combining with the estimates proposed in Sections 6.3.2 and 6.3.4, the general direction of σ1 in the Suanjingzi region should range from 0 to N18^{o}E. This leads to the formation of two fault groups:

(1) Group 1: The NE-SW trended faults such as F_h, F_e and F_b, which have relatively low angles to relative to σ1 that behave less compressively (or more extensionally) and are more strike-slip (sinistral) in nature.
(2) Group 2: The NW-SE trended faults such as F_1, F_2 and F_d, which are relatively high angle to σ1, which behave more compressively with less horizontal shearing compared to Group 1 (F_h, F_e, and F_b).

These faults were generated due to the σ1 in the NE-SW and a σ3 in the NW-SE, which can be explained based on the kinematic theory introduced in Section 6.2. This leads to a maximum compression in the NE-SW and an extension (minimum compression) in the NW-SE. Collectively, these faults lead to the deformations in Figure 6.6 A to D.

6.4 Characterizing active faulting at Jiujing granite outcrop

Based on the kinematic theories introduced in Section 6.2, this section mapped and characterized the active faults of the Jiujing region granite outcrops using InSAR. It verified the activation of the faults (F_1, F_6, F_{14}, F_{15}, $F_{16\text{-}1}$, $F_{16\text{-}2}$, F_{17}, F_{18}, F_{19}, $F_{20\text{-}1}$, $F_{20\text{-}2}$, $F_{20\text{-}3}$, and $F_{20\text{-}4}$) introduced by literature [34, 49] in Jiujing area based on the InSAR displacement rate patterns (D_{los}^{asc}, D_{los}^{des}, D_U, and D_E). These PSI results and the traced faults (included both previously mapped and newly identified) have been presented in Figures 6.15 (A), (B), (C), and (D). Their characteristics are summarized in Table 6.2 and the detailed explanations are presented as fellows in sub-Sections 6.4.1 to 6.4.7.

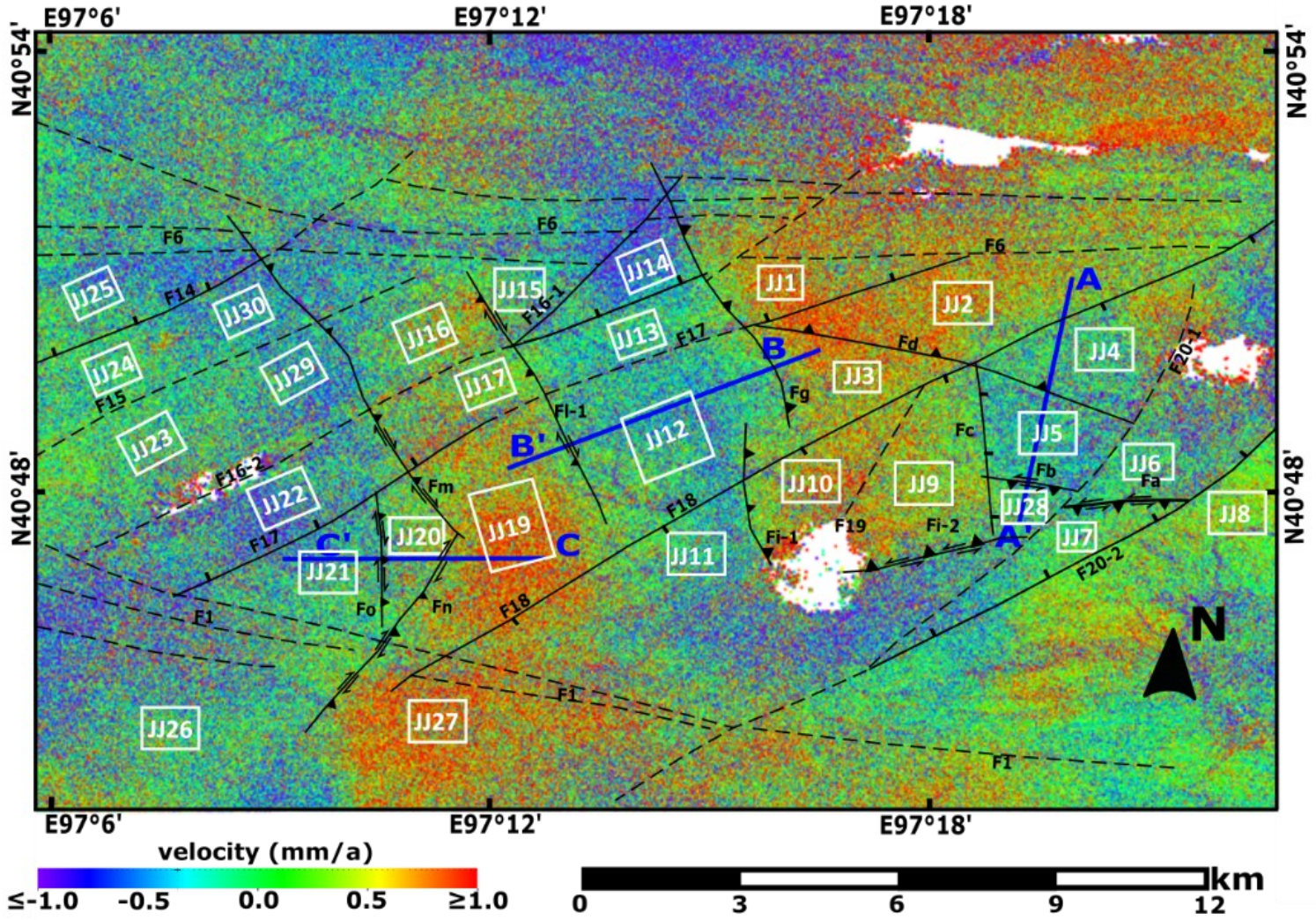


Figure 6.15 (A) The LoS displacement (D_{los}^{asc}) pattern of Jiujing region reprocessed from ascending Sentinel-1 data, where the positive values (upper, red side of colour axis) refer to the uplift and negative values (blue, lower side of colour axis) refers to subsidence. It illustrates the correlations between active faults and deformation patterns.

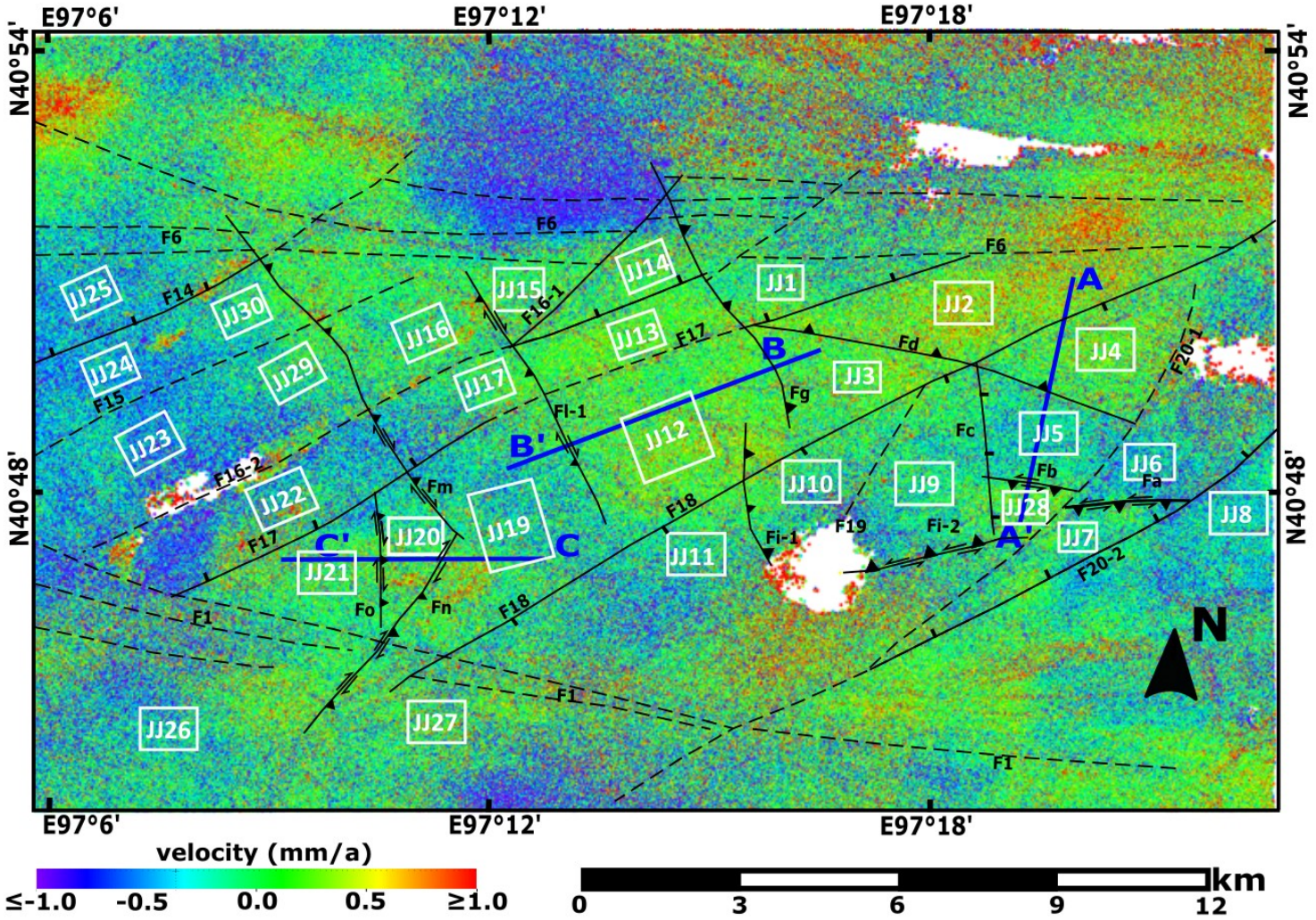


Figure 6.15(B) The LoS displacement (D_{los}^{des}) pattern of Jiujing region reprocessed from descending Sentinel-1 data, where the positive values (upper, red side of colour axis) refer to the uplift and negative values (blue, lower side of colour axis) refers to subsidence. It illustrates the correlations between active faults and deformation patterns.

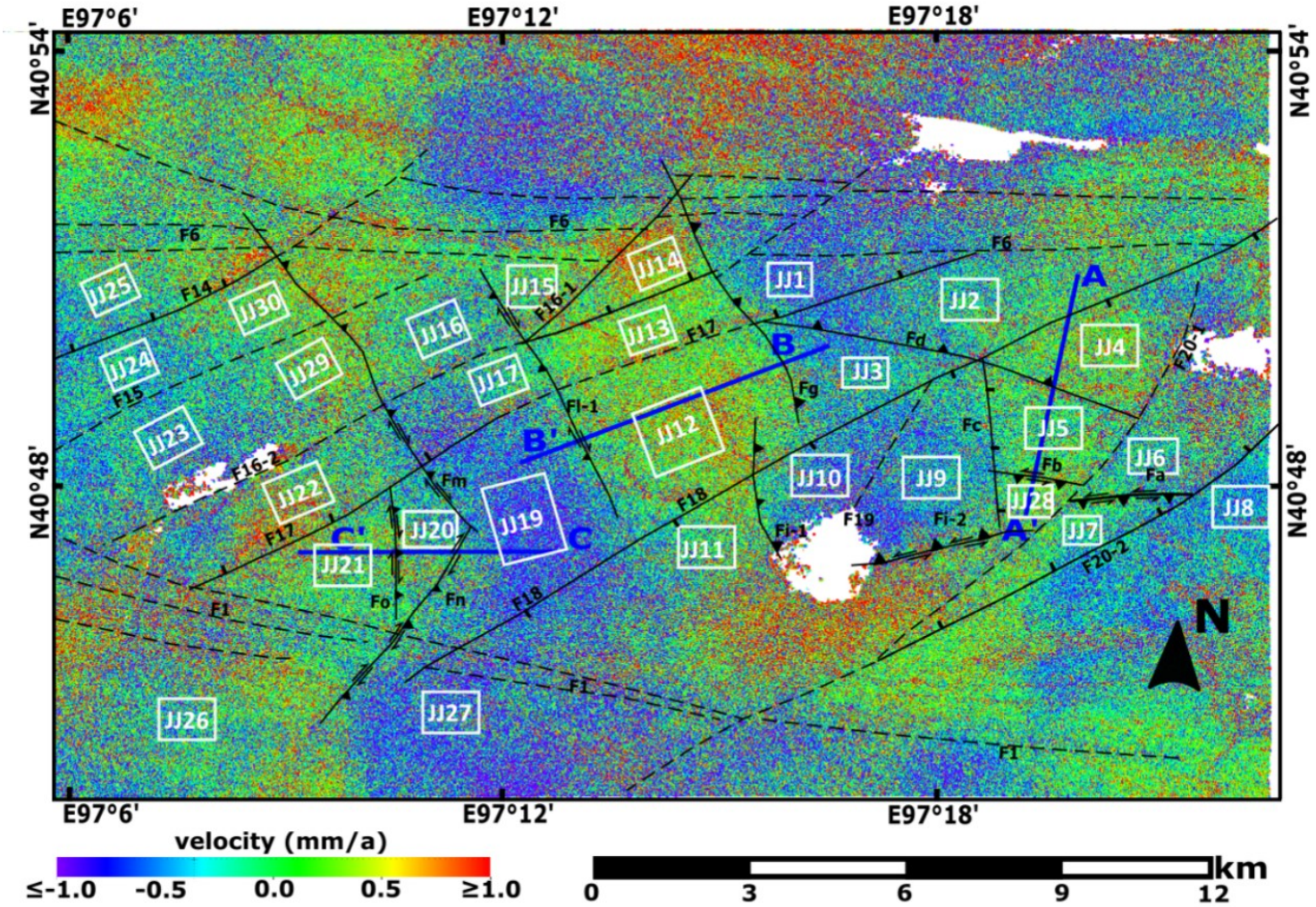


Figure 6.15(C) The pattern of horizontal displacement (D_E) in the Jiujing region computed through the combination of descending and ascending Sentinel-1 data based on the theory introduced in Section 4.3, where the positive values (red and yellow coloured) refer to eastward horizontal displacements and the negative values (blue coloured) refers to westward displacements. It illustrates the correlations between active faults and deformation patterns.

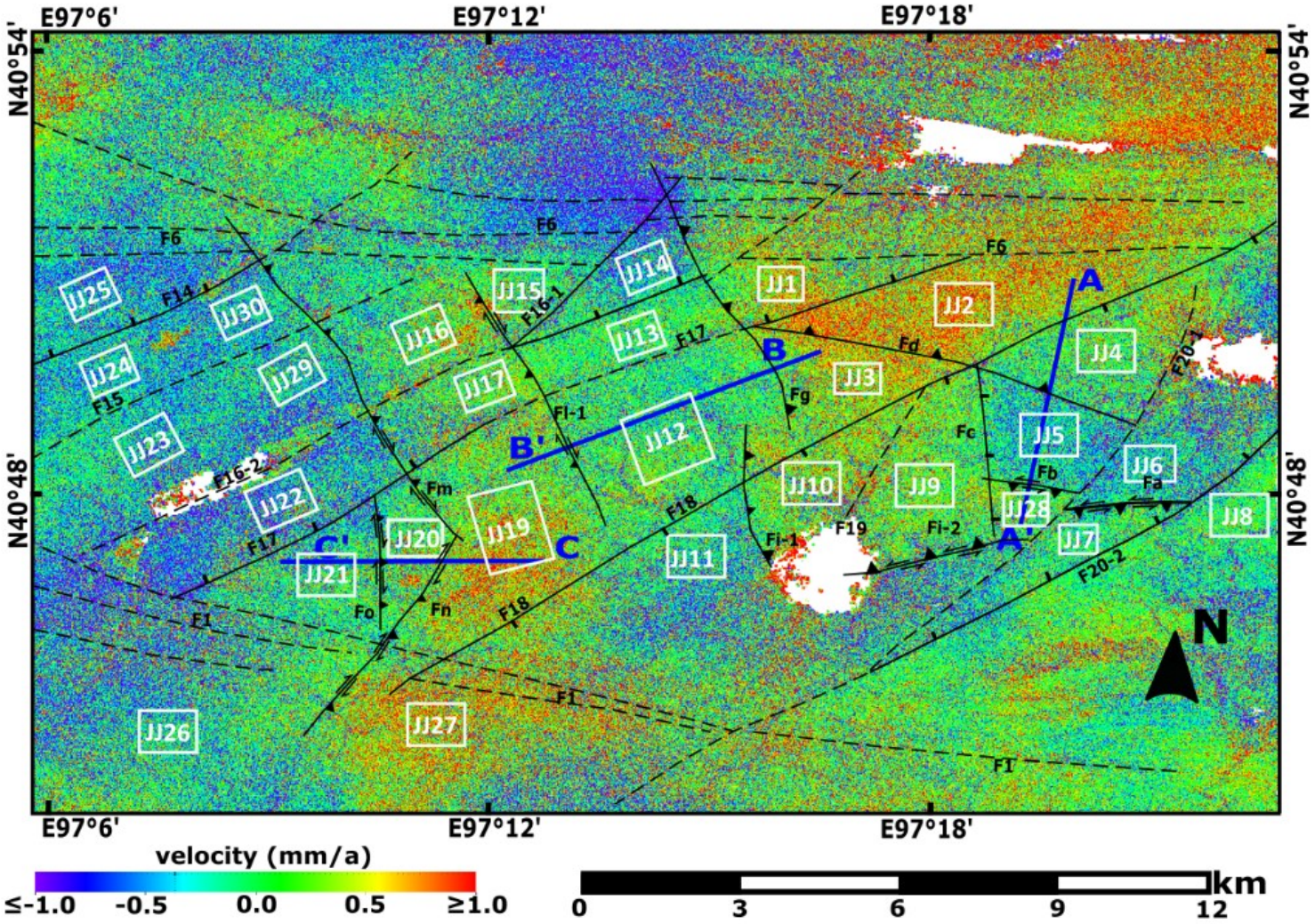


Figure 6.15(D) The pattern of vertical displacement (D_U) in the Jiujing region computed through the combination of descending and ascending Sentinel-1 data based on the theory introduced in Section 4.3, where the positive values (upper, red side of colour axis) refer to the uplift and negative values (blue, lower side of colour axis) refers to subsidence. It illustrates the correlations between active faults and deformation patterns.

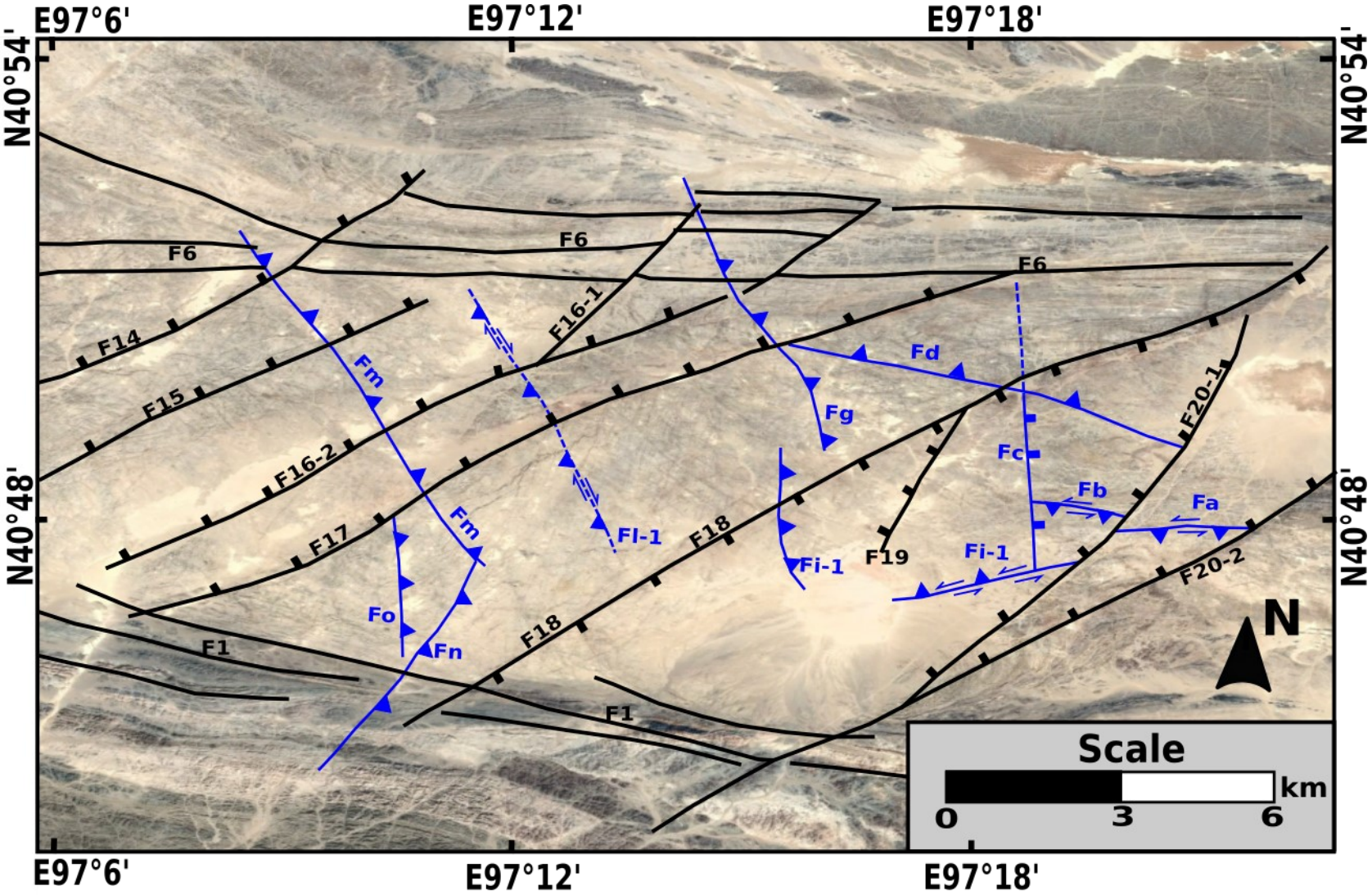


Figure 6.15 (E) The distribution of faults in the Jiujing region on the Google Earth image, where faults found in the literature are highlighted by black lines and the newly identified faults are highlighted by blue lines.

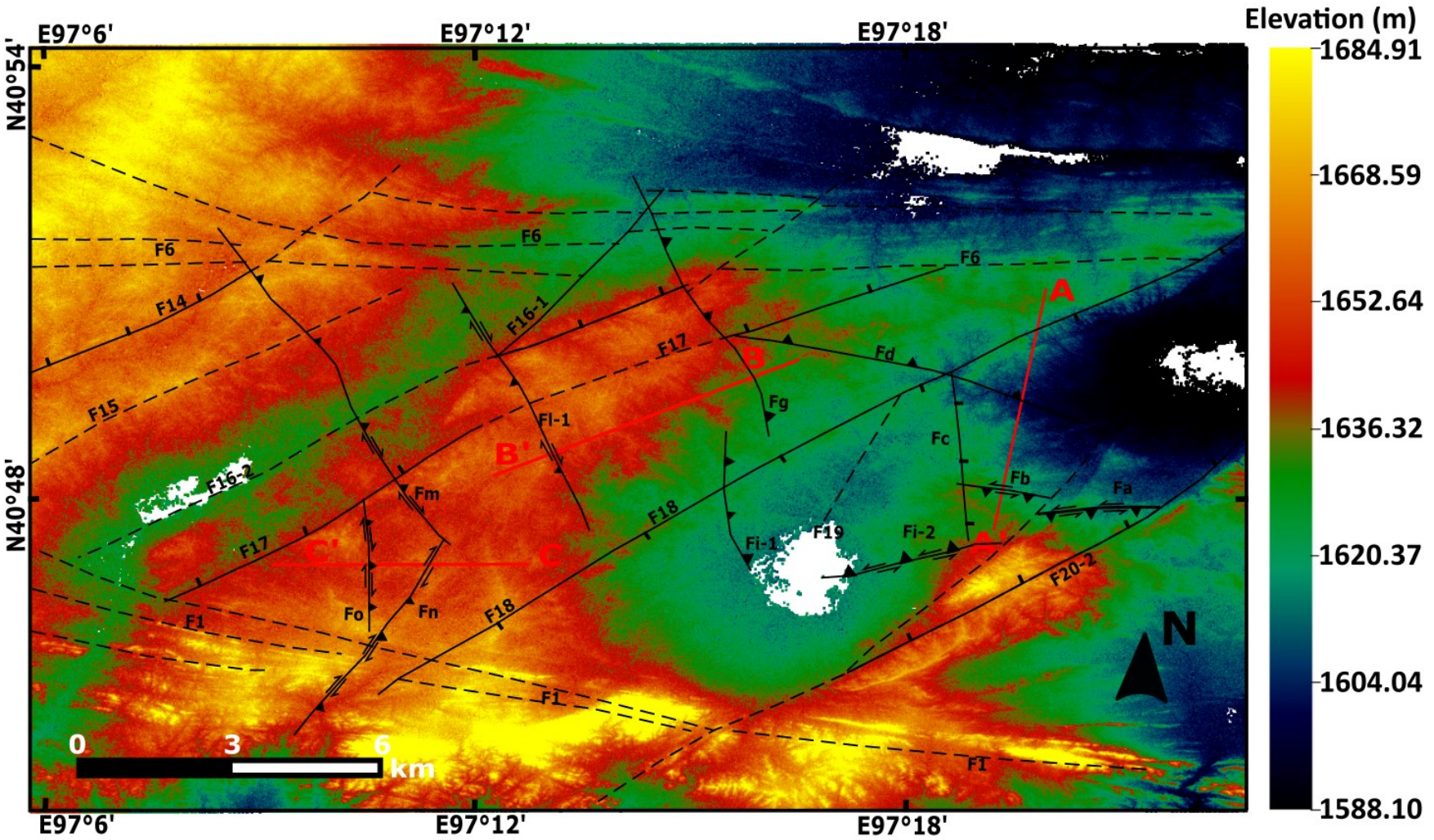


Figure 6.15 (F). The digital elevation model (DEM) across the Jiujing study area illustrates the spatial correlation between faults and the topography. The DEM is a third-party product provided by the NASA Shuttle Radar Topography Mission (SRTM). This provides a topographic representation of the earth surface. The solid line represents the on-going active faults and the dash line represent the recent inactive faults (or those whose activity cannot be sorely interpreted based on D_E and D_U deformation).

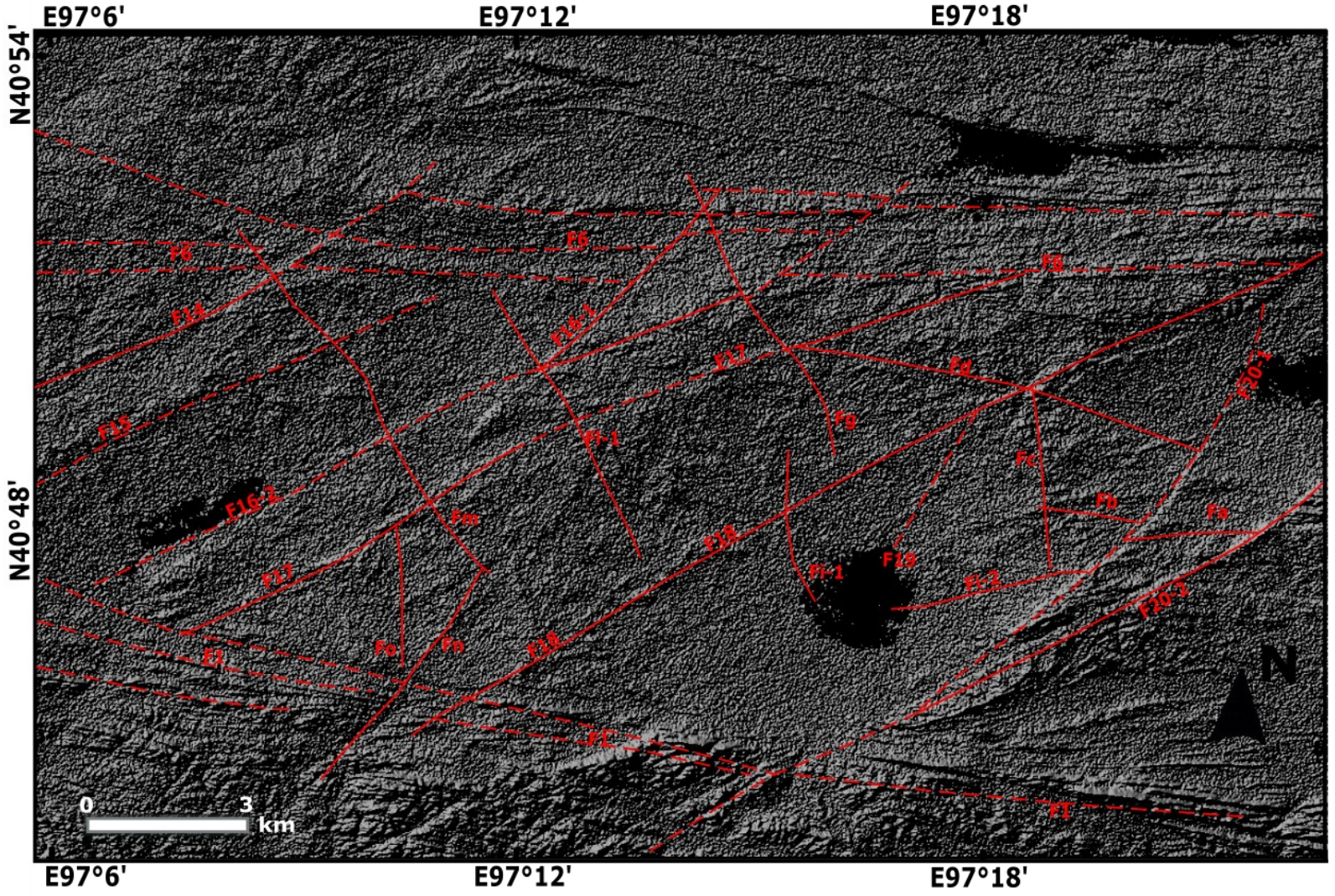


Figure 6.15 (G). The hill-shaded Digital Elevation Model map which overlays the location of active (solid lines) and inactive (dash lines) faults across the Jiujing study area. The figure is produced through the processing of DEM data in Figure 6.15 (F) using the QGIS Hillshade analysing tool.

Table 6.2 The characteristics of newly identified active faults in Jiujing region

Fault No.	Dipping direction	Vertical shearing Component	Lateral Shearing Component
F_a	South	Reverse	Sinistral
F_b	South	Reverse	Sinistral
F_c	East	Normal	--
F_g	Northeast	Reverse	Dextral
F_{i-1}	East	Reverse	--
F_{i-2}	North	Reverse	Sinistral
F_{l-1}	Southwest	Reverse	Dextral
F_m	East	Reverse	--
F_n	East	Reverse	--
F_o	East	Reverse	--

The fault interpretation and characterization in this section is assumes that the direction of maximum horizontal compression (σ1) in the Jiujing region ranges from N25°E to N45°E (N35°E in average). This is based on the in-situ stress measurements at Borehole BS01 introduced in Table 2.1, Section 2.2.3. σ1 is expected to align with the direction of horizontal movement (D_H), allowing for an estimation of the northing deformation rate (D_N) (method introduced in Section 4.4). To better describe the deformation patterns, the Jiujing region has been divided into 30 blocks, labelled from JJ1 to JJ30. The frequency distribution curves are presented to express the displacement rate difference between the blocks along the fault plane (Figure 6.16 A to G). The time-series analyses conducted across several major blocks (JJ3, JJ4, JJ5, JJ6, JJ7, JJ12, JJ19, and JJ21) presents the temporal variation of vertical displacement (shown in Figure 6.17 A to F and the original data is presented in Appendix Table S6 and S7). This is achieved through the averaging of the displacement values of thousands of PS points within each block (number presented in Table 5.2). Meanwhile, three cross-sections (AA', BB', and CC', Figure 6.18, 6.19, and 6.20) were generated to show the spatial distribution of vertical displacement.

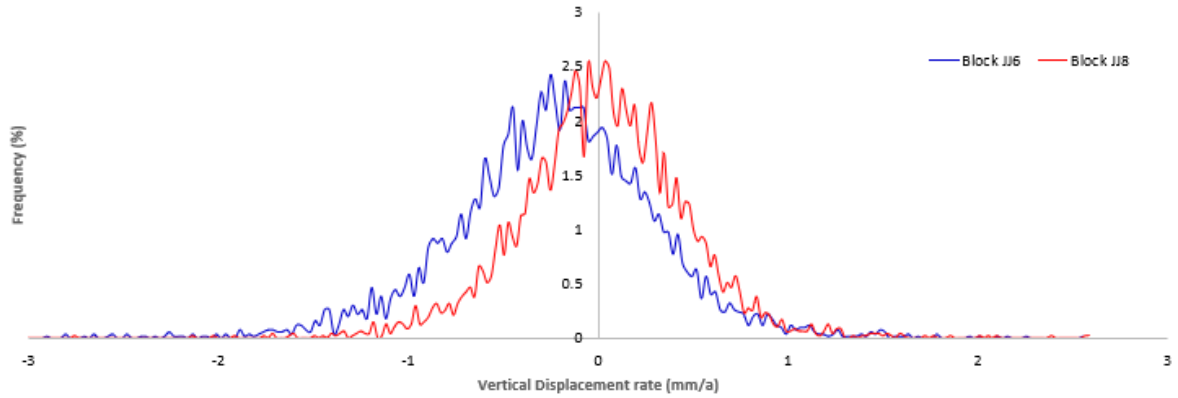


Figure 6.16 (A) illustrates the frequency distribution of vertical displacement rates (D_U) at Block JJ6 and JJ8. Statistically, around 68.6% scatterers at JJ6 are displacing downward and 51.7% at JJ8 are displacing upward. The means and standard deviations at JJ6 and JJ8 are -0.20±0.70 mma^{-1} and 0.02±0.43 mma^{-1} respectively.

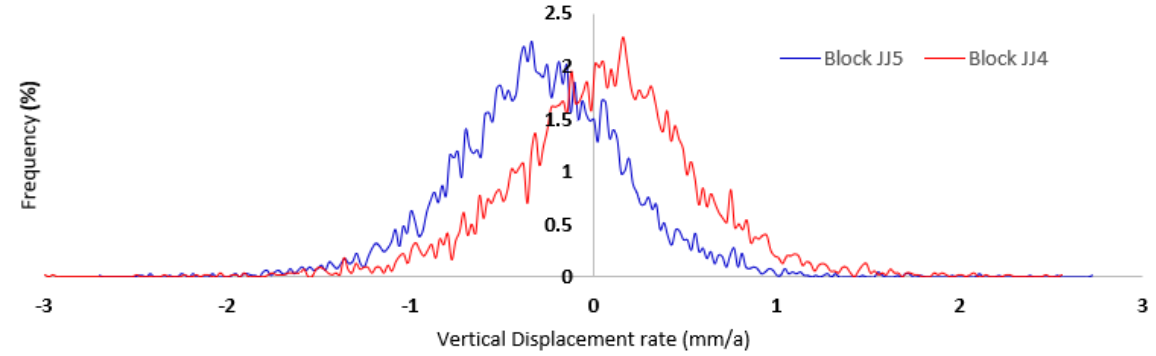


Figure 6.16 (B) illustrates the aerial frequency distribution of vertical displacement rates (D_U) at Block JJ5 and JJ4. Statistically, around 74.0% scatterers at JJ5 are displacing downward and 56.3% at JJ4 are displacing upward. The means and standard deviations at JJ5 and JJ4 are -0.26±0.51 mm a^{-1} and 0.06±0.53 mma^{-1} respectively.

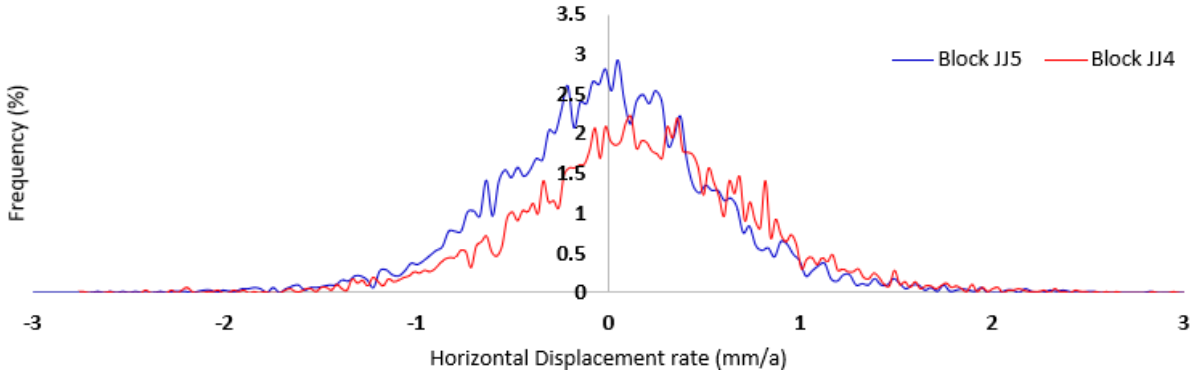


Figure 6.16 (C) illustrates the frequency distribution of easting displacement rates (D_E) at Block JJ5 and JJ4. Statistically, around 74.0% scatterers at JJ5 are displacing eastwards and 56.3% at JJ4 are displacing eastwards. The means and standard deviations at JJ5 and JJ4 are 0.02±0.59 mma^{-1} and 0.18±0.63 mma^{-1} respectively.

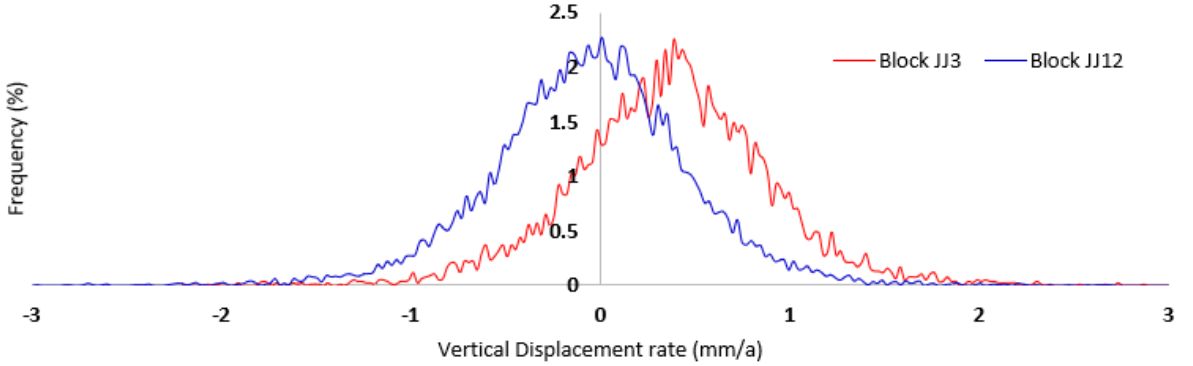


Figure 6.16 (D) illustrates the aerial frequency distribution of vertical displacement rates (D_U) at Block JJ3 and JJ12. Statistically, around 53.9% scatterers at JJ12 are displacing downward and 78.8% at JJ3 are displacing upward. The means and standard deviations at JJ3 and JJ12 are 0.42±0.53 mma^{-1} and -0.05±0.53 mma^{-1} respectively.

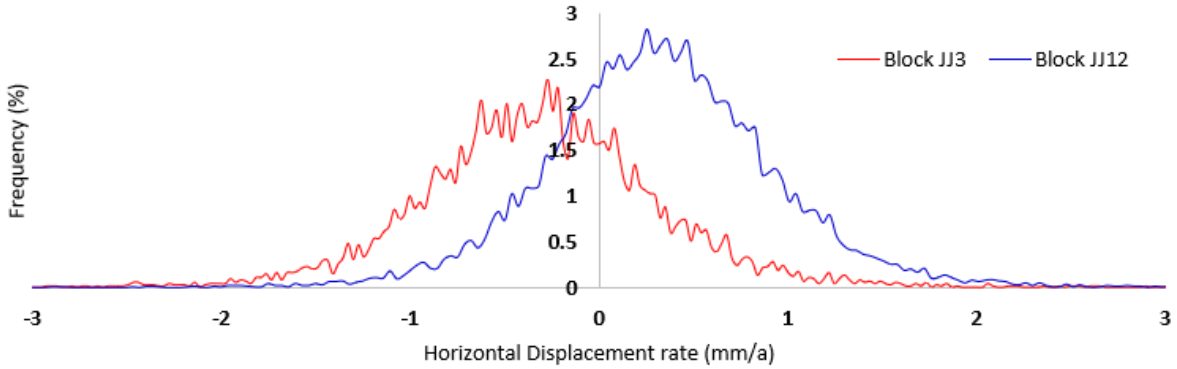


Figure 6.16 (E) illustrates the aerial frequency distribution of easting displacement rates (D_E) at Block JJ3 and JJ12. Statistically, around 72.6% scatterers at JJ12 are displacing eastwards and 72.1% at JJ3 are displacing westwards. The means and standard deviations at JJ3 and JJ12 are -0.26±0.66 mma^{-1} and 0.22±0.64 mma^{-1} respectively.

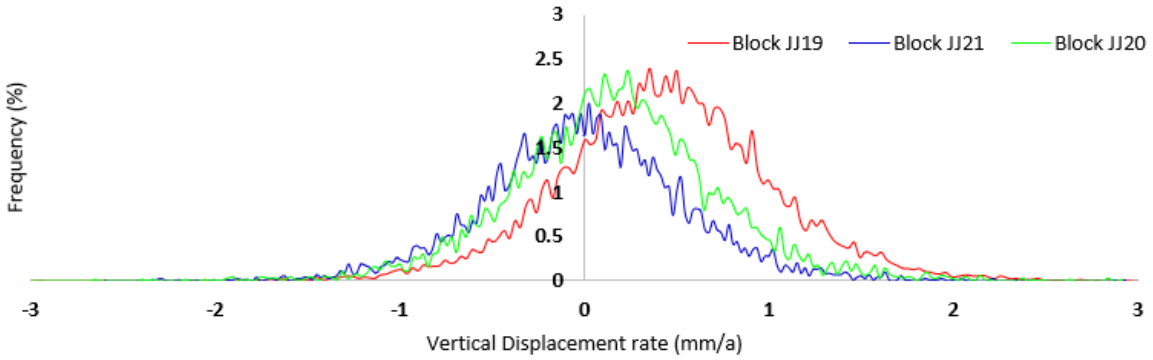


Figure 6.16 (F) illustrates the aerial frequency distribution of vertical displacement rates (D_U) at Block JJ19, JJ20 and JJ21. Statistically, around 79.7% scatterers at JJ19 are displacing upwards, 64.2% scatterers at JJ20 are displacing upwards, and only 50.4% scatterers at JJ21 are displacing upwards. The means and standard deviations at JJ19, JJ20 and JJ21 are 0.35±0.60 mma^{-1}, 0.16±0.59 mma^{-1}, and -0.03±0.58 mma^{-1} respectively.

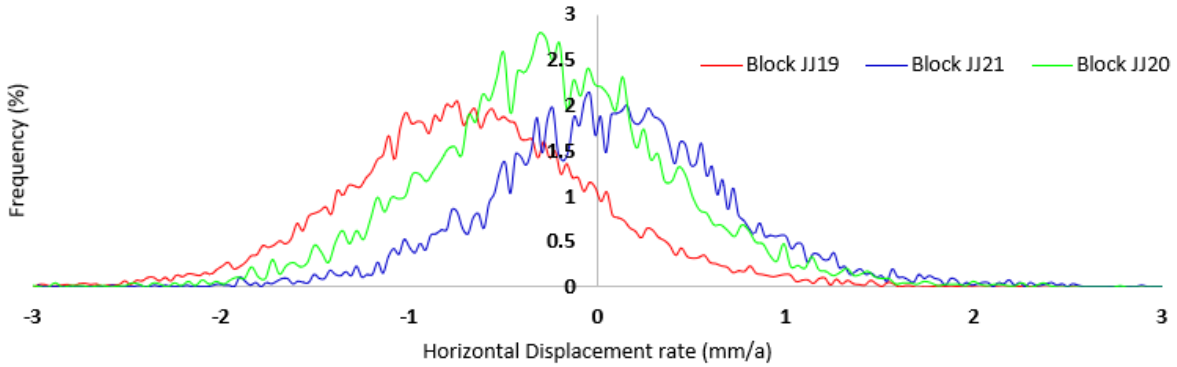
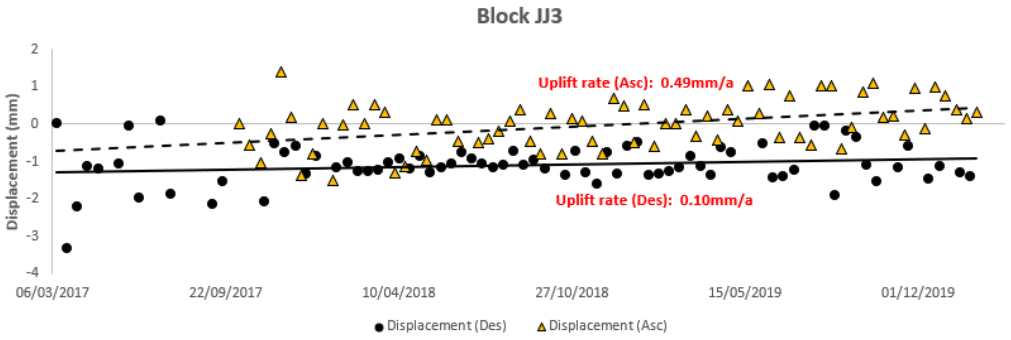
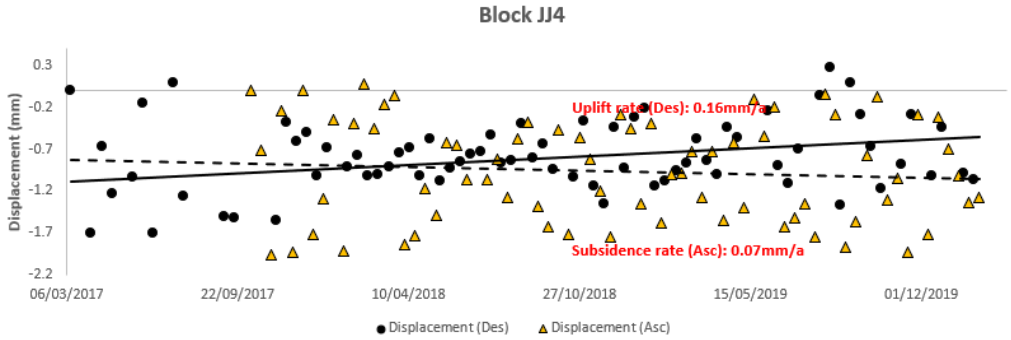


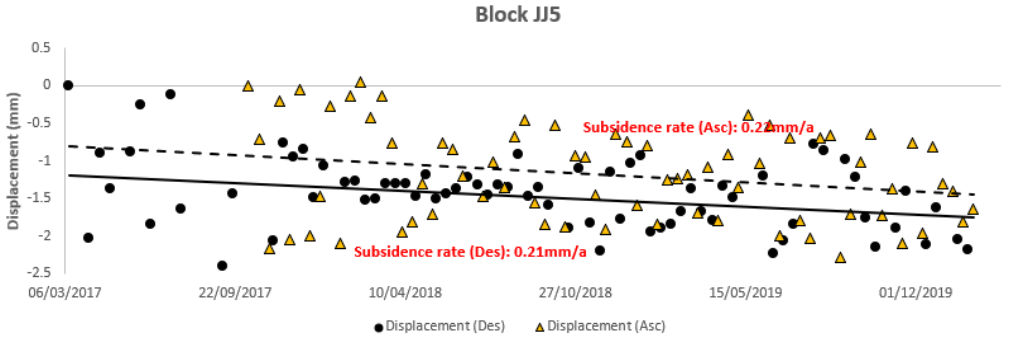
Figure 6.16 (G) illustrates the aerial frequency distribution of easting displacement rates (D_U) at Block JJ19, JJ20 and JJ21. Statistically, around 85.0% scatterers at JJ19 are displacing westwards, 66.7% scatterers at JJ20 are displacing westwards, and only 46.1% scatterers at JJ21 are displacing westwards. The means and standard deviations at JJ19, JJ20 and JJ21 are -0.54±0.69 mma^{-1}, -0.20±0.69 mma^{-1}, and 0.05±0.64 mma^{-1} respectively.


Block JJ3
Uplift rate (Asc): 0.49mm/a
Uplift rate (Des): 0.10mm/a
Displacement (mm)
2
1
0
-1
-2
-3
-4
06/03/2017
22/09/2017
10/04/2018
27/10/2018
15/05/2019
01/12/2019
Displacement (Des)
Displacement (Asc)

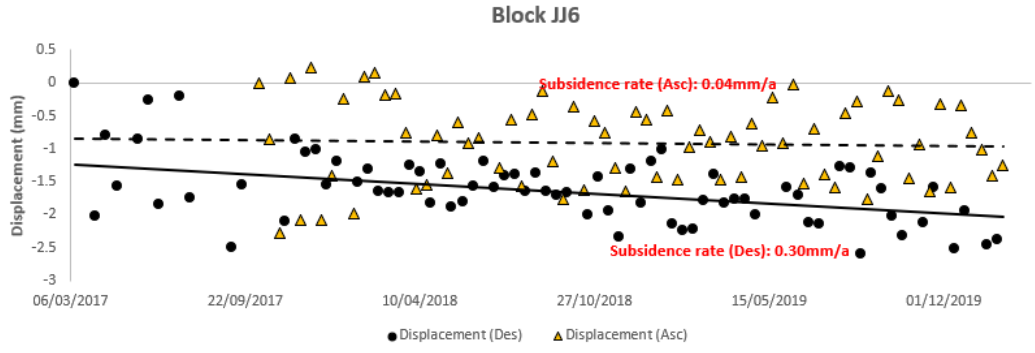
(A)


Block JJ4
Uplift rate (Des): 0.16mm/a
Subsidence rate (Asc): 0.07mm/a
Displacement (mm)
0.3
-0.2
-0.7
-1.2
-1.7
-2.2
06/03/2017
22/09/2017
10/04/2018
27/10/2018
15/05/2019
01/12/2019
Displacement (Des)
Displacement (Asc)

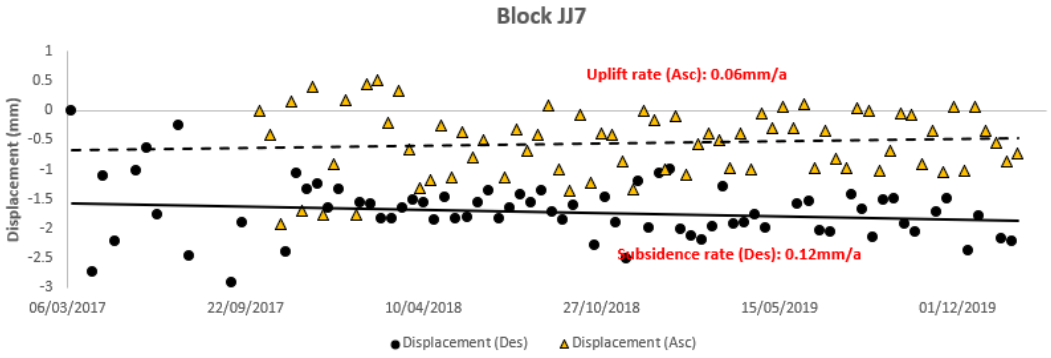
(B)


Block JJ5
Subsidence rate (Asc): 0.22mm/a
Subsidence rate (Des): 0.21mm/a
Displacement (mm)
0.5
0
-0.5
-1
-1.5
-2
-2.5
06/03/2017
22/09/2017
10/04/2018
27/10/2018
15/05/2019
01/12/2019
Displacement (Des)
Displacement (Asc)

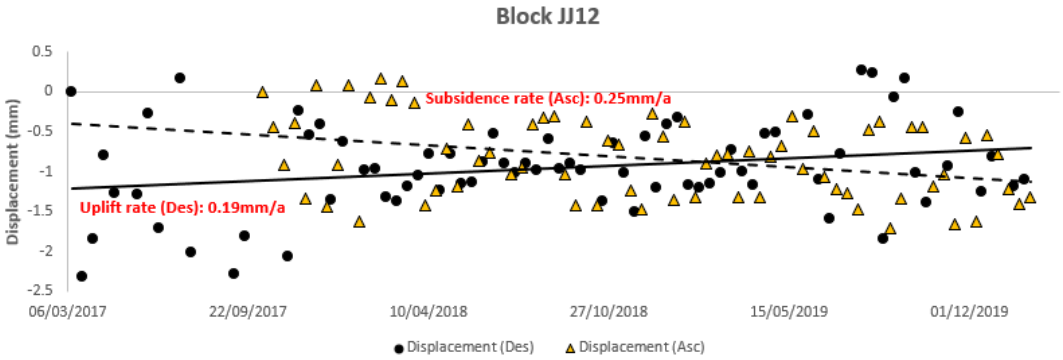
(C)


Block JJ6
Subsidence rate (Asc): 0.04mm/a
Subsidence rate (Des): 0.30mm/a
Displacement (mm)
0.5
0
-0.5
-1
-1.5
-2
-2.5
-3
06/03/2017
22/09/2017
10/04/2018
27/10/2018
15/05/2019
01/12/2019
Displacement (Des)
Displacement (Asc)

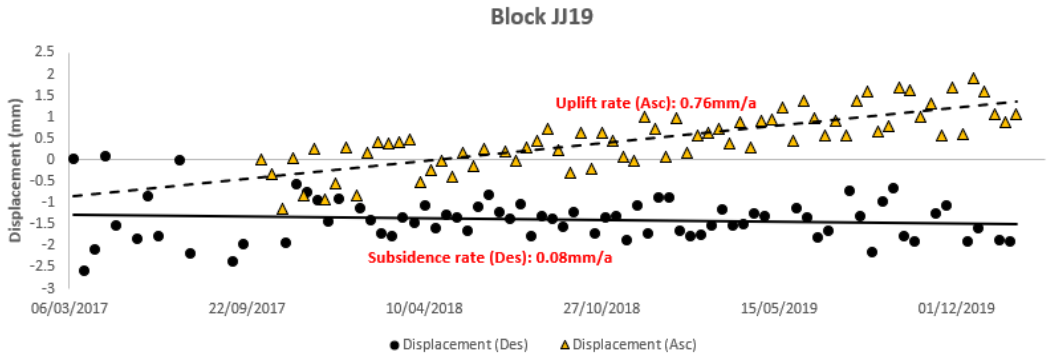
(D)



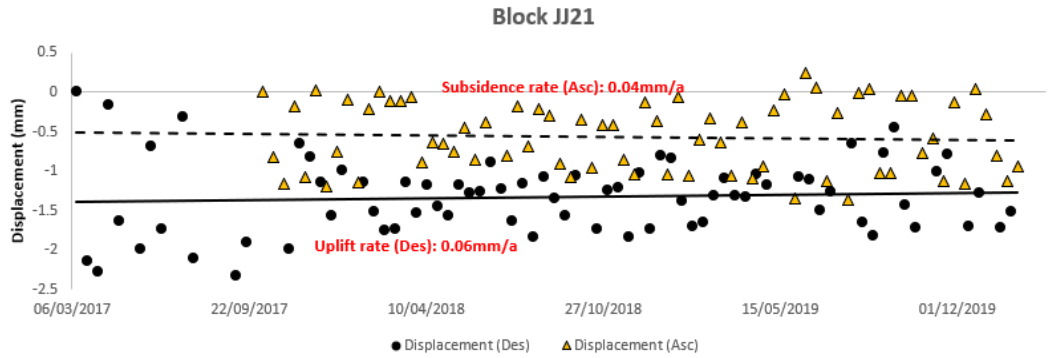
(E)



(F)



(G)



(H)

Figure 6.17 (A, B, C, D, E, and F). (A) The average time-series analysis for JJ6 along F_a. JJ6 subsided by 0.5mm from Oct 2017 to Feb 2020, equivalent to an annual rate around 0.2mm; (B) The average time-series analysis for JJ7 along F_a. JJ7 uplifted by 0.20 mm from Oct 2017 to Feb 2020, equivalent to an annual rate about 0.07 mm; (C) The average time-series analysis for JJ3 along F_g. JJ3 uplifted by 1.0 mm from Oct 2017 to Feb 2020, equivalent to an annual rate about 0.40 mm; (D) The average time-series analysis for JJ12 along F_g. JJ12 subsided by 0.5mm from Oct 2017 to Feb 2020, equivalent

to an annual rate about 0.2 mm a^{-1}; (E) The average time-series analysis for JJ19 along F_m, F_n and F_o. JJ19 uplifted by 1 mm from Oct 2017 to Feb 2020, equivalent to an annual rate around 0.40 mm; (F) The average time-series analysis for JJ21 along F_m, F_n and F_o suggests 21 subsidized slightly by 0.03 mm a^{-1} from Oct 2017 to Feb 2020.

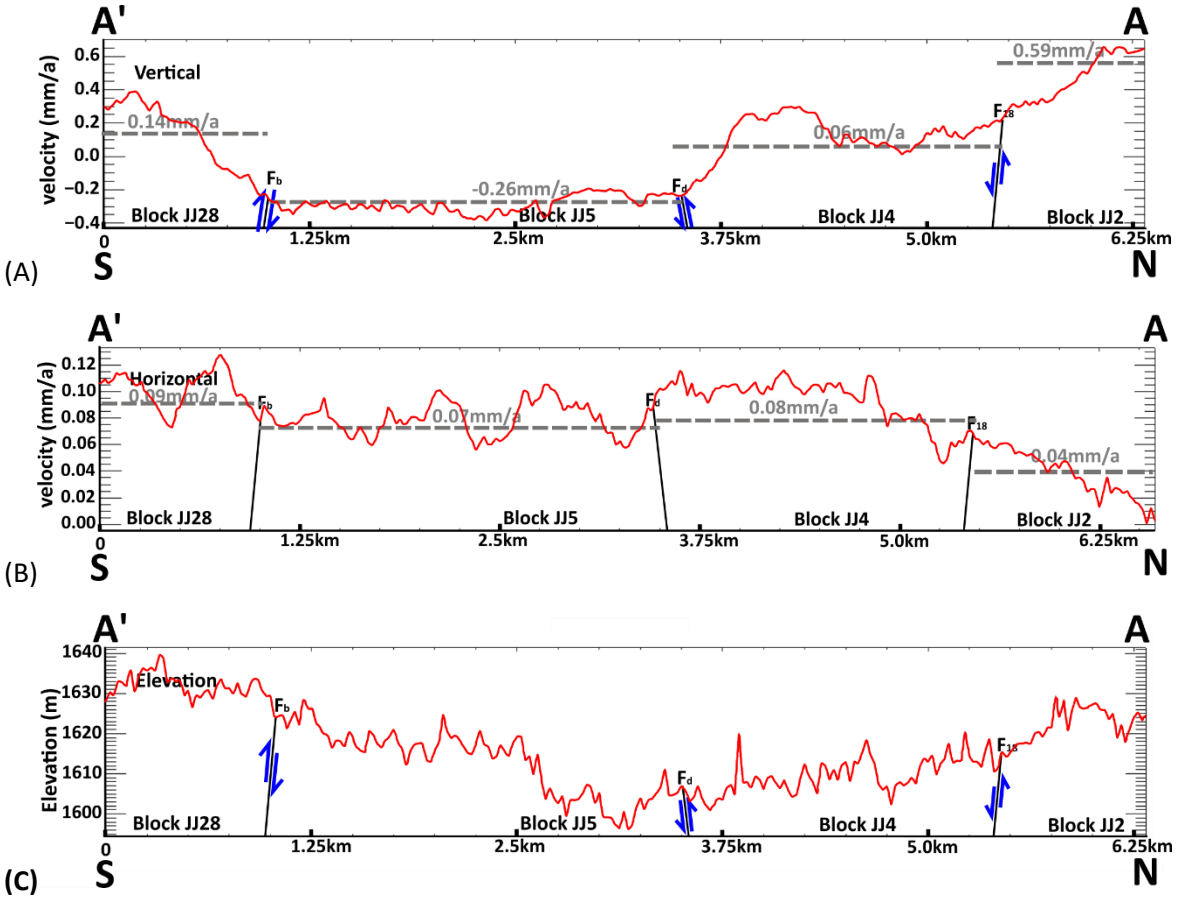


Figure 6.18 (A), (B) and (C). The distribution of vertical displacement (D_U), horizontal displacement (D_E), and elevation along cross-section AA' in Figures 6.15. This cross-section is formed from thousands of PS displacement values sampled along the cross-section line and shows the annual relative movements within each fault block. The faults marked are interpreted from the PS displacement maps, they are illustrative showing the sense of fault movement and general direction of faults. The horizontal gray dash lines highlighted the average displacement rates along the cross section over each block.

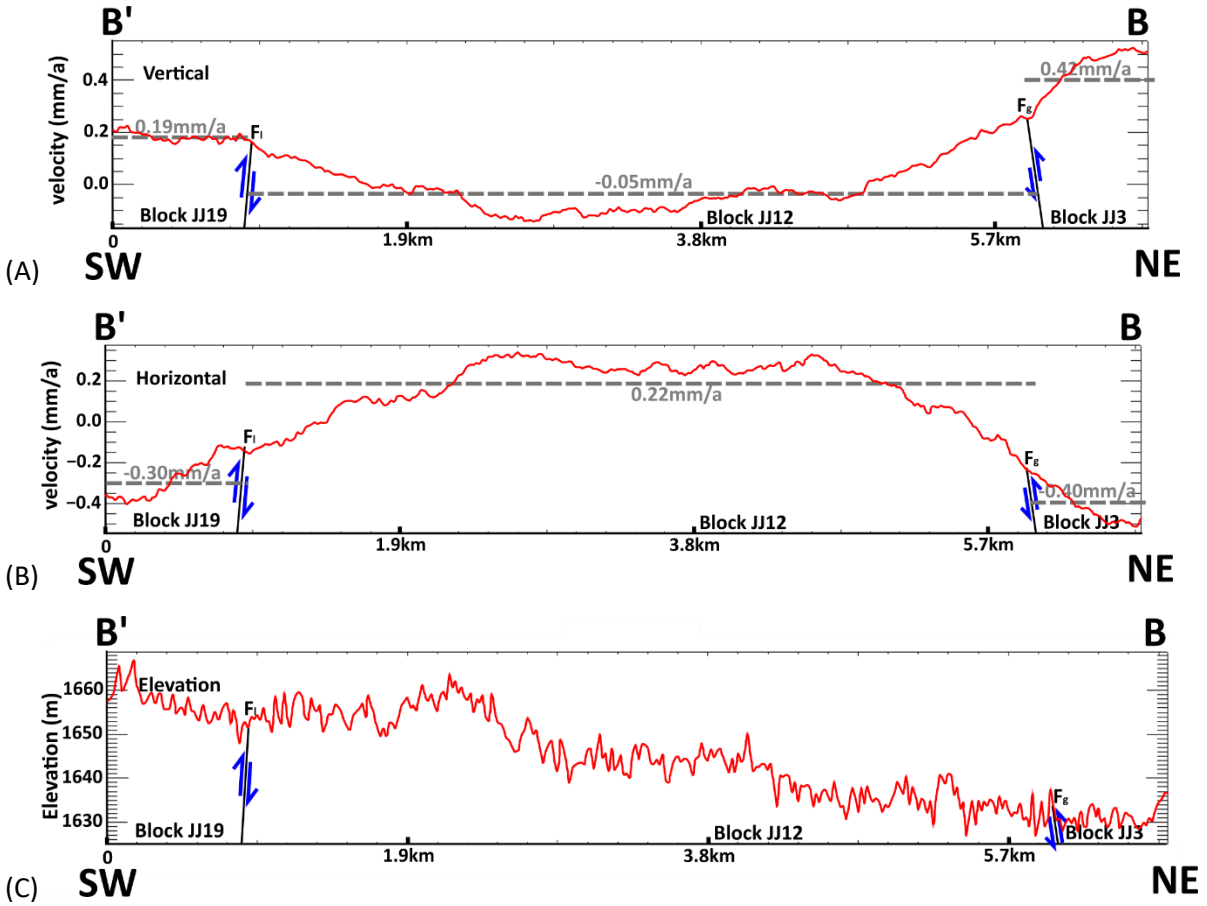
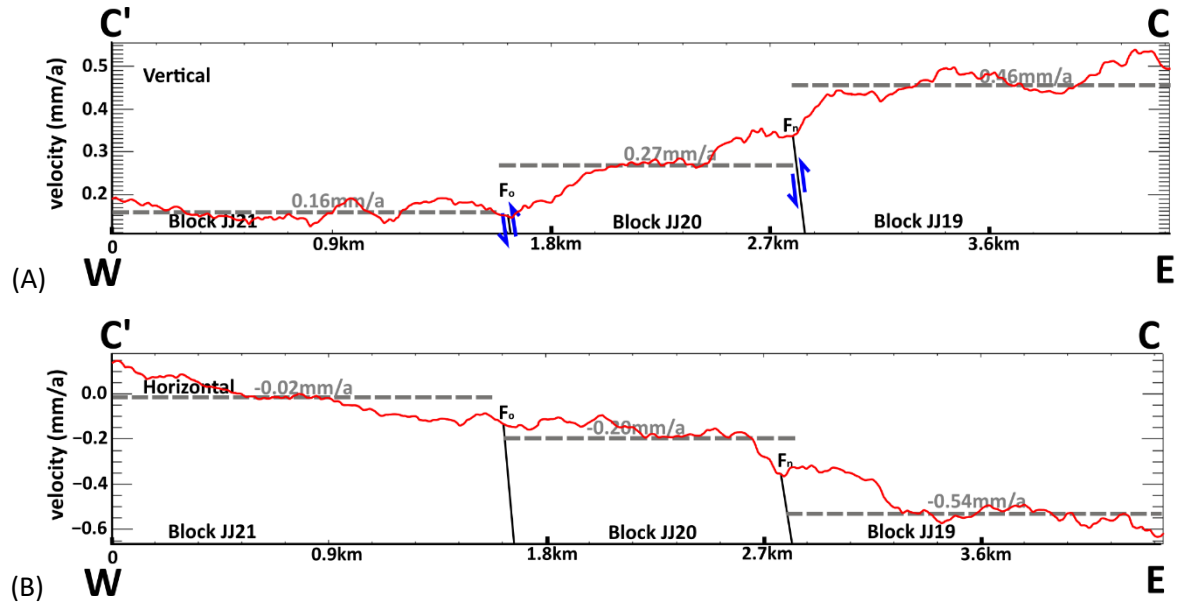
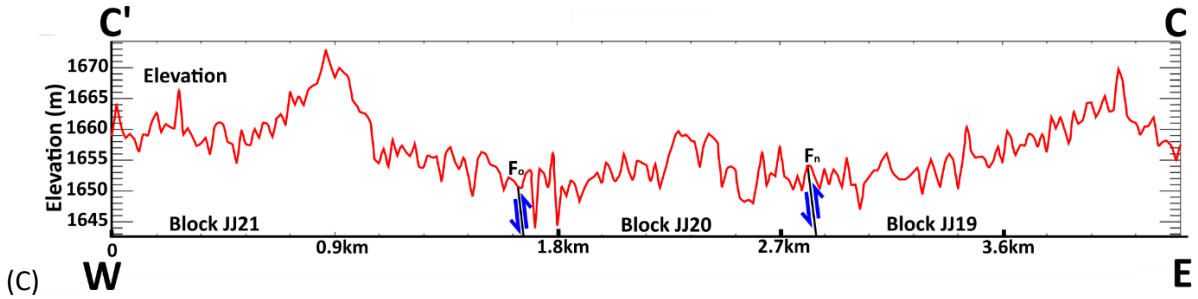


Figure 6.19 (A), (B) and (C). The distribution of vertical displacement (D_U), horizontal displacement (D_E), and elevation along cross-section BB' in Figures 6.15. This cross-section is formed from thousands of PS values sampled along the cross-section line and shows the annual relative movements within each fault block. The faults marked are interpreted from the PS, they are illustrative showing the sense of fault movement and general direction of faults. The horizontal gray dash lines highlighted the average displacement rates along the cross section over each block.





(C)

Figure 6.20 (A), (B) and (C). The distribution of vertical displacement (D_U), horizontal displacement (D_E), and elevation along cross-section CC' in Figures 6.15. This cross-section is formed from thousands of PS values sampled along the cross-section line and shows the annual relative movements within each fault block. The fault marked are interpreted from the PS, they are illustrative showing the sense of fault movement and general direction of faults. The horizontal gray dash lines highlighted the average displacement rates along the cross section over each block. The horizontal gray dash lines highlighted the average displacement rates along the cross section over each block.

6.4.1 Evidence of $F_{16\text{-}2}$, F_{17}, F_{18} and $F_{20\text{-}2}$ as active faults in modern time

The PSI results in Figures 6.15 (A to D) clearly show the NE-SW trending normal faults $F_{16\text{-}2}$, F_{17}, F_{18} and $F_{20\text{-}2}$ are still vertically active, where the PSI data show small but measurable movements along these known faults. These challenges accepted arguments [34, 49], which suggest that these faults are currently inactive. The direct evidence of this vertical movement comes from the patterns of D_U across the fault planes, where there is a clear difference in the relative vertical motion of the blocks on either side of the fault lines.

$F_{20\text{-}2}$ controls the eastern boundary of the Jiujing region. The eastern side of the fault (Block JJ8) has a maximum elevation difference of 90 m, with the Jiujing Basin on the western side of the fault (JJ6); caused by past tectonic activity [34, 49]. The Sentinel-1 data in Figure 6.15 (D) indicates the western side of $F_{20\text{-}2}$ in JJ6 is subsiding by 0.20 mm a^{-1} on average whilst the eastern side of the fault (JJ8) is uplifting by an average of 0.02 mm a^{-1}. This leads to a vertical displacement rate around 0.22 mm a^{-1}. This kind of D_U deviation between the two blocks have been presented in Figure 6.16 (A). These differences in vertical displacement rates and the relative subsidence at JJ6 confirm that $F_{20\text{-}2}$ is a normal fault dipping to the northwest [34, 49], where JJ6 and JJ7 form the hanging wall of that fault and are expected to move downwards relative to JJ8.

The PSI results also indicate the average displacement rates on the southern side of F_{18} (JJ4, JJ5, JJ9, JJ10, JJ11) range from −0.26 to 0.26 mm a^{-1}, while displacement of the northern side of the fault (JJ2, JJ3, JJ12 and JJ19) ranges from -0.05 to 0.60 mm a^{-1}. This shows F_{18} is a vertically active normal fault

dipping towards the southwest. This vertical velocity difference along cross section AA' in Figure 6.15 has been presented in Figure 6.18.

Conversely, the southern side of F_{17} (JJ2, JJ3, JJ12, JJ19, JJ20 and JJ21) is uplifting faster compared to the northern side (JJ1, JJ13, JJ17, JJ18 and JJ22). The vertical displacement rates on the southern and northern sides range from −0.05 to 0.6 mm a^{-1} and −0.41 to 0.33 mm a^{-1} respectively, indicating that F_{17} is a normal fault dipping towards the northwest, consistent with the literature.

In Figure 6.15 (D) along the fault $F_{16\text{-}2}$, between blocks JJ13 and JJ14, indicate the average vertical deformation patterns of JJ13 is uplifting (0.04 mm a^{-1}) and block JJ14 on the northern side of fault $F_{16\text{-}2}$ is subsiding (JJ14, -0.32 mm a^{-1}), confirming that $F_{16\text{-}2}$ is a northwest dipping normal fault, whereas the northern side of the fault (JJ14) is expected to subside relative to the southern side, showing this part of fault $F_{16\text{-}2}$ is vertically active.

In general, it is believed $F_{16\text{-}2}$, F_{17}, F_{18} and $F_{20\text{-}2}$ are more likely to be extensional rather than compressional. That is because these faults are generally NE-SW trending, which tend to be parallel with σ1. Based on the discussion in Section 6.2.1, the angle between fault planes and σ1 ($|\theta\text{-}\alpha|$) is highly likely to be low. This would lead to a very low compression (σ_{1v}) perpendicular to the fault but there is no clear deformation displacement along F_1, F_6, F_{14}, F_{15}, $F_{16\text{-}1}$, F_{19}, $F_{20\text{-}1}$, $F_{20\text{-}3}$, and $F_{20\text{-}4}$, either in vertical (D_U) or easting (D_E) directions. This agrees with the literature descriptions [34, 49] and suggests that these faults are currently inactive.

6.4.2 Thrust with sinistral strike-slip, F_a

The average vertical velocity difference between JJ6 (−0.20 mm a^{-1}) and JJ7 (-0.04 mm a^{-1}) suggests F_a is vertically active (Figure 6.15 (D)). The average time-series displacements of these two blocks along F_a are presented in Figures 6.17 (D) and (E), where the gradients of the linear trend lines show the rates of subsidence or uplift. A positive gradient refers to an upwards displacement and a negative gradient refers to a downwards displacement. This applies to all parts (A-H) of Figure 6.17.

The average horizontal velocity indicates JJ7 is relatively stable, with a westward deformation rate of only 0.15 mm a^{-1} (with descending and ascending viewed vertical velocity of -0.12mm a^{-1} and 0.06 mm a^{-1} respectively). Meanwhile, the northern side (JJ6) has an average westward deformation rate of 0.20 mm a^{-1} (with descending and ascending viewed vertical velocity of -0.30 mm a^{-1} and -0.04 mm a^{-1} respectively), indicating a low sinistral shear sense along F_a.

Based on the method introduced in Section 4.4 to calculate D_H, it can be estimated that JJ6 is moving towards the southwest at a higher velocity than JJ7, which indicates a crustal shortening along F_a. The uplift of JJ7, relative to JJ6, suggests JJ7 is in the hanging wall of the reverse fault, meaning F_a is dipping towards the south.

6.4.3 Factors contributing the subsidence of block JJ5

Block JJ5 is subsiding by 0.26 mm a^{-1} (Figure 6.15 (D)), this likely caused by movements on F_c, F_b and F_d. Along F_b, JJ28 (southern side) and JJ5 (northern side) are displacing eastwards by 0.09 mm a^{-1} and 0.02 mm a^{-1} respectively (Figure 6.15 (C)). JJ5 is clearly stable (with very similar ascending and descending viewed displacements) but based on the orthogonal decomposition of maximum velocity (§3.6), JJ28 is displacing towards the northeast (N35°E) at 0.16 mm a^{-1}, indicating crustal shortening along F_b in the direction of northeast and that F_b is a reverse fault. The vertical deformation pattern in Figure 6.15 (D) indicates JJ28 has an average uplift rate of 0.14 mm a^{-1}, whereas JJ5 has subsided by 0.26 mm a^{-1}. This indicates F_b is dipping towards the south and JJ28 is the hanging wall of the reverse fault.

F_c appears to be another active fault causing the subsidence of JJ5. JJ5 is horizontally stable while, as shown in Figure 6.15 (C), JJ9 (the west side of F_c) is displacing towards the west by 0.33 mma^{-1}. This indicates crustal extension along F_c in an east-west direction. Figure 6.15 (D) also shows a vertical velocity contrast between the eastern and western sides of F_c, where JJ9 is uplifting by 0.17 mma^{-1} on average, whilst JJ5 is subsiding (-0.26 mma^{-1}). These indicate JJ9 and JJ5 represent the footwall and hanging wall of F_c respectively, and that F_c is a normal fault dipping towards the east.

The difference in vertical displacement between JJ5 (subsidence rate 0.26 mm a^{-1}) and JJ4 (uplift rate 0.06 mm a^{-1}) is 0.32 mma^{-1}, shown in Figure 6.15 (D), Figure 6.16 (B) and Figure 6.18 (A), which indicates that F_d is vertically active. There is no visible horizontal deformation displacement along F_d, whereas the E-W displacements along the two sides of the fault plane are similar, according to Figures 6.15 (C), 6.16 (C) and 6.18 (B). This indicates F_d is horizontally inactive. Since F_d is NW-SE oriented and because the entire Jiujing granite pluton region is influenced by a NE-SW direction maximum principal compression, F_d is more likely to be compressional than extensional. According to the vertical deformation pattern in Figure 15 (D), it can be estimated that F_d is northward dipping. In this way, JJ5 is part of the F_d footwall.

There are significant D_U discontinuities and indistinct or gradational D_E discontinuities along F_d, as discussed in Section 6.2.1, which is likely because σ1 tends to be perpendicular to the fault plane (|θ-

α|=90°), where σ1H tends to be 0 and the impacts of σ1V are maximized. As illustrated in Figure 6.21, F_d is NW-SE trending, and the estimated striking angle (θ) is around 118°. If σ1 is perpendicular to F_d, the direction of σ1 (α) can be estimated as N28°E. This agrees with the in-situ stress measurements at Borehole BS01, which indicate θ ranges from N25°E to N45°E. Hence, it can be confirmed F_d is being impacted by σ1, which is perpendicular to the fault plane.

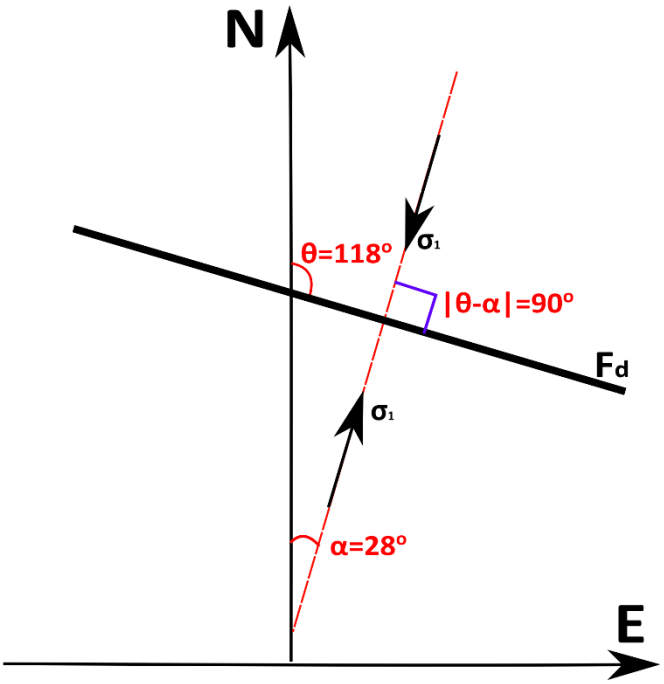


Figure 6.21 The schematic figure illustrates the spatial correlation between F_d and the maximum horizontal compression (σ1). σ1 tends to be in perpendicular to F_d, this leads to little horizontal shearing along fault plane.

$F_{20\text{-}1}$ is a normal fault dipping towards the northwest [34, 49] and JJ5 is a part of the $F_{20\text{-}1}$ hanging wall in theory. The PSI data in Figure 6.15 (D) indicate a slight vertical displacement rate difference between the two sides of $F_{20\text{-}1}$, where JJ5 (the western side) is subsiding on average 0.26 mma^{-1} more than JJ6 (subsiding at 0.20 mma^{-1}). In conclusion, JJ5 is the normal faults' hanging wall of F_c and F_d and the reverse fault footwall of F_b. The combined effect of F_c, F_b, and F_d contributes to the overall subsidence of JJ5.

6.4.4 Eastwards/north-eastwards dipping reverse faults, F_g and $F_{i\text{-}1}$

Along fault F_g (Figure 6.15 (C)) the eastern side JJ1 and JJ3 are displacing towards the west by 0.46, and 0.26 mm a^{-1} respectively, meanwhile, blocks on the western side of the fault (JJ12, JJ13 and JJ14) are moving towards the east by 0.22, 0.22 and 0.29 mm a^{-1} respectively. This indicates a crustal convergence along F_g, showing it is a reverse fault (Figure 6.16 (E)).

Figure 6.15 (D) shows JJ1, JJ2 and JJ3 on the eastern side of F_g are uplifting by 0.33 to 0.60mma^{-1}, meanwhile, on the western side, JJ13 is uplifting by only 0.04 mm a^{-1}, whilst JJ12 and JJ14 are subsiding by an average of 0.05 and 0.32 mm a^{-1} respectively. This kind of vertical displacement difference is clearly illustrated by the cross-section BB' in Figure 19 and by the average time-series analyses from both descending and ascending views at JJ3 (Figure 6.17 (A)) and JJ12 (Figure 6.17 (F)), illustrating vertical deformation rate variability along F_g (Figure 6.16 (D)). Generally, the blocks on the eastern side are moving upwards relative to those on the western side, indicating they are part of a reverse fault hanging wall and that F_g is dipping towards the northeast.

Similarly, when comparing the average vertical (Figure 6.15 (D)) and horizontal (Figure 6.15 (C)) deformation rates at JJ11 and JJ12 on the western side and JJ10 on the eastern side, it can be speculated that F_{i-1} is another east-dipping reverse fault.

6.4.5 Northwards dipping reverse fault, F_{i-2}

F_{i-2} is another reverse fault, where JJ9 and JJ11 lie on northern and southern sides respectively. JJ11 lies on the southern side of F_{i-2}; horizontally it is displacing towards the east by 0.27 mm a^{-1}, whilst the northern side of the fault (JJ9) is displacing towards the west by 0.33 mm a^{-1}. This indicates a sinistral shear sense on F_{i-2}, and since the maximum compressive stress is in a north-easterly direction (average N35°E) [33, 49], based on the method introduced in Section 3.6, it is estimated that JJ11 displaces towards the northeast by 0.47 mm a^{-1} and JJ9, on the northern side of $F_{i-2,}$ displaces towards the southwest by 0.58 mm a^{-1}. This kind of crustal convergence indicates a shortening along F_{i-2} and thus F_{i-2} is a reverse fault. Vertically, Figure 6.15 shows JJ11 is subsiding by *ca* 0.18 mm a^{-1}, whilst JJ9 on the northern side of the fault is uplifting by *ca* 0.17 mma^{-1}. This indicates that JJ11 and JJ9 represent the footwall and hanging wall sides of F_{i-2} respectively, and that F_{i-2} is dipping towards the north.

6.4.6 The major thrust along F_m, F_n and F_o

On the western side of F_m, Figure 6.15 (C) shows JJ22 and JJ30 are displacing slightly towards the east by 0.06 and 0.01 mm a^{-1} respectively and JJ20 and JJ29 on the eastern side are displacing towards the west by 0.20 and 0.03 mm a^{-1}. Meanwhile, as mentioned above, JJ16, JJ17, and JJ19 on the east side of F_m are displacing westwards by 0.10 to 0.54 mm a^{-1}. Therefore, F_m has been interpreted as a reverse fault due to the crustal convergence along it. Figure 6.15(C) also shows that both JJ20 and JJ19 are moving westwards but JJ19 is moving at an average rate of 0.54 mm a^{-1} which is higher than that at JJ20 moving at an average rate of 0.20 mm a^{-1}. This generates a crustal shortening along F_n and may be interpreted as a reverse fault.

Vertically, JJ16, JJ17 and JJ19 on the eastern side of F_m and F_n are uplifting by 0.16 to 0.35 mm a^{-1}; whilst JJ30, JJ29 and JJ22 on the western side of F_m is subsiding by 0.33, 0.28 and 0.41 mm a^{-1} respectively. JJ20 is uplifting, but the rate of uplift (0.16 mm a^{-1}) is lower than its eastern counterpart JJ19, which is uplifting at 0.35 mm a^{-1}. These all indicate the western side blocks are generally moving downwards relative to eastern side fault blocks along F_m and F_n, suggesting F_m and F_n are eastward dipping reverse faults, where Blocks JJ16, JJ17 and JJ19 are part of the hanging wall and JJ30, JJ29 and JJ22 are the footwall.

Fault F_o is another east-dipping reverse fault generated by the convergence of JJ20 and JJ21 shown in Figures 6.15 C and D, where the east side (JJ20) is displacing towards the west by 0.20 mma^{-1} and is uplifting by 0.16 mma^{-1}, and the western side of the fault (JJ21) is displacing towards the east by 0.05 mm a^{-1} and subsiding by 0.03 mma^{-1}. This kind of horizontal crustal shortening indicates F_o is a reverse fault, and the uplift of JJ20 relative to JJ21 indicates that JJ20 is part of the hanging wall and F_o is dipping towards the east.

In general, due to the impact of F_m, F_n and F_o, JJ21 is subsiding at 0.03 mm a^{-1} whilst JJ20 is uplifting at 0.16 mm a^{-1} and JJ19 has the greatest rate of uplift at 0.35 mm a^{-1}. This shows the average time-series analyses at JJ19, JJ20 and JJ21 (cross-section CC', Figure 6.20) have a stepped vertical displacement pattern with gradual uplift from west to east. These has been illustrated in Figure 6.16 (F, G) and Figure 6.20 respectively.

6.4.7 Thrust fault with dextral strike-slip, F_{I-1}

Horizontally, on the western side of F_{i-1}, the PSI data in Figure 6.15C show that JJ16, JJ17, and JJ19 are displacing towards the west by 0.10, 0.29, and 0.54 mma^{-1} respectively, whilst, as mentioned above, JJ12 to JJ15 on the eastern side of F_{i-1} are displacing eastwards by 0.12 to 0.22 mma^{-1}. As summarized in Table 5.2, this is demonstrated in the ascending data by uplifting displacement of blocks JJ16, JJ17 and JJ19 and subside displacement of blocks JJ12 and JJ15. This kind of crustal divergence indicates F_{I-1} is a normal fault but this interpretation assumes that maximum horizontal displacement is homogeneous across the entire granite section. If this is the case, a possible explanation for F_{I-1}'s extensional feature is F_m formed a thrust ramp fold with F_g, followed by F_{I-1} then forming a graben along the top of the thrust ramp fold which is behind and parallel to the primary thrust (F_m). This is mainly due to the compressional variation between the two sides of the fault plane, therefore the lower compression along one side leading to an extension along the fault plane.

However, since the entire Jiujing granite pluton is dominated by a NE-SW trending compression, the existence of extensional structures F_{l-1} is kinematically and mechanically incompatible with the compressional structures such as F_m and F_g; In this way, another more convinced explanation is that F_{l-1} is a dextral reverse fault, dipping to the southwest, as illustrated in Figure 6.22. This could initially be triggered by a NE-SW maximum compression (σ_1) at a very low angle with the fault plane (Step 1). Based on the previous hypothesis that D_H should generally be in line with σ_1, where the east (JJ12-15) and west side (JJ16, JJ17, JJ19) blocks are expected to converge, pushing the east side blocks (JJ12-15) towards the southwest and pushing the west side blocks (JJ16, JJ17, JJ19) towards the northeast. However, the maximum compression (σ_1) may not always be homogeneous across the entire granite section. The impeding and resisting of the opposite blocks may change the direction of σ_1, converting it to NW-SE trend due to the internal shearing around F_{l-1} (Figure 6.22, Step 2). The horizontal component (σ_H) leads to a right-lateral sliding along the fault plane, where the east side (JJ12, JJ13, JJ14 and JJ15) and west side (JJ16, JJ17 and JJ19) are displacing towards the southeast and northwest respectively. This might be the most persuasive theory to explain the existence of this divergent pattern along F_{l-1} in Figure 6.15 (C) in the compressive direction. Vertically, the uplifting of JJ16, JJ17 and JJ19 and the relative subsidence of JJ12 to JJ15 (shown in Figure 6(D)) indicate that the hanging walls lie to the west and the footwalls to the east of these reverse faults respectively, which suggests F_{l-1} is westwards dipping.

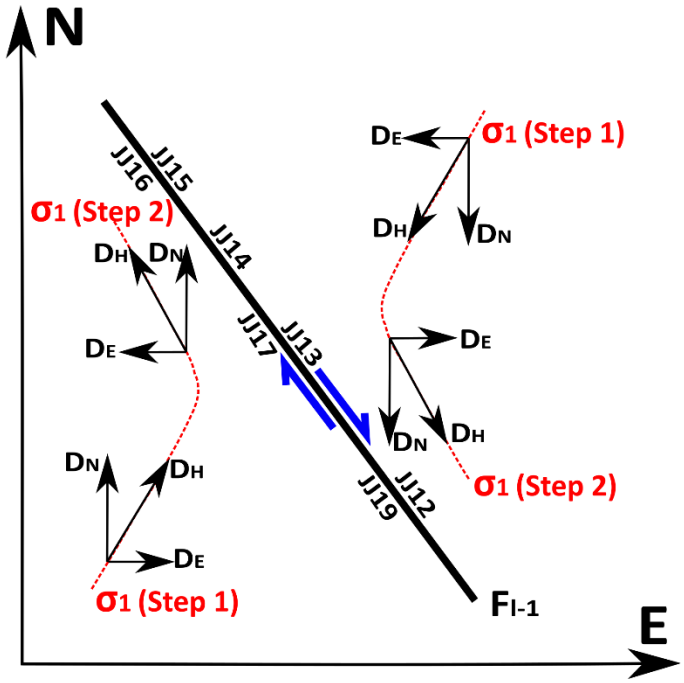


Figure 6.22 A schematic figure illustrating the direction of σ_1 and D_H in Step 1 and 2 due to direction change and the two horizontal deformation components (D_E and D_N) along F_{l-1}. This leads to dextral strike slip along the fault plane, so that JJ12 to JJ15 are finally sliding towards the southeast and JJ16, JJ17 and JJ19 are sliding towards northwest.

6.4.8 Summary

As a part of a convergent wrench fault zone, the maximum compressive stress in NE-SW direction leads to the crustal shortening in the NE-SW direction and in turn, this leads to the formation of reverse faults (mostly trending NW-SE and/or E-W) F_a, F_b, F_g, F_{i-1}, F_{i-2}, F_m, F_n and F_o. Meanwhile, the NW-SE direction is relatively elongated due to low compression, which may generate NE-SW trending normal faults such as F_{20-2}, F_{20-1}, F_{18}, F_{17}, F_{16-2}, F_{15} and F_{14}. The superposition of above compressional and extensional structures leads to the surface deformation in Figure 6.15 (A, B, C and D). Especially for vertical deformation (D_U), this section argues the impacts of NW-SE and/or E-W trending reverse faults are more prominent than NE-SW extensional structures.

6.5 Characterizing the active faults at Xinchang granite outcrop

This section aims to investigate the on-going active faults at Xinchang granite outcrop. The interpretation is based on the precondition that the Xinchang study region is impacted by a maximum compression (σ1) with direction range from N45°E to N77°E (the average is around N60°E) [33, 49] which has been measured in boreholes BS06, BS017, BS018, and BS019 and the data are presented in Table 2.2). This allows for the estimation of D_N and in turn supports the fault characterization.

Figures 6.23 (A), (B), (C), and (D) show the patterns of D_{los}^{asc}, D_{los}^{des}, D_U and D_E and the traced active faults in the Xinchang region. This research compares these deformation patterns with the structural geology map, concluding that F_{22-4}, F_{29-1}, F_{29}, F_{31} and F_6 are still active or partially active, before tracing four previously unknown active faults (labelled as F_a, F_b, F_e and F_h). Their characteristics are summarized in Table 6.3 and detailed explanations are presented in sub-sections 6.5.1 to 6.5.5.

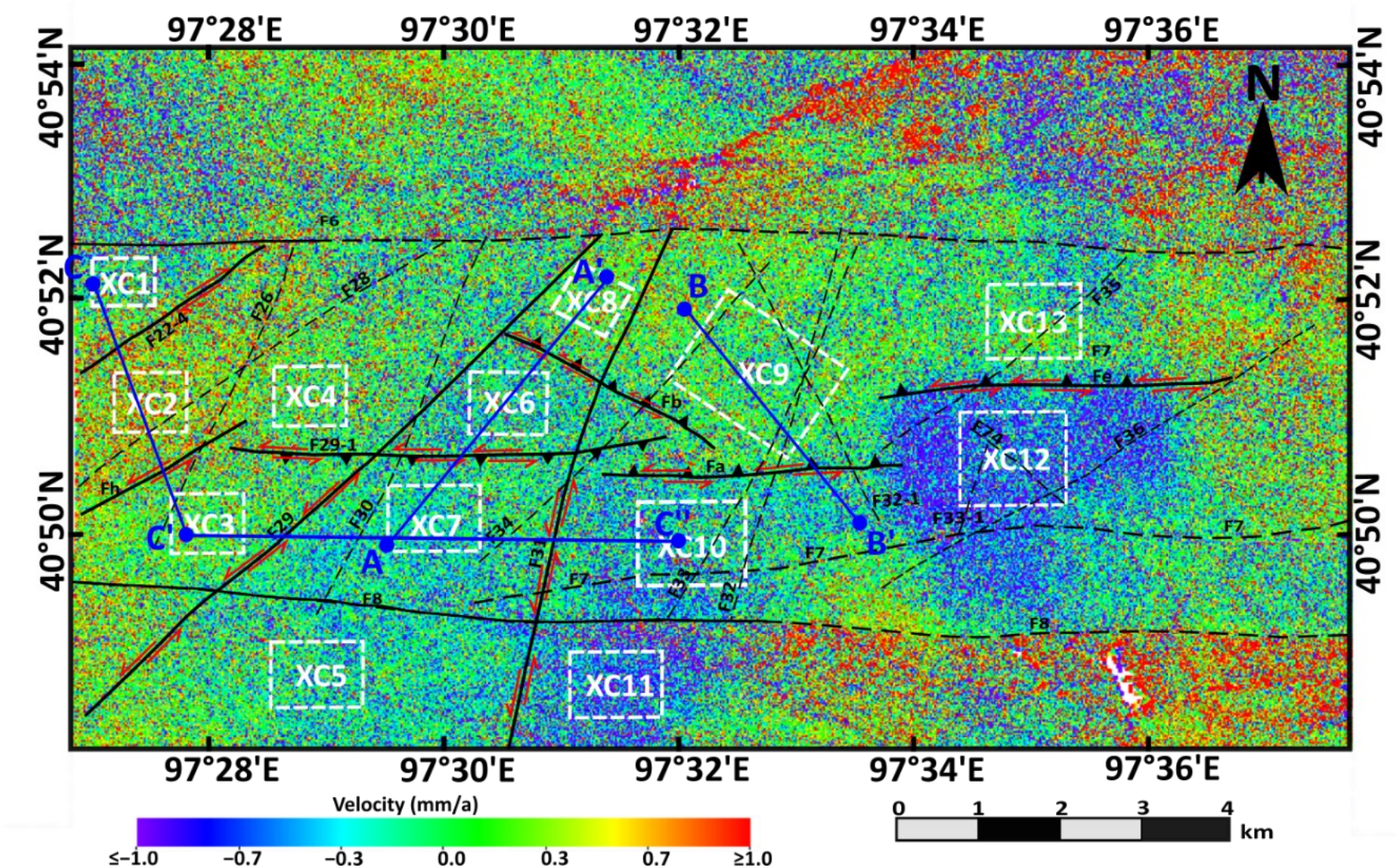


Figure 6.23 (A). The pattern of LoS displacement at Xinchang region in ascending orbit (D_{los}^{asc}), where the positive values (upper, red side of colour axis) refer to the uplift and negative values (lower, blue side of colour axis) refers to subsidence. It illustrates the correlations between active faults and deformation patterns.

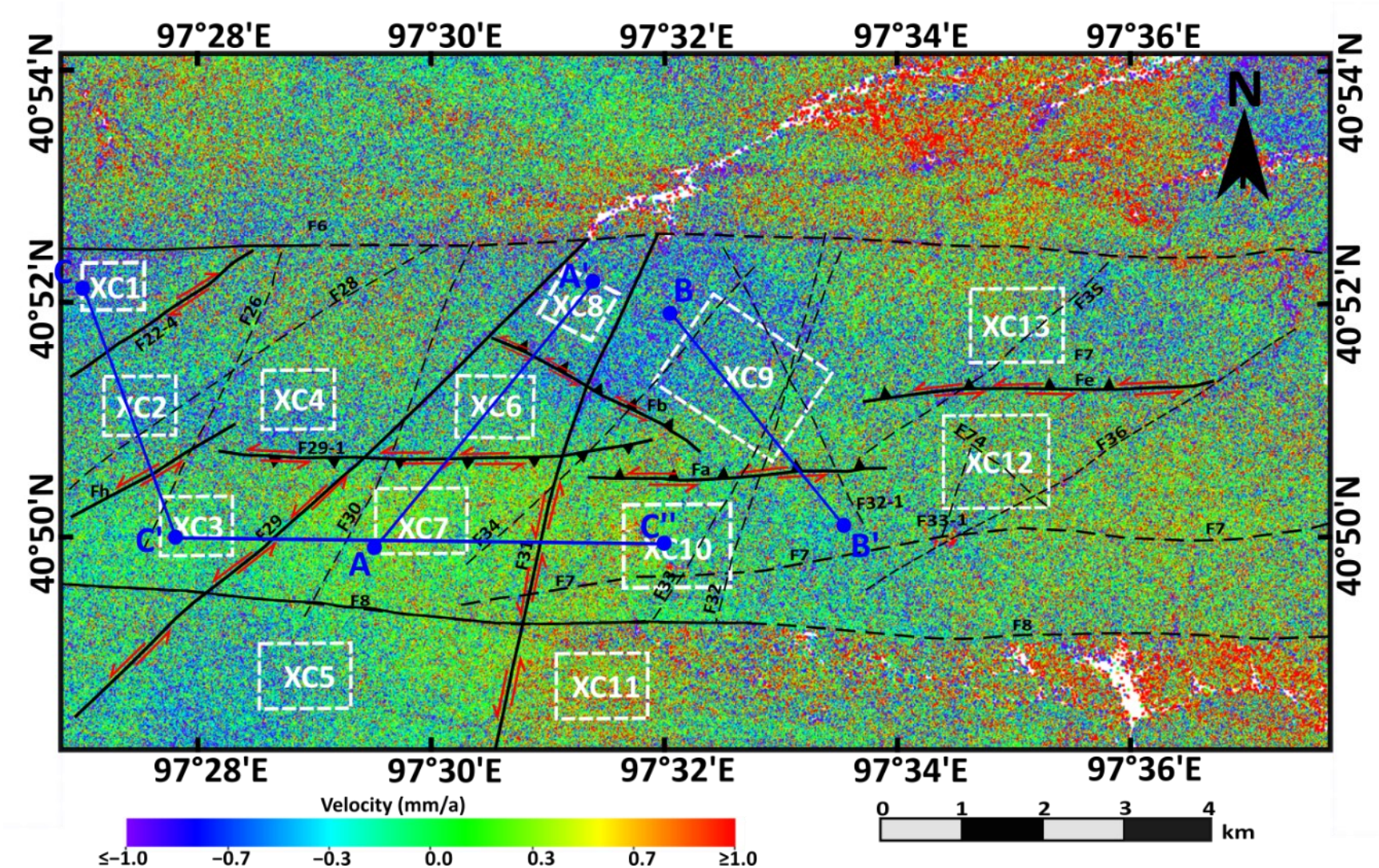


Figure 6.23 (B). The pattern of LoS displacement at Xinchang region in descending orbit (D_{los}^{des}), where the positive values (upper, red side of colour axis) refer to the uplift and negative values (lower, blue side of colour axis) refers to subsidence. It illustrates the correlations between active faults and deformation patterns.

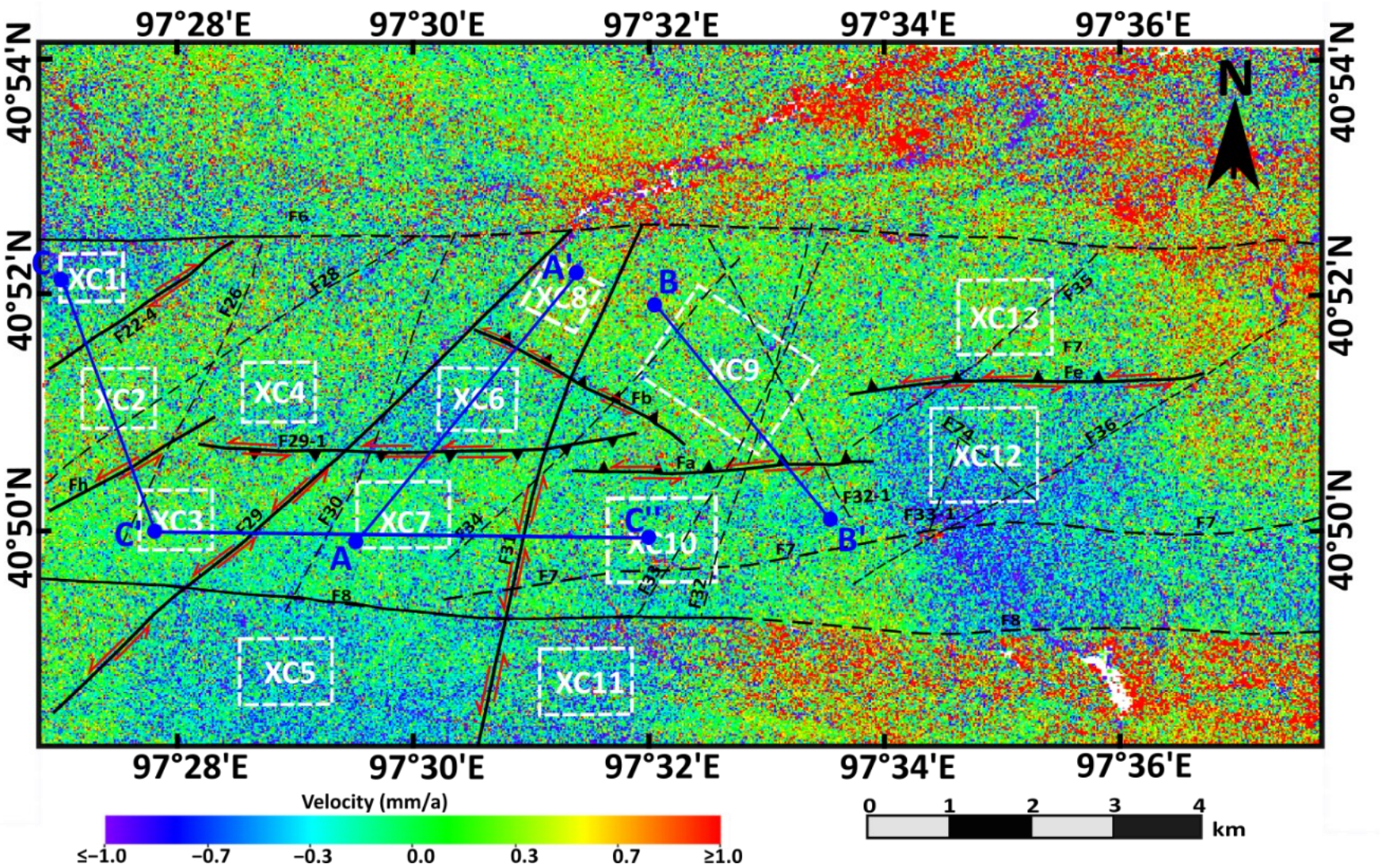


Figure 6.23 (C). The pattern of vertical displacement (D_U) at Xinchang region computed through the combination of ascending and descending data, where the positive values (upper, red side of colour axis) refer to the uplift and negative values (lower, blue side of colour axis) refers to subsidence. It illustrates the correlations between active faults and deformation patterns.

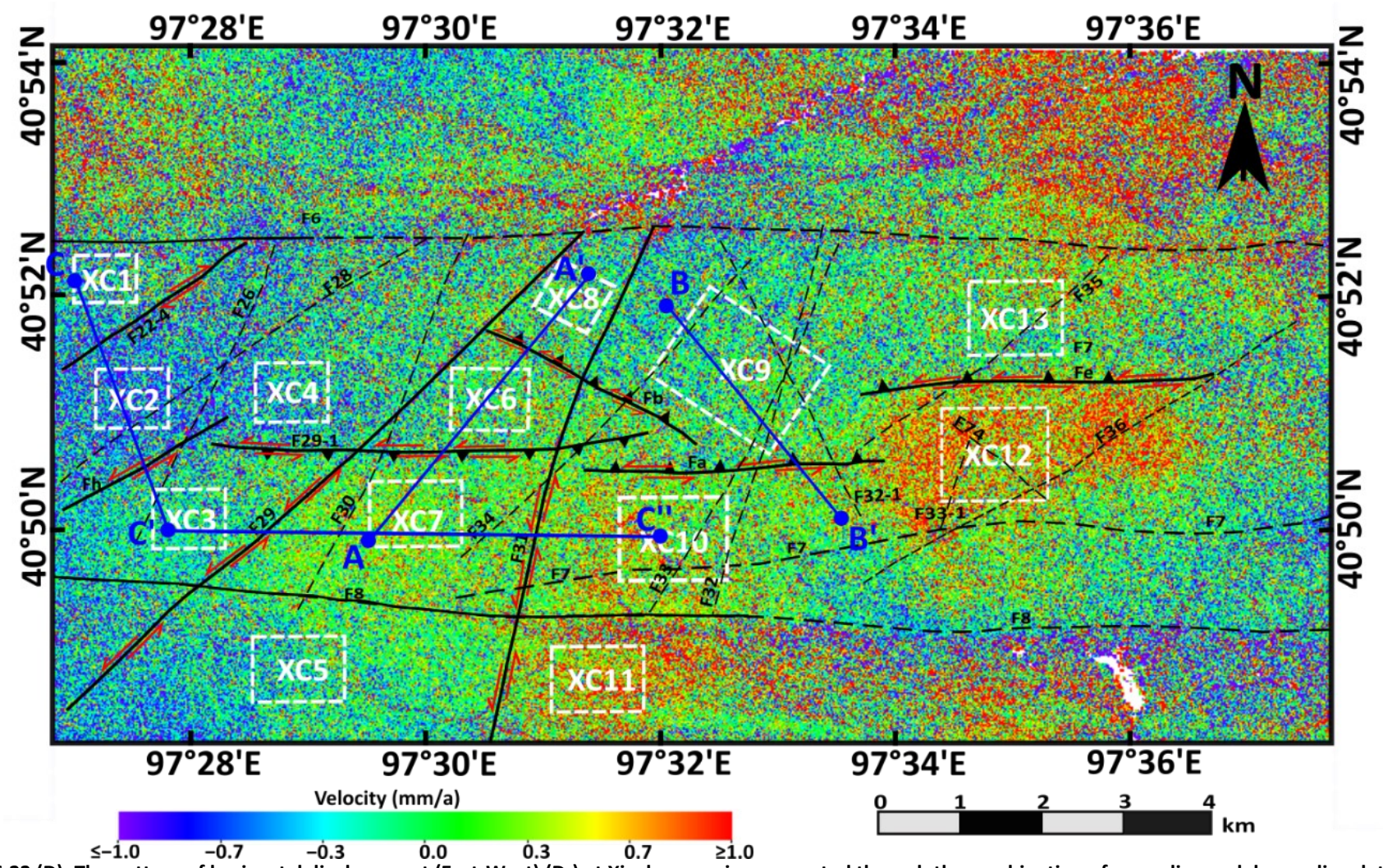


Figure 6.23 (D). The pattern of horizontal displacement (East-West) (D_E) at Xinchang region computed through the combination of ascending and descending data, where the positive values (red and yellow coloured) refer to eastward displacements and the negative values (blue coloured) refers to westward displacements. It illustrates the correlations between active faults and deformation patterns.

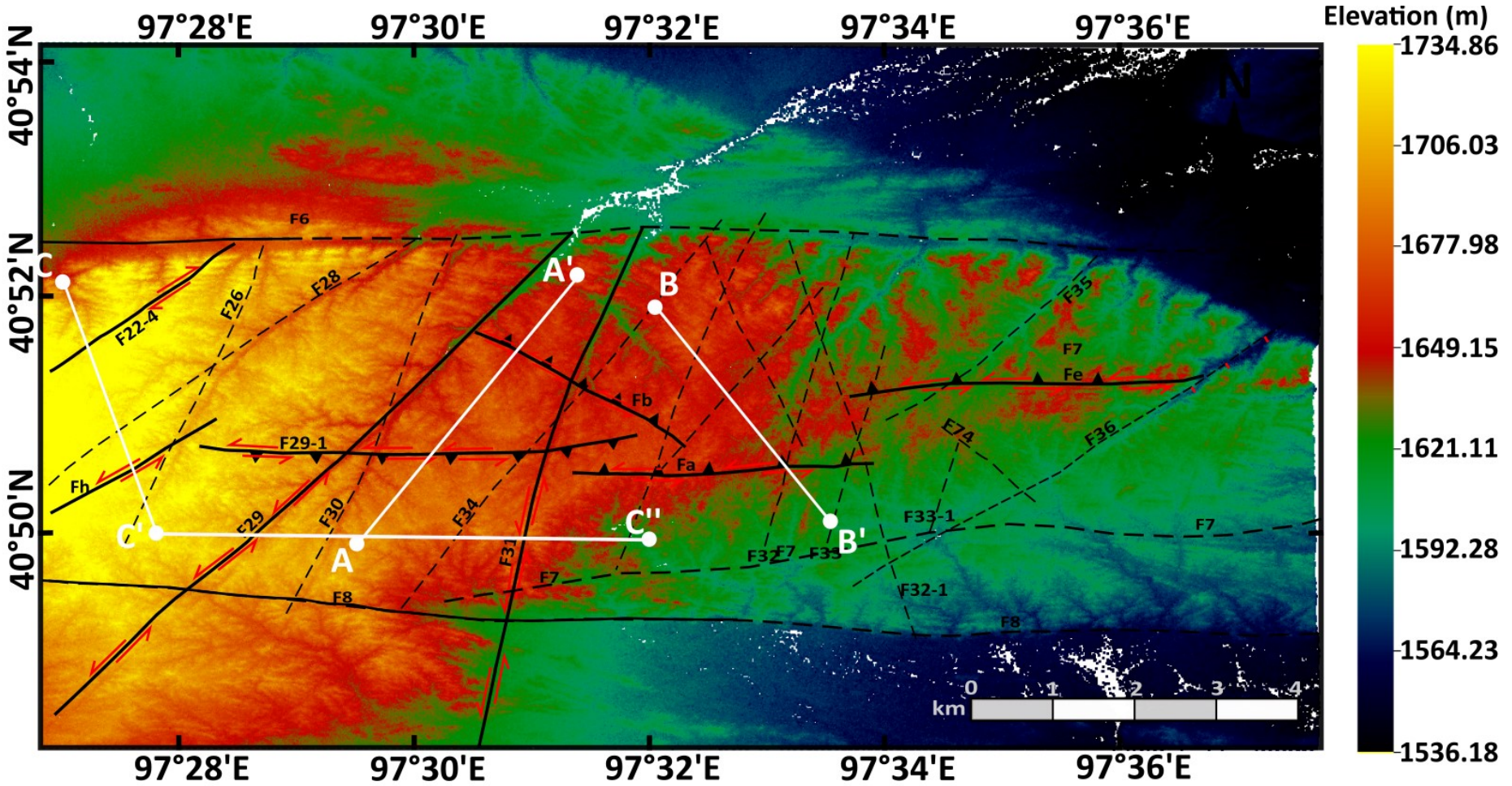


Figure 6.23 (E). The digital elevation model (DEM) across the Xinchang study area illustrates the spatial correlation between faults and the topography. The DEM is a third-party product provided by the NASA Shuttle Radar Topography Mission (SRTM). This provides a topographic representation of the earth surface. The solid line represents the on-going active faults and the dash line represent the recent inactive faults (or those whose activity cannot be sorely interpreted based on D_E and D_U deformation).

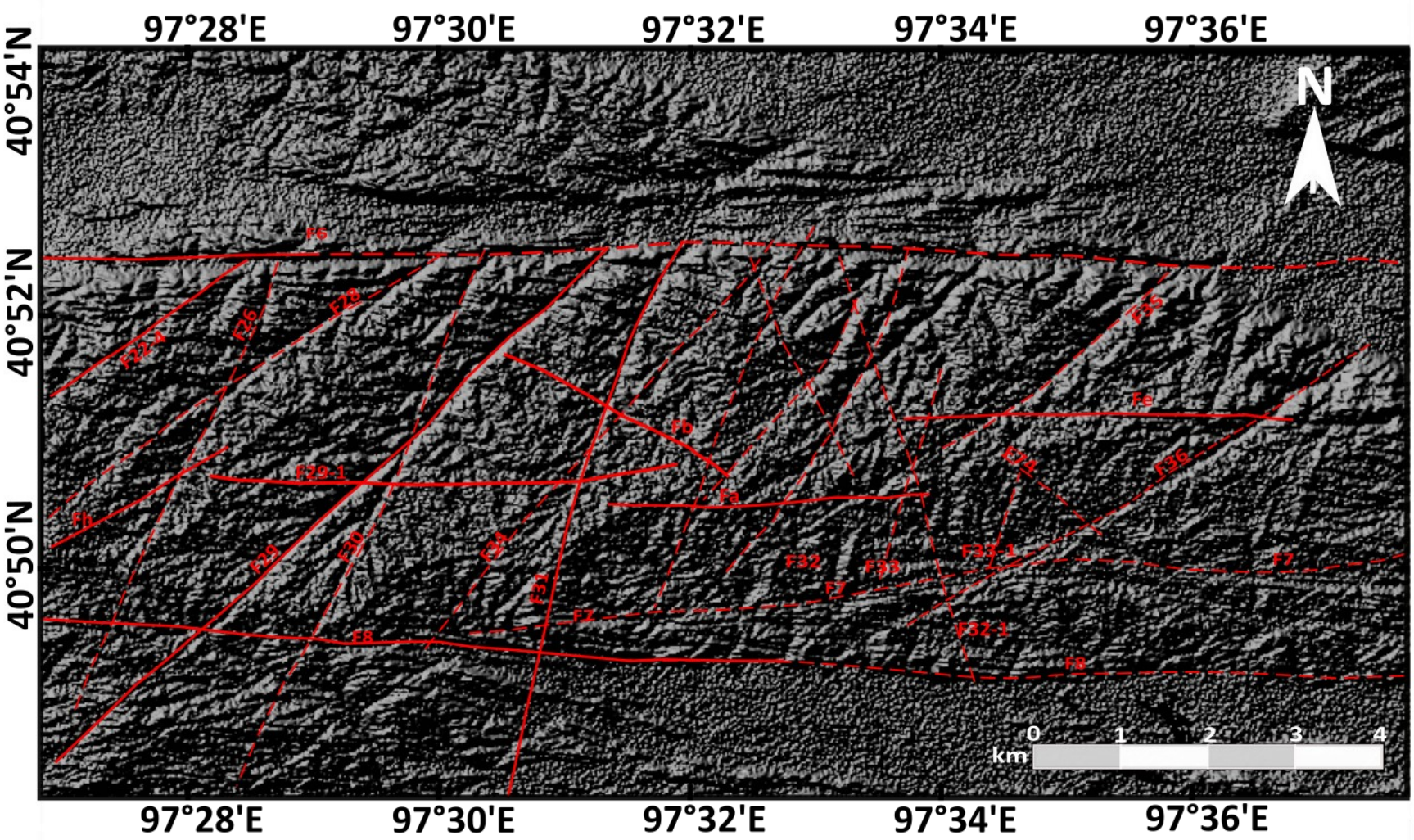


Figure 6.23 (F). The hill-shaded Digital Elevation Model map which overlays the location of active (solid lines) and inactive (dash lines) faults across the Xinchang study area. The figure is produced through the processing of DEM data in Figure 6.23 (E) using the QGIS Hillshade analysing tool.

Table 6.3 The characteristics of active faults in Xinchang region

Fault No.	Dipping direction	Vertical shearing Component	Lateral Shearing Component
F_6	South	Normal	--
F_7	South	Normal	--
$F_{22\text{-}4}$	Northwest	Normal	--
F_{29}	--	Normal	Sinistral
$F_{29\text{-}1}$	South	Reverse	Sinistral
F_{31}	--	Normal	Sinistral
$F_{32\text{-}1}$	Northwest	Normal	--
F_{32}	Southeast	Reverse	--
F_a	North	Reverse	Sinistral
F_b	Northwest	Reverse	Sinistral
F_e	North	Reverse	Sinistral
F_h	Southwest	Normal	Sinistral

To better describe the deformation patterns, the Xinchang region has been divided into 13 blocks labelled from XC1 to XC13. The average deformation rates from the vertical direction (D_U), ascending view (D_{los}^{asc}), descending view (D_{los}^{des}) and easting direction (D_E) have been summarized in Table 5.3. The frequency distribution curves are adopted to illustrate the displacement rate difference between two blocks along active faults (Figure 6.24 A to C). Time series analyses at Blocks XC6, XC7, XC8, XC9 and XC10 have been conducted to show the temporal variation of vertical displacement in both ascending and descending directions (Figure 6.25 (A) to (E)), which is achieved through the averaging of thousands of PS in each block. Meanwhile, three cross sections AA' (Figure 6.26), BB' (Figure 6.27) and CC'C'' (Figure 6.28) have been generated to show the spatial distribution of deformation and elevation. This could improve the demonstration of the velocity displacements between the two sides of the fault plane, hence proving the activity of the faults.

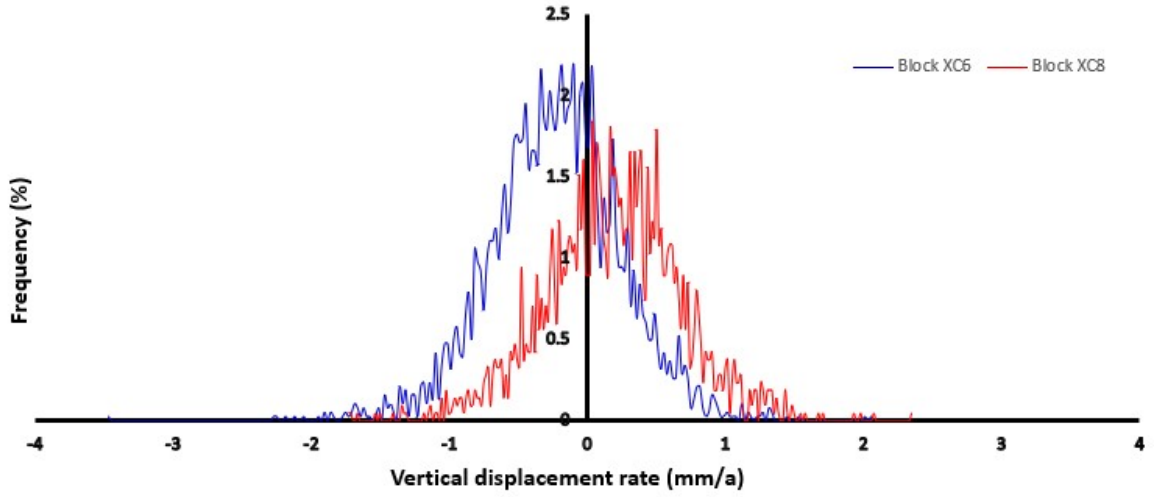


Figure 6.24 (A) illustrates the aerial frequency distribution of vertical displacement rates (D_U) at Block XC6 and XC8. Statistically, 69.8% scatterers at XC6 are displacing downwards and 66.0% at XC8 are displacing upwards. The means and standard deviations at XC6 and XC8 are -0.22±0.48 mma^{-1} and 0.19±0.49 mma^{-1} respectively.

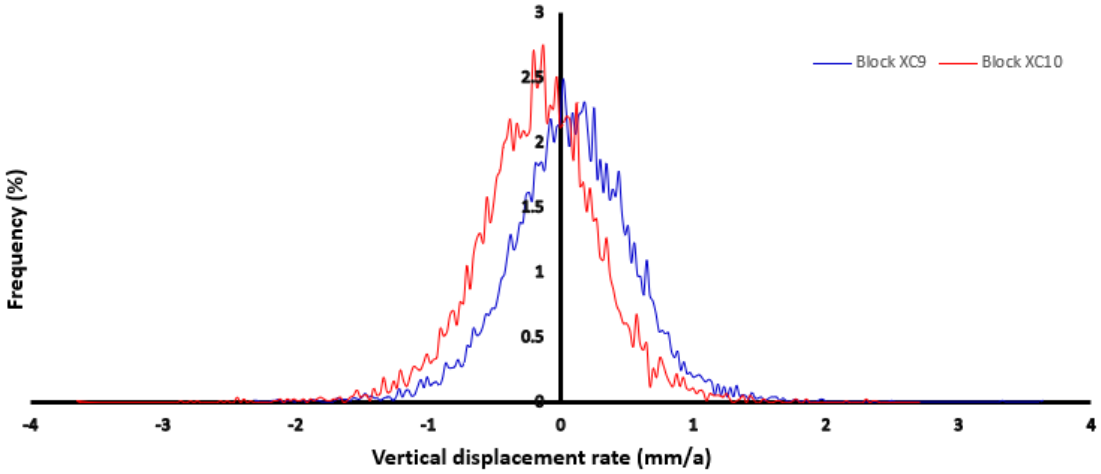


Figure 6.24 (B) illustrates the aerial frequency distribution of vertical displacement rates (D_U) at Block XC9 and XC10. Statistically, around 56.9% scatterers at XC9 are displacing upwards and 65.4% at XC10 are displacing downwards. The means and standard deviations at XC9 and XC10 are 0.09±0.47 mma^{-1} and -0.15±0.48 mma^{-1} respectively.

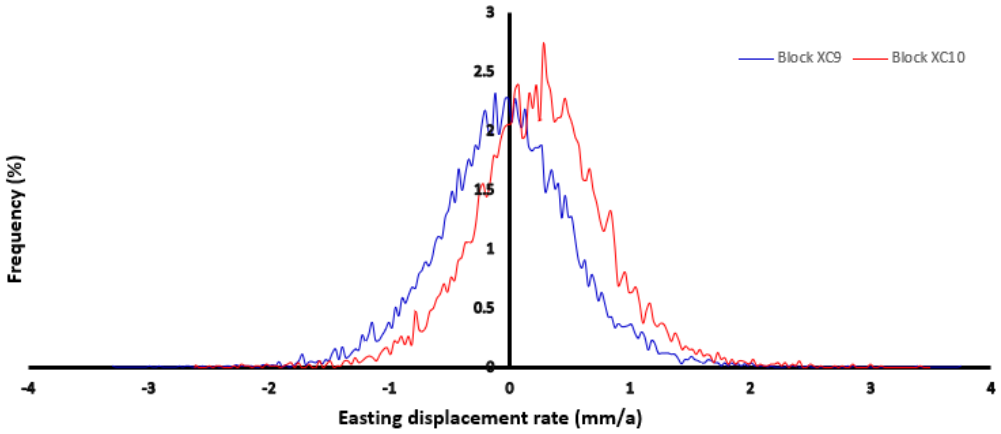
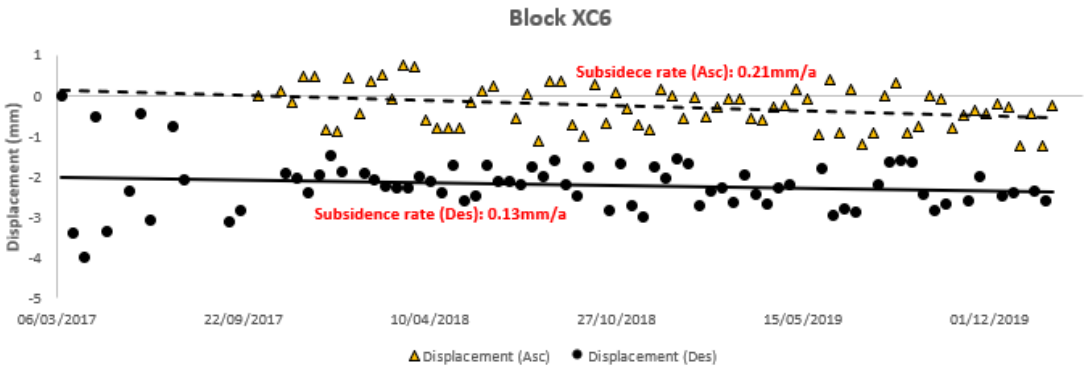
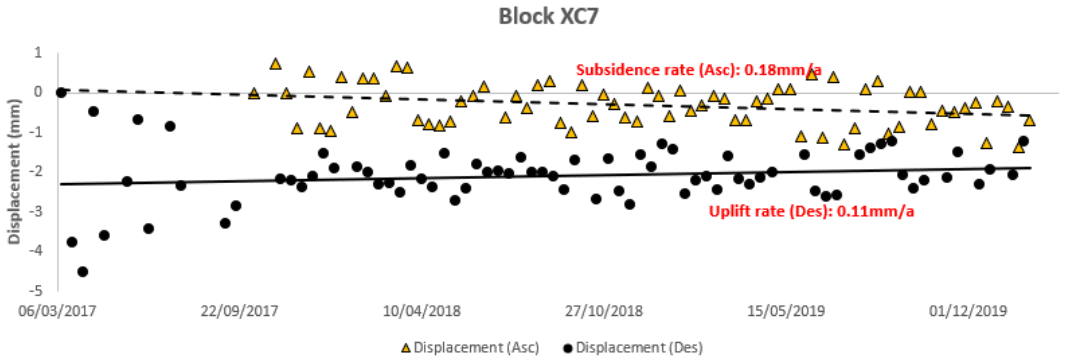


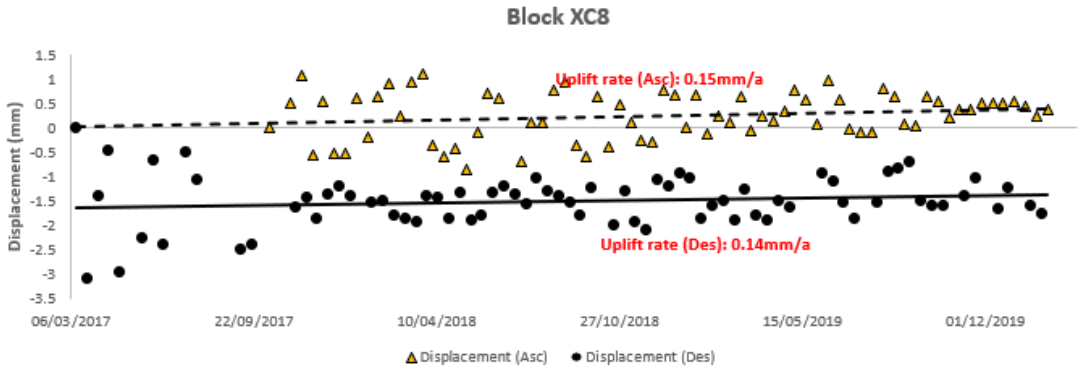
Figure 6.24 (C) illustrates the aerial frequency distribution of easting displacement rates (D_E) at Block XC9 and XC10. Statistically, around 53.0% scatterers at XC9 are displacing westwards and 68.6% at XC10 are displacing eastwards. The means and standard deviations at XC9 and XC10 are -0.02±0.57 mma^{-1} and 0.27±0.58 mma^{-1} respectively.



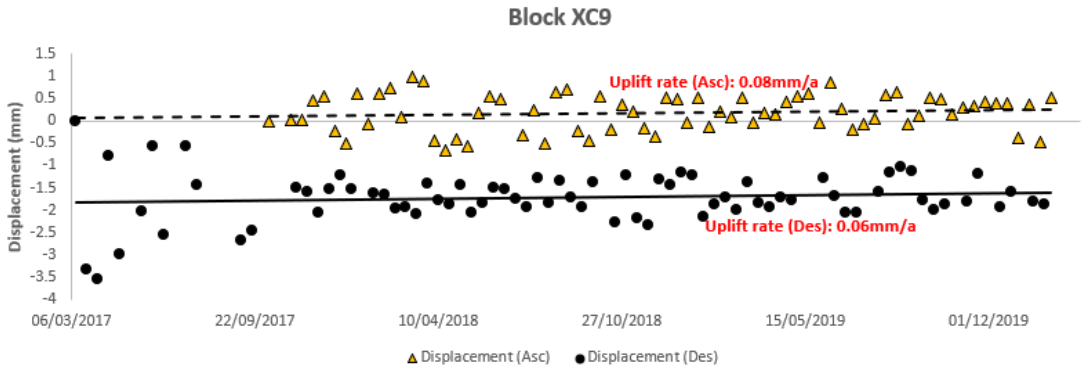
(A)



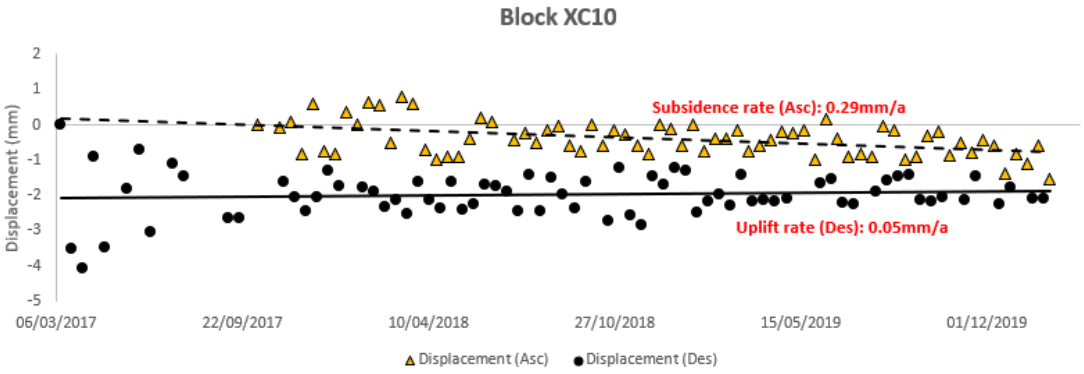
(B)



(C)



(D)



(E)

Figure 6.25 (A) to (E). The average time-series displacement of Blocks XC6 (A), XC7 (B), XC8 (C), XC9(D), and XC10 (E) in the ascending (01/10/2017 to 07/02/2020) and descending (11/03/2017 to 31/01/2020) scene. The dash lines represent the trends of ascending viewed displacements, and the solid lines represent the descending viewed displacements. The gradients of the linear trend lines show the rates of subsidence or uplift. A positive gradient refers to an upward displacement and a

negative gradient refers to a downward displacement. The uplift or subsidence rates are highlighted red in the figures.

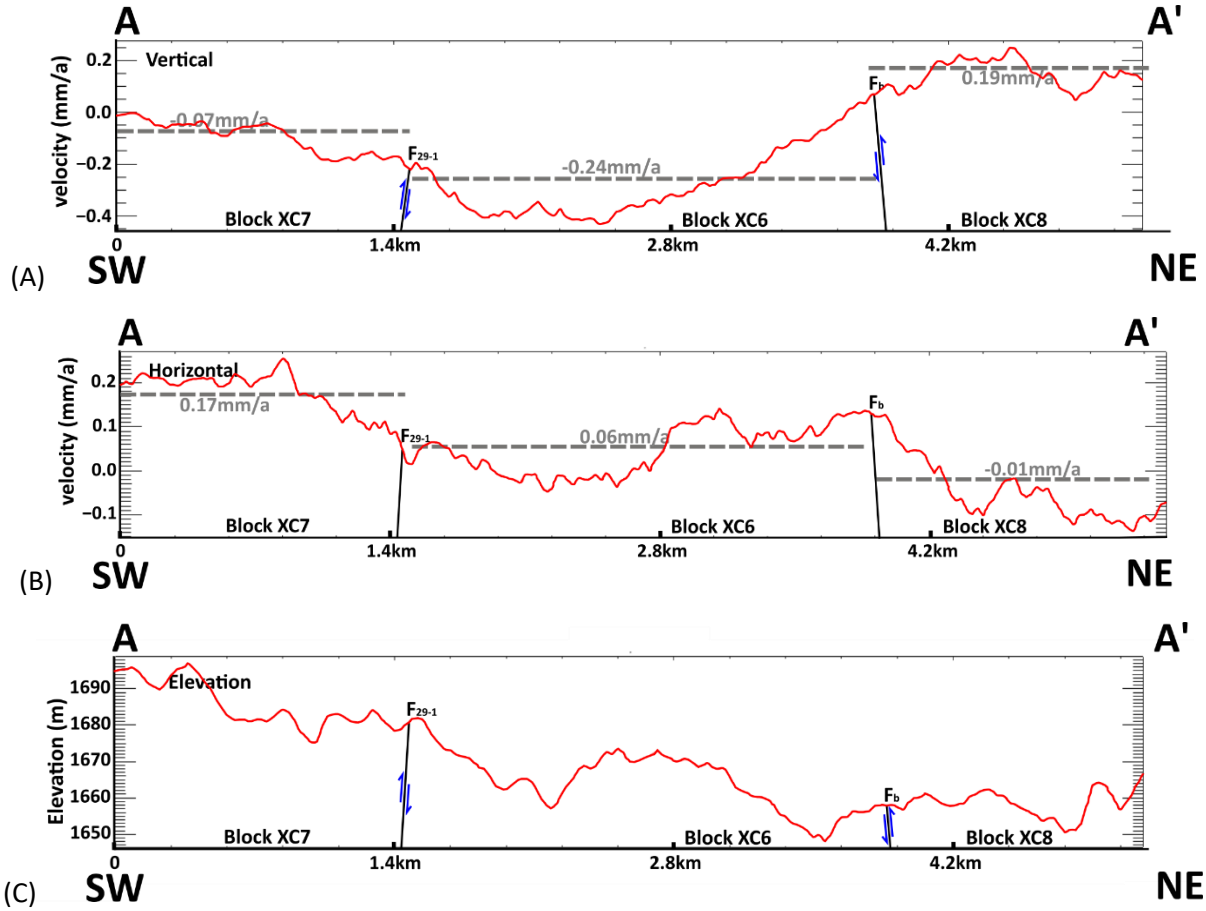
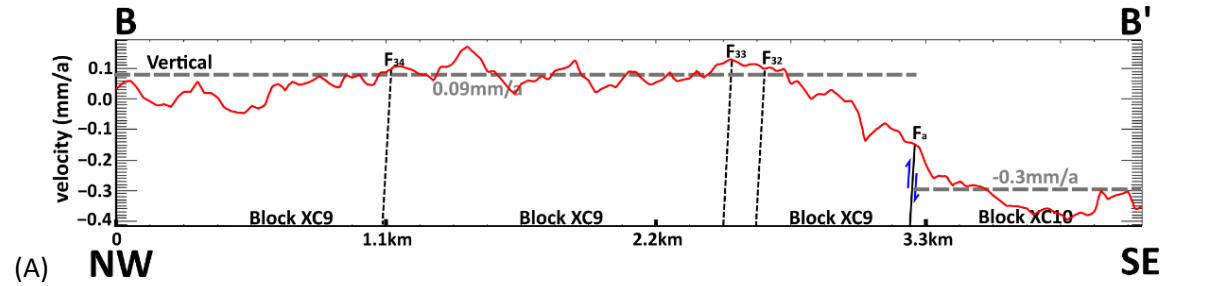


Figure 6.26 (A), (B) and (C). The distribution of vertical displacement (D_U), horizontal displacement (D_E), and elevation along cross-section AA' in Figures 6.23. This cross-section is formed from Persistent Scatterer (PS) values sampled along the cross-section line and shows the annual relative movements within each fault block (Block XC7, XC6, and XC8). The solid marked faults ($F_{29\text{-}1}$ and F_b) are tectonically active. These faults are illustrative, showing the sense of fault movement and general direction of faults. They are either interpreted from the PS or extracted from published literature. The horizontal gray dash lines highlighted the average displacement rates along the cross section over each block.



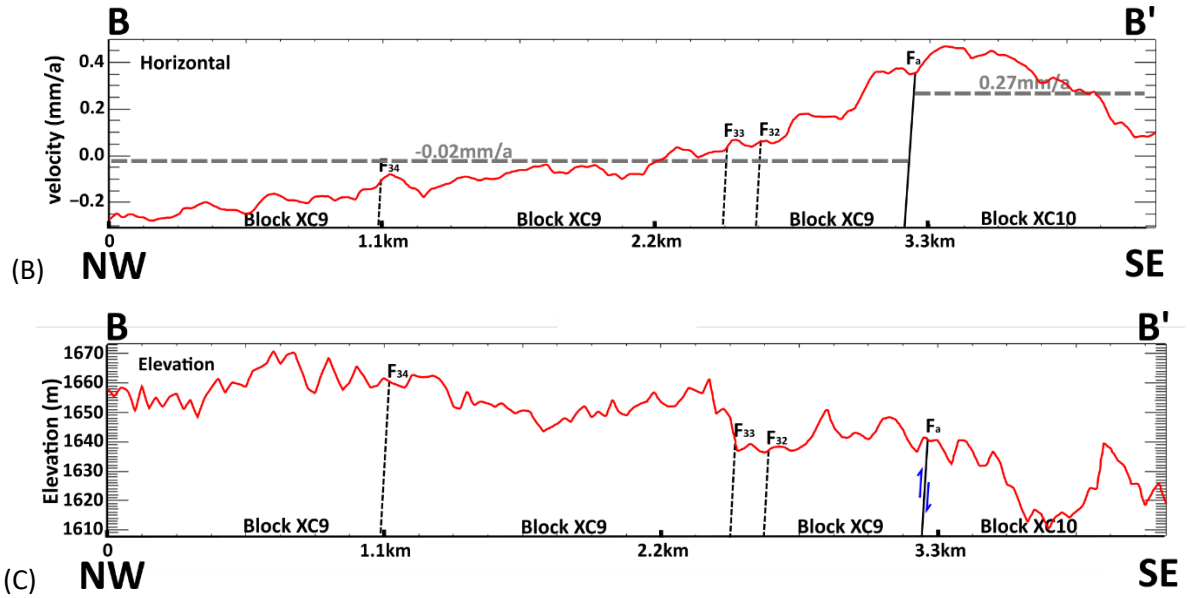


Figure 6.27 (A), (B) and (C). The distribution of vertical displacement (D_U), horizontal displacement (D_E), and elevation along cross-section BB' in Figures 6.23. This cross-section is formed from Persistent Scatterer (PS) values sampled along the cross-section line and shows the annual relative movements within each fault block (Block XC9 and XC10). The solid marked faults (F_a) are tectonically active, and the dash marked are believed as inactive (F_{34}, F_{33}, and F_{32}). These faults are illustrative, showing the sense of fault movement and general direction of faults. They are either interpreted from the PS or extracted from published literature. The horizontal gray dash lines highlighted the average displacement rates along the cross section over each block.

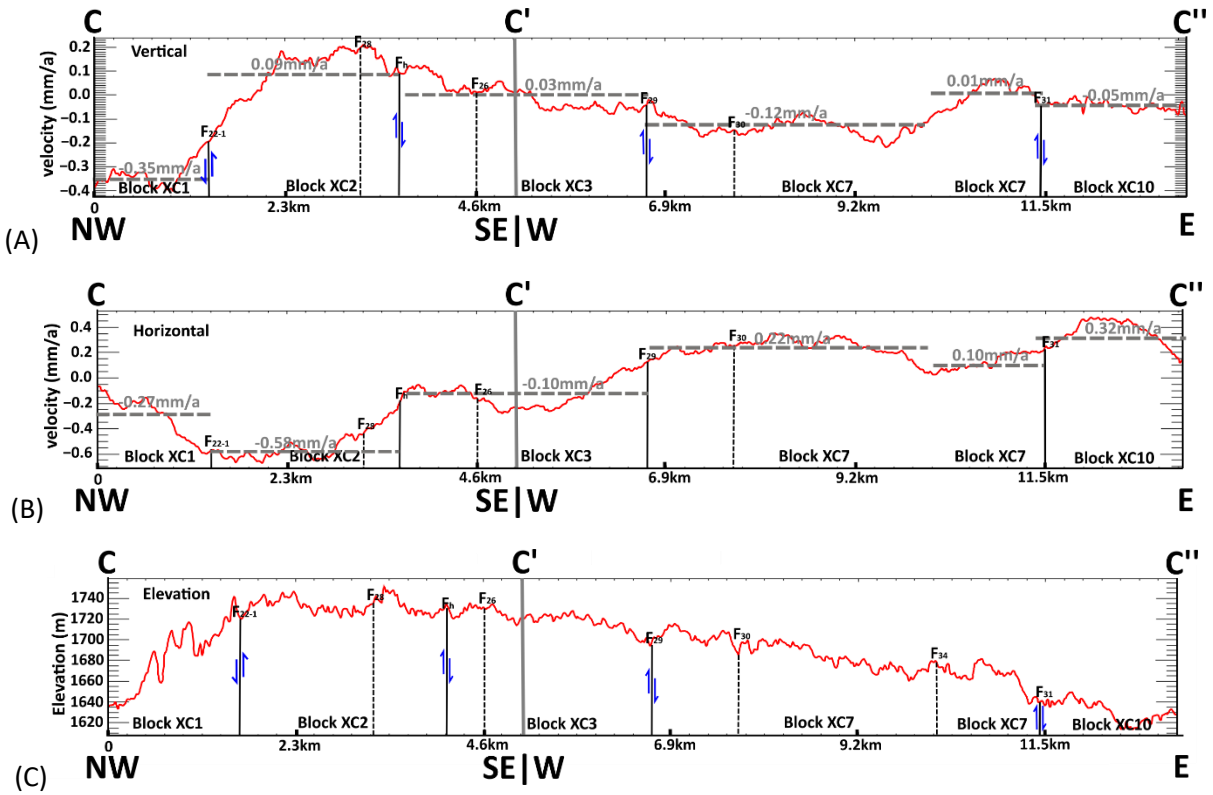


Figure 6.28 (A), (B) and (C). The distribution of vertical displacement (D_U), horizontal displacement (D_E), and elevation along cross-section CC'C'' in Figures 6.23. This cross-section is formed from Persistent Scatterer (PS) values sampled along the cross-section line and shows the annual relative movements within each fault block (Block XC1, XC2, XC3, XC7 and XC10). The solid marked faults (F_h, F_{22-1}, F_{29}, and F_{31}) are tectonically active, and the dash marked are believed as inactive (F_{28}, F_{26}, F_{30}, and F_{34}). These faults are illustrative, showing the sense of fault movement. They are either interpreted from the PS or extracted from published literature. The horizontal gray dash lines highlighted the average displacement rates along the cross section over each block.

6.5.1 Evidence of F_{31}, F_{29}, F_h and F_{22-4} as active faults in modern time

This research maintains F_{31}, F_{29}, F_h and F_{22-4} are active faults, with direct evidence coming from the vertical and horizontal displacement discontinuities along the fault planes. The vertical and horizontal variations across F_{31}, F_{29}, F_h and F_{22-4} have been clearly illustrated in cross-section CC'C'' in Figure 6.28.

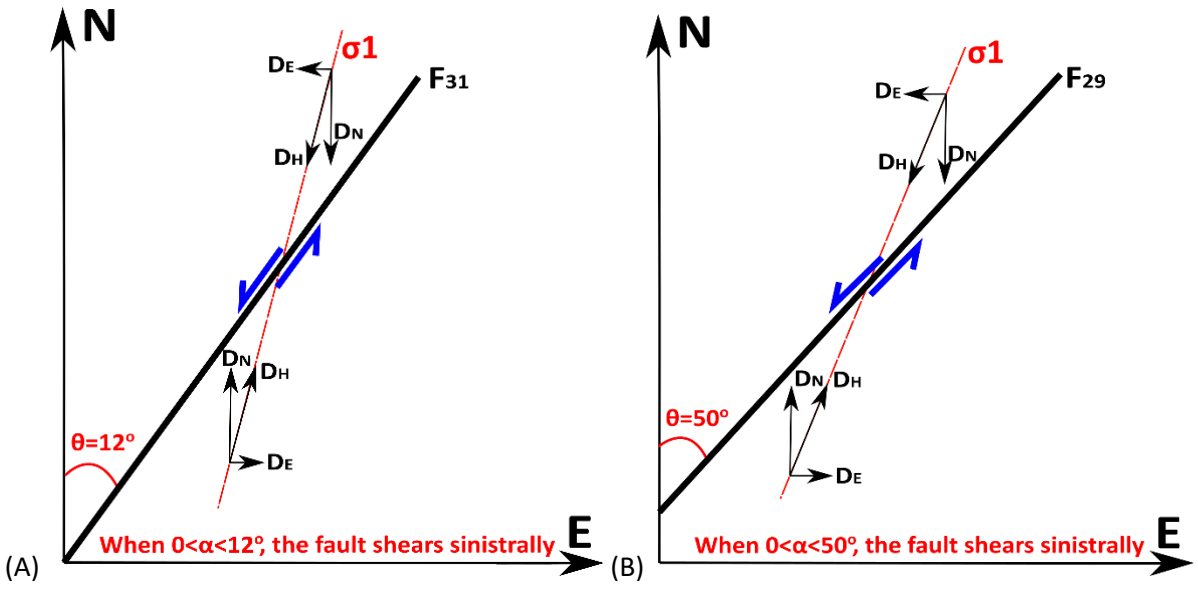
Starting from F_{31}, Block XC10 is on the east side of F_{31}, which is subsiding by 0.15 mma^{-1} and moving eastwards by 0.27 mma^{-1}. This is reflected by a significant deviation between ascending and descending displacement rates, where the vertical displacement rates from the ascending view (-0.29 mma^{-1}) are subsiding more than those from descending view (0.05 mma^{-1}), indicating a strong movement away from the view of the ascending satellite (time series displacement in Figure 6.25(E)). Meanwhile, the west side (Block XC7) has a very low vertical displacement rate (-0.04 mma^{-1}), suggesting the whole block is vertically stable. Compared with XC10, there is a similar ascending-descending displacement rate deviation at XC7, which is subsiding by 0.18 mma^{-1} in ascending view and uplifting by 0.11 mma^{-1} in descending view (time series displacement in Figure 6.25(B)), reflecting a movement towards the descending satellite. However, the ascending-descending difference at XC7 is slightly lower than that at XC10, which is equivalent to a slightly lower eastward displacement rate at XC7 (D_E = 0.22 mma^{-1}). These vertical and horizontal discontinuities have been presented in Figures 6.23 (C) and (D). The in-situ stress measurements at Boreholes BS06, BS017, BS018, and BS019 suggest the direction of maximum compressive stress at Xinchang ranges from N52^{o}E to N67^{o}E (N60^{o}E on average). As the orientation of horizontal stress is governed by the tectonic movements [48], it therefore reflects how both XC10 and XC7 are displacing towards the northeast. However, the displacement rate at XC10 is higher than that at XC7, which in turn indicates a sinistral shearing property along F_{31}.

Compared to F_{31}, F_{29} is vertically stable, where the east (XC7) and west (XC3) sides have very low vertical displacement rates around -0.04 mma^{-1} and 0.03 mma^{-1}respectively, but this still presents a slight vertical discontinuity (Figure 7.6(C)). Meanwhile, XC3 is displacing westwards by 0.1 mma^{-1}

(where D_{los}^{asc} = 0.09 mma^{-1} and D_{los}^{des} = -0.04 mma^{-1}) and XC7 is displacing eastwards by 0.22 mma^{-1} (where D_{los}^{asc} = -0.18 mma^{-1} and D_{los}^{des} = 0.11 mma^{-1}). This reflects how XC3 and XC7 are displacing towards the southwest and northeast respectively, indicating a sinistral shearing property along F_{29} (Figure 7.6(A), 7.6(B) and 7.6(D)), which agrees with descriptions in the literature [59, 60].

Further west, a previous unmapped active fault (F_h) has been identified based on the displacements of D_U and D_E between Blocks XC2 and XC3, in which XC2 (D_U= 0.09 mma^{-1}) is uplifting slightly more than XC3 (D_U= 0.03 mma^{-1}) (Figure 6.25C). As presented in Table 5.3, XC2 has a much larger difference between and with subsiding more rapidly which leads to a significant D_E pattern displacement along F_h (Figure 6.25D), where the D_E at XC2 and XC3 are subsiding at -0.51 mma^{-1} and -0.10 mma^{-1} respectively. The horizontal stress direction controls the tectonic movements and the maximum compressive stress in the Xinchang region is NE-SW, which indicates how XC2 and XC3 are displacing towards the southwest, and the high D_E at XC2 indicates sinistral shearing properties along F_h.

Finally, the distinct D_U pattern discontinuity between XC1 and XC2 indicates $F_{22\text{-}4}$ is still active, where XC2 is uplifting by 0.09 mma^{-1} and XC1 is subsiding by 0.35 mma^{-1} (Figure 6.25C). Meanwhile, XC1 (D_E = -0.27 mma^{-1}) has much higher westwards displacement rates than XC2 (D_E = -0.51 mma^{-1}) (Figure 6.25D), which reflects a dextral shearing along $F_{22\text{-}4}$.



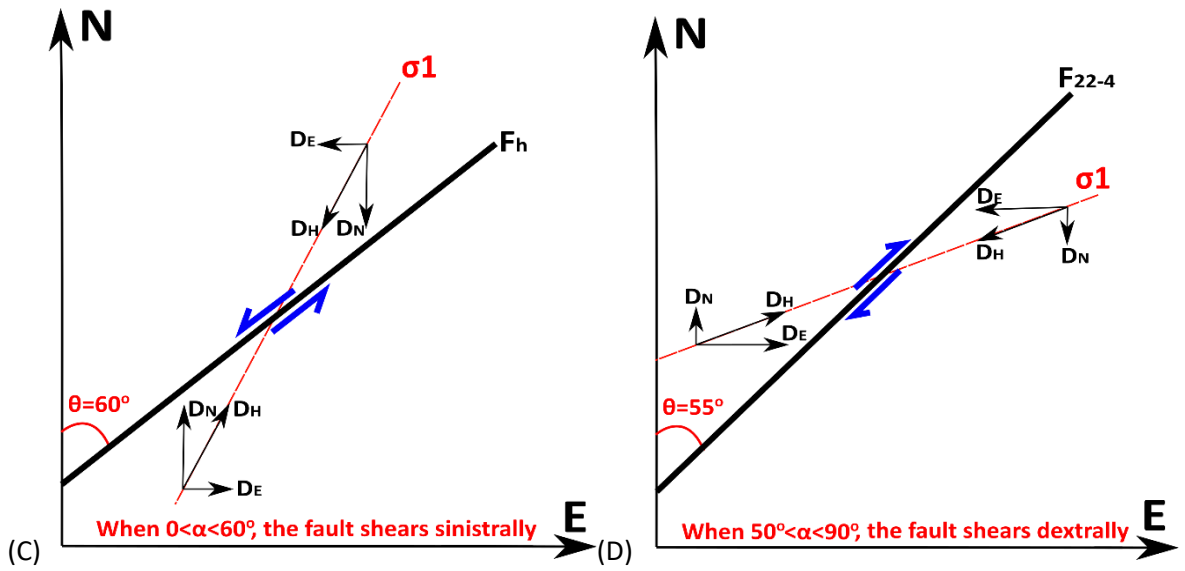


Figure 6.29 (A), (B), (C), and (D) The schematic graphs illustrate the spatial correlation between maximum horizontal compression (σ1) and fault strike angle along Fault F_{31} (Figure 6.29A), F_{29} (Figure 6.29B), F_h (Figure 6.29C), and $F_{22\text{-}4}$ (Figure 6.29D).

The striking angles (θ) along F_{31}, F_{29}, F_h and $F_{22\text{-}4}$ are measured as N12°E, N50°E, N60°E and N55°E respectively. The variations of shearing properties and fault strike angles (θ) indicate a spatial variation of the σ1 direction (α) among F_{31}, F_{29}, F_h and $F_{22\text{-}4}$. Based on the conclusion proposed in Section 6.2.2 (Figure 6.4), from Figure 6.29 (A) to (C), the sinistrally sheared F_{31}, F_{29}, and F_h indicate the σ1 direction (α), ranging from 0 to N12°E, 0 to N50°E, and 0 to N60°E respectively.

The D_E pattern in Figure 6.25 (C) indicate $F_{22\text{-}4}$ is shearing dextrally. The trending angle of $F_{22\text{-}4}$ is around 55°. Based on the kinematic theory illustrated in Figure 6.29 (D), the dextral strike-slip along $F_{22\text{-}4}$ can only be achieved when the σ1 direction (α) along it should range from N55°E to N90°E. This therefore allows us to roughly estimate the direction of maximum compression along $F_{22\text{-}4}$. From F_{31} to $F_{22\text{-}4}$, the spatial variation of the σ1 direction (α) reflects a domino-shaped compression pattern, which shows an anticlockwise rotation and reflects how the σ1 direction (α) is increasing towards the west.

Just like $F_{16\text{-}2}$, F_{17}, F_{18} and $F_{20\text{-}2}$ in the Jiujing region discussed in Section 6.4.1, F_{31}, F_{29}, F_h and $F_{22\text{-}4}$, which are NE-SW trending, tend to have low angles with σ1 (hence |θ-α| tends to be low). Therefore, this study argues the deformations along F_{31}, F_{29}, F_h and $F_{22\text{-}4}$ is strike-slip dominated, and this is more likely to be extensional in nature.

6.5.2 Subsidence at block XC6: the impact of $F_{29\text{-}1}$ and F_b

XC6 is subsiding by 0.22 mma^{-1} and displacing slightly eastwards by 0.06 mma^{-1}. The block is subsiding in the LoS in both the descending, and ascending views with LoS displacements of -0.13 mma^{-1} and -

0.21 mma^{-1} respectively (Figure 6.23, and Table 5.3). This research argues that the NE-SW trending compressive stress leads to the formation of F_b and $F_{29\text{-}1}$, where block XC6 is a part of the F_b and $F_{29\text{-}1}$ footwall and subsides relatively due to the squeezing up of XC8 and XC7. The deformation rate (D_U, D_E, D_{los}^{des}, and D_{los}^{asc}) discontinuities at XC6, XC7, and XC8 in relation to F_b and $F_{29\text{-}1}$ have been presented in cross-section AA' (Figure 6.26).

There is a distinct D_U discontinuity between XC6 and XC8 along F_b (Figure 6.23C, Figure 24A), where XC8 is uplifting by 0.19 mma^{-1}. In general block XC8 has similar ascending and descending viewed LoS deformation (D_{los}^{asc} = 0.14 mma^{-1} and D_{los}^{des}= 0.15 mma^{-1}, time series analysis in Figure 6.25 (C)) and low westwards displacement rates (D_E= -0.01 mma^{-1}). As the maximum compressive stress is NE-SW trending, it can be speculated that F_b is a northeast dipping reverse fault with low sinistral shearing.

The low horizontal shearing rate along F_b indicates the maximum compression (σ1) and the fault plane are nearly vertical (|θ-α|≈90°), meaning the deformation at F_b is vertically dominated. Meanwhile, the sinistral shearing properties indicate |θ-α|is slightly lower than 90°. These have been illustrated in Figure 6.30.

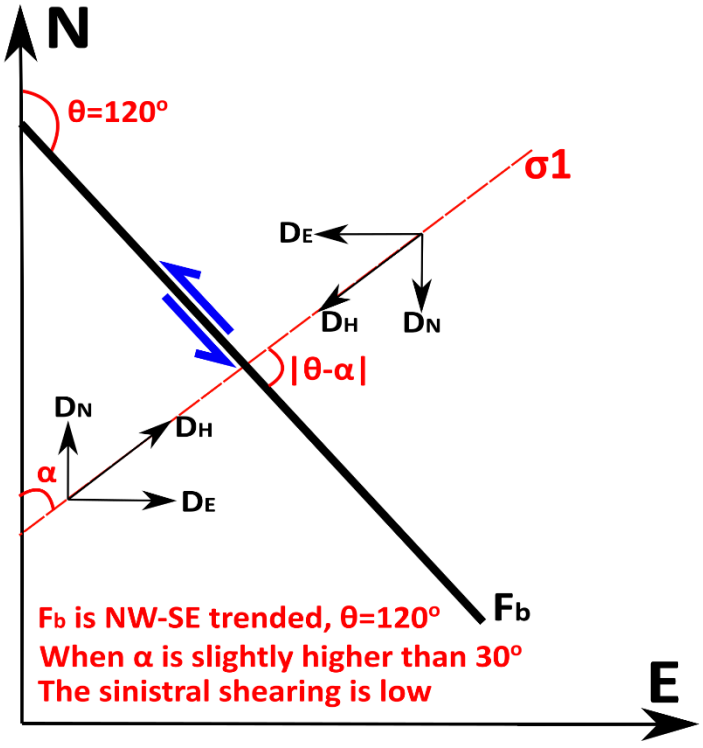


Figure 6.30 The schematic graph illustrates the spatial correlation between maximum horizontal compression (σ1) and fault strike angle along Fault F_b

The striking angle (θ) of F_b has been measured as 120° from Figure 6.23. If |θ-α| is slightly lower than 90°, one can estimate that the direction of maximum compression (α) around F_b is slightly higher than N30°E. This value is lower than the in-situ stress measurements at Boreholes BS06, BS017, BS018, and BS019 (Table 2.2), however, considering the spatial variation of the maximum compressive stress direction across the region, this study maintains the deviation is within an acceptable range.

The vertical and horizontal deformation discontinuities between XC6 and XC7 indicate $F_{29\text{-}1}$ is still active, which has been illustrated in Figures 6.23 (C) and (D). XC6 (D_E= 0.06 mma^{-1}) displacing eastward less rapidly than XC7 (D_E= 0.22 mma^{-1}), which indicates a sinistral shearing along $F_{29\text{-}1}$. As the maximum compressive stress in Xinchang region is NE-SW trending, this indicates XC7 is moving towards the northeast at a higher rate than XC6, which in turn shows a crustal shortening along $F_{29\text{-}1}$. Meanwhile, as XC6 (D_U= -0.22 mma^{-1}) is subsiding more rapidly than XC7 (D_U= -0.04 mma^{-1}), it, in turn, indicates $F_{29\text{-}1}$ is a south dipping reverse fault, where XC7 and XC6 are the hanging wall and footwall respectively. This agrees with the description in the literature [60].

The easting displacement rate (D_E) difference along $F_{29\text{-}1}$ is 0.16 mma^{-1}, which is slightly higher than that along F_b (0.07 mma^{-1}). This study argues this is due to the faults striking at different angles. If the direction of σ1 is more than N30°E, or even ranging from N45°E to N77°E according to borehole in-situ stress measurements, the |θ-α| value around F_b is obviously higher than that around $F_{29\text{-}1}$. This has, therefore, led to a higher horizontal shearing rate along $F_{29\text{-}1}$ which is consistent with the conclusions proposed in Section 6.2.1 and 6.2.2.

6.5.3 Thrust faults with sinistral strike-slip, F_a and F_e

Along with F_{31}, F_{29}, F_h, $F_{22\text{-}4}$, $F_{29\text{-}1}$ and F_b, this research also identifies F_a and F_e as active faults with sinistral reverse properties. This comes from the evidence of vertical and horizontal deformation contrasts along the fault planes (cross-section BB' in Figure 6.27).

XC9 has been chosen as the GDF host block within Xinchang. Compared with many other blocks within the study area, XC9 is vertically and horizontally stable, and has D_U and D_E of 0.09 mma^{-1} (in which, D_{los}^{des} = 0.06 mma^{-1} and D_{los}^{asc} = 0.08 mma^{-1}, shown in Figure 6.25D) and -0.02 mma^{-1} respectively. However, the south side of F_a, XC10 is subsiding vertically at 0.15 mma^{-1}. However, the rate of subsidence in ascending view (subside by 0.29 mma^{-1}) is more significant than that in descending view (uplift by 0.05 mma^{-1}) (Figure 6.25E). This is mainly due to a significant displacement to the east (D_E= 0.27 mma^{-1}) towards the descending satellite. This has led to a crustal shortening along F_a with a sinistral shearing property. The vertical and horizontal deformation rate deviations between XC9 and

XC10 are presented in Figures 24 (B) and (C). Since XC9 moves upwards relative to XC10, it can be speculated that F_a is dipping towards the north, where XC9 and XC10 are the hanging wall and footwall of the reverse fault respectively.

Using the same approach to compare the vertical and horizontal deformation rates between XC12 and XC13, F_e has been identified as another north dipping reverse fault with sinistral behaviour. Compared to F_a, the hanging wall XC13 has the same D_U as the F_a hanging wall XC9, however, the D_U and D_E (-0.34 mma^{-1} and 0.56 mma^{-1} respectively) at XC12 are much higher than that at XC10. This indicates F_e is more active than F_a.

It is important to note that the high subsidence rates from the ascending view (D_{los}^{asc}) of block XC12 (-0.63 mma^{-1}) may be due to the impacts of atmospheric phase (APS) residual (Figure 6.23A). The overall displacement rates in the Xinchang region are around 0.2 mma^{-1} in ascending view. The high subsidence patterns at XC12 in Figure 6.23 (A) looks abrupt and kinematically incompatible with the displacement in XC9 and XC13. The deformation did not distribute along the surface discontinuities in Google Earth imagery and were decorrelated to the deformation pattern in descending view (D_{los}^{des}) (Figure6.23B). This further impacts the D_U and D_E patterns in Figure 6.23 (C) and (D), which is computed through the combination of ascending and descending data. This may influence the precision of F_e characterization but does not impact kinematic interpretation as a whole in the Xinchang region.

6.5.4 The activity of F_8

F_8 controls the south boundary of the Xinchang granite section, which is dipping towards the south [59, 61, 65]. The PSI results indicate XC7 is displacing eastwards by 0.22 mma^{-1} and XC5 is displacing westwards by 0.18 mma^{-1}, which therefore suggests XC7 and XC5 are moving towards the northeast and southwest and indicates a dextral shearing and crustal elongation along F_8. It can therefore be concluded that F_8 is a normal fault. The D_U discontinuity between XC7 and XC5 has validated this speculation. In theory, as F_8 is a south dipping normal fault, the south side (XC5) is the hanging wall and expected to subside relative to the footwall side (XC7). This is proven by the PSI results, where XC7 is uplifting by 0.04 mma^{-1} and XC5 is subsiding by 0.32 mma^{-1}. This has further confirmed F_8 as a south dipping normal fault.

6.5.5 Inactive faults

Finally, this research maintains the previously mapped faults F_{26}, F_{28}, F_{30}, F_{32}, $F_{32\text{-}1}$, F_{33}, $F_{33\text{-}1}$, F_{34}, F_{35}, F_{36}, F_{74} and F_7, and most of F_6 are tectonically inactive. This is because there are no distinct vertical or

horizontal deformation patterns along these discontinuities. These have been marked as a dashed line in Figure 6.23 and clearly illustrated by cross-section BB' and CC'C'' in Figure 6.27 and Figure 6.28.

6.5.6 Summary

This study identifies deformation (D_E and D_U) in the Xinchang granite region resulting from eight active faults, including four NE-SW trended strike-slipped faults ($F_{22\text{-}4}$, F_h, F_{29}, and F_{31}) and four NW-SE or W-E trending reverse faults (F_b, $F_{29\text{-}1}$, F_a, and F_e). Most of the vertical deformation is controlled by the four reverse faults. The strike-slip faults $F_{22\text{-}4}$, F_h, F_{29}, and F_{31} control the eastward deformation in the southeast part of the Xinchang granite region (Blocks XC1, XC2, XC3, XC7 and XC10), which also reflects the spatial variation of the maximum compressive direction in the region. These collectively lead to the deformation patterns observed in Figure 6.23.

6.6 Summary

In this chapter the InSAR deformation patterns in vertical and horizontal (E-W) directions are interpreted over the area exposed by granite outcrops in the Suanjingzi, Jiujing and Xinchang regions. Tectonic activity (the movements of active faults) is shown to be the main factor driving the surface displacement in these areas. The fault characterization in based on the assumption that Beishan is part of a convergent wrench fault zone subject to a NE-SW maximum compression. The kinematic theory (Section 6.2) suggests the dip-slip and strike-slip shearing properties of the fault plane are controlled by the correlation between fault strike and maximum compression.

Based on the assertions in Section 6.2, Section 6.3, 6.4, and 6.5 mapped and characterized the active faults over Suanjingzi, Jiujing and Xinchang respectively. This has been achieved by tracing the InSAR displacement discontinuities along the surface cracks observed in Google Earth Imagery and is supported by evidence from the frequency distribution curves, cross sections, and time series displacements curves. As summarized in Table 6.1, 6.2, and 6.3, there are 15 active faults in Suanjingzi, 15 in Jiujing and 8 in Xinchang region. These include both known faults but also previously unidentified and unmapped faults, which have only been elucidated as a result of this approach. Generally, these active faults can be divided into two groups, which are NE-SW trended sinistrally strike-slipped faults influenced by the NW-SE minimum compression (or extension) and the NW-SE trended dip-slipped reverse faults. The superposition of these compressional and extensional structures might collectively contribute the surface displacements observed in Figure 6.6, 6.15, and 6.23.

By identifying, mapping and characterizing the active faults, this chapter improves the understanding of the local structural geology. This will ultimately support the ongoing GDF site investigation for the purpose of permanent HLW isolation. The results also benefit the studies of the regional tectonic activity around the Arjen Fault Zone, Shulehe Fault Zone and Sanweishan Fault zone in the northern boundary of Qinghai-Tibetan Plateau. Most importantly, this chapter demonstrates a new approach to mapping and characterizing the active faults. The recent structural geological mapping work is based on field observations and satellite images (such as Google Earth Imagery); however, this will likely omit those with slight movements and indistinct surface fault planes. The InSAR technique provides a new mapping option which significantly improves the mapping accuracy, making active fault mapping in environmentally harsh rural areas much more feasible.

The outcomes presented in this chapter assume PSInSAR is an appropriate method of monitoring real ground displacements over the granite outcrop areas in Suanjingzi, Jiujing and Xinchang. To support the results in this Chapter, Chapter 7 will aim to validate the results and discuss the possible why the standard deviations are high. (Table 5.1, 5.2, and 5.3).

7. Discussion

7.1 Regional tectonic

Beishan is a part of the Tarim Basin, whose southern boundary is controlled by the Arjen strike-slip fault zone, which is tectonically active, and motion is driven by the collision between the Indian Plate and Eurasian Plate (Chapter 2). This in turn leads to the formation of a NE-SW trending maximum compression (and, therefore, the surface deformation). The Arjen Fault Zone is a NE trending reverse fault dipping towards the southeast with components of sinistral strike slip, which also controls the northern boundary of the Qinghai-Tibetan Plateau. The strike-slip component of the Arjen Fault led to the formation of the Sanweishan Fault [22**,** 35]. Jiujing and Xinchang are at the northeast end of the Sanweishan Fault Zone, which activates the faults in these two regions. It may also activate the Suanjingzi faults in a similar way.

This research demonstrates that tectonically induced displacement occurs, within all the three study regions (Suanjingzi, Jiujing and Xinchang) in Beishan, with ground motions rates ranging from -0.5 mm a^{-1} to 0.5 mm a^{-1}. The time series analysis curves in Figures 6.8, 6.17, and 6.25 demonstrate continuous trends of displacements over time, therefore, this could distinguish the tectonically induced displacements from seismically induced, which are expected to behave as sudden movements. Compared to the Arjen strike-slip fault zone, which has displacement rates around 10 mm a^{-1} to 30 mm a^{-1} [35], Beishan is relatively tectonically stable but tectonic movements could still be observed and interpreted. That is because the effects of strike-slip motion, transmitted from the Arjen Fault Zone, is largely absorbed and attenuated by Qilian Mountain range [22**,** 34, 35], which finally lead to weak tectonic activities within Beishan and significantly reduced the tectonic displacement rates to less than 1 mm a^{-1}. It has been widely described as 'the most stable region within an active zone' by geoscientists and considered for long-term HLW waste disposal.

Inheriting the activation energy from the Arjen Fault and Sanweishan Fault, this study maintains the active faults in the three study regions can be divided into two groups: NE-SW trending strike-slip faults and the NW-SE, or E-W trending reverse faults. These include published literature mapped faults and previously unidentified faults. Their fault characteristics (striking angle, dipping direction, vertical and horizontal shearing components) are closely related to the direction of maximum horizontal compression.

The NE-SW trending strike-slip faults include F_h, F_e, and F_b in the Suanjingzi region (Table 6.1), $F_{20\text{-}2}$, $F_{20\text{-}1}$, F_{18}, F_{17}, $F_{16\text{-}2}$, F_{15}, F_{14} in the Jiujing region (Table 6.2) and $F_{22\text{-}4}$, F_h, F_{29}, and F_{31} in the Xinchang region

(Table 6.3). They are formed due to the minimum compression, in a NW-SE direction, having a low angle to maximum compression (low $|\theta-\alpha|$). In general, these faults are characterized by high horizontal shearing rates along the fault planes, therefore usually having significant D_E discontinuities along the fault plane in SAR deformation imagines. Their horizontal shearing properties (sinistral or dextral) are controlled by the relative direction between the maximum compression and fault plane. However, since these faults were activated by the left strike slipped Sanweishan Fault, it can be found that most NE-SW trending strike-slip faults are in fact shearing sinistrally.

As illustrated in Figure 6.1, this study concludes the vertical shearing properties along these faults are highly likely to be extensional. Future studies applying northing displacement rates (D_N) supported by a field trip will solidify this judgement. Yun [32] indicates how the strong left-strike-slip (sinistral shearing) of the Sanweishan Fault led to an extensional environment at the north-eastern end in Jiujing, which may also apply to Xinchang and Suanjingzi. This could in turn have led to the formation of extensional sinistral branch faults. Meanwhile, the low angle to maximum compression (low $|\theta-\alpha|$) leads to low compression along fault planes, which indicates the forming of extensional structures in NE-SW trends at Beishan is theoretically feasible.

The NW-SE or W-E trending reverse faults mainly include F_1, F_2 and F_d in the Suanjingzi region, F_a, F_b, F_g, F_{i-1}, F_{i-2}, F_m, F_n and F_o in Jiujing and F_b, F_{29-1}, F_a, and F_e in the Xinchang region. They are formed due to compression in a NE-SW direction, having a high angle maximum compression ($|\theta-\alpha|$ trends to 90^o) and reflecting significant crustal shortening. These faults are usually dip-slip and are mainly characterized by distinct D_U discontinuities in the SAR deformation patterns. There may be some strike-slip characteristics along the fault plane, however, the D_E discontinuities along the fault planes are usually topographically very low and unclear in the image.

In general, the spatial correlations between deformation patterns and faults indicate the NW-SE trending reverse faults make a more prominent contribution to vertical deformation (D_U) than NE-SW strike-slip faults, and the NE-SW strike-slip faults may have a higher impact on horizontal deformation (D_E) than NW-SE trending reverse faults. The coexistence and superposition of these compressional and extensional structures finally leads to the surface deformation in Figures 6.5 (A to D), 6.15 (A to D), and 6.23 (A to D). Comparing the deformation rates (D_{los}^{des}, D_{los}^{asc}, D_E, and D_U) over the three study regions (data presented in Tables 5.1, 5.2 and 5.3), this study maintains the surface displacement rates at Suanjingzi are the highest, then followed by Jiujing and Xinchang.

7.2 The potential contributing sources of the data standard deviations

The mean deformation rates in each of the selected blocks in the Suanjingzi, Jiujing and Xinchang regions are summarized in Tables 5.1, 5.2 and 5.3. The errors presented in these tables are representations of standard deviation, presenting the uncertainty within the data and reflect the dispersion of data sets relative to its mean. It is derived based on a standard deviation formula. The mean deformation rates and standard deviations are calculated from the spatial average of thousands to tens of thousands of PS points within each block area (the number depends on the block size). The standard deviation is a widely adopted measure of the error in PSI measurements.

This study argues the standard deviations are reasonable with respect to the measured displacement rates. The standard deviation is generated from the internal variation of velocity/displacement, which means the deformation rate within each block may not be spatially uniform. This might be influenced by geomorphological processes and the spatially inconsistent movement (such as tilting and concaving) within each block.

As discussed in Chapter 5, the impacts of geomorphological processes such as erosion and deposition may increase the standard deviation significantly. This study has reduced the data noise by setting a high coherence of 0.75 (the most widely adopted value for InSAR-related studies). However, it still seems unrealistic to remove all geomorphologically induced displacement. The residual geomorphologically related scatterer points may generate extreme high or low displacement values (higher than tectonic induced) to improve the standard deviation. For example, the tectonic induced displacements rate in Suanjingzi are between -0.3 to 0.3 mm a^{-1} between 08/10/2017 to 26/01/2020. The Quaternary sediments covering the area (Block SJZ0) which are characterized by low coherence (lower than 0.7) are severely impacted by erosion (Chapter 5). This leads to a higher deformation rate around 0.68 mm a^{-1}.

Tectonically, the displacements in many blocks may not be simple vertical movements and may in fact be tilting, concaving up or concaving down due to the impact of compression. This phenomenon is reflected by the cross sections in Figures 6.9, 6.10, 6.19, 6.20, 6.26, 6.27 and 6.28. Tilting refers to two sides of a block moving such that one side has higher vertical deformation rate than the other. This may be due to the processes of thrusting (uplift) or subducting. The most typical examples include Blocks JJ20 and JJ19 in the Jiujing region in cross-section CC' (Figure 6.20) and Blocks SJZ7a and SJZ11 in the Suanjingzi region in cross-sections AA' (Figure 6.9) and BB' (Figure 6.10) respectively.

When under compression, the granite blocks may also deform elastically vertically before the rupture point (which generates active faults), this may cause a concave or convex block ground deformation pattern. In theory, this makes the displacement rates between the middle and the edges of the blocks different. When the block has a concave upwards motion, the middle part has a higher D_U than the surroundings. Examples include Block SJZ6 in the Suanjingzi region presented in cross-section BB' (Figure 6.10), Block JJ4 in the Jiujing region presented in cross-section AA' (Figure 6.18), and Block XC2 in the Xinchang region presented in cross-section CC'C'' (Figure 6.28). When the blocks are convex upwards, the middle part has a lower D_U than the side parts. Examples include Block SJZ1 in the Suanjingzi region presented in cross-section BB' (Figure 6.10), Block JJ12 in the Jiujing region presented in cross-section BB' (Figure 6.19), and Block XC6 in the Xinchang region presented in cross-section AA' (Figure 6.26).

In general, even though the geomorphological processes, tilting and convex/concave displacement led to high standard deviations, these displacements are low compared to the clear tectonic movements between blocks. Therefore, this does not impact this study's ability to identify or quantify the tectonic offsets and discontinuities between blocks. This is the case for two reasons. Firstly, the upper and lower error bar are always consistent with the trends of average time series displacement, therefore reflecting the overall vertical displacement direction of the block. Second, as presented in Figures 6.6 (A to D), 6.16 (A to G) and 6.24 (A to C), the frequency distributions of the PS displacement within each block are generally comparable, which are clear enough to reflect the PS in blocks moving in different directions or rates. This indicates deformation data might be reliable to reflect the deformation rate differences among blocks.

7.3 The result validation

This research demonstrates that InSAR can be used as a tool for detecting deformation patterns and estimating displacement rates and might be a reliable tool to reflect the real tectonic movements within three study areas, despite the overall low displacement rates (-0.5 mma^{-1} to 0.5 mma^{-1}). In addition, structural kinematic analysis can be used to interpret individual fault type and movement along with understanding of the regional tectonic environment. To conclude and synthesis previous discussions, there are several arguments to which support this theory.

First, the coherence measurements presented in Table 5.4, 5.6, and 5.7 at Section 5.3, 5.4 and 5.5 in Chapter 5 suggest that more than 90% of pixels at Xinchang and Jiujing and 70% of pixels at Suanjingzi granite outcrop have a coherence greater than 0.70 between 08/10/2017 to 26/01/2020, this may

effectively exclude the impacts of geomorphological processes (erosion and deposition) on surface deformation. This may also exclude the impacts of seismic activities. That is because the seismically induced movement are usually in sudden, which is expected to demonstrate a very significant displacement discontinuity (probably with extent more than 1000mm) on time series analysis curves. However, this kind of sudden discontinuity was not found in time series displacement curves. Meanwhile, the seismic induced movements may also lead to significant decoherence due to the impact of volumetric decorrelation. Therefore, these leave tectonic activities as the sole factor triggering the surface displacements.

Second, a stack of 69 ascending and 71 descending SAR interferograms, which span over 2 to 3 years respectively have showed distinct and consistent ground movement trends from the time series analysis over time. Similar studies generally only employed 20-40 interferograms, the high number of interferograms used have significantly reduced the instrumental (satellite) measuring error and further effectively remove the atmospheric related effects. According to Adam [213], the instrumental error for PS-InSAR velocity can be expressed as:

$$\textbf{Velocity Error} = \frac{\mathbf{1.3}}{\sqrt{\mathbf{N}}} \quad \textbf{Eq. 7.1}$$

where N is the number of interferograms. In this research, the velocity error was estimated to be only 0.16 mma^{-1}. This indicates the tectonic displacement observed in the InSAR measurements for this study should have a high confidence being reliable and accurate.

Third, the Sentinel-1 data were reprocessed by SARScape. This is a reputable satellite data (notably Sentinel-1) reprocessing software developed by Harris Geospatial Solutions. A series peer reviewed studies include Agarwal [148], Trevoho [209], Smolianinova [145] and Khan [146] have demonstrated data processed by SARScape is technically reliable. The SARScape PSI technique used in this research is developed from an algorithm introduced by Ferretti [81] and [82]. This is one of the most popular techniques for time series analysis model [27]. Therefore, the deformation patterns may reflect the real movement at the ground surface.

Fourth, the residual of atmospheric phase screen (APS) may impact the estimated displacement rate, but in general, it has been appropriately eliminated in this study. The evidence comes from the deformation patterns in Figure 6.5 (A to D), 6.15 (A to D) and 6.23 (A to D). By coupling the optical imagery (Google Earth) with the SAR images it provides evidence that actual ground movements observed in the SAR images are represented as offsets on either side of the surface discontinuities

(faults). However, the APS would be distributed randomly (depends on the clouds) rather than along discontinuity lines.

Meanwhile, the accuracy of the mean APS is dependent on the density of PS [82]. In the study areas, especially the areas where granite is exposed, the coherence is high, this in turn leads to a high PS density. This could significantly reduce the APS and improve the atmospheric filters during the deformation rate estimations. This provides the confidence that the results are actual ground surface movements. The exception is where the InSAR deformation pattern has been affected by atmospheric errors around Block XC12 at Xinchang. This can be observed from the ascending view deformation pattern (Figure 6.23A). This error is believed to result from the atmospheric phase removal stage during the Sentinel-1 data reprocessing in SARScape. The SAR deformation is affected by APS residue and can be easily identified due to its kinematical incompatibility with the surrounding blocks. The deformation patterns are spatially decorrelated to the surface gullies and discontinuities observed by Google Earth imagery. The reason for such deformation incompatibility and decorrelation around Block XC12 is unclear in Figure 6.23 (B) (the deformation pattern in descending LoS direction), but in both cases could be the result of cloud cover or the near surface dust with a high dielectric material (e.g., iron-rich). Overall, this may impact the accuracy of F_e characterization but will not exert significant influence on regional kinematic interpretation at Xinchang as a whole.

Fifth, the deformation pattern discontinuities indicate the active faults. The difference in the displacement rates at the two blocks along the fault plane are statistically comparable. The main evidence come from the deformation rates' frequency distribution curves (Figure 6.6 (A to C), 6.16 (A to G), and 6.24 (A to C)) and the cross sections (Figure 6.9 (A to D), 6.10 (A to D), 6.18 (A to D), 6.20 (A to D), 6.26 (A to D), 6.27 (A to D), and 6.28 (A to D)).

Sixth, the displacement rates measured in this study are within the monitoring capability of PS-InSAR technique. That is because the results presented are calculated annual velocities, which is defined as the rate of displacement change over 2 to 3 years of satellite data acquisition which is then annualized for comparison purposes. This is equivalent to an overall displacement in millimetres over acquisition time period, which is within the monitoring capability of InSAR. There are multiple peer reviewed publications demonstrating that PS-InSAR technique can be applied to measure the regional displacement rates less than 1 mm a^{-1}, these include Mason et al., 2015 [141] and Fuhrmann et al., 2013, 2015 [227, 228]. This shows using the InSAR to measure regional micro-displacements rates of less than 1 mma^{-1} is feasible if sufficient data is available.

Finally, the overall displacement rate measurements (-0.5 mm a^{-1} to 0.5 mm a^{-1}) in this research are generally in agreement with the published literature and reflect tectonic displacement rates in Beishan Region. This is supported by several studies investigating the fault displacement rates around Beishan showing similar results. For example, Yang [46] estimated the sinistral strike-slip rate and vertical displacement rate along the Sanweishan Fault were between 0.06-1.25 mma^{-1} and 0.05-0.08 mma^{-1} since the late Pleistocene; Yang [46] also indicates the vertical displacement rate along the Beihewan Fault (around Beishan) was around 0.35 mma^{-1}. Wang [34] estimated that the vertical and horizontal displacement rates along the Jiujing Fault (F_{20}) are 0.03±0.01 mma^{-1} and 0.18 mma^{-1} respectively. Wang [10] and Zhang [229] suggested the crust in the Beishan area has been uplifting slowly at a rate of 0.6 mma^{-1} to 0.8 mm a^{-1} since the Tertiary Period. These all confirm the slow deformation rates around Beishan are in the power of 10^{-1} mm a^{-1} and may have proved the small-scale tectonic movements observed and quantified in this research are precise and accurate.

7.4 The validation of fault micro-displacements using ICSAR

To improve the understanding of Sentinel-1 data reprocessing, to support the development of ICSAR software, and to validate the SARScape results in Chapter 6, this Section compares the deformation pattern of the two independent systems ICSAR and SARScape software. The descending Sentinel-1 data set which were first reprocessed using SARScape in previous chapters (Chapter 4, 5 and 6) (presented in Table S2) were re-analysed using ICSAR algorithm. In this work, the Jiujing study area was chosen as case study area to compare the two-software due to its typical deformation patterns.

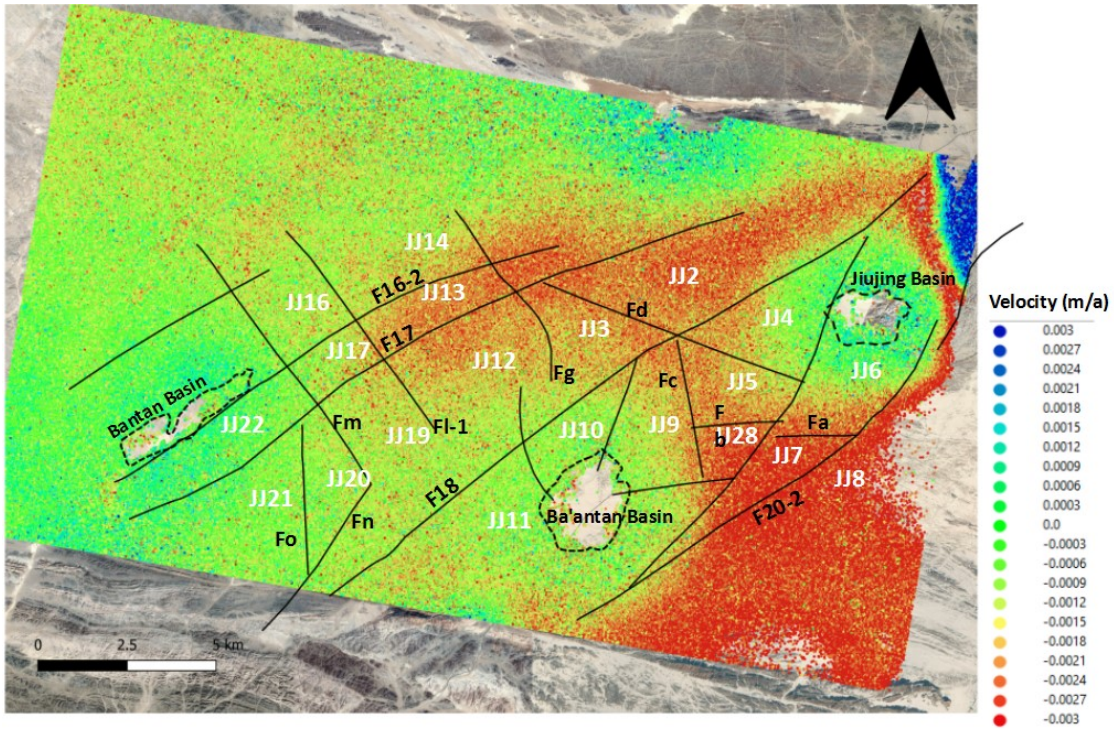


Figure 7.1 Patterns of LoS displacement rate in descending direction across the Jiujing study area over period 11/03/2017 reprocessed by ICSAR. The negative values (green-to-red colours) refers to decrease in LoS distance, therefore indicate uplift; and the positive values (blue-to-green colours) refers to increase in LoS distance, therefore, indicate subsidence.

Figure 7.1 shows the pattern of displacement rates reprocessed by ICSAR across the Jiujing study area and can be compared with Figure 6.15 (B) in Chapter 6. In general, Figure 7.1 and Figure 6.15 (B) show very similar patterns of surface displacements over the period 11/03/2017 to 31/01/2020 across Jiujing study area. The notable uplifting areas in Block JJ2, JJ3, JJ5, JJ12, JJ13, JJ17, JJ19 and JJ20 and the highly subsiding areas in Block J6, JJ11, JJ21 and JJ22 between these two reprocessing very similar providing confidence in the results. The new ICSAR software which is still in early stages of development is reliable enough to reflect the moving direction of the surface displacements. It also demonstrates the displacement rate discontinuities along major faults such as F_a, F_c, F_g, F_{l-1}, F_m, F_n, F_o F_{18}, F_d, and F_{17} which were previously identified as active at Section 6.4 in Chapter 6. This therefore provided confidence that SARScape is reliable enough to reflect the real micro-movements along active faults. As the Sentinel-1 data in Xinchang and Suanjingzi are reprocessed in same way with exactly same Sentinel-1 data set as that in Jiujing, in this way, it is believed the ICSAR results in Jiujing is broadly representative and provides confidence in the results.

Even though the ICSAR and SARScape results show similar displacement rate patterns, it should be recognized that there is a difference in the magnitude of displacement rates. The SARScape descending LoS displacements are generally distributed in the range between -0.5 to 0.5 mm a^{-1}, while

the magnitude of ICSAR displacement rates is generally in the range between -3 to 3 mm a^{-1}. It believes the SARScape results are more accurately reflect the real magnitude of the displacement rates over study area. As previously mentioned in Section 2.2 and 7.1, the published literature confirms that Beishan annual displacement rates are in the range of 0.1 mm, which is general in agreement with the SARScape results. Therefore, the ICSAR measured displacement rates of 3 mm a^{-1} are considered erroneous. This investigating using ICSAR was one of the first attempts to use the software are so errors can be expected of the software which is still in development.

As discussed in Section 7.2, the unstable scatterers impacted by geomorphological processes that is mistakenly selected as Persistent Scatterer Candidates (PSCs) might be one of a potential factor contribute the high displacement rates. Meanwhile, the different methods used by SARScape and ICSAR in selection of the Master image geocoding, the atmospheric phase residual (APS) removal and the PSI inversion may also lead to result deviations. In any case, although the ICSAR results are encouraging and providing a robust comparison, further works is required to improve the displacement rate estimations of ICSAR.

7.5 Limitations and suggested future works

Validating the results from this work is challenging due to difficulties in acquiring field based geodetic movement data to validate the modelled deformation. Substantial work has been undertaken to improve the robustness of this research and in this section the results and limitations are critically assessed, and areas of further work are considered.

This research measures the surface deformation rates through the reprocessing of around 70 Sentinel-1 data using the PSInSAR method in SARScape software package. The estimated deformation patterns with deformation rates are generally in the power of 10^{-1} mma^{-1} which make it possible to identify and characterise active faults which forms the main outcomes in this research. However, since SARScape is proprietary, the end users cannot fully understand the software's working mechanisms from a technical perspective as the algorithms being used are not known. Therefore, it is understandable if the reliability of the results is questioned. The best way to validate the results is through direct field measurements and observations. Originally it was planned for this research programme to include a geological fieldwork campaign focused on field measuring and mapping the structural geology in Beishan (at Suanjingzi, Jiujing, and Xinchang) in Gansu Province, China to further verify the InSAR results in Chapter 6. However, due to Covid-related travel restrictions, this was not feasible. To compensate for the fact no direct field measures were taken other methods were used to validate the

results, but recognising their limitations, these included literature-based data comparison, coherence change detection and ICSAR validation.

A geological fieldwork campaign ground truthing the results and coupling them with the InSAR and photogrammetry of the region, especially to trace the new active faults, would be of benefit. To ensure that faults are correctly characterized, the strike and dip directions and the dip angles of potential planes (valleys, gullies and cracks) should be surveyed. The InSAR displacement rates can be validated directly using a seismometer or drone, the method is introduced by Carpenter [236], which might be adopted by future studies. Meanwhile, the InSAR results can also be validated by the in-situ measurement of dip-slipped and strike-slipped displacements along the fault planes. Finally, fieldtrips also provide the opportunities to collect data in relation to the geomorphology and earth surface processes (surface sediments, the degree of erosion, the soil water contents, and vegetation). This would support the result validation in Chapter 5.

This research quantifies the displacement rates by reprocessing the Sentinel-1 data downloaded from the Alaska Satellite Facility's website. At the time 72 descending (11/March/2017 to 31/January/2020) and 69 ascending (08/October/2017 to 07/February/2020) scenes were available, this equates to approximately a three-year observation period. The three years of Sentinel-1 data processed for this research has shown distinct and consistent ground movement trends from the time series analysis, this allows the estimation of displacement rates. However, the literature review in Chapter 2 revealed the fault displacements in Beishan are usually varying temporally. Therefore, the modelled InSAR results may only reflect the surface deformation rates over the observing period but may not be a reliable indicator to predict the surface deformation over 100,000 years' period which are the time scales which are interest to geological disposal facilities.

To reinforce the results and further reduce the instrumental (satellite) measuring error (which is 0.16 mma^{-1} in this research), this research also suggests the future studies re-examining the data using the methods developed for this research but extending the analysis to over 5 years of data. This could significantly improve the measuring precision of the InSAR technique. Further, the ENVISAT ASAR, ALOS, TerraSAR-X, and ERS-1/2 satellite data recorded in this area during same time period could be used to validate the Sentinel-1 results, this would improve the robustness and confidence of the data.

8. Conclusion

By way of conclusion, the final chapter summarizes the outcomes achieved by this research, highlights their significance, lists the research limitations and provides suggestions for future works.

8.1 Introduction and research background

As a part of a convergent wrench fault zone in Northwest China, the granite outcrops at Suanjingzi, Jiujing, and Xinchang in Beishan have long been investigated for the permanent disposal of HLW in a GDF. This research intended to contribute to this significant topic through a combined perspective of structural geology and remote sensing. The main aim of this research is to improve the understanding of local tectonic stability to support the ongoing GDF site investigation, this includes the identifying, mapping, and characterizing the active faults by interpreting the InSAR deformation patterns in both descending-LoS and ascending-LoS directions.

8.2 Research achievements

The main aims in this research are (1) to identify, map, and characterize the micro-displacements along active faults and (2) to assess and conceptualize the structural regime at three study areas (Suanjingzi, Jiujing, and Xinchang) in Beishan Region to support the permanent disposal of HLW in China. To achieve these two aims, this research first identified and distinguish the temporal and spatial impacts of geomorphological processes (erosion and deposition) on LoS displacements in Chapter 5, and then investigated the impacts of the tectonic activity on surface displacements.

8.2.1 Geomorphology

As discussed in Chapter 5, this research first distinguished and separated the geomorphologically induced and tectonically induced deformation in three study areas at Suanjingzi, Jiujing and Xinchang. This is achieved through the application of the coherence change detection method by gathering two time-separated high-resolution satellite radar images of one geographic area for coherence comparison in order to detect and measure the surface changes.

The Quaternary sediments covering the low land areas are more susceptible to the aeolian and fluvial erosion than granite/granodiorite exposed areas based on the conclusion in Chapter 5. This is supported by the extent of temporal decoherence. The granite outcrop areas are characterized by high coherence (>0.7) whilst the area covered by Quaternary sediments are characterized by low coherence (less than 20% of pixels have coherence greater than 0.70) over the monitoring period 08/10/2017 to 26/01/2020. This is because the granite outcrop areas are more resistant to erosion,

so there is less surface weathering as a consequence of aeolian and fluvial processes. These highlighted geomorphological processes have very a low impact on deformation over the granite outcrop areas, so the resulting movement can be associated with tectonic activity.

Further, this research also demonstrated the feasibility of PSInSAR method in measuring slow erosional and depositional rates. PSInSAR (and other PSI methods) measured surface deformation based on the selection of stable scatterers with high interferogram threshold coherence that is controlled by the time interval between the Master and Slave SAR images. The geomorphological processes may continuously but slightly change the surface in study area, therefore, it is possible to generate an interferogram with coherence at the chosen threshold value (0.65 to 0.75), this allows for the monitoring of slow geomorphological processes using PSI, such as the development in incised ephemeral channels.

8.2.2 Tectonics

If as demonstrated tectonic activity is the main cause of surface deformation in the granite outcrop areas (Chapter 6), it is possible to correlate mapping and characterization of active faults. To correlate the visible discontinuities (valleys, gullies, or cracks) in Google Earth's satellite imagery with the SAR image deformation rate patterns, the actual fault movements are identified in the SAR images with distinct displacement rate discontinuities between the two sides of the fault planes.

The InSAR results suggested the tectonic induced displacements in the three study areas generally range from -0.4 to 0.4 mm a^{-1} and are dominated by tectonic fault movements. The overall tectonic movement rates are low, and this is supported by the literature (Chapter 2). This research successfully mapped and characterized more than 30 active faults in the three study areas (Suanjingzi, Jiujing, and Xinchang), which include both known faults and more importantly identified previously undiscovered, unmapped faults. The movements observed were based on their shearing properties and trending directions. These faults can be grouped into two, (1) NE-SW trending sinistrally strike-slipped faults and (2) NW-SE trending dip-slipped reverse faults. These faults are summarized in Table 8.1. The superposition of these compressional and extensional structures collectively contributed the surface displacements monitored by the InSAR technique in this research.

Table 8.1 A summary of the active fault identified in Suanjingzi, Jiujing, and Xinchang

	NE-SW trended	NW-SE or W-E trended
Suanjingzi	F_h, F_e, F_b	F_1, F_2, F_d
Jiujing	$F_{20\text{-}2}$, $F_{20\text{-}1}$, F_{18}, F_{17}, $F_{16\text{-}2}$, F_{15}, F_{14}	F_a, F_b, F_g, $F_{i\text{-}1}$, $F_{i\text{-}2}$, F_m, F_n, F_o
Xinchang	$F_{22\text{-}4}$, F_h, F_{29}, F_{31}	F_b, $F_{29\text{-}1}$, F_a, F_e

Through the identification and the characterization of active faults, this research also improved the understanding of local structural geology. This is based on the theory that the direction of maximum horizontal deformation is aligned with the direction of the maximum in situ compressive stress field (σ1), as a part of the convergent wrench fault zone, where the maximum compression and minimum compression (or extension) are in the directions of NE-SW and NW-SE respectively. The dip-slip and strike-slip shearing properties of the fault plane are believed to be controlled by the correlation between fault strike (θ) and σ1 direction (α). This is tenable under the assumption that the magnitude of σ1 remains constant.

The NE-SW trended strike-slip faults are formed by the NW-SE minimum compression. Their horizontal shearing properties are controlled by the relative direction between fault strike (θ) and σ1 direction (α). A decrease in |θ-α| would lead to a reduction in fault compression and an increase in fault horizontal shearing rates. This would cause the fault motion to be purely strike-slip when |θ-α|tends to be zero. As the faults in Jiujing, Xinchang and even Suanjingzi are originally activated by the sinistrally sheared Sanweishan Fault, most of the faults in these areas are shearing sinistrally.

In contrast, the NW-SE or W-E trending reverse faults are formed due to the compression in the NE-SW direction, which has a high angle to maximum compression (|θ-α| tends to 90^o) and is characterized by distinct vertical discontinuities in the SAR deformation imaginary. An increase in |θ-α| leads to an increased compression and a decrease in fault horizontal shearing rates. This would ultimately generate a purely dip-slipped fault with no horizontal shearing when |θ-α|is 90^o.

8.3 The significance of this research

This research has significant implications for geological and civil engineering applications. Geologically, by identifying, mapping and characterizing the active faults, it improves the understanding of the stress regime and the structural geology in Beishan. The results can be used to explain the correlation between the direction of NE-SW trending maximum compression and the strike- and dip-slipped characteristics of active faults. The results support the relevant studies regarding the tectonic activities

around Arjen Fault Zone, Shulehe Fault Zone and Sanweishan Fault zone in the northern boundary of Qinghai-Tibetan Plateau. The InSAR has demonstrated that faults thought to be inactive are actually still active, albeit displacing very slowly, and it has identified previously unknown faults. In addition, the magnitude of the InSAR displacement rates calculated quantify the rate and type of movement, allowing for the interpretation of the past and present active structural regime at a regional scale. The approach also demonstrates monitoring fault micro-movements over a large region in suitable conditions is possible using InSAR.

Through the comparison of vertical offset rates along active faults, this research indicates Xinchang is tectonically the most stable, followed by Jiujing and Suanjingzi, but critically demonstrating that all regions continue to be tectonically active, underlining the value of this technique with regard to civil infrastructure applications, such as the siting of a GDF that requires safe isolation of radioactive waste for tens of thousands of years. Importantly, the approach developed during this research could be used for long term monitoring of any potential Chinese GDF's in this region. The approach should have wider applications and could be used as an analogue to investigate similar tectonically active regions globally. The applied benefit of this is improving long term monitoring tools for civil infrastructure projects.

This thesis successfully demonstrates a new approach to the mapping and characterizing of active faults through the measurements of micro-displacement rates using PSInSAR technique. The approach of using Earth Observation techniques to undertake structural geology mapping is another tool to be used in conjunction with field observations. But the approach used here tracing the InSAR deformation pattern discontinuities improves the accuracy in positioning the fault plane and make the fault mapping in rural areas with harsh environment (such as Gobi Desert) more feasible.

9. Reference

[1] The subsidiary ledger of the radioactive wastes in China(中国核废料存量的明细账) Available at: http://www.djzhj.com/Item/32033.aspx

[2] THE PEOPLE'S REPUBLIC OF CHINA Third National Report for the Joint Convention on the Safety of Spent Fuel Management and on the Safety of Radioactive Waste Management. Available at: http://nnsa.mee.gov.cn/gjhz_9050/gjgybg/201512/P020151223562288196956.pdf

[3] The situation of the radioactive waste in China in 2018 and the analysis of future development trends. (2018 年我国核废料行业市场现状及发展趋势分析). Available at: https://www.chyxx.com/industry/201805/643813.html

[4] Alley, William M., and Rosemarie Alley. Too hot to touch: the problem of high-level nuclear waste. Cambridge University Press, 2012.

[5] Apted, M.J. and Ahn, J. eds., 2017. Geological repository systems for safe disposal of spent nuclear fuels and radioactive waste. Woodhead Publishing.

[6] Wang, Ju. "On area-specific underground research laboratory for geological disposal of high-level radioactive waste in China." Journal of Rock Mechanics and Geotechnical Engineering 6.2 (2014): 99-104. Available at: https://doi.org/10.1016/j.jrmge.2014.01.002

[7] INTERNATIONAL ATOMIC ENERGY AGENCY, Scientific and Technical Basis for the Geological Disposal of Radioactive Wastes, Technical Reports Series No. 413, IAEA, Vienna (2003)

[8] Nuclear Decommissioning Authority (NDA)., 2013. Geological Disposal-Overview of international siting processes. Available at: https://assets.publishing.service.gov.uk/government/uploads/system/uploads/attachment_data/file/456820/Overview_of_international_siting_processes_September_2013.pdf

[9] Available at: https://www.swissinfo.ch/eng/waste-storage_radioactive-waste--japan-learns-from-switzerland-s-mistakes/44812352

[10] Wang, J., 2010. High-level radioactive waste disposal in China: update 2010. Journal of Rock Mechanics and Geotechnical Engineering, 2(1), pp.1-11.

[11] Jin Yuanxin, Wenguang Wang, and Zhangru Chen. Selection of the host rock for high level radioactive waste repository in China. No. CNIC--01551. China Nuclear Information Centre, 2001.

[12] Ding, H., 2015. The geological conditions and lithological characteristics of the clay rock in Nanbaxian Pre-selected area, Qaidam (Doctoral dissertation, East China University of Technology) (丁鸿. 柴达木盆地西北缘南八仙预选区地质条件与粘土岩特征研究[D]. 东华理工大学, 2015.)

[13] Xu, Guoqing, et al. "Study of the crustal stability of the Beishan area, Gansu province, China-the preselected area for China's high-level radioactive waste repository." The progress report of geological disposal of high-level radioactive waste in China in the past ten years. 2004.

[14] Wang, J., 2019. Progress of geological disposal of high-level radioactive waste in China in the 21st Century. Atomic Energy Science and Technology, 53(10), pp.2072-2081.

[15] Timing of High-level Waste Disposal: https://www.oecd-nea.org/ndd/pubs/2008/6244-timing-waste-disposal.pdf

[16] Bennett, D.G. and Gens, R., 2008. Overview of European concepts for high-level waste and spent fuel disposal with special reference waste container corrosion. Journal of Nuclear Materials, 379(1-3), pp.1-8.

[17] Wei, H., 2012. Research on radionuclide migration in the groundwater of the geological disposal preliminary site of HLW (Doctoral dissertation, China University of Geosciences, Beijing, China) (韦红钢, 2012. 核素在高放废物地质处置预选场的迁移行为研究 (Doctoral dissertation, 北京: 中国地质大学).)

[18] Qiu, G., Li, Q. and Jin, Y., 2014. Investigation on present environmental protection and land use of Jijicao and Xinchang rock mass in Beishan region, Gansu province. World Nuclear Geoscience, 31(suppl. 1), pp.178-183.

[19] Xian, L., 2011. Gansu Rural Yearbook (2011) [M]. Gansu Rural Yearbook Editorial Committee, Lanzhou, China (鲜力群, 2011 甘肃农村年鉴[M] 兰州: 甘肃农村年鉴编委会, 2011.)

[20] Fan, H., and Xian, L., 2011. Gansu Development Yearbook (2011) [M]. China Statistical Publishing House, Beijing, China (樊怀玉, 鲜力群, 甘肃发展年鉴[M] 北京: 中国统计出版社, 2011.)
[21] Jiuquan Climate Weather Averages, World Weather Online, accessed 20 March 2021, <https://www.worldweatheronline.com/jiuquan-weather-averages/gansu/cn.aspx>.
[22] Guo, J.; Zhang, Z.; Wang, J.; Chen, W. The Preliminary Assessment of the Tectonic Activity in Beishan Area; Chinese Society of Mineralogy, Petrology and Geochemistry: Guiyang, China, 2007; Volume 11. (郭召杰, 张志诚, 王驹 and 陈伟明, 2007. 北山候选区构造活动性评价初步研究. 中国矿物岩石地球化学学会第 11 届学术年会论文集.)
[23] Guo, Y.H., Wang, J., Xiao, F., Wang, Z.M., Liu, S.F., Rui, S., Zong, Z.H., Li, Y.W. and Wang, H.L., 2010. Groundwater formation in Beishan (Gansu) preselected area of high-level radioactive waste disposal repository. Geological Journal of China Universities, 16(1), pp.13-18.
[24] Li, J.B., Su, R., Zhou, Z.C., Guo, Y.H., Ji, R.L., Zhang, M., and Wang, H.B., Estimation of shallow groundwater recharge using the environmental tracer chloride method in Beishan Area. Arid Land Geography, 43(1), pp.135-143. (李杰彪, 苏锐, 周志超, 郭永海, 季瑞利, 张明 and 王洪斌, 2020. 基于环境示踪剂氯的北山地区浅部地下水补给研究,干旱区地理, 43(1), pp.135-143.) Available at: https://doi:10.12118/j.issn.1000- 6060.2020.01.16
[25] Zhou, Z., 2014. An investigation of the forming mechanisms of the deep groundwater in Beishan pre-selected area for high-level radioactive waste disposal repository (Doctoral dissertation, Beijing Research Institute of Uranium Geology). (周志超, 2014. 高放废物处置库北山预选区深部地下水成因机制研究 [D] (Doctoral dissertation, 核工业北京地质研究院).)
[26] Liu, S., Guo, Y., Wang, J., Wang, Z., Zong, Z. and Zhou, J., 2007. Groundwater formation and distribution in the preselected Beishan area of repository for high level radioactive waste. Uranium Geology, 23(6), pp.356-362.
[27] Osmanoğlu, B., Sunar, F., Wdowinski, S. and Cabral-Cano, E., 2016. Time series analysis of InSAR data: Methods and trends. ISPRS Journal of Photogrammetry and Remote Sensing, 115, pp.90-102. Available at:
[28] Massonnet, D. and Feigl, K.L., 1998. Radar interferometry and its application to changes in the Earth's surface. Reviews of geophysics, 36(4), pp.441-500.
[29] Wilcox, R.E.; Harding, T.T.; Seely, D.R. Basic wrench tectonics. AAPG Bull. 1973, 57, 74–96. Available at: https://www.semanticscholar.org/paper/Basic-Wrench-Tectonics-Wilcox-Harding/7738acc4a212ef6677df4e37bf8a0ea186000d73
[30] Tchalenko, J.S., 1970. Similarities between shear zones of different magnitudes. Geological Society of America Bulletin, 81(6), pp.1625-1640. Available at: https://doi.org/10.1130/0016-7606(1970)81[1625:SBSZOD]2.0.CO;2
[31] Schreurs, G. and Colletta, B., 1998. Analogue modelling of faulting in zones of continental transpression and transtension. Geological Society, London, Special Publications, 135(1), pp.59-79.
[32] Yun, L., Wang, J., Yang, X. and Song, F., 2015. Neotectonics subdivision and moderate, strong earthquake distribution of preselected site for high-level radioactive waste disposal repository in Beishan. World Nuclear Geoscience, 32(3), pp.172-178. (云龙, 王驹, 杨晓平 and 宋方敏, 2015. 高放废物处置库场址北山预选区新构造运动分区与中, 强地震分布特征. 世界核地质科学, 32(03), pp.3706-0.) Available at: https://doi.org/10.3969/j.issn.1672-0636.2015.03.008
[33] Niu, L., 2015. In-situ stress measurement in nuclear waste disposal sites preselected area (Master's thesis, Chinese Academy of Geological Sciences). (牛琳琳, 2015. 核废料处置场址预选区地应力测量研究 (Master's thesis, 中国地质科学院).)
[34] Wang, F., Wang, J., Fan, H.H., Su, G., Xu, J. and Wang, H.Z., 2005. Distribution of Late Quaternary active faults and its tectonic significance in the Beishan region, Gansu Province, China. Geol Rev, 51, pp.250-259. (王峰, 王驹, 范洪海, 苏刚, 徐健 and 王焕贞, 2005. 甘肃北山旧井地区晚第四纪活动断裂分布及其构造意义. 地质论评, 51(3), pp.250-256.)
[35] Guo, Z., Zhang, Z., Zhang, C., Liu, C., Zhang, Y., Wang, J. and Chen, W., 2008. The Cenozoic strike-slip faults and TTHE regional crust stability of Beishan area. In Proceedings of the 2nd academic

seminar on waste underground disposal. (郭召杰, 张志诚, 张臣, 刘畅, 张宇, 王驹 and 陈伟明, 2008. 甘肃北山地区晚新生代走滑构造与地壳稳定性初步评价. 第二届废物地下处置学术研讨会论文集.)
[36] Guo, J., Zhang, Z., and Wang, J., 1998. Study on the formation and evolution of the Solcuri Basin and its relationship with the Arjen Fault Zone. Geological Journal of China Universities, 4(1), p.59. (郭召杰, 张志诚 and 王建君, 1998. 索尔库里盆地的形成, 演化及其与阿尔金断裂带的关系研究. 高校地质学报, 4(1), p.59.)
[37] Ritts, B.D. and Biffi, U., 2000. Magnitude of post–Middle Jurassic (Bajocian) displacement on the central Altyn Tagh fault system, northwest China. Geological Society of America Bulletin, 112(1), pp.61-74. Available at: https://doi.org/10.1130/0016-7606(2000)112<61:MOPJBD>2.0.CO;2
[38] Matte, P., Tapponnier, P., Arnaud, N., Bourjot, L., Avouac, J.P., Vidal, P., Qing, L., Yusheng, P. and Yi, W., 1996. Tectonics of Western Tibet, between the Tarim and the Indus. Earth and Planetary Science Letters, 142(3-4), pp.311-330. Available at: https://doi.org/10.1016/0012-821X(96)00086-6
[44] Meng, Q.R., Hu, J.M. and Yang, F.Z., 2001. Timing and magnitude of displacement on the Altyn Tagh fault: constraints from stratigraphic correlation of adjoining Tarim and Qaidam basins, NW China. Terra Nova, 13(2), pp.86-91. Available at: https://doi.org/10.1046/j.1365-3121.2001.00320.x
[45] Molnar, P., Burchfiel, B.C., K'uangyi, L. and Ziyun, Z., 1987. Geomorphic evidence for active faulting in the Altyn Tagh and northern Tibet and qualitative estimates of its contribution to the convergence of India and Eurasia. Geology, 15(3), pp.249-253. Available at: https://doi.org/10.1130/0091-7613(1987)15<249:GEFAFI>2.0.CO;2
[46] Yang, H., 2020. Kinematics of active faults and block interactions along the northern Tibetan margin and southern Beishan, China (Doctoral dissertation, Institute of Geology, China Earthquake Administration) (杨海波, 2020. 青藏高原北缘及北山南部活动断层运动学及块体相互作用 (Doctoral dissertation, 中国地震局地质研究所).)
[47] Hudson, J.A., Cosgrove, J.W., Kemppainen, K. and Johansson, E., 2011. Faults in crystalline rock and the estimation of their mechanical properties at the Olkiluoto site, western Finland. Engineering geology, 117(3-4), pp.246-258. Available at: https://doi.org/10.1016/j.enggeo.2010.11.004
[48] Zhao, X.G., Wang, J., Cai, M., Ma, L.K., Zong, Z.H., Wang, X.Y., Su, R., Chen, W.M., Zhao, H.G., Chen, Q.C. and An, Q.M., 2013. In-situ stress measurements and regional stress field assessment of the Beishan area, China. Engineering Geology, 163, pp.26-40. Available at: https://doi.org/10.1016/j.enggeo.2013.05.020
[49] Ma, L.K., 2017. Study on the Long-term stability of Beishan Granitic host rock for high-level radioactive waste repository in the Beishan area in Gansu Province (Doctoral dissertation, Beijing Research Institute of Uranium Geology). (马利科, 2017. 高放废物处置库甘肃北山花岗岩围岩长期稳定性研究 (Doctoral dissertation, 核工业北京地质研究院).)
[50] Tian, X., 2013. The geochemical properties of the granite fracture fillings in Beishan pre-selected area, Gansu Province (Doctoral dissertation, Beijing Research Institute of Uranium Geology) (田霄, 2013. 高放废物地质处置甘肃北山预选区花岗岩裂隙充填物的地球化学特征研究 (Doctoral dissertation, 北京: 核工业北京地质研究院).)
[51] Jiang, S., Luo, H., Chen, WM., et al. Suitability of geological conditions in Suanjingzi area for the disposal of high-level radioactive wastes [J]. Geophysical and Geochemical Exploration. 2021, 45(5): 1208-1216. (蒋实, 罗辉, 陈伟明, 等. 高放废物地质处置算井子地段地质条件适宜性研究[J].物探与化探, 2021, 45 (5): 1208-1216) Available at: http://doi.org/10.11720/wtyht.2021.0388
[52] Zhao, H.G., Liang, J.W., Wang, J., Su, R., Jin, Y.X., Tian, X. and Luo, H., 2019. Geochronology and geochemical characteristics of the Suanjingzi adakitic granites in the Beishan Mountains, Gansu Province, China, and their tectonic significance. Acta Geologica Sinica, 93(2), pp.329-352. (赵宏刚, 梁积伟, 王驹, 苏锐, 金远新, 田霄 and 罗辉, 2019. 甘肃北山算井子埃达克质花岗岩年代学, 地球化学特征及其构造意义. 地质学报, 93(2), pp.329-352.) Available at: http://www/geojournals.cn/dzxb/ch/index.aspx

[53] Wang, J., Chen, W., Jin, Y. and Su, R., 2004. Geology of Jiujing section, Beishan area, Gansu province-the preselected area for China's high level radioactive waste repository (on the scale of 1/50,000). In The progress report of geological disposal of high-level radioactive waste in China in the past ten years. (王驹, 陈伟明, 金远新 and 苏锐, 2004. 旧井地段 1/5 万区域地质特征研究. 中国高放废物地质处置十年进展.)
[54] Wang, J., Su, R., Chen, W.M., Guo, Y.H., Jin, Y.X., Wen, Z.J. and Liu, Y.M., 2006. Deep geological disposal of high-level radioactive wastes in China. Chinese Journal of Rock Mechanics and Engineering, 25(4), pp.649-658.
[55] Li, j., 2014. An investigation of the groundwater recharging from atmospheric precipitation in arid area: a case study at Xinchang-Xiangyangshan pre-selected region in Beishan, China (Master's thesis, Beijing Research Institute of Uranium Geology). (李杰彪, 2014. 干旱地区大气降水入渗补给研究 (Master's thesis, 核工业北京地质研究院).)
[56] Xiao, F., Wang, J., Guo, Y., Wang, Z. and Su, R., 2011. Progress of hydrogeological studies in Beishan preselected area of disposal repository for high level radioactive waste in China. Uranium Geology, 27(3), pp.185-192.
[57] Guo, L., Wu, L., Zhang, J., Liao, M. and Ji, Y., 2020. Identification of homogeneous region boundaries of fractured rock masses in candidate sites for Chinese HLW repository. BULLETIN OF ENGINEERING GEOLOGY AND THE ENVIRONMENT.
[58] Yun L, Zhang J, Wang J, Zhao Z, Bao Y, Zhuang H, Chen S, Zhang J, Zhang J, Zhao H, Zhang B. Discovery of active faults in the southern Beishan area, NW China: Implications for regional tectonics. Journal of Geomechanics, 2021, 27(2): 195-207. (云龙, 张进, 王驹, 赵志涛, 宝音图, 庄海洋, 陈苏, 张竞嘉, 张佳, 赵衡, 张北航. 甘肃北山南部活动断裂的发现及其区域构造意义. 地质力学学报, 2021, 27(2): 195-207.) Available at: http://doi.org/10.12090/j.issn.1006-6616.2021.27.02.019
[59] Yun, L., 2014. An investigation of the tectonic stability at potential GDF host rock in Xinchang and Jijicao (Doctoral dissertation, Beijing Research Institute of Uranium Geology) (云龙, 2014. 高放废物处置库新场和芨芨槽预选场址地壳稳定性研究(Doctoral dissertation, 核工业北京地质研究院).)
[60] Luo, H., 2019. Study on geological characteristics and 3D geological modelling of Xinchang Underground Laboratory Site (Doctoral dissertation, Beijing Research Institute of Uranium Geology). (罗辉, 2019. 地下实验室新场场址地质特征研究与三维地质建模 (Doctoral dissertation, 核工业北京地质研究院).)
[61] Wan, H., 2015. Electromagnetic method detection of granite body distribution and internal structure in Xinchang Area of Beishan, Gansu (Master's thesis, East China Institute of Technology). (万海涛, 2015. 甘肃北山新场地段花岗岩体展布及内部结构电磁法探测 (Master's thesis, 东华理工大学).)
[62] Zong, Z., Wang, J. and Su, R., 2006. Fractal characteristic of fractures in Jiujing, Beishan area, Gansu province. The potential site for high level radioactive waste repository in China. World Nuclear Geoscience, 23(2), pp.107-113. (宗自华, 王驹 and 苏锐, 2006. 甘肃北山预选区旧井地段断裂的分形特征——中国高放废物处置的潜在场址. 世界核地质科学, 23(02), pp.3172-0.)
[63] Wang, J., Chen, L., Su, R. and Zhao, X., 2018. The Beishan underground research laboratory for geological disposal of high-level radioactive waste in China: planning, site selection, site characterization and in situ tests. Journal of Rock Mechanics and Geotechnical Engineering, 10(3), pp.411-435. Available at: https://doi.org/10.1016/j.jrmge.2018.03.002
[64] Jin, Y.X., Min, M.Z., Chen, W.M. and Zhao, H.G., 2007. Study on granite characteristics of Xinchang section of candidate Beishan area, Gansu Province. Chinese Journal of Rock Mechanics and Engineering, 26(Suppl 2), pp.3975-3981. (金远新, 闵茂中, 陈伟明 and 赵宏刚, 2007. 甘肃北山预选区新场地段花岗岩类岩石特征研究. 岩石力学与工程学报, (S2), pp.3974-3981.)
[65] Lei, G., 2015. Study on rock mass joints geometric feature and three-dimension network simulation (Doctoral dissertation, Chongqing University, Chongqing, China) (雷光伟, 2015. 岩体节理几何特征研究及三维网络模拟 (Doctoral dissertation, 重庆: 重庆大学).)

[66] Ling, H., Wang, J., and Chen, W., 2018. Preliminary evaluation of radioactive effect of candidate sites in Suanjingzi sub-area for geological disposal of high-level radioactive waste. Uranium Geology, 34(2), pp.118-123. (凌辉, 王驹 and 陈伟明, 2018. 高放废物地质处置算井子候选场址核素迁移模拟研究. 铀矿地质, 34(02), pp.3853-0.)
[67] Zhang, S., He, Z., Hu, E., Wang, Y.N., Wang, B. and Chen, Q., 2018. The discovery of Mesozoic overthrust nappe tectonics and an analysis of its control of mineralization in Shapoquan area, Ejin Banner, Inner Mongolia. *Geological Bulletin of China*, *37*(2-3), pp.435-445. (张善明, 贺中银, 胡二红, 王亚楠, 王博 and 陈强, 2018. 内蒙古额济纳旗沙坡泉地区发现中生代逆冲推覆构造及其控矿作用. 地质通报, 37(2-3), pp.435-445.) Available at: http://en.cgsjournals.com/article/id/6153fea0ed73f876a05b5eb1
[68] Yun, L., Xu, W., Wang, J., and Liu, Z., 2018. Study on fault activity in near region of Suanjingzi section for disposal of High-level radioactive waste in Beishan preselected area. 7th Symposium on Underground Waste Disposal, 2018-08-24, International Conference. (云龙, 徐伟, 王驹, 刘志成. 高放废物北山预选区算井子地段近区域断裂活动性研究. 第七届废物地下处置学术研讨会论文集 2018-08-24 国际会议)
[69] Zhang, J.L., Pan, Z.L., Chen, C., Zhang, G.F., Zhang, H., Li, Q.Z., Wang, S., Zhang, L.G. and Zhang, Y.Q., 2017. Sedimentary characteristics and age of the Early Cretaceous Chijinbao Formation in the Sandaomingshui of Beishan area, Inner Mongolia. North China Geology, (1), pp.29-34. (张金龙, 潘志龙, 陈超, 张桂凤, 张欢, 李庆喆, 王硕, 张立国 and 张运强, 2017. 内蒙古北山地区三道明水一带早白垩世赤金堡组沉积特征及时代厘定. 地质调查与研究, 40(1), pp.29-34.) Available at: http://doi.org/10.3969/j.issn.1672-4135.2017.01.004
[70] Wang, S., 1990. The stratigraphy of the Dahuoluoshan Group in Beishan, Gansu. Northwest Geoscience, (2). (王树洗, 1990. 甘肃北山大豁落山群的时代. 西北地质科学, 2.)
[71] Wang, L.S., Yang, J.G., Xie, C.L. and Wang, Y.X., 2007. The discovery and geological significance of an early Paleozoic ophiolite melange belt in the Huoshishan part of Beishan Mountain, Gansu Province, China. Geoscience, 21(3), p.45. (王立社, 杨建国, 谢春林 and 王育习, 2007. 甘肃北山火石山地区早古生代蛇绿混杂岩的发现及其地质意义. 现代地质, 21(3), p.451.)
[72] Guo, Y., Wang, J., Wang, Z., Xiao, F., Liu, S., Su, R., Zong, Z. and Li, Y., 2010. Dynamic characteristic of underground water table in Beishan preselection area of high-level radioactive waste disposal repository. Uranium Geology, 26(1), pp.46-50.
[73] Xiao, F., Guo, Y. and Wang, Z., 2012. Outlook of isotopic hydrologic study in Beishan preselected area of high-level waste repository. Uranium Geology, 28(2), pp.83-114.
[74] Zheng, M., Zhang, Q., Huang, Y., Lu, D., Yu, X. and Liu, Y., 2016. Determination of representative groundwater for corrosion assessment of candidate materials used in Beishan area preselected for high-level radioactive waste disposal repository. Journal of Chinese Society for Corrosion and protection, 36(2), pp.185-190. (郑珉, 张琦超, 黄彦良, 路东柱, 余秀明 and 刘月妙, 2016. 中国高放废物处置库甘肃北山预选区腐蚀研究用代表性地下水成分的确定. 中国腐蚀与防护学报, 36(2), pp.185-190.) Available at: https://www.jcscp.org/EN/abstract/abstract24505.shtml
[75] Liu, S., Guo, Y., Su, R., Wang, H., Dong, J., Ji, R. and Zong, Z., 2012. The groundwater chemical characteristics of Xinchang-Xiangyangshan section in Beishan preselected area for Chinese high level radioactive waste repository.
[76] Li, Y., 2020. An investigation of the groundwater geochemical evolution and water-rock interaction in Beishan pre-selected area, Gansu Province (Doctoral dissertation, Beijing Research Institute of Uranium Geology). (李亚楠, 2020. 甘肃北山预选区地下水化学演化规律及水岩作用研究 (Doctoral dissertation, 核工业北京地质研究院).)
[77] Zhang, M., Ji, R., Su, R., Li, J. and Zhou, Z., 2014. Comparison of CHI test data interpretation method in Xinchang block. World Nuclear Geoscience, 31(1), pp.32-38. (张明, 季瑞利, 苏锐, 李杰彪 and 周志超, 2014. 新场岩体定压力压水试验数据解译方法的对比. 世界核地质科学, 31(01), pp.3616-0.)

[78] Guo, L., 2015. Study on seepage characteristics of granite joint and fracture system and fracture structure (Doctoral dissertation, Nanjing university, Nanjing, China) (郭亮, 2015. 花岗岩体节理裂隙系统与断裂构造渗流特性研究 (Doctoral dissertation, 南京: 南京大学).)
[79] Zhang, R., Guo, Y., Xiao, H., Liu, Y. and Li, X., 2019. Microscopic study on permeability test of core in fracture zone [J]. Journal of Engineering Geology, 27(S1): 497-504. (张锐, 郭义, 肖涉恒, 刘洋 and 李晓昭, 2019. 断裂破碎带核部渗透特性试验的微观研究. 工程地质学报, 27(S1), pp.497-504.) Available at: https://doi.org/10.13544/j.cnki.jeg.2019029
[80] https://www.permanet-alpinespace.eu/archive/pdf/WP6_1_dinsar.pdf
[81] Ferretti, A., Prati, C. and Rocca, F., 2000. Nonlinear subsidence rate estimation using permanent Scatterer in differential SAR interferometry. IEEE Transactions on geoscience and remote sensing, 38(5), pp.2202-2212. Available at: https://doi.org/10.1109/36.868878
[82]Ferretti, A., Prati, C. and Rocca, F., 2001. Permanent scatterers in SAR interferometry. IEEE Transactions on geoscience and remote sensing, 39(1), pp.8-20. Available at: https://doi.org/10.1109/36.898661
[83] Scoular, J., Ghail, R., Mason, P. and Lawrence, J., 2022. Are measured InSAR displacements a function of the chosen processing method. Quarterly Journal of Engineering Geology and Hydrogeology, pp. qjegh2022-049. Available at: https://doi.org/10.1144/qjegh2022-049
[84] Perissin, D. and Ferretti, A., 2007. Urban-target recognition by means of repeated spaceborne SAR images. IEEE Transactions on Geoscience and Remote Sensing, 45(12), pp.4043-4058. Available at: https://doi.org/10.1109/TGRS.2007.906092
[85] Ferretti, A., Fumagalli, A., Novali, F., Prati, C., Rocca, F. and Rucci, A., 2011. A new algorithm for processing interferometric data-stacks: SqueeSAR. IEEE transactions on geoscience and remote sensing, 49(9), pp.3460-3470. Available at: https://doi.org/10.1109/TGRS.2011.2124465
[86] Soergel, U., 2010. Review of radar remote sensing on urban areas. In Radar remote sensing of urban areas (pp. 1-47). Springer, Dordrecht.
[87] Werner, C., Wegmuller, U., Strozzi, T. and Wiesmann, A., 2003, July. Interferometric point target analysis for deformation mapping. In IGARSS 2003. 2003 IEEE International Geoscience and Remote Sensing Symposium. Proceedings (IEEE Cat. No. 03CH37477) (Vol. 7, pp. 4362-4364). IEEE. Available at: https://doi.org/10.1109/IGARSS.2003.1295516
[88] Kampes, B. 2005. Displacement Parameter Estimation using Permanent
Scatterer Interferometry. PhD Thesis, Technische Universieit Delft
[89] Lanari, R., Casu, F., Manzo, M., Zeni, G., Berardino, P., Manunta, M. and Pepe, A., 2007. An overview of the small baseline subset algorithm: A DInSAR technique for surface deformation analysis. Deformation and Gravity Change: Indicators of Isostasy, Tectonics, Volcanism, and Climate Change, pp.637-661.
[90] Berardino, P., Fornaro, G., Lanari, R. and Sansosti, E., 2002. A new algorithm for surface deformation monitoring based on small baseline differential SAR interferograms. IEEE Transactions on geoscience and remote sensing, 40(11), pp.2375-2383. Available at: https://doi.org/10.1109/TGRS.2002.803792
[90] Hooper, A., Zebker, H., Segall, P. and Kampes, B., 2004. A new method for measuring deformation on volcanoes and other natural terrains using InSAR persistent scatterers. *Geophysical research letters*, *31*(23). Available at: https://doi.org/10.1029/2004GL021737
[91] Hooper, A., 2008. A multi-temporal InSAR method incorporating both persistent scatterer and small baseline approaches. Geophysical Research Letters, 35(16). Available at: https://doi.org/10.1029/2008GL034654
[92] Rocca, F., Rucci, A., Ferretti, A. and Bohane, A., 2013. Advanced InSAR interferometry for reservoir monitoring. First break, 31(5). Available at: https://doi.org/10.3997/1365-2397.31.5.68075
[93] Ferretti, A., Novali, F., Fumagalli, A., Prati, C., Rocca, F. and Rucci, A., 2009, December. Beyond PSInSAR: the SqueeSAR approach. In AGU fall meeting abstracts (Vol. 2009, pp. G31A-02).
[94] Rosi, A., Tofani, V., Tanteri, L., Stefanelli, C.T., Agostini, A., Catani, F. and Casagli, N., 2018. The new landslide inventory of Tuscany (Italy) updated with PS-InSAR: geomorphological features and

landslide distribution. Landslides, 15(1), pp.5-19. Available at: https://doi.org/10.1007/s10346-017-0861-4
[95] Bozzano, F., Mazzanti, P., Perissin, D., Rocca, A., De Pari, P. and Discenza, M.E., 2017. Basin scale assessment of landslides geomorphological setting by advanced InSAR analysis. Remote Sensing, 9(3), p.267. Available at: https://doi.org/10.3390/rs9030267
[96] Oommen, T. and Escobar-Wolf, R., 2018. Mapping of slow landslides on the Palos Verdes Peninsula using the California landslide inventory and persistent scatterer interferometry. Landslides, 15(3), pp.439-452. Available at: https://doi.org/10.1007/s10346-017-0882-z
[97] Deffontaines, B., Chang, K.J., Champenois, J., Lin, K.C., Lee, C.T., Chen, R.F., Hu, J.C. and Magalhaes, S., 2018. Active tectonics of the onshore Hengchun Fault using UAS DSM combined with ALOS PS-InSAR time series (Southern Taiwan). *Natural Hazards and Earth System Sciences*, *18*(3), pp.829-845. Available at: https://doi.org/10.5194/nhess-18-829-2018
[98] Declercq, P.Y., Gerard, P., Pirard, E., Perissin, D., Walstra, J. and Devleeschouwer, X., 2017. Subsidence related to groundwater pumping for breweries in Merchtem area (Belgium), highlighted by Persistent Scatterer Interferometry. International journal of applied earth observation and geoinformation, 63, pp.178-185. Available at: https://doi.org/10.1016/j.jag.2017.07.012
[99] Grzovic, M. and Ghulam, A., 2015. Evaluation of land subsidence from underground coal mining using TimeSAR (SBAS and PSI) in Springfield, Illinois, USA. *Natural Hazards*, *79*(3), pp.1739-1751. Available at: https://doi.org/10.1007/s11069-015-1927-z
[100] Zhao, C., Kang, Y., Zhang, Q., Lu, Z. and Li, B., 2018. Landslide identification and monitoring along the Jinsha River catchment (Wudongde reservoir area), China, using the InSAR method. Remote Sensing, 10(7), p.993. Available at: https://doi.org/10.3390/rs10070993
[101] Jia, H., Zhang, H., Liu, L. and Liu, G., 2019. Landslide deformation monitoring by adaptive distributed scatterer interferometric synthetic aperture radar. Remote Sensing, 11(19), p.2273. Available at: https://doi.org/10.3390/rs11192273
[102] Liu, B., Luo, Y., Zhang, J., Gong, L., Jiang, W. and Ren, L., 2010, July. PS-InSAR time series analysis for measuring surface deformation before the L'Aquila earthquake. In *2010 IEEE International Geoscience and Remote Sensing Symposium* (pp. 4604-4607). IEEE. Available at: https://doi.org/10.1109/IGARSS.2010.5650971
[103] Motagh, M., Shamshiri, R., Haghighi, M.H., Wetzel, H.U., Akbari, B., Nahavandchi, H., Roessner, S. and Arabi, S., 2017. Quantifying groundwater exploitation induced subsidence in the Rafsanjan plain, southeastern Iran, using InSAR time-series and in situ measurements. Engineering geology, 218, pp.134-151. Available at: https://doi.org/10.1016/j.enggeo.2017.01.011
[104] Champenois, J., Fruneau, B., Pathier, E., Deffontaines, B., Lin, K.C. and Hu, J.C., 2012. Monitoring of active tectonic deformations in the Longitudinal Valley (Eastern Taiwan) using Persistent Scatterer InSAR method with ALOS PALSAR data. Earth and Planetary Science Letters, 337, pp.144-155. Available at: https://doi.org/10.1016/j.epsl.2012.05.025
[105] Yazici, B.V. and Tunc Gormus, E., 2020. Investigating persistent scatterer InSAR (PSInSAR) technique efficiency for landslides mapping: a case study in Artvin dam area, in Turkey. Geocarto International, pp.1-19. Available at: https://doi.org/10.1080/10106049.2020.1818854
[106] Cetin, E., Cakir, Z., Meghraoui, M., Ergintav, S. and Akoglu, A.M., 2014. Extent and distribution of aseismic slip on the Ismetpaşa segment of the North Anatolian Fault (Turkey) from Persistent Scatterer InSAR. Geochemistry, Geophysics, Geosystems, 15(7), pp.2883-2894. Available at: https://doi.org/10.1002/2014GC005307
[107] Siles, G.L., Alcérreca-Huerta, J.C., López-Quiroz, P. and Hernández, J.C., 2015. On the potential of time series InSAR for subsidence and ground rupture evaluation: application to Texcoco and Cuautitlan–Pachuca subbasins, northern Valley of Mexico. Natural Hazards, 79(2), pp.1091-1110. Available at: https://doi.org/10.1007/s11069-015-1894-4
[108] Fatholahi, N., Akhoondzadeh, M. and Bahroudi, A., 2020. An investigation of surface deformation over oilfield in Southwest Iran (2003–2010) using InSAR and physical modelling.

International Journal of Remote Sensing, 41(14), pp.5355-5370. Available at: https://doi.org/10.1080/01431161.2020.1731929
[109] Tong, X. and Schmidt, D., 2016. Active movement of the Cascade landslide complex in Washington from a coherence based InSAR time series method. Remote Sensing of Environment, 186, pp.405-415. Available at: https://doi.org/10.1016/j.rse.2016.09.008
[110] Lauknes, T.R., Shanker, A.P., Dehls, J.F., Zebker, H.A., Henderson, I.H.C. and Larsen, Y., 2010. Detailed rockslide mapping in northern Norway with small baseline and persistent scatterer interferometric SAR time series methods. Remote Sensing of Environment, 114(9), pp.2097-2109. Available at: https://doi.org/10.1016/j.rse.2010.04.015
[111] Yang, C.S., Zhang, Q., Zhao, C.Y., Wang, Q.L. and Ji, L.Y., 2014. Monitoring land subsidence and fault deformation using the small baseline subset InSAR technique: a case study in the Datong Basin, China. Journal of Geodynamics, 75, pp.34-40. Available at: https://doi.org/10.1016/j.jog.2014.02.002
[112] Yang, C., Zhang, Q. and Zhao, C., 2016, July. Ground deformation investigation over Taiyuan Basin (China) by InSAR technology. In *2016 IEEE International Geoscience and Remote Sensing Symposium (IGARSS)* (pp. 6831-6834). IEEE. Available at: https://doi.org/10.1109/IGARSS.2016.7730783
[113] Funning, G.J., Bürgmann, R., Ferretti, A., Novali, F. and Fumagalli, A., 2007. Creep on the Rodgers Creek fault, northern San Francisco Bay area from a 10-year PS-InSAR dataset. *Geophysical Research Letters*, *34*(19). Available at: https://doi.org/10.1029/2007GL030836
[114] Parcharidis, I., Foumelis, M., Kourkouli, P. and Wegmuller, U., 2009. Persistent Scatterer InSAR to detect ground deformation over Rio-Antirio area (Western Greece) for the period 1992–2000. Journal of Applied Geophysics, 68(3), pp.348-355. Available at: https://doi.org/10.1016/j.jappgeo.2009.02.005
[115] Jin, L. and Funning, G.J., 2017. Testing the inference of creep on the northern Rodgers Creek fault, California, using ascending and descending persistent scatterer InSAR data. Journal of Geophysical Research: Solid Earth, 122(3), pp.2373-2389. Available at: https://doi.org/10.1002/2016JB013535
[116] Halldén, T.H., 2017. Measuring coastal erosion along the coast of Ystad municipality using PSInSAR and SBAS.
[117] Jiang, C. and Fan, W., 2019. Rader Tracer Erosion Analysis of Dongzhiyu District Based on Radar Imagery. 대한지질공학회 학술발표논문집, 2019(2), pp.159-159.
[118] Mider, G., Lawrence, J., Mason, P. and Ghail, R., 2020. Monitoring Littoral Platform Downwearing Using Differential SAR Interferometry. Remote Sensing, 12(19), p.3243. Available at: https://doi.org/10.3390/rs12193243
[119] Jiang, C., Fan, W., Yu, N. and Nan, Y., 2021. A New Method to Predict Gully Head Erosion in the Loess Plateau of China Based on SBAS-InSAR. *Remote Sensing*, *13*(3), p.421. Available at: https://doi.org/10.3390/rs13030421
[120] Sajinkumar, K.S., Bincy, H.S., Bouali, E.H., Oommen, T., Vishnu, C.L., Anilkumar, Y., Thrivikramji, K.P. and Keerthy, S., 2021. Picturing beach erosion and deposition trends using PSInSAR: an example from the non-barred southern west coast of India. Wetlands Ecology and Management, 29(5), pp.775-788. Available at: https://doi.org/10.1007/s11273-020-09706-3
[121] Aswathi, J., Sajinkumar, K.S., Rajaneesh, A., Oommen, T., Bouali, E.H., Binojkumar, R.B., Rani, V.R., Thomas, J., Thrivikramji, K.P., Ajin, R.S. and Abioui, M., 2022. Furthering the precision of RUSLE soil erosion with PSInSAR data: An innovative model. Geocarto International, (just-accepted), pp.1-22. Available at: https://doi.org/10.1080/10106049.2022.2105407
[122] Mason, P.J., Bischoff, C.A., Hughes, G., Petrone, C.M., Varley, N.R., Nicholas, G. and Ferretti, A., 2022. Monitoring ground movement at Volcán de Colima, Mexico, using Sentinel-1 data and SqueeSAR®. Quarterly Journal of Engineering Geology and Hydrogeology, pp. qjegh2022-047. Available at: https://doi.org/10.1144/qjegh2022-0
[123] Dehghani, M., Zoej, M.J.V., Hooper, A., Hanssen, R.F., Entezam, I. and Saatchi, S., 2013. Hybrid conventional and persistent scatterer SAR interferometry for land subsidence monitoring in the

Tehran Basin, Iran. ISPRS journal of photogrammetry and remote sensing, 79, pp.157-170. Available at: https://doi.org/10.1016/j.isprsjprs.2013.02.012
[124] Dang, V.K., Nguyen, T.D., Dao, N.H., Duong, T.L., Dinh, X.V. and Weber, C., 2021. Land subsidence induced by underground coal mining at Quang Ninh, Vietnam: persistent scatterer interferometric synthetic aperture radar observation using Sentinel-1 data. International Journal of Remote Sensing, 42(9), pp.3563-3582. Available at: https://doi.org/10.1080/01431161.2021.1875513
[125] Qu, F., Lu, Z., Zhang, Q., Bawden, G.W., Kim, J.W., Zhao, C. and Qu, W., 2015. Mapping ground deformation over Houston–Galveston, Texas using multi-temporal InSAR. Remote Sensing of Environment, 169, pp.290-306. Available at: https://doi.org/10.1016/j.rse.2015.08.027
[126] Chen, F., Lin, H., Zhang, Y. and Lu, Z., 2012. Ground subsidence geo-hazards induced by rapid urbanization: Implications from InSAR observation and geological analysis. Natural Hazards and Earth System Sciences, 12(4), pp.935-942. Available at: https://doi.org/10.5194/nhess-12-935-2012
[127] Zeng, R.Q., Meng, X.M., Wasowski, J., Dijkstra, T., Bovenga, F., Xue, Y.T. and Wang, S.Y., 2014. Ground instability detection using PS-InSAR in Lanzhou, China. Quarterly journal of engineering geology and hydrogeology, 47(4), pp.307-321. Available at: https://doi.org/10.1144/qjegh2014-040
[128] Yang, Q., Ke, Y., Zhang, D., Chen, B., Gong, H., Lv, M., Zhu, L. and Li, X., 2018. Multi-scale analysis of the relationship between land subsidence and buildings: A case study in an eastern Beijing Urban Area using the PS-InSAR technique. Remote Sensing, 10(7), p.1006. Available at: https://doi.org/10.3390/rs10071006
[129] Hu, L., Dai, K., Xing, C., Li, Z., Tomás, R., Clark, B., Shi, X., Chen, M., Zhang, R., Qiu, Q. and Lu, Y., 2019. Land subsidence in Beijing and its relationship with geological faults revealed by Sentinel-1 InSAR observations. *International Journal of Applied Earth Observation and Geoinformation*, *82*, p.101886. Available at: https://doi.org/10.1016/j.jag.2019.05.019
[130] Haghighi, M.H. and Motagh, M., 2019. Ground surface response to continuous compaction of aquifer system in Tehran, Iran: Results from a long-term multi-sensor InSAR analysis. Remote sensing of environment, 221, pp.534-550. Available at: https://doi.org/10.1016/j.rse.2018.11.003
[131] Zhang, Z., Wang, C., Tang, Y., Zhang, H. and Fu, Q., 2015. Analysis of ground subsidence at a coal-mining area in Huainan using time-series InSAR. International Journal of Remote Sensing, 36(23), pp.5790-5810. Available at: https://doi.org/10.1080/01431161.2015.1109725
[132] Osmanoğlu, B., Dixon, T.H., Wdowinski, S., Cabral-Cano, E. and Jiang, Y., 2011. Mexico City subsidence observed with persistent scatterer InSAR. International Journal of Applied Earth Observation and Geoinformation, 13(1), pp.1-12. Available at: https://doi.org/10.1016/j.jag.2010.05.009
[133] Cigna, F., Osmanoğlu, B., Cabral-Cano, E., Dixon, T.H., Ávila-Olivera, J.A., Garduño-Monroy, V.H., DeMets, C. and Wdowinski, S., 2012. Monitoring land subsidence and its induced geological hazard with Synthetic Aperture Radar Interferometry: A case study in Morelia, Mexico. Remote Sensing of Environment, 117, pp.146-161. Available at: https://doi.org/10.1016/j.rse.2011.09.005
[134] van der Horst, T., Rutten, M.M., van de Giesen, N.C. and Hanssen, R.F., 2018. Monitoring land subsidence in Yangon, Myanmar using Sentinel-1 persistent scatterer interferometry and assessment of driving mechanisms. Remote sensing of environment, 217, pp.101-110. Available at: https://doi.org/10.1016/j.rse.2018.08.004
[135] Bonì, R., Cigna, F., Bricker, S., Meisina, C. and McCormack, H., 2016. Characterisation of hydraulic head changes and aquifer properties in the London Basin using Persistent Scatterer Interferometry ground motion data. Journal of Hydrology, 540, pp.835-849. Available at: https://doi.org/10.1016/j.jhydrol.2016.06.068
[136] Temporim, F.A., Gama, F.F., Mura, J.C., Paradella, W.R. and Silva, G.G., 2017. Application of persistent scatterers interferometry for surface displacements monitoring in N5E open pit iron mine using TerraSAR-X data, in Carajás Province, Amazon region. Brazilian Journal of Geology, 47, pp.225-235. Available at: https://doi.org/10.1590/2317-4889201720170006
[137] El Kamali, M., Papoutsis, I., Loupasakis, C., Abuelgasim, A., Omari, K. and Kontoes, C., 2021. Monitoring of land surface subsidence using persistent scatterer interferometry techniques and

ground truth data in arid and semi-arid regions, the case of Remah, UAE. Science of The Total Environment, 776, p.145946. Available at: https://doi.org/10.1016/j.scitotenv.2021.145946
[138] Jiang, Y., Liao, M., Wang, H., Zhang, L. and Balz, T., 2016. Deformation monitoring and analysis of the geological environment of Pudong international airport with persistent scatterer SAR interferometry. Remote Sensing, 8(12), p.1021. Available at: https://doi.org/10.3390/rs8121021
[139] Catalao, J., Raju, D. and Nico, G., 2020. InSAR maps of land subsidence and sea level scenarios to quantify the flood inundation risk in coastal cities: The case of Singapore. *Remote Sensing*, *12*(2), p.296. Available at: https://doi.org/10.3390/rs12020296
[140] Ng, A.H.M., Ge, L., Li, X., Abidin, H.Z., Andreas, H. and Zhang, K., 2012. Mapping land subsidence in Jakarta, Indonesia using persistent scatterer interferometry (PSI) technique with ALOS PALSAR. International Journal of Applied Earth Observation and Geoinformation, 18, pp.232-242. Available at: https://doi.org/10.1016/j.jag.2012.01.018
[141] Mason, P.J., Ghail, R.C., Bischoff, C. and Skipper, J.A., 2015. Detecting and monitoring small-scale discrete ground movements across London, using Persistent Scatterer InSAR (PSI).[unpublished]
[142] Bell, J.W., Amelung, F., Ferretti, A., Bianchi, M. and Novali, F., 2008. Permanent scatterer InSAR reveals seasonal and long-term aquifer-system response to groundwater pumping and artificial recharge. *Water Resources Research*, *44*(2). Available at: https://doi.org/10.1029/2007WR006152
[143] Kim, S.W., Wdowinski, S., Dixon, T.H., Amelung, F., Kim, J.W. and Won, J.S., 2010. Measurements and predictions of subsidence induced by soil consolidation using persistent scatterer InSAR and a hyperbolic model. Geophysical Research Letters, 37(5). Available at: https://doi.org/10.1029/2009GL041644
[144] Heleno, S.I., Oliveira, L.G., Henriques, M.J., Falcão, A.P., Lima, J.N., Cooksley, G., Ferretti, A., Fonseca, A.M., Lobo-Ferreira, J.P. and Fonseca, J.F., 2011. Persistent scatterers interferometry detects and measures ground subsidence in Lisbon. Remote Sensing of Environment, 115(8), pp.2152-2167. Available at: https://doi.org/10.1016/j.rse.2011.04.021
[145] Smolianinova, E.I., Mikhailov, V.O. and Dmitriev, P.N., 2020. Subsidence monitoring in the Imereti Lowland (the Big Sochi region) using multifrequency InSAR data for 2007–2019. Sovremennye problemy distantsionnogo zondirovaniya Zemli iz kosmosa, 17(5), pp.103-113. Available at: https://doi.org/10.21046/2070-7401-2020-17-5-103-113
[146] Khan, S.D., Huang, Z. and Karacay, A., 2014. Study of ground subsidence in northwest Harris County using GPS, LiDAR, and InSAR techniques. Natural Hazards, 73(3), pp.1143-1173. Available at: https://doi.org/10.1007/s11069-014-1067-x
[147] Ge, W., Li, Y., Wang, Z., ZHANG, C. and Yang, H., 2021. Spatial-Temporal Ground Deformation Study of Baotou Based on the PS-InSAR Method. Acta Geologica Sinica-English Edition, 95(2), pp.674-683. Available at: https://doi.org/10.1111/1755-6724.14651
[148] Agarwal, V., Kumar, A., L Gomes, R. and Marsh, S., 2020. Monitoring of ground movement and groundwater changes in London using InSAR and GRACE. Applied Sciences, 10(23), p.8599. Available at: https://doi.org/10.3390/app10238599
[149] Razi, P., Sumantyo, J.T.S., Perissin, D., Kuze, H., Chua, M.Y. and Panggabean, G.F., 2018. 3D land mapping and land deformation monitoring using persistent scatterer interferometry (PSI) ALOS PALSAR: Validated by Geodetic GPS and UAV. IEEE Access, 6, pp.12395-12404. Available at: https://doi.org/10.1109/ACCESS.2018.2804899
[150] Beladam, O., Balz, T., Mohamadi, B. and Abdalhak, M., 2019. Using ps-insar with sentinel-1 images for deformation monitoring in northeast Algeria. Geosciences, 9(7), p.315. Available at: https://doi.org/10.3390/geosciences9070315
[151] Pratesi, F., Tapete, D., Del Ventisette, C. and Moretti, S., 2016. Mapping interactions between geology, subsurface resource exploitation and urban development in transforming cities using InSAR Persistent Scatterers: Two decades of change in Florence, Italy. Applied Geography, 77, pp.20-37. Available at: https://doi.org/10.1016/j.apgeog.2016.09.017

[152] Gao, M., Gong, H., Chen, B., Zhou, C., Chen, W., Liang, Y., Shi, M. and Si, Y., 2016. InSAR time-series investigation of long-term ground displacement at Beijing Capital International Airport, China. Tectonophysics, 691, pp.271-281. Available at: https://doi.org/10.1016/j.tecto.2016.10.016
[153] Cigna, F., Lasaponara, R., Masini, N., Milillo, P. and Tapete, D., 2014. Persistent scatterer interferometry processing of COSMO-SkyMed StripMap HIMAGE time series to depict deformation of the historic centre of Rome, Italy. Remote Sensing, 6(12), pp.12593-12618. Available at: https://doi.org/10.3390/rs61212593
[154] Declercq, P.Y., Walstra, J., Gérard, P., Pirard, E., Perissin, D., Meyvis, B. and Devleeschouwer, X., 2017. A Study of Ground Movements in Brussels (Belgium) Monitored by Persistent Scatterer Interferometry over a 25-Year Period. Geosciences, 7(4), p.115. Available at: https://doi.org/10.3390/geosciences7040115
[155] Jung, J., Kim, D.J., Lavalle, M. and Yun, S.H., 2016. Coherent change detection using InSAR temporal decorrelation model: A case study for volcanic ash detection. IEEE Transactions on Geoscience and Remote Sensing, 54(10), pp.5765-5775. Available at: https://doi.org/10.1109/TGRS.2016.2572166
[156] Bischoff, C., Mason, P. J., Ghail, R. C. & Davis, J., 2019. Revealing mm-scale ground movements in London using SqueeSARTM, Quarterly Journal of Geology & Hydrology, 53(1):3. Available at: https://doi.org/10.1144/qjegh2018-075
[157] Monti-Guarnieri, A.V., Brovelli, M.A., Manzoni, M., d'Alessandro, M.M., Molinari, M.E. and Oxoli, D., 2018. Coherent change detection for multipass SAR. IEEE Transactions on Geoscience and Remote Sensing, 56(11), pp.6811-6822. Available at: https://doi.org/10.1109/TGRS.2018.2843560
[158] Closson, D. and Milisavljevic, N., 2017. InSAR Coherence and Intensity Changes Detection. Mine Action-The Research Experience of the Royal Military Academy of Belgium.
[159] Havivi, S., Amir, D., Schvartzman, I., August, Y., Maman, S., Rotman, S.R. and Blumberg, D.G., 2018. Mapping dune dynamics by InSAR coherence. Earth Surface Processes and Landforms, 43(6), pp.1229-1240. Available at: https://doi.org/10.1002/esp.4309
[160] Kim, J., Dorjsuren, M., Choi, Y. and Purevjav, G., 2020. Reconstructed Aeolian Surface Erosion in Southern Mongolia by Multi-Temporal InSAR Phase Coherence Analyses. Front. Earth Sci, 8, p.531104. Available at: https://doi.org/10.3389/feart.2020.531104
[161] Kim, J.R., Lin, C.W. and Lin, S.Y., 2021. The Use of InSAR Phase Coherence Analyses for the Monitoring of Aeolian Erosion. Remote Sensing, 13(12), p.2240. Available at: https://doi.org/10.3390/rs13122240
[162] Jordan, T.E., Lohman, R.B., Tapia, L., Pfeiffer, M., Scott, C.P., Amundson, R., Godfrey, L. and Riquelme, R., 2020. Surface materials and landforms as controls on InSAR permanent and transient responses to precipitation events in a hyperarid desert, Chile. *Remote Sensing of Environment*, *237*, p.111544. Available at: https://doi.org/10.1016/j.rse.2019.111544
[163] Gaber, A., Abdelkareem, M., Abdelsadek, I.S., Koch, M. and El-Baz, F., 2018. Using InSAR coherence for investigating the interplay of fluvial and aeolian features in arid lands: implications for groundwater potential in Egypt. *Remote Sensing*, *10*(6), p.832. Available at: https://doi.org/10.3390/rs10060832
[164] Li, Y., Martinis, S. and Wieland, M., 2019. Urban flood mapping with an active self-learning convolutional neural network based on TerraSAR-X intensity and interferometric coherence. ISPRS Journal of Photogrammetry and Remote Sensing, 152, pp.178-191. Available at: https://doi.org/10.1016/j.isprsjprs.2019.04.014
[165] Selmi, S., Abdallah, W.B. and Abdelfatteh, R., 2014. Flood mapping using InSAR coherence map. The International Archives of Photogrammetry, Remote Sensing and Spatial Information Sciences, 40(7), p.161. Available at: https://doi.org/10.5194/isprsarchives-XL-7-161-2014
[166] Schepanski, K., Wright, T.J. and Knippertz, P., 2012. Evidence for flash floods over deserts from loss of coherence in InSAR imagery. Journal of Geophysical Research: Atmospheres, 117(D20). Available at: https://doi.org/10.1029/2012JD017580

[167] Chaabani, C., Chini, M., Abdelfattah, R., Hostache, R. and Chokmani, K., 2018. Flood mapping in a complex environment using bistatic TanDEM-X/TerraSAR-X InSAR coherence. Remote sensing, 10(12), p.1873. Available at: https://doi.org/10.3390/rs10121873
[168] Cabré, A., Remy, D., Aguilar, G. and Riquelme, R., 2018, April. Coherence-loss from InSAR data in the Atacama Desert after the March 2015 extreme event. In EGU General Assembly Conference Abstracts (p. 13591).
[169] Cabré, A. et al., 2020. Mapping rainstorm erosion associated with an individual storm from InSAR coherence loss validated by field evidence for the Atacama Desert. Earth Surface Processes and Landforms, 45(9), pp.2091–2106. Available at: http://dx.doi.org/10.1002/esp.4868.
[170] Geudtner, D., Winter, R. and Vachon, P.W., 1996, May. Flood monitoring using ERS-1 SAR interferometry coherence maps. In IGARSS'96. 1996 International Geoscience and Remote Sensing Symposium (Vol. 2, pp. 966-968). IEEE. Available at: https://doi.org/10.1109/IGARSS.1996.516536
[171] Chini, M., Papastergios, A., Pulvirenti, L., Pierdicca, N., Matgen, P. and Parcharidis, I., 2016, July. SAR coherence and polarimetric information for improving flood mapping. In 2016 IEEE International Geoscience and Remote Sensing Symposium (IGARSS) (pp. 7577-7580). IEEE. Available at: https://doi.org/10.1109/IGARSS.2016.7730976
[172] Chini, M., Pelich, R., Pulvirenti, L., Pierdicca, N., Hostache, R. and Matgen, P., 2019. Sentinel-1 InSAR coherence to detect floodwater in urban areas: Houston and Hurricane Harvey as a test case. Remote Sensing, 11(2), p.107. Available at: https://doi.org/10.3390/rs11020107
[173] Chini, M., Hostache, R., Pelich, R., Matgen, P., Pulvirenti, L. and Pierdicca, N., 2019, July. Probabilistic Urban Flood Mapping Using SAR Data. In IGARSS 2019-2019 IEEE International Geoscience and Remote Sensing Symposium (pp. 4643-4645). IEEE. Available at: https://doi.org/10.1109/IGARSS.2019.8898523
[174] Giordano, F., Goccia, M. and Dellepiane, S., 2005, September. Segmentation of coherence maps for flood damage assessment. In IEEE International Conference on Image Processing 2005 (Vol. 2, pp. II-233). IEEE. Available at: https://doi.org/10.1109/ICIP.2005.1530034
[175] Corr, D.G. and Rodrigues, A., 1998, July. Coherent change detection of vehicle movements. In IGARSS'98. Sensing and Managing the Environment. 1998 IEEE International Geoscience and Remote Sensing. Symposium Proceedings. (Cat. No. 98CH36174) (Vol. 5, pp. 2451-2453). IEEE. Available at: https://doi.org/10.1109/IGARSS.1998.702243
[176] Angelliaume, S., Oriot, H. and Dupuis, X., 2008, June. A coherent change detection analysis using multi-pass airborne interferometric data at X-band. In *7th European Conference on Synthetic Aperture Radar* (pp. 1-4). VDE. Available at: https://ieeexplore.ieee.org/xpl/conhome/5757081/proceeding
[177] Oriot, H., Dupuis, X. and Du Plessis, O.R., 2010, June. Coherent change detection in urban environment. In 8th European Conference on Synthetic Aperture Radar (pp. 1-3). VDE. Available at: https://ieeexplore.ieee.org/xpl/conhome/5757416/proceeding
[178] Mattar, K.E. and Secker, J., 2015, July. Coherent stacks of RADARSAT-2 spotlight mode interferometry data for monitoring Arctic DEW Line Clean-Up. In 2015 IEEE International Geoscience and Remote Sensing Symposium (IGARSS) (pp. 1519-1522). IEEE. Available at: https://doi.org/10.1109/IGARSS.2015.7326069
[179] Milisavljević, N., Closson, D. and Bloch, I., 2010, July. Detecting potential human activities using coherent change detection. In 2010 2nd International Conference on Image Processing Theory, Tools, and Applications (pp. 482-485). IEEE. Available at: https://doi.org/10.1109/IPTA.2010.5586772
[180] Wang, S., Lu, X., Chen, Z., Zhang, G., Ma, T., Jia, P. and Li, B., 2020. Evaluating the Feasibility of illegal open-pit mining identification using InSAR coherence. Remote Sensing, 12(3), p.367. Available at: https://doi.org/10.3390/rs12030367
[181] Abdel-Hamid, A., Dubovyk, O. and Greve, K., 2021. The potential of sentinel-1 InSAR coherence for grasslands monitoring in Eastern Cape, South Africa. International Journal of Applied Earth Observation and Geoinformation, 98, p.102306. Available at: https://doi.org/10.1016/j.jag.2021.102306

[182] Brisco, B., Ahern, F., Murnaghan, K., White, L., Canisus, F. and Lancaster, P., 2017. Seasonal change in wetland coherence as an aid to wetland monitoring. Remote Sensing, 9(2), p.158. Available at: https://doi.org/10.3390/rs9020158
[183] Canisius, F., Brisco, B., Murnaghan, K., Van Der Kooij, M. and Keizer, E., 2019. SAR backscatter and InSAR coherence for monitoring wetland extent, flood pulse and vegetation: A study of the Amazon lowland. Remote Sensing, 11(6), p.720. Available at: https://doi.org/10.3390/rs11060720
[184] Babu, A. and Kumar, S., 2019. InSAR coherence and backscatter images-based analysis for the Anak Krakatau volcano eruption. In Multidisciplinary digital publishing institute proceedings (Vol. 24, No. 1, p. 21). Available at: https://doi.org/10.3390/IECG2019-06216
[185] Natsuaki, R., Nagai, H., Tomii, N. and Tadono, T., 2018. Sensitivity and limitation in damage detection for individual buildings using InSAR coherence—A case study in 2016 Kumamoto earthquakes. Remote Sensing, 10(2), p.245. Available at: https://doi.org/10.3390/rs10020245
[186] Goorabi, A., 2020. Detection of landslide induced by large earthquake using InSAR coherence techniques–Northwest Zagros, Iran. The Egyptian Journal of Remote Sensing and Space Science, 23(2), pp.195-205. Available at: https://doi.org/10.1016/j.ejrs.2019.04.002
[187] Tzouvaras, M., Danezis, C. and Hadjimitsis, D.G., 2020. Small scale landslide detection using Sentinel-1 interferometric SAR coherence. Remote Sensing, 12(10), p.1560. Available at: https://doi:10.3390/rs12101560
[188] Jacquemart, M. and Tiampo, K., 2020. Radar coherence and NDVI ratios as landslide early warning indicators. Natural Hazards and Earth System Sciences Discussions, 2020, pp.1-16. Available at: https://doi.org/10.5194/nhess-2020-227
[189] Ullmann, T., Sauerbrey, J., Hoffmeister, D., May, S.M., Baumhauer, R. and Bubenzer, O., 2019. Assessing spatiotemporal variations of sentinel-1 InSAR coherence at different time scales over the atacama desert (Chile) between 2015 and 2018. *Remote Sensing*, *11*(24), p.2960. Available at: https://doi.org/10.3390/rs11242960
[190] Lee, H., and Liu, J.G., 2001. Analysis of topographic decorrelation in SAR interferometry using ratio coherence imagery. *IEEE Transactions on Geoscience and Remote Sensing*, *39*(2), pp.223-232. Available at: https://doi.org/10.1109/36.905230
[191] Liu, J.G., Mason, P.J., Hilton, F. & Lee, H., 2004. Detection of Rapid Erosion in SE Spain: a GIS Approach Based on ERS SAR Coherence Imagery. Photogrammetric Engineering and Remote Sensing, 70, Number 10, 1179-1185. Available at: https://doi.org/10.1117/12.413954
[192] Ballou, Glen (2005). Handbook for sound engineers (3 ed.). Focal Press, Gulf Professional Publishing. p. 1499. ISBN 978-0-240-80758-4.
[193] Castellazzi, Pascal; Schmid, Wolfgang. Ground displacements in the Lower Namoi region. NSW DPIE: CSIRO; 2020. Available at: http://hdl.handle.net/102.100.100/367006?index=1
[194] Miky, Y.H., 2019. Multitemporal Sentinel-1 SAR Interferometry for Surface Deformation Monitoring near High Dam in Aswan, Egypt. *American Journal of Geographic Information System*, *8*(2), pp.96-102.
[195] Xu, B., Li, Z., Zhu, Y., Shi, J. and Feng, G., 2020. SAR interferometric baseline refinement based on flat-earth phase without a ground control point. *Remote Sensing*, *12*(2), p.233.
[196] Xiang, Z., Wang, K. and Liu, X., 2008, March. A new DEM reconstruction method based on an accurate flattening algorithm in interferometric SAR. In *2008 IEEE International Conference on Acoustics, Speech and Signal Processing* (pp. 1093-1096). IEEE.
[197] Baek, J., Kim, S.W., Park, H.J., Jung, H.S., Kim, K.D. and Kim, J.W., 2008. Analysis of ground subsidence in coal mining area using SAR interferometry. Geosciences Journal, 12(3), pp.277-284.
[198] Xueliang, W.A.N.G., Zhenhua, H.A.N., Luqing, Z.H.A.N.G. and Jian, Z.H.O.U., 2018. Regional engineering geology suitability assessment for high-level radioactive waste disposal of pre-selected Alxa area. *Journal of Engineering Geology*, *26*(6), pp.1715-1723.
[199] Jiang, S., Shi, F., Hu, B., Wang, W. and Lin, Q., 2017, December. Monitoring of the Ground Subsidence in Macao Using the PSI Technique. In *International Conference on Geo-Spatial Knowledge and Intelligence* (pp. 250-261). Springer, Singapore.

[200] Hu, B., Chen, J. and Zhang, X., 2019. Monitoring the land subsidence area in a coastal urban area with InSAR and GNSS. *Sensors*, *19*(14), p.3181.
[201] Fárová, K., Jelének, J., Kopačková-Strnadová, V. and Kycl, P., 2019. Comparing DInSAR and PSI techniques employed to Sentinel-1 data to monitor highway stability: a case study of a massive Dobkovičky landslide, Czech Republic. *Remote Sensing*, *11*(22), p.2670.
[202]Dai, K., Liu, G., Li, Z., Li, T., Yu, B., Wang, X. and Singleton, A., 2015. Extracting vertical displacement rates in Shanghai (China) with multi-platform SAR images. Remote Sensing, 7(8), pp.9542-9562.
[203] Ng, A.H.M., Ge, L., Zhang, K., Chang, H.C., Li, X., Rizos, C. and Omura, M., 2011. Deformation mapping in three dimensions for underground mining using InSAR–Southern highland coalfield in New South Wales, Australia. *International Journal of Remote Sensing*, *32*(22), pp.7227-7256.
[204] Fialko, Y., Simons, M. and Agnew, D., 2001. The complete (3-D) surface displacement field in the epicentral area of the 1999 Mw7. 1 Hector Mine earthquake, California, from space geodetic observations. *Geophysical research letters*, *28*(16), pp.3063-3066.
[205] Hu, J., Li, Z., Zhu, J., Ren, X. and Ding, X., 2010. Inferring three-dimensional surface displacement field by combining SAR interferometric phase and amplitude information of ascending and descending orbits. Science China Earth Sciences, 53(4), pp.550-560.
[206] Zebker, H.A. and Villasenor, J., 1992. Decorrelation in interferometric radar echoes. *IEEE Transactions on geoscience and remote sensing*, *30*(5), pp.950-959.
[207] Ahmed, R., Siqueira, P., Hensley, S., Chapman, B. and Bergen, K., 2011. A survey of temporal decorrelation from spaceborne L-Band repeat-pass InSAR. Remote Sensing of Environment, 115(11), pp.2887-2896.
[208] https://www.baesystems.com/en-us/definition/what-is-coherent-change-detection#:~:text=Coherent%20Change%20Detection%2C%20also%20known,measure%20changes%20to%20that%20area.
[209] Trevoho, I., Chetverikov, B., Babiy, L. and Malanchuk, M., 2020. Monitoring of displacements and deformations of the earth's surface near the Stebnyk city using radar images of Sentinel-1. Geodesy and Cartography, 69(1).
[210] SARScape Help, User Guide. Sarmap 2015, SARScape 5.2.0. Available online: https://www.l3harrisgeospatial.com/docs/pdf/sarscape_help.pdf (accessed on 21 November 2021)
[211] Shirani, K. and Pasandi, M., 2019. Detecting and monitoring of landslides using persistent scattering synthetic aperture radar interferometry. *Environmental Earth Sciences*, *78*(1), pp.1-24.
[212] Guo, Y., Wang, J., Liu, S., Su, R. and Lu, C., 2004. Groundwater chemical characteristics of the Yemaquan section. The preselected area for China's high-level radioactive waste repository. Atomic Energy Science and Technology, 38(Suppl.), pp.143-147.
[213] Adam, N., Parizzi, A., Eineder, M. and Crosetto, M., 2009. Practical persistent scatterer processing validation in the course of the Terrafirma project. Journal of Applied Geophysics, 69(1), pp.59-65. Available at: https://doi.org/10.1016/j.jappgeo.2009.07.002
[214] Matmon, A., Mushkin, A., Enzel, Y., Grodek, T. and ASTER Team, 2013. Erosion of a granite inselberg, Gross Spitzkoppe, Namib desert. Geomorphology, 201, pp.52-59.
[215] Small, E.E., Anderson, R.S., Repka, J.L. and Finkel, R., 1997. Erosion rates of alpine bedrock summit surfaces deduced from in situ 10Be and 26Al. Earth and Planetary Science Letters, 150(3-4), pp.413-425.
[216] Nishiizumi, K., Kohl, C.P., Arnold, J.R., Dorn, R., Klein, I., Fink, D., Middleton, R. and Lal, D., 1993. Role of in situ cosmogenic nuclides 10Be and 26Al in the study of diverse geomorphic processes. Earth surface processes and landforms, 18(5), pp.407-425.
[217] Bierman, P.R., 1993. Cosmogenic isotopes and the evolution of granitic landforms. *Unpublished Doctoral Thesis, University of Washington*.
[218] Bierman, P. and Turner, J., 1995. 10Be and 26Al evidence for exceptionally low rates of Australian bedrock erosion and the likely existence of pre-Pleistocene landscapes. Quaternary Research, 44(3), pp.378-382.

[219] Granger, D.E., Kirchner, J.W. and Finkel, R., 1996. Spatially averaged long-term erosion rates measured from in situ-produced cosmogenic nuclides in alluvial sediment. *The Journal of Geology*, *104*(3), pp.249-257.
[220] Prospero, J.M., Ginoux, P., Torres, O., Nicholson, S.E. and Gill, T.E., 2002. Environmental characterization of global sources of atmospheric soil dust identified with the Nimbus 7 Total Ozone Mapping Spectrometer (TOMS) absorbing aerosol product. Reviews of geophysics, 40(1), pp.2-1. Available at: https://doi.org/10.1029/2000RG000095
[221] Wang, X.M., Lang, L.L., Hua, T., Zhang, C.X. and Wang, Z.T., 2013. Gravel cover of Gobi Desert and its significance for wind erosion: an experimental study. Journal of Desert Research, 33(2), pp.313-319. Available at: http://www.desert.ac.cn/EN/10.7522/j.issn.1000-694X.2013.00044
[222] Wang, X., Cai, D., Sun, J., Lu, H., Liu, W., Qiang, M., Cheng, H., Che, H., Hua, T. and Zhang, C., 2019. Contributions of modern Gobi Desert to the Badain Jaran Desert and the Chinese Loess Plateau. Scientific reports, 9(1), pp.1-4. Available at: https://doi.org/10.1038/s41598-018-37635-y
[223] Shi, P., Yan, P., Yuan, Y. and Nearing, M.A., 2004. Wind erosion research in China: past, present and future. Progress in physical geography, 28(3), pp.366-386. Available at: https://doi.org/10.1191/0309133304pp416ra
[224] Barrett, B.W., Dwyer, E. and Whelan, P., 2009. Soil moisture retrieval from active spaceborne microwave observations: An evaluation of current techniques. Remote Sensing, 1(3), pp.210-242. 730 Available at: https://doi.org/10.3390/rs1030210
[225] Bader, W. J. Wrench Fault Tectonics. North American: Geo News, January 2020, pp. 20–24. Available online: https://www.dmr.nd.gov/ndgs/documents/newsletter/2020Winter/Wrench_Fault_Tectonics.pdf.
[226] Yang, H.; Cunningham, D.; Yang, X. Quaternary crustal reactivation of the southwestern Beishan, NW China: The Liuyuan sinistral transgressional duplex. *Tectonophysics* 2021, *803*, 228758.
[227] Fuhrmann, T., Knöpfler, A., Mayer, M., Schenk, A., Westerhaus, M., Zippelt, K. and Heck, B., 2013. Towards a fusion of SAR-interferometry, GNSS and precise levelling in the Upper Rhine Graben Area, Southwest Germany. ESA Special Publication, 722, p.57. Available at: https://ftp.space.dtu.dk/pub/Ioana/papers/s361_1fuhr.pdf.
[228] Fuhrmann, T., Caro Cuenca, M., Knöpfler, A., Van Leijen, F.J., Mayer, M., Westerhaus, M., Hanssen, R.F. and Heck, B., 2015. Estimation of small surface displacements in the Upper Rhine Graben area from a combined analysis of PS-InSAR, levelling and GNSS data. Geophysical Journal International, 203(1), pp.614-631. Available at: https://doi.org/10.1093/gji/ggv328
[229] Zhang, C., Chen, Q., Qin, X., Hong, B., Meng, W. and Zhang, Q., 2017. In-situ stress and fracture characterization of a candidate repository for spent nuclear fuel in Gansu, northwestern China. *Engineering Geology*, *231*, pp.218-229.
[230] Ojovan, Michael I., and William E. Lee. An introduction to nuclear waste immobilization. Newness, 2013.
[231] Agar, S., 2023. Transient scattering effects in Sentinel 1 ground deformation analyses of the rural UK (Doctoral dissertation, Imperial College London, UK).
[232] Carpenter, A. and Agar, S. ICSAR Tutorial Document. Imperial College London, May 2020.
[233] Pei, S., Zhao, J., Sun, Y., Xu, Z., Wang, S., Liu, H., Rowe, C.A., Toksöz, M.N. and Gao, X., 2007. Upper mantle seismic velocities and anisotropy in China determined through Pn and Sn tomography. Journal of Geophysical Research: Solid Earth, 112(B5). Available at: https://doi.org/10.1029/2006JB004409
[234] Gatinsky, Y., Rundquist, D., Vladova, G. and Prokhorova, T., 2011. Up-to-date geodynamics and seismicity of Central Asia. International Journal of Geosciences, 2(01), p.1. Available at: https://www.scirp.org/html/3934.html
[235] Wu, J., Wang, C., He, X., Wang, X. and Li, N., 2017. Spatiotemporal changes in both asset value and GDP associated with seismic exposure in China in the context of rapid economic growth from 1990 to 2010. Environmental research letters, 12(3), p.034002. Available at: https://doi.org/10.1088/1748-9326/aa5d47

[236] Carpenter, A., Lawrence, J.A., Ghail, R. and Mason, P.J., 2023. The Development of Copper Clad Laminate Horn Antennas for Drone Interferometric Synthetic Aperture Radar. Drones, 7(3), p.215. Available at: https://www.mdpi.com/2504-446X/7/3/215

10. Supplementary materials

Table S1. Details of 69 ascending viewed Sentinel-1 data reprocessed in this research (Time span: 08/01/2017 to 07/02/2020).

No.	Platform	Acquisition Date	Absolute Orbit	Polarization	Production Type	Flight Direction	Beam Mode	Path	Frame
1	Sentinel-1A	08/10/2017	18721	VV+VH	SLC	Ascending	IW	99	1315
2	Sentinel-1A	01/11/2017	19071	VV+VH	SLC	Ascending	IW	99	1315
3	Sentinel-1A	13/11/2017	19246	VV+VH	SLC	Ascending	IW	99	1315
4	Sentinel-1A	25/11/2017	19421	VV+VH	SLC	Ascending	IW	99	1315
5	Sentinel-1A	07/12/2017	19596	VV+VH	SLC	Ascending	IW	99	1315
6	Sentinel-1A	19/12/2017	19771	VV+VH	SLC	Ascending	IW	99	1315
7	Sentinel-1A	31/12/2017	19946	VV+VH	SLC	Ascending	IW	99	1315
8	Sentinel-1A	12/01/2018	20121	VV+VH	SLC	Ascending	IW	99	1315
9	Sentinel-1A	24/01/2018	20296	VV+VH	SLC	Ascending	IW	99	1315
10	Sentinel-1A	05/02/2018	20471	VV+VH	SLC	Ascending	IW	99	1315
11	Sentinel-1A	17/02/2018	20646	VV+VH	SLC	Ascending	IW	99	1315
12	Sentinel-1A	01/03/2018	20821	VV+VH	SLC	Ascending	IW	99	1315
13	Sentinel-1A	13/03/2018	20996	VV+VH	SLC	Ascending	IW	99	1315
14	Sentinel-1A	25/03/2018	21171	VV+VH	SLC	Ascending	IW	99	1315
15	Sentinel-1A	06/04/2018	21346	VV+VH	SLC	Ascending	IW	99	1315
16	Sentinel-1A	18/04/2018	21521	VV+VH	SLC	Ascending	IW	99	1315
17	Sentinel-1A	30/04/2018	21696	VV+VH	SLC	Ascending	IW	99	1315
18	Sentinel-1A	12/05/2018	21871	VV+VH	SLC	Ascending	IW	99	1315
19	Sentinel-1A	24/05/2018	22046	VV+VH	SLC	Ascending	IW	99	1315
20	Sentinel-1A	05/06/2018	22221	VV+VH	SLC	Ascending	IW	99	1315
21	Sentinel-1A	17/06/2018	22396	VV+VH	SLC	Ascending	IW	99	1315
22	Sentinel-1A	11/07/2018	22746	VV+VH	SLC	Ascending	IW	99	1315
23	Sentinel-1A	23/07/2018	22921	VV+VH	SLC	Ascending	IW	99	1315
24	Sentinel-1A	04/08/2018	23096	VV+VH	SLC	Ascending	IW	99	1315
25	Sentinel-1A	16/08/2018	23271	VV+VH	SLC	Ascending	IW	99	1315

26	Sentinel-1A	28/08/2018	23446	VV+VH	SLC	Ascending	IW	99	1315
27	Sentinel-1A	09/09/2018	23621	VV+VH	SLC	Ascending	IW	99	1315
28	Sentinel-1A	21/09/2018	23796	VV+VH	SLC	Ascending	IW	99	1315
29	Sentinel-1A	03/10/2018	23971	VV+VH	SLC	Ascending	IW	99	1315
30	Sentinel-1A	15/10/2018	24146	VV+VH	SLC	Ascending	IW	99	1315
31	Sentinel-1A	27/10/2018	24321	VV+VH	SLC	Ascending	IW	99	1315
32	Sentinel-1A	08/11/2018	24496	VV+VH	SLC	Ascending	IW	99	1315
33	Sentinel-1A	20/11/2018	24671	VV+VH	SLC	Ascending	IW	99	1315
34	Sentinel-1A	02/12/2018	24846	VV+VH	SLC	Ascending	IW	99	1315
35	Sentinel-1A	14/12/2018	25021	VV+VH	SLC	Ascending	IW	99	1315
36	Sentinel-1A	26/12/2018	25196	VV+VH	SLC	Ascending	IW	99	1315
37	Sentinel-1A	07/01/2019	25371	VV+VH	SLC	Ascending	IW	99	1315
38	Sentinel-1A	19/01/2019	25546	VV+VH	SLC	Ascending	IW	99	1315
39	Sentinel-1A	31/01/2019	25721	VV+VH	SLC	Ascending	IW	99	1315
40	Sentinel-1A	24/02/2019	26071	VV+VH	SLC	Ascending	IW	99	1315
41	Sentinel-1A	08/03/2019	26246	VV+VH	SLC	Ascending	IW	99	1315
42	Sentinel-1A	20/03/2019	26421	VV+VH	SLC	Ascending	IW	99	1315
43	Sentinel-1A	01/04/2019	26596	VV+VH	SLC	Ascending	IW	99	1315
44	Sentinel-1A	13/04/2019	26771	VV+VH	SLC	Ascending	IW	99	1315
45	Sentinel-1A	25/04/2019	26946	VV+VH	SLC	Ascending	IW	99	1315
46	Sentinel-1A	07/05/2019	27121	VV+VH	SLC	Ascending	IW	99	1315
47	Sentinel-1A	19/05/2019	27296	VV+VH	SLC	Ascending	IW	99	1315
48	Sentinel-1A	31/05/2019	27471	VV+VH	SLC	Ascending	IW	99	1315
49	Sentinel-1A	12/06/2019	27646	VV+VH	SLC	Ascending	IW	99	1315
50	Sentinel-1A	24/06/2019	27821	VV+VH	SLC	Ascending	IW	99	1315
51	Sentinel-1A	06/07/2019	27996	VV+VH	SLC	Ascending	IW	99	1315
52	Sentinel-1A	18/07/2019	28171	VV+VH	SLC	Ascending	IW	99	1315
53	Sentinel-1A	30/07/2019	28346	VV+VH	SLC	Ascending	IW	99	1315
54	Sentinel-1A	11/08/2019	28521	VV+VH	SLC	Ascending	IW	99	1315
55	Sentinel-1A	23/08/2019	28696	VV+VH	SLC	Ascending	IW	99	1315

56	Sentinel-1A	04/09/2019	28871	VV+VH	SLC	Ascending	IW	99	1315
57	Sentinel-1A	16/09/2019	29046	VV+VH	SLC	Ascending	IW	99	1315
58	Sentinel-1A	28/09/2019	29221	VV+VH	SLC	Ascending	IW	99	1315
59	Sentinel-1A	10/10/2019	29396	VV+VH	SLC	Ascending	IW	99	1315
60	Sentinel-1A	22/10/2019	29571	VV+VH	SLC	Ascending	IW	99	1315
61	Sentinel-1A	03/11/2019	29746	VV+VH	SLC	Ascending	IW	99	1315
62	Sentinel-1A	15/11/2019	29921	VV+VH	SLC	Ascending	IW	99	1315
63	Sentinel-1A	27/11/2019	30096	VV+VH	SLC	Ascending	IW	99	1315
64	Sentinel-1A	09/12/2019	30271	VV+VH	SLC	Ascending	IW	99	1315
65	Sentinel-1A	21/12/2019	30446	VV+VH	SLC	Ascending	IW	99	1315
66	Sentinel-1A	02/01/2020	30621	VV+VH	SLC	Ascending	IW	99	1315
67	Sentinel-1A	14/01/2020	30796	VV+VH	SLC	Ascending	IW	99	1315
68	Sentinel-1A	26/01/2020	30971	VV+VH	SLC	Ascending	IW	99	1315
69	Sentinel-1A	07/02/2020	31146	VV+VH	SLC	Ascending	IW	99	1315

Table S2. Details of 72 descending viewed Sentinel-1 data reprocessed in this research (Time span: 11/03/2017 to 31/02/2020).

No.	Platform	Acquisition Date	Absolute Orbit	Polarization	Production Type	Flight Direction	Beam Mode	Path	Frame
1	Sentinel-1A	11/03/2017	15651	VV+VH	SLC	Descending	IW	4	456
2	Sentinel-1A	23/03/2017	15826	VV+VH	SLC	Descending	IW	4	456
3	Sentinel-1A	04/04/2017	16001	VV+VH	SLC	Descending	IW	4	456
4	Sentinel-1A	16/04/2017	16176	VV+VH	SLC	Descending	IW	4	456
5	Sentinel-1A	28/04/2017	16351	VV+VH	SLC	Descending	IW	4	456
6	Sentinel-1A	22/05/2017	16701	VV+VH	SLC	Descending	IW	4	456
7	Sentinel-1A	03/06/2017	16876	VV+VH	SLC	Descending	IW	4	456
8	Sentinel-1A	15/06/2017	17051	VV+VH	SLC	Descending	IW	4	456
9	Sentinel-1A	09/07/2017	17401	VV+VH	SLC	Descending	IW	4	456
10	Sentinel-1A	21/07/2017	17576	VV+VH	SLC	Descending	IW	4	456
11	Sentinel-1A	07/09/2017	18276	VV+VH	SLC	Descending	IW	4	456
12	Sentinel-1A	19/09/2017	18451	VV+VH	SLC	Descending	IW	4	456
13	Sentinel-1A	06/11/2017	19151	VV+VH	SLC	Descending	IW	4	456
14	Sentinel-1A	18/11/2017	19326	VV+VH	SLC	Descending	IW	4	456
15	Sentinel-1A	30/11/2017	19501	VV+VH	SLC	Descending	IW	4	456
16	Sentinel-1A	12/12/2017	19676	VV+VH	SLC	Descending	IW	4	456
17	Sentinel-1A	24/12/2017	19851	VV+VH	SLC	Descending	IW	4	456
18	Sentinel-1A	05/01/2018	20026	VV+VH	SLC	Descending	IW	4	456
19	Sentinel-1A	29/01/2018	20376	VV+VH	SLC	Descending	IW	4	456
20	Sentinel-1A	10/02/2018	20551	VV+VH	SLC	Descending	IW	4	456
21	Sentinel-1A	22/02/2018	20726	VV+VH	SLC	Descending	IW	4	456
22	Sentinel-1A	06/03/2018	20901	VV+VH	SLC	Descending	IW	4	456
23	Sentinel-1A	18/03/2018	21076	VV+VH	SLC	Descending	IW	4	456
24	Sentinel-1A	30/03/2018	21251	VV+VH	SLC	Descending	IW	4	456
25	Sentinel-1A	11/04/2018	21426	VV+VH	SLC	Descending	IW	4	456
26	Sentinel-1A	23/04/2018	21601	VV+VH	SLC	Descending	IW	4	456
27	Sentinel-1A	05/05/2018	21776	VV+VH	SLC	Descending	IW	4	456

28	Sentinel-1A	17/05/2018	21951	VV+VH	SLC	Descending	IW	4	456
29	Sentinel-1A	29/05/2018	22126	VV+VH	SLC	Descending	IW	4	456
30	Sentinel-1A	10/06/2018	22301	VV+VH	SLC	Descending	IW	4	456
31	Sentinel-1A	22/06/2018	22476	VV+VH	SLC	Descending	IW	4	456
32	Sentinel-1A	04/07/2018	22651	VV+VH	SLC	Descending	IW	4	456
33	Sentinel-1A	16/07/2018	22826	VV+VH	SLC	Descending	IW	4	456
34	Sentinel-1A	28/07/2018	23001	VV+VH	SLC	Descending	IW	4	456
35	Sentinel-1A	09/08/2018	23176	VV+VH	SLC	Descending	IW	4	456
36	Sentinel-1A	21/08/2018	23351	VV+VH	SLC	Descending	IW	4	456
37	Sentinel-1A	14/09/2018	23701	VV+VH	SLC	Descending	IW	4	456
38	Sentinel-1A	26/09/2018	23876	VV+VH	SLC	Descending	IW	4	456
39	Sentinel-1A	20/10/2018	24226	VV+VH	SLC	Descending	IW	4	456
40	Sentinel-1A	01/11/2018	24401	VV+VH	SLC	Descending	IW	4	456
41	Sentinel-1A	13/11/2018	24576	VV+VH	SLC	Descending	IW	4	456
42	Sentinel-1A	25/11/2018	24751	VV+VH	SLC	Descending	IW	4	456
43	Sentinel-1A	07/12/2018	24926	VV+VH	SLC	Descending	IW	4	456
44	Sentinel-1A	19/12/2018	25101	VV+VH	SLC	Descending	IW	4	456
45	Sentinel-1A	31/12/2018	25276	VV+VH	SLC	Descending	IW	4	456
46	Sentinel-1A	12/01/2019	25451	VV+VH	SLC	Descending	IW	4	456
47	Sentinel-1A	24/01/2019	25626	VV+VH	SLC	Descending	IW	4	456
48	Sentinel-1A	05/02/2019	25801	VV+VH	SLC	Descending	IW	4	456
49	Sentinel-1A	17/02/2019	25976	VV+VH	SLC	Descending	IW	4	456
50	Sentinel-1A	01/03/2019	26151	VV+VH	SLC	Descending	IW	4	456
51	Sentinel-1A	13/03/2019	26326	VV+VH	SLC	Descending	IW	4	456
52	Sentinel-1A	25/03/2019	26501	VV+VH	SLC	Descending	IW	4	456
53	Sentinel-1A	06/04/2019	26676	VV+VH	SLC	Descending	IW	4	456
54	Sentinel-1A	18/04/2019	26851	VV+VH	SLC	Descending	IW	4	456
55	Sentinel-1A	30/04/2019	27026	VV+VH	SLC	Descending	IW	4	456
56	Sentinel-1A	05/06/2019	27551	VV+VH	SLC	Descending	IW	4	456
57	Sentinel-1A	17/06/2019	27726	VV+VH	SLC	Descending	IW	4	456

58	Sentinel-1A	29/06/2019	27901	VV+VH	SLC	Descending	IW	4	456
59	Sentinel-1A	11/07/2019	28076	VV+VH	SLC	Descending	IW	4	456
60	Sentinel-1A	04/08/2019	28426	VV+VH	SLC	Descending	IW	4	456
61	Sentinel-1A	16/08/2019	28601	VV+VH	SLC	Descending	IW	4	456
62	Sentinel-1A	28/08/2019	28776	VV+VH	SLC	Descending	IW	4	456
63	Sentinel-1A	09/09/2019	28951	VV+VH	SLC	Descending	IW	4	456
64	Sentinel-1A	21/09/2019	29126	VV+VH	SLC	Descending	IW	4	456
65	Sentinel-1A	03/10/2019	29301	VV+VH	SLC	Descending	IW	4	456
66	Sentinel-1A	15/10/2019	29476	VV+VH	SLC	Descending	IW	4	456
67	Sentinel-1A	08/11/2019	29826	VV+VH	SLC	Descending	IW	4	456
68	Sentinel-1A	20/11/2019	30001	VV+VH	SLC	Descending	IW	4	456
69	Sentinel-1A	14/12/2019	30351	VV+VH	SLC	Descending	IW	4	456
70	Sentinel-1A	26/12/2019	30526	VV+VH	SLC	Descending	IW	4	456
71	Sentinel-1A	19/01/2020	30876	VV+VH	SLC	Descending	IW	4	456
72	Sentinel-1A	31/01/2020	31051	VV+VH	SLC	Descending	IW	4	456

Table S3 (Part 1). The temporal variation of ascending LoS displacements (mm) at Block SJZ9, SJZ14, and SJZ15 in Suanjingzi study area

Date	SJZ15			SJZ14			SJZ9		
	Pixel amount	displacement	stdev	Pixel amount	displacement	stdev	Pixel amount	displacement	stdev
08/10/2017	2569	0	0	3219	0	0	6531	0	0
20/10/2017	2569	1.692888	1.254149	3219	2.343314	1.316363	6531	1.578044	1.198517
01/11/2017	2569	1.017037	1.084232	3219	1.088381	1.237569	6531	1.060711	1.10146
13/11/2017	2569	0.366618	1.15392	3219	0.496784	1.244204	6531	0.255005	1.148944
25/11/2017	2569	0.543814	1.275046	3219	0.416022	1.470655	6531	0.719732	1.25908
07/12/2017	2569	0.863745	1.327336	3219	0.94962	1.536673	6531	0.842712	1.302046
19/12/2017	2569	0.696973	1.360449	3219	0.679116	1.565978	6531	0.863933	1.334907
31/12/2017	2569	0.331022	1.637108	3219	0.316577	1.893874	6531	0.334567	1.475078
12/01/2018	2569	1.118732	1.245817	3219	1.061796	1.357532	6531	1.063494	1.286162
24/01/2018	2569	1.021039	1.348942	3219	1.10455	1.483127	6531	0.758023	1.327271
05/02/2018	2569	0.721477	1.266846	3219	0.641657	1.516355	6531	0.930017	1.294882
17/02/2018	2569	-0.223954	1.222513	3219	-0.077562	1.352103	6531	-0.236006	1.277913
01/03/2018	2569	0.466856	1.234835	3219	-0.068225	1.324504	6531	0.418108	1.291165
13/03/2018	2569	-0.366211	1.338534	3219	-0.13893	1.422018	6531	-0.290776	1.339619
25/03/2018	2569	1.547366	1.347023	3219	1.803289	1.417325	6531	1.494382	1.31587
06/04/2018	2569	0.08416	1.319609	3219	0.233091	1.391198	6531	0.134064	1.264329
18/04/2018	2569	-0.579152	1.244736	3219	-0.268893	1.351999	6531	-0.483767	1.248998
30/04/2018	2569	0.702144	1.375412	3219	1.300859	1.407061	6531	0.676546	1.234897
12/05/2018	2569	-0.492773	1.462394	3219	-0.258785	1.601277	6531	-0.519756	1.335363
24/05/2018	2569	0.967499	1.532131	3219	1.01193	1.702293	6531	1.078645	1.368863
05/06/2018	2569	1.128988	1.446804	3219	0.981411	1.487012	6531	1.385607	1.296622
17/06/2018	2569	0.576751	1.391971	3219	0.863583	1.603348	6531	0.977099	1.264045
11/07/2018	2569	0.776799	1.582983	3219	1.010597	1.770249	6531	0.993352	1.55962
23/07/2018	2569	0.04784	1.483332	3219	1.486256	1.583697	6531	0.014061	1.563839
04/08/2018	2569	0.244197	2.51507	3219	0.925663	2.532421	6531	0.387241	2.118437
16/08/2018	2569	-0.203043	1.837721	3219	0.139278	1.84711	6531	-0.063863	1.862509

28/08/2018	2569	0.802326	1.854587	3219	1.292752	1.754998	6531	0.930489	1.791016
09/09/2018	2569	0.778806	1.726597	3219	1.437744	1.778571	6531	0.492868	1.786081
21/09/2018	2569	0.099098	1.631367	3219	0.398072	1.643343	6531	0.531961	1.618914
03/10/2018	2569	0.588467	1.63726	3219	1.575297	1.618643	6531	0.450409	1.597453
15/10/2018	2569	0.575978	1.667719	3219	1.692062	1.783931	6531	0.53688	1.571657
27/10/2018	2569	0.419374	1.520792	3219	1.092528	1.534367	6531	0.266088	1.478018
08/11/2018	2569	0.231972	1.681627	3219	0.766798	1.905275	6531	0.426814	1.580225
20/11/2018	2569	0.493314	1.599055	3219	1.344422	1.769576	6531	0.638322	1.497974
02/12/2018	2569	0.443856	1.689488	3219	1.133515	1.829055	6531	0.561573	1.636827
14/12/2018	2569	0.247714	1.658213	3219	0.851572	1.718395	6531	0.208416	1.627529
26/12/2018	2569	0.168345	1.662324	3219	1.020737	1.863723	6531	-0.039925	1.572204
07/01/2019	2569	0.630797	1.797415	3219	1.360012	1.961348	6531	0.70673	1.626075
19/01/2019	2569	0.207354	2.139611	3219	1.109109	2.182323	6531	-0.139895	1.969441
31/01/2019	2569	0.829693	1.718103	3219	1.397472	1.679268	6531	0.786898	1.779949
12/02/2019	2569	0.159183	1.317585	3219	0.956818	1.3318	6531	0.191813	1.249294
24/02/2019	2569	-0.216225	1.777705	3219	0.859221	1.932393	6531	-0.116864	1.653941
08/03/2019	2569	-0.427186	1.682396	3219	0.389173	1.787188	6531	-0.378035	1.600114
20/03/2019	2569	0.955648	1.692846	3219	1.668278	1.739366	6531	0.944816	1.578084
01/04/2019	2569	-0.641068	1.715411	3219	0.091452	1.831018	6531	-0.224917	1.604462
13/04/2019	2569	-0.122666	1.913241	3219	0.889734	1.926968	6531	0.084645	1.897098
25/04/2019	2569	0.296052	2.176095	3219	1.359035	2.332792	6531	0.280056	2.09986
07/05/2019	2569	-0.379626	2.29949	3219	1.151954	2.507524	6531	-0.350046	2.284903
19/05/2019	2569	-0.365858	1.873814	3219	0.429476	1.933144	6531	-0.397124	1.859259
31/05/2019	2569	-0.458402	1.903925	3219	0.612938	2.114209	6531	-0.080635	1.805274
12/06/2019	2569	1.032712	1.928698	3219	1.852775	2.003388	6531	0.996164	1.849093
24/06/2019	2569	-0.389896	2.256127	3219	1.905647	2.507879	6531	-0.368477	2.030326
06/07/2019	2569	-1.08121	1.895346	3219	0.194461	1.971714	6531	-0.852546	1.833738
18/07/2019	2569	0.7213	2.234368	3219	1.59959	2.207203	6531	0.050652	2.258923
30/07/2019	2569	0.344467	2.071046	3219	1.400795	2.066766	6531	0.282333	2
11/08/2019	2569	0.753086	2.183035	3219	1.144541	2.255122	6531	0.648225	2.123438

23/08/2019	2569	0.725984	2.124161	3219	2.050329	2.352786	6531	0.706551	2.087777
04/09/2019	2569	0.828502	1.948992	3219	1.913461	2.092351	6531	0.538758	1.920856
16/09/2019	2569	0.852851	2.056831	3219	1.71692	2.05814	6531	0.568827	2.07156
28/09/2019	2569	0.766664	2.021279	3219	1.583675	1.994036	6531	0.464955	1.914922
10/10/2019	2569	-0.651328	1.897696	3219	0.641782	1.934254	6531	-0.288376	1.852706
22/10/2019	2569	-0.435041	2.011377	3219	0.755177	2.035233	6531	-0.198529	1.954068
03/11/2019	2569	-0.950456	1.972764	3219	0.46159	2.084219	6531	-0.712027	1.907745
15/11/2019	2569	-0.896892	1.94429	3219	0.330089	1.939914	6531	-0.624949	1.845831
27/11/2019	2569	-0.919952	1.99141	3219	0.251895	2.121279	6531	-0.797829	1.858919
09/12/2019	2569	-0.517673	1.988512	3219	0.701517	2.105599	6531	-0.31938	1.872734
21/12/2019	2569	0.679839	1.968678	3219	1.864819	2.009771	6531	0.643069	1.892524
02/01/2020	2569	-0.891906	2.022656	3219	0.445032	2.069367	6531	-0.856504	1.987348
14/01/2020	2569	0.095178	2.074532	3219	1.390277	2.073569	6531	-0.128815	1.945152
26/01/2020	2569	0.237574	2.002897	3219	1.718496	2.057887	6531	0.298494	1.884453
07/02/2020	2569	0.534381	1.988521	3219	1.823956	2.138426	6531	0.53608	1.888203

Table S3 (Part 2). The temporal variation of ascending LoS displacements (mm) at Block SJZ0, SJZ1, and SJZ2 in Suanjingzi study area

Date	SJZ0			SJZ1			SJZ2		
	Pixel amount	displacement	stdev	Pixel amount	displacement	stdev	Pixel amount	displacement	stdev
08/10/2017	6607	0	0	6160	0	0	3367	0	0
20/10/2017	6607	-1.328223	1.567328	6160	-1.041571	1.138255	3367	-1.27631	1.070405
01/11/2017	6607	-0.559273	1.57615	6160	-1.48991	1.050119	3367	-0.423105	0.972498
13/11/2017	6607	-0.51025	1.618938	6160	-0.215833	1.045464	3367	-1.035006	0.992488
25/11/2017	6607	-0.471958	1.631194	6160	-1.534233	1.179121	3367	-0.353473	1.074591
07/12/2017	6607	-0.708397	1.705006	6160	-0.566868	1.193919	3367	-0.176606	1.211908
19/12/2017	6607	-0.853673	1.766294	6160	-1.537949	1.214177	3367	-0.577257	1.240798
31/12/2017	6607	-0.669381	1.765295	6160	-1.394114	1.337535	3367	-0.686691	1.39715
12/01/2018	6607	-0.823503	2.034882	6160	-0.990663	1.199021	3367	-0.243697	1.256955
24/01/2018	6607	-0.412235	1.852268	6160	-0.940846	1.280753	3367	-0.203467	1.243374
05/02/2018	6607	-0.396756	1.915214	6160	-0.517893	1.224252	3367	0.082067	1.182632
17/02/2018	6607	-1.112831	1.763548	6160	-1.810565	1.166744	3367	-0.765629	1.111297
01/03/2018	6607	-0.519555	1.721747	6160	-1.046579	1.200566	3367	-0.145298	1.13701
13/03/2018	6607	-0.413261	1.812172	6160	-0.678249	1.291069	3367	-0.148638	1.295061
25/03/2018	6607	-0.885704	1.746937	6160	-1.038197	1.209053	3367	0.10461	1.21822
06/04/2018	6607	-0.661634	1.727231	6160	-1.06772	1.211189	3367	-0.214605	1.145446
18/04/2018	6607	-1.299512	1.698528	6160	-1.661928	1.173934	3367	0.400009	1.12227
30/04/2018	6607	-0.85266	1.771953	6160	-0.556118	1.175961	3367	0.083575	1.124813
12/05/2018	6607	-1.029674	1.899089	6160	-1.431269	1.251263	3367	-0.57865	1.256226
24/05/2018	6607	-1.059685	1.912913	6160	-0.712544	1.338559	3367	-0.599642	1.265172
05/06/2018	6607	-0.685501	1.883186	6160	-0.874485	1.211652	3367	-0.18688	1.236253
17/06/2018	6607	-1.178577	1.918839	6160	-1.52181	1.178367	3367	-0.471381	1.172552
11/07/2018	6607	-0.795868	2.161698	6160	-1.554692	1.52264	3367	-0.447693	1.711874
23/07/2018	6607	-0.796941	2.486879	6160	-1.378734	1.422829	3367	-0.493502	1.564565
04/08/2018	6607	-1.0934	3.163503	6160	-1.357644	2.11377	3367	-0.334193	2.235601
16/08/2018	6607	-1.16138	2.863651	6160	-1.078112	1.726628	3367	-0.04319	1.804706

28/08/2018	6607	-0.942741	2.670767	6160	-1.105413	1.639716	3367	-0.290169	1.732535
09/09/2018	6607	-0.943717	2.675819	6160	-1.351005	1.578139	3367	-0.463013	1.63791
21/09/2018	6607	-0.981789	2.524291	6160	-1.225946	1.442109	3367	-0.350274	1.540346
03/10/2018	6607	-1.615643	2.489658	6160	-1.474902	1.407886	3367	-0.645978	1.478189
15/10/2018	6607	-0.868273	2.45216	6160	-1.40397	1.384905	3367	-0.299091	1.441499
27/10/2018	6607	-1.56816	2.414322	6160	-1.532975	1.298579	3367	-0.630895	1.380299
08/11/2018	6607	-0.675376	2.480974	6160	-1.003329	1.438192	3367	-0.211836	1.551099
20/11/2018	6607	-0.820948	2.481301	6160	-1.154945	1.29561	3367	-0.25049	1.414672
02/12/2018	6607	-0.637289	2.548437	6160	-1.033732	1.445489	3367	-0.161953	1.511728
14/12/2018	6607	-1.49248	2.606594	6160	-1.609094	1.57882	3367	-0.897353	1.63514
26/12/2018	6607	-2.075814	2.525569	6160	-2.039415	1.394379	3367	-1.138849	1.469482
07/01/2019	6607	-0.592691	2.564503	6160	-0.761292	1.475304	3367	0.004643	1.54818
19/01/2019	6607	-2.226876	2.651316	6160	-1.95526	1.722343	3367	-1.17431	1.849822
31/01/2019	6607	-0.442474	2.813902	6160	-0.914162	1.507768	3367	0.01616	1.647378
12/02/2019	6607	-1.542833	2.08485	6160	-1.486673	1.126133	3367	-0.567686	1.197891
24/02/2019	6607	-2.248909	2.656996	6160	-1.560457	1.528557	3367	-0.674397	1.588531
08/03/2019	6607	-1.798924	2.532711	6160	-2.038623	1.422281	3367	-0.926007	1.521957
20/03/2019	6607	-0.675154	2.533794	6160	-0.771324	1.431682	3367	0.016595	1.530947
01/04/2019	6607	-1.474825	2.533625	6160	-1.674899	1.460139	3367	-0.602319	1.561353
13/04/2019	6607	-1.435314	3.324257	6160	-1.395164	1.829305	3367	-0.185083	2.046889
25/04/2019	6607	-1.153623	3.099737	6160	-1.224847	1.877071	3367	-0.185019	1.967179
07/05/2019	6607	-2.567681	3.515214	6160	-1.661685	2.186075	3367	-1.023218	2.366214
19/05/2019	6607	-2.59679	3.243676	6160	-2.266595	1.746467	3367	-1.32988	1.875332
31/05/2019	6607	-1.54563	3.566542	6160	-1.260716	1.742421	3367	-0.463665	1.851151
12/06/2019	6607	-0.625232	3.29256	6160	-0.721944	1.891975	3367	-0.006899	1.888543
24/06/2019	6607	-1.455583	3.470868	6160	-2.25412	1.865628	3367	-1.168633	1.989172
06/07/2019	6607	-2.627689	3.151953	6160	-2.354425	1.685476	3367	-1.208551	1.806171
18/07/2019	6607	-2.598805	3.657177	6160	-2.269475	2.219555	3367	-0.926646	2.116481
30/07/2019	6607	-1.462651	3.465296	6160	-1.023858	1.958977	3367	-0.159661	1.930643
11/08/2019	6607	-1.378174	3.71524	6160	-1.488863	2.141699	3367	-0.22577	2.123484

23/08/2019	6607	-2.503942	3.599823	6160	-1.416273	2.137828	3367	0.387973	2.150171
04/09/2019	6607	-1.630684	3.367597	6160	-1.461811	1.969121	3367	0.376471	1.943759
16/09/2019	6607	-1.667506	3.702066	6160	-1.190072	2.064786	3367	-0.375667	2.068866
28/09/2019	6607	-1.730755	3.430908	6160	-1.200242	1.926641	3367	-0.449802	1.968945
10/10/2019	6607	-2.413734	3.328133	6160	-1.694523	1.849661	3367	0.678125	1.820379
22/10/2019	6607	-1.956337	3.409707	6160	-2.107333	1.851172	3367	0.406906	1.871972
03/11/2019	6607	-2.411479	1.85024	6160	-2.411479	1.85024	3367	1.178335	1.859654
15/11/2019	6607	-2.639482	3.409153	6160	-2.005419	1.823868	3367	0.998207	1.830819
27/11/2019	6607	-2.797651	3.389204	6160	-2.340082	1.816521	3367	0.409074	1.798015
09/12/2019	6607	-2.092022	3.386352	6160	-1.904742	1.848223	3367	-0.719205	1.837436
21/12/2019	6607	-1.852396	3.443096	6160	-1.258367	1.841437	3367	-0.158017	1.842719
02/01/2020	6607	-2.840254	3.435974	6160	-2.401374	1.810912	3367	0.425524	1.829714
14/01/2020	6607	-2.40653	3.42395	6160	-1.472607	1.837618	3367	-0.587651	1.829197
26/01/2020	6607	-2.157992	3.445826	6160	-1.642913	1.843733	3367	0.592392	1.856759
07/02/2020	6607	-2.176501	3.450507	6160	-1.314392	1.849457	3367	0.399824	1.877042

Table S3 (Part 3). The temporal variation of ascending LoS displacements (mm) at Block SJZ6a, SJZ6b, and SJZ11 in Suanjingzi study area

Date	SJZ6b			SJZ6a			SJZ11		
	Pixel amount	displacement	stdev	Pixel amount	displacement	stdev	Pixel amount	displacement	stdev
08/10/2017	9710	0	0	9381	0	0	7138	0	0
20/10/2017	9710	1.901753	1.250919	9381	1.833572	1.187327	7138	2.294659	1.125033
01/11/2017	9710	0.664066	1.218345	9381	-0.121775	1.181692	7138	0.196184	1.032239
13/11/2017	9710	0.187139	1.259324	9381	0.103536	1.163241	7138	0.195164	1.06326
25/11/2017	9710	0.351438	1.305166	9381	-0.224214	1.244737	7138	-0.032136	1.199845
07/12/2017	9710	0.577119	1.346642	9381	0.324864	1.290274	7138	0.424692	1.229496
19/12/2017	9710	0.382496	1.334701	9381	-0.18141	1.300162	7138	0.036204	1.208145
31/12/2017	9710	0.106672	1.391301	9381	-0.471901	1.36371	7138	-0.231262	1.306381
12/01/2018	9710	0.808134	1.530663	9381	0.289885	1.385736	7138	0.500598	1.180925
24/01/2018	9710	0.397468	1.431118	9381	0.067925	1.378886	7138	0.04852	1.264191
05/02/2018	9710	0.779607	1.406901	9381	0.392363	1.389302	7138	0.285564	1.225625
17/02/2018	9710	-0.121685	1.351044	9381	-0.727294	1.312125	7138	-0.730128	1.18767
01/03/2018	9710	0.604981	1.380586	9381	-0.166622	1.377556	7138	-0.00269	1.223264
13/03/2018	9710	0.177791	1.47466	9381	0.142173	1.464331	7138	-0.140107	1.370392
25/03/2018	9710	1.201536	1.47197	9381	0.847176	1.39556	7138	1.060576	1.335684
06/04/2018	9710	0.274584	1.349472	9381	0.0476	1.369667	7138	0.007401	1.238938
18/04/2018	9710	-0.117247	1.32223	9381	-0.542279	1.31997	7138	-0.444662	1.22015
30/04/2018	9710	1.04893	1.327208	9381	0.953582	1.334721	7138	0.738396	1.248214
12/05/2018	9710	0.071706	1.389401	9381	-0.429143	1.354009	7138	-0.33345	1.299643
24/05/2018	9710	1.034617	1.402858	9381	0.598141	1.373065	7138	0.664794	1.326295
05/06/2018	9710	0.956654	1.383522	9381	0.607158	1.344072	7138	0.493067	1.319249
17/06/2018	9710	0.260004	1.435438	9381	-0.275683	1.350498	7138	0.005082	1.289296
11/07/2018	9710	0.760737	1.826741	9381	-0.072679	1.827172	7138	0.091123	1.757213
23/07/2018	9710	0.701548	1.720596	9381	-0.092617	1.644454	7138	0.123131	1.522452
04/08/2018	9710	0.447554	2.165331	9381	0.212634	2.23944	7138	-0.019817	2.17749
16/08/2018	9710	0.618853	2.150368	9381	0.414229	2.010917	7138	0.172315	1.919834

28/08/2018	9710	0.683427	2.335434	9381	0.346793	2.160419	7138	-0.005564	2.050885
09/09/2018	9710	0.698911	2.06647	9381	0.191114	1.853951	7138	0.313353	1.75301
21/09/2018	9710	0.671115	1.88301	9381	0.212815	1.73134	7138	-0.125646	1.594621
03/10/2018	9710	0.546359	1.814579	9381	0.245322	1.611932	7138	0.263159	1.515209
15/10/2018	9710	0.740346	1.764224	9381	0.20986	1.573007	7138	0.269947	1.501981
27/10/2018	9710	0.512108	1.721997	9381	0.168571	1.534625	7138	0.23865	1.424541
08/11/2018	9710	0.822437	1.764726	9381	0.326524	1.632618	7138	0.062399	1.556153
20/11/2018	9710	0.878796	1.704439	9381	0.421642	1.57184	7138	0.075699	1.444627
02/12/2018	9710	0.939611	1.803731	9381	0.461557	1.721041	7138	0.099459	1.584808
14/12/2018	9710	0.500429	1.923862	9381	0.053425	1.902645	7138	-0.147778	1.686751
26/12/2018	9710	0.175806	1.802076	9381	-0.199314	1.662545	7138	-0.222295	1.558248
07/01/2019	9710	1.216551	1.835374	9381	0.734108	1.743556	7138	0.276352	1.638733
19/01/2019	9710	0.112307	2.078489	9381	-0.105437	1.963405	7138	-0.068491	1.889161
31/01/2019	9710	1.318714	1.983171	9381	0.802485	1.846056	7138	0.357369	1.683269
12/02/2019	9710	0.690166	1.380959	9381	0.302395	1.318007	7138	0.063134	1.240025
24/02/2019	9710	0.232014	1.888934	9381	0.39555	1.777169	7138	0.231475	1.635069
08/03/2019	9710	0.222674	1.812835	9381	-0.182978	1.715978	7138	-0.455892	1.595724
20/03/2019	9710	1.316862	1.793982	9381	0.969226	1.684212	7138	0.697708	1.630227
01/04/2019	9710	0.439873	1.800004	9381	-0.030689	1.710228	7138	-0.470252	1.601483
13/04/2019	9710	1.259099	2.287969	9381	0.689841	2.144352	7138	0.268049	1.996957
25/04/2019	9710	0.983066	2.342083	9381	0.66151	2.154844	7138	0.314363	2.105915
07/05/2019	9710	0.611312	2.681971	9381	0.160201	2.438615	7138	0.353395	2.361579
19/05/2019	9710	0.196549	2.176999	9381	-0.248045	2.070653	7138	-0.550201	1.953677
31/05/2019	9710	0.67683	2.083213	9381	0.619152	1.948214	7138	0.800574	1.855999
12/06/2019	9710	1.451533	2.231399	9381	1.095234	1.981683	7138	0.669517	2.003804
24/06/2019	9710	0.156553	2.299787	9381	-0.137049	2.126293	7138	-0.310424	2.128919
06/07/2019	9710	0.169478	2.068663	9381	-0.000247	1.930972	7138	-0.645586	1.858307
18/07/2019	9710	1.1063	2.613334	9381	0.359543	2.526294	7138	-0.422337	2.330011
30/07/2019	9710	0.932845	2.217666	9381	0.861072	2.069937	7138	0.640817	1.958804
11/08/2019	9710	1.277016	2.324907	9381	0.604299	2.22012	7138	-0.094531	2.09461

23/08/2019	9710	1.302819	2.237474	9381	0.845418	2.11681	7138	0.516076	2.055081
04/09/2019	9710	1.306939	2.070534	9381	0.791868	1.984606	7138	0.530074	1.850717
16/09/2019	9710	1.33242	2.382462	9381	0.758498	2.265938	7138	0.594797	2.184085
28/09/2019	9710	1.224776	2.165052	9381	0.762697	2.051366	7138	0.566797	1.961972
10/10/2019	9710	0.622164	2.124365	9381	0.468098	1.974058	7138	0.11867	1.894803
22/10/2019	9710	0.566193	2.109576	9381	0.18544	1.984168	7138	-0.486956	1.935299
03/11/2019	9710	0.435657	2.097425	9381	0.063217	1.965129	7138	-0.612285	1.876453
15/11/2019	9710	0.594977	2.094283	9381	0.364871	1.936188	7138	-0.302271	1.853235
27/11/2019	9710	0.263905	2.072393	9381	-0.110628	1.932437	7138	-0.760163	1.912036
09/12/2019	9710	0.699453	2.076951	9381	0.339389	1.987979	7138	-0.203324	1.931346
21/12/2019	9710	1.579511	2.068584	9381	1.15577	1.96509	7138	0.613033	1.904508
02/01/2020	9710	0.252568	2.10952	9381	-0.11257	1.997056	7138	-0.798404	1.925002
14/01/2020	9710	1.278732	2.101102	9381	1.096788	1.982195	7138	0.417469	1.927441
26/01/2020	9710	0.265295	2.078697	9381	0.86467	1.983145	7138	0.406754	1.895536
07/02/2020	9710	1.493989	2.098139	9381	1.160485	2.012598	7138	0.683936	1.95783

Table S3 (Part 4). The temporal variation of ascending LoS displacements (mm) at Block SJZ12 and Fluvial Channel 2 in Suanjingzi study area

Date	SJZ12			Fluvial Channel 2		
	Pixel amount	displacement	stdev	Pixel amount	displacement	stdev
08/10/2017	5626	0	0	3140	0	0
20/10/2017	5626	2.037297	1.142538	3140	1.936607	1.383054
01/11/2017	5626	1.233367	1.119606	3140	1.129936	1.268519
13/11/2017	5626	0.365458	1.089152	3140	0.306094	1.361054
25/11/2017	5626	1.009259	1.212674	3140	0.893552	1.409772
07/12/2017	5626	0.926187	1.22986	3140	0.831234	1.459027
19/12/2017	5626	1.046024	1.249283	3140	0.953447	1.418483
31/12/2017	5626	0.706442	1.321412	3140	0.619029	1.509431
12/01/2018	5626	1.130975	1.309894	3140	0.933695	1.542661
24/01/2018	5626	1.087742	1.361491	3140	1.053033	1.594326
05/02/2018	5626	0.963489	1.3497	3140	1.000191	1.557348
17/02/2018	5626	0.176196	1.276832	3140	0.17821	1.476145
01/03/2018	5626	0.702248	1.307011	3140	0.378341	1.475815
13/03/2018	5626	0.357506	1.425112	3140	0.062739	1.58081
25/03/2018	5626	1.06135	1.350427	3140	0.96542	1.519858
06/04/2018	5626	0.832531	1.312978	3140	0.564074	1.518806
18/04/2018	5626	0.292477	1.268333	3140	-0.019855	1.434679
30/04/2018	5626	1.207369	1.210036	3140	0.913873	1.470204
12/05/2018	5626	0.324073	1.328083	3140	-0.001361	1.574508
24/05/2018	5626	1.109164	1.367967	3140	0.963727	1.648038
05/06/2018	5626	1.191217	1.415371	3140	0.992982	1.610926
17/06/2018	5626	1.148662	1.422669	3140	0.839638	1.629816
11/07/2018	5626	0.939674	1.832341	3140	0.558776	1.906682
23/07/2018	5626	0.997171	1.742566	3140	0.531852	1.771629
04/08/2018	5626	0.367172	2.300785	3140	0.348347	2.387625
16/08/2018	5626	1.238802	2.338669	3140	0.523835	2.660602

28/08/2018	5626	0.580271	2.171248	3140	0.748294	2.523094
09/09/2018	5626	1.320277	2.198787	3140	0.76855	2.320673
21/09/2018	5626	0.368598	1.986846	3140	0.063561	2.170902
03/10/2018	5626	1.059218	1.863766	3140	0.712941	2.072588
15/10/2018	5626	1.085698	1.822696	3140	0.65957	1.997916
27/10/2018	5626	1.159831	1.828628	3140	0.621702	2.055455
08/11/2018	5626	0.576802	1.837514	3140	0.266528	2.058461
20/11/2018	5626	0.925424	1.809786	3140	0.453041	2.023391
02/12/2018	5626	0.688016	1.873148	3140	0.464429	2.242611
14/12/2018	5626	0.694721	1.881747	3140	0.346179	2.131374
26/12/2018	5626	0.429712	1.810618	3140	0.206735	2.142633
07/01/2019	5626	1.009999	1.842616	3140	0.686477	2.172662
19/01/2019	5626	0.358286	2.156215	3140	0.021606	2.380634
31/01/2019	5626	1.277046	2.076175	3140	0.843434	2.378022
12/02/2019	5626	0.697939	1.482581	3140	0.266388	1.659902
24/02/2019	5626	0.086327	1.968546	3140	-0.284439	2.204212
08/03/2019	5626	-0.024959	1.902341	3140	-0.413052	2.198937
20/03/2019	5626	1.58998	1.8975	3140	1.109377	2.191534
01/04/2019	5626	0.137329	1.897195	3140	-0.573756	2.117512
13/04/2019	5626	0.795275	2.430213	3140	0.085088	2.720005
25/04/2019	5626	1.177941	2.544361	3140	0.579875	2.879422
07/05/2019	5626	-0.033369	2.932844	3140	-0.345805	3.23594
19/05/2019	5626	0.482629	2.259174	3140	-0.125028	2.57459
31/05/2019	5626	0.163327	2.161909	3140	-0.736835	2.321698
12/06/2019	5626	1.590781	2.16734	3140	0.820339	2.361678
24/06/2019	5626	0.941858	2.433329	3140	0.467061	2.784889
06/07/2019	5626	0.155924	2.062079	3140	-0.802293	2.399753
18/07/2019	5626	0.387216	2.52367	3140	0.532612	2.852905
30/07/2019	5626	0.829791	2.263389	3140	0.354661	2.593363
11/08/2019	5626	1.115158	2.430115	3140	0.772502	2.771395

23/08/2019	5626	1.113152	2.337034	3140	0.483401	2.695721
04/09/2019	5626	1.054064	2.125002	3140	0.662404	2.493238
16/09/2019	5626	1.265251	2.428834	3140	0.816824	2.69284
28/09/2019	5626	1.222264	2.175279	3140	0.578467	2.44702
10/10/2019	5626	0.419364	2.144952	3140	-0.38049	2.413427
22/10/2019	5626	0.505779	2.419761	3140	-0.087513	2.725785
03/11/2019	5626	-0.063799	2.219919	3140	-0.737844	2.534405
15/11/2019	5626	0.084025	2.182282	3140	-0.57561	2.494661
27/11/2019	5626	-0.108007	2.159105	3140	-0.729159	2.469575
09/12/2019	5626	0.372562	2.189099	3140	-0.278945	2.464991
21/12/2019	5626	1.429457	2.184718	3140	0.737491	2.481504
02/01/2020	5626	-0.215895	2.311543	3140	-0.822069	2.60014
14/01/2020	5626	0.490046	2.185792	3140	-0.043102	2.523306
26/01/2020	5626	1.081859	2.239821	3140	0.447873	2.541153
07/02/2020	5626	1.398046	2.252661	3140	0.718543	2.54511

Table S4 (Part 1). The temporal variation of descending LoS displacements (mm) at Block SJZ9, SJZ14, and SJZ15 in Suanjingzi study area

Date	SJZ15			SJZ14			SJZ9		
	Pixel amount	displacement	stdev	Pixel amount	displacement	stdev	Pixel amount	displacement	stdev
11/03/2017	2569	0	0	3219	0	0	6531	0	0
23/03/2017	2569	2.036223	1.744218	3219	0.104522	1.765142	6531	0.582167	1.245896
04/04/2017	2569	-0.20086	1.723708	3219	-1.741964	1.898998	6531	-0.472687	1.289122
16/04/2017	2569	0.029373	1.682968	3219	-0.225906	1.857584	6531	-0.173912	1.37566
28/04/2017	2569	-0.347848	2.153387	3219	-2.060668	2.199346	6531	-0.589697	1.667918
22/05/2017	2569	0.196965	1.591263	3219	-0.983849	1.607963	6531	-0.331566	1.363253
03/06/2017	2569	0.500345	1.704066	3219	0.141989	1.760891	6531	-0.163854	1.422884
15/06/2017	2569	-0.17678	1.963094	3219	-0.935006	2.086901	6531	-0.463915	1.449665
09/07/2017	2569	-0.474881	1.753466	3219	-1.573167	1.765228	6531	-0.382011	1.408554
21/07/2017	2569	0.587255	1.808221	3219	-0.383684	1.79185	6531	-0.307111	1.597104
07/09/2017	2569	0.80248	1.746153	3219	-0.613847	1.723111	6531	0.082886	1.48519
19/09/2017	2569	0.701694	1.733678	3219	-0.486149	1.628313	6531	0.063307	1.468788
06/11/2017	2569	0.833128	1.644419	3219	-0.228652	1.687513	6531	0.181307	1.502834
18/11/2017	2569	-0.044628	1.666631	3219	-0.37939	1.734353	6531	-0.823734	1.50787
30/11/2017	2569	0.757228	1.706855	3219	-0.363581	1.783627	6531	0.266359	1.475997
12/12/2017	2569	0.017944	1.823137	3219	-0.670933	1.824997	6531	-0.591679	1.544445
24/12/2017	2569	0.569409	1.88032	3219	-0.435389	1.954862	6531	-0.091618	1.527886
05/01/2018	2569	-0.061245	1.833258	3219	-0.760796	1.930261	6531	-0.835363	1.565762
29/01/2018	2569	-0.153546	1.717802	3219	-0.848601	1.785638	6531	-0.778945	1.455937
10/02/2018	2569	0.593902	1.713198	3219	-0.424325	1.784945	6531	0.087134	1.455303
22/02/2018	2569	-0.298414	2.026067	3219	-1.374566	2.171007	6531	-0.878263	1.475245
06/03/2018	2569	0.537672	2.132321	3219	-0.521911	2.316148	6531	0.016143	1.473611
18/03/2018	2569	0.87803	1.680306	3219	-0.016239	1.773945	6531	0.477608	1.424067
30/03/2018	2569	0.492409	1.699608	3219	-0.366707	1.730894	6531	0.126279	1.421987
11/04/2018	2569	0.621665	1.720341	3219	0.064228	1.797162	6531	-0.211403	1.480313
23/04/2018	2569	0.308102	1.904591	3219	-0.750188	2.047287	6531	-0.495644	1.467502

05/05/2018	2569	-0.19544	2.046086	3219	-1.595233	2.060289	6531	-0.896881	1.482009
17/05/2018	2569	0.781322	1.804815	3219	0.204883	1.868653	6531	0.309916	1.488271
29/05/2018	2569	0.367248	2.016965	3219	-1.027877	1.958996	6531	-0.57484	1.519985
10/06/2018	2569	0.126926	1.943021	3219	-0.997909	1.902037	6531	-0.94034	1.58948
22/06/2018	2569	0.644013	2.230262	3219	0.424809	2.316184	6531	-0.314083	1.873263
04/07/2018	2569	0.751182	2.191719	3219	0.198004	2.534249	6531	0.07971	1.635699
16/07/2018	2569	0.425707	1.960458	3219	-0.385893	1.982131	6531	-0.641621	1.802848
28/07/2018	2569	0.334286	2.40031	3219	0.503283	2.415014	6531	-0.257646	1.791077
09/08/2018	2569	0.607814	2.159705	3219	-0.130546	2.139175	6531	-0.233704	1.883557
21/08/2018	2569	0.207341	2.227632	3219	-0.903863	2.32388	6531	-0.66604	1.725986
02/09/2018	2569	0.528849	1.57019	3219	-0.357213	1.583775	6531	-0.369228	1.266467
14/09/2018	2569	0.581363	2.015026	3219	-0.388295	2.079884	6531	-0.126933	1.697492
26/09/2018	2569	0.684369	1.96405	3219	-0.269033	1.969689	6531	-0.806149	1.706255
20/10/2018	2569	0.695028	1.897911	3219	-0.222859	2.016124	6531	-0.715753	1.64564
01/11/2018	2569	0.329393	1.955915	3219	-0.607985	2.040994	6531	-0.242281	1.610618
13/11/2018	2569	0.784103	1.917536	3219	-0.020295	1.946113	6531	-0.031945	1.603346
25/11/2018	2569	0.84117	2.006054	3219	-0.002075	2.043118	6531	-0.410517	1.653328
07/12/2018	2569	0.509521	2.399234	3219	0.07867	2.595073	6531	-0.510471	1.846792
19/12/2018	2569	0.438977	2.024758	3219	-0.234921	2.082425	6531	-0.799809	1.666379
31/12/2018	2569	0.545777	2.012787	3219	-0.263438	2.10463	6531	-0.275877	1.646132
12/01/2019	2569	0.465449	2.061452	3219	-0.474168	2.065883	6531	-0.270427	1.646716
24/01/2019	2569	0.707227	2.337668	3219	0.355432	2.349318	6531	-0.681004	1.907493
05/02/2019	2569	0.393254	1.98362	3219	-0.357405	2.047964	6531	-0.731621	1.659323
17/02/2019	2569	0.529393	1.989489	3219	-0.116096	2.004475	6531	-0.488072	1.657952
01/03/2019	2569	0.733896	2.05827	3219	-0.408555	2.060999	6531	-0.268352	1.644105
13/03/2019	2569	0.343835	2.374753	3219	-1.022485	2.416945	6531	-0.571897	1.669711
25/03/2019	2569	0.905391	2.125775	3219	-0.094326	2.094043	6531	-0.31023	1.666926
06/04/2019	2569	0.395232	2.038665	3219	-0.457073	2.045315	6531	-0.531661	1.687193
18/04/2019	2569	0.685372	2.219697	3219	-0.123105	2.242304	6531	-0.343872	1.841329
30/04/2019	2569	0.796772	2.328201	3219	-0.161	2.283128	6531	-0.331259	1.875191

05/06/2019	2569	1.076464	2.186316	3219	0.134046	2.240793	6531	-0.060506	1.831311
17/06/2019	2569	1.432851	2.340783	3219	0.566749	2.409364	6531	0.061105	2.02473
29/06/2019	2569	0.43936	2.310838	3219	-0.701777	2.286355	6531	-1.026718	1.949628
11/07/2019	2569	0.04208	2.37879	3219	-1.206047	2.451223	6531	-1.026788	2.069152
04/08/2019	2569	-0.062085	2.305268	3219	-0.480396	2.330266	6531	-1.106747	1.965653
16/08/2019	2569	1.717454	2.427265	3219	1.051339	2.438189	6531	0.128609	2.06608
28/08/2019	2569	-0.319975	2.408572	3219	-1.563366	2.333775	6531	-1.270071	1.947689
09/09/2019	2569	1.948668	2.62149	3219	1.583636	2.749459	6531	0.308473	2.359512
21/09/2019	2569	-0.142073	2.414057	3219	-1.228316	2.391221	6531	-1.111117	2.013339
03/10/2019	2569	0.930107	2.447452	3219	-0.213217	2.443996	6531	-0.531405	2.022512
15/10/2019	2569	1.736975	2.477446	3219	1.018532	2.483922	6531	0.188379	2.171652
08/11/2019	2569	0.353852	2.352431	3219	-0.91499	2.348257	6531	-0.873117	1.969517
20/11/2019	2569	1.021674	2.461946	3219	0.643552	2.416808	6531	-0.449588	1.942107
14/12/2019	2569	1.373514	2.542634	3219	0.821908	2.607661	6531	0.006401	2.029141
26/12/2019	2569	0.102944	2.83493	3219	-0.910173	2.991589	6531	-1.325174	2.221275
19/01/2020	2569	1.341648	2.391623	3219	0.394104	2.400567	6531	-0.035345	1.940185
31/01/2020	2569	1.020602	2.381496	3219	-0.027535	2.426463	6531	-0.406095	1.909806

Table S4 (Part 2). The temporal variation of descending LoS displacements (mm) at Block SJZ0, SJZ1, and SJZ2 in Suanjingzi study area

Date	SJZ0			SJZ1			SJZ2		
	Pixel amount	displacement	stdev	Pixel amount	displacement	stdev	Pixel amount	displacement	stdev
11/03/2017	6599	0	0	6116	0	0	3367	0	0
23/03/2017	6599	0.267779	2.054852	6116	-0.176259	1.167845	3367	-0.765864	1.186361
04/04/2017	6599	-0.855943	2.046584	6116	-1.425998	1.222337	3367	-0.868798	1.25037
16/04/2017	6599	-0.865852	2.217762	6116	-0.928198	1.310179	3367	-0.593837	1.298827
28/04/2017	6599	-0.401712	2.263028	6116	-0.322564	1.423012	3367	-0.9234	1.511221
22/05/2017	6599	-0.533141	2.342237	6116	-1.042174	1.181897	3367	-0.428106	1.199485
03/06/2017	6599	0.15222	2.385782	6116	0.039385	1.265051	3367	0.120857	1.278546
15/06/2017	6599	-1.154178	2.480946	6116	-1.547889	1.312663	3367	1.134966	1.321082
09/07/2017	6599	-1.074398	2.383124	6116	-1.647296	1.273827	3367	-1.354929	1.262078
21/07/2017	6599	-0.115575	2.383568	6116	-0.776486	1.281119	3367	-0.836588	1.236815
07/09/2017	6599	-0.131741	2.457127	6116	0.114513	1.434088	3367	-0.048268	1.307648
19/09/2017	6599	0.296123	2.427727	6116	-0.01971	1.337348	3367	-0.186483	1.338107
06/11/2017	6599	0.279935	2.453201	6116	-0.041982	1.37119	3367	0.074566	1.371553
18/11/2017	6599	-0.412382	2.479268	6116	-1.25465	1.366878	3367	-0.808546	1.351948
30/11/2017	6599	0.334155	2.4517	6116	-0.137462	1.356178	3367	-0.038838	1.370981
12/12/2017	6599	-0.916966	2.499969	6116	-1.188085	1.392503	3367	-1.120144	1.425321
24/12/2017	6599	0.191878	2.470623	6116	-0.318448	1.415882	3367	-0.023747	1.436474
05/01/2018	6599	-0.861265	2.584121	6116	-1.304418	1.461099	3367	-1.249702	1.532856
29/01/2018	6599	-1.355331	2.62883	6116	-1.484704	1.346014	3367	-1.504221	1.446671
10/02/2018	6599	0.484008	2.53526	6116	-0.356051	1.328884	3367	0.111003	1.362259
22/02/2018	6599	0.666962	2.455532	6116	-0.157178	1.367245	3367	0.2988	1.407138
06/03/2018	6599	0.217892	2.519777	6116	-0.163218	1.426734	3367	0.117323	1.44949
18/03/2018	6599	0.622707	2.381477	6116	0.023269	1.318124	3367	0.511875	1.297182
30/03/2018	6599	0.690237	2.461354	6116	-0.015733	1.300176	3367	0.486851	1.302251
11/04/2018	6599	-1.196633	2.450785	6116	-0.825587	1.283857	3367	-1.345901	1.322303
23/04/2018	6599	-0.963829	2.433885	6116	-1.397052	1.332769	3367	-1.467125	1.415539

05/05/2018	6599	-0.836077	2.443901	6116	-0.814473	1.337141	3367	-0.697712	1.458159
17/05/2018	6599	-0.417608	2.522091	6116	-0.408796	1.34568	3367	-0.068238	1.367419
29/05/2018	6599	-1.073983	2.492242	6116	-1.434345	1.383781	3367	-1.52451	1.460502
10/06/2018	6599	-0.499083	2.595534	6116	-1.111523	1.40164	3367	-1.095707	1.459242
22/06/2018	6599	0.232238	3.100617	6116	-1.151943	1.708869	3367	-0.796426	1.752992
04/07/2018	6599	0.011795	2.70436	6116	-0.400066	1.617474	3367	-0.066515	1.558644
16/07/2018	6599	-0.251702	3.310509	6116	-0.564892	1.646745	3367	-0.216331	1.794639
28/07/2018	6599	-0.765102	2.759026	6116	-1.01722	1.541979	3367	-0.986596	1.663799
09/08/2018	6599	-0.636959	3.236052	6116	-1.080567	1.723048	3367	-1.024088	1.754155
21/08/2018	6599	-0.322649	3.078489	6116	-0.713998	1.580271	3367	-0.265378	1.614683
02/09/2018	6599	-0.26164	2.289201	6116	-0.745571	1.127183	3367	-0.480817	1.174632
14/09/2018	6599	-0.788556	3.050905	6116	-0.950442	1.561098	3367	-0.961833	1.56517
26/09/2018	6599	-0.324666	2.975043	6116	-0.789618	1.54166	3367	-0.274451	1.536031
20/10/2018	6599	-0.322005	2.907995	6116	-0.802738	1.423595	3367	-0.275598	1.483218
01/11/2018	6599	-0.044281	2.894053	6116	-0.677653	1.463255	3367	-0.664337	1.533255
13/11/2018	6599	0.116824	2.925726	6116	-0.552184	1.410304	3367	-0.415687	1.530415
25/11/2018	6599	-0.488506	2.920738	6116	-0.85806	1.474011	3367	-0.263487	1.517777
07/12/2018	6599	-0.288494	3.07861	6116	-0.975841	1.899994	3367	-0.634591	1.896824
19/12/2018	6599	-0.779044	2.994159	6116	-1.07793	1.569716	3367	-0.666947	1.559565
31/12/2018	6599	0.243129	2.965508	6116	-0.617581	1.47596	3367	-0.427866	1.525478
12/01/2019	6599	0.225082	2.986131	6116	-0.514817	1.451313	3367	-0.352994	1.528383
24/01/2019	6599	-0.90041	3.019651	6116	-1.051375	1.743164	3367	-0.581424	1.80392
05/02/2019	6599	-0.705799	3.053082	6116	-0.939982	1.465374	3367	-0.607049	1.501624
17/02/2019	6599	-0.020622	3.197974	6116	-0.849314	1.606657	3367	-0.528563	1.677824
01/03/2019	6599	0.1631	2.961502	6116	-0.719754	1.447474	3367	-0.384953	1.529082
13/03/2019	6599	-0.206942	3.009397	6116	-0.857481	1.503397	3367	-0.60508	1.59248
25/03/2019	6599	-0.368507	2.956451	6116	-0.759718	1.461401	3367	-0.296703	1.592862
06/04/2019	6599	-0.086804	2.967086	6116	-0.850374	1.481876	3367	-0.54825	1.587121
18/04/2019	6599	-0.329315	3.449133	6116	-0.797851	1.747134	3367	-0.446892	1.765185
30/04/2019	6599	-0.502066	3.277909	6116	-0.586922	1.734244	3367	-0.437177	1.746519

05/06/2019	6599	-0.18552	3.476539	6116	-0.341621	1.744888	3367	-0.01915	1.775184
17/06/2019	6599	0.136136	3.840235	6116	-0.871351	2.019671	3367	0.40487	2.117009
29/06/2019	6599	-0.164671	3.559245	6116	-1.341268	1.797641	3367	-0.868713	1.884774
11/07/2019	6599	-0.263438	3.890336	6116	-0.408518	2.04798	3367	-0.489344	2.01342
04/08/2019	6599	-0.085284	3.554618	6116	-1.522174	1.931906	3367	-1.089818	1.853136
16/08/2019	6599	-0.114334	3.72863	6116	0.048995	2.096985	3367	0.497841	1.925757
28/08/2019	6599	-0.711694	3.646305	6116	-1.567347	1.951219	3367	-1.408631	1.833283
09/09/2019	6599	0.49989	4.092384	6116	-0.63958	2.390925	3367	-0.114308	2.32826
21/09/2019	6599	-0.912602	3.720767	6116	-1.14917	2.013419	3367	-0.844286	1.891645
03/10/2019	6599	-0.188722	3.615064	6116	-1.42773	1.996724	3367	-0.937046	1.918451
15/10/2019	6599	0.4792	3.548037	6116	0.015012	1.873106	3367	0.411059	1.85982
08/11/2019	6599	-0.660985	3.550921	6116	-0.539693	1.898589	3367	-0.574452	1.836359
20/11/2019	6599	-0.618199	3.592264	6116	-1.167117	1.876624	3367	-0.771492	1.837717
14/12/2019	6599	0.2643	3.621111	6116	-0.395119	1.917328	3367	-0.154086	1.870073
26/12/2019	6599	-0.186532	3.537825	6116	-1.410841	1.958945	3367	-0.755275	1.873138
19/01/2020	6599	-0.61447	3.599126	6116	-0.4933	1.805149	3367	-0.112473	1.830493
31/01/2020	6599	0.081581	3.607482	6116	-0.542709	1.801911	3367	-1.033932	1.814495

Table S4 (Part 3). The temporal variation of descending LoS displacements (mm) at Block SJZ6a, SJZ6b, and SJZ11 in Suanjingzi study area

Date	SJZ6b			SJZ6a			SJZ11		
	Pixel amount	displacement	stdev	Pixel amount	displacement	stdev	Pixel amount	displacement	stdev
11/03/2017	9710	0	0	9381	0	0	7055	0	0
23/03/2017	9710	0.629795	1.291828	9381	0.523942	1.292771	7055	0.064821	1.239952
04/04/2017	9710	-1.163989	1.363037	9381	-1.091434	1.342891	7055	-1.311497	1.262583
16/04/2017	9710	-0.305715	1.52995	9381	-0.071188	1.434717	7055	-0.999349	1.434966
28/04/2017	9710	-0.837866	1.966318	9381	-0.427801	1.772223	7055	-0.446437	1.69028
22/05/2017	9710	-0.509143	1.505735	9381	-0.529717	1.422225	7055	-0.765492	1.366232
03/06/2017	9710	0.078153	1.544661	9381	0.214612	1.40504	7055	-0.042215	1.418196
15/06/2017	9710	-0.920988	1.594686	9381	-0.947545	1.49154	7055	-1.080757	1.48101
09/07/2017	9710	-1.029762	1.546421	9381	-1.145095	1.451929	7055	-1.415846	1.433215
21/07/2017	9710	-0.657808	1.538886	9381	-0.627367	1.445906	7055	-0.92623	1.429326
07/09/2017	9710	-0.110937	1.578858	9381	0.094829	1.48227	7055	-0.313041	1.494028
19/09/2017	9710	-0.101146	1.591481	9381	0.240989	1.555176	7055	-0.419195	1.514417
06/11/2017	9710	0.013711	1.641122	9381	0.233888	1.539877	7055	-0.493969	1.569467
18/11/2017	9710	-0.679503	1.620725	9381	-0.429089	1.541336	7055	-0.837078	1.517278
30/11/2017	9710	0.034293	1.617135	9381	0.145063	1.531407	7055	-0.569678	1.550927
12/12/2017	9710	-0.834803	1.652677	9381	-0.683366	1.566907	7055	-0.843812	1.551013
24/12/2017	9710	0.318173	1.675917	9381	0.403155	1.576579	7055	-0.260174	1.573064
05/01/2018	9710	-1.033971	1.750351	9381	-0.822696	1.655606	7055	-1.031096	1.661656
29/01/2018	9710	-1.34532	1.716357	9381	-1.095399	1.584952	7055	-1.382997	1.546206
10/02/2018	9710	0.301579	1.625685	9381	0.192337	1.53421	7055	-0.409988	1.530421
22/02/2018	9710	-0.74637	1.623078	9381	0.148748	1.541327	7055	-1.005696	1.533365
06/03/2018	9710	0.425595	1.62951	9381	0.543536	1.595697	7055	-0.196414	1.590666
18/03/2018	9710	0.688806	1.549283	9381	0.772056	1.489561	7055	-0.081687	1.517754
30/03/2018	9710	0.335492	1.572362	9381	0.720337	1.51711	7055	-0.136836	1.510743
11/04/2018	9710	-0.257175	1.590824	9381	-0.532776	1.505718	7055	-0.845734	1.536819
23/04/2018	9710	-0.870227	1.611434	9381	-0.892619	1.504361	7055	-1.172505	1.560073

05/05/2018	9710	-0.625004	1.628511	9381	-0.220462	1.554564	7055	-0.695333	1.561036
17/05/2018	9710	0.485476	1.608651	9381	0.702149	1.578819	7055	-0.069114	1.601378
29/05/2018	9710	-1.014616	1.63831	9381	-0.892017	1.565374	7055	-1.275193	1.604788
10/06/2018	9710	-0.914218	1.723581	9381	-0.502154	1.618868	7055	-1.49351	1.822564
22/06/2018	9710	-0.562435	2.146583	9381	-0.460706	1.897418	7055	-0.877031	1.959321
04/07/2018	9710	0.02182	1.832354	9381	0.330691	1.705067	7055	-0.43607	1.700364
16/07/2018	9710	-0.288664	2.099515	9381	-0.129217	1.899883	7055	-0.559498	1.864818
28/07/2018	9710	-0.776815	1.8164	9381	-0.686894	1.666167	7055	-1.210304	1.704252
09/08/2018	9710	-0.99762	2.174973	9381	-0.797677	1.968974	7055	-1.056132	1.988987
21/08/2018	9710	-0.266011	1.907929	9381	0.053459	1.745072	7055	-0.714684	1.828484
02/09/2018	9710	-0.342804	1.37895	9381	-0.112433	1.280223	7055	-0.816164	1.356444
14/09/2018	9710	-0.873441	2.022977	9381	-0.597831	1.739335	7055	-1.136018	1.833785
26/09/2018	9710	-0.219324	1.94123	9381	0.130736	1.700141	7055	-0.824298	1.736781
20/10/2018	9710	-0.062833	1.817372	9381	0.336174	1.658754	7055	-0.700971	1.695461
01/11/2018	9710	-0.57314	1.813651	9381	-0.348164	1.619583	7055	-0.987172	1.680662
13/11/2018	9710	-0.154221	1.812299	9381	0.065581	1.624933	7055	-0.850568	1.672777
25/11/2018	9710	0.118682	1.824315	9381	0.274601	1.658948	7055	-0.677598	1.71101
07/12/2018	9710	-0.825103	2.221864	9381	-0.329959	2.142311	7055	-0.982678	2.087032
19/12/2018	9710	-0.55625	1.964282	9381	-0.165352	1.814671	7055	-0.898122	1.791212
31/12/2018	9710	-0.476004	1.884441	9381	-0.166569	1.72688	7055	-0.868318	1.744772
12/01/2019	9710	-0.309492	1.85546	9381	-0.080794	1.697067	7055	-0.834173	1.730941
24/01/2019	9710	-0.566108	2.0557	9381	-0.130117	1.94365	7055	-0.925517	1.921916
05/02/2019	9710	-0.602238	1.845839	9381	-0.027057	1.699602	7055	-0.749872	1.729413
17/02/2019	9710	-0.468481	1.889217	9381	-0.24527	1.822363	7055	-1.15874	1.723756
01/03/2019	9710	-0.12009	1.83357	9381	-0.085903	1.699264	7055	-0.976393	1.731896
13/03/2019	9710	-0.381646	1.884652	9381	-0.216232	1.720255	7055	-1.008188	1.79652
25/03/2019	9710	-0.019444	1.860271	9381	0.305821	1.712562	7055	-0.303496	1.773829
06/04/2019	9710	-0.357949	1.856191	9381	-0.230099	1.733054	7055	-1.33057	1.779103
18/04/2019	9710	-0.307572	2.115114	9381	-0.088268	1.924575	7055	-0.929575	2.019073
30/04/2019	9710	-0.137531	2.159678	9381	0.074502	1.934046	7055	-0.724087	2.047915

05/06/2019	9710	0.223021	2.04519	9381	0.470894	1.888114	7055	-0.544423	1.946667
17/06/2019	9710	0.272958	2.418397	9381	0.971899	2.160546	7055	-0.096159	2.276298
29/06/2019	9710	-0.986404	2.144194	9381	-0.704608	1.967423	7055	-1.465248	2.055361
11/07/2019	9710	-0.710426	2.421615	9381	-0.216998	2.171668	7055	-1.173076	2.21035
04/08/2019	9710	-1.157151	2.227589	9381	-1.073573	2.050451	7055	-2.064973	2.075598
16/08/2019	9710	0.686067	2.185037	9381	1.136996	2.067523	7055	0.233517	2.098912
28/08/2019	9710	-1.395663	2.113224	9381	-1.021763	1.952732	7055	-1.608389	2.030255
09/09/2019	9710	-0.3542	2.704587	9381	-0.206439	2.44031	7055	-1.164933	2.518846
21/09/2019	9710	-0.82099	2.259431	9381	-0.072671	2.070447	7055	-1.541463	2.140595
03/10/2019	9710	-0.512867	2.193195	9381	-0.668163	1.995657	7055	-1.918247	2.1026
15/10/2019	9710	0.691859	2.251532	9381	0.885372	2.00253	7055	-0.053875	2.066069
08/11/2019	9710	-0.673747	2.127144	9381	-0.141401	1.963233	7055	-1.540603	2.056294
20/11/2019	9710	0.158888	2.111379	9381	0.332822	1.957836	7055	-0.304889	2.043792
14/12/2019	9710	0.503319	2.164234	9381	0.609577	1.999238	7055	-0.294723	2.102062
26/12/2019	9710	-1.052014	2.233419	9381	-0.435348	2.032558	7055	-0.670778	2.181602
19/01/2020	9710	0.376528	2.133747	9381	0.448769	1.926406	7055	-0.806932	2.055409
31/01/2020	9710	0.137973	2.117459	9381	0.487491	1.965822	7055	-0.647815	2.074639

Table S4 (Part 4). The temporal variation of descending LoS displacements (mm) at Block SJZ12 and Fluvial Channel 2 in Suanjingzi study area

Date	SJZ12			Fluvial Channel 2		
	Pixel amount	displacement	stdev	Pixel amount	displacement	stdev
11/03/2017	5626	0	0	3169	0	0
23/03/2017	5626	1.401302	1.418123	3169	2.125937	1.630328
04/04/2017	5626	0.441855	1.35206	3169	0.749906	1.739431
16/04/2017	5626	0.18323	1.481257	3169	0.026443	1.766239
28/04/2017	5626	0.367587	1.880104	3169	0.015789	1
22/05/2017	5626	0.136058	1.530441	3169	0.670117	1.852765
03/06/2017	5626	0.286872	1.613496	3169	0.659728	1.894869
15/06/2017	5626	0.267343	1.606122	3169	0.640143	1.923858
09/07/2017	5626	0.096691	1.62402	3169	0.545173	1.937836
21/07/2017	5626	-0.094801	1.726831	3169	0.480543	2.010496
07/09/2017	5626	0.377006	1.620802	3169	0.567702	1.934158
19/09/2017	5626	0.366949	1.65078	3169	0.621449	1.964946
06/11/2017	5626	0.64144	1.652612	3169	0.956087	1.952085
18/11/2017	5626	-0.033608	1.647527	3169	0.340974	1.965072
30/11/2017	5626	0.725178	1.659934	3169	1.122337	1.933764
12/12/2017	5626	-0.018273	1.669358	3169	0.451179	1.946185
24/12/2017	5626	0.472871	1.673578	3169	0.820935	1.970645
05/01/2018	5626	-0.15149	1.778749	3169	0.306613	2.101981
29/01/2018	5626	-0.329106	1.629892	3169	0.19949	1.985027
10/02/2018	5626	0.4925	1.635355	3169	0.927439	1.998351
22/02/2018	5626	-0.102315	1.639311	3169	0.137417	1.9097
06/03/2018	5626	0.361083	1.654623	3169	0.883705	1.950043
18/03/2018	5626	0.756241	1.594924	3169	1.286817	1.901294
30/03/2018	5626	0.627457	1.580865	3169	1.042468	1.884506
11/04/2018	5626	0.486041	1.583456	3169	1.030494	1.934807
23/04/2018	5626	0.108172	1.62234	3169	0.645114	1.940355

05/05/2018	5626	0.062964	1.650495	3169	0.274124	2.014525
17/05/2018	5626	0.716425	1.663121	3169	1.235714	1.922477
29/05/2018	5626	0.54468	1.714127	3169	0.965027	2.098268
10/06/2018	5626	0.242161	1.759022	3169	0.3279	2.12559
22/06/2018	5626	-0.025592	2.261674	3169	0.648493	2.705564
04/07/2018	5626	0.312018	1.876425	3169	0.946705	2.107087
16/07/2018	5626	-0.34416	2.234429	3169	0.027109	2.288815
28/07/2018	5626	-0.659014	1.939967	3169	0.079378	2.083845
09/08/2018	5626	0.071324	2.369748	3169	0.372606	2.552006
21/08/2018	5626	-0.310973	2.120815	3169	-0.051586	2.394881
02/09/2018	5626	0.108146	1.467083	3169	0.552942	1.691241
14/09/2018	5626	0.322421	2.096466	3169	0.605636	2.364555
26/09/2018	5626	-0.324765	2.074031	3169	0.250214	2.195358
20/10/2018	5626	-0.209912	1.906529	3169	0.447547	2.177558
01/11/2018	5626	0.172355	1.937711	3169	0.548529	2.193142
13/11/2018	5626	0.255292	1.953489	3169	0.735679	2.188537
25/11/2018	5626	0.135753	1.942681	3169	0.631975	2.190673
07/12/2018	5626	-0.043345	2.096393	3169	0.537228	2.30652
19/12/2018	5626	-0.113116	1.947195	3169	0.368717	2.254733
31/12/2018	5626	0.109659	1.920393	3169	0.627403	2.225422
12/01/2019	5626	0.042401	1.945509	3169	0.425575	2.22947
24/01/2019	5626	-0.376573	2.152681	3169	0.147491	2.329985
05/02/2019	5626	-0.329184	1.973504	3169	0.080168	2.276412
17/02/2019	5626	-0.103279	1.936781	3169	0.493932	2.229335
01/03/2019	5626	0.283602	1.91935	3169	0.799842	2.219452
13/03/2019	5626	-0.105767	1.974685	3169	0.223526	2.253103
25/03/2019	5626	0.449705	1.964457	3169	0.983323	2.245866
06/04/2019	5626	0.001891	1.925351	3169	0.458895	2.212705
18/04/2019	5626	0.244138	2.168735	3169	0.664231	2.420647
30/04/2019	5626	0.142465	2.2264	3169	0.564538	2.518003

05/06/2019	5626	0.529354	2.131882	3169	1.017585	2.384888
17/06/2019	5626	0.268094	2.463469	3169	0.8406	2.823298
29/06/2019	5626	-0.657331	2.260763	3169	0.087383	2.578432
11/07/2019	5626	-0.647269	2.53675	3169	-0.27936	2.846639
04/08/2019	5626	-0.584384	2.322843	3169	-0.088053	2.557963
16/08/2019	5626	0.423008	2.306943	3169	1.142599	2.588384
28/08/2019	5626	-0.580957	2.261898	3169	-0.267951	2.541349
09/09/2019	5626	0.492476	2.934418	3169	0.986721	3.144888
21/09/2019	5626	-0.534796	2.357766	3169	-0.241587	2.506372
03/10/2019	5626	0.063874	2.31507	3169	0.775841	2.483139
15/10/2019	5626	0.480804	2.721847	3169	0.806372	2.93379
08/11/2019	5626	-0.510724	2.299443	3169	0.115301	2.449257
20/11/2019	5626	-0.232773	2.285639	3169	0.352494	2.501709
14/12/2019	5626	0.321937	2.243552	3169	1.012955	2.489271
26/12/2019	5626	-0.627441	2.427728	3169	-0.115322	2.71453
19/01/2020	5626	0.316168	2.271176	3169	0.917868	2.499061
31/01/2020	5626	0.0209	2.258301	3169	0.75367	2.504953

Table S5 (Part 1). The temporal variation of coherence at Block SJZ0, SJZ1 and SJZ2 in Suanjingzi study area

Date	SJZ0			SJZ1			SJZ2		
	Pixel amount	Coherence	stdev	Pixel amount	Coherence	stdev	Pixel amount	Coherence	stdev
01/11/2017	6552	0.873425	0.036042	6020	0.928116	0.023959	3404	0.924892	0.022766
13/11/2017	6552	0.864072	0.036059	6020	0.930235	0.024785	3404	0.92549	0.024312
25/11/2017	6552	0.852819	0.03932	6020	0.84869	0.049828	3404	0.878967	0.032176
07/12/2017	6552	0.828188	0.040595	6020	0.90724	0.031871	3404	0.897421	0.030083
19/12/2017	6552	0.831756	0.042147	6020	0.90386	0.031559	3404	0.896045	0.031215
31/12/2017	6552	0.822735	0.042783	6020	0.872297	0.039677	3404	0.879321	0.030739
12/01/2018	6552	0.763387	0.05292	6020	0.896081	0.037456	3404	0.882185	0.034782
24/01/2018	6552	0.794784	0.047669	6020	0.86094	0.037683	3404	0.864813	0.034379
05/02/2018	6552	0.791177	0.049339	6020	0.86441	0.036992	3404	0.866778	0.033192
17/02/2018	6552	0.823576	0.044482	6020	0.892749	0.033129	3404	0.885995	0.031308
01/03/2018	6552	0.832083	0.043782	6020	0.892319	0.031792	3404	0.886055	0.030196
13/03/2018	6552	0.817844	0.043179	6020	0.873247	0.040261	3404	0.87359	0.033662
25/03/2018	6552	0.828122	0.043592	6020	0.87999	0.034029	3404	0.874941	0.030798
06/04/2018	6552	0.825986	0.044721	6020	0.877502	0.032146	3404	0.873216	0.031854
18/04/2018	6552	0.837141	0.045989	6020	0.904893	0.029468	3404	0.896858	0.027634
30/04/2018	6552	0.832968	0.047749	6020	0.917854	0.026989	3404	0.905827	0.028693
12/05/2018	6552	0.798806	0.060699	6020	0.821933	0.056217	3404	0.850147	0.038517
24/05/2018	6552	0.788097	0.060981	6020	0.780386	0.072871	3404	0.830018	0.044408
05/06/2018	6552	0.792505	0.060143	6020	0.852387	0.044698	3404	0.865839	0.035251
17/06/2018	6552	0.790539	0.062619	6020	0.892265	0.034758	3404	0.88779	0.02889
11/07/2018	6552	0.737961	0.064429	6020	0.852169	0.047485	3404	0.835587	0.04336
23/07/2018	6552	0.662489	0.080444	6020	0.801359	0.054829	3404	0.79013	0.049086
04/08/2018	6552	0.507955	0.08125	6020	0.709911	0.076725	3404	0.708507	0.065979
16/08/2018	6552	0.520551	0.087707	6020	0.732261	0.073185	3404	0.718024	0.066064
28/08/2018	6552	0.591176	0.086831	6020	0.799857	0.056982	3404	0.754484	0.059338
09/09/2018	6552	0.596307	0.081181	6020	0.812923	0.056401	3404	0.770944	0.057531

21/09/2018	6552	0.62848	0.083957	6020	0.81089	0.053194	3404	0.777241	0.05383
03/10/2018	6552	0.651801	0.08041	6020	0.82597	0.051491	3404	0.79573	0.049734
15/10/2018	6552	0.665122	0.077064	6020	0.770854	0.068342	3404	0.77552	0.050797
27/10/2018	6552	0.681678	0.073983	6020	0.867168	0.041666	3404	0.828594	0.045519
08/11/2018	6552	0.675178	0.073466	6020	0.857528	0.045095	3404	0.820795	0.046815
20/11/2018	6552	0.672284	0.078578	6020	0.86927	0.04496	3404	0.831916	0.044706
02/12/2018	6552	0.649992	0.081724	6020	0.842969	0.049024	3404	0.810835	0.048496
14/12/2018	6552	0.647309	0.082551	6020	0.818512	0.054071	3404	0.792502	0.054201
26/12/2018	6552	0.664325	0.082255	6020	0.830686	0.049794	3404	0.808834	0.046486
07/01/2019	6552	0.659466	0.082669	6020	0.839457	0.051539	3404	0.807196	0.051677
19/01/2019	6552	0.632305	0.082347	6020	0.79242	0.05867	3404	0.759138	0.055896
31/01/2019	6552	0.600864	0.087072	6020	0.814432	0.057932	3404	0.775572	0.055393
12/02/2019	6552	0.632679	0.082505	6020	0.810697	0.054602	3404	0.773411	0.054069
24/02/2019	6552	0.620155	0.083535	6020	0.78057	0.060398	3404	0.763095	0.05436
08/03/2019	6552	0.646757	0.083552	6020	0.801756	0.054924	3404	0.776025	0.051532
20/03/2019	6552	0.661831	0.078601	6020	0.831869	0.049156	3404	0.791512	0.051068
01/04/2019	6552	0.668561	0.076039	6020	0.794407	0.056314	3404	0.772621	0.049641
13/04/2019	6552	0.425707	0.092762	6020	0.702618	0.075364	3404	0.687496	0.068939
25/04/2019	6552	0.451628	0.091049	6020	0.611743	0.09601	3404	0.631084	0.073232
07/05/2019	6552	0.382437	0.093036	6020	0.678863	0.085328	3404	0.647232	0.077538
19/05/2019	6552	0.496126	0.092205	6020	0.751942	0.068827	3404	0.729363	0.064757
31/05/2019	6552	0.373238	0.096688	6020	0.722356	0.067325	3404	0.700903	0.066979
12/06/2019	6552	0.481657	0.10598	6020	0.76871	0.066615	3404	0.709441	0.067829
24/06/2019	6552	0.442635	0.098615	6020	0.708552	0.074314	3404	0.683388	0.071358
06/07/2019	6552	0.54419	0.094757	6020	0.771906	0.061101	3404	0.739689	0.061665
18/07/2019	6552	0.404432	0.100561	6020	0.690433	0.080175	3404	0.67452	0.077024
30/07/2019	6552	0.481144	0.098059	6020	0.735174	0.069843	3404	0.71267	0.069879
11/08/2019	6552	0.37829	0.097658	6020	0.619705	0.090674	3404	0.637163	0.076533
23/08/2019	6552	0.412149	0.09609	6020	0.611839	0.094138	3404	0.647423	0.077771
04/09/2019	6552	0.51491	0.091481	6020	0.688593	0.0782	3404	0.701764	0.066897

16/09/2019	6552	0.3992	0.100482	6020	0.693144	0.08293	3404	0.679061	0.076545
28/09/2019	6552	0.51331	0.093893	6020	0.718531	0.073358	3404	0.714473	0.066303
10/10/2019	6552	0.538618	0.090257	6020	0.758433	0.067549	3404	0.744561	0.062804
22/10/2019	6552	0.498517	0.093173	6020	0.748069	0.06744	3404	0.727731	0.065235
03/11/2019	6552	0.545511	0.087872	6020	0.716653	0.071664	3404	0.722091	0.062254
15/11/2019	6552	0.555652	0.086989	6020	0.74157	0.06684	3404	0.73938	0.059982
27/11/2019	6552	0.568101	0.089519	6020	0.785285	0.063082	3404	0.765965	0.058007
09/12/2019	6552	0.555174	0.09114	6020	0.774994	0.065278	3404	0.752547	0.060771
21/12/2019	6552	0.551198	0.087346	6020	0.762023	0.065104	3404	0.743674	0.059986
02/01/2020	6552	0.555732	0.092717	6020	0.759693	0.064058	3404	0.742587	0.061577
14/01/2020	6552	0.555733	0.091026	6020	0.756837	0.064589	3404	0.742213	0.060106
26/01/2020	6552	0.554472	0.089001	6020	0.764549	0.06382	3404	0.745215	0.059879
07/02/2020	6552	0.555244	0.089939	6020	0.771728	0.065298	3404	0.748537	0.6032

Table S5 (Part 2): The temporal variation of coherence at Block SJZ11. SJZ12, and Fluvial Channel 2 in Suanjingzi study area

Date	SJZ11			SJZ12			Fluvial Channel 2		
	Pixel amount	Coherence	stdev	Pixel amount	Coherence	stdev	Pixel amount	Coherence	stdev
01/11/2017	7055	0.92552	0.025936	5529	0.926911	0.030784	3191	0.915145	0.024524
13/11/2017	7055	0.923914	0.028796	5529	0.943087	0.022788	3191	0.911842	0.027765
25/11/2017	7055	0.859769	0.043286	5529	0.768224	0.021546	3191	0.889851	0.028892
07/12/2017	7055	0.899516	0.034371	5529	0.925499	0.029444	3191	0.88281	0.030387
19/12/2017	7055	0.897292	0.034133	5529	0.917972	0.030903	3191	0.882898	0.032271
31/12/2017	7055	0.86892	0.040195	5529	0.847151	0.077918	3191	0.876838	0.030839
12/01/2018	7055	0.893888	0.038212	5529	0.924468	0.029344	3191	0.8652	0.039491
24/01/2018	7055	0.860949	0.040524	5529	0.83223	0.070915	3191	0.858483	0.035192
05/02/2018	7055	0.86303	0.039842	5529	0.837057	0.073453	3191	0.865002	0.033819
17/02/2018	7055	0.883762	0.037879	5529	0.89809	0.036536	3191	0.875316	0.032348
01/03/2018	7055	0.880293	0.038057	5529	0.895319	0.035408	3191	0.875461	0.030927
13/03/2018	7055	0.858742	0.044651	5529	0.890387	0.03705	3191	0.846838	0.039155
25/03/2018	7055	0.867769	0.039554	5529	0.875204	0.044974	3191	0.860631	0.035014
06/04/2018	7055	0.864666	0.04027	5529	0.871224	0.049189	3191	0.864659	0.034812
18/04/2018	7055	0.888375	0.03571	5529	0.908004	0.035039	3191	0.880786	0.033565
30/04/2018	7055	0.901883	0.034157	5529	0.941575	0.022916	3191	0.886348	0.033732
12/05/2018	7055	0.82386	0.052079	5529	0.75081	0.127994	3191	0.855836	0.040022
24/05/2018	7055	0.794474	0.063222	5529	0.686545	0.154207	3191	0.832269	0.050818
05/06/2018	7055	0.847339	0.047399	5529	0.816546	0.094245	3191	0.839217	0.051818
17/06/2018	7055	0.876577	0.042509	5529	0.888156	0.045824	3191	0.838293	0.053343
11/07/2018	7055	0.820138	0.056322	5529	0.862321	0.038499	3191	0.742087	0.076061
23/07/2018	7055	0.797428	0.057264	5529	0.768984	0.0918	3191	0.724611	0.074216
04/08/2018	7055	0.724948	0.073165	5529	0.742934	0.067292	3191	0.651332	0.071744
16/08/2018	7055	0.713981	0.074598	5529	0.673025	0.108146	3191	0.552157	0.094521
28/08/2018	7055	0.712394	0.078115	5529	0.777005	0.070084	3191	0.5773	0.089543
09/09/2018	7055	0.776965	0.065836	5529	0.815736	0.057032	3191	0.594444	0.101329

21/09/2018	7055	0.778604	0.063952	5529	0.7954	0.078108	3191	0.633338	0.094906
03/10/2018	7055	0.792641	0.05946	5529	0.797729	0.081952	3191	0.659156	0.089796
15/10/2018	7055	0.757118	0.06702	5529	0.681894	0.139465	3191	0.669121	0.084051
27/10/2018	7055	0.839234	0.05415	5529	0.878542	0.03959	3191	0.686081	0.086898
08/11/2018	7055	0.826834	0.0554	5529	0.860859	0.047688	3191	0.680438	0.088314
20/11/2018	7055	0.839288	0.053894	5529	0.889598	0.038503	3191	0.688641	0.08853
02/12/2018	7055	0.812715	0.058032	5529	0.860933	0.046014	3191	0.67245	0.086292
14/12/2018	7055	0.800924	0.061352	5529	0.861437	0.045631	3191	0.677322	0.0817
26/12/2018	7055	0.805314	0.058418	5529	0.811499	0.067311	3191	0.685476	0.081746
07/01/2019	7055	0.805292	0.062051	5529	0.857739	0.04743	3191	0.676133	0.084244
19/01/2019	7055	0.75981	0.068772	5529	0.792664	0.060816	3191	0.629467	0.079935
31/01/2019	7055	0.782028	0.065543	5529	0.830258	0.050783	3191	0.617948	0.082643
12/02/2019	7055	0.775341	0.063827	5529	0.796158	0.065316	3191	0.627083	0.079123
24/02/2019	7055	0.763914	0.063777	5529	0.74814	0.095543	3191	0.646417	0.07975
08/03/2019	7055	0.775728	0.062439	5529	0.77414	0.084746	3191	0.665244	0.079094
20/03/2019	7055	0.801439	0.058322	5529	0.839787	0.051693	3191	0.676864	0.07831
01/04/2019	7055	0.771703	0.061858	5529	0.744596	0.10259	3191	0.677821	0.076141
13/04/2019	7055	0.688574	0.07819	5529	0.688699	0.105303	3191	0.514857	0.105164
25/04/2019	7055	0.59735	0.09141	5529	0.50687	0.154038	3191	0.472201	0.099912
07/05/2019	7055	0.662017	0.088828	5529	0.71709	0.077539	3191	0.419774	0.119925
19/05/2019	7055	0.727489	0.07436	5529	0.796873	0.058978	3191	0.577869	0.102233
31/05/2019	7055	0.720531	0.071913	5529	0.715669	0.112942	3191	0.632863	0.090213
12/06/2019	7055	0.732379	0.074983	5529	0.839222	0.051488	3191	0.642817	0.086712
24/06/2019	7055	0.691694	0.079287	5529	0.724822	0.081689	3191	0.521269	0.10414
06/07/2019	7055	0.755336	0.066744	5529	0.810642	0.059309	3191	0.634525	0.087735
18/07/2019	7055	0.645535	0.090718	5529	0.75117	0.068945	3191	0.522809	0.102773
30/07/2019	7055	0.724101	0.073384	5529	0.769901	0.069708	3191	0.59563	0.092908
11/08/2019	7055	0.642147	0.082714	5529	0.608071	0.134206	3191	0.516099	0.10043
23/08/2019	7055	0.636286	0.083558	5529	0.56972	0.146154	3191	0.533496	0.095776
04/09/2019	7055	0.708048	0.071841	5529	0.684035	0.122529	3191	0.623537	0.087483

16/09/2019	7055	0.688424	0.085085	5529	0.761227	0.070539	3191	0.560654	0.098849
28/09/2019	7055	0.724571	0.073731	5529	0.772283	0.077761	3191	0.627007	0.088219
10/10/2019	7055	0.755241	0.069027	5529	0.825671	0.05497	3191	0.646414	0.086177
22/10/2019	7055	0.738082	0.070111	5529	0.773918	0.068114	3191	0.522153	0.103397
03/11/2019	7055	0.71436	0.068987	5529	0.693564	0.115373	3191	0.592271	0.094091
15/11/2019	7055	0.738294	0.067917	5529	0.756838	0.089297	3191	0.620552	0.090317
27/11/2019	7055	0.769247	0.068011	5529	0.852721	0.049981	3191	0.636663	0.088996
09/12/2019	7055	0.75974	0.069788	5529	0.843882	0.051953	3191	0.627351	0.089456
21/12/2019	7055	0.746644	0.070064	5529	0.815995	0.05615	3191	0.627043	0.08891
02/01/2020	7055	0.738667	0.070117	5529	0.79935	0.061081	3191	0.609465	0.088156
14/01/2020	7055	0.738448	0.069565	5529	0.796884	0.062548	3191	0.620948	0.087679
26/01/2020	7055	0.746515	0.070184	5529	0.817698	0.056923	3191	0.624999	0.086432
07/02/2020	7055	0.752762	0.069151	5529	0.839285	0.05289	3191	0.62624	0.091592

Table S6 (Part 1). The temporal variation of ascending LoS displacements (mm) at Block JJ3, JJ4, and JJ5 in Jiujing study area

Date	JJ3			JJ4			JJ5		
	Pixel amount	displacement	stdev	Pixel amount	displacement	stdev	Pixel amount	displacement	stdev
08/10/2017	7482	0	0	5600	0	0	6205	0	0
20/10/2017	7482	-0.54578	1.31393	5600	-0.71040	1.02379	6205	-0.71246	0.97661
01/11/2017	7482	-1.02955	1.26202	5600	-1.96492	1.03358	6205	-2.16088	0.95313
13/11/2017	7482	-0.26441	1.24144	5600	-0.24082	1.02557	6205	-0.20418	0.98744
25/11/2017	7482	-1.42078	1.33282	5600	-1.93338	1.08444	6205	-2.05576	1.06194
07/12/2017	7482	0.19173	1.33692	5600	0.00377	1.07542	6205	-0.05200	1.04920
19/12/2017	7482	-1.36369	1.32655	5600	-1.72096	1.10570	6205	-2.00094	1.08629
31/12/2017	7482	-0.79833	1.36930	5600	-1.28619	1.13757	6205	-1.47748	1.11211
12/01/2018	7482	0.00539	1.30918	5600	-0.34343	1.06106	6205	-0.27573	1.07331
24/01/2018	7482	-1.52337	1.64032	5600	-1.92369	1.44499	6205	-2.10485	1.31002
05/02/2018	7482	-0.00456	1.50998	5600	-0.38884	1.35800	6205	-0.13571	1.23909
17/02/2018	7482	0.53835	1.61413	5600	0.08463	1.44457	6205	0.05530	1.42119
01/03/2018	7482	0.02802	1.45354	5600	-0.45563	1.24017	6205	-0.41940	1.18999
13/03/2018	7482	0.51258	1.37359	5600	-0.16869	1.15508	6205	-0.12867	1.14969
25/03/2018	7482	0.33448	1.33389	5600	-0.06052	1.15310	6205	-0.76439	1.12966
06/04/2018	7482	-1.31057	1.38384	5600	-1.83830	1.16851	6205	-1.94543	1.12010
18/04/2018	7482	-1.11905	1.29794	5600	-1.72903	1.05625	6205	-1.81432	1.03514
30/04/2018	7482	-0.73991	1.32261	5600	-1.16754	1.10562	6205	-1.29947	1.06462
12/05/2018	7482	-0.96704	1.35663	5600	-1.49025	1.11776	6205	-1.70650	1.09329
24/05/2018	7482	0.13121	1.40043	5600	-0.61577	1.09378	6205	-0.75679	1.12706
05/06/2018	7482	0.10236	1.36774	5600	-0.65074	1.12445	6205	-0.84703	1.15958
17/06/2018	7482	-0.46347	1.33252	5600	-1.06979	1.12196	6205	-1.19954	1.05453
11/07/2018	7482	-0.49866	1.59169	5600	-1.06628	1.28490	6205	-1.46871	1.26364
23/07/2018	7482	-0.39661	1.44344	5600	-0.82108	1.38035	6205	-1.01100	1.19603
04/08/2018	7482	-0.17418	2.55741	5600	-1.27400	2.59791	6205	-1.34934	2.68680
16/08/2018	7482	0.07949	2.87661	5600	-0.58004	2.67948	6205	-0.68123	2.48222

28/08/2018	7482	0.38495	2.58272	5600	-0.38436	2.39005	6205	-0.45909	2.50377
09/09/2018	7482	-0.45372	1.57601	5600	-1.37595	1.40524	6205	-1.56443	1.33079
21/09/2018	7482	-0.81201	1.57988	5600	-1.62860	1.36616	6205	-1.85326	1.22570
03/10/2018	7482	0.29167	1.49019	5600	-0.46850	1.26957	6205	-0.53240	1.14304
15/10/2018	7482	-0.79056	1.45172	5600	-1.72280	1.22430	6205	-1.87921	1.14505
27/10/2018	7482	0.14033	1.44211	5600	-0.55319	1.21765	6205	-0.92475	1.08983
08/11/2018	7482	0.07450	1.51232	5600	-0.82642	1.22996	6205	-0.95377	1.19282
20/11/2018	7482	-0.46742	1.68300	5600	-1.20191	1.52037	6205	-1.44982	1.44089
02/12/2018	7482	-0.80832	1.95437	5600	-1.74697	1.71692	6205	-1.91534	1.67047
14/12/2018	7482	0.69847	1.87635	5600	-0.28655	1.64438	6205	-0.64097	1.61203
26/12/2018	7482	0.48485	1.74613	5600	-0.45523	1.47306	6205	-0.74700	1.45760
07/01/2019	7482	-0.47742	1.68110	5600	-1.35058	1.49679	6205	-1.58657	1.39861
19/01/2019	7482	0.52743	2.09224	5600	-0.38809	1.91850	6205	-0.79111	1.91987
31/01/2019	7482	-0.59328	1.97888	5600	-1.58496	1.73801	6205	-1.85512	1.71336
12/02/2019	7482	0.00221	1.18836	5600	-1.00682	1.06862	6205	-1.26036	1.03150
24/02/2019	7482	0.00941	1.64097	5600	-0.98777	1.33933	6205	-1.24042	1.30122
08/03/2019	7482	0.38408	1.54584	5600	-0.73348	1.29933	6205	-1.19179	1.23929
20/03/2019	7482	-0.32598	1.51572	5600	-1.27721	1.28367	6205	-1.69327	1.23874
01/04/2019	7482	0.20465	1.52369	5600	-0.73094	1.29475	6205	-1.07799	1.22193
13/04/2019	7482	-0.42378	2.77511	5600	-1.55754	2.53731	6205	-1.78754	2.36965
25/04/2019	7482	0.37542	2.59988	5600	-0.62255	2.29067	6205	-0.91043	2.27213
07/05/2019	7482	0.09379	3.06722	5600	-1.39597	2.79187	6205	-1.34716	2.66240
19/05/2019	7482	1.02740	2.68793	5600	-0.10225	2.33181	6205	-0.38542	2.43103
31/05/2019	7482	0.29317	1.82965	5600	-0.55125	1.51973	6205	-1.04004	1.60379
12/06/2019	7482	1.07027	2.01868	5600	-0.19601	1.46648	6205	-0.52868	1.59769
24/06/2019	7482	-0.34073	3.15575	5600	-1.62363	2.94476	6205	-2.00302	2.81761
06/07/2019	7482	0.76676	2.32657	5600	-1.52515	2.58235	6205	-0.70035	2.59945
18/07/2019	7482	-0.35349	3.35885	5600	-1.35544	3.28550	6205	-1.79168	2.96111
30/07/2019	7482	-0.54497	2.25710	5600	-1.74285	2.19639	6205	-2.03979	1.97442
11/08/2019	7482	1.02375	2.67619	5600	-0.04595	2.44070	6205	-0.69153	2.28641

23/08/2019	7482	1.03981	2.30569	5600	-0.28792	2.14220	6205	-0.65453	1.98350
04/09/2019	7482	-0.64850	1.91323	5600	-1.86985	1.80342	6205	-2.28565	1.69188
16/09/2019	7482	-0.09706	2.54434	5600	-1.55920	2.24668	6205	-1.71012	2.12484
28/09/2019	7482	0.87529	1.96026	5600	-0.78082	1.86872	6205	-1.02111	1.70890
10/10/2019	7482	1.10793	1.80956	5600	-0.06622	1.74566	6205	-0.64616	1.66033
22/10/2019	7482	0.18360	1.80679	5600	-1.30799	1.74155	6205	-1.73001	1.62190
03/11/2019	7482	0.20722	1.78367	5600	-1.04773	1.71277	6205	-1.37440	1.62401
15/11/2019	7482	-0.29410	1.85572	5600	-1.92898	1.79669	6205	-2.09458	1.71590
27/11/2019	7482	0.97775	1.79734	5600	-0.27861	1.76340	6205	-0.75845	1.63892
09/12/2019	7482	-0.12345	1.80883	5600	-1.72227	1.76667	6205	-1.95694	1.64201
21/12/2019	7482	1.01032	1.85821	5600	-0.31912	1.80119	6205	-0.80811	1.70664
02/01/2020	7482	0.76629	2.00891	5600	-0.69149	1.88710	6205	-1.31287	1.83714
14/01/2020	7482	0.40228	1.91547	5600	-1.01681	1.84880	6205	-1.40435	1.74409
26/01/2020	7482	0.16483	1.92404	5600	-1.34160	1.80728	6205	-1.81532	1.78098
07/02/2020	7482	0.33290	1.88290	5600	-1.28220	1.77069	6205	-1.63764	1.67702

Table S6 (Part 2). The temporal variation of ascending LoS displacements (mm) at Block JJ6, JJ7, and JJ12 in Jiujing study area

Date	JJ6			JJ7			JJ12		
	Pixel amount	displacement	stdev	Pixel amount	displacement	stdev	Pixel amount	displacement	stdev
08/10/2017	4919	0	0	3312	0	0	13820	0	0
20/10/2017	4919	-0.84779	1.03139	3312	-0.40691	1.05344	13820	-0.43724	1.19313
01/11/2017	4919	-2.28538	0.94715	3312	-1.91454	1.01931	13820	-0.91892	1.04967
13/11/2017	4919	0.07901	0.99326	3312	0.16036	0.98097	13820	-0.38596	1.10236
25/11/2017	4919	-2.08895	1.03936	3312	-1.69495	1.08744	13820	-1.33391	1.17161
07/12/2017	4919	0.23124	1.06536	3312	0.40478	1.12624	13820	0.09171	1.14617
19/12/2017	4919	-2.07606	1.07717	3312	-1.77178	1.16337	13820	-1.44411	1.15925
31/12/2017	4919	-1.41052	1.12871	3312	-0.91651	1.16143	13820	-0.92009	1.20293
12/01/2018	4919	-0.24736	1.07644	3312	0.17520	1.12755	13820	0.08470	1.14140
24/01/2018	4919	-1.97195	1.41730	3312	-1.76784	1.31571	13820	-1.61995	1.41517
05/02/2018	4919	0.08959	1.25145	3312	0.43636	1.24921	13820	-0.06247	1.37399
17/02/2018	4919	0.15704	1.44955	3312	0.50279	1.43040	13820	0.17412	1.47445
01/03/2018	4919	-0.17441	1.27235	3312	-0.20644	1.29672	13820	-0.10343	1.29568
13/03/2018	4919	-0.16706	1.19795	3312	0.34383	1.15760	13820	0.13515	1.19879
25/03/2018	4919	-0.76003	1.21052	3312	-0.65942	1.18085	13820	-0.14169	1.21397
06/04/2018	4919	-1.61470	1.17451	3312	-1.31510	1.18836	13820	-1.42590	1.29226
18/04/2018	4919	-1.55189	1.05148	3312	-1.17121	1.08660	13820	-1.23155	1.13491
30/04/2018	4919	-0.79963	1.12768	3312	-0.24999	1.16016	13820	-0.70724	1.17975
12/05/2018	4919	-1.36073	1.16673	3312	-1.14346	1.11639	13820	-1.18724	1.19324
24/05/2018	4919	-0.60053	1.13468	3312	-0.37162	1.19680	13820	-0.40303	1.21653
05/06/2018	4919	-0.91138	1.11966	3312	-0.78939	1.16578	13820	-0.85838	1.23157
17/06/2018	4919	-0.83879	1.13476	3312	-0.49182	1.20424	13820	-0.76385	1.18622
11/07/2018	4919	-1.28083	1.23898	3312	-1.13602	1.31480	13820	-1.02795	1.45951
23/07/2018	4919	-0.55281	1.23824	3312	-0.32359	1.23871	13820	-0.95202	1.35513
04/08/2018	4919	-1.56890	2.85456	3312	-0.67587	2.54607	13820	-0.40954	2.66058
16/08/2018	4919	-0.47347	2.70848	3312	-0.40609	2.65591	13820	-0.32632	2.72993

28/08/2018	4919	-0.12831	2.31210	3312	0.07571	2.22859	13820	-0.31109	2.49863
09/09/2018	4919	-1.18484	1.36662	3312	-1.00068	1.37551	13820	-1.02871	1.53265
21/09/2018	4919	-1.76861	1.30016	3312	-1.36868	1.29922	13820	-1.42945	1.44771
03/10/2018	4919	-0.35632	1.21816	3312	-0.06301	1.22068	13820	-0.38120	1.39595
15/10/2018	4919	-1.62789	1.14843	3312	-1.21853	1.21584	13820	-1.42353	1.33505
27/10/2018	4919	-0.57821	1.16513	3312	-0.38662	1.17009	13820	-0.61713	1.29982
08/11/2018	4919	-0.75492	1.20701	3312	-0.40837	1.26006	13820	-0.65514	1.35178
20/11/2018	4919	-1.27998	1.49598	3312	-0.85581	1.49138	13820	-1.24355	1.50557
02/12/2018	4919	-1.64356	1.66479	3312	-1.34168	1.84547	13820	-1.47652	2.00825
14/12/2018	4919	-0.43364	1.64964	3312	-0.00739	1.64245	13820	-0.27976	1.75884
26/12/2018	4919	-0.56189	1.47898	3312	-0.16784	1.45532	13820	-0.56650	1.56461
07/01/2019	4919	-1.42957	1.42585	3312	-0.99112	1.46169	13820	-1.35897	1.50723
19/01/2019	4919	-0.42194	1.82804	3312	-0.08700	1.93392	13820	-0.37023	2.09766
31/01/2019	4919	-1.47138	1.67376	3312	-1.09035	1.91769	13820	-1.32703	1.90516
12/02/2019	4919	-0.96561	1.06222	3312	-0.57396	1.06143	13820	-0.90659	1.14513
24/02/2019	4919	-0.72080	1.35493	3312	-0.39688	1.38686	13820	-0.79812	1.49290
08/03/2019	4919	-0.89124	1.32497	3312	-0.49228	1.35013	13820	-0.77788	1.43285
20/03/2019	4919	-1.46739	1.28609	3312	-0.97558	1.31973	13820	-1.32521	1.40119
01/04/2019	4919	-0.81176	1.27032	3312	-0.39626	1.27851	13820	-0.75108	1.42445
13/04/2019	4919	-1.42231	2.63085	3312	-0.98867	2.46741	13820	-1.31904	2.58843
25/04/2019	4919	-0.61113	2.35742	3312	-0.06195	2.18678	13820	-0.81283	2.29806
07/05/2019	4919	-0.95267	2.84240	3312	-0.29611	2.78917	13820	-0.67244	2.88983
19/05/2019	4919	-0.21889	2.64566	3312	0.06912	2.47570	13820	-0.30691	2.59946
31/05/2019	4919	-0.90613	1.67766	3312	-0.29857	1.62673	13820	-0.96332	1.87989
12/06/2019	4919	-0.01846	1.64858	3312	0.11518	1.55670	13820	-0.49785	2.11097
24/06/2019	4919	-1.53535	3.04091	3312	-0.98186	2.94513	13820	-1.06737	2.70037
06/07/2019	4919	-0.68875	2.38053	3312	-0.33999	2.06662	13820	-1.21657	2.24476
18/07/2019	4919	-1.38958	3.30138	3312	-0.81562	3.12581	13820	-1.27382	3.15414
30/07/2019	4919	-1.57684	2.18295	3312	-0.97233	1.93453	13820	-1.47378	2.02887
11/08/2019	4919	-0.45985	2.45809	3312	0.03653	2.19237	13820	-0.47558	2.31483

23/08/2019	4919	-0.28907	2.09838	3312	-0.01358	1.95622	13820	-0.38020	2.11912
04/09/2019	4919	-1.75909	1.80547	3312	-1.02700	1.64425	13820	-1.71371	1.72983
16/09/2019	4919	-1.12019	2.24475	3312	-0.68804	2.04584	13820	-1.33111	2.49359
28/09/2019	4919	-0.11849	1.78986	3312	-0.04519	1.68332	13820	-0.43426	1.86237
10/10/2019	4919	-0.25967	1.71737	3312	-0.07865	1.61080	13820	-0.44304	1.70826
22/10/2019	4919	-1.44498	1.72046	3312	-0.90195	1.53700	13820	-1.17903	1.71579
03/11/2019	4919	-0.92486	1.70584	3312	-0.34224	1.56505	13820	-1.04212	1.66932
15/11/2019	4919	-1.63722	1.78071	3312	-1.05476	1.63160	13820	-1.65711	1.74912
27/11/2019	4919	-0.32903	1.69064	3312	0.05148	1.57806	13820	-0.57164	1.67386
09/12/2019	4919	-1.58004	1.77170	3312	-1.03355	1.55379	13820	-1.63061	1.69485
21/12/2019	4919	-0.33357	1.76956	3312	0.05916	1.60998	13820	-0.54810	1.71663
02/01/2020	4919	-0.76303	1.89720	3312	-0.35491	1.79301	13820	-0.77411	1.88996
14/01/2020	4919	-1.01388	1.82537	3312	-0.53835	1.70367	13820	-1.22480	1.81267
26/01/2020	4919	-1.40376	1.79000	3312	-0.85756	1.70474	13820	-1.41019	1.83316
07/02/2020	4919	-1.24770	1.77553	3312	-0.73705	1.64943	13820	-1.32673	1.74179

Table S6 (Part 3). The temporal variation of ascending LoS displacements (mm) at Block JJ19 and JJ21 in Jiujing study area

Date	JJ19			JJ21		
	Pixel amount	displacement	stdev	Pixel amount	displacement	stdev
08/10/2017	15243	0	0	6717	0	0
20/10/2017	15243	-0.33376	1.46249	6717	-0.82830	1.26690
01/11/2017	15243	-1.12170	1.40075	6717	-1.16651	1.27725
13/11/2017	15243	0.03315	1.35060	6717	-0.18525	1.25581
25/11/2017	15243	-0.82151	1.46361	6717	-1.06775	1.34347
07/12/2017	15243	0.26009	1.43211	6717	0.02814	1.36391
19/12/2017	15243	-0.92734	1.49555	6717	-1.19279	1.33644
31/12/2017	15243	-0.55188	1.50073	6717	-0.75098	1.39152
12/01/2018	15243	0.27976	1.47531	6717	-0.08989	1.33241
24/01/2018	15243	-0.81900	1.69694	6717	-1.14463	1.57549
05/02/2018	15243	0.16476	1.70487	6717	-0.21639	1.59093
17/02/2018	15243	0.41774	1.79655	6717	0.00222	1.69491
01/03/2018	15243	0.39328	1.58844	6717	-0.10919	1.50841
13/03/2018	15243	0.43090	1.52204	6717	-0.11083	1.41144
25/03/2018	15243	0.48851	1.51199	6717	-0.06527	1.37810
06/04/2018	15243	-0.52026	1.59968	6717	-0.89543	1.49778
18/04/2018	15243	-0.24571	1.48714	6717	-0.64104	1.33518
30/04/2018	15243	-0.02351	1.49178	6717	-0.64517	1.32004
12/05/2018	15243	-0.38510	1.46137	6717	-0.75289	1.35176
24/05/2018	15243	0.15938	1.53888	6717	-0.44667	1.37000
05/06/2018	15243	-0.14040	1.56042	6717	-0.86207	1.35704
17/06/2018	15243	0.25806	1.50914	6717	-0.38697	1.39039
11/07/2018	15243	0.18633	1.79424	6717	-0.80168	1.73305
23/07/2018	15243	-0.02101	1.98266	6717	-0.18088	1.80949
04/08/2018	15243	0.28400	2.89657	6717	-0.67998	3.02176
16/08/2018	15243	0.43628	3.17469	6717	-0.20906	2.91107

28/08/2018	15243	0.71558	2.88513	6717	-0.29725	2.79033
09/09/2018	15243	0.22039	1.82918	6717	-0.90276	1.60662
21/09/2018	15243	-0.29610	1.78824	6717	-1.07175	1.63273
03/10/2018	15243	0.64294	1.64683	6717	-0.35009	1.47024
15/10/2018	15243	-0.20982	1.65560	6717	-0.95097	1.49673
27/10/2018	15243	0.63534	1.64827	6717	-0.42256	1.43662
08/11/2018	15243	0.45735	1.67761	6717	-0.42248	1.51475
20/11/2018	15243	0.08910	1.79754	6717	-0.86137	1.64650
02/12/2018	15243	-0.01924	2.28090	6717	-1.04877	2.17815
14/12/2018	15243	1.02300	2.05655	6717	-0.12974	1.99548
26/12/2018	15243	0.74018	1.91417	6717	-0.36919	1.82721
07/01/2019	15243	0.07419	1.88482	6717	-1.03890	1.80875
19/01/2019	15243	0.98552	2.37458	6717	-0.06634	2.21149
31/01/2019	15243	0.18360	2.20717	6717	-1.05970	2.16798
12/02/2019	15243	0.58438	1.36969	6717	-0.60044	1.24667
24/02/2019	15243	0.64035	1.82051	6717	-0.32983	1.66837
08/03/2019	15243	0.71485	1.75494	6717	-0.63392	1.62976
20/03/2019	15243	0.39290	1.74514	6717	-1.06124	1.55844
01/04/2019	15243	0.88791	1.75482	6717	-0.38411	1.57257
13/04/2019	15243	0.29305	2.98389	6717	-1.09987	2.75830
25/04/2019	15243	0.92994	2.58592	6717	-0.94189	2.39797
07/05/2019	15243	0.94260	3.31528	6717	-0.22968	3.08689
19/05/2019	15243	1.21774	2.97601	6717	-0.03382	2.74694
31/05/2019	15243	0.44341	2.10711	6717	-1.35025	1.89873
12/06/2019	15243	1.38914	2.13202	6717	0.25016	2.10015
24/06/2019	15243	0.96270	3.10465	6717	0.05602	2.87762
06/07/2019	15243	0.57575	2.48940	6717	-1.12339	2.31102
18/07/2019	15243	0.90813	3.66552	6717	-0.25494	3.47435
30/07/2019	15243	0.58041	2.37979	6717	-1.37018	2.27908
11/08/2019	15243	1.36722	2.72123	6717	-0.00597	2.57750

23/08/2019	15243	1.59399	2.40142	6717	0.03541	2.36566
04/09/2019	15243	0.66452	2.08405	6717	-1.01817	1.93210
16/09/2019	15243	0.80303	2.85861	6717	-1.01947	2.73005
28/09/2019	15243	1.69311	2.22537	6717	-0.03858	2.08411
10/10/2019	15243	1.64429	2.02539	6717	-0.05009	1.90167
22/10/2019	15243	1.02349	1.97855	6717	-0.77610	1.86679
03/11/2019	15243	1.31309	1.95560	6717	-0.57653	1.86653
15/11/2019	15243	0.58579	2.04821	6717	-1.11841	1.93278
27/11/2019	15243	1.70285	1.98174	6717	-0.12064	1.87255
09/12/2019	15243	0.61639	1.99779	6717	-1.16870	1.89565
21/12/2019	15243	1.90154	2.02557	6717	0.04222	1.89829
02/01/2020	15243	1.61192	2.26629	6717	-0.27725	2.15538
14/01/2020	15243	1.07467	2.13215	6717	-0.80736	2.00838
26/01/2020	15243	0.87423	2.20672	6717	-1.12773	2.12013
07/02/2020	15243	1.06236	2.09864	6717	-0.94328	2.02600

Table S7 (Part 1). The temporal variation of descending LoS displacements (mm) at Block JJ3, JJ4, and JJ5 in Jiujing study area

Date	JJ3			JJ4			JJ5		
	Pixel amount	displacement	stdev	Pixel amount	displacement	stdev	Pixel amount	displacement	stdev
11/03/2017	7457	0	0	5607	0	0	6210	0	0
23/03/2017	7457	-3.33633067	2.05233284	5607	-3.15860254	1.80174994	6210	-3.25248826	1.691613
04/04/2017	7457	-2.23398091	1.61074947	5607	-1.70145137	1.33023964	6210	-2.02878141	1.291211
16/04/2017	7457	-1.12172942	2.03207995	5607	-0.66756894	1.58456791	6210	-0.89723223	1.626412
28/04/2017	7457	-1.18936032	2.30217431	5607	-1.23783826	2.07691306	6210	-1.36838256	1.907895
22/05/2017	7457	-1.07894959	1.74175373	5607	-1.03197078	1.45514659	6210	-0.87581318	1.335837
03/06/2017	7457	-0.04348676	1.81559845	5607	-0.14128859	1.54260561	6210	-0.25211035	1.417001
15/06/2017	7457	-1.98569081	1.70565206	5607	-1.70041001	1.54698091	6210	-1.84985533	1.388859
09/07/2017	7457	0.08087694	1.71430836	5607	0.10186811	1.58751444	6210	-0.12216423	1.411968
21/07/2017	7457	-1.87096394	3.05951787	5607	-1.26731777	2.90037001	6210	-1.64520884	2.634386
07/09/2017	7457	-2.14762565	1.78019177	5607	-1.51002447	1.66480089	6210	-2.41304231	1.491129
19/09/2017	7457	-1.5253704	1.77532891	5607	-1.51532731	1.63339343	6210	-1.44534788	1.470234
06/11/2017	7457	-2.09421622	1.8454977	5607	-1.55609575	1.6726204	6210	-2.07162851	1.495796
18/11/2017	7457	-0.51207048	1.85915802	5607	-0.38472451	1.69511332	6210	-0.7644686	1.508463
30/11/2017	7457	-0.74726996	1.88886008	5607	-0.60936086	1.71667095	6210	-0.95534694	1.553082
12/12/2017	7457	-0.59187557	1.89714923	5607	-0.50016386	1.72978713	6210	-0.85096145	1.574107
24/12/2017	7457	-1.35248423	1.88722878	5607	-1.01389726	1.69081326	6210	-1.48751272	1.554361
05/01/2018	7457	-0.85663421	1.89708519	5607	-0.67572838	1.72956039	6210	-1.07318583	1.56822
29/01/2018	7457	-1.15463806	2.01315793	5607	-0.90489202	1.90134765	6210	-1.28342033	1.647704
10/02/2018	7457	-1.02005097	2.14899653	5607	-0.77336748	1.97873024	6210	-1.26566875	1.820737
22/02/2018	7457	-1.27973626	1.8472048	5607	-1.01521712	1.67997197	6210	-1.52893435	1.501355
06/03/2018	7457	-1.27550663	1.80521456	5607	-1.00429862	1.66235698	6210	-1.50301654	1.476147
18/03/2018	7457	-1.24964215	1.78961127	5607	-0.91114896	1.60489168	6210	-1.30947174	1.466051
30/03/2018	7457	-1.02299123	1.78580721	5607	-0.74252933	1.62615673	6210	-1.29864735	1.487178
11/04/2018	7457	-0.92608789	1.81157732	5607	-0.68973216	1.64424528	6210	-1.30150694	1.496979
23/04/2018	7457	-1.21200126	1.84967784	5607	-1.02015972	1.67265467	6210	-1.46787359	1.537182

05/05/2018	7457	-0.86099914	1.91900371	5607	-0.57650213	1.7638513	6210	-1.19153504	1.597646
17/05/2018	7457	-1.29263028	1.83596737	5607	-1.07397797	1.66685999	6210	-1.50195433	1.531344
29/05/2018	7457	-1.17920077	1.88655879	5607	-0.92350821	1.72418578	6210	-1.43481008	1.587918
10/06/2018	7457	-1.07941297	1.9142421	5607	-0.85181381	1.7400006	6210	-1.3657645	1.613027
22/06/2018	7457	-0.77096433	2.56868397	5607	-0.75988042	2.02260876	6210	-1.21730088	2.01638
04/07/2018	7457	-0.94445424	2.18909307	5607	-0.72056876	1.92030635	6210	-1.32501521	1.695169
16/07/2018	7457	-1.06915321	1.87263663	5607	-0.53265263	2.06984976	6210	-1.45836668	1.532772
28/07/2018	7457	-1.16206855	2.25351984	5607	-0.87014134	2.20331615	6210	-1.31583142	2.544916
09/08/2018	7457	-1.08639252	1.81454974	5607	-0.8285335	1.64773712	6210	-1.35409046	1.479072
21/08/2018	7457	-0.71635225	2.16939526	5607	-0.38517477	1.90802011	6210	-0.91190892	1.808368
02/09/2018	7457	-1.09289892	1.50905736	5607	-0.80891753	1.37616703	6210	-1.46712491	1.239355
14/09/2018	7457	-0.96216571	1.93773679	5607	-0.63253753	1.69122876	6210	-1.36144098	1.531079
26/09/2018	7457	-1.21292261	1.86762548	5607	-0.94137578	1.66536993	6210	-1.59409569	1.510012
20/10/2018	7457	-1.38762522	1.87416417	5607	-1.03507448	1.69732056	6210	-1.90051606	1.560127
01/11/2018	7457	-0.72854091	1.89397318	5607	-0.35574349	1.72401382	6210	-1.10492302	1.577226
13/11/2018	7457	-1.29313264	1.89994552	5607	-1.1409386	1.70987594	6210	-1.83153135	1.574786
25/11/2018	7457	-1.61446074	1.94250645	5607	-1.34988549	1.71719959	6210	-2.19781427	1.5644
07/12/2018	7457	-0.76825029	2.43116796	5607	-0.43823164	2.17330221	6210	-1.1496186	2.193478
19/12/2018	7457	-1.3461631	2.13013992	5607	-0.92130329	1.93058762	6210	-1.77319715	1.887404
31/12/2018	7457	-0.59555388	2.02848684	5607	-0.31673775	1.86080257	6210	-1.04148698	1.779651
12/01/2019	7457	-0.50643697	2.00604954	5607	-0.21051677	1.84038593	6210	-0.92967635	1.749297
24/01/2019	7457	-1.37402594	2.38980155	5607	-1.14432652	2.13959532	6210	-1.95075754	2.200297
05/02/2019	7457	-1.34130998	2.06477679	5607	-1.07245111	1.71826454	6210	-1.89055314	1.645553
17/02/2019	7457	-1.27164995	1.9068936	5607	-0.96018736	1.68179612	6210	-1.85359705	1.548118
01/03/2019	7457	-1.16541241	1.89572696	5607	-0.86221311	1.65328984	6210	-1.66963881	1.535196
13/03/2019	7457	-0.84950241	1.98136076	5607	-0.57442507	1.78800177	6210	-1.37509635	1.637577
25/03/2019	7457	-1.12121942	2.01368896	5607	-0.84142172	1.7983678	6210	-1.67459462	1.652584
06/04/2019	7457	-1.37242609	1.94940154	5607	-1.00323008	1.7639922	6210	-1.80072697	1.608446
18/04/2019	7457	-0.61590001	2.24854899	5607	-0.43375197	1.93371248	6210	-1.33379204	1.83947
30/04/2019	7457	-0.76343624	2.03042314	5607	-0.56388048	1.74536717	6210	-1.48845214	1.618786

05/06/2019	7457	-0.52258512	2.0193254	5607	-0.23817525	1.71564826	6210	-1.21032108	1.605903
17/06/2019	7457	-1.44593927	2.83001214	5607	-0.89487281	2.48245635	6210	-2.23366704	2.445053
29/06/2019	7457	-1.41988798	2.53123801	5607	-1.10270059	2.52086418	6210	-2.07257431	2.345465
11/07/2019	7457	-1.25109235	2.88371929	5607	-0.69313511	2.70231773	6210	-1.84395671	2.521331
04/08/2019	7457	-0.05161043	2.24569705	5607	-0.05488131	2.02496825	6210	-0.7832902	1.926763
16/08/2019	7457	-0.06217161	2.26259122	5607	0.28044103	2.08630832	6210	-0.86026818	1.952322
28/08/2019	7457	-1.92652468	2.25118104	5607	-1.3665649	1.98092608	6210	-2.51383773	1.914412
09/09/2019	7457	-0.19540904	2.37474544	5607	0.10160132	2.19434104	6210	-0.97696865	1.970893
21/09/2019	7457	-0.3607288	2.24637671	5607	-0.28621822	2.01956581	6210	-1.22667359	1.921164
03/10/2019	7457	-1.11793357	2.1805397	5607	-0.66148086	1.9558297	6210	-1.76677213	1.881837
15/10/2019	7457	-1.53601885	2.15142555	5607	-1.17284328	1.93043605	6210	-2.14801598	1.843751
08/11/2019	7457	-1.16805749	2.4883533	5607	-0.88258024	2.29194334	6210	-1.89942386	2.270697
20/11/2019	7457	-0.58139101	2.11912006	5607	-0.28059509	1.93474278	6210	-1.40241164	1.885217
14/12/2019	7457	-1.46053478	2.19556925	5607	-1.0158844	1.99259123	6210	-2.11001028	1.900216
26/12/2019	7457	-1.13657708	2.42559231	5607	-0.43807396	2.1985074	6210	-1.62033749	2.183082
19/01/2020	7457	-1.30794916	2.24650294	5607	-0.98043064	2.08169534	6210	-2.05552952	2.006766
31/01/2020	7457	-1.40893977	2.15421972	5607	-1.05880222	2.00213276	6210	-2.18187925	1.905042

Table S7 (Part 2). The temporal variation of descending LoS displacements (mm) at Block JJ6, JJ7, and JJ12 in Jiujing study area

Date	JJ6			JJ7			JJ12		
	Pixel amount	displacement	stdev	Pixel amount	displacement	stdev	Pixel amount	displacement	stdev
11/03/2017	4947	0	0	3327	0	0	13804	0	0
23/03/2017	4947	-3.36999713	1.79165363	3327	-3.60202279	1.533098	13804	-3.31779207	1.726722
04/04/2017	4947	-2.02828238	1.39175957	3327	-2.7354682	1.243825	13804	-1.84458889	1.28055
16/04/2017	4947	-0.78701628	1.89791	3327	-1.11758464	1.868276	13804	-0.79240976	1.811847
28/04/2017	4947	-1.56897014	2.08129387	3327	-2.22661945	2.096319	13804	-1.27597683	2.170951
22/05/2017	4947	-0.86316048	1.42587298	3327	-1.02526228	1.296362	13804	-1.29308773	1.373254
03/06/2017	4947	-0.26779616	1.52643285	3327	-0.62961417	1.430038	13804	-0.27651729	1.428696
15/06/2017	4947	-1.85173214	1.50699817	3327	-1.76598079	1.466792	13804	-1.71037023	1.418732
09/07/2017	4947	-0.195325	1.49768249	3327	-0.26087875	1.435223	13804	0.16739183	1.400777
21/07/2017	4947	-1.74193176	2.72398837	3327	-2.4645874	2.614151	13804	-2.0141495	2.752125
07/09/2017	4947	-2.48672265	1.61055445	3327	-2.90960484	1.484053	13804	-2.28868139	1.462312
19/09/2017	4947	-1.54882708	1.55627609	3327	-1.91416301	1.504923	13804	-1.80859991	1.442063
06/11/2017	4947	-2.090471	1.59618876	3327	-2.39320839	1.545543	13804	-2.06984982	1.494195
18/11/2017	4947	-0.85946585	1.61261617	3327	-1.07286446	1.593506	13804	-0.24024568	1.492548
30/11/2017	4947	-1.04755164	1.6374266	3327	-1.32915267	1.583672	13804	-0.53717691	1.488164
12/12/2017	4947	-1.01083439	1.65076395	3327	-1.24927307	1.632901	13804	-0.41304794	1.535678
24/12/2017	4947	-1.54600102	1.65815999	3327	-1.66084772	1.60911	13804	-1.35966811	1.521159
05/01/2018	4947	-1.19299075	1.64816576	3327	-1.34507823	1.609543	13804	-0.62124543	1.503993
29/01/2018	4947	-1.49870901	1.7799419	3327	-1.56771204	1.659794	13804	-0.98107242	1.705649
10/02/2018	4947	-1.31430201	1.97219986	3327	-1.59569573	1.796937	13804	-0.96509198	1.898041
22/02/2018	4947	-1.65181585	1.62272583	3327	-1.84472559	1.553691	13804	-1.324043	1.540322
06/03/2018	4947	-1.67327891	1.55361085	3327	-1.83587744	1.533098	13804	-1.36998708	1.462253
18/03/2018	4947	-1.65640354	1.56811744	3327	-1.66364953	1.56887	13804	-1.18455858	1.43508
30/03/2018	4947	-1.25148006	1.56793672	3327	-1.52138267	1.487152	13804	-1.05029174	1.443799
11/04/2018	4947	-1.34056456	1.58029081	3327	-1.57506993	1.554335	13804	-0.78459104	1.437266
23/04/2018	4947	-1.82606196	1.65113465	3327	-1.8675084	1.56587	13804	-1.22848859	1.523842

05/05/2018	4947	-1.23462107	1.73350283	3327	-1.46528636	1.709182	13804	-0.7878357	1.557659
17/05/2018	4947	-1.8898145	1.6496513	3327	-1.82875768	1.579553	13804	-1.14786096	1.497733
29/05/2018	4947	-1.79926899	1.71297444	3327	-1.81449785	1.70288	13804	-1.12740125	1.550991
10/06/2018	4947	-1.5715258	1.74468261	3327	-1.56383844	1.691224	13804	-0.88646008	1.603565
22/06/2018	4947	-1.1821015	2.25600912	3327	-1.35405258	2.135885	13804	-0.5240734	2.359148
04/07/2018	4947	-1.57877925	1.68209723	3327	-1.82763349	1.543437	13804	-0.90204637	1.873221
16/07/2018	4947	-1.40814675	1.6915179	3327	-1.66591212	1.585806	13804	-1.0190261	1.579973
28/07/2018	4947	-1.39460275	2.95201742	3327	-1.43014055	2.732281	13804	-0.90323852	2.165209
09/08/2018	4947	-1.64187651	1.62190772	3327	-1.56947376	1.498325	13804	-0.98659583	1.493706
21/08/2018	4947	-1.35980247	1.98109579	3327	-1.37195833	1.789335	13804	-0.58613673	1.906148
02/09/2018	4947	-1.63621501	1.36217312	3327	-1.72250114	1.257064	13804	-0.9631473	1.190073
14/09/2018	4947	-1.69873541	1.68738534	3327	-1.86402396	1.592938	13804	-0.89849644	1.779127
26/09/2018	4947	-1.66017769	1.6501596	3327	-1.61445071	1.579026	13804	-0.97534204	1.519262
20/10/2018	4947	-1.99928614	1.69124575	3327	-2.27766	1.619077	13804	-1.37039175	1.552613
01/11/2018	4947	-1.41945302	1.74283569	3327	-1.46528864	1.67536	13804	-0.64276123	1.548425
13/11/2018	4947	-1.93943626	1.70878893	3327	-1.90459835	1.647819	13804	-1.02467058	1.577683
25/11/2018	4947	-2.32974724	1.72707518	3327	-2.51054433	1.609202	13804	-1.51367764	1.568121
07/12/2018	4947	-1.31140716	2.23259207	3327	-1.19203567	2.234581	13804	-0.56590702	2.214783
19/12/2018	4947	-1.82618132	1.94735187	3327	-1.99152205	1.897682	13804	-1.20741907	1.838935
31/12/2018	4947	-1.1928387	1.89110478	3327	-1.06553645	1.833428	13804	-0.4005054	1.745768
12/01/2019	4947	-1.00498798	1.82290007	3327	-0.99885553	1.779062	13804	-0.32998472	1.694274
24/01/2019	4947	-2.14814276	2.13538245	3327	-2.00984563	2.223103	13804	-1.16940241	2.229452
05/02/2019	4947	-2.24761974	1.74865501	3327	-2.13882521	1.740161	13804	-1.19897885	1.735045
17/02/2019	4947	-2.21646091	1.68948617	3327	-2.19489016	1.605015	13804	-1.14812154	1.568355
01/03/2019	4947	-1.78610902	1.63982357	3327	-1.97376315	1.629299	13804	-1.01637297	1.546537
13/03/2019	4947	-1.3927532	1.78725385	3327	-1.29901845	1.738828	13804	-0.72432626	1.649411
25/03/2019	4947	-1.82518302	1.77032427	3327	-1.92560191	1.720038	13804	-0.99214921	1.614044
06/04/2019	4947	-1.7696719	1.75327156	3327	-1.89913531	1.685105	13804	-1.17648657	1.569899
18/04/2019	4947	-1.75586687	1.96901667	3327	-1.76806917	1.780129	13804	-0.52307684	1.930337
30/04/2019	4947	-1.99201932	1.74282635	3327	-1.99289617	1.62253	13804	-0.50177291	1.701472

05/06/2019	4947	-1.58401128	1.76343891	3327	-1.5774302	1.712677	13804	-0.28612809	1.731241
17/06/2019	4947	-1.69780796	2.60931826	3327	-1.5364155	2.361336	13804	-1.09330285	2.531534
29/06/2019	4947	-2.11974096	2.50351839	3327	-2.03016151	2.251026	13804	-1.5944643	2.077843
11/07/2019	4947	-2.1408687	2.79277882	3327	-2.05626471	2.412586	13804	-0.78440016	2.453079
04/08/2019	4947	-1.26068561	2.12943286	3327	-1.42645242	1.884197	13804	0.27251527	1.913678
16/08/2019	4947	-1.29319212	2.06236732	3327	-1.68352151	1.894369	13804	0.24238953	1.933478
28/08/2019	4947	-2.58380113	2.07645599	3327	-2.16014554	1.862245	13804	-1.84355478	1.859312
09/09/2019	4947	-1.35880065	2.16547766	3327	-1.52777573	1.880912	13804	-0.06513259	2.002577
21/09/2019	4947	-1.60587978	2.09176	3327	-1.49197732	1.900938	13804	0.16609165	2.093714
03/10/2019	4947	-2.02132053	2.03824026	3327	-1.92849243	1.822701	13804	-1.01084484	1.849915
15/10/2019	4947	-2.30715409	2.02619629	3327	-2.06714242	1.762204	13804	-1.38147189	1.909397
08/11/2019	4947	-2.11035538	2.4572301	3327	-1.72745124	2.195563	13804	-0.93688541	2.241498
20/11/2019	4947	-1.58537033	2.06039794	3327	-1.49475571	1.861814	13804	-0.25323828	1.772509
14/12/2019	4947	-2.50901859	2.04817522	3327	-2.38167804	1.896339	13804	-1.25424651	1.785188
26/12/2019	4947	-1.948615	2.31806467	3327	-1.79778436	2.160336	13804	-0.8106873	2.169487
19/01/2020	4947	-2.45900623	2.16437424	3327	-2.17036522	2.05461	13804	-1.19264962	1.992991
31/01/2020	4947	-2.3836087	2.08739997	3327	-2.21587478	1.882734	13804	-1.10830143	1.849368

Table S7 (Part 3). The temporal variation of descending LoS displacements (mm) at Block JJ19 and JJ21 in Jiujing study area

Date	JJ19			JJ21		
	Pixel amount	displacement	stdev	Pixel amount	displacement	stdev
11/03/2017	15239	0	0	6720	0	0
23/03/2017	15239	-2.59271857	2.097887	6720	-3.13582192	1.864103
04/04/2017	15239	-2.10162002	1.78142	6720	-2.27766418	1.656042
16/04/2017	15239	0.09179184	2.469351	6720	-0.15789912	2.487856
28/04/2017	15239	-1.54929787	2.606943	6720	-1.64215308	2.471195
22/05/2017	15239	-1.83895336	1.944588	6720	-1.98843843	1.789073
03/06/2017	15239	-0.8468327	1.9058	6720	-0.68147754	1.823891
15/06/2017	15239	-1.80102302	1.939586	6720	-1.73963401	1.806424
09/07/2017	15239	-0.0167396	1.914574	6720	-0.32155318	1.710896
21/07/2017	15239	-2.17927999	3.400169	6720	-2.10673412	3.038599
07/09/2017	15239	-2.38042684	1.909639	6720	-2.32557378	1.76045
19/09/2017	15239	-1.95794145	1.914468	6720	-1.90892219	1.724239
06/11/2017	15239	-1.93145549	1.942504	6720	-1.98275803	1.826274
18/11/2017	15239	-0.59020454	1.939225	6720	-0.65223879	1.816755
30/11/2017	15239	-0.76363534	1.979094	6720	-0.8179682	1.801837
12/12/2017	15239	-0.94700833	1.966675	6720	-1.14871259	1.857626
24/12/2017	15239	-1.45357771	1.982196	6720	-1.5630734	1.84493
05/01/2018	15239	-0.90633908	1.965436	6720	-0.99397649	1.846213
29/01/2018	15239	-1.13477031	2.147842	6720	-1.13981098	2.072679
10/02/2018	15239	-1.42218063	2.279133	6720	-1.5204401	2.15592
22/02/2018	15239	-1.71681794	1.960314	6720	-1.7472288	1.806104
06/03/2018	15239	-1.78405783	1.912435	6720	-1.73946936	1.750498
18/03/2018	15239	-1.3594208	1.900087	6720	-1.14142135	1.733728
30/03/2018	15239	-1.46754881	1.89236	6720	-1.52958194	1.754581
11/04/2018	15239	-1.0618788	1.927873	6720	-1.17415265	1.745086
23/04/2018	15239	-1.58997042	1.986492	6720	-1.44849078	1.795021

05/05/2018	15239	-1.28335955	2.0022	6720	-1.57256227	1.908334
17/05/2018	15239	-1.3546872	1.959336	6720	-1.17993379	1.802105
29/05/2018	15239	-1.64807304	1.994584	6720	-1.27434729	1.824077
10/06/2018	15239	-1.10470757	2.02779	6720	-1.26644981	1.922762
22/06/2018	15239	-0.8308151	2.688542	6720	-0.89680018	2.581099
04/07/2018	15239	-1.2270954	2.382621	6720	-1.22784794	2.251306
16/07/2018	15239	-1.37457688	2.187676	6720	-1.63005705	2.01481
28/07/2018	15239	-1.05436753	2.706507	6720	-1.16122528	2.37913
09/08/2018	15239	-1.77693636	2.004943	6720	-1.844954	1.834896
21/08/2018	15239	-1.32627249	2.253896	6720	-1.08061862	2.11379
02/09/2018	15239	-1.39635076	1.567344	6720	-1.33964531	1.435355
14/09/2018	15239	-1.56319093	2.554219	6720	-1.56297614	2.525394
26/09/2018	15239	-1.24248115	2.016571	6720	-1.05708381	1.849778
20/10/2018	15239	-1.73592781	2.001405	6720	-1.73410933	1.80835
01/11/2018	15239	-1.35174934	1.997275	6720	-1.24834974	1.852275
13/11/2018	15239	-1.31621699	2.003044	6720	-1.20422719	1.825629
25/11/2018	15239	-1.88166812	2.038801	6720	-1.84510614	1.835459
07/12/2018	15239	-1.07159295	2.596057	6720	-1.01713646	2.60185
19/12/2018	15239	-1.7358305	2.247197	6720	-1.73614645	2.166398
31/12/2018	15239	-0.88234771	2.221179	6720	-0.80010984	2.077212
12/01/2019	15239	-0.88506659	2.136791	6720	-0.83630306	1.999403
24/01/2019	15239	-1.64729012	2.584231	6720	-1.38353854	2.403883
05/02/2019	15239	-1.78109841	2.229346	6720	-1.70846401	2.040468
17/02/2019	15239	-1.75325437	2.07055	6720	-1.65945557	1.913798
01/03/2019	15239	-1.53118732	2.040319	6720	-1.31915471	1.864699
13/03/2019	15239	-1.17186236	2.153488	6720	-1.09956103	1.952753
25/03/2019	15239	-1.55306859	2.116294	6720	-1.3125292	1.961107
06/04/2019	15239	-1.51540682	2.078283	6720	-1.33353492	1.902707
18/04/2019	15239	-1.25689364	2.435807	6720	-1.05049795	2.244683
30/04/2019	15239	-1.30928128	2.157702	6720	-1.18450021	1.977518

05/06/2019	15239	-1.12370668	2.161725	6720	-1.07546306	2.005089
17/06/2019	15239	-1.36086407	2.904754	6720	-1.10909099	2.794559
29/06/2019	15239	-1.81814955	2.536257	6720	-1.50325725	2.367701
11/07/2019	15239	-1.65749622	2.729289	6720	-1.26780458	2.595481
04/08/2019	15239	-0.72457289	2.379445	6720	-0.65862294	2.235338
16/08/2019	15239	-1.32095649	2.410619	6720	-1.6484891	2.299586
28/08/2019	15239	-2.14937599	2.311873	6720	-1.82673868	2.138027
09/09/2019	15239	-0.99368326	2.52771	6720	-0.76682041	2.379462
21/09/2019	15239	-0.66395775	2.546152	6720	-0.45040725	2.447813
03/10/2019	15239	-1.78346104	2.312219	6720	-1.42385561	2.154322
15/10/2019	15239	-1.9174072	2.26318	6720	-1.71332027	2.059147
08/11/2019	15239	-1.25516129	2.617133	6720	-1.00174433	2.518899
20/11/2019	15239	-1.06559686	2.223903	6720	-0.79293046	2.081788
14/12/2019	15239	-1.92223932	2.273937	6720	-1.7089663	2.101806
26/12/2019	15239	-1.60383914	2.592385	6720	-1.27425748	2.568783
19/01/2020	15239	-1.89439693	2.510062	6720	-1.7272865	2.482206
31/01/2020	15239	-1.91496644	2.320466	6720	-1.51544545	2.284529

Table S8 (Part 1). The temporal variation of coherence at BB1, BB2 and JB1 areas in Jiujing study area

Date	BB1			BB2			JB1		
	Pixel amount	Coherence	stdev	Pixel amount	Coherence	stdev	Pixel amount	Coherence	stdev
01/11/2017	3721	0.262331	0.146707	6205	0.786638	0.059702	1886	0.75329	0.056227
13/11/2017	3721	0.252848	0.148082	6205	0.774408	0.060913	1886	0.671419	0.071752
25/11/2017	3721	0.263903	0.139849	6205	0.763582	0.062981	1886	0.550268	0.101636
07/12/2017	3721	0.242569	0.139315	6205	0.740887	0.064413	1886	0.446449	0.121791
19/12/2017	3721	0.238643	0.138843	6205	0.746681	0.063672	1886	0.371503	0.138699
31/12/2017	3721	0.245545	0.141599	6205	0.741307	0.061485	1886	0.353619	0.140554
12/01/2018	3721	0.225254	0.142072	6205	0.739776	0.067481	1886	0.259751	0.138155
24/01/2018	3721	0.241497	0.125807	6205	0.704644	0.071323	1886	0.213657	0.12183
05/02/2018	3721	0.257955	0.135172	6205	0.694834	0.071604	1886	0.19801	0.111346
17/02/2018	3721	0.233837	0.138034	6205	0.665398	0.068081	1886	0.191616	0.11069
01/03/2018	3721	0.229862	0.13934	6205	0.702951	0.063995	1886	0.222913	0.119567
13/03/2018	3721	0.253719	0.144288	6205	0.727657	0.062635	1886	0.309717	0.134058
25/03/2018	3721	0.249904	0.142216	6205	0.732833	0.061521	1886	0.370551	0.14914
06/04/2018	3721	0.266704	0.137518	6205	0.729679	0.058963	1886	0.408417	0.156902
18/04/2018	3721	0.274548	0.139593	6205	0.747345	0.059685	1886	0.440266	0.161891
30/04/2018	3721	0.269682	0.143447	6205	0.739299	0.065525	1886	0.44315	0.164879
12/05/2018	3721	0.23903	0.138733	6205	0.732042	0.062841	1886	0.44196	0.162307
24/05/2018	3721	0.245232	0.147102	6205	0.714614	0.066323	1886	0.431713	0.157278
05/06/2018	3721	0.239433	0.138012	6205	0.720589	0.065044	1886	0.42135	0.151431
17/06/2018	3721	0.25111	0.143415	6205	0.718443	0.066936	1886	0.389043	0.148122
11/07/2018	3721	0.216546	0.134921	6205	0.653386	0.066271	1886	0.353111	0.123394
23/07/2018	3721	0.191538	0.111916	6205	0.580817	0.076484	1886	0.330006	0.132342
04/08/2018	3721	0.216744	0.134724	6205	0.495925	0.083882	1886	0.264939	0.10419
16/08/2018	3721	0.166394	0.11101	6205	0.38206	0.09297	1886	0.250304	0.097056
28/08/2018	3721	0.18538	0.109738	6205	0.48655	0.08809	1886	0.258131	0.109008
09/09/2018	3721	0.206198	0.105738	6205	0.567917	0.087735	1886	0.270185	0.129781

21/09/2018	3721	0.192977	0.104694	6205	0.559751	0.082838	1886	0.266229	0.127802
03/10/2018	3721	0.198046	0.10698	6205	0.585369	0.087678	1886	0.27923	0.135256
15/10/2018	3721	0.20027	0.10017	6205	0.599415	0.084574	1886	0.28098	0.130271
27/10/2018	3721	0.186171	0.105938	6205	0.595007	0.090412	1886	0.289764	0.130597
08/11/2018	3721	0.196827	0.104351	6205	0.594307	0.086888	1886	0.271184	0.126353
20/11/2018	3721	0.213003	0.112437	6205	0.579709	0.086821	1886	0.24129	0.117076
02/12/2018	3721	0.175305	0.096986	6205	0.474747	0.086717	1886	0.219175	0.10229
14/12/2018	3721	0.17788	0.099421	6205	0.507051	0.10257	1886	0.169083	0.095725
26/12/2018	3721	0.198445	0.093213	6205	0.527965	0.099014	1886	0.166742	0.096219
07/01/2019	3721	0.202586	0.100207	6205	0.53837	0.096049	1886	0.155107	0.087705
19/01/2019	3721	0.161917	0.097152	6205	0.470679	0.090343	1886	0.144078	0.080727
31/01/2019	3721	0.157337	0.091757	6205	0.472741	0.106969	1886	0.146093	0.079373
12/02/2019	3721	0.173309	0.096935	6205	0.524423	0.091943	1886	0.151432	0.079035
08/03/2019	3721	0.190527	0.098309	6205	0.56208	0.091671	1886	0.165044	0.090114
20/03/2019	3721	0.212649	0.10477	6205	0.582779	0.087558	1886	0.187631	0.102285
01/04/2019	3721	0.193288	0.102956	6205	0.575684	0.089828	1886	0.204123	0.103473
13/04/2019	3721	0.15927	0.097518	6205	0.393003	0.087436	1886	0.194594	0.105398
25/04/2019	3721	0.17161	0.094593	6205	0.483471	0.086735	1886	0.205731	0.109285
07/05/2019	3721	0.160228	0.103189	6205	0.318347	0.094565	1886	0.190353	0.097416
19/05/2019	3721	0.145249	0.079104	6205	0.412694	0.088841	1886	0.238117	0.114029
31/05/2019	3721	0.16202	0.082605	6205	0.504379	0.086882	1886	0.229844	0.123099
12/06/2019	3721	0.167678	0.088573	6205	0.541937	0.088516	1886	0.234635	0.122072
24/06/2019	3721	0.134049	0.078766	6205	0.331617	0.095339	1886	0.135972	0.065099
06/07/2019	3721	0.147756	0.077526	6205	0.483568	0.0923	1886	0.140667	0.079786
18/07/2019	3721	0.130524	0.078224	6205	0.267412	0.098666	1886	0.126713	0.064016
30/07/2019	3721	0.159184	0.083556	6205	0.485227	0.094821	1886	0.129844	0.067175
11/08/2019	3721	0.135438	0.073206	6205	0.389627	0.08923	1886	0.136079	0.070788
23/08/2019	3721	0.144221	0.077677	6205	0.44917	0.090069	1886	0.130689	0.063978
04/09/2019	3721	0.154142	0.075505	6205	0.512506	0.095441	1886	0.138322	0.07349
16/09/2019	3721	0.147244	0.07679	6205	0.405949	0.089547	1886	0.146671	0.071805

28/09/2019	3721	0.163635	0.079784	6205	0.494488	0.091212	1886	0.145371	0.075956
10/10/2019	3721	0.152079	0.078784	6205	0.516968	0.092979	1886	0.139962	0.072471
22/10/2019	3721	0.149095	0.079803	6205	0.520595	0.096088	1886	0.140251	0.080231
03/11/2019	3721	0.169265	0.085183	6205	0.536419	0.094925	1886	0.142891	0.084121
15/11/2019	3721	0.169334	0.082219	6205	0.515879	0.099614	1886	0.146767	0.07518
27/11/2019	3721	0.15487	0.079458	6205	0.521744	0.098889	1886	0.142893	0.07695
09/12/2019	3721	0.153323	0.077832	6205	0.514937	0.096863	1886	0.136957	0.070953
21/12/2019	3721	0.162481	0.081489	6205	0.515335	0.094834	1886	0.135849	0.069531
02/01/2020	3721	0.141985	0.073261	6205	0.466117	0.103932	1886	0.132124	0.068872
14/01/2020	3721	0.148432	0.078534	6205	0.477851	0.10051	1886	0.131231	0.066425
07/02/2020	3721	0.14902	0.077868	6205	0.492217	1.100202	1886	0.124486	0.065436

Table S8 (Part 2). The temporal variation of coherence at Block JJ5 and JJ12 in Jiujing study area

Date	JJ12			JJ5		
	Pixel amount	Coherence	stdev	Pixel amount	Coherence	stdev
01/11/2017	3538	0.936068	0.019894	2067	0.935643	0.018413
13/11/2017	3538	0.928638	0.020067	2067	0.93127	0.017342
25/11/2017	3538	0.913748	0.023541	2067	0.91849	0.017686
07/12/2017	3538	0.906458	0.023995	2067	0.905344	0.021409
19/12/2017	3538	0.905246	0.02507	2067	0.905247	0.021188
31/12/2017	3538	0.900928	0.026262	2067	0.902495	0.020311
12/01/2018	3538	0.910311	0.02661	2067	0.909976	0.021662
24/01/2018	3538	0.856705	0.031191	2067	0.856192	0.029866
05/02/2018	3538	0.867937	0.030818	2067	0.871849	0.026845
17/02/2018	3538	0.834065	0.034052	2067	0.822818	0.03327
01/03/2018	3538	0.878156	0.029203	2067	0.874196	0.025749
13/03/2018	3538	0.89484	0.024725	2067	0.894622	0.023426
25/03/2018	3538	0.902093	0.024772	2067	0.902892	0.02303
06/04/2018	3538	0.884089	0.027069	2067	0.891539	0.024125
18/04/2018	3538	0.917868	0.023033	2067	0.916279	0.019401
30/04/2018	3538	0.920974	0.023543	2067	0.922732	0.019529
12/05/2018	3538	0.903079	0.025306	2067	0.904226	0.2143
24/05/2018	3538	0.895979	0.025834	2067	0.896264	0.023109
05/06/2018	3538	0.903253	0.02481	2067	0.902815	0.021799
17/06/2018	3538	0.912647	0.024077	2067	0.909036	0.020519
11/07/2018	3538	0.855985	0.03187	2067	0.858646	0.028062
23/07/2018	3538	0.855816	0.034158	2067	0.883329	0.024132
04/08/2018	3538	0.506156	0.083574	2067	0.501163	0.092598
16/08/2018	3538	0.483443	0.093315	2067	0.476506	0.086307
28/08/2018	3538	0.520256	0.077095	2067	0.467895	0.088268
09/09/2018	3538	0.832116	0.040593	2067	0.853286	0.031549

21/09/2018	3538	0.838915	0.038365	2067	0.869788	0.026855
03/10/2018	3538	0.865008	0.036101	2067	0.888238	0.025198
15/10/2018	3538	0.867441	0.035164	2067	0.883244	0.026144
27/10/2018	3538	0.875118	0.034048	2067	0.889144	0.027246
08/11/2018	3538	0.868341	0.034329	2067	0.880512	0.02712
20/11/2018	3538	0.823083	0.037571	2067	0.829147	0.0352
02/12/2018	3538	0.728031	0.049697	2067	0.790683	0.039205
14/12/2018	3538	0.785685	0.047513	2067	0.806815	0.038116
26/12/2018	3538	0.822897	0.040702	2067	0.832675	0.036151
07/01/2019	3538	0.824436	0.040788	2067	0.827168	0.037026
19/01/2019	3538	0.673172	0.055368	2067	0.712161	0.054272
31/01/2019	3538	0.721633	0.056755	2067	0.754382	0.050333
12/02/2019	3538	0.79329	0.042768	2067	0.799865	0.040151
08/03/2019	3538	0.854203	0.034916	2067	0.865717	0.030004
20/03/2019	3538	0.859038	0.034734	2067	0.872398	0.027133
01/04/2019	3538	0.858005	0.032887	2067	0.867801	0.028386
13/04/2019	3538	0.507617	0.090839	2067	0.473883	0.092057
25/04/2019	3538	0.580342	0.068147	2067	0.509335	0.0799
07/05/2019	3538	0.470542	0.086906	2067	0.476013	0.085204
19/05/2019	3538	0.509643	0.0839	2067	0.48471	0.083946
31/05/2019	3538	0.74458	0.055302	2067	0.774202	0.04463
12/06/2019	3538	0.664375	0.078545	2067	0.827414	0.035292
24/06/2019	3538	0.482077	0.089858	2067	0.416073	0.090353
06/07/2019	3538	0.738812	0.060015	2067	0.692793	0.056041
18/07/2019	3538	0.407215	0.097043	2067	0.407486	0.089315
30/07/2019	3538	0.717995	0.059474	2067	0.696139	0.057659
11/08/2019	3538	0.594841	0.070576	2067	0.558777	0.070593
23/08/2019	3538	0.669659	0.061792	2067	0.652133	0.060703
04/09/2019	3538	0.792812	0.050756	2067	0.788827	0.042929
16/09/2019	3538	0.557793	0.079351	2067	0.569798	0.07409

28/09/2019	3538	0.75196	0.054943	2067	0.776338	0.043921
10/10/2019	3538	0.792206	0.050269	2067	0.808167	0.037075
22/10/2019	3538	0.784489	0.051718	2067	0.8058	0.040128
03/11/2019	3538	0.80938	0.045252	2067	0.812124	0.038535
15/11/2019	3538	0.787965	0.050275	2067	0.796324	0.041146
27/11/2019	3538	0.811594	0.045541	2067	0.814044	0.042911
09/12/2019	3538	0.801979	0.047525	2067	0.806755	0.04302
21/12/2019	3538	0.791759	0.046954	2067	0.796968	0.040912
02/01/2020	3538	0.754344	0.051768	2067	0.771842	0.045943
14/01/2020	3538	0.770877	0.047518	2067	0.777385	0.046443
07/02/2020	3538	0.788224	0.048034	2067	0.794437	0.042825

Table S9 (Part 1). The temporal variation of ascending LoS displacements (mm) at Block XC6, XC7 and XC8 in Xinchang study area

Date	XC6			XC7			XC8		
	Pixel amount	displacement	stdev	Pixel amount	displacement	stdev	Pixel amount	displacement	stdev
08/10/2017	3790	0	0	6257	0	0	2116	0	0
01/11/2017	3790	0.119174	1.015695	6257	0.724663	0.964771	2116	0.51734	1.02404
13/11/2017	3790	-0.182965	1.029481	6257	-0.01806	0.974976	2116	1.07847	0.997943
25/11/2017	3790	0.458849	1.120962	6257	-0.87687	1.05896	2116	-0.5422	1.101201
07/12/2017	3790	0.461912	1.156081	6257	0.516657	1.082817	2116	0.52803	1.098285
19/12/2017	3790	-0.846491	1.177704	6257	-0.90917	1.088335	2116	-0.5102	1.111526
31/12/2017	3790	-0.882983	1.251961	6257	-0.9662	1.162553	2116	-0.5354	1.195681
12/01/2018	3790	0.446888	1.222233	6257	0.382464	1.0615	2116	0.5976	1.194179
24/01/2018	3790	-0.461546	1.581484	6257	-0.4732	1.318078	2116	-0.1717	1.565607
05/02/2018	3790	0.369729	1.604052	6257	0.351287	1.359872	2116	0.63399	1.663666
17/02/2018	3790	0.490529	1.597626	6257	0.372522	1.391519	2116	0.90569	1.548052
01/03/2018	3790	-0.104683	1.351151	6257	-0.06964	1.24026	2116	0.24058	1.330674
13/03/2018	3790	0.747796	1.297892	6257	0.666999	1.196291	2116	0.94774	1.274257
25/03/2018	3790	0.697561	1.29285	6257	0.616273	1.201084	2116	1.092	1.281188
06/04/2018	3790	-0.596769	1.273686	6257	-0.69577	1.168268	2116	-0.3405	1.23062
18/04/2018	3790	-0.800163	1.150945	6257	-0.78905	1.105567	2116	-0.6	1.164023
30/04/2018	3790	-0.81189	1.161655	6257	-0.83992	1.127512	2116	-0.4156	1.261252
12/05/2018	3790	-0.799698	1.205594	6257	-0.73994	1.119801	2116	-0.8535	1.207166
24/05/2018	3790	-0.186483	1.254124	6257	-0.22428	1.171428	2116	-0.0747	1.225634
05/06/2018	3790	0.108954	1.215788	6257	-0.06398	1.103318	2116	0.71581	1.171102
17/06/2018	3790	0.224304	1.192989	6257	0.141091	1.099655	2116	0.61721	1.164073
11/07/2018	3790	-0.573956	1.336044	6257	-0.62253	1.2009	2116	-0.6857	1.411019
23/07/2018	3790	0.012189	1.323548	6257	-0.09703	1.259529	2116	0.12109	1.342881
04/08/2018	3790	-1.121772	2.370734	6257	-0.3809	2.165896	2116	0.11809	2.420525
16/08/2018	3790	0.362132	1.900589	6257	0.1787	1.821489	2116	0.76098	1.791753
28/08/2018	3790	0.354388	1.916028	6257	0.289297	2.01776	2116	0.95808	1.66879

09/09/2018	3790	-0.707644	1.603581	6257	-0.76292	1.438409	2116	-0.354	1.499208
21/09/2018	3790	-0.999612	1.498078	6257	-0.9961	1.271499	2116	-0.5836	1.409855
03/10/2018	3790	0.269872	1.366106	6257	0.205308	1.221682	2116	0.64856	1.314542
15/10/2018	3790	-0.692988	1.374866	6257	-0.58072	1.202008	2116	-0.3825	1.281682
27/10/2018	3790	0.06659	1.345027	6257	-0.05799	1.150081	2116	0.48934	1.304796
08/11/2018	3790	-0.308833	1.393334	6257	-0.29991	1.231426	2116	0.09694	1.355417
20/11/2018	3790	-0.714629	1.526306	6257	-0.62667	1.37094	2116	-0.2442	1.410754
02/12/2018	3790	-0.827657	1.857581	6257	-0.72287	1.737318	2116	-0.3005	1.747827
14/12/2018	3790	0.143883	1.750207	6257	0.130667	1.590498	2116	0.77635	1.756842
26/12/2018	3790	0.009165	1.554067	6257	-0.07578	1.375687	2116	0.67969	1.436466
07/01/2019	3790	-0.555306	1.554619	6257	-0.57295	1.416551	2116	0.01351	1.438828
19/01/2019	3790	-0.040702	1.925576	6257	0.059294	1.748908	2116	0.67165	1.788786
31/01/2019	3790	-0.53297	1.830347	6257	-0.44372	1.618484	2116	-0.1323	1.761154
12/02/2019	3790	-0.302918	1.106827	6257	-0.31008	0.990601	2116	0.25644	1.050876
24/02/2019	3790	-0.072648	1.514791	6257	-0.08326	1.355613	2116	0.11517	1.488905
08/03/2019	3790	-0.081495	1.46666	6257	-0.1318	1.32396	2116	0.62772	1.462487
20/03/2019	3790	-0.569773	1.483165	6257	-0.6844	1.308154	2116	-0.0657	1.418478
01/04/2019	3790	-0.606986	1.460414	6257	-0.68378	1.33841	2116	0.24452	1.419679
13/04/2019	3790	-0.296937	1.894374	6257	-0.2094	1.773064	2116	0.13018	1.778293
25/04/2019	3790	-0.248633	1.867346	6257	-0.13643	1.751211	2116	0.35111	1.844505
07/05/2019	3790	0.158449	2.45157	6257	0.092446	2.431989	2116	0.78685	2.315838
19/05/2019	3790	-0.085556	2.019829	6257	0.073557	1.858862	2116	0.5741	1.940504
31/05/2019	3790	-0.981338	1.630617	6257	-1.08666	1.526721	2116	0.06982	1.636834
12/06/2019	3790	0.397505	1.663747	6257	0.476468	1.512716	2116	0.98644	1.645767
24/06/2019	3790	-0.9186	2.164616	6257	-1.13159	2.11083	2116	0.58227	2.112859
06/07/2019	3790	0.146414	2.354466	6257	0.40773	1.877774	2116	-0.0107	1.56362
18/07/2019	3790	-1.196119	1.838252	6257	-1.29991	1.69545	2116	-0.0942	1.675849
30/07/2019	3790	-0.91542	1.614036	6257	-0.87909	1.497821	2116	-0.0788	1.573465
11/08/2019	3790	-0.021981	1.808399	6257	0.091996	1.634779	2116	0.82307	1.694005
23/08/2019	3790	0.304191	1.749498	6257	0.302501	1.625119	2116	0.65476	1.60828

04/09/2019	3790	-0.939132	1.545179	6257	-1.0152	1.395841	2116	0.08215	1.510258
16/09/2019	3790	-0.777193	1.785865	6257	-0.87528	1.688101	2116	0.03669	1.663841
28/09/2019	3790	-0.019923	1.599704	6257	0.031227	1.442623	2116	0.63239	1.553283
10/10/2019	3790	-0.068034	1.534186	6257	0.006154	1.392298	2116	0.55191	1.436713
22/10/2019	3790	-0.812626	1.532761	6257	-0.80793	1.339983	2116	0.22111	1.393032
03/11/2019	3790	-0.471923	1.539404	6257	-0.44522	1.380471	2116	0.39031	1.429269
15/11/2019	3790	-0.375385	1.595582	6257	-0.47256	1.403954	2116	0.37409	1.470471
27/11/2019	3790	-0.441079	1.573841	6257	-0.36985	1.39766	2116	0.50142	1.452619
09/12/2019	3790	-0.210722	1.545283	6257	-0.26034	1.419178	2116	0.52716	1.50807
21/12/2019	3790	-0.296356	1.609601	6257	-1.27526	1.44594	2116	0.5054	1.466406
02/01/2020	3790	-1.246042	1.718325	6257	-0.20614	1.509329	2116	0.5471	1.591943
14/01/2020	3790	-0.453862	1.644062	6257	-0.35506	1.450157	2116	0.43556	1.568134
26/01/2020	3790	-1.244539	1.606325	6257	-1.3516	1.450567	2116	0.24428	1.554821
07/02/2020	3790	-0.24561	1.629856	6257	-0.69342	1.472304	2116	0.37128	1.556223

Table S9 (Part 2). The temporal variation of ascending LoS displacements (mm) at Block XC9 and XC10 in Xinchang study area

Date	XC9			XC10		
	Pixel amount	displacement	stdev	Pixel amount	displacement	stdev
08/10/2017	11083	0	0	7211	0	0
01/11/2017	11083	0.030855	1.002564	7211	-0.0638	0.997744
13/11/2017	11083	0.029603	1.020933	7211	0.083972	1.055086
25/11/2017	11083	0.465656	1.112227	7211	-0.84303	1.130661
07/12/2017	11083	0.547241	1.156843	7211	0.595555	1.124829
19/12/2017	11083	-0.22294	1.147451	7211	-0.75821	1.134493
31/12/2017	11083	-0.49483	1.263433	7211	-0.81165	1.255482
12/01/2018	11083	0.621263	1.217574	7211	0.360127	1.138605
24/01/2018	11083	-0.06142	1.619852	7211	0.006191	1.399299
05/02/2018	11083	0.621954	1.589776	7211	0.630928	1.383692
17/02/2018	11083	0.726831	1.527833	7211	0.556697	1.402783
01/03/2018	11083	0.0972	1.310911	7211	-0.49628	1.302146
13/03/2018	11083	0.993552	1.269828	7211	0.780225	1.273323
25/03/2018	11083	0.905263	1.235155	7211	0.584091	1.252774
06/04/2018	11083	-0.4382	1.241836	7211	-0.72273	1.237093
18/04/2018	11083	-0.6662	1.142813	7211	-0.97449	1.189245
30/04/2018	11083	-0.4098	1.2015	7211	-0.91191	1.179556
12/05/2018	11083	-0.56068	1.218466	7211	-0.92227	1.235523
24/05/2018	11083	0.168453	1.257333	7211	-0.40474	1.241773
05/06/2018	11083	0.548309	1.208146	7211	0.204782	1.18618
17/06/2018	11083	0.490846	1.196549	7211	0.092277	1.174298
11/07/2018	11083	-0.30661	1.332413	7211	-0.42991	1.357507
23/07/2018	11083	0.23402	1.294747	7211	-0.22759	1.311425
04/08/2018	11083	-0.49143	2.205899	7211	-0.50378	1.742894
16/08/2018	11083	0.639005	1.845116	7211	-0.17305	1.879108
28/08/2018	11083	0.708309	1.916632	7211	-0.01871	2.119097

09/09/2018	11083	-0.2235	1.511536	7211	-0.5966	1.598056
21/09/2018	11083	-0.43762	1.377118	7211	-0.76525	1.432347
03/10/2018	11083	0.553275	1.301848	7211	0.003752	1.360552
15/10/2018	11083	-0.18675	1.258996	7211	-0.60439	1.353057
27/10/2018	11083	0.368334	1.248588	7211	-0.14853	1.302918
08/11/2018	11083	0.212422	1.330666	7211	-0.26427	1.370195
20/11/2018	11083	-0.15029	1.447769	7211	-0.58791	1.531398
02/12/2018	11083	-0.33407	1.731848	7211	-0.8325	1.713047
14/12/2018	11083	0.525014	1.70274	7211	0.012595	1.609887
26/12/2018	11083	0.476978	1.481795	7211	-0.1026	1.442174
07/01/2019	11083	-0.03861	1.481593	7211	-0.59309	1.476009
19/01/2019	11083	0.52293	1.823118	7211	-0.00395	1.846338
31/01/2019	11083	-0.12572	1.712884	7211	-0.72975	1.641436
12/02/2019	11083	0.20794	1.062598	7211	-0.40611	1.085778
24/02/2019	11083	0.083978	1.43264	7211	-0.40483	1.477177
08/03/2019	11083	0.51134	1.420732	7211	-0.1582	1.463865
20/03/2019	11083	-0.03297	1.373512	7211	-0.73159	1.427222
01/04/2019	11083	0.169399	1.38255	7211	-0.58731	1.463369
13/04/2019	11083	0.15394	1.814756	7211	-0.42319	1.850393
25/04/2019	11083	0.413189	1.799191	7211	-0.20267	1.876358
07/05/2019	11083	0.563844	2.333529	7211	-0.2233	2.457246
19/05/2019	11083	0.606915	1.914089	7211	-0.1594	1.922377
31/05/2019	11083	-0.04995	1.635933	7211	-0.96669	1.640422
12/06/2019	11083	0.851816	1.614895	7211	0.16749	1.616769
24/06/2019	11083	0.263813	1.955232	7211	-0.39675	2.135643
06/07/2019	11083	-0.18385	1.565051	7211	-0.8878	2.161153
18/07/2019	11083	-0.07797	1.722923	7211	-0.83925	1.765538
30/07/2019	11083	0.045722	1.541257	7211	-0.89182	1.593222
11/08/2019	11083	0.580199	1.735946	7211	-0.04663	1.764736
23/08/2019	11083	0.63475	1.708227	7211	-0.15188	1.758104

04/09/2019	11083	-0.05852	1.459461	7211	-0.99276	1.559101
16/09/2019	11083	0.110017	1.660565	7211	-0.90011	1.708096
28/09/2019	11083	0.518605	1.510975	7211	-0.29423	1.555308
10/10/2019	11083	0.504463	1.436372	7211	-0.17865	1.528636
22/10/2019	11083	0.1468	1.428374	7211	-0.88399	1.49468
03/11/2019	11083	0.309231	1.468762	7211	-0.52337	1.605116
15/11/2019	11083	0.340962	1.507379	7211	-0.77179	1.602993
27/11/2019	11083	0.425102	1.484181	7211	-0.43511	1.60312
09/12/2019	11083	0.398533	1.495657	7211	-0.57576	1.601095
21/12/2019	11083	0.403808	1.513718	7211	-1.38074	1.626151
02/01/2020	11083	-0.37263	1.583429	7211	-0.83981	1.625531
14/01/2020	11083	0.365525	1.56303	7211	-1.09651	1.648762
26/01/2020	11083	-0.46542	1.531066	7211	-0.58534	1.636343
07/02/2020	11083	0.510921	1.528828	7211	-1.52231	1.683728

Table S10 (Part 1). The temporal variation of descending LoS displacements (mm) at Block XC6, XC7 and XC8 in Xinchang study area

Date	XC6			XC7			XC8		
	Pixel amount	displacement	stdev	Pixel amount	displacement	stdev	Pixel amount	displacement	stdev
11/03/2017	3790	0	0	6257	0	0	2116	0	0
23/03/2017	3790	-3.37972	1.639075	6257	-3.77555	1.381894	2116	-3.08291	2.060097
04/04/2017	3790	-4.00312	1.518801	6257	-4.501683	1.332723	2116	-1.37714	1.927986
16/04/2017	3790	-0.50764	1.922173	6257	-0.477885	1.6101	2116	-0.46742	2.145791
28/04/2017	3790	-3.36822	2.034879	6257	-3.601607	1.817624	2116	-2.93445	2.374765
22/05/2017	3790	-2.37702	1.659893	6257	-2.232982	1.378026	2116	-2.25262	1.902904
03/06/2017	3790	-0.45899	1.645448	6257	-0.692841	1.396693	2116	-0.64125	2.098981
15/06/2017	3790	-3.09135	1.739155	6257	-3.425704	1.55635	2116	-2.37389	2.125652
09/07/2017	3790	-0.75405	1.861645	6257	-0.8482	1.440508	2116	-0.50096	2.384452
21/07/2017	3790	-2.06591	2.396257	6257	-2.352408	2.176529	2116	-1.05928	2.90557
07/09/2017	3790	-3.10726	1.835829	6257	-3.309055	1.44469	2116	-2.48515	2.361134
19/09/2017	3790	-2.8354	1.848707	6257	-2.869023	1.432469	2116	-2.36556	2.340912
06/11/2017	3790	-1.90838	1.843861	6257	-2.164742	1.43542	2116	-1.59953	2.388442
18/11/2017	3790	-2.05786	1.827647	6257	-2.211401	1.409247	2116	-1.42405	2.371716
30/11/2017	3790	-2.39758	1.83027	6257	-2.398047	1.372524	2116	-1.84397	2.371034
12/12/2017	3790	-1.96072	1.878556	6257	-2.100552	1.414207	2116	-1.36079	2.413716
24/12/2017	3790	-1.47	1.861523	6257	-1.52103	1.431062	2116	-1.19142	2.370187
05/01/2018	3790	-1.86439	1.919003	6257	-1.917977	1.450658	2116	-1.38491	2.554129
29/01/2018	3790	-1.92809	2.257095	6257	-1.887121	1.714636	2116	-1.51631	2.779231
10/02/2018	3790	-2.06845	2.406602	6257	-2.016423	1.90565	2116	-1.48075	2.810183
22/02/2018	3790	-2.24525	1.889337	6257	-2.310169	1.440899	2116	-1.79716	2.508912
06/03/2018	3790	-2.29819	1.774902	6257	-2.276522	1.362937	2116	-1.85783	2.388342
18/03/2018	3790	-2.29658	1.73933	6257	-2.529259	1.330521	2116	-1.90518	2.334754
30/03/2018	3790	-2.01073	1.791556	6257	-1.848541	1.329601	2116	-1.39696	2.32359
11/04/2018	3790	-2.11525	1.791274	6257	-2.168664	1.35463	2116	-1.41417	2.350498
23/04/2018	3790	-2.38621	1.82245	6257	-2.398781	1.423143	2116	-1.83667	2.329248

05/05/2018	3790	-1.73268	1.858867	6257	-1.529128	1.39823	2116	-1.3161	2.380525
17/05/2018	3790	-2.59392	1.843872	6257	-2.710138	1.396096	2116	-1.89481	2.363949
29/05/2018	3790	-2.46341	1.853368	6257	-2.415119	1.461958	2116	-1.77643	2.401964
10/06/2018	3790	-1.73039	1.912032	6257	-1.822112	1.511249	2116	-1.32179	2.414918
22/06/2018	3790	-2.10603	2.03601	6257	-2.022523	1.63789	2116	-1.17917	2.534956
04/07/2018	3790	-2.11385	1.981413	6257	-1.970614	1.633818	2116	-1.3524	2.466405
16/07/2018	3790	-2.20997	2.0301	6257	-2.039025	1.63406	2116	-1.54978	2.577415
28/07/2018	3790	-1.76094	2.278221	6257	-1.648273	2.093331	2116	-1.01379	2.715983
09/08/2018	3790	-2.01713	1.95673	6257	-2.024485	1.513734	2116	-1.28448	2.438004
21/08/2018	3790	-1.59944	2.007645	6257	-2.007452	1.598678	2116	-1.37747	2.521188
02/09/2018	3790	-2.19489	1.601971	6257	-2.101468	1.176061	2116	-1.51471	2.137782
14/09/2018	3790	-2.46186	1.979776	6257	-2.464334	1.525891	2116	-1.77539	2.510335
26/09/2018	3790	-1.76776	1.958182	6257	-1.717781	1.502813	2116	-1.21599	2.429579
20/10/2018	3790	-2.82598	1.894596	6257	-2.690621	1.470553	2116	-1.98384	2.431661
01/11/2018	3790	-1.69937	1.933694	6257	-1.67885	1.485094	2116	-1.28534	2.500035
13/11/2018	3790	-2.71505	1.893576	6257	-2.490036	1.475783	2116	-1.92912	2.443712
25/11/2018	3790	-3.00427	1.891558	6257	-2.818481	1.459375	2116	-2.08592	2.449446
07/12/2018	3790	-1.76675	2.504572	6257	-1.581703	2.122169	2116	-1.05448	2.893109
19/12/2018	3790	-2.02544	2.099502	6257	-1.882371	1.658497	2116	-1.17923	2.624639
31/12/2018	3790	-1.5662	2.063316	6257	-1.312138	1.601143	2116	-0.93195	2.541087
12/01/2019	3790	-1.67922	2.046342	6257	-1.419514	1.576137	2116	-1.0163	2.515313
24/01/2019	3790	-2.71971	2.324471	6257	-2.549395	1.90859	2116	-1.84099	2.74173
05/02/2019	3790	-2.36974	1.939871	6257	-2.206577	1.491367	2116	-1.56635	2.449356
17/02/2019	3790	-2.27641	1.904899	6257	-2.114209	1.470855	2116	-1.49152	2.420005
01/03/2019	3790	-2.65131	1.845853	6257	-2.465168	1.440634	2116	-1.89081	2.390118
13/03/2019	3790	-1.94591	1.946351	6257	-1.608644	1.537582	2116	-1.2439	2.451613
25/03/2019	3790	-2.42206	1.953473	6257	-2.174587	1.517186	2116	-1.7876	2.42965
06/04/2019	3790	-2.67795	1.925816	6257	-2.322387	1.516609	2116	-1.8681	2.439724
18/04/2019	3790	-2.28224	2.097295	6257	-2.15217	1.593484	2116	-1.48355	2.562466
30/04/2019	3790	-2.20675	2.025747	6257	-2.003641	1.607306	2116	-1.61077	2.584494

05/06/2019	3790	-1.80965	2.05006	6257	-1.579174	1.586748	2116	-0.93104	2.52434
17/06/2019	3790	-2.96109	2.339641	6257	-2.492341	1.896848	2116	-1.08626	2.729273
29/06/2019	3790	-2.78218	2.172169	6257	-2.627931	1.782999	2116	-1.52104	2.627341
11/07/2019	3790	-2.88484	2.140843	6257	-2.597516	1.686775	2116	-1.83232	2.562813
04/08/2019	3790	-2.18988	2.152282	6257	-1.558245	1.698243	2116	-1.50577	2.597561
16/08/2019	3790	-1.63797	2.105724	6257	-1.415949	1.661237	2116	-0.86993	2.579309
28/08/2019	3790	-1.59982	2.082716	6257	-1.300705	1.654416	2116	-0.80388	2.539554
09/09/2019	3790	-1.63521	2.398548	6257	-1.234319	1.803608	2116	-0.67342	2.92137
21/09/2019	3790	-2.44318	2.200933	6257	-2.080826	1.675558	2116	-1.49604	2.61861
03/10/2019	3790	-2.82187	2.14471	6257	-2.419698	1.675861	2116	-1.577	2.582754
15/10/2019	3790	-2.68454	2.063054	6257	-2.226066	1.600049	2116	-1.58389	2.526826
08/11/2019	3790	-2.59752	2.551841	6257	-2.130306	2.040031	2116	-1.37826	2.902135
20/11/2019	3790	-1.9974	2.120566	6257	-1.497447	1.620755	2116	-1.02161	2.561814
14/12/2019	3790	-2.48275	2.134919	6257	-2.31412	1.648175	2116	-1.64828	2.585933
26/12/2019	3790	-2.39602	2.418673	6257	-1.93763	1.833319	2116	-1.20962	2.837157
19/01/2020	3790	-2.34765	2.229429	6257	-2.065552	1.642343	2116	-1.56804	2.62598
31/01/2020	3790	-2.59119	2.141315	6257	-1.23383	1.587842	2116	-1.74083	2.586495

Table S10 (Part 2). The temporal variation of descending LoS displacements (mm) at Block XC9 and XC10 in Xinchang study area

Date	XC9			XC10		
	Pixel amount	displacement	stdev	Pixel amount	displacement	stdev
11/03/2017	11083	0	0	7211	0	0
23/03/2017	11083	-3.33423	2.035846	7211	-3.49908	1.549749
04/04/2017	11083	-3.54496	1.847985	7211	-4.05048	1.411022
16/04/2017	11083	-0.78137	2.113167	7211	-0.89334	1.701082
28/04/2017	11083	-2.9848	2.306013	7211	-3.46371	1.885407
22/05/2017	11083	-2.01886	1.864932	7211	-1.83195	1.484948
03/06/2017	11083	-0.56535	1.852867	7211	-0.70405	1.57922
15/06/2017	11083	-2.54992	2.127955	7211	-3.04505	1.659906
09/07/2017	11083	-0.56447	2.287033	7211	-1.09417	1.684667
21/07/2017	11083	-1.43828	2.748734	7211	-1.45002	2.328173
07/09/2017	11083	-2.6671	2.241186	7211	-2.64593	1.675505
19/09/2017	11083	-2.46709	2.25531	7211	-2.65563	1.680224
06/11/2017	11083	-1.4904	2.249892	7211	-1.61651	1.654948
18/11/2017	11083	-1.58802	2.250527	7211	-2.06031	1.62406
30/11/2017	11083	-2.05838	2.235826	7211	-2.43418	1.60842
12/12/2017	11083	-1.54265	2.242862	7211	-2.07201	1.634836
24/12/2017	11083	-1.21525	2.246664	7211	-1.28867	1.660594
05/01/2018	11083	-1.52141	2.38159	7211	-1.73107	1.686603
29/01/2018	11083	-1.61525	2.595591	7211	-1.75861	1.799884
10/02/2018	11083	-1.65465	2.725414	7211	-1.89395	1.930363
22/02/2018	11083	-1.9698	2.301015	7211	-2.33111	1.67225
06/03/2018	11083	-1.91995	2.204718	7211	-2.13851	1.627368
18/03/2018	11083	-2.08197	2.196188	7211	-2.51035	1.577313
30/03/2018	11083	-1.41767	2.204079	7211	-1.60794	1.545354
11/04/2018	11083	-1.78125	2.217684	7211	-2.14399	1.595996
23/04/2018	11083	-1.86326	2.222204	7211	-2.35196	1.636176

05/05/2018	11083	-1.43398	2.246126	7211	-1.60714	1.624234
17/05/2018	11083	-2.05674	2.240358	7211	-2.42614	1.654181
29/05/2018	11083	-1.84119	2.2605	7211	-2.23171	1.653176
10/06/2018	11083	-1.49089	2.302812	7211	-1.68876	1.689853
22/06/2018	11083	-1.52413	2.375559	7211	-1.73839	1.905519
04/07/2018	11083	-1.74473	2.345024	7211	-1.89312	1.793449
16/07/2018	11083	-1.93791	2.406583	7211	-2.45618	1.834621
28/07/2018	11083	-1.28529	2.6924	7211	-1.40485	2.354913
09/08/2018	11083	-1.83373	2.323657	7211	-2.44084	1.720115
21/08/2018	11083	-1.3439	2.390786	7211	-1.51771	1.887701
02/09/2018	11083	-1.714	1.99745	7211	-1.98328	1.413343
14/09/2018	11083	-1.91942	2.322372	7211	-2.35139	1.789965
26/09/2018	11083	-1.36067	2.29921	7211	-1.60385	1.749329
20/10/2018	11083	-2.27075	2.286088	7211	-2.73367	1.7304
01/11/2018	11083	-1.2251	2.301151	7211	-1.22351	1.747171
13/11/2018	11083	-2.19186	2.300926	7211	-2.56215	1.731772
25/11/2018	11083	-2.34451	2.279349	7211	-2.85283	1.715333
07/12/2018	11083	-1.32454	2.747594	7211	-1.45306	2.165726
19/12/2018	11083	-1.44983	2.43231	7211	-1.71398	1.836636
31/12/2018	11083	-1.15842	2.384258	7211	-1.22443	1.778694
12/01/2019	11083	-1.22254	2.350395	7211	-1.28863	1.763328
24/01/2019	11083	-2.13658	2.644042	7211	-2.49739	2.054448
05/02/2019	11083	-1.85601	2.29123	7211	-2.16717	1.722075
17/02/2019	11083	-1.71851	2.27871	7211	-1.98117	1.683483
01/03/2019	11083	-1.9859	2.264436	7211	-2.28806	1.687418
13/03/2019	11083	-1.36916	2.298654	7211	-1.40636	1.756486
25/03/2019	11083	-1.82597	2.300175	7211	-2.18327	1.750997
06/04/2019	11083	-1.94834	2.293367	7211	-2.12756	1.735422
18/04/2019	11083	-1.71574	2.428939	7211	-2.1909	1.827811
30/04/2019	11083	-1.77724	2.406542	7211	-2.08009	1.848507

05/06/2019	11083	-1.29546	2.403318	7211	-1.65895	1.815819
17/06/2019	11083	-1.68882	2.637163	7211	-1.54127	2.036312
29/06/2019	11083	-2.05209	2.527521	7211	-2.19274	2.001847
11/07/2019	11083	-2.05038	2.469089	7211	-2.23157	1.947674
04/08/2019	11083	-1.59463	2.459956	7211	-1.89061	1.959105
16/08/2019	11083	-1.16855	2.459065	7211	-1.5797	1.930589
28/08/2019	11083	-1.03646	2.425272	7211	-1.45637	1.938371
09/09/2019	11083	-1.13496	2.664535	7211	-1.41337	2.01014
21/09/2019	11083	-1.79088	2.46441	7211	-2.1306	1.987105
03/10/2019	11083	-1.98832	2.46145	7211	-2.18578	1.978202
15/10/2019	11083	-1.86612	2.40938	7211	-2.06204	1.952293
08/11/2019	11083	-1.81894	2.750263	7211	-2.11939	2.310744
20/11/2019	11083	-1.18347	2.406863	7211	-1.45709	1.943889
14/12/2019	11083	-1.94138	2.429531	7211	-2.24922	2.004942
26/12/2019	11083	-1.60567	2.607479	7211	-1.79284	2.031484
19/01/2020	11083	-1.80363	2.449216	7211	-2.10572	1.962453
31/01/2020	11083	-1.86345	2.406054	7211	-2.10634	1.968362

Table S11 (Part 1). The temporal variation of coherence at Block XC4, XC5 and XC6 in Xinchang study area

Date	XC4			XC5			XC6		
	Pixel amount	Coherence	stdev	Pixel amount	Coherence	stdev	Pixel amount	Coherence	stdev
01/11/2017	2305	0.9319624	0.02354582	4201	0.93827311	0.02031154	3788	0.92747504	0.022315
13/11/2017	2305	0.9346855	0.02251079	4201	0.93713899	0.022152	3788	0.92901748	0.023496
25/11/2017	2305	0.8800863	0.04274643	4201	0.88547013	0.03180888	3788	0.88126113	0.030661
07/12/2017	2305	0.9054605	0.02969578	4201	0.91198471	0.02601594	3788	0.89909619	0.029207
19/12/2017	2305	0.9052557	0.03070217	4201	0.9098689	0.02670403	3788	0.89848216	0.029536
31/12/2017	2305	0.8853729	0.03429495	4201	0.89182749	0.02976168	3788	0.87948581	0.029412
12/01/2018	2305	0.9035821	0.03244961	4201	0.91791943	0.02612666	3788	0.88991789	0.035905
24/01/2018	2305	0.8241405	0.0403789	4201	0.85149851	0.03706672	3788	0.80158707	0.050631
05/02/2018	2305	0.8184933	0.04372437	4201	0.8598142	0.03710451	3788	0.80273292	0.05305
17/02/2018	2305	0.8254359	0.04579714	4201	0.84188555	0.04355879	3788	0.82253086	0.046925
01/03/2018	2305	0.8692828	0.03736014	4201	0.87527835	0.03043083	3788	0.86245813	0.036533
13/03/2018	2305	0.8809985	0.03379371	4201	0.88896652	0.02936641	3788	0.87089965	0.034642
25/03/2018	2305	0.8855954	0.03154505	4201	0.88929676	0.0287728	3788	0.87600604	0.034483
06/04/2018	2305	0.8793609	0.03575248	4201	0.88966297	0.02826663	3788	0.87334822	0.035303
18/04/2018	2305	0.9075959	0.03154177	4201	0.91547933	0.02520378	3788	0.89790254	0.031879
30/04/2018	2305	0.9157914	0.03066627	4201	0.91291087	0.02670287	3788	0.90685251	0.028621
12/05/2018	2305	0.8540296	0.05067575	4201	0.86648492	0.03906012	3788	0.85430983	0.040872
24/05/2018	2305	0.8292685	0.06468643	4201	0.8441456	0.04930715	3788	0.83649103	0.043361
05/06/2018	2305	0.8733246	0.04411281	4201	0.88455851	0.03302174	3788	0.87197898	0.032516
17/06/2018	2305	0.8968188	0.04107278	4201	0.90611491	0.02747334	3788	0.88826463	0.031051
11/07/2018	2305	0.8902159	0.04154617	4201	0.91238616	0.02736528	3788	0.87727937	0.036828
23/07/2018	2305	0.8379182	0.0463551	4201	0.85441897	0.03597085	3788	0.83872519	0.038716
04/08/2018	2305	0.6261703	0.08131507	4201	0.83552155	0.04334096	3788	0.70767735	0.064993
16/08/2018	2305	0.7018163	0.07415018	4201	0.68862955	0.07342393	3788	0.7006556	0.06616
28/08/2018	2305	0.7334549	0.07353975	4201	0.65747016	0.08521098	3788	0.70776904	0.07219
09/09/2018	2305	0.795444	0.05361731	4201	0.83661521	0.05264871	3788	0.80174321	0.05069

21/09/2018	2305	0.8151562	0.04830355	4201	0.85044668	0.04951976	3788	0.8204605	0.045054
03/10/2018	2305	0.8311398	0.05231128	4201	0.86307554	0.04248219	3788	0.84058264	0.041728
15/10/2018	2305	0.8052593	0.05942239	4201	0.82776327	0.05008797	3788	0.81890629	0.042963
27/10/2018	2305	0.8560378	0.04682468	4201	0.8841767	0.04012118	3788	0.861822	0.040148
08/11/2018	2305	0.8495893	0.04993548	4201	0.86833447	0.0411831	3788	0.85589545	0.037753
20/11/2018	2305	0.8172659	0.05450099	4201	0.82987751	0.04675107	3788	0.82613468	0.044503
14/12/2018	2305	0.7746792	0.06102223	4201	0.80005586	0.06133459	3788	0.77740894	0.058063
26/12/2018	2305	0.8096468	0.05268562	4201	0.83114589	0.04953237	3788	0.81136059	0.050717
07/01/2019	2305	0.8162349	0.05576862	4201	0.83864894	0.04956768	3788	0.81638117	0.047403
19/01/2019	2305	0.7274887	0.06687877	4201	0.7474819	0.05979753	3788	0.74017248	0.063991
31/01/2019	2305	0.7624456	0.06403185	4201	0.7805184	0.05955649	3788	0.77149366	0.058698
12/02/2019	2305	0.7945995	0.05359383	4201	0.80932406	0.04840535	3788	0.79637885	0.050678
24/02/2019	2305	0.8009538	0.05441024	4201	0.81831485	0.04548361	3788	0.80407867	0.048318
08/03/2019	2305	0.8130751	0.05198852	4201	0.83321821	0.04390123	3788	0.81698094	0.047244
20/03/2019	2305	0.8351675	0.05014261	4201	0.85629343	0.04520659	3788	0.83349312	0.045359
01/04/2019	2305	0.8099113	0.05529636	4201	0.83566366	0.04443076	3788	0.8205425	0.043919
13/04/2019	2305	0.6910308	0.07373722	4201	0.69857316	0.07446949	3788	0.70179303	0.068258
25/04/2019	2305	0.6456537	0.07760253	4201	0.66597509	0.07317926	3788	0.64088316	0.072581
07/05/2019	2305	0.5998804	0.08749364	4201	0.58581096	0.08929763	3788	0.62123719	0.085012
19/05/2019	2305	0.699251	0.07938449	4201	0.70399048	0.07634184	3788	0.70702698	0.071224
31/05/2019	2305	0.7568273	0.07125682	4201	0.77483282	0.05410578	3788	0.76465351	0.054261
12/06/2019	2305	0.8063498	0.06597881	4201	0.82843248	0.0489348	3788	0.81522778	0.048096
24/06/2019	2305	0.6613315	0.09265915	4201	0.66094781	0.08071192	3788	0.68425829	0.074747
06/07/2019	2305	0.7766432	0.07465495	4201	0.80533946	0.05174465	3788	0.80139755	0.049136
18/07/2019	2305	0.7575083	0.07447417	4201	0.79665636	0.05067129	3788	0.78093633	0.052432
30/07/2019	2305	0.7884405	0.07674374	4201	0.83074713	0.04449981	3788	0.80753428	0.048018
11/08/2019	2305	0.6917919	0.08538346	4201	0.71265561	0.06440365	3788	0.70910402	0.05949
23/08/2019	2305	0.701463	0.08292875	4201	0.72087338	0.06277071	3788	0.7101115	0.05711
04/09/2019	2305	0.7739003	0.07559003	4201	0.80907383	0.05158063	3788	0.79716648	0.045958
16/09/2019	2305	0.748204	0.0774876	4201	0.78311635	0.05626779	3788	0.76636514	0.057145

28/09/2019	2305	0.7851742	0.07416573	4201	0.82698578	0.04834501	3788	0.80634836	0.044858
10/10/2019	2305	0.8114153	0.07877981	4201	0.85290951	0.04231712	3788	0.83422312	0.042957
22/10/2019	2305	0.8069349	0.07163811	4201	0.84385518	0.04556565	3788	0.83114831	0.04122
03/11/2019	2305	0.7854483	0.0758296	4201	0.82469604	0.04825393	3788	0.81227232	0.043338
15/11/2019	2305	0.7880057	0.07333909	4201	0.83385719	0.04588508	3788	0.80891674	0.04733
27/11/2019	2305	0.8117538	0.07369174	4201	0.85535304	0.04314318	3788	0.83042791	0.044542
09/12/2019	2305	0.8044563	0.0751321	4201	0.85033255	0.0442687	3788	0.82455749	0.046961
21/12/2019	2305	0.7932086	0.07298309	4201	0.83797657	0.04451229	3788	0.81010577	0.048621
02/01/2020	2305	0.771697	0.07504818	4201	0.83529122	0.04569298	3788	0.79444606	0.052522
14/01/2020	2305	0.7762892	0.07042034	4201	0.83483853	0.0461702	3788	0.80063832	0.049193
26/01/2020	2305	0.7853667	0.07506129	4201	0.83783201	0.04589856	3788	0.80923862	0.048709
07/02/2020	2305	0.799526	0.07070224	4201	0.84667115	0.04588793	3788	0.81581388	0.047963

Table S11 (Part 2). The temporal variation of coherence at Block XC9, XC10 and XC11 in Xinchang study area

Date	XC9			XC10			XC11		
	Pixel amount	Coherence	stdev	Pixel amount	Coherence	stdev	Pixel amount	Coherence	stdev
01/11/2017	11082	0.92643737	0.027697	7228	0.9302637	0.023485	4416	0.86232639	0.06203062
13/11/2017	11082	0.92629062	0.029896	7228	0.928957	0.024359	4416	0.84440818	0.06842327
25/11/2017	11082	0.85830287	0.065407	7228	0.8853199	0.031163	4416	0.83796737	0.06580308
07/12/2017	11082	0.89507785	0.037702	7228	0.8997897	0.030684	4416	0.80675274	0.08106282
19/12/2017	11082	0.89267935	0.036979	7228	0.9021153	0.02874	4416	0.79924386	0.08541984
31/12/2017	11082	0.85062274	0.049847	7228	0.8781346	0.033875	4416	0.77437516	0.09186711
12/01/2018	11082	0.8770425	0.045499	7228	0.8986523	0.033383	4416	0.78054446	0.10125833
24/01/2018	11082	0.78831184	0.061959	7228	0.8304069	0.0465	4416	0.7103214	0.11303102
05/02/2018	11082	0.79492566	0.06323	7228	0.8338644	0.046957	4416	0.72066644	0.11136276
17/02/2018	11082	0.81301355	0.060958	7228	0.8387719	0.045084	4416	0.67866177	0.12399075
01/03/2018	11082	0.85137568	0.050437	7228	0.8630701	0.038452	4416	0.7173858	0.11770171
13/03/2018	11082	0.86177877	0.047937	7228	0.8739913	0.034966	4416	0.73778165	0.11479949
25/03/2018	11082	0.86481463	0.04528	7228	0.8755325	0.034887	4416	0.74794237	0.10952951
06/04/2018	11082	0.86613687	0.046734	7228	0.8754821	0.036499	4416	0.74473621	0.11322204
18/04/2018	11082	0.88916605	0.043201	7228	0.8974863	0.034863	4416	0.76639411	0.11181772
30/04/2018	11082	0.89653813	0.04317	7228	0.9005171	0.035008	4416	0.75963987	0.11567907
12/05/2018	11082	0.82132015	0.080276	7228	0.8633867	0.041606	4416	0.74792438	0.11473444
24/05/2018	11082	0.78946094	0.102558	7228	0.846389	0.047019	4416	0.73729421	0.11639204
05/06/2018	11082	0.84428445	0.063583	7228	0.8786777	0.038954	4416	0.74155689	0.11840269
17/06/2018	11082	0.87354475	0.054926	7228	0.8952267	0.036084	4416	0.73989717	0.12787585
11/07/2018	11082	0.8681654	0.054653	7228	0.8830953	0.041315	4416	0.74074771	0.11714051
23/07/2018	11082	0.81425094	0.065647	7228	0.8483763	0.044866	4416	0.72321573	0.12114993
04/08/2018	11082	0.76654691	0.085608	7228	0.8418969	0.047425	4416	0.69513654	0.12268687
16/08/2018	11082	0.70753364	0.082771	7228	0.7030232	0.077784	4416	0.43449904	0.14040779
28/08/2018	11082	0.72021212	0.096648	7228	0.6673142	0.085146	4416	0.3535043	0.12555241
09/09/2018	11082	0.81147278	0.06518	7228	0.8165736	0.056931	4416	0.63271494	0.1700132

21/09/2018	11082	0.82179874	0.063416	7228	0.8321733	0.053191	4416	0.66858182	0.15463486
03/10/2018	11082	0.83304485	0.065414	7228	0.8444011	0.049562	4416	0.6851277	0.14516505
15/10/2018	11082	0.78984228	0.093112	7228	0.8236116	0.052904	4416	0.68431421	0.13944524
27/10/2018	11082	0.86414836	0.055609	7228	0.8600936	0.05095	4416	0.69778411	0.13559693
08/11/2018	11082	0.84849957	0.056857	7228	0.8518578	0.049114	4416	0.68214986	0.13761112
20/11/2018	11082	0.83139069	0.060167	7228	0.817748	0.054765	4416	0.64731314	0.1286803
14/12/2018	11082	0.77742216	0.072258	7228	0.7880832	0.064911	4416	0.63187778	0.14278083
26/12/2018	11082	0.80677555	0.066511	7228	0.8157735	0.05748	4416	0.64243603	0.14863938
07/01/2019	11082	0.81377858	0.063716	7228	0.8169534	0.058494	4416	0.6462248	0.13955021
19/01/2019	11082	0.73385777	0.077202	7228	0.732945	0.063283	4416	0.57877758	0.13724664
31/01/2019	11082	0.7609621	0.076135	7228	0.7748807	0.06088	4416	0.59323308	0.13559749
12/02/2019	11082	0.79547216	0.06632	7228	0.7980366	0.055008	4416	0.63063276	0.13906217
24/02/2019	11082	0.79308423	0.071257	7228	0.8010375	0.053891	4416	0.64844448	0.1365124
08/03/2019	11082	0.80766378	0.066868	7228	0.8132027	0.05331	4416	0.65621527	0.1373106
20/03/2019	11082	0.83525461	0.05994	7228	0.8307163	0.051616	4416	0.66281789	0.13296879
01/04/2019	11082	0.80662432	0.070356	7228	0.8144509	0.054586	4416	0.66453492	0.13285459
13/04/2019	11082	0.70097358	0.082943	7228	0.7060197	0.077751	4416	0.43002938	0.14344756
25/04/2019	11082	0.63239232	0.112014	7228	0.6598862	0.077976	4416	0.50518927	0.15081958
07/05/2019	11082	0.63448456	0.099827	7228	0.6000164	0.092737	4416	0.32893335	0.13164973
19/05/2019	11082	0.71868421	0.087043	7228	0.7098244	0.078466	4416	0.42247992	0.14310198
31/05/2019	11082	0.75438197	0.075808	7228	0.7709375	0.063008	4416	0.55319686	0.15578128
12/06/2019	11082	0.8100568	0.067063	7228	0.8111982	0.058815	4416	0.60484211	0.15391449
24/06/2019	11082	0.67136761	0.094404	7228	0.6914238	0.081095	4416	0.3570399	0.13458457
06/07/2019	11082	0.7945117	0.070027	7228	0.8031815	0.058853	4416	0.55414471	0.14721965
18/07/2019	11082	0.78061221	0.071096	7228	0.7882698	0.060988	4416	0.59864215	0.14439259
30/07/2019	11082	0.79800406	0.068563	7228	0.8068532	0.058885	4416	0.62451995	0.14874929
11/08/2019	11082	0.67645656	0.092027	7228	0.709322	0.070284	4416	0.48573474	0.15800149
23/08/2019	11082	0.67259111	0.100377	7228	0.713944	0.068167	4416	0.5474927	0.1498682
04/09/2019	11082	0.76179633	0.084324	7228	0.7937866	0.059721	4416	0.64197194	0.14444067
16/09/2019	11082	0.78257925	0.073337	7228	0.795227	0.059399	4416	0.60611825	0.14545607

28/09/2019	11082	0.79533848	0.070736	7228	0.808689	0.057021	4416	0.63589587	0.1426372
10/10/2019	11082	0.82355632	0.066311	7228	0.827975	0.055605	4416	0.64921906	0.14364739
22/10/2019	11082	0.8120875	0.068068	7228	0.8196133	0.056686	4416	0.65108004	0.14047897
03/11/2019	11082	0.78085004	0.080263	7228	0.8092457	0.056216	4416	0.64849476	0.14091751
15/11/2019	11082	0.79431124	0.069725	7228	0.8114562	0.055791	4416	0.63619785	0.147989
27/11/2019	11082	0.81778249	0.0641	7228	0.8240588	0.055597	4416	0.63854839	0.14948673
09/12/2019	11082	0.81472976	0.066005	7228	0.8188425	0.056513	4416	0.63040289	0.14869266
21/12/2019	11082	0.80124286	0.066931	7228	0.8073462	0.058609	4416	0.62867026	0.14775316
02/01/2020	11082	0.79421556	0.070084	7228	0.8047408	0.058945	4416	0.62652881	0.14447694
14/01/2020	11082	0.79338245	0.070061	7228	0.8015751	0.060133	4416	0.62468666	0.14598034
26/01/2020	11082	0.80398536	0.066416	7228	0.8088715	0.057834	4416	0.62869541	0.14502528
07/02/2020	11082	0.80979985	0.066054	7228	0.8135521	0.057866	4416	0.62999958	0.14561183

Table S11 (Part 3). The temporal variation of coherence at Qh1 area in Xinchang study area

	Qh1		
Date	Pixel amount	Coherence	stdev
01/11/2017	3371	0.72720458	0.086335
13/11/2017	3371	0.67945927	0.106133
25/11/2017	3371	0.67145305	0.103561
07/12/2017	3371	0.62462709	0.124281
19/12/2017	3371	0.62046896	0.12291
31/12/2017	3371	0.6107874	0.114448
12/01/2018	3371	0.60275398	0.126932
24/01/2018	3371	0.52364964	0.132785
05/02/2018	3371	0.51062157	0.144068
17/02/2018	3371	0.47267101	0.143413
01/03/2018	3371	0.4977739	0.151453
13/03/2018	3371	0.5105102	0.145444
25/03/2018	3371	0.50830299	0.154639
06/04/2018	3371	0.49594223	0.1606
18/04/2018	3371	0.50934563	0.161768
30/04/2018	3371	0.46453021	0.154357
12/05/2018	3371	0.46012823	0.163632
24/05/2018	3371	0.46014647	0.168166
05/06/2018	3371	0.44733655	0.17505
17/06/2018	3371	0.44955991	0.17338
11/07/2018	3371	0.44359865	0.174656
23/07/2018	3371	0.44209704	0.16228
04/08/2018	3371	0.41871363	0.155002
16/08/2018	3371	0.24696013	0.11571
28/08/2018	3371	0.24111871	0.104776
09/09/2018	3371	0.40283601	0.16551
21/09/2018	3371	0.40915022	0.173962
03/10/2018	3371	0.41928519	0.171335
15/10/2018	3371	0.42427273	0.17287
27/10/2018	3371	0.42559385	0.171217
08/11/2018	3371	0.41080568	0.172558
20/11/2018	3371	0.41002273	0.164477
14/12/2018	3371	0.39062651	0.165385
26/12/2018	3371	0.39459488	0.166104
07/01/2019	3371	0.3971189	0.166624
19/01/2019	3371	0.36128423	0.145084
31/01/2019	3371	0.37074435	0.160665
12/02/2019	3371	0.38294466	0.157281
24/02/2019	3371	0.39934158	0.164747
08/03/2019	3371	0.40808832	0.166457
20/03/2019	3371	0.41057659	0.171918
01/04/2019	3371	0.39891897	0.169862

13/04/2019	3371	0.2714591	0.129206
25/04/2019	3371	0.2991119	0.122121
07/05/2019	3371	0.1959048	0.097871
19/05/2019	3371	0.23467983	0.110504
31/05/2019	3371	0.30987111	0.141603
12/06/2019	3371	0.34915724	0.156054
24/06/2019	3371	0.24311191	0.115687
06/07/2019	3371	0.35989723	0.156169
18/07/2019	3371	0.34827955	0.156627
30/07/2019	3371	0.35224344	0.161242
11/08/2019	3371	0.25532909	0.11572
23/08/2019	3371	0.28204903	0.131361
04/09/2019	3371	0.36468357	0.164351
16/09/2019	3371	0.34062867	0.151286
28/09/2019	3371	0.3590489	0.157637
10/10/2019	3371	0.36935544	0.162233
22/10/2019	3371	0.37049456	0.161798
03/11/2019	3371	0.35831119	0.166282
15/11/2019	3371	0.34999151	0.155644
27/11/2019	3371	0.34816222	0.167555
09/12/2019	3371	0.34453636	0.162132
21/12/2019	3371	0.3420444	0.164018
02/01/2020	3371	0.3497791	0.162322
14/01/2020	3371	0.34848407	0.162178
26/01/2020	3371	0.35007721	0.158302
07/02/2020	3371	0.34250352	0.164871